School of
Civil Engineering and Geosciences

Newcastle University

Analysis of the Stability of Shallow Abandoned Colliery Workings

Peter Rennie Helm

BSc (Hons) Geology

MSc Geotechnical Engineering

A thesis submitted in fulfilment of the requirements for the award of Doctor of Philosophy in the School of Civil Engineering and Geosciences, Newcastle University, January 2011

Abstract

Subsidence related to shallow abandoned mine workings are considered an inherent threat to safety, particularly of the transport infrastructure. In order to better constrain the conditions that can lead to subsidence, a study taking the form of a parametric analysis to investigate the features and properties significant in the causes of abandoned mine working instability has been undertaken within the numerical modelling code FLAC3D. The effect on stability of variations in excavation geometry along with variations of the *in-situ* stresses related to the overburden loading have also been investigated.

Use has been made of interface elements to allow the modelling of coal measures rocks as a horizontally laminated assemblage of strata whereby discrete or discontinuous behaviour representative of the failure of layered rock masses over abandoned mine workings can be modelled. The modelling of variably dipping discontinuity features commonly present in rock masses has also been undertaken using an anisotropic constitutive model.

The effects of fluctuations in the groundwater table are modelled as variations in pore water pressures on the stability of excavations have also been investigated. The modelling results indicate that the friction angle of the rock mass (which may be considered a composite of the intact rock and discontinuity friction angles) is a key parameter in controlling the geometry of failure of the strata forming the excavation roof. Pore water pressures are also shown to be significant in causing the initiation of instability. Empirical tools to allow the estimation of the height of collapse before arching or choking of the void occurs are also introduced as well as a numerical based methodology to allow the modelling of collapse propagation in rock masses above excavations. Numerical modelling was also undertaken of the subsidence event that occurred at Dolphingstone in Scotland which suggests that the increase in the ground water table may have been responsible for the collapse.

Acknowledgements

Firstly I would like to express my gratitude to Network Rail and Newcastle University for providing the funding, equipment and facilities that made this project possible.

I would specifically like to thank my supervisors Dr. Colin Davie and Dr. Stephanie Glendinning of the School of Civil Engineering and Geosciences for their support, advice and time throughout the course of the project.

I would also like to express my gratitude to John Stothard and Brian Bell of Network Rail for offering me the opportunity to undertake this research project and also their support during the project and allowing me access to the Network Rail mining office archive enabling the acquisition of site investigation report and other data related to the subsidence events at Dolphingstone.

To all my friends who have stood by me, thank you for the laughter.

Finally I would also like to take this opportunity to offer my heartfelt thanks to my parents and my brother for their support.

Table of Contents

List of Figures

List of Tables

Chapter

1

Introduction

1 Introduction

The history of mineral extraction in the UK predates the Roman occupation of this country and the extraction of coal on a significant scale began to occur in the 13th Century (Bell and de Bruyn, 1999). From the 16th Century onwards coal mining was a major industry supporting the industrial revolution (Jones *et al*., 2005). However there have been a number of negative impacts of subsurface mining and of particular concern is the inherent threat to safety posed by the collapse of subsurface voids.

To highlight the threat posed by mining subsidence, the following case study is relevant: During May and June 2001 a pair of crown holes of approximate diameter 1.5 m were found near the East Coast Main Line (ECML) track at a site near Dolphingstone in East Lothian in Scotland. The presence of these crown holes and the possibility of further subsidence at this site prompted Network Rail to divert the ECML over a distance of approximately 1.6 kilometres (Donaldson Associates Ltd, 2002).

During the site investigation work, it was found that the most likely cause of this subsidence was the collapse of shallow abandoned mine workings beneath the area. The solution adopted was the diversion of the ECML. This required the construction of a continuous raft supported on end bearing piles and although the remedial measures were successful they were highly expensive.

As this example demonstrates, the legacy of past mining is a growing concern, particularly in relation to transport systems. Further to this, the threat of mining subsidence is not just limited to the UK but is of concern globally. A report commissioned by Network Rail following the subsidence event at Dolphingstone (Jones *et al*., 2005) with the aim of reviewing current practice associated with the management and treatment of subsurface voids as they influence transport networks contains case studies from nine different countries including France and Germany (amongst other European countries), the USA, Canada and the Republic of South Africa (RSA). Another aim of the report was to suggest areas where further research was required. One such research topic identified was the use of advanced numerical / computer modelling of the site at Dolphingstone to attempt to better understand the causes of failure. Further to this it was decided to undertake a numerical modelling study to

investigate the relative importance of varying parameters in the initial stability and potential instability of sub surface excavations.

1.1 Thesis Layout

This thesis is split into 10 chapters, including this initial introduction (chapter 1). Chapter 2 consists of a literature review where a summary is presented of the published information related to shallow abandoned mine workings, shallow mining subsidence, the collapse of horizontally layered strata above excavations and void migration. As numerical modelling requires the derivation of strength and stiffness parameters of the rock mass, a review is undertaken of rock mass characterisation methods along with relations to allow the derivation of input parameters for numerical modelling. A review is also made of the numerical techniques commonly employed in rock mechanics modelling and mining engineering along with a review of the published work related to the numerical modelling of the stability of underground excavations of varying types and at varying depths thought relevant to this thesis whether due to methodology employed or the specific problem investigated (section 2.5).

Chapter 3 is related to the numerical modelling undertaken to investigate the parameters that broadly influence the stability of shallow abandoned mine workings. Initially the numerical modelling code FLAC3D is discussed including descriptions of the primary constitutive models and yield mechanisms used in the modelling. Following on from this, a preliminary numerical modelling parametric study is discussed in which the parameters that are thought to be of primary significance for the initial stability of the roof strata of subsurface excavations based on information derived from the literature review are investigated.

In chapter 4 further modelling is undertaken making use of an advanced constitutive model that captures the anisotropic behaviour of rock masses in an equivalent continuum to simulate dipping discontinuity surfaces using the Strain-Softening Ubiquitous-Joint model.

In chapter 5 the parameters initially identified in the previous sections as significant such as excavation width and level of ground water table / pore water pressure within the rock mass are then investigated in more detail with the introduction of increased complexity into the modelling whereby the behaviour of stratified rock masses are

modelled with non linear post yield behaviour and with material anisotropy to allow investigation of the effects of discontinuities in the rock mass as a discrete assemblage of individual stratum modelled as Strain-Softening Mohr-Coulomb materials separated by interface elements along which slip and separation of the model grid can occur and which simulate the delamination and sagging behaviour of layered strata.

Chapter 6 introduces some empirical tools that can be used to estimate the height of collapse of a void before arching or bulking may occur. These are compared to other published methods and also to the numerical modelling results from Chapter 5. A numerical tool is also introduced which was developed to allow the progressive collapse of roof strata and the migration of voids through the rock mass to be modelled.

Chapter 7 is a case study of the collapse that occurred at the Dolphingstone site giving an overview of the geology and mining history along with an overview of the significant information from the site investigation that was undertaken. A numerical modelling investigation is then described in which a large parametric study was undertaken in order to attempt to identify the likely causes of failure. The results and potential implications of this work are then discussed.

Chapter 8 introduces a system used to assess the potential relative hazard posed by abandoned mine workings which was developed by the US Department of Transport's Federal Highway Administration (FHA) to assess the risk posed by mine workings to road infrastructure (Ruegsegger, 1999) The main features of the FHA system are summarised and are discussed in terms of the numerical modelling and empirical parametric studies undertaken

Chapter 9 presents the general conclusions of the work undertaken and also includes suggestions for further work and Chapter 10 lists the references cited in this work.

Chapter

2

A Review of Underground Excavation Stability, Shallow Mining Subsidence and the Numerical Modelling of Mine Workings and Other Subsurface Voids

2 A Review of Underground Excavation Stability, Shallow Mining Subsidence and the Numerical Modelling of Mine Workings and Other Subsurface Voids

2.1 Shallow Mine Workings

Coal mining began on a significant scale in the United Kingdom in the 13th century (Bell and De Bruyn, 1999). This took the form of adits driven into the base of quarry faces, or along the coal outcrops in hilly terrain. The depths of workings were limited by the requirements for natural drainage and ventilation.

This type of working began to be replaced in the 14th century by bell pits – shallow workings <12 m deep where a shaft was driven through the overburden material, until the coal seam was reached. This seam would then be mined away from the base of the shaft, until signs of imminent collapse were observed (Waltham, 1989). At this stage the pit was abandoned, and a new shaft driven close by. By the 15th and 16th Century (Bell and de Bruyn, 1999, Healy and Head, 1984), the pillar and stall method of extraction began to become more common. This was a process where pillars of the mineral deposit (in this case coal) are left in place to support the roof of the mine (Attewell and Taylor, 1984). The most common type of pillar and stall workings comprised regular square pillars, however it should also be noted that by the end of the 17th Century (Healy and Head, 1984), different geographical localities developed differing pillar and stall geometries depending on varying local conditions as illustrated in Figure 2.1.

As a general trend it has been observed that the layout of the workings typically became more regular over time and as the mining became more systematic (Bell, 1975). This led to the introduction of pillars of a constant size and a gradual tendency to increase the size of the rooms (also known as stalls or bords). An example of the regular stoop and room or pillar and stall workings found at shallow depths is shown in Figure 2.2.

Room and pillar workings are still commonly used to this day in the USA, but have largely been replaced in the UK by longwall mining. This means that any subsidence that occurs due to pillar and stall workings within the UK are likely to be associated with mine workings abandoned over a century ago due to the transition to longwall mining methods (Attewell and Taylor, 1984, Waltham, 1989).

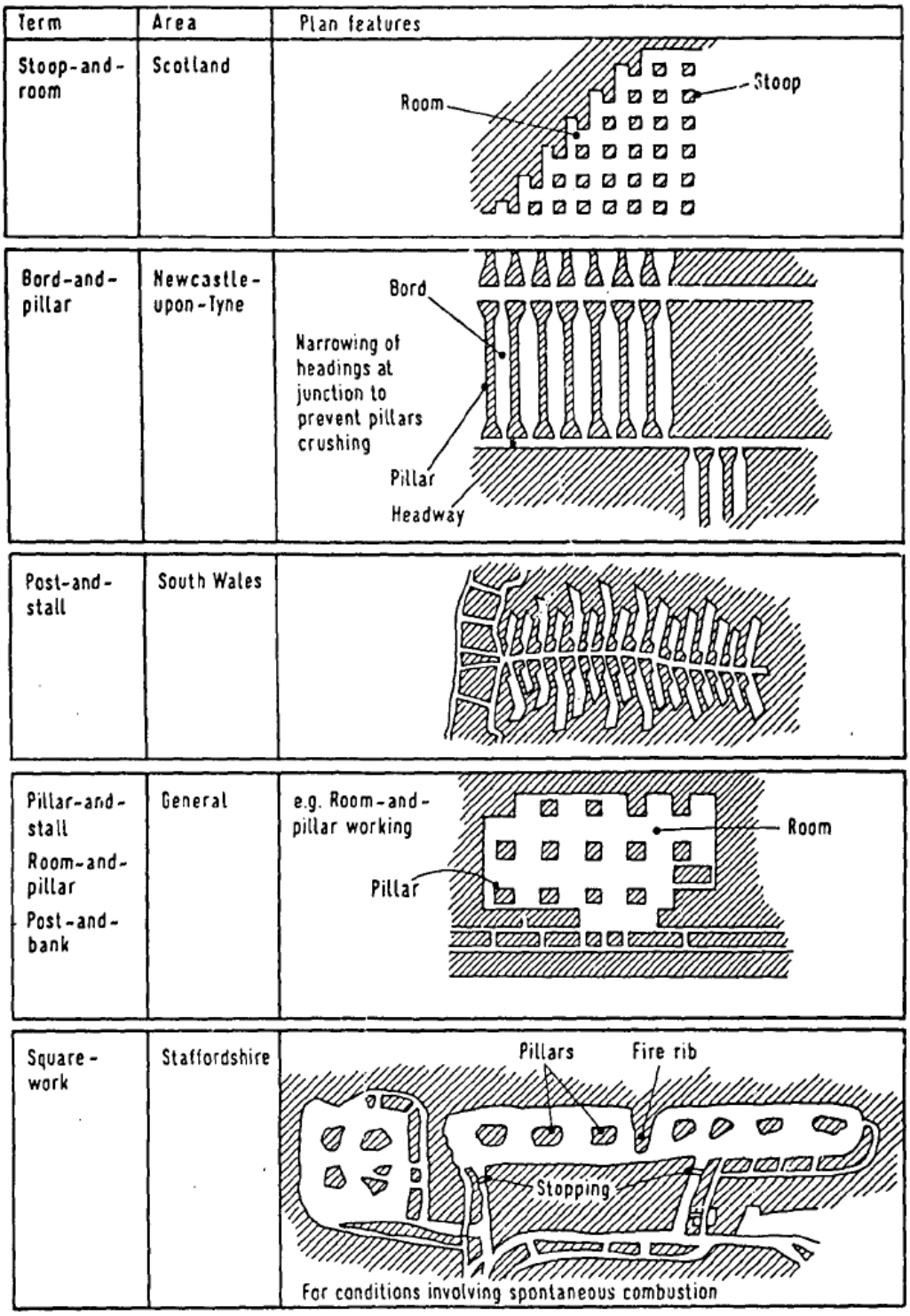

Figure 2.1: Variations in the geometry of pillar and stall workings (after Healy and Head, 1984).

This is supported by data from the USA where crown hole subsidence occurrences have been reported as long as 100 years after the closure of mine workings in Pennsylvania (Dyne, 1998). It is estimated that there are over 70,000 old mine workings in the UK (Deb and Choi, 2006) and based on research in Britain, the USA and South Africa (Bell, 1992, Bell and de Bruyn, 1999) it is common to define shallow workings as those within 30 m of the surface.

Figure 2.2: Shallow pillar and stall workings of the Young Wallsend Seam, exposed after 'lifting the roof' off the former Wallsend Borehole Colliery to remove the remnant pillar coal (after McNally, 2000).

The reasoning behind the choice of this 30 m depth was analysis of case studies in the above mentioned countries suggesting that caving rarely proceeds higher than ten times the seam's working thickness, which is generally less than 3 m (McNally, 2000). The process of void migration is covered in more detail in section 2.2.4. One of the main reasons that shallow workings cause building and development problems is because the dimensions and condition of the rooms and pillars are often very difficult to ascertain (Healy and Head, 1984). This is due to a number of factors:

- Entering the workings to directly establish the condition of pillars *etc*. is potentially very dangerous. Also gaining access to the workings may be difficult depending on how they were sealed and the nature of the original means of access (*e.g.* adit or shaft)
- Mine abandonment plans were rarely accurate (discussed further in section 2.2.2)
- The geometry of the workings varies depending on the region and age of the workings (as indicated in Figure 2.1 and previously in this section). This increases site investigation costs as there is a requirement for closely spaced bore holes to establish pillar and room dimensions and geometry

2.2 Subsidence Mechanisms

Healy and Head (1984) state that the three main mechanisms of deterioration and collapse of workings are:

1. Floor heave
2. Crushing of pillars
3. Roof collapse.

When these processes occur they ultimately lead to the stabilisation (by closure or infilling) of the workings and in order to determine the subsidence mechanism, it is important to identify the dominant deterioration mechanism. The three main mechanisms are illustrated in Figure 2.3.

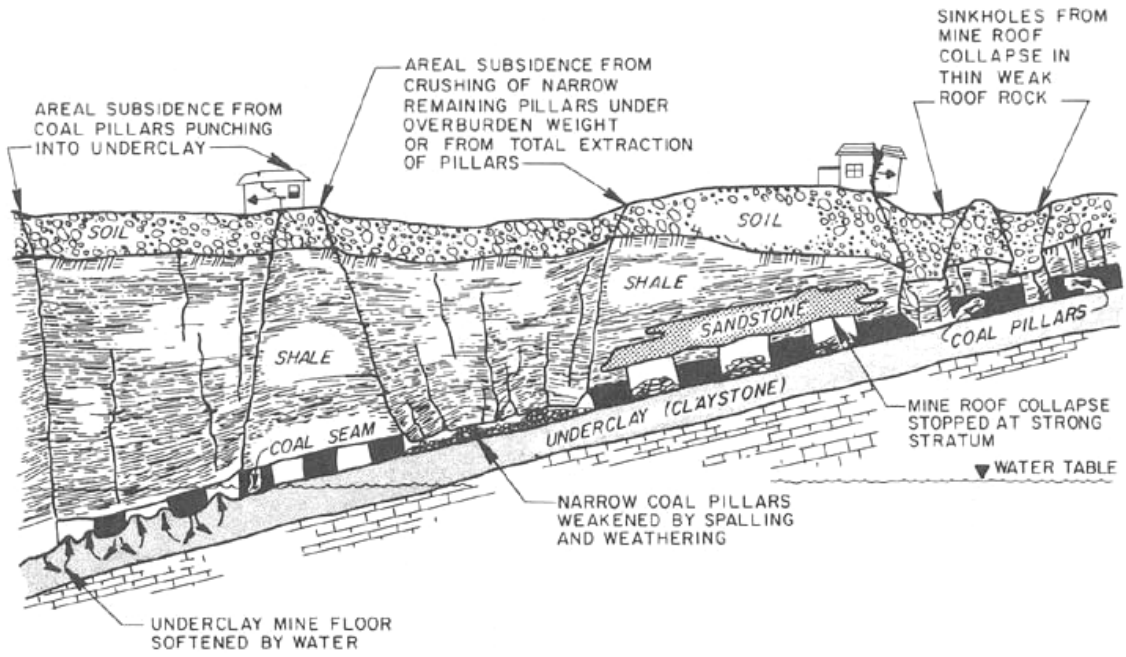

Figure 2.3: The three main mechanisms of subsidence in shallow workings (after Gray, 1988).

2.2.1 Floor Heave

Floor heave is a process where the imposed overburden load is transmitted through the pillars onto the floor of the workings causing plastic deformation or heave of the floor material into the mined void. This is most commonly found in mines where very weak "seatearths" or "underclays" form the floor of mine workings. Attewell and Taylor, (1984) state that the degree of floor heave is controlled by:

- Imposed load
- Mineralogical composition of the floor layer

The most common triggering mechanism for floor heave is flooding of the mine (typically when first abandoned). The presence of highly active expandable clay minerals within the seatearth or underclay, combined with the ingress of water into the mine, lead to swelling and softening of the mine floor. When coupled with the pillar loading on the floor of the workings this effectively causes a bearing capacity failure at the base of the pillar, where the floor material is squeezed out from under the pillars laterally into the workings, which can lead to the pillars punching into the floor. However, the heave of floor material into the workings can also provide lateral support to the pillars, thus reducing the rate of pillar spalling and effectively reducing the risk of pillar failure (Waltham, 1989). Floor heave is illustrated in Figure 2.4.

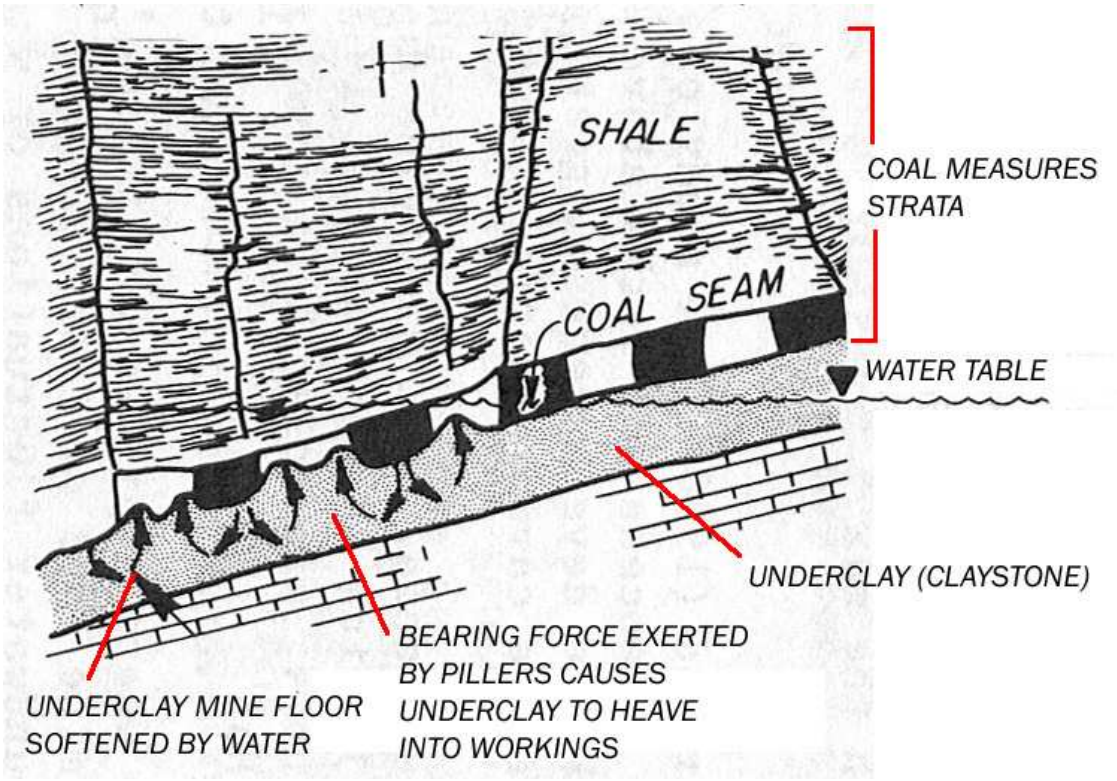

Figure 2.4: Floor heave due to clay softening at base of pillars (after Gray, 1988).

The settlement by pillars punching through the floor ultimately results in the lowering of the ground surface, with strains and tilting occurring around the periphery of the settlement basin. This form of subsidence at the surface appears very similar to that observed due to pillar failure (as illustrated in Figure 2.5). Any additional loading at the surface can cause new settlement of the pillars into the floor or restart old movements.

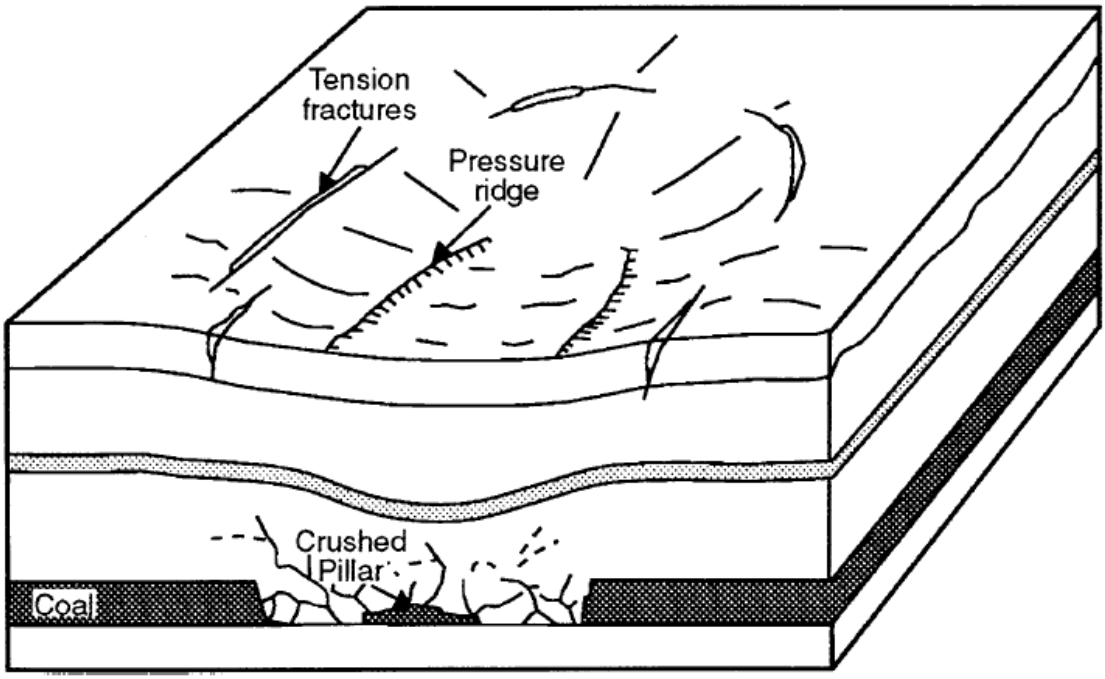

Figure 2.5: Typical sag subsidence configuration (after Bell and DeBruyn, 1999)

2.2.2 Pillar Failure

In pillar and stall workings the pillars sustain the entire weight of the overburden. This results in the pillars themselves and the rocks immediately above being subjected to increased compressive stress. Between the pillars, the unsupported roof beds tend to sag, adding further stress to the edge of the pillars. Although the intrinsic strength of coal varies, according to Bell and deBruyn, (1999) the stability of pillars is largely controlled by:

a) The ratio of seam thickness to pillar width;
b) Depth below ground level;
c) Dimensions of the mined void.
d) Strength of roof rock
e) Compressive strength of coal

A method of determining pillar strength in mine workings known as the Holland-Gaddy equation (Farmer, 1992) incorporating the above factors is given below:

$$\sigma_{MPS} = \sigma_{ci}\left(0.65 + 0.35\frac{P_w}{P_H}\right) \quad 2.1$$

Where:

σ_{MPS} = mine pillar strength (MPa),

σ_{ci} = Uniaxial compressive strength of pillar material (MPa),

P_w = pillar width (m)

P_H = pillar height (m)

The pillar load (P_L) may then be calculated based on:

$$P_L = \frac{T_O \rho_O}{(1 - E_{rat})} \quad 2.2$$

Where:

T_O = overburden thickness,

ρ_O = overburden density

E_{rat} = extraction ratio (ratio of volume of coal extracted in rooms to the total volume of the ore body, expressed as a percentage; Farmer, 1992).

The extraction ratio may be difficult to establish in old workings where there is no abandonment plan and where some roof material has already collapsed into the voids making it difficult to establish the width of rooms and the thickness of pillars during SI).

The position of the pillars within the mine can also influence the potential for failure: pillars in the centre of the mined void are subjected to greater stresses than those at the periphery. Collapse in one pillar can bring about collapse in others in a chain reaction as increasing loads are placed on the adjacent pillars. In general the greater the ratio of pillar width to its height (*i.e.* worked seam thickness), the greater its load bearing capacity. However as has been stated above, stress concentrations tend to develop at the edges of pillars, leading to spalling of the pillar margins (Healy and Head, 1984). This process leads to further weakening of the pillar as it reduces the constraint on the core of the pillar and increases the stress within the pillar. This then causes further spalling

(hence decreasing the pillar width to height ratio), leading to a cyclical process of progressive pillar weakening which may eventually lead to pillar failure.

Another factor which can influence the ratio of pillar height to width is roof failure in the area between the pillars, where the pillar height effectively increases over time and hence structural stability is reduced.

Subsidence due to pillar failure in shallow mines can be greater than that which occurs in mines where total extraction has taken place as the pillars restrict the bulking of strata immediately above them. This is an important mechanism in halting void migration caused by roof failure and will be discussed in section 2.2.4.

Where a significant structural weakness such as a fault occurs, the combination of deconfinement and reduced shear strength will also increase the likelihood of pillar failure leading to subsidence.

The yielding of a large number of pillars can create shallow subsidence over a large surface area. These broad shallow subsidence events are referred to as sags. Here the ground surface is displaced radially inwards towards the area of maximum subsidence as illustrated in Figure 2.5.

To further complicate matters it was common practice to rob pillars in UK pillar and stall workings as the mine approached the end of its working life, hence decreasing their cross sectional area; leading to an increase in the stress imposed on individual pillars, and increasing the roof span between them. Both these factors will increase the chance of a collapse, either of the overstressed pillars or of the roof strata. This was rarely recorded on the mine abandonment plan created by the mine owners and when combined with the possibility of later roof falls and instability, caution is recommended, as the mining plan may not accurately reflect the final state of the workings. See Figure 2.6.

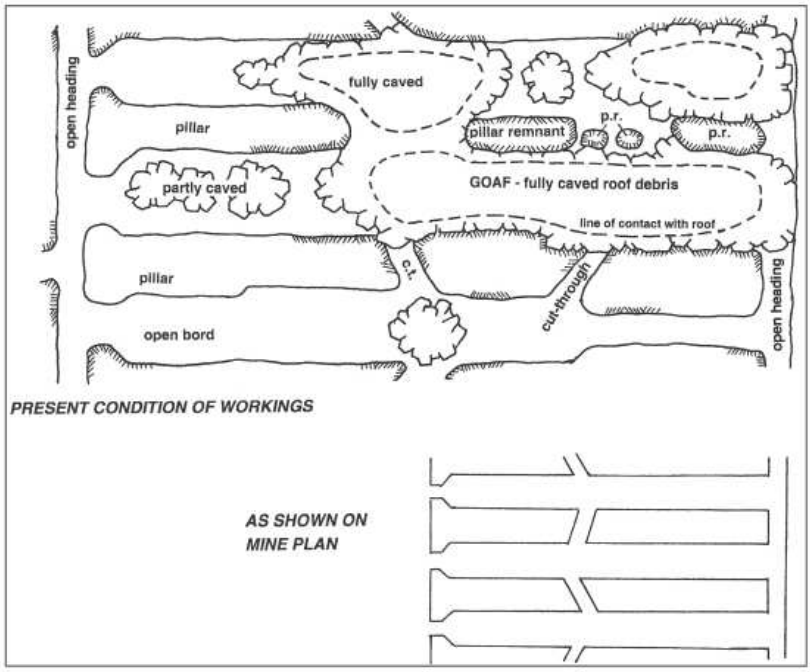

Figure 2.6: Comparison of mine abandonment plan with condition of workings at a later date (after McNally, 2000).

In mines at moderate depth (or greater) the removal of roof support would lead to a very rapid closure of the goaf or mined void (Bell and de Bruyn, 1999). At shallow depths however, the overburden pressure may not reach a level capable of exceeding the strength of the pillars, therefore roof closure may be much more variable. This coupled with the fact that wooden roof supports with an unknown life span were commonly used; vastly increases the difficulty of assessing the state of abandoned historical workings.

2.2.3 Roof Failure

According to Healy and Head, (1984), the "disintegration and deformation" of roof strata is the primary closure mechanism in shallow mine workings, and is the greatest problem in subsidence engineering practice.

Roof failure within pillar and stall workings most commonly leads to surface subsidence in the form of crown holes or depressions. Roof failures most commonly occur at roadway crossings due to the span of the roof being at a maximum at these points (Attewell and Taylor, 1984). See Figure 2.7.

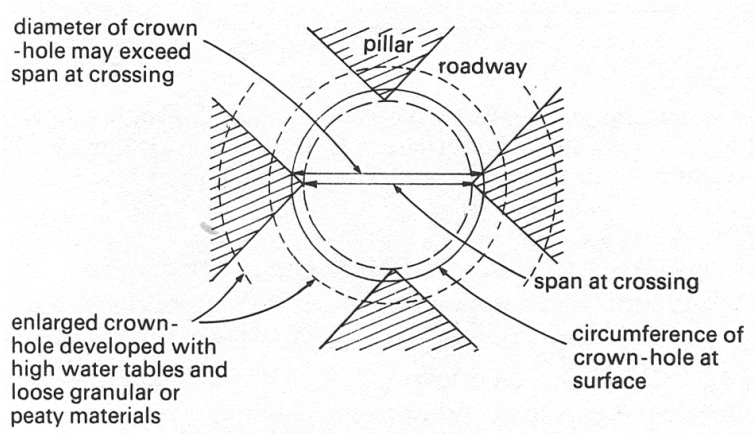

Figure 2.7: Failure most commonly occurs at roadway intersections due to increased span (after Attewell and Taylor, 1984).

Roof collapse seems to be considered by the majority of authors as a progressive phenomenon, where the void formed during mineral extraction migrates upwards through the overlying strata (void migration). The mine opening will remain stable as long as the strength of the roof rock exceeds the stress upon it (Dyne, 1998).

A number of factors affect the stress acting on the roof of the workings and on the roof strength:

a) The presence of water – fluctuations in the ground water may alter the hydrostatic head and the pore pressure within the rock mass. Also variations in water content can cause mineral alteration, weathering and slaking. All of which have the potential to reduce the strength of the roof material.
b) Creep deformations – deformation of the roof rocks by the process of creep alter the stress distributions above openings and may also exceed the plastic limits of the rock leading to roof failure.

Conditions Leading to Roof Collapse

In order for void migration to occur, the roof of the workings must fail. Typically when the overburden load is taken by the pillars, tensile stresses develop in the immediate roof, and compressive stresses build at the upper corners of the workings (Attewell and Taylor, 1984, Twiss and Moores, 1992, Dyne, 1998).

Also prior to the formation of any cavity, the stresses in the earth will reach an equilibrium state. Formation of a void can cause the overlying strata to become fractured due to sudden shock loading. This fractured material is made stable by the

confining stress. Any disturbance in the *in-situ* stress at this point can also lead to roof failure (Thigpen, 1984).

If the roof contains vertical joints or fractures, the tensile stresses may be alleviated by the propagation of these fractures or joints through the roof strata (Twiss and Moores, 1992), along with a downward deflection of the roof as illustrated in Figure 2.8. In this case it is assumed that the roof strata are behaving as a voussoir beam as in the following diagram.

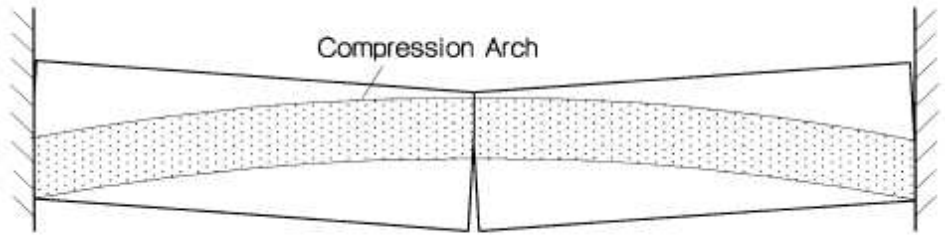

Figure 2.8:Voussoir beam analogue (after Diederichs and Kaiser, 1999).

There are a number of mechanisms (Hibbeler, 1999; Alejano *et al.,* 2009) that may lead to the failure of a voussoir beam, these include:

- Snap-through or buckling failure
- Lateral compressive failure (crushing) at the midspan and abutments
- Abutment slip or shear failure

Snap-through failure and crushing are observed in thin beams or roof strata while shear failure is observed in thick beams (Diederichs and Kaiser, 1999; Alejano *et al.,* 2009). See Figure 2.9 for details.

Snap through failure (Figure 2.9a) is most common in high strength roof strata with a high span to thickness ratio, that tend to sag initially, then fail under their own weight (Diederichs, 2003). This may also be known as flexural failure (Singh and Dhar, 1997). Snap through or flexural failure can occur due to:

a) High vertical stress
b) Low ratio of horizontal to vertical stress
c) The presence of thinly bedded or separated roof strata where shearing occurs along the interfaces between bedding planes (Twiss and Moores, 1992)
d) Bending of the strata generating tensile stresses which exceed the tensile strength of the rock. Flexural deformation is illustrated in Figure 2.10.

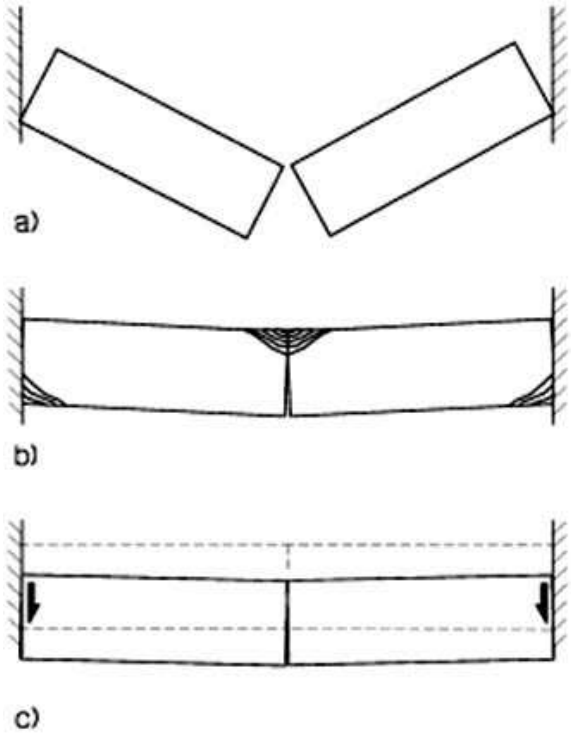

Figure 2.9: Failure modes of the voussoir beam: (a) snap through; (b) crushing; (c) shearing or abutment slip (after Diederichs, 1999).

It should be noted that the above failure mechanisms are related to higher strength rock strata. In lower strength strata the thinly bedded stratum will yield by the mechanism of self weight sagging (Whittles *et al.*, 2007).

Crushing failure is most common in thicker strata where less sagging occurs and which are overlain by thinner strata. In this case the load of the thinner strata is passed on into the thicker underlying strata and passed through the compressive arch into the abutments or coal pillars. If the load exceeds the shear strength of the rock or more likely the coal / roof interface, this would result in compressive failure of the shaded point of the beam (shown in Figure 2.9b) leading to a failure of the arch (Goodman, 1989).

Crushing failure most commonly occurs in the following conditions:

a) High ratio of horizontal to vertical stress
b) The pillars are stiffer than the roof material (causing stress to concentrate at the boundary between the roof and the pillar leading to shear failure).
c) Shear strength of the roof material being exceeded by stress concentrations at the pillar roof boundary.

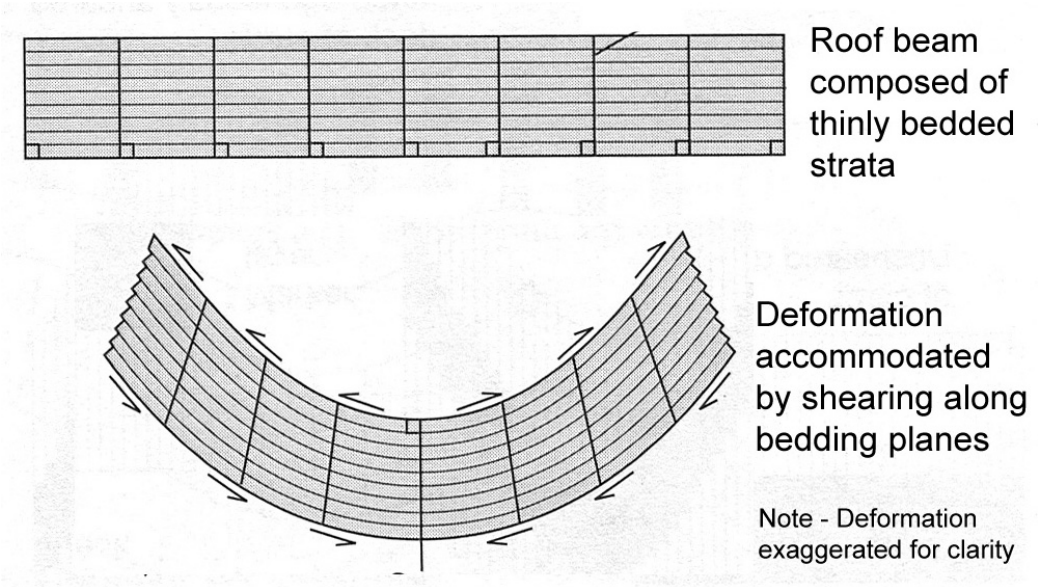

Figure 2.10: Flexural deformation of the roof strata (after Twiss and Moores, 1992).

Shearing failure (Figure 2.9c) occurs where coal measure rocks, are affected by defects that disrupt the lateral continuity of bedded planes. These defects can range from features on a microscopic scale to major faults offsetting beds for kilometres, however the size of the features that most often affect coal beds can be measured from centimetres to metres (Molinda, 2003).

Jointing that occurred during the depositional process will only affect that specific strata, whereas joint formation due to post depositional tectonic activity may affect the rock mass in its entirety. In situations where the roof is affected by the presence of these defects, it is in effect composed of blocks of rock bounded by vertical joints / discontinuities. In shear failure, the roof fails due to sliding occurring along the joint planes where the vertical stress exceeds the shear strength of the discontinuity (Singh and Dhar, 1997). These types of failures are illustrated in more detail in Figure 2.11.

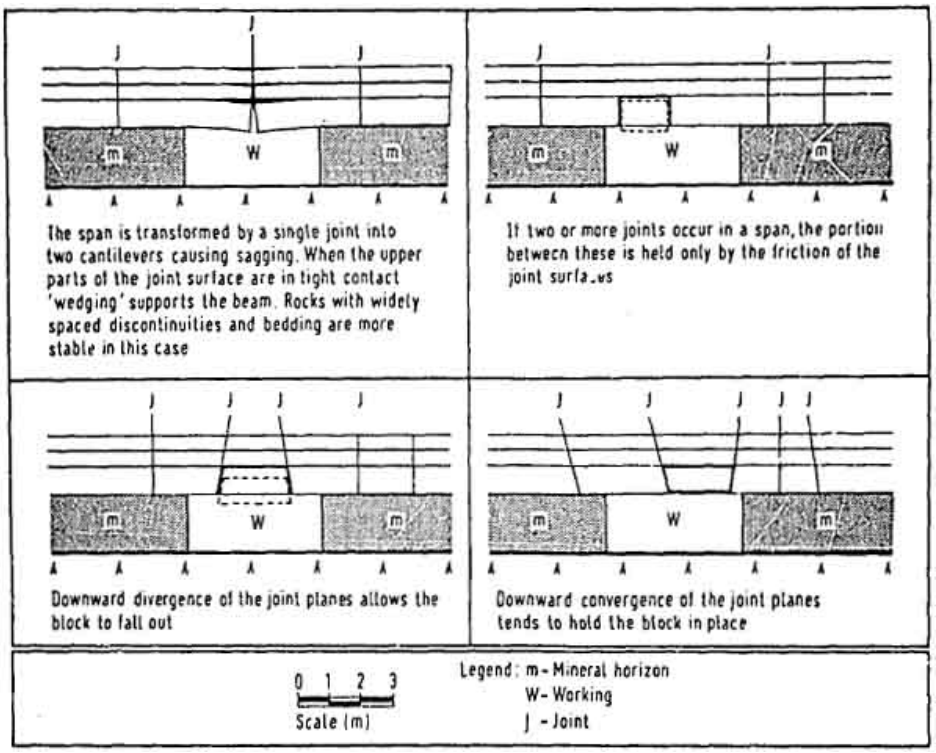

Figure 2.11: Effect of discontinuities on stability of mine workings (after Healy and Head, 1984).

2.2.4 Void Migration

Once void migration has commenced, it will continue until the void becomes choked due to bulked roof material filling the void and supporting the roof, it is arrested by natural arching or by the presence of massive roof strata (*i.e.* very thickly bedded strata) in the overlying rock mass (Bell, 1992).

The height to which a void will migrate before it is halted by bulking is dependent on the bulking factor of the material, the volume available within the workings to store the bulked debris, the geometry of collapse and the angle of repose of the debris pile. These vary depending on the rock mass properties of the strata in question.

The volume change of strata from the *in-situ* to the broken state is denoted by its bulking factor, BF (%):

$$BF = \frac{V_C - V_I}{V_I} \times 100 \qquad 2.3$$

Where

V_I = volume of intact, unbroken strata

V_C = volume of the collapse debris in a loose broken state

The value of BF for Coal Measure strata is typically between 30 and 50% (Healy and Head, 1984).

Tincelin (Bell, 1975; Bell *et al.*, 1988) proposed a relation based on the average density of colliery waste (approximately 2000 kg/m^3 – where the colliery spoil is considered representative of broken roof strata) compared to the intact density of coal measures strata (approximately 2240 kg/m^3). Using these density contrasts a relation was proposed between collapse height (H_C) and the extracted thickness of the coal seam (T_C).

$$H_C = T_C \left[\frac{\rho_C}{\rho_I} \Big/ 1 - \frac{\rho_C}{\rho_I} \right] \qquad 2.4$$

Where:

ρ_C = Bulk density of collapse debris

ρ_I = Bulk density of intact rock

The density ratio in this case indicates a bulking factor of 1.12 (112%) which is lower than that commonly used in coal measures strata of 1.3-1.5 (130-150%).

Wardell and Eynon (Bell, 1975) proposed the following relation based on the cone geometry of a collapse and the bulking factor of the rock mass:

$$H_C = \frac{3 \times T_C}{BF_R} \qquad 2.5$$

Where:

BF_R = bulking factor as a ratio (normally quoted as between 1.3 and 1.5 for coal measures strata).

According to Healy and Head (1984) a simple relationship for an initial evaluation of ground surface movement, S_S, can be determined based on the ground geometry and porosity, n, of collapsed material as follows:

$$S_S = 2T_C - T_R \left(\frac{n}{1-n} \right) \qquad 2.6$$

Where:

T_R = rock cover thickness

The above relationship assumes that pillars do not experience failure and it considers only a prismal element of strata having vertical sides. Vertical settlement prediction is complex and the expression, presented graphically in Figure 2.12 should only be used to estimate, rather than calculate movements.

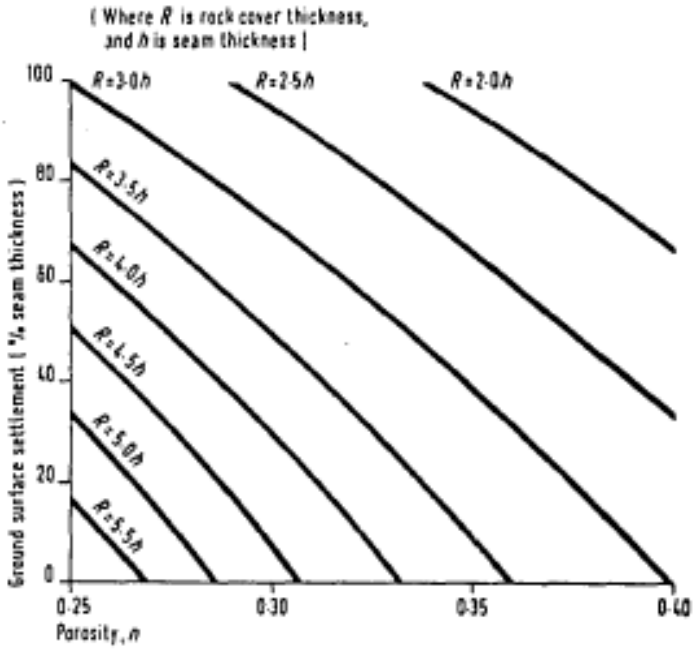

Figure 2.12: Ground subsidence assessment using prismal theory (after Healy and Head, 1984).

Crown hole development is strongly influenced by the cover rocks between the mine and the surface. Void migration, or upward stoping, may be stopped by the formation of a stable arch, which may form in any rock type. Typically flatter arches seem to form in stronger rock types (*i.e.* those with greater tensile strength). The height to which a void will migrate before it is halted by arching is dependent on the caving angle of the material. Das (2000) has identified from empirical observations, a relationship between the uniaxial compressive strength of the strata and the resultant angle of caving where an increase in the uniaxial compressive strength of the rock mass is linked to a decrease in the angle of caving. As such the height of collapse before a stable arch is formed will decrease.

This arching process seems to occur predominantly where the roof failure mechanism is either snap through or buckling failure and occurs because as a roof layer fails, it flexes downwards due to yielding (the degree of actual deformation is dependent on the thickness and stiffness properties of the roof beam). This leads to the development of cracks at the point where the roof strata meets the pillar. Fractures also develop at the roof centreline on the base of the layer forming the roof. The initial yielding can be seen in Figure 2.13, and the progression of failure can be seen in Figure 2.14.

Due to the nature of the stress field at the ends of the roof layers, these cracks propagate diagonally away from the pillars into the strata above the excavation (Goodman, 1989). Ultimate collapse of the first beam leaves a pair of cantilevers as abutments for the overlying roof strata, effectively reducing the span of the excavation.

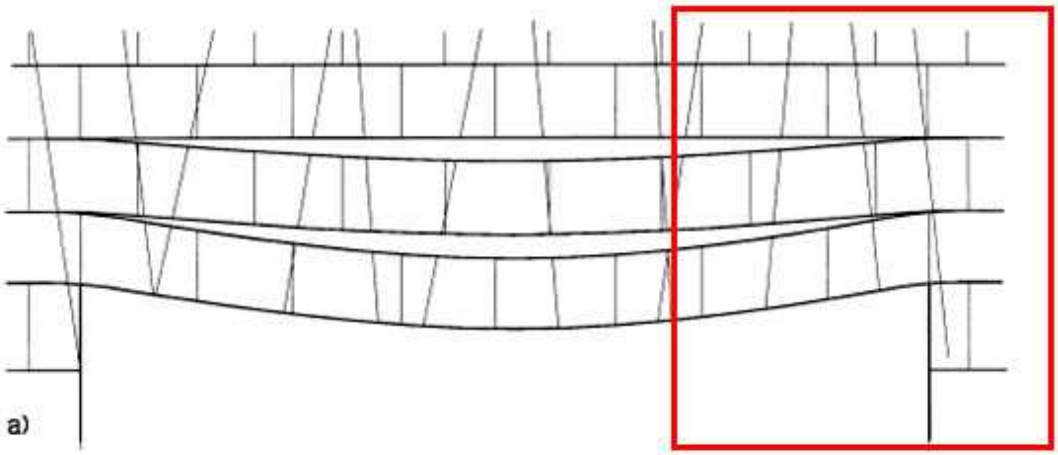

Figure 2.13: Yielding of roof strata over an excavation. The red zone marks the detailed area in Figure 2.14 (Figures adapted from Diederichs and Kaiser, 1999).

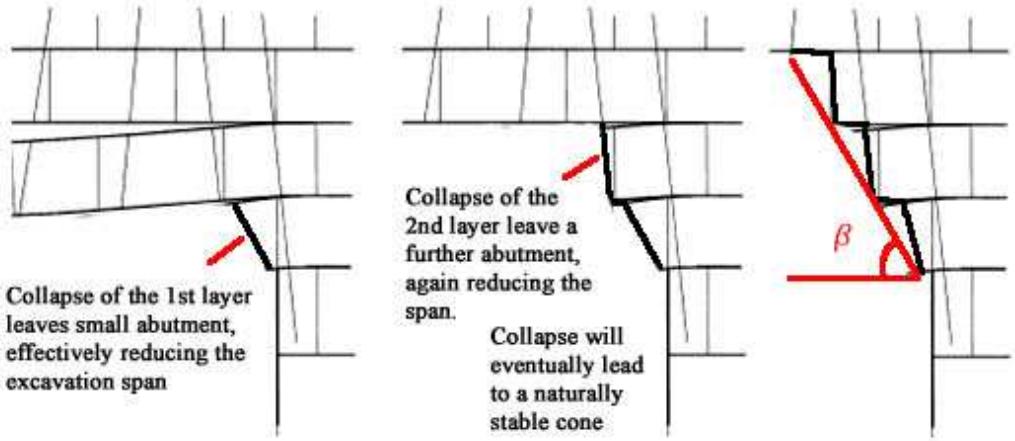

Figure 2.14: Progressive failure leading to void stabilisation by arching (Figures adapted from Diederichs and Kaiser, 1999).

Figure 2.14 above shows an excavation roof yielding with roof beams sagging and delaminating from the layers above. The area indicated in detail in Figure 2.14 shows the progressive failure of layers, and the resulting abutments which act to decrease the span width. The angle β represents the caving angle of the strata. Continued failure and roof collapse will naturally lead to a stable, conical void assuming sufficient height to rock head (Goodman, 1989).

This mode of failure has also been demonstrated in physical modelling undertaken by a number of researchers using basal friction test machines. This work is summarised in a

number of text books including Bieniawski (1984) and Goodman (1989). One very good example of this methodology is the work of Mark, summarised in Bieniawski (1984), where the effects of varying roof strata thickness and the presence of weak layers in the mine roof were successfully modelled. An example from this work is shown in Figure 2.15 where the sagging of the roof strata due to tensile delamination of the bedding planes and the resultant fracturing which propagates into the rock strata above the excavation leading to the formation of cantilevered abutments can clearly be seen.

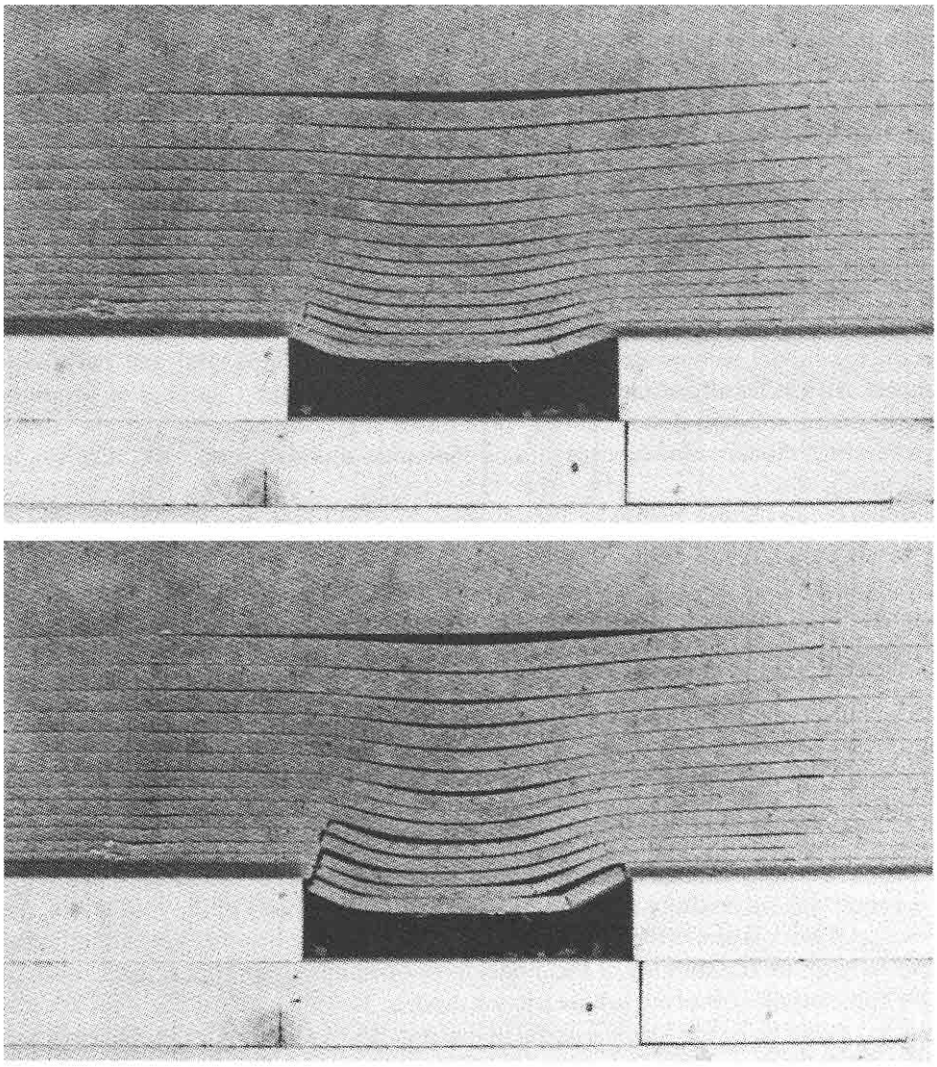

Figure 2.15: Physical modelling of the initiation and progression of failure of an unsupported coal mine roof composed of uniform strata (Bieniawski, 1984).

It was noted at the beginning of Section 2.1, that it is common to define shallow workings as those within 30 m of the surface. The choice of this value is based in part on empirical data suggesting that voids migrate to a height equal to a maximum of ten times the worked thickness of the coal seam (derived from the relations proposed by Wardell and Eynon and where the maximum thickness of excavations is typically 3m).

According to some authors (Bell, 1975; Fernando, 1988; Attewell and Taylor, 2003), this value is overly conservative and they suggest that it is uncommon to find voids migrating to more than 6 times the worked seam thickness, and that a value of 8 times the worked thickness of the seam is a more realistic maximum extent of void migration. However these rules are typically contentious, and should be viewed with caution.

If a void does eventually reach the surface then a crown hole will form. At the surface, crown holes are rarely more than 5 m in diameter or depth, and typically have vertical or overhanging sides. A diagrammatic cross section through a typical crown hole is shown in Figure 2.16 and a photograph of a cross section through a crown hole is shown in Figure 2.17. If remedial measures are not taken quickly, then the walls of the sinkhole may be eroded by water drainage which will increase the dimensions of the pit (Dyne, 1998).

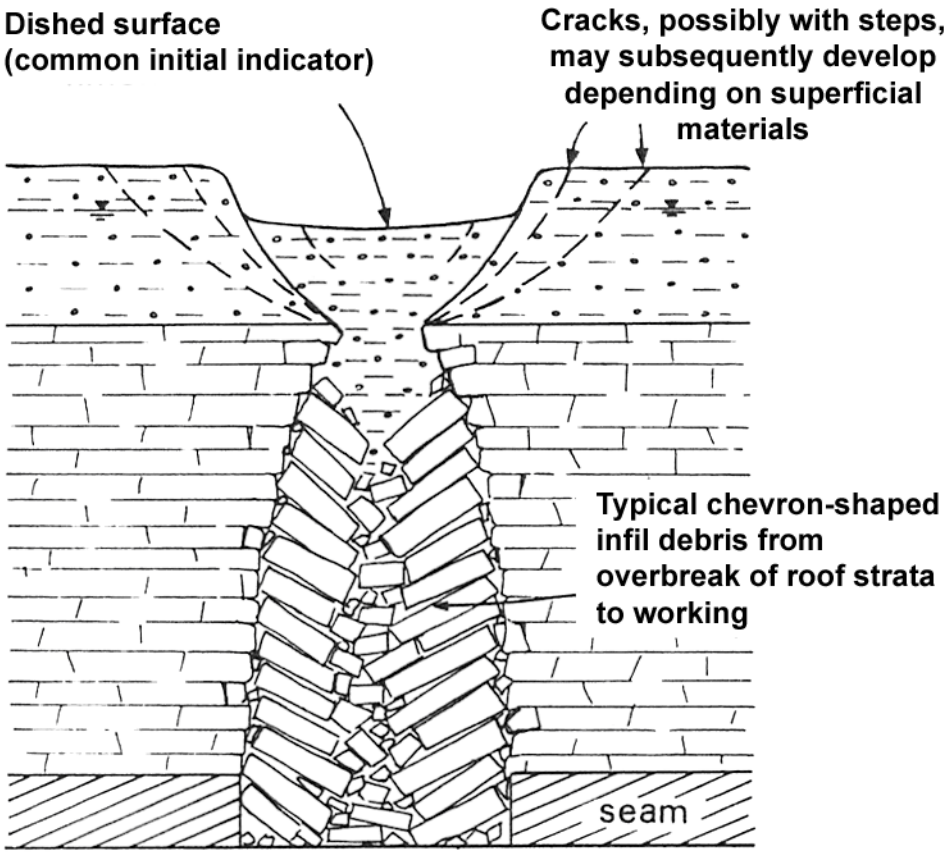

Figure 2.16: Typical cross section through a fully developed crown hole (after Attewell and Taylor, 1984).

Figure 2.17: A choked historical mining void, found during opencast mining / quarrying (after Attewell and Taylor, 1984).

As crown holes are the direct result of roof collapse between stable pillars, they mostly form over the wider stalls of shallow old mines. The presence of a competent stratum with a tensile strength large enough to allow the roof to span the opening (in coal measures rocks this is likely to be a thick bedded sand stone layer) will also halt void migration. These conditions are illustrated in Figure 2.18 and Figure 2.19.

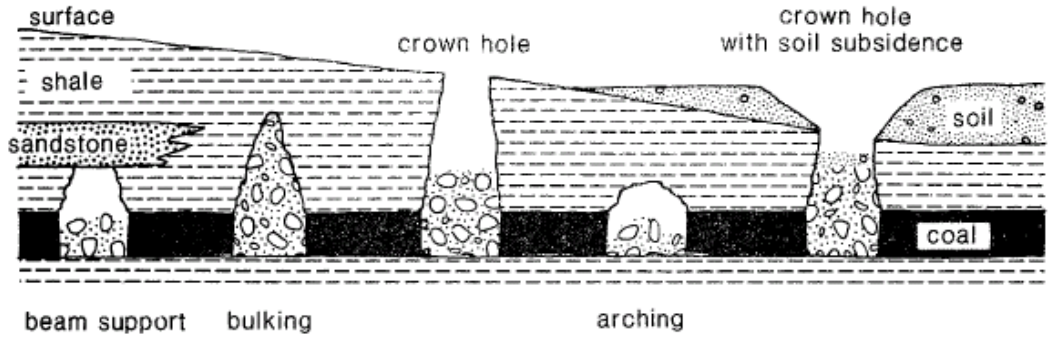

Figure 2.18: Types of roof failure in shallow workings (after Waltham, 1989).

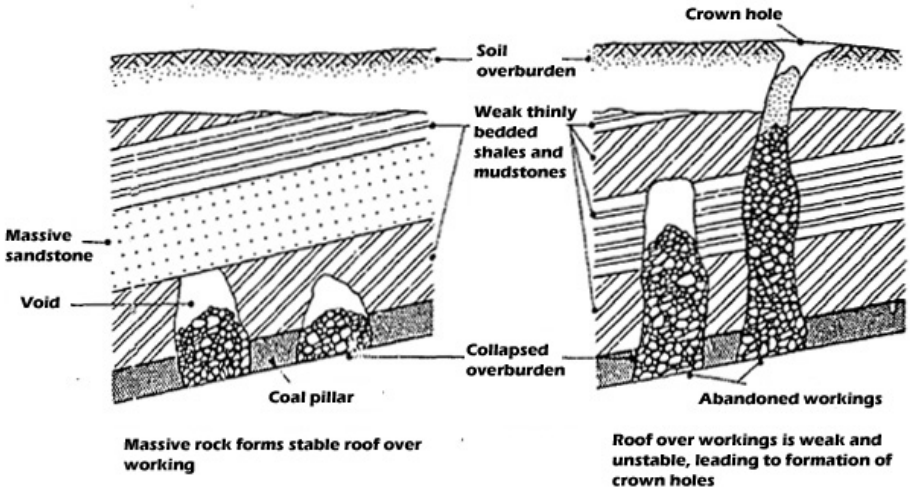

Figure 2.19: Extent of void migration in varying ground conditions (after Healy and Head, 1984).

2.3 Rock Mass Characterisation and Strength Assessment

2.3.1 Introduction

Bieniawski (1988) made the following observations about the reasons for the success of rock mass characterisation and strength assessment systems:

1. Provide a methodology for characterizing rock mass strength using simple measurements;
2. Allow geologic information to be converted into quantitative engineering data;
3. Improve communication between geologists and engineers; and
4. Enable the comparison of ground control experiences between sites, even when the geologic conditions are very different.

From the above it seems reasonable to assume that these systems may be of use in both the development of a hazard assessment or ranking system (point 4) as well as in the derivation of parameters for numerical modelling (Point 2). With reference to deriving strength and stiffness properties for numerical modelling the importance of rock mass characterisation and strength assessment methods is highlighted by Jing (2003) and Wiles (2006) when they state that:

> "*...in rock mechanics and engineering design, having insufficient data is a way of life…and that is why the empirical approaches (i.e. classification systems) have been developed and are still required...*"
>
> "*...rock mechanics problems are considered to be data limited...*"

The statement above originates from the 21st century, but the requirement for an empirical approach to rock mass characterisation has been recognised by geologists and mining engineers for considerably longer. Hoek (2007) states that attempts to create rock mass characterisation schemes have been ongoing for over 130 years since the first published attempt to create an empirical scheme for use in the design of tunnel roof support by W. Ritter in 1879. Since then a number of differing systems have been proposed, some more successful than others. It is intended here to briefly summarise the history of rock mass characterisation systems and then to concentrate on the more modern systems that are more directly applicable to numerical modelling and abandoned (and working) mines and to those systems that may be more easily applied to large data sets (such as the large number of varying ground conditions found at sites of abandoned mine workings).

2.3.2 The Development and History of Rock Mass Characterisation and Rock Mass Strength Assessment Methods

It is generally accepted (Bieniawski, 1984; Crabb, 1997; Price-Jones, 2004; Hoek, 2007) that the first publication of a rock characterisation system was made by Terzaghi in 1946 known as the Rock Load Classification (Bieniawski, 1984). Of most interest are his rock mass descriptions as he identifies the characteristics that control or dominate the rock mass response. This is a descriptive system so is of little use in deriving numerical modelling parameters as it provides no quantitative information on the properties of the rock mass (Bieniawski, 1984; Bieniawski, 1989). However it provides a very useful introduction to understanding the factors that control rock mass behaviour (*e.g.* presence of joints / discontinuities and joint spacing and persistence). The first numerical system was devised in 1964 by Deere (Deere, 1964; Bieniawski, 1984; Bieniawski, 1989; Crabb, 1997; Hoek, 2007; Hung *et al.*, 2009) and was intended to provide a quantitative estimate of rock mass quality from drill core logs (Hoek, 2007) and is a very commonly used index of rock mass fracturing (Bieniawski, 1984; Bieniawski, 1989; Crabb, 1997).

In 1972 Wickham *et al.* developed the Rock Structure Rating (RSR) system (Bieniawski, 1984; Bieniawski, 1989; Crabb, 1997; Price-Jones, 2004; Hoek, 2007). This is a partly quantitative nine-parameter, weighted classification system for determining rock quality (Crabb, 1997) and uses assessment of a number of parameters which take account of the local geological structure, the pattern and orientation of joints relative to the tunnel direction and groundwater and joint condition (Price-Jones, 2004) to produce an RSR value between 0 and 100 (Bieniawski, 1984; Bieniawski, 1989, Crabb, 1997 and Hoek, 2007) where the higher the value the higher the rock mass quality.

The RSR scheme is considered to be the precursor to the modern rock characterisation schemes which produce a numerical result or parameter to define rock mass quality that are in use today (Bieniawski, 1984; Bieniawski, 1989 and Hoek, 2007). The most commonly used of which are the Council for Scientific and Industrial Research Rock Mass Rating system (CSIR RMR system) developed by Bieniawski in 1973 and the Norwegian Geotechnical Institute Tunnelling Quality Index (NGI Q-System) developed by Barton *et al.* (Crabb, 1997, Price-Jones, 2004; Hoek, 2007 and Hung *et al.*, 2009). The RMR and NGI Q-System have been continuously updated and a number of other

systems have been derived or are based on modified versions of the RMR System (the Mining Rock Mass Rating (MRMR) system, rock mass Strength classification (RMS) and the Rock Condition Rating (RCR)) and the NGI Q-System (Rock Mass Number - (N) system) as described by Edelbro (2004).

2.3.3 Rock Mass Characterisation and Strength Assessment Methods

In this section more detail will be given on the different methods of rock mass characterisation and strength assessment that are currently used or that may be useful in making an initial assessment of rock mass strength based on limited data such as that found during a desk study or preliminary site investigation.

2.3.4 Rock Quality Designation Index (RQD)

The Rock Quality Designation (RQD) was developed to allow a quantitative assessment of rock mass quality to be made from drill core logs (Bieniawski, 1984; Bieniawski, 1989; Brady and Brown, 1993; Crabb, 1997; Hoek, 2007 and Hung *et al.*, 2009). The RQD is defined as the intact core recovered that is longer than 0.1 m divided by the total core run and expressed as a percentage (Bieniawski, 1984; Bieniawski, 1989; Crabb, 1997). See Equation 2.7 and Figure 2.20.

$$\text{RQD} = \frac{\sum \text{Length of Core Pieces} > 0.1\,\text{m}}{\text{Total Length of Core Run (m)}} \times 100 \qquad 2.7$$

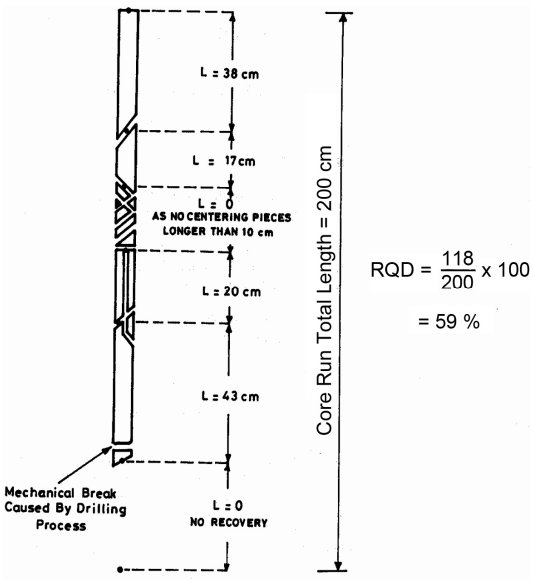

Figure 2.20: Procedure for measurement and calculation of Rock Quality Designation (after Deere and Deere, 1988).

The RQD value is related to the engineering quality of the rock mass as follows:

Table 2.1: Relation between RQD and rock mass quality (Deere and Deere, 1988 and Crabb, 1997).

RQD (%)	Rock Quality
< 25	Very Poor
25 - 50	Poor
50 - 75	Fair
75 - 90	Good
90 - 100	Excellent

One of the major drawbacks of the RQD system is its scale dependence (Crabb, 1997) especially in rock masses with a discontinuity spacing close to 0.1 m. *E.g.* for a discontinuity spacing equal to 0.11 m the RQD rating would be 100% however for a discontinuity spacing of 0.09 m, the RQD value would be 0%, suggesting the rock masses were of excellent and very poor quality respectively, entirely due to the arbitrary nature of the intact core size cut off length of 0.1 m. Another important factor is the directional dependence of the RQD system and its value may change significantly depending on the orientation of the borehole relative to the discontinuities (Hoek, 2007).

2.3.5 Rock Mass Rating (RMR) System

The Rock Mass Rating (RMR) system, sometimes also known as the Geomechanics System was initially introduced by Bieniawski in 1973 (Bieniawski, 1984; Brady and Brown, 1993; Hoek *et al.*, 1995; Crabb, 1997; Hoek, 2007; Hung *et al.*, 2009). The current RMR system involves the analysis of 351 case studies (Crabb, 1997; Hoek, 2007). Both the 1976 and 1989 (the most up to date) version of the RMR system allow the derivation of rock mass strength properties (Hoek, 1995; Hoek, 2007) however the older version will be presented here as the most commonly used rock mass failure criteria (Hoek-Brown and Shoerey criteria) recommend the use of the 1976 version (Edelbro, 2004) for derivation of numerical modelling parameters.

The RMR system uses 6 parameters to classify the rock mass and their ratings are summed to derive the RMR value. These parameters are as follows (Bieniawski, 1984):

1. Uniaxial compressive strength of intact rock material;
2. Rock quality designation (RQD);
3. Joint or discontinuity spacing;
4. Joint condition;
5. Ground water condition; and
6. Joint orientation.

The rock mass is zoned into regions with differing structure and each is assessed separately. These boundaries are usually located at points where a change of rock type or major structural feature (*e.g.* fault) occurs, but may also be applied to locations where significant changes in discontinuity spacing occur within the same rock type (Hoek *et al.*, 1995).

Of the six parameters listed above, the first five represent the basic RMR parameters (RMR_{basic}), however the sixth is treated separately as the influence of discontinuity orientation is dependent on the engineering application *i.e.* it differs for tunnels, foundations, and rock slopes (Crabb, 1997).

Each of the six parameters of the RMR system are further subdivided into 5 classes, each of which is assigned a numerical value, weighted to account for its relative importance. The values for the first five parameters are summed, and then are adjusted using parameter six, based on the relative orientation of the excavation and joints / discontinuities (Bieniawski, 1984). See Equation 2.8 and 2.9.

$$RMR_{Basic} = \sum \text{parameters} (1 + 2 + 3 + 4 + 5) \quad 2.8$$

$$RMR = RMR_{Basic} + \text{Adjustment for Joint Orientation} \quad 2.9$$

The final RMR value (range from 0 – 100) is used to place the rock mass into one of five rock masses classes (see Table 2.2), with a higher value of RMR representing a higher quality and condition of rock mass (Bieniawski, 1984; Crabb, 1997).

Table 2.2: Rock mass classes and rock mass strength parameters derived from the RMR values (after Bieniawski, 1984).

Parameter/ Property of Rock Mass	**Rock Mass Rating (Rock class)**				
Rating	100-81	80-61	60-41	40-21	< 20
Classification of Rock Mass	Very Good	Good	Fair	Poor	Very Poor
Average Stand-up Time (Unsupported)	10 years for 15 m span	6 months for 8 m span	1 week for 5 m span	10 hours for 2.5 m span	30 minutes for 1 m span
Cohesion of the Rock Mass (kPa)	> 400	300-400	200-300	100-200	< 100
Friction Angle of the Rock Mass (°)	45	35 - 45	25 - 35	15 - 25	< 15

Overall, the RMR system is considered simple to use, and the classification parameters are easy to obtain from either borehole data or underground mapping. To date, most of the applications of RMR have been in the field of tunnelling but also in the stability analysis of caverns and mining openings (Edelbro, 2004).

2.3.6 Norwegian Geotechnical Institute Tunnelling Quality Index (NGI Q-System)

Barton *et a1.*, (1974) of the Norwegian Geotechnical Institute developed the rock tunnelling quality index (Q-system) in 1974 and is currently based around analysis of a database of approximately 1200 excavation / tunnelling case studies in varying rock types in many differing countries (Crabb, 1997; Edelbro, 2004). It was originally developed to assist in determination of rock mass characteristics (Hoek, 2007; Hung *et al.*, 2009) and the empirical design of tunnel and cavern support and reinforcement (Barton, 2002).

The numerical value of the index Q varies on a logarithmic scale from 0.001 to a maximum of 1,000 (Hoek, 2007) and is defined by the following:

$$Q = \frac{RQD}{J_n} \times \frac{J_r}{J_a} \times \frac{J_w}{SRF} \qquad 2.10$$

Where:

RQD = Rock quality designation

J_n = Joint set number

J_r = Joint roughness number

J_a = Joint alteration number

J_w = Joint water reduction factor

SRF = Stress reduction factor

The three ratios represent the following (Barton, 2002):

1. RQD / J_n = Relative block size.
2. J_r / J_a = Relative frictional strength (least favourable joint set / discontinuity).
3. J_w / SRF = Active stress.

Ratio one (relative block size) represents the structure of the rock mass, ratio two represents the roughness and frictional properties of the joint walls or joint fill. This ratio is weighted to favour unaltered joints in direct contact and which are expected to be close to peak strength and undergo strong dilation when sheared. The higher this ratio, the more stable the excavation in the rock mass will be (Hoek, 2007) and because of this ratio, it is considered that the Q-System gives the most detailed assessment of the discontinuity properties on stability of all the systems summarised here thus far (Crabb, 1997). The third ratio accounts for the relative effect of water, faulting, strength/stress

ratio and squeezing or swelling ground conditions (Barton, 2002). Once the Q parameter is derived the rock mass is classified based on the following (See Table 2.3):

Table 2.3: Q-System rock mass classification (Derived from Barton, 2002).

Q Value	Group	Classification
400 - 1000	A	Exceptionally Good
100 - 400		Extremely Good
40 - 100		Very Good
10 - 40	B	Good
4.0 - 10.0	C	Fair
1.0 - 4.0	D	Poor
0.1 - 1.0	E	Very Poor
0.01 - 0.1	F	Extremely Poor
0.001 - 0.01	G	Exceptionally Poor

While originally intended to allow the design of roof support for tunnelling, work has been undertaken to correlate Q values to rock mass strength parameters suitable for input to numerical modelling software.

2.3.7 Geological Strength Index and the Hoek-Brown Criterion

Geological Strength Index

The Geological Strength Index (GSI) system was developed by Hoek and first published in 1994 (Hoek *et al.*, 1995; Marinos and Hoek, 2007).

It was introduced to allow a rapid and simple classification of both strong and weak rock masses to be made based on a visual inspection of the geological conditions (Zhang, 2005) in part because it was felt that the numbers associated with the RMR and Q-systems were largely meaningless for weak or highly heterogeneous rock masses due to their reliance on RQD as an input parameter and also as it was intended to allow a system that could be used to estimate rock mass parameters rather than in the design of tunnel roof reinforcement and support (Marinos *et al.*, 2005).

The system is based on the reasoning that the strength of discontinuous rock masses is dependent on the properties of both the intact rock and also upon the freedom of these rock blocks to slide and rotate under differing stress conditions (Hoek and Brown, 1997).

As such the GSI system is broadly based on two main parameters. (1) The density of discontinuities in the rock mass and (2) the conditions of the surfaces of the discontinuities as indicated by joint roughness and alteration.

The density of discontinuities / discontinuity spacing is split broadly into 6 main categories (Hoek, 1999):

- Intact / Massive
- Blocky
- Very blocky
- Blocky / disturbed
- Disintegrated
- Foliated / laminated

The conditions of the joints are separated into 5 main categories as below:

- Very good
- Good
- Fair
- Poor
- Very poor

The scheme was originally intended for application to homogeneous rock masses and so was originally broadly similar to RMR however it was modified in 1998 (after experience from tunnelling in very poor quality rock masses) to improve its use in such conditions (Hoek *et al.*, 1998) and to allow its use in heterogeneous rock masses (Marinos *et al.*, 2001).

The current charts that are used in the estimation of GSI in homogeneous and heterogeneous rock masses can be seen in Figure 2.21 and Figure 2.22 respectively.

Whereby it is intended that an assessment of the lithology, structure and condition of discontinuity surfaces in the rock mass either from visual examination of exposed outcrops, in surface excavations or tunnel faces and in borehole cores is made and the most appropriate GSI value from the tables is chosen.

From those tables it can be seen broadly that in homogeneous rock masses as the discontinuity spacing / block size decreases and or the condition of the joints / discontinuities become poorer, the GSI value decreases. The same is broadly true for heterogeneous rock masses however the composition is also factored into the assessment along with the structure of the rock mass so that for example the progression of a massively bedded sandstone, through small laminations of siltstone, through to

siltstone or shale with thin layers of sandstone will result in a decrease in the GSI value of the rock mass.

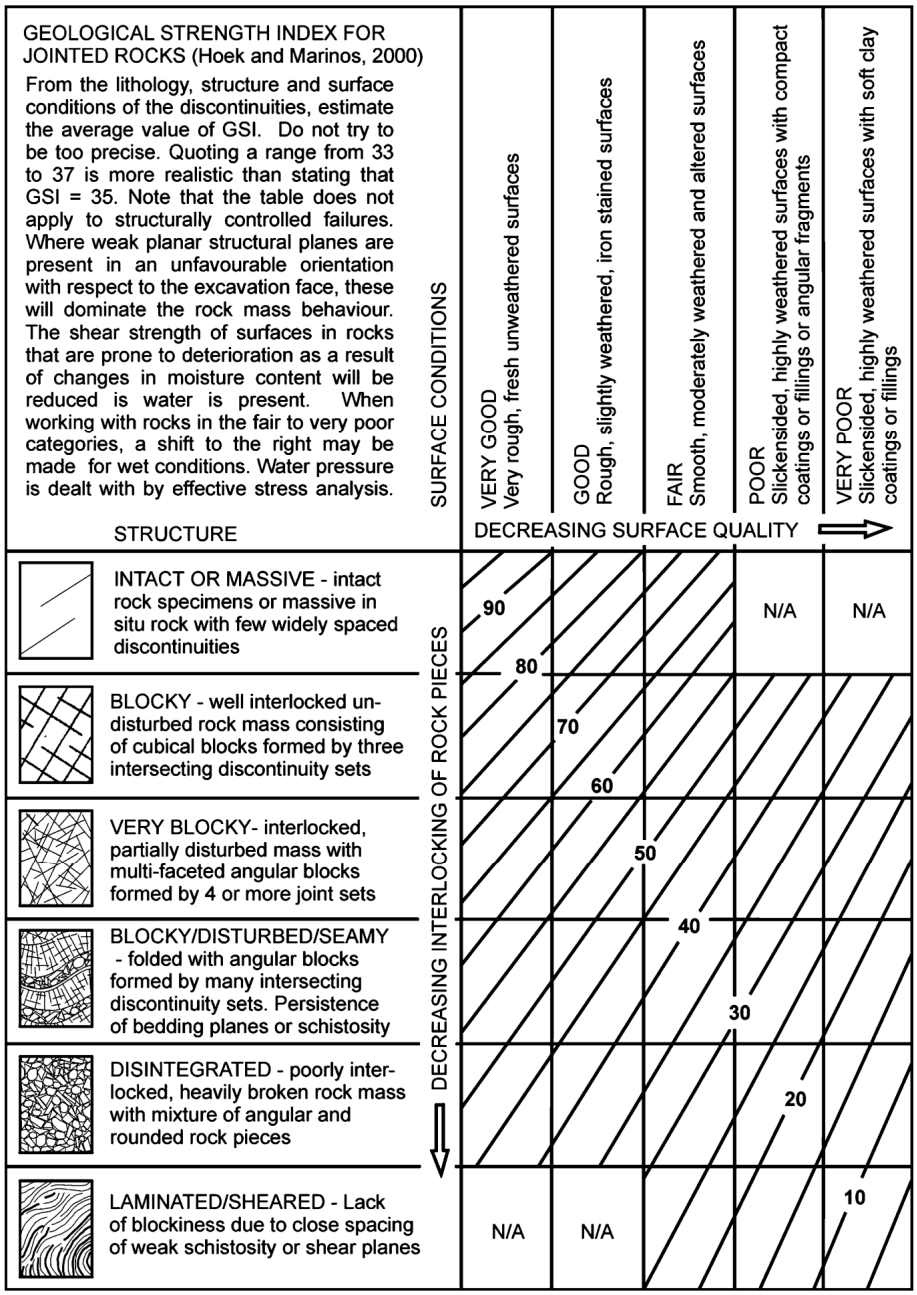

Figure 2.21: Chart for estimating GSI values for broadly homogenous rock masses (After Marinos *et al.*, 2005).

Once a GSI value is derived, it is necessary to convert it into a parameter of use in design. This requires the use of the Hoek-Brown failure criterion discussed in more detail below.

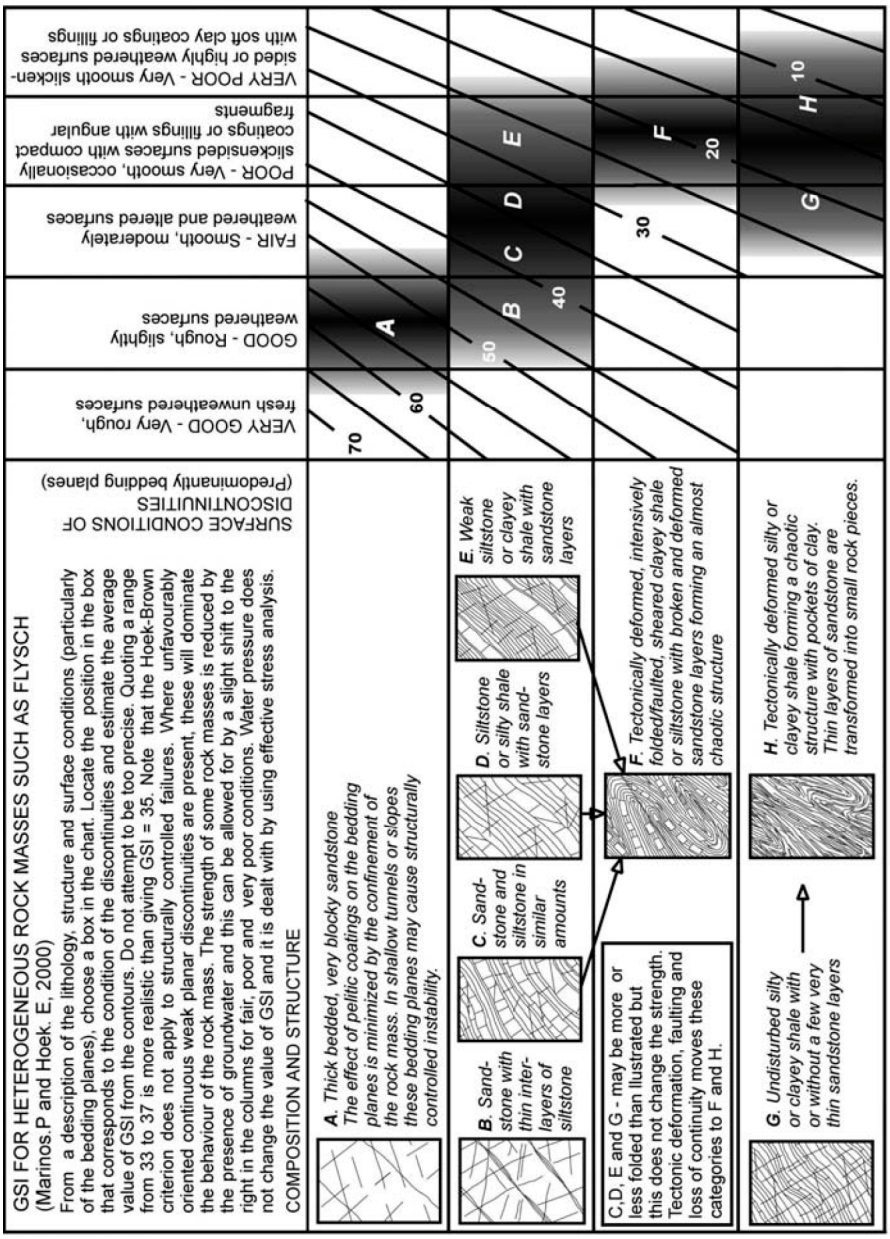

Figure 2.22: Chart for estimating GSI values for weak and or heterogeneous rock masses (After Marinos *et al.*, 2005).

Hoek-Brown Criterion

The Hoek-Brown criterion was developed as the authors identified a requirement for estimating rock mass design parameters for use in underground excavations and was initially based on investigations into the brittle failure of rock and the behaviour of jointed rock masses by Hoek and Brown respectively (Hoek *et al.*, 2002).

The criterion is based on the assumption that the strength parameters of an intact rock can be scaled to account for the presence of discontinuities in a rock mass (Marinos and Hoek, 2007).

For intact rock, the criterion takes the form:

$$\sigma_1^{'} = \sigma_3^{'} + \sigma_{ci}\left(m_i \frac{\sigma_3^{'}}{\sigma_{ci}} + HB_s \right)^{0.5} \qquad 2.11.$$

Where:

$\sigma_1^{'}$ = Major effective principal stress at failure

$\sigma_3^{'}$ = Minor effective principal stress at failure

σ_{ci} = Uniaxial compressive stress of intact rock material

m_i = Intact constant dependent on rock type

HB_s = 1 (for intact rock).

This relationship is empirically based and was originally derived based on triaxial testing on intact rock specimens (Hoek *et al.*, 2002).

In order to allow this criterion to be used with the majority of numerical modelling software and in design, it was necessary to identify a relationship between the Hoek-Brown criterion (Equation 2.11) written in terms of the maximum and minimum principal stresses with the non linear HB_s and m_i terms with the Mohr-Coulomb criterion formed in terms of the normal and shear stresses at failure and the linear parameters of friction angle (ϕ') and cohesion (c') (Hoek *et al.*, 2002; Marinos and Hoek, 2007).

This was achieved in 1983 (Marinos and Hoek, 2007) and on reviewing this solution Hoek identified the possibility of adjusting the square root parameter in Equation 2.11 with a variable term to allow an adjustment of the failure envelope. This ultimately resulted in the derivation of the generalised Hoek-Brown failure criterion for rock masses containing adjustments to allow for the derivation of rock mass parameters as shown in Equation 2.12.

$$\sigma_1^{'} = \sigma_3^{'} + \sigma_{ci}\left(m_b \frac{\sigma_3^{'}}{\sigma_{ci}} + HB_s \right)^{HB_a} \quad 2.12.$$

Where:

m_b = is a reduced value of m_i (a material constant – see Equation 2.13)

HB_s = rock mass constant (see Equation 2.14)

HB_a = rock mass constant (see Equation 2.15)

m_b can be found using the following:

$$m_b = m_i \exp\left(\frac{GSI - 100}{28 - 14D} \right) \quad 2.13$$

Where:

GSI = Selected value of geological strength index

D = Disturbance factor dependent on the degree to which rock mass has been affected by stress relaxation or blast damage where D = 0 for an undisturbed rock mass and a maximum of 1 for very significant disturbance for example due to very poor quality blasting.

The parameter HB_s is found using the following:

$$HB_S = \exp\left(\frac{GSI - 100}{9 - 3D} \right) \quad 2.14.$$

And the parameter HB_a is found using the following:

$$HB_a = \frac{1}{2} + \frac{1}{6}\left(e^{\frac{-GSI}{15}} - e^{\frac{-20}{3}} \right) \quad 2.15.$$

The uniaxial compressive strength of the rock mass (σ_c) is derived by setting the value of $\sigma_3^{'}$ in Equation 2.12 equal to zero yielding the following (Hoek *et al.*, 2002):

$$\sigma_c = \left(\sigma_{ci} HB_s \right)^{HB_a} \quad 2.16.$$

And the tensile strength (σ_t) can be derived using Equation 2.17:

$$\sigma_t = -\left(\frac{HB_s \sigma_{ci}}{m_b} \right) \quad 2.17.$$

To derive the normal ($\sigma_n^{'}$) and shear (τ) stresses, the following equations (Equation 2.17 and Equation 2.18) are used:

$$\sigma_n^{'} = \frac{\sigma_1^{'} + \sigma_3^{'}}{2} + \frac{\sigma_1^{'} - \sigma_3^{'}}{2}\left(\frac{\left(d\sigma_1^{'}/d\sigma_3^{'}\right) - 1}{\left(d\sigma_1^{'}/d\sigma_3^{'}\right) + 1}\right) \qquad 2.18$$

$$\tau = \sigma_1^{'} + \sigma_3^{'}\frac{\sqrt{\left(d\sigma_1^{'}/d\sigma_3^{'}\right)}}{\left(d\sigma_1^{'}/d\sigma_3^{'}\right) + 1} \qquad 2.19$$

Where:

$$d\sigma_1^{'}/d\sigma_3^{'} = 1 + HB_a m_b \left(m_b \sigma_3^{'}/\sigma_{ci} + HB_s\right)^{HB_a - 1} \qquad 2.20$$

Finally the rock mass elastic modulus (E_m) is derived using the following (see Equation 2.21).

$$E_m(GPa) = \left(1 - \frac{D}{2}\right)\sqrt{\frac{\sigma_{ci}}{100}} \times 10^{\left((GSI - 10)/40\right)} \qquad 2.21$$

To derive the Mohr-Coulomb values of friction angle (ϕ' - see Equation 2.22) and cohesion (c' - see Equation 2.23) as used in the vast majority of constitutive models in numerical modelling software, it is necessary to fit an average linear relationship to the curve generated by solving Equation 2.12 for a range of minor principal stress values defined by $\sigma_t < \sigma_3 < \sigma_{3\max}$. An example of this curve fit is shown in Figure 2.23.

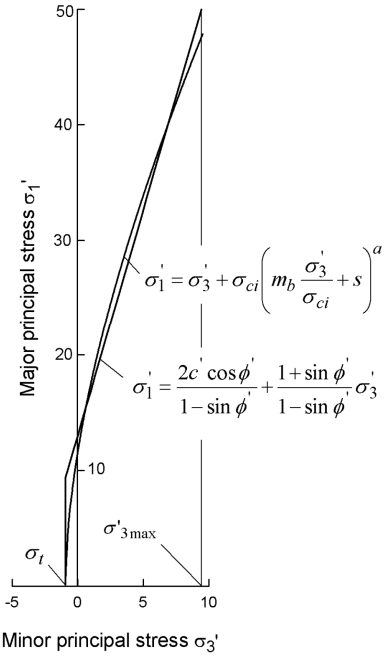

Figure 2.23: Relationship between major and minor principal stresses for Hoek-Brown and equivalent Mohr-Coulomb criteria (after Hoek *et al.*, 2002).

The fitting process involves balancing the areas above and below the Mohr-Coulomb plot and which results in the following equations (Hoek *et al.*, 2002):

$$\phi' = \sin^{-1}\left[\frac{6HB_a m_b \left(HB_s + m_b \sigma'_{3n}\right)^{HB_a - 1}}{2(1+HB_a)(2+HB_a) + 6am_b \left(HB_s + m_b \sigma'_{3n}\right)^{HB_a - 1}}\right] \qquad 2.22$$

$$c' = \frac{\sigma_{ci}\left[(1+2HB_a)HB_s + (1-HB_a)m_b \sigma'_{3n}\right]\left(HB_s + m_b \sigma'_{3n}\right)^{HB_a - 1}}{(1+HB_a)(2+HB_a)\sqrt{1+\left(6HB_a m_b \left(HB_s + m_b \sigma'_{3n}\right)^{HB_a - 1}\right)/\left((1+HB_a)(2+HB_a)\right)}} \qquad 2.23$$

Where:

$$\sigma'_{3n} = \frac{\sigma'_{3\max}}{\sigma_{ci}} \qquad 2.24$$

$\sigma'_{3\max}$ = upper limit of confining stress over which the relationship between the Hoek-Brown and Mohr-Coulomb parameters are applicable. This is significant as the value of friction angle as derived will be significantly higher at low confining pressures and increases with increasing depth, so this parameter should be selected with care.

One other outcome of the derivation of these relationships which is of interest is the concept of a uniaxial compressive strength of the rock mass (σ'_{cm}) which is calculated using Equation 2.25.

$$\sigma'_{cm} = \sigma_{ci} \times \frac{\left(m_b + 4HB_s - HB_a\left(m_b - 8HB_s\right)\right)\left(m_b/4 + HB_s\right)^{HB_a - 1}}{2(1+HB_a)(2+HB_a)} \qquad 2.25$$

The value of $\sigma'_{3\max} / \sigma_{ci}$ for tunnelling as used in Equation 2.24 can then be estimated using Equation 2.26.

$$\frac{\sigma'_{3\max}}{\sigma_{ci}} = \left(\frac{\sigma'_{cm}}{\gamma H}\right)^{-0.94} \qquad 2.26$$

Where:

γ = Unit weight of overburden rock mass (MNm^{-3})

H = Depth of excavation below the surface

It should be readily apparent from the above that the derivation of the Mohr-Coulomb parameters from the Generalised Hoek-Brown criterion and ultimately from the GSI value is a complex process however it has been greatly simplified by the publication of a software program known as ROCLAB (Rocscience, 2010) where the process is largely automated.

2.3.8 Coal Mine Roof Rating (CMRR)

The CMRR system starts with the premise that the rock mass strength is controlled by the presence of discontinuities (Mark and Molinda, 2007). However unlike the characterisation and classification systems discussed previously it is specifically developed for use in horizontally to sub horizontally bedded coal measures. The CMRR system employs the same format as that used in the RMR system giving a CMRR value in the range of 0 - 100 and was developed based on case histories and from mines in the US, India and South Africa (Mark and Molinda, 2007) and from an extensive literature review of the factors affecting the stability of coal mine roof rock.

Based on these case histories a number of geological features were found to be a recurring element in roof (in)stability and these are summarised below:

1. Bedding features are most likely to cause problems with roof stability, with the most common examples being weak laminations in shale and thinly interbedded sandstone and shales.
2. Strata Strength - In bedded coal measures rocks the roof of an excavation will commonly consist of several layers with varying strength and stiffness properties.
3. Moisture Sensitivity - Moisture sensitive shales can undergo significant loss of strength or even total disintegration in the presence of groundwater, as well as compromising roof stability through the development of swelling pressure (Mark and Molinda, 2007).
4. Slickensides and Other Discontinuities - The CMRR system allows for small scale localised discontinuities that may have a large effect on roof stability such as slickensides.

To account for these features the CMRR is composed of five primary and 3 secondary parameters (Mark *et al.*, 2002; Mark and Molinda, 2007):

1. Uniaxial compressive strength of the intact rock;
2. Intensity (spacing and persistence) of bedding and other discontinuities;
3. Shear strength (cohesion and roughness) of bedding and other discontinuities;
4. Moisture sensitivity of the rock;
5. Presence of a strong bed in the bolted interval.
6. Number of layers (secondary parameter);
7. Presence of groundwater (secondary parameter);
8. Surcharge from overlying weak beds (secondary parameter).

One significant drawback of the CMRR system for application towards abandoned mine workings is the fact it was developed for use in working coal mines in the USA where by law, all mine roof strata must use rock bolting as reinforcement. This is clearly not the case for other coal mines; particularly the old abandoned mine workings of the UK.

2.3.9 Coal Measure Classification (CMC)

The Coal Measure Classification system was developed to derive strength and stiffness properties that account for the anisotropic nature of coal measures strata whereas the majority of empirical systems assume that a rock mass is isotropic (Whittles *et al.*, 2007).

The approach taken is to identify the parameters that have an impact on stability and their relative importance. In order to do this it was first necessary to identify the modes of deformation and failure which may occur in stratified coal measures rock masses. The five that affect the roof are summarised in Figure 2.24. The relative importance of the parameters was then assessed based on the degree to which they influence the above deformation and failure mechanisms (Whittles *et al.*, 2007).

Ultimately this resulted in six parameters being identified as very significant in the majority of deformation and failure mechanism considered. These are outlined below:

- Unconfined compressive strength of the intact rock
- Bedding/lamination characteristics
    a. Bedding plane spacing
    b. Bedding plane strength
- Joint properties
    a. Joint set number
    b. Joint set orientation
    c. Joint set spacing
    d. Joint strength
- Degree of fissility (shaleyness)
- Water flow
- Moisture sensitivity of the rock type

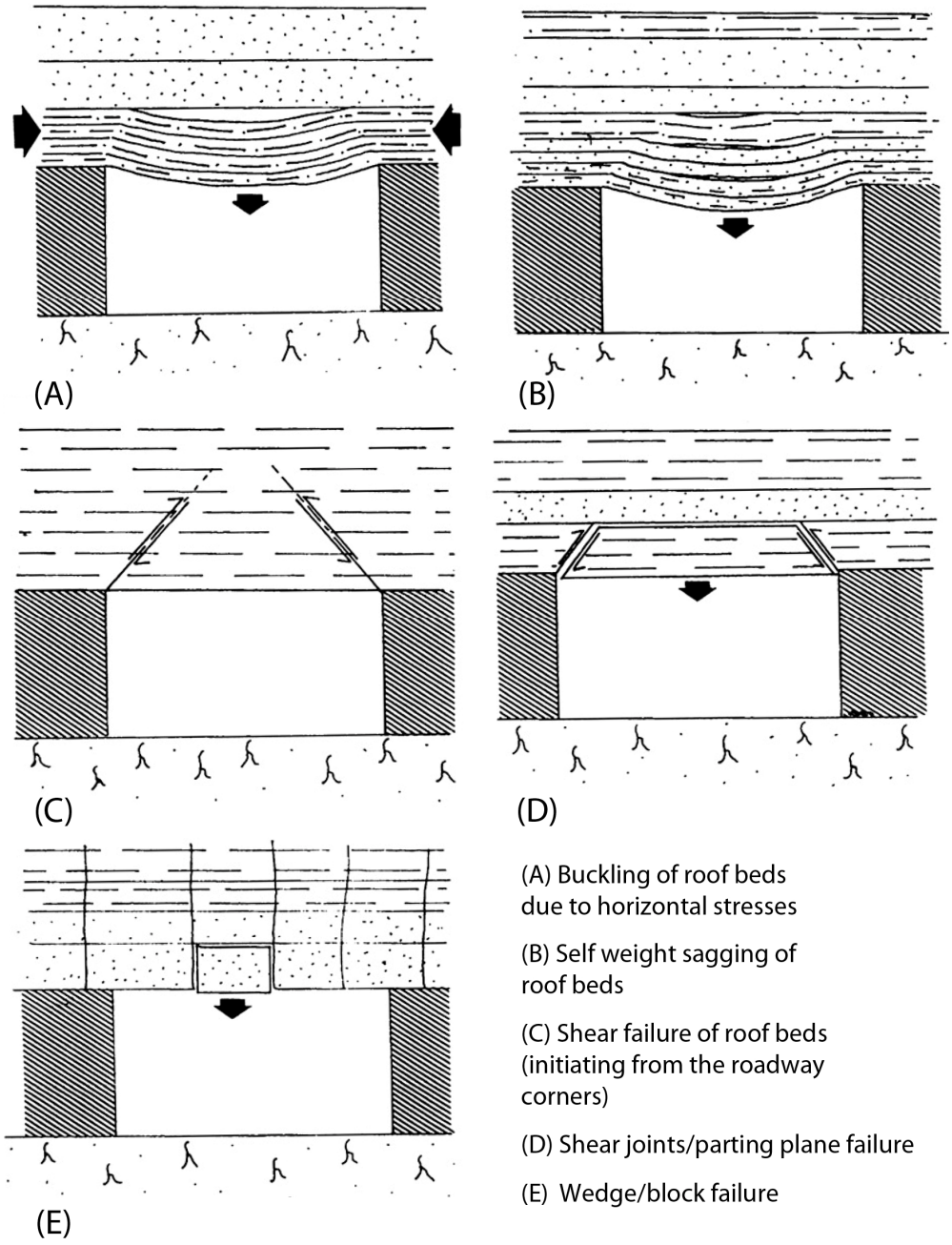

Figure 2.24: Five modes of roof failure (Whittles *et al.*, 2007).

The relative importance of these six main parameters was then derived based on the estimated effect on stability in the differing failure and deformation mechanisms of an unfavourable value for a parameter when compared to the other parameters. As such each parameter was assumed to play a role of varying importance and so was allocated a variable percentage score for a given failure mechanism depending on its presumed importance.

Once this process was completed for the failure mechanisms, the percentage score of each parameter was then summed giving a total score for each of the individual

parameters allowing an estimate to be made of its general importance in the stability of coal measures strata. The finalised ratings can be seen in Table 2.4**.**

Table 2.4: Parameter ratings as derived in the CMC system (after Whittles *et al.*, 2007).

Parameters	Total Ratings	Adjusted Ratings
UCS	390	19
Joint set number	174.5	8
Joint set spacing	174.5	8
Joint set orientation	87	4
Joint strength	87	4
Bedding plane spacing	299	14
Bedding plane strength	254	12
Degree of fissility	283	14
Water flow	182	9
Moisture sensitivity	160	8
Total	2092	100

It is readily apparent that in this system, the intact rock strength and the strength and spacing of the horizontal discontinuities (*i.e.* the bedding planes and degree of fissility) are very significant parameters accounting for approximately 60% of potential (in)stability. In order to use the system, the rock mass is assessed both normal and parallel to bedding.

2.4 Numerical Methods in Modelling

Numerical modelling has been characterised by Alejano *et al.*, (2008) as:

> "*a mathematical abstraction that describes the most significant aspects of a phenomenon*"

This highlights an important factor in that numerical models provide a simplification of the true problem whilst capturing significant behaviour. Rock masses are considered difficult to model numerically as the rock mass properties have to be established rather than designed in a manufacturing process (Jing, 2003), leading rock masses to be described as Discontinuous, Anisotropic, Inhomogeneous and Not-Elastic or DIANE materials (Harrison and Hudson, 2000). To define the independent components of such a system may require an infinite subdivision of the area to be modelled. This requires the mathematical assumption of an infinitesimal element requiring an infinite number of sub components with infinite degrees of freedom and as such differential equations are required to describe the behaviour of the system (Jing, 2003). Problems of this type are described as continuous or continuum systems.

2.4.1 Numerical Methods

Numerical methods in rock mechanics can generally be divided into 3 main areas:

- Continuum methods
- Discrete or discontinuum methods
- Hybrid methods

These methods are discussed in the following sub sections along with a summary of their advantages and disadvantages.

2.4.2 Continuum Methods

In continuum models the problem domain is divided into a series of smaller areas or elements whose behaviour can be approximated using simplified numerical techniques with finite degrees of freedom. This process is known as discretisation and allows the approximation of a continuum with infinite degrees of freedom to be modelled using a discrete system with finite degrees of freedom (Jing, 2003). There are a number of techniques used in the modelling of continua and these are broadly summarised in the following sections.

Finite Element Method

The Finite Element Method (FEM) is very commonly used in geotechnical analysis and involves the division of a continuum into a number of elements of smaller sizes and standard shapes with a fixed number of nodes at the vertices and/or on the sides (Jing, 2003). The degrees of freedom of these nodes are limited and correspond to the unknowns in the problem to be analysed. Most commonly these unknowns correspond to displacement components (Brinkgreve *et al.*, 2010).

The main advantages and disadvantages for geotechnical analysis are as follows.
Advantages

- Structural features in the rock mass, such as closely spaced parallel sets of joints or fissures can be modelled (for example by the application of a homogenisation technique).
- Time-dependent material behaviour may be introduced.
- The method has been extensively applied to solve practical problems and thus a lot of experience is already available.

Disadvantages

The majority of the disadvantages listed below are more severe when three-dimensional problems are considered, and are much less of a problem where two-dimensional models are concerned (Carter *et al.*, 2000).

- Discretisation of the entire volume of the model requires large pre- and post-processing efforts.
- Due to the requirement of FEM analysis to generate (sometimes very large) matrices that must be stored in the computer's memory, the analysis duration and memory requirements may be very high.
- If the mechanical behaviour of the medium in question is dominated by randomly oriented joint or fracture sets, then FEM analysis is generally not suitable.

Explicit Finite Difference Method

The finite difference method (FDM) produces a direct approximation of the governing partial differential equations (PDEs) of the objective functions *e.g.* displacement, (Jing and Hudson, 2002) by replacing them with finite differences (in the form of algebraic equations with the unknowns at certain spatial intervals in the coordinate directions and located at grid points) spread over the area of interest (Itasca, 2005; Jing and Hudson, 2002; Jing, 2003). This grid system allows the creation of objective function values at sampling points with small enough intervals between them, so that errors thus introduced are small enough to be acceptable.

FDM codes like FLAC differ from FEM codes in their use of an explicit solution scheme, coupled with their use of the full dynamic equations of motion even for static problems. These factors make FDM codes better suited to solving problems with non linear and physically unstable behaviour than FEM codes – for example large strain behaviour of the sort seen in mining collapse problems (Itasca, 2005).

The FDM method used in FLAC is comparable to the finite element method (Itasca, 2005) and as such some of the advantages listed above for FEM methods are also applicable to the finite difference method as well. However some additional advantages and disadvantages can be identified due the explicit solution technique employed (Carter *et al.*, 2000):

Advantages

- The explicit solution method avoids the solution of large sets of equations and therefore reduces processing time, and memory requirements.
- Simple problems are very easy to prepare within the model.

Disadvantages

- The method is less efficient than FEM for linear or moderately nonlinear problems.
- Because FDM is based on Newton's law of motion no converged solution for static problems exists, as is the case in static finite element analysis. It is the subjective judgement of the user as to whether a sufficient number of time steps have been run to reach failure.

2.4.3 Discrete / Discontinuum Methods

The aim of discrete or discontinuum methods is to represent the fractured material as assemblages of blocks formed by connected fractures in the area of interest, and to solve the equations of motion of these blocks through continuous detection and treatment of contacts between the blocks (Jing, 2003). The continuum mechanics methods described up to this point are restricted to problems where the behaviour of the material is not governed by the effects of discontinuities. If discontinuities do control the strength of the rock mass, then discrete element methods are most suitable.

Discrete Element Method

These methods may be characterised as follows:

- Finite displacements and rotations of discrete blocks (deformable or rigid) are calculated (Carter *et al.*, 2000) .
- Blocks that are originally connected may separate during the analysis (Carter *et al.*, 2000) .
- New contacts which develop between blocks due to displacements and rotations are detected automatically (Itasca, 2005b) .

Without the first two attributes, the program cannot replicate the behaviour of a discontinuous material or medium; without the third, the program is limited to small numbers of bodies for which the interactions are known in advance, hence negating the requirement for modelling said interaction (Itasca, 2005c).

The most commonly used software based around DEM methods are the ITASCA programs UDEC and PFC, which both employ an explicit finite difference scheme, as in the program FLAC (all of which are products of ITASCA consulting group and are described in more detail below). It is considered inappropriate to directly compare discontinuum and continuum techniques; however the following should be noted: The majority of finite element, boundary element and Lagrangian finite difference programs allow the creation of interface elements or "slide lines" within the model geometry; this typically allows them to model discontinuous materials to a limited extent.
However, they usually have the following drawbacks (Itasca, 2005b, Itasca, 2005c):

- They are not suitable to deal with large numbers of intersecting discontinuities.
- They are unable to recognize new contacts between regions bounded by discontinuities.
- Typically they are limited to allowing only small displacements or rotations.

Advantages of DEM

- Large numbers of irregular joints can be taken into account in a physically rational way.

Disadvantages

- Generating an accurate three-dimensional model is very time consuming.
- Determination of the parameters required for joint strength can be difficult as they may not be available from experiment.
- Processing and run times for three-dimensional analyses are usually quite high.

2.4.4 Hybrid Numerical Methods

A useful way of minimising the disadvantages of some of the individual methods described above is to combine them (Jing, 2003, Carter *et al.*, 2000).

Coupled Finite Element - Discrete Element Method

Rock failure is typically a complex problem which involves both deformation of the continuum, movement along pre-existing discontinuities and the formation of new fractures within the rock mass (Eberhardt, 2003). To model the combined continuum - discontinuum behaviour of rock failure a number of hybrid finite - discrete element software codes have been developed.

In order to model continuum and discontinuum, software programs such as ELFEN (Eberhardt *et al.*, 2003) incorporate a system known as adaptive remeshing which is described by Stead *et al.*, (2001) a summary of which is given below:

Adaptive remeshing is a process where the rock mass is represented initially by a finite-element mesh. This is coupled with a discrete-element model able to model deformation involving joints or joint bounded blocks within the model. If the stresses within the rock mass exceed the failure strength of the material within the finite-element model a crack is initiated. (Eberhardt *et al.*, 2003, Eberhardt *et al.*, 2004) Remeshing allows the development and propagation of cracks through the finite-element mesh to be simulated, where fracture propagation within the continuum can occur. This may eventually result in the formation of a discrete element as the rock fragments. Subsequent motion of these discrete elements and further fracturing of both the remaining continuum and previously created discrete elements is then simulated. This process is continued until either the system comes to equilibrium or up to the time of interest (Eberhardt *et al.*, 2003).

Hybrid codes with adaptive remeshing routines, have been successfully applied to the simulation of intense fracturing associated with surface mine blasting, mineral grinding, retaining wall failure, rock slope failure and underground rock caving (Stead *et al.*, 2001).

Hybrid methods combine the inherent advantages provided by both continuum and discontinuum numerical codes, however it should be noted that as this is a relatively new technique, the availability of published information regarding the application of continuum – discontinuum modelling to rock mechanics problems is limited.

2.5 A Review of the Numerical Modelling of Underground Excavation and Mine Working Stability

2.5.1 Introduction

There has been a significant amount of research undertaken into the stability of deep hard rock excavations, deep pillar and stall workings and active long wall coal mine roof stability, particularly during face advance and to assess the effectiveness of roof support. This has been undertaken using a range of commercial and custom software codes.

In this section it is intended to summarise the work undertaken on underground excavation stability and to identify lessons that can be applied to this research project.

2.5.2 A Review of Underground Excavation Stability Modelling

The following subsections are a review of articles on the numerical modelling of mine workings and are separated into pillar and stall and longwall mining. Typically, for mine workings, numerical modelling is undertaken for stability analysis or reinforcement design. Occasionally it is also undertaken to back analyse a failure event. Case studies are presented where appropriate or of particular interest.

2.5.3 Longwall Mine Workings

Numerical modelling work on Longwall mine workings is predominantly undertaken to assess roof stability with the aim of identifying the requirements for roof support (Zipf, 2006, González-Nicieza *et al.*, 2008 and Lawrence, 2009). Work is also undertaken to model top coal caving which is a specialised form of longwall mining where thick coal seams are present (Xie *et al.*, 1999, Yasitli and Unver, 2005 and Singh and Singh, 2009).

Zipf (2006) has undertaken work with the aim of reducing the danger posed by roof instability in US coal mines, where it is estimated that 50% of all fatalities were caused by ground failure. In order to develop improved ground control (*i.e.* roof support such as rock bolting) designs and design methodologies the author has undertaken numerical modelling work with the finite difference program FLAC.

The methodology suggested by the author requires core logging and point load testing to be undertaken on rock core to accurately estimate the unconfined compressive strength of the rock. This has the advantage of being accurate and is very useful for individual mines but may not be feasible where there are a large number of differing sites with differing ground conditions. The intact rock properties were then used to derive strength and stiffness properties for the rock mass using the RMR and GSI systems.

The detailed core logs and strength parameters allow a very high resolution model to be created of the strata around the excavation to be modelled and the author indicates that the modelling results closely match the observed deformations in the mine in question and appears to be a very useful tool for designing a suitable roof support system. The most important conclusion drawn from this work is the importance of identifying strata of significantly lower strength or major bedding planes with low strength infill which will control the deformation behaviour of the roof strata. However the whole aim of the modelling undertaken by the author is to reduce instability so no effort is made to model post failure behaviour or roof collapse mechanisms.

González-Nicieza *et al.* (2008) also used numerical modelling software (FLAC and FLAC3D) to assess suitable roof support in longwall mine workings in Northern Spain. Similarly to the modelling work by Zipf (2006), the authors had access to the mine workings they were modelling and were able to directly take very detailed cores and samples for a full range of characterisation, strength and stiffness tests to derive intact rock properties. They then used the RMR, GSI and Q systems to derive rock mass properties and support requirements. The major difference between this work and that undertaken by Zipf (2006) is in the use of three-dimensional modelling and the use of a parametric study to identify the minimum supporting pressure necessary to stabilise the roof. As such they obtained results for sub-critical support pressures (*i.e.* pressures that were insufficient to adequately support the roof) resulting in failure. An example of this is shown in Figure 2.25, where large vertical velocity vectors can be seen oriented down from the roof into the void space and a significant shear strain has occurred both within the excavation roof and into the rock mass above the un-mined coal seam. The non-zero velocity vectors and shear strain rate contours indicate that the failure is progressive and that the roof is currently unstable and further displacement and shear strains will occur.

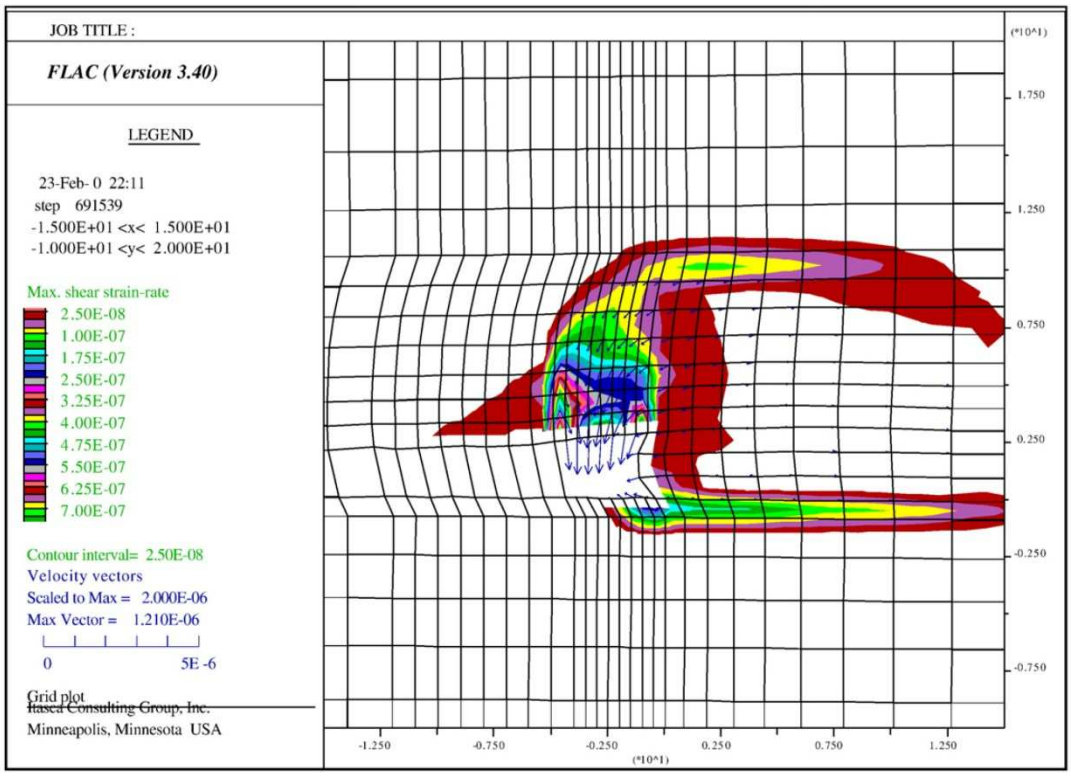

Figure 2.25: Plot of shear strain rate and velocity vectors around a longwall face with a sub-critical support pressure resulting in roof failure (after González-Nicieza *et al.*, 2008).

As well as two-dimensional modelling, the authors undertook three-dimensional modelling to investigate the effect of variations on seam dip on roof stability and support requirements. During this portion of the work it was found that there was a negligible difference between the results for two and three-dimensional modelling or due to the 30° dip of the seam in the three-dimensional model, with a critical support pressure of 77 kPa and 75 kPa for the two and three-dimensional models respectively. Of more impact was the initial *in-situ* stress in the model, whereby the authors found that increasing the ratio of horizontal to vertical stress (or co-efficient of lateral earth pressure - K_o) led to an increase in the critical support pressure suggesting that increase in horizontal stress were leading to a decrease in roof stability. However the authors did not consider this especially significant as large variations in K_o caused only small variations in the critical support pressure.

Laurence (2009) has undertaken an investigation into gateroad roof support requirements in longwall mine workings in Australia using the three-dimensional FDM code FLAC3D with the aim of developing a design criterion for roof support. The specific numerical modelling results are not applicable to the problem of mining subsidence however the conclusions drawn by the author on the choice of rock mass

characterisation systems is of direct interest in that use was made of both the CMRR and GSI systems to derive the numerical modelling parameters, which is further evidence for their usefulness (particularly GSI) in mining studies.

Yasitli and Unver (2005) and Xie *et al.,* (1999) have undertaken three-dimensional modelling of thick seam long wall mining in a Turkish coal mine and a coal mine in China respectively. In both cases the studies were undertaken using the three-dimensional numerical modelling code FLAC3D. The longwall mines in question are of greater depth (circa 225 m of overburden) with resultant increased *in-situ* stresses and a very different geometry than a UK shallow pillar and stall working with large 450 m – 650 m long, by 90 m – 150 m wide panels as opposed to the much smaller room and pillar workings common to UK shallow workings). See Figure 2.26.

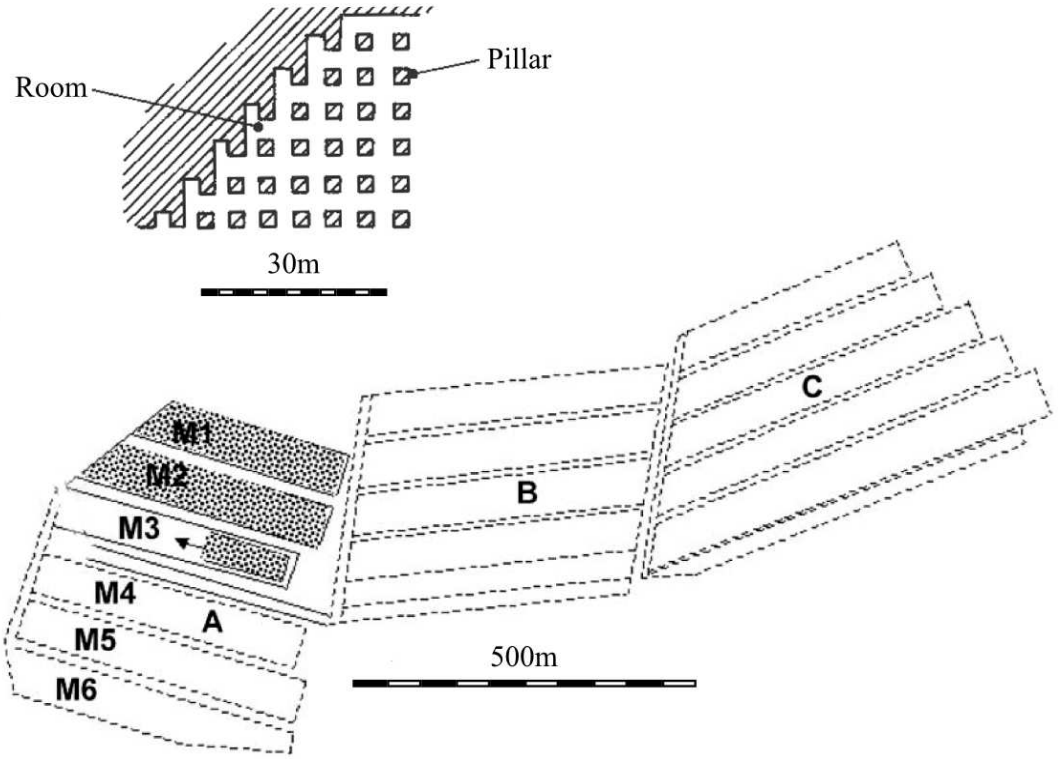

Figure 2.26: Difference in geometry and scale between a typical UK shallow room and pillar working and Turkish longwall mine workings (adapted from Healy and Head, 2003 and Yasitli and Unver, 2005).

Despite these differences the work in question is still of interest as the authors of the paper have modelled top coal caving in thick seam workings (seam thickness greater than 4.8 m). Top coal caving is a process whereby the face is located at the floor of the seam and the coal above the face is extracted by means of roof collapse (either due to the presence of natural fractures or blasting) through windows (of 1.5 m – 3 m width) located in the shields (roof supports) behind the face. In both papers the aim of the

modelling is to identify how to improve or increase the “draw” of coal through the windows to maximise extraction volume and extraction rate. In this case draw is defined as the flow of coal through the shield window into the working.

This is important as numerical modelling is predominantly used to assess roof stability (or lack thereof) and then allow the design of roof support to prevent failure, rather than to model the collapse mechanism of a failed roof as in these papers. As such the methodology outlined in here is of interest as it suggests that the modelling of the initial roof instability which occurs in pillar and stall workings should be feasible as the windows in the support shields can be considered analogous to the span of an unsupported roof at room intersections.

An example of the output from FLAC3D collapse modelling in Yasitli and Unver’s paper (2005) is given below in Figure 2.27.

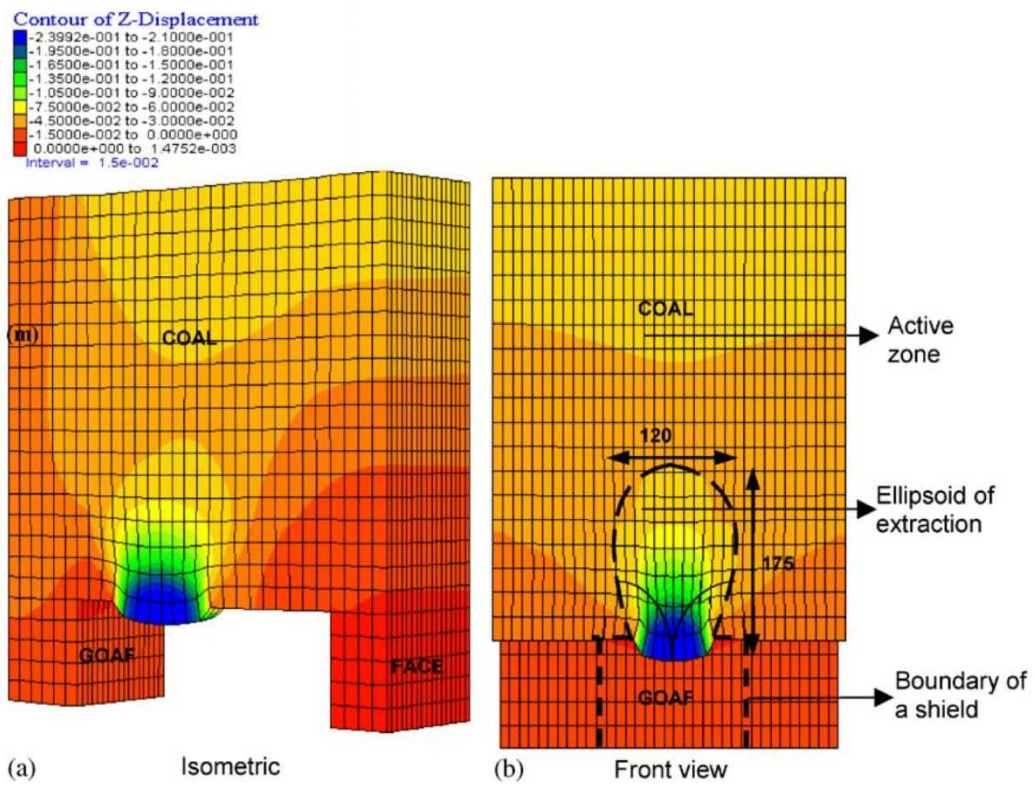

Figure 2.27: Contours of displacement (in metres) indicating the deformation in the zone of collapse in the top coal (after Yasitli and Unver, 2005).

Figure 2.27 shows the contours of displacement above the window in the shield where top coal caving has occurred. In this example the top coal has assumed to have undergone blasting with explosives (effects of blasting are assumed to simply cause a

reduction in strength properties as the blasting is assumed to create heterogeneous fractures which are very difficult / impossible to model discretely in FLAC3D) to assess the effect on the failure mechanism and the total displacement of the roof above the shield window. Predictably the maximum displacement occurs in the top coal directly above the window (the blue contour indicating a displacement of between 0.21 and 0.24 m).

A significant drawback with this methodology however exists in that although it appears to be very useful in assessing the geometry of the zone of initial ductile yielding within the roof strata that occurs while the roof is still behaving as a continuum (*i.e.* the sagging of roof strata as shown in Figure 2.13) it is unable to model the brittle failure that results in the roof strata collapsing into the workings, which in turn results in the void migration that occurs when shallow pillar and stall mine working collapse (the mechanism demonstrated in Figure 2.9 and Figure 2.14).

In an attempt to overcome this problem Singh and Singh (2009) while improving the modelling of powered roof support in longwall mine workings in India, have also modelled the progressive caving of roof strata using the two-dimensional finite difference code FLAC.

Their aim was to identify the optimum time to emplace powered roof support in response to roof deformation. To achieve this they modelled the post excavation roof deformation behaviour. This commences with an immediate post excavation elastic stage, through an arching and self-supporting stage and as excavation continued a stage where failure would ultimately occur.

These stages are represented in Figure 2.28 where the section of the ground response curve between points A and B represents the elastic displacement of the roof at very high stresses. The section between points B and C represents the arching of the rock mass above the excavation with a reduction in stress and finally beyond point C with continued excavation failure occurs resulting in roof collapse.

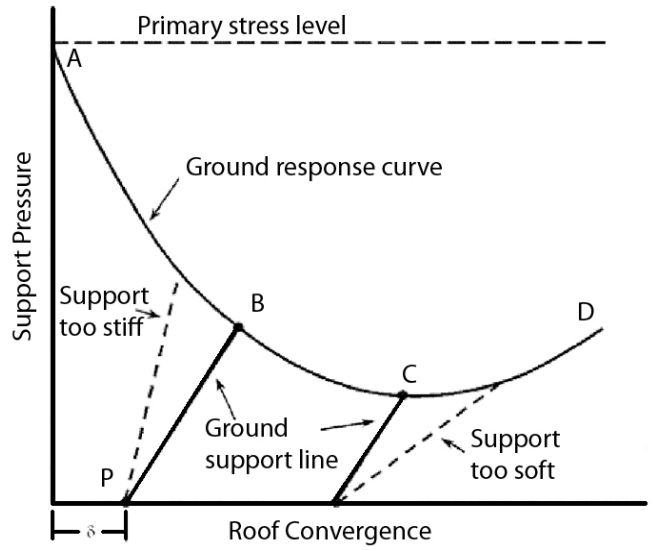

Figure 2.28: Stages of roof response related to support requirement (after Singh and Singh, 2009).

In this research the authors selected the Mohr-Coulomb constitutive model to simulate roof failure as it required the lowest number of assumptions about the rock mass while giving an accurate representation of the rock mass behaviour under the stress conditions encountered under excavation.

However Singh and Singh (2009) concluded that while the Mohr-Coulomb criteria is suitable for modelling the initial elastic and plastic yielding of the roof, it would require modification to better approximate the post failure or caving behaviour of the roof strata using a custom FISH function (FISH being FLAC's inbuilt programming language, Itasca, 2005). In their work a function was written that would monitor the shear strain and vertical displacement of an element that was shown to have failed in tension (based on the tension cut off method used in the Mohr-Coulomb model). Initially on detection of tensile failure, the elements cohesion would be set to zero (justified based on their observations of laboratory data) and the FISH function would continue to monitor the vertical displacement and shear strain within the element. If these parameters exceeded a prescribed level (0.25 strain or 1 m vertical displacement) the element was assumed to have caved and was removed from the model.

The progression of roof collapse over the longwall workings during face advance can be seen in Figure 2.29.

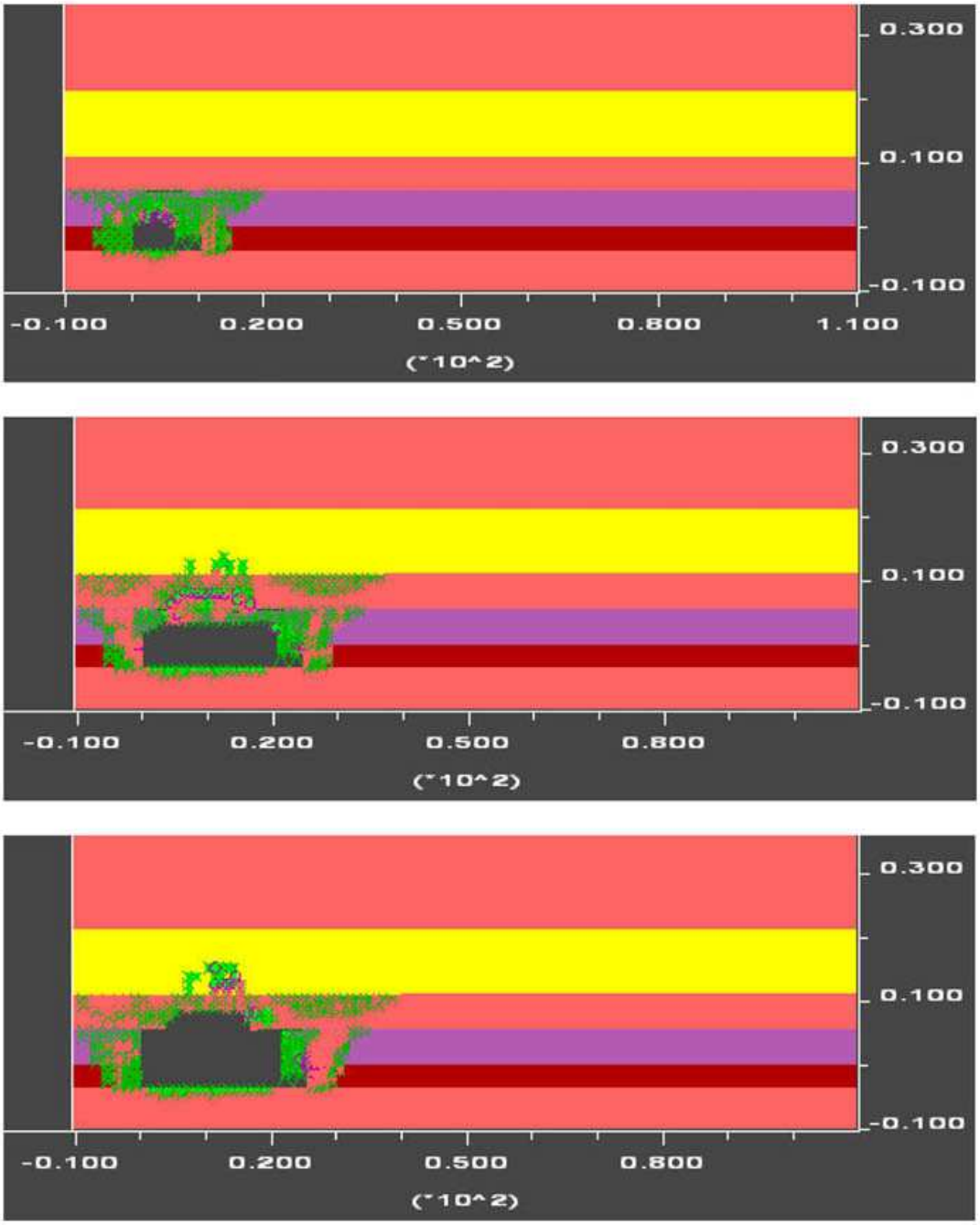

Figure 2.29: Progressive roof collapse during longwall face advance (Singh and Singh, 2009).

2.5.4 Pillar and Stall Mine Workings

Singh *et al.*, (2002) and Zipf (2005) investigated instability in contiguous or multi seam pillar and stall and longwall coal mines in India and the USA respectively. In both papers use was made of the continuum finite difference code FLAC (and in the case of Singh *et al.*, (2002) FLAC3D modelling was also undertaken) to investigate the parameters affecting parting stability in these types of workings.

In India, coal seams are defined as contiguous if the parting (*i.e.* non mined strata) thickness between any two seams is less than 9m. In these situations the pillars and roadways in under and overlying seams must be super imposed. However even where this rule is followed, collapse events have still occurred. The authors of the paper ran a parametric study to identify the key factors in parting (in)stability with the aim of creating a simple tool to estimate the stability of differing partings and to suggest suitable methods of roof support. In the U.S. example however interburden (or parting thickness) is defined as being either close (7 m) or intermediate with a parting thickness of 24 m.

The main parameters investigated in these studies were as follows:

1. Depth of cover (Singh *et al.*, 2002 and Zipf, 2005).
2. Parting thickness / interburden thickness (Singh *et al.*, 2002 and Zipf, 2005).
3. Lateral shift or eccentricity between top and bottom seam roadways (Singh *et al.*, 2002).
4. Extraction ratio (varying both pillar and roadway widths; Singh *et al.*, 2002).
5. *In-situ* stress field (Singh *et al.*, 2002 and Zipf, 2005).
6. Rock mass strength (Singh *et al.*, 2002 and Zipf, 2005).
7. Order of extraction (Zipf, 2005).

Depth of Cover

The depths of cover chosen for the numerical investigation undertaken by Singh *et al.*, (2002) ranged between 100 m – 250 m in 50 m increments. Zipf (2005) chose overburden values commensurate with *in-situ* vertical stresses of 3 MPa, 6 MPa and 9 MPa roughly equivalent to a depth of 120 m, 240 m and 360 m respectively. These values are significantly deeper than that which is defined as a shallow working in the UK (<30 m) and hence will lead to a much higher *in-situ* stress field. The results for variation of cover depth on stability were predictable in that with increased depth of cover (and hence greater *in-situ* stress) and where all other parameters remain constant, the factor of safety for roof stability decreased (Singh *et al.*, 2002) as shown in Figure 2.30 and the size of the failed zone within the roof or floor of the excavation became larger (Zipf, 2005) as shown in Figure 2.31 where the rock mass around the excavation and as a whole shows progressively increasing failures as the vertical stress increases.

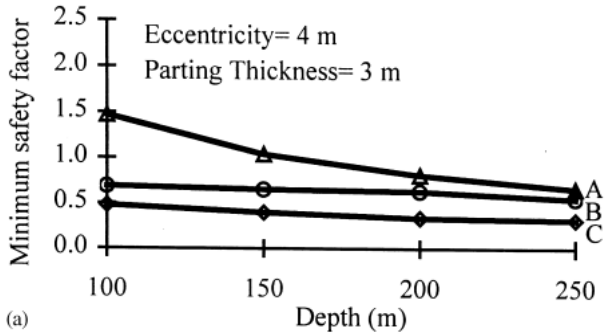

Figure 2.30: Variation of roof stability factor of safety with increasing cover depth (after Singh *et al.*, 2002).

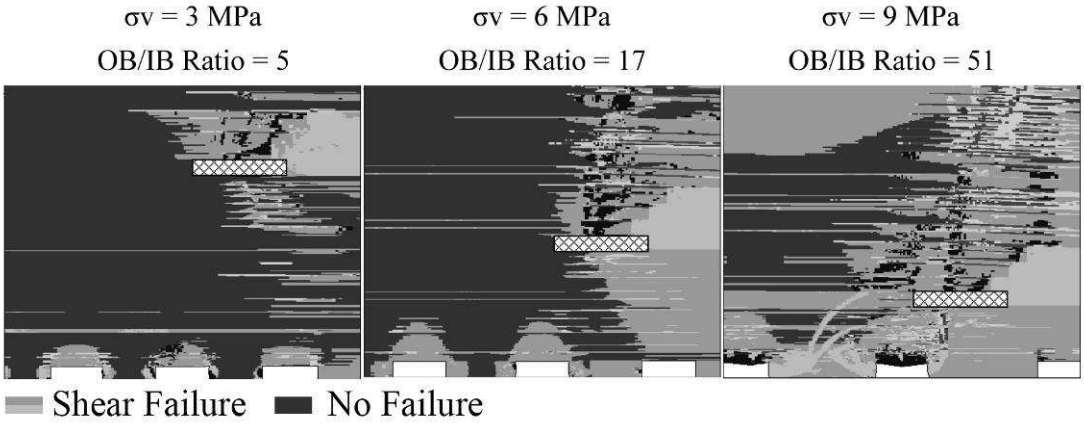

Figure 2.31: Variation in failure of rock mass around excavations with increasing vertical stress and increasing ratio of overburden thickness to interburden thickness (after Zipf, 2005).

One very interesting point that Singh *et al.*, (2002) made and which may be significant in terms of the choice of numerical modelling code for the investigation of roof instability was their decision to discard the inbuilt constitutive model (in this case the Mohr-Coulomb criterion in FLAC) in favour of their own criterion based on estimating safety factors within the parting using the Sheorey rock mass failure criteria. They reached this decision as they indicated that during the modelling of an obviously competent parting formation the initial model run using an elastic constitutive model gave high safety factors in the roof suggesting that no failure in the roof should occur, however, subsequent elasto-plastic analysis of the same problem led to yielding.

Unfortunately the authors have not presented any examples of this phenomenon in their paper so it is difficult to identify a cause. There are a number of possible explanations however. The constitutive models in FLAC may be unsuitable for this type of investigation. This is unlikely as FLAC was developed for the mining and geotechnics industry and so was expressly designed for investigations such as this. Also FLAC has been widely used by other authors (Yasitli and Unver, 2005; Xie *et al.*, 1999; Zipf, 2005; Zipf, 2006; Singh and Singh, 2009) in investigations into the stability of

underground excavations, none of whom seem to report the same problem. Another potential factor in this case is the subjective nature of the interpretation of failure in FLAC. The user's manual (Itasca, 2005) states that "plastic indicators" usually indicate that plastic flow is occurring, although an element may simply sit on the yield surface without any significant flow occurring. As such, it is necessary to examine the whole pattern of plasticity indicators to see if a mechanism has developed. Such a mechanism is indicated if there is a continuous line of active plastic zones that join two surfaces. This can be further confirmed if the velocity plot also indicates motion corresponding to the same mechanism.

Another potential cause of this erroneous yielding is the dynamic nature of the FLAC solution scheme which is quasi-static (*i.e.* the full equations of motion are used during model stepping, as such, to provide a "static" solution damping is used to remove kinetic energy from the system). Ultimately this means that any sudden changes to the model *e.g.* sudden excavation of the road ways can lead to a disturbance of the forces at grid points which in turn can induce unexpected yielding such as found by the authors. The FLAC manual contains a number of solutions to this problem however it is not clear whether this may have been an issue in this particular modelling study as the authors have not described their modelling procedure, particularly the steps taken in installing boundary conditions or in the excavation of the roadways.

Parting Thickness / Interburden Thickness

Parting thicknesses in the Singh *et al.*, (2002) study ranged from 1.2 m to 9 m. As parting thickness increased, the minimum factor of safety (FoS.) increased. This is unsurprising as the stress disturbance from the normal *in-situ* values will diminish with increased distance from the excavations and so with a greater parting thickness there will be less interaction between the stress fields around the two excavations. In their results they found that the variation in the minimum FoS reached a plateau at a parting thickness of approximately 6 m for all cover depths tested and for all eccentricity values. This would suggest that at parting thicknesses greater than this value, the stress fields around the under and overlying excavations are no longer interacting. However the strength and stiffness properties of the rock mass or coal seam for these initial studies has not been varied, as such this 6 m limiting value is site specific and not more widely applicable to other coal measures strata around the world.

Zipf (2005) states that interburden or parting thickness alone is a less significant parameter than the ratio of the overburden thickness (and hence vertical stress) to the interburden thickness described as the overburden/interburden (OB/IB) ratio. Based on case studies (undertaken on previous contiguous mine workings) by Ellenberger (2003) it was found that an OB/IB ratio of 7 was the critical value below which no interaction occurred and conditions in the seam were identical to those areas where no contiguous mining had occurred. An OB/IB ratio of greater than 7 indicated that multi seam interaction would occur that may potentially lead to damage but this interaction was described as "moderate" (defined as the potential for damage to the rock mass, but where mining was still possible). Finally OB/IB ratios greater than 16 may lead to "extreme interactions" with significant implications for both coal extraction and mine safety as parts of the coal seam were rendered "unmineable".

The numerical modelling work undertaken by Zipf (2005) supported this hypothesis suggesting that workings with an OB/IB ratio of 5 or below would not interact under any circumstances whereas extreme interaction would occur in all cases where the OB/IB ratio was equal to 50. Sites where intermediate OB/IB ratios of around 17 were modelled showed mixed interaction of multi seam workings (ranging from none, through moderate to severe as defined by Ellenberger (2003)) depending on other parameters such as rock mass strength and horizontal stress.

Lateral shift or Eccentricity of the Workings

Eccentricity of the workings was investigated by Singh *et al.,* (2002) who define this as the horizontal distance between the centreline of the overlying and underlying roadways (assuming equal pillar size). The eccentricity value is at a minimum when the over and underlying roadway centre lines are exactly aligned vertically and at a maximum when the overlying seam roadway centreline overlies the centre of the underlying pillar (see Figure 2.32).

Interestingly they found that stability increased as the eccentricity increased, reaching a maximum factor of safety at the maximum eccentricity with the minimum FoS found when the eccentricity value was equal to 0.5 m, however it is worth noting that in this study, the pillar widths were kept constant at 24 m and the roadway widths at 4 m.

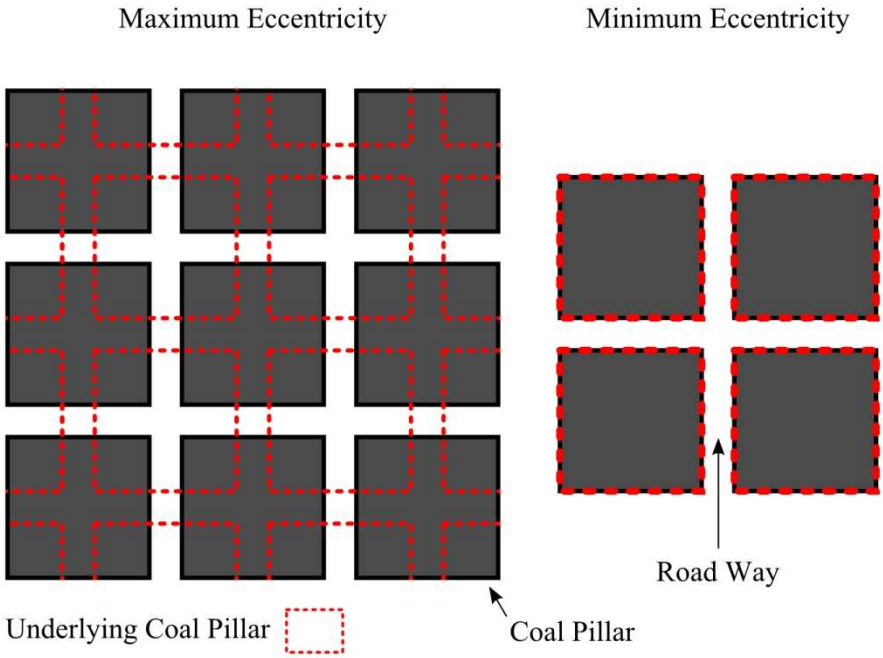

Figure 2.32: Variation in eccentricity of contiguous pillar and stall workings.

This pillar thickness is significantly larger than the width expected in UK shallow workings where pillar thicknesses range from 2.5 - 9.5 m (Attewell and Taylor (1984) and Waltham (1989). The roadway thickness is also at the upper boundary of the range of values expected in the UK, where excavation widths are commonly in the range of 2 – 5 m (Attewell and Taylor, 1984). The variation between a typical UK and Indian pillar and stall contiguous seam working with maximum eccentricity is shown in Figure 2.33.

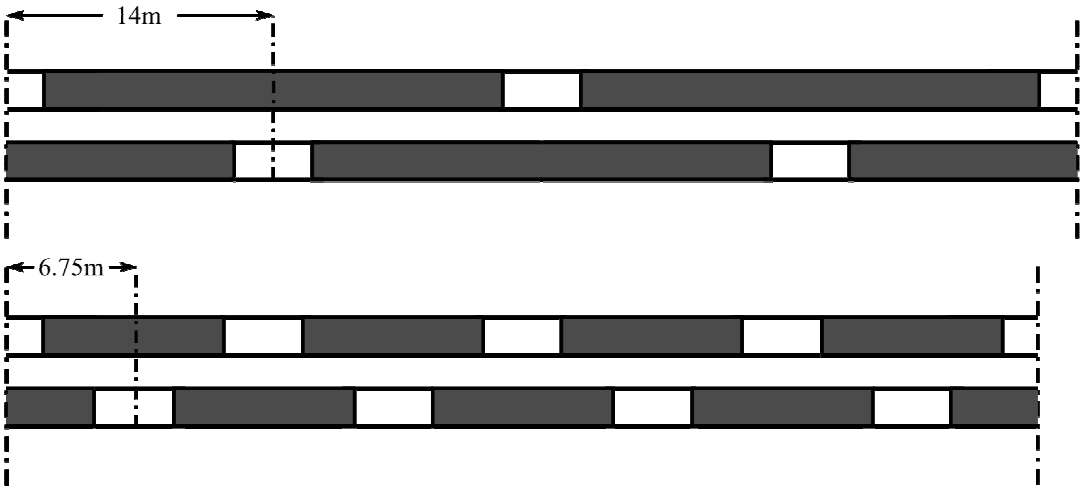

Figure 2.33: Plot of variation in geometry at maximum eccentricity between the specific Indian mine modelled (Top) in the study and a UK contiguous pillar and stall working (Bottom).

From the above it is clear that the maximum eccentricity is limited by the relatively narrow coal pillars and roadways found in shallow pillar and stall workings within the UK (in Figure 2.33 the maximum suggested values of pillar and room width are used for the UK example), as such the increased stability found with increasing eccentricity will be of lesser importance in UK workings. The graphs presented by the authors (and reproduced here, see Figure 2.34) appear to demonstrate that the importance of eccentricity in stability is influenced strongly by both the parting thickness and the *in-situ* horizontal stress field. With increasing parting thickness, any increase in eccentricity results in progressively lower improvements in the minimum FoS, with the limiting value of parting thickness being approximately 6 m (*i.e.* above this value, the variation in eccentricity makes virtually no difference to the roof stability minimum FoS). Of more interest is the sudden reduction in FoS found when the eccentricity drops below 1 m (for all values of parting thickness, *in-situ* horizontal stress and depth of cover) as this value is within the range that may be found in UK shallow abandoned workings and so this phenomenon may also occur in shallower workings. The variation in *in-situ* horizontal stress also appears to have a strong influence on the stability of the excavations at all the eccentricity values tested here and would seem, from the results presented by the authors to be a significant parameter in parting stability.

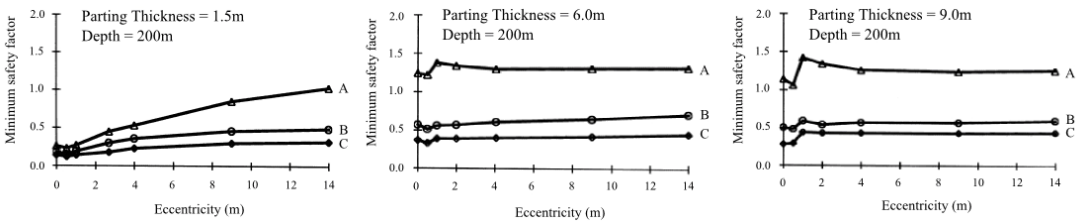

Figure 2.34: Variation in minimum factor of safety with varying eccentricity for differing *in-situ* stresses and parting thickness (after Singh *et al.*, 2002).

Variation in Extraction Ratio / Pillar and Room Thickness

Singh *et al.*, (2002) investigated the effect of varying the extraction ratio in two differing ways, the pillar widths were varied from 4 – 24 m while maintaining a constant roadway (stall) width of 4 m and the roadway widths were varied from 3 to 8 m while maintaining a constant pillar width of 24 m. The roadway widths are in excess of those expected in shallow UK workings and the pillar widths are significantly larger than the UK examples where excavation widths are commonly in the range of 2 - 5 m (Attewell and Taylor, 1984) and pillar thicknesses range from 2.5 - 9.5 m (Attewell and Taylor (1984) and Waltham (1989). Zipf (2005) did not vary the dimensions of the excavated workings as a parameter; instead keeping them constant with 6 m wide rooms

and pillars (these values being much closer to the dimensions of UK shallow abandoned workings).

The results of Singh *et al.,* (2002) appear to indicate that it is the variation in the roadway (stall) thickness that has the greatest impact on stability rather than the thickness of the pillar or the extraction ratio (a combination of variation of both pillar width and roadway width).

In-situ Stress Field

Singh *et al.,* (2002) found that for a given depth of cover, the stability of the roof in the pillar and stall workings decreases as the applied horizontal stress increases relative to the vertical stress. Based on the three-dimensional modelling they observed that where the horizontal stresses were anisotropic, the major horizontal stress had a much greater impact on roof stability than the minimum horizontal stress (which they considered to have a negligible effect on roof stability). Zipf (2005) took a differing approach and rather than varying the initial horizontal stress applied a constant value for all models and instead monitored the variations in the stress fields as the contiguous mining was simulated in the model. Their results suggest that the ratio of horizontal to vertical stress and horizontal stress to roof strength are important parameters in mine working stability.

Rock Mass Strength

Variation in rock mass strength of the roof strata showed (unsurprisingly) that as the rock mass strength increased, the roof stability also increased. The study by Singh *et al.,* (2002) used the Rock Mass Rating (RMR) system of Bieniawski (1976) to define rock mass strength and stiffness properties; however no explanation was given for the choice of this system over any other rock mass strength assessment method. The RMR value was varied from 50 – 80 in increments of 10. Zipf (2005) used the Coal Mine Roof Rating system to derive rock mass properties which is the preferred method of the National Institute for Occupational Safety and Health (NIOSH) in the US and is intended to be used to aid the design of roof support in active coal mines. As Zipf (2005) had access to detailed core logs and lab test data, he chose to use the ubiquitous joint strain softening model available within FLAC, however derivation of the necessary parameters without laboratory test data is difficult so this model is not always suitable.

Perhaps the most interesting conclusion drawn by Singh *et al.,* (2002) is that there is very little difference between the results obtained for two-dimensional and three-dimensional modelling of pillar and stall workings. The statistical analysis of the two sets of results gave a coefficient of determination of 0.97 (*i.e.* 97% of the two and three dimensional model results are a match). This appears to be supported by the results of González-Nicieza *et al.,* (2008) who found that the two and three-dimensional modelling results (in this case for the critical roof support pressure required to stabilise a longwall mine roof) were nearly identical.

Back Analysis Using Discrete Element Modelling

While predominantly numerical modelling of stability of mine workings is undertaken using continuum codes, the discrete element method is also used and an interesting case study of its use is presented here.

Alejano *et al.,* (2008) have undertaken a numerical investigation into a roof failure that occurred in a hard rock pillar and stall mine in Spain using the two-dimensional discrete element code UDEC.

The mine in question is a magnesite mine with room and pillars of 12 m and 7 m widths respectively. No instability of the pillars had been reported, however the roof strata were of relatively low geotechnical quality, so a 1 m thickness of magnesite is left in place to strengthen the roof and rock bolting is used for further reinforcement. In March 2004, on advancement of a room, a normal fault was crossed with a throw of 0.5 m. This advancement continued for around 20 m without any reinforcement. However the fault throw had reduced the thickness of the magnesite roof beam to 0.5 m. The roof was initially stable, but during excavation of a neighbouring room, failure of the roof in the whole of the unsupported area of the original room occurred. This affected the magnesite roof beam and extended a further 2 m up into the overlying strata leaving what the authors describe as a bell shaped zone formed in the roof which appears to have stabilised due to natural arching.

In order to model the failure accurately using the discrete element code, the authors undertook a laboratory test program on the rocks including UCS testing, triaxial testing, Young’s modulus and Poisson's ratio tests as well as point load, tensile strength and tilt

tests. Further to the laboratory testing, a detailed discontinuity survey was undertaken in the area surrounding the collapse, where a total of 135 discontinuities were measured and all relevant geomechanical information for each was recorded. Upon stereographic analysis it was found that there were five main joint sets (one due to bedding, two cross joint (*i.e.* normal to bedding) and two secondary

This highlights the very detailed information required for the use of discrete element models and the authors state that for the back analysis of a single problem, distinct element codes such as UDEC are very useful in that they can very accurately recreate the orientation and spacing of the discontinuous rock mass, however, the modelling process needs to be painstaking, due to the difficulty in estimating the geomechanical parameters of rocks and discontinuities realistically (requiring laboratory tests) and the detailed site investigation or (as in this case) access to the workings to directly assess discontinuity spacing and orientation.

The authors also undertook rock mass characterisation using the RMR and Q-systems and used these systems to derive strength and stiffness properties for the rock mass. They ultimately produced a numerical model of three parallel rooms and their pillars and incorporated the joint sets found in the discontinuity survey to produce a highly detailed model of the workings where the failure occurred as shown in Figure 2.35. This also shows the boundary conditions applied to the model, with a vertical stress applied to the upper boundary equivalent to 200 m of overburden and horizontal stresses equal to approximately 1.1 times the vertical stress for a given depth. The roof strata itself is assumed to behave as a voussoir arch as suggested by Diederichs and Kaiser (1999) and discussed in section 2.2.3. In order to attempt to recreate the roof failure event as described, the authors undertook a phased excavation process. Initially the central room was excavated and ultimtely stabilised with a roof deflection of around 55 mm. This is shown in Figure 2.36. Then the excavation of the parallel room was simulated which ultimately leads to roof failure in the original room as seen in Figure 2.37.

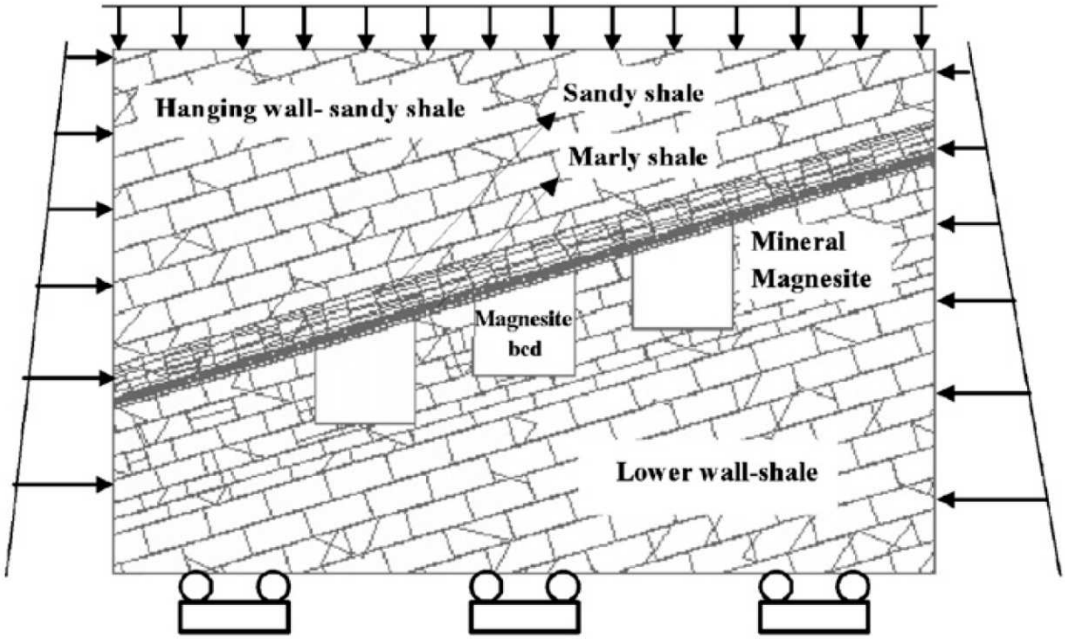

Figure 2.35: Model geometry and boundary conditions (after Alejano *et al.*, 2008).

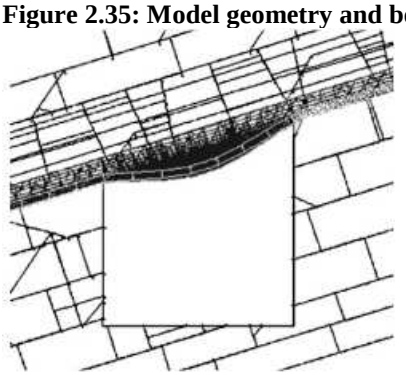

Figure 2.36: Excavation of first room. Initially roof is stable with a deflection of 55 mm (after Alejano *et al.*, 2008).

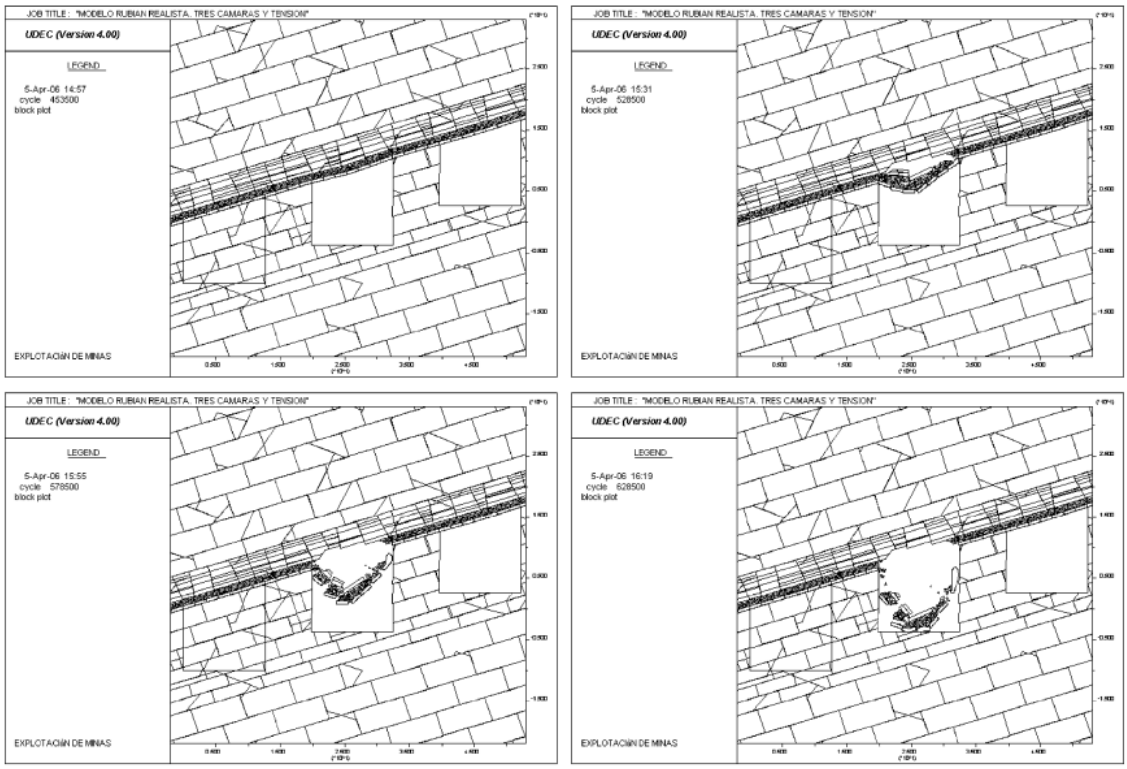

Figure 2.37: Failure of central room roof due to excavation of parallel room causing stress relaxation and ultimately failure (after Alejano *et al.*, 2008).

2.6 Conclusions

In this chapter a review of the types of shallow mining subsidence (sag / areal subsidence, void migration) has been undertaken along with the common causes (pillar crushing or punching of the pillar through soft underlying material along with roof failure). Differing causes of roof failure were reviewed and summarised in greater detail as the phenomenon of void migration is predominantly controlled by the failure and collapse of the strata forming the excavation roof in abandoned coal mine workings.

Observations of void migration chimneys in the field (for example during excavations in open cast mines) suggest that the primary factors that halt void migration are choking of the void by bulked collapse debris, the presence of a high strength / thickly bedded stratum in the overlying rock mass or by arching (the formation of a natural stable arch over the void). As rock masses are highly anisotropic, heterogeneous and discontinuous materials it is necessary to derive rock mass strength and stiffness properties form intact laboratory properties. A number of rock mass strength assessment systems were reviewed that allowed the derivation of scaled strength and stiffness parameters for modelling that account for the reduction in strength and stiffness due to the presence of discontinuity surfaces.

In order to allow the effective modelling of the behaviour of rock masses representative of coal measures strata, a review of numerical methods and numerical modelling software was undertaken. In this section, examples of the modelling of mines and subsurface excavations were also summarised in order to better understand the methodology commonly employed in subsidence or roof collapse modelling and also in deriving appropriate numerical modelling parameters.

In the next chapter, the numerical modelling code FLAC 3D is discussed and a preliminary numerical modelling study is undertaken to investigate the parameters that are important in the stability of shallow abandoned colliery workings.

Chapter

3

Parametric Study Phase 1 – Initial Numerical Modelling of Shallow Abandoned Mine Roof Stability

3 Parametric Study Phase 1 – Initial Numerical Modelling of Shallow Abandoned Mine Roof Stability

In this chapter the finite difference numerical modelling code FLAC3D is introduced and some of its significant features are described. Following this a phased numerical modelling study is introduced to investigate the parameters that the literature review indicated may be significant in terms of stability of shallow mine workings and other subsurface voids in rock.

Initial studies were undertaken using a linear elastic perfectly plastic model to investigate these parameters using the continuum assumption and a Mohr-Coulomb plasticity model. Once the key parameters were identified, a second phase of modelling work was undertaken using more sophisticated constitutive models including the strain softening ubiquitous joint model which allows the anisotropic behaviour of a rock mass with a persistent joint set, in which the joint dip angle and the joint properties can be varied from that of the rock mass as a whole to be captured. The standard strain softening Mohr-Coulomb model was also used which replicates post yield strength loss by varying the values of cohesion, friction and tensile strength which more accurately captures the failure behaviour of rock masses.

3.1 Fast Lagrangian Analysis of Continua in 3 Dimensions – FLAC3D

FLAC3D is a three-dimensional explicit finite-difference program for engineering mechanics computation, simulating the behaviour of three-dimensional structures built of soil, rock or other materials. FLAC3D was developed primarily for geotechnical engineering applications, mainly problems in the fields of mining, underground engineering, rock mechanics and research (Itasca, 2005).

In FLAC3D the structure to be modelled is represented as a series of elements or zones forming a mesh or grid. The user can adjust the grid shape to recreate the geometry of the object of interest. For each element in the mesh, the behaviour is controlled according to a prescribed linear or nonlinear stress/strain law in response to applied forces or boundary restraints. This allows the material to yield and flow, and the grid to deform and move with the material that is represented (Itasca, 2005).

3.1.1 FLAC Solution Scheme

As stated in section 2.4.2, FLAC3D uses an explicit time marching scheme in order to find the solution to a given problem. A diagram illustrating this process is included. Please see Figure 3.1.

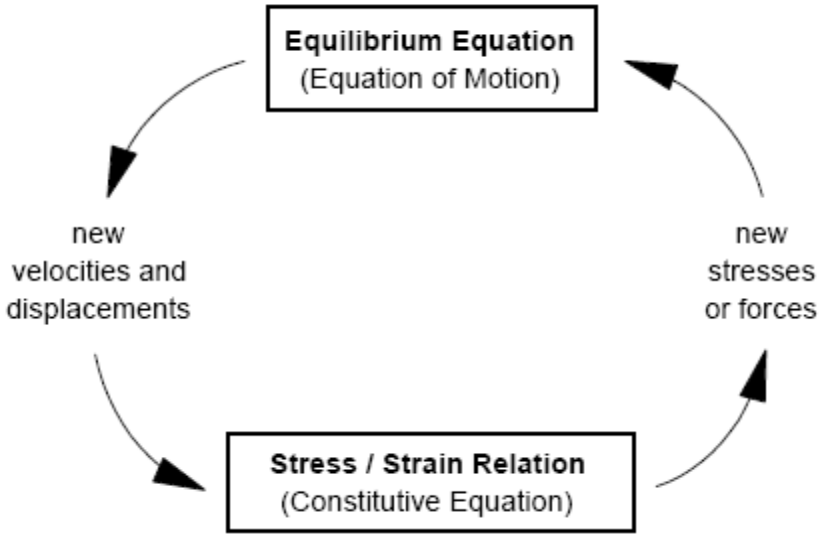

Figure 3.1: FLAC basic explicit calculation cycle diagram (Itasca, 2005).

Figure 3.1 shows the cycle of one calculation step. Within the upper box the equations of motion are invoked to calculate velocities and displacements from the stress and forces of the problem to be modelled. These velocities and displacements are then used to derive strain rates, from which updated stresses or forces are calculated using the specified constitutive model as shown in the lower box (Itasca, 2005). For each calculation cycle the variables remain fixed and are known.

In order for this approach to be valid, the time step for each calculation cycle must be smaller than the time taken for information to propagate from one zone to another. The size of the time step is controlled by the stiffness of the modelled materials and the grid spacing.

3.1.2 Problem Solving using FLAC

The general solution procedure as used by FLAC is summarised in the following section.

In order to setup and run a model in FLAC it is necessary to specify three main components:

1. The finite difference grid
2. Constitutive models and material properties
3. Boundary and initial conditions

The grid is used to define the geometry of the problem within FLAC3D. The constitutive behaviour and related material properties control the response the model will display when it is disturbed. The boundary and initial conditions define the *in-situ* state (*i.e.* the condition before a change or disturbance in the problem state is introduced). After these conditions are defined in FLAC3D, the initial equilibrium state is calculated for the model. An alteration is then made (*e.g.*, excavate material or change boundary conditions), and the resulting response of the model is calculated.

3.1.3 Elastic Bulk Modulus and Elastic Shear Modulus

The bulk and shear modulus parameters control the pre failure elastic deformation of the material under loading and are derived from Young's modulus and Poisson's ratio (Itasca, 2005).

$$K = \frac{E}{3(1-2\nu)} \tag{3.1}$$

$$G = \frac{E}{2(1+\nu)} \tag{3.2}$$

Where

K = Bulk modulus (Pa)

G = Shear modulus (Pa)

E = Young's modulus (Pa)

ν = Poisson's ratio

Where Young's modulus (E) defines the relationship between the axial stress (σ_n) and axial strain (ε_n) and Poisson's ratio (υ) defines the relationship between the radial strain (ε_r) (*i.e.* the strain occurring in a direction normal to applied load) and the axial or parallel strain (ε_n).

$$E = \frac{\sigma_n}{\varepsilon_n} \tag{3.3}$$

$$\nu = \frac{\varepsilon_r}{\varepsilon_n} \tag{3.4}$$

Young's modulus for most intact rocks = 5 GPa to 70 GPa

Poisson's ratio for most intact rocks = 0.25 to 0.4

Typical values taken from Bell (1992a), Goodman (1980), Twiss and Moores (1992) and Itasca (2005). However, the elastic values for the rock mass are likely to be significantly lower and as such it will be necessary to apply a correction factor, such as that used in the Hoek-Brown criterion to derive strength and stiffness properties from the GSI system to in turn derive the elastic modulus of the rock mass from intact rock strength and stiffness properties.

3.1.4 Constitutive Models and Yield Mechanisms

The models within FLAC can be divided into null, elastic and plastic models. Within the elastic models the stress/strain relationship is linear and all strains are recoverable. The plastic models within FLAC involve some degree of non-recoverable deformation. The constitutive models used in this work are summarised in the following sections.

Null Model

In FLAC3D a null material model is used to represent material that is removed or excavated. As such, all stresses in the affected zones are set to zero.

For sequential static analyses, such as that undertaken in this work, it is necessary to minimise the effect of transient waves when problem conditions are changed suddenly (Itasca, 2005) such as during the instantaneous creation of the void zones in the model representing the gradual process of excavation of the rooms in pillar and stall workings. The FLAC manual (Itasca, 2005) recommends the following methods to ensure that unbalanced forces due to instantaneous creation of null spaces do not initiate failure:

There are two ways to make a FLAC3D solution more static:

1. When a sudden change is made (*e.g.*, by nulling zones to simulate excavation), set the strength properties to high values and step to equilibrium. Then set the properties to realistic values and step again to ensure that out-of-balance forces are low. In this way, failure will not be triggered due to transients.
2. Use a FISH function or table history to gradually reduce loads when material is removed

Mohr-Coulomb Model

This constitutive model is the most widely known and commonly used failure criterion for rocks (Goodman, 1989) and is the recommended model for making initial

investigations into geomechanics problems where yielding or failure is possible, but the post failure response of the material is less important and for problems with limited lab test or site investigation derived strength parameters (Itasca, 2005). Although this is well suited for modelling the conditions leading to initial failure (*i.e.* collapse initiation), it is not ideally suited for modelling the post failure response of the system (*i.e.* caving),

as this model assumes that when the strength of the material has been exceeded, it yields in a ductile fashion rather than a brittle manner. As such, cohesion is maintained and is still able to support a stress equal to the failure strength. This is adequate for initial sagging of roof strata, but not for ultimate collapse.

The Mohr-Coulomb failure criterion represents the linear envelope that is obtained from a plot of the shear strength of a material versus the applied principal normal deviatoric stress from triaxial tests (Parry, 2004).

This relation is usually expressed in the following form (Parry, 2004):

$$\tau_f = c' + \sigma_n \tan(\phi') \qquad 3.5$$

Where:

τ_f = shear strength,

σ_n = normal stress,

c' = cohesion (the intercept of the failure envelope with the τ axis)

ϕ' = angle of internal friction (slope of the failure envelope).

This two-dimensional relation is shown in Figure 3.2. The Mohr-Coulomb criterion in FLAC3D is expressed in terms of the principal stresses; σ_1, σ_2 and σ_3 which are the three components of the generalized stress vector for this model. The components of the corresponding generalized strain vector are the principal strains ε_1, ε_2 and ε_3 (Itasca 2005).

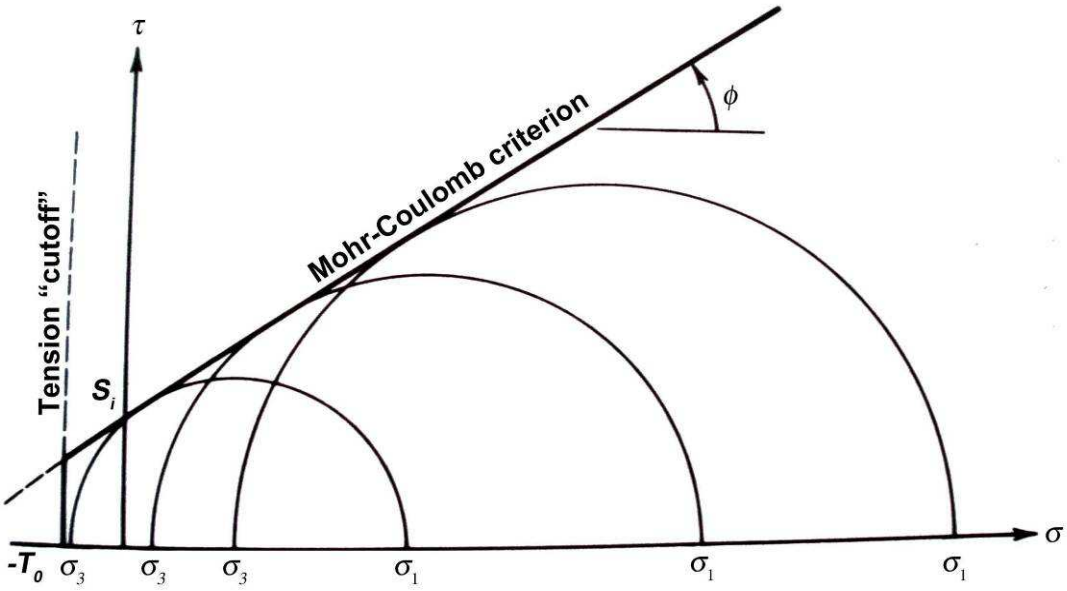

Figure 3.2: Mohr-Coulomb failure criterion with tension cut off (after Goodman, 1989).

Within FLAC3D compressive stresses are negative, therefore the principal stresses are ordered:

$$\sigma_1 \le \sigma_2 \le \sigma_3 \qquad 3.6$$

Corresponding strains Δe, are composed of elastic strains Δe^e and plastic strains Δe^p:

$$\Delta e = \Delta e^e + \Delta e^p \qquad 3.7$$

However the plastic increment of the total strain is zero if plastic deformation does not occur. In this situation where strain is purely elastic, the stress strain relationship is linear and follows Hooke's law, where the incremental expression of Hooke's law in terms of the generalized stress and stress increments is as shown below (Itasca, 2005):

$$\Delta\sigma_1 = \alpha_1 \Delta\varepsilon_1^e + \alpha_2(\Delta\varepsilon_2^e + \Delta\varepsilon_3^e) \qquad 3.8$$

$$\Delta\sigma_2 = \alpha_1 \Delta\varepsilon_2^e + \alpha_2(\Delta\varepsilon_1^e + \Delta\varepsilon_3^e) \qquad 3.9$$

$$\Delta\sigma_3 = \alpha_1 \Delta\varepsilon_3^e + \alpha_2(\Delta\varepsilon_1^e + \Delta\varepsilon_2^e) \qquad 3.10$$

Where α_1 and α_2 are material constants defined in terms of the shear modulus, G, and bulk modulus, K:

$$\alpha_1 = K + \frac{4}{3}G \qquad 3.11$$

$$\alpha_2 = K - \frac{2}{3}G \qquad 3.12$$

The Mohr-Coulomb criterion can be represented in the plane (σ_1, σ_3)as shown in Figure 3.3. The failure envelope in this case is defined by the line A-B in Figure 3.3 by the Mohr-Coulomb failure shear criteria $f_s = 0$.

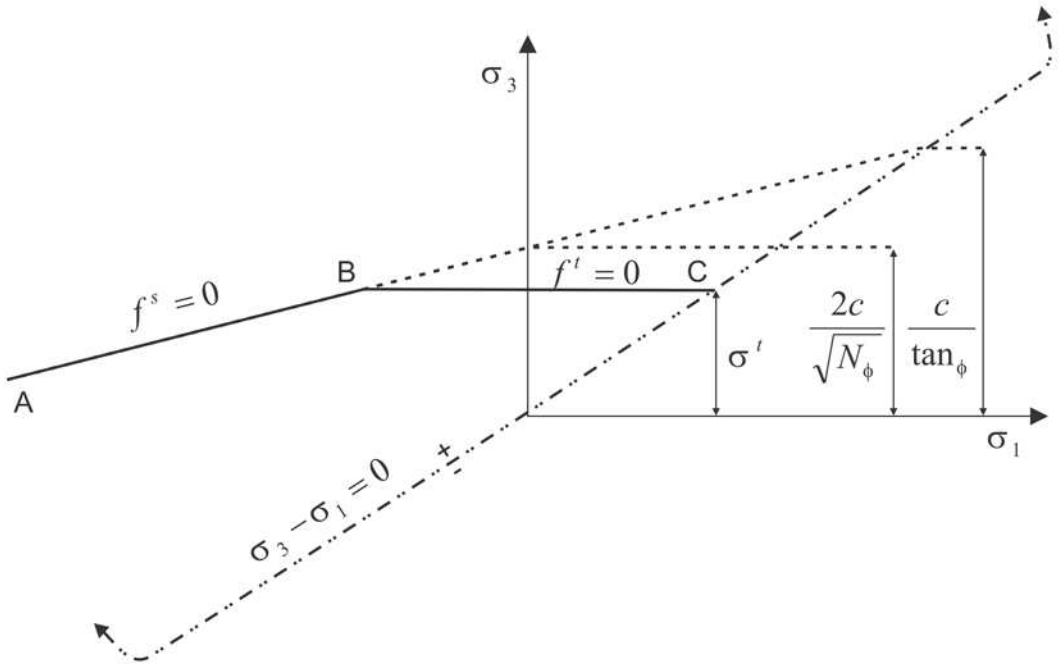

Figure 3.3: Mohr-Coulomb criterion in the plane (σ_1, σ_3) (Itasca, 2005).

$$f_s = \sigma_1 - \sigma_3 N_\phi + 2_c \sqrt{N_\phi} \qquad 3.13$$

And the tensile failure criteria which makes up the second portion of the overall failure envelope is defined by the line joining points B and C which takes the form $f_t = 0$

$$f_t = \sigma_3 - \sigma_t \qquad 3.14$$

Where:

ϕ' =friction angle (º)

c' = cohesion (Pa)

σ_t =tensile strength (Pa)

N_ϕ = see Equation 3.15

$$N_\phi = \frac{1+\sin\phi'}{1-\sin\phi'} \qquad 3.15$$

From Figure 3.3 it should also be noted that the tensile strength of the material cannot exceed the value of σ_3 which corresponds to the intersection point of lines $f_s = 0$ **and** $\sigma_1 = \sigma_3$ in the $f(\sigma_1, \sigma_3)$plane. This maximum value is given by:

$$\sigma_t \max = \frac{c'}{\tan\phi'} \qquad 3.16$$

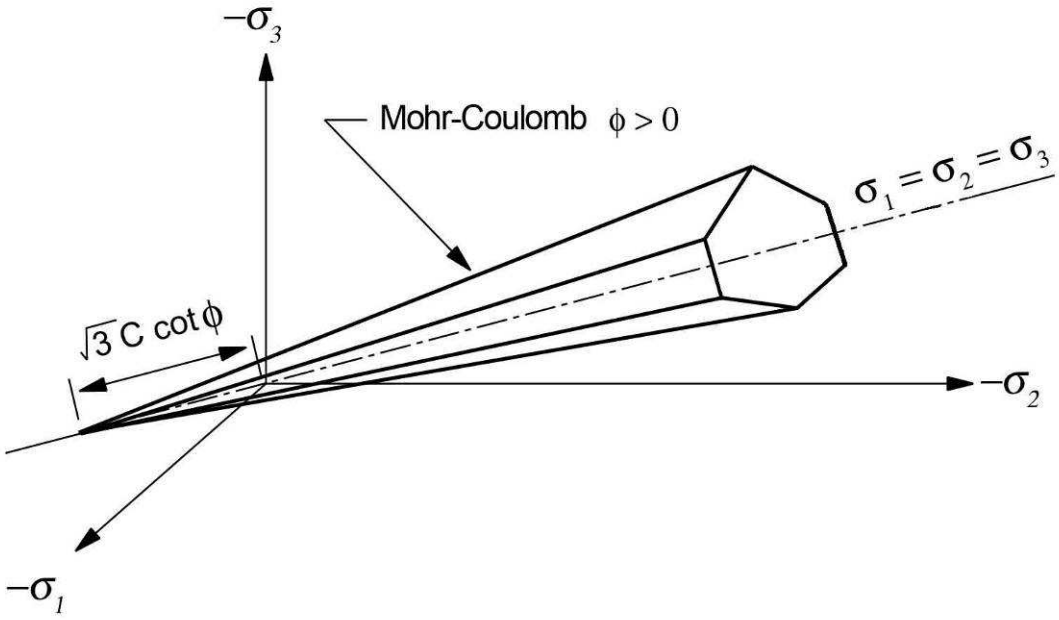

Figure 3.4: Mohr-Coulomb yield surface in principal stress space (after Itasca, 2005)

Strain-Softening Mohr-Coulomb and Ubiquitous-Joint Mohr-Coulomb Models

The strain-softening model allows FLAC to represent nonlinear material softening behaviour appropriate for materials that show an increase or degradation in shear and tensile strength when loaded beyond the initial failure limit. This softening behaviour is based on user prescribed variations of the Mohr-Coulomb model properties (cohesion, friction, tensile strength) as functions of the deviatoric plastic and tensile strains (Itasca, 2005). An example of this is included below.

A one-dimensional stress-strain curve, σ versus ε, which softens once the yield criterion is reached and then attains a residual strength value, is shown in Figure 3.5. The stress-strain curve is linear up to the point of yield. In this range, the strain is elastic only: $\varepsilon = \varepsilon^E$. After yielding has occurred however, the total strain is composed of both elastic and a plastic component: $\varepsilon = \varepsilon^E + \varepsilon^P$. The cohesion, friction angle and tensile strength all vary as a function of the plastic component, ε^P, of the total strain. The variation of each of the parameters with increasing strain would form a curve which is approximated in FLAC3D as a set of linear segments as shown in Figure 3.6.

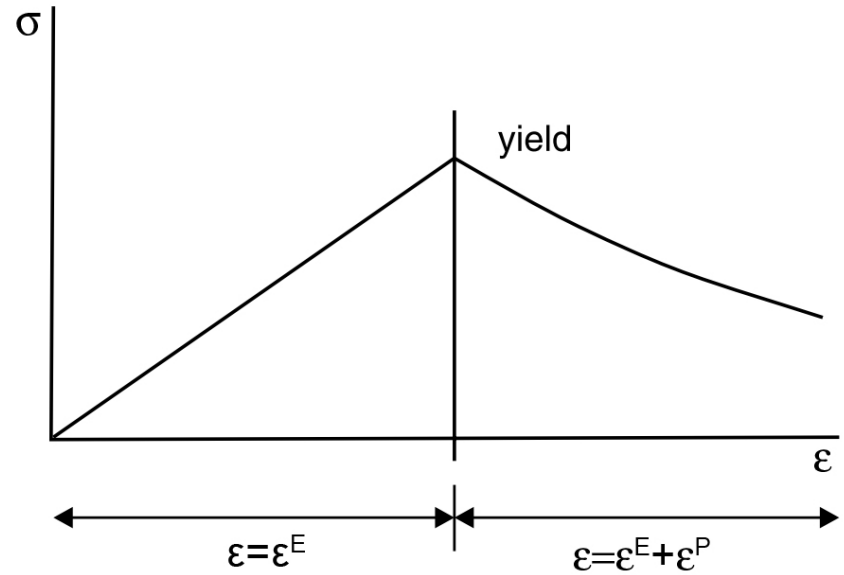

Figure 3.5: Example stress strain curve showing post yield softening behaviour (after Itasca, 2005).

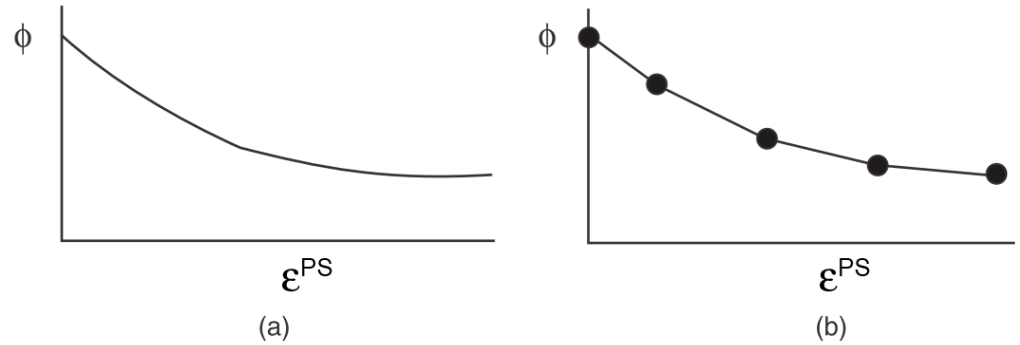

Figure 3.6: Approximation of curve of variation in friction angle with increased plastic strain by linear segments (after Itasca, 2005).

The softening behaviour for the cohesion and friction in relation to the shear plastic strain and for the tensile strength in terms of the tensile plastic strain are input into the model in the form of tables where each table contains pairs of values for the parameter and the corresponding property value. It is important to note that FLAC assumes that the property varies linearly between two consecutive parameter entries in the table so the more points specified, the more closely the modelled parameters will match the true stress-strain curve (Itasca, 2005). The strain-softening ubiquitous-joint model is an anisotropic plasticity model that includes weak planes of user specified orientation (*i.e.* variable strike and dip) embedded in a Mohr-Coulomb solid which is also able to represent nonlinear material softening behaviour of both the weak plane and the material matrix as per the method used in the strain-softening model.

3.1.5 Interface Elements

Coal measures strata that form the roof of shallow mine workings typically display strong horizontal to sub horizontal discontinuities in the form of bedding planes. FLAC3D incorporates zero thickness elements to allow the representation of planes along which sliding or separation can occur (Itasca, 2005). In FLAC3D these are described as interface elements characterised by Coulomb sliding and/or tensile and shear bonding (Itasca, 2005). Interfaces in FLAC3D have the following properties:

- Friction
- Cohesion
- Dilation
- Normal stiffness
- Shear stiffness
- Tensile strength
- Shear bond strength

Interfaces are represented as triangular elements defined by three nodes, one at each element vertex. Interface elements are attached to the face of model zones, with two triangular interface elements being defined for every one quadrilateral model zone face. When another part of the grid comes into contact with an interface, the contact is detected by the interface nodes and the resultant behaviour is characterized by normal and shear stiffnesses, and sliding properties.

Each interface element distributes its area to its nodes in a weighted fashion and so each interface node has an associated representative area. The entire interface is thus divided into active interface nodes representing the total area of the interface. Figure 3.7 illustrates the relation between interface elements and interface nodes, and the representative area associated with an individual node.

Any contact between the interface and any other zone face is detected by the interface nodes and at each timestep, the absolute normal penetration and the relative shear velocity are calculated for each interface node and its contacting face. These values are then used by the interface constitutive model to calculate a normal force and a shear-force vector.

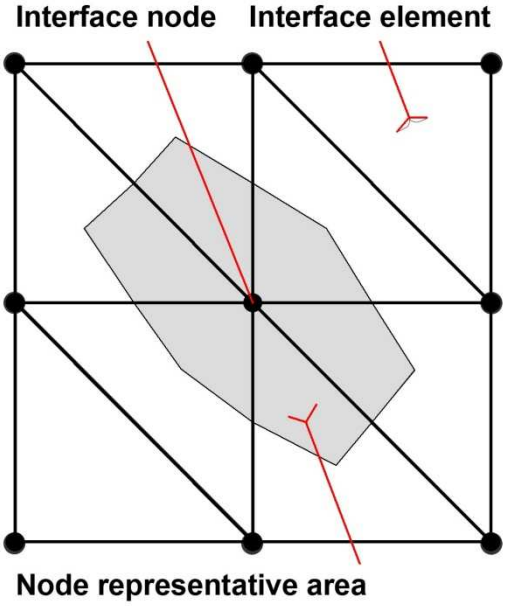

Figure 3.7: Relation between interface elements and interface nodes and the distribution of representative areas to interface nodes (after Itasca, 2005).

The constitutive model is defined by a linear Coulomb shear-strength criterion acting to limit the shear forces at interface nodes and incorporates the normal and shear stiffnesses, tensile and shear bond strengths, and a dilation angle that causes an increase in effective normal force on the face after the shear-strength limit is reached. A schematic diagram representing the interface constitutive model behaviour is shown in Figure 3.8

The Coulomb shear-strength criterion limits the shear force (F_s) to a maximum value (F_{smax}) using the following relation (Itasca, 2005):

$$F_{smax} = c' A_i + \tan\phi' (F_n - \mu A_i) \qquad 3.17$$

Where:

c' = cohesion along the interface (Pa)

A_i = representative area associated with the interface node

F_n = normal force (N)

ϕ' = friction angle of the interface surface (degrees)

μ = pore pressure (Pa)

If the criterion is satisfied (*i.e.*, if $F_s \geq F_{smax}$), then sliding is assumed to occur.

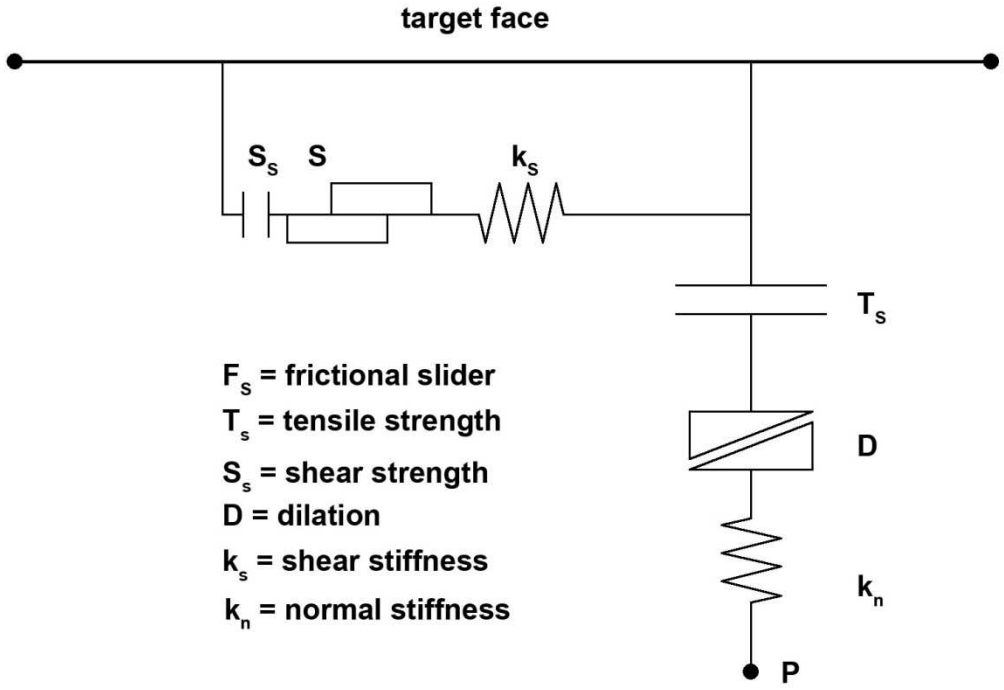

.

Figure 3.8: Components of the bonded interface constitutive model (after Itasca, 2005).

Interface Stiffness

The selection of appropriate normal and shear stiffness parameters for interfaces is undertaken using the recommended method in the FLAC user's manual (Itasca, 2005).

The discontinuity / interface normal (k_n) and shear (k_s) stiffness properties can be estimated based on the following (Itasca, 2005):

$$k_n = \frac{EE_r}{Int_S(E_r - E)} \qquad 3.18$$

Where:

E = rock mass Young's modulus

E_r = intact rock Young's modulus

Int_S = joint spacing

A similar expression can be derived for joint shear stiffness, k_s:

$$k_s = \frac{GG_r}{Int_S(G_r - G)} \qquad 3.19$$

Where:

G = rock mass shear modulus

G_r = intact rock shear modulus

However it should also be noted that there is a maximum practical limit to the joint normal and shear stiffness values and the FLAC3D manual (Itasca, 2005) recommends

that the interface normal and shear stiffness be set to a maximum of ten times the equivalent stiffness of the stiffest neighbouring zone to avoid excessively long numerical solution times due to large contrasts in stiffness. The equivalent stiffness (k_e) can be found using the following relation (Itasca, 2005):

$$k_e = \max\left[\frac{K + \frac{4}{3}G}{\Delta Z_{\min}}\right] \qquad 3.20$$

Where:

K = Bulk modulus (Pa)

G = Shear modulus (Pa)

$\Delta Z_{\min}$ = smallest width of an adjoining zone in the normal direction (m)

N.B. In FLAC3D, the equivalent stiffness parameter as well as the interface stiffness parameters has the units of Pa/m.

3.2 Parametric Study Phase 1 – Initial Continuum Modelling

The main objective of these parametric investigations is to identify the parameters fundamental in the initial collapse of shallow excavations in rock masses and the resultant propagation of voids. The overall aim being to suggest improvements to the management strategy of sites potentially affected by shallow mine workings.

Best practice in the assessment of the danger posed by shallow mine workings is currently based on the empirical evidence available from previous failures. Based on this evidence, generalized relationships (with a number of important assumptions) are identified and used to formulate "rules" which guide shallow mine working hazard assessment. This is the approach currently suggested by professional bodies (*e.g.* CIRIA (Healy and Head, 1984) and in the majority of text books (*e.g.* Bell, 1975; Attewell and Taylor, 1984; Waltham 1989).

Often the rules derived from empirical evidence prove very contentious. It would seem sensible, with improvements in numerical modelling software, to test the validity of these assumptions and to attempt to identify, in a physically valid manner, the key parameters that control the failure of shallow workings and the resultant void migration.

3.2.1 Parametric Study Introduction

From the summary list of parameters on the following page, it can be seen that there are a large number of variables that may affect the collapse of shallow excavations and the resultant void migration. Where ranges of parameters are suggested for testing they are derived from the expected ranges of values derived from the literature.

As numerical models are data limited systems, exact knowledge of the ground conditions can not be known. Furthermore, the objective of the initial phase of the modelling is to investigate the mechanisms of collapse with the aim being to gain information on collapse behaviour that can be applied to varying ground conditions rather than one specific site. The initial models may be relatively simple, with assumed data that is consistent with known field data and engineering judgment. It is a waste of effort to construct a very large and complicated model that may be just as difficult to understand as the real case. (Cundall, 2003). As such, some simplifying assumptions must be made. These are described for each phase of the parametric study. Once the parameters found to be significant are identified, further more detailed modelling work using more sophisticated constitutive models is then undertaken on those of interest.

In the initial phase, modelling was undertaken to investigate the effects on stability of the geometry of the mine workings along with variations in the over lying rock mass strength. Then results for the investigation into the effects of the strength of the coal pillar and underlying rock mass on excavation stability are presented. This was followed by an investigation into the effects of variations in the overburden thickness and density and finally the effects of fluctuations in the water table (modelled as variations in pore water pressure) were investigated. The parameters from the literature which were considered to be of potential importance are summarised in Table 3.1 and the broad significance of the parameters is indicated in Table 3.2.

Table 3.1: Parameters derived from literature review

Model Geometry Parameters	**Symbol**	**Units**	**Values**
Pillar Width		(m)	2.5 - 10
Width of Working		(m)	1 - 5
Extraction Height		(m)	< 3
Overburden Thickness		(m)	< 30
Material Parameters			
Dry Density	ρ_d	(kgm^{-3})	
Porosity	n		
Saturation	S_w		0 - 1
Bulking Factor	BF		1.3 - 1.5
Debris Slope Angle		(°)	30 - 45
Constitutive Model Parameters			
Mohr - Coulomb			
Elastic Bulk Modulus	K	(Pa)	
Elastic Shear Modulus	G	(Pa)	
Tension Limit	σ^t	(Pa)	
Cohesion	c'	(Pa)	
Internal Angle of Friction	ϕ'	(°)	
Strain-Softening			
Shear Strain Softening Parameter			
Tensile Strain Softening Parameter			
Interface Properties			
Interface Normal Stiffness	K_n	(Pa/m)	
Interface Shear Stiffness	K_s	(Pa/m)	
Interface Cohesion	c'^i	(Pa)	
Interface Internal Angle of Friction	ϕ'^i	(°)	
Interface Normal Tensile Strength	σ^{ti}	(Pa)	

3.2.2 Significance of Parameters

Table 3.2: Significance of parameters derived from literature review

Model Geometry Parameters	**Failure**	**Collapse Height**	***In-situ* Stress**
Pillar Width	x		
Width of Working	x	x	
Extraction Height	x	x	
Overburden Thickness	x	x	x
Material Parameters			
Dry Density	x		x
Porosity			x
Saturation	x		x
Bulking Factor		x	
Debris Slope Angle		x	
Constitutive Model Parameters			
Mohr - Coulomb			
Elastic Bulk Modulus	Elastic Response		x
Elastic Shear Modulus	Elastic Response		x
Tension Limit	Tensile Yield	x	
Cohesion	Shear Yield	x	
Internal Angle of Friction	Shear Yield	x	
Strain-Softening			
Shear Strain Softening Parameter	Shear Yield	x	
Tensile Strain Softening Parameter	Tensile Yield	x	
Ubiquitous Joint			
Joint Normal Stiffness	Elastic Response		x
Joint Shear Stiffness	Elastic Response		x
Joint Cohesion	Shear Yield	x	
Joint Internal Angle of Friction	Shear Yield	x	
Joint Normal Tensile Strength	Tensile Yield	x	
Interface Properties			
Interface Normal Stiffness	Interface Interpenetration		x
Interface Shear Stiffness	Elastic Shear		x
Interface Cohesion	Shear Sliding	x	
Interface Internal Angle of Friction	Shear Sliding	x	
Interface Normal Tensile Strength	Interface Delamination	x	

3.3 Effect of Choice of Shallow Tunnel GSI Values versus the Generalised Rock Mass GSI Values on the Modelling of Shallow Excavations

Due to the method in which the Mohr-Coulomb criterion values are derived from a given GSI value and the resultant Hoek-Brown criterion by fitting a straight line to the Hoek-Brown failure envelope (see section 2.3.7 for more information), the value of cohesion (c') and friction angle (ϕ') is either based upon a line which broadly fits the whole Hoek-Brown failure envelope over a full range of potential confining stresses (described from here as the generalised GSI Mohr-Coulomb parameter - MC-G) or is dependent on the maximum confining stress of the region of interest (whereby it is necessary to specify the ratio between the maximum confining stress and the rock mass strength) and the Mohr-Coulomb failure envelope is fitted to this portion of the Hoek-Brown criterion only (described from here as the confining stress dependent GSI Mohr-Coulomb parameter - MC-Sigma3).

This is significant as the Mohr-Coulomb cohesion value at low confining stress is typically significantly over estimated using the generalised curve fitting methodology (MC-G) and the friction angle is typically significantly underestimated. To illustrate this, a plot of the Hoek-Brown failure envelope and the resultant generalised best fit (MC-G) Mohr-Coulomb failure envelope is shown in Figure 3.9 along with the envelope derived for the maximum confining stress dependent GSI Mohr-Coulomb parameter (MC-Sigma3).

In Figure 3.9 it can be clearly seen that the generalised Mohr-Coulomb envelope significantly over estimates the cohesion of the material (by approximately 1.7 MPa in this example) and underestimates the angle of friction at low confining stresses (in this case at a confining stress roughly equivalent to 30 m below the surface where the over burden has a density of 3000 kg/m^3 with a σ'_{3max} value ≈ 0.5 MPa) the MC-Sigma3 Mohr-Coulomb failure surface has a friction angle equal to 47° whereas the MC-G Mohr-Coulomb failure surface has a friction angle equal to approximately 22°. Conversely the MC-Sigma3 Mohr-Coulomb envelope is not applicable at confining stresses higher than the specified value of σ'_{3max} as above this value the MC-Sigma3 Mohr-Coulomb envelope begins to significantly over estimate the friction angle.

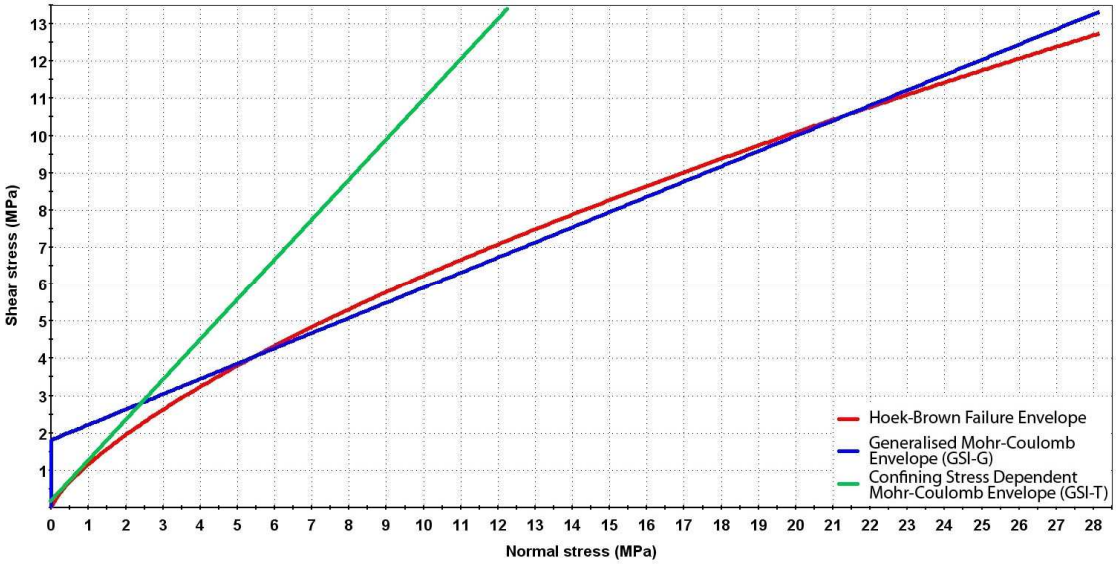

Figure 3.9: Plot of Hoek-Brown failure envelope with the general Mohr-Coulomb fitted failure envelope (MC-G) and the maximum confining stress dependant Mohr-Coulomb envelope (MC-Sigma3) for sandstone with a GSI value of 10.

As shallow abandoned mine workings are typically considered to be those that are at less than 30 m depth below the surface and it is clear from the above that the confining stress has a significant impact on the Mohr-Coulomb parameters and as the cohesion and friction angle of the rock mass potentially have a very significant effect on the modelling results it was decided to compare the effect on the stability of shallow voids when modelling was undertaken using the generalised Mohr-Coulomb and confining stress dependant Mohr-Coulomb properties.

In the modelling results presented here the averaged rock mass strength parameters were varied to investigate their impact on the stability of shallow excavations (*i.e.* the friction angle of the discontinuities is assumed to be equal to that of the material forming the bedding planes – hence averaged rock mass strength – note it is acknowledged that this would yield a higher than expected strength of the rock mass for the apparent discontinuity spacing, however as it is the relative effect of two differing methods of deriving the Mohr-Coulomb parameters which is being investigated and the higher than normal frictional strength of the discontinuity planes effects both models equally it will not affect the result).The two sets of Mohr-Coulomb strength and stiffness parameters are outlined in Table 3.3.

Table 3.3: Rock mass generalised Mohr-Coulomb and confining stress dependant Mohr-Coulomb properties.

GSI	Bulk Mod.	Shear Mod.	MC-Sigma3 Mohr-Coulomb			MC-G Mohr-Coulomb		
			Cohesion	Friction Angle	Tensile Strength	Cohesion	Friction Angle	Tensile Strength
10	0.874	0.28	0.13	47	0.005	1.81	22	0.005
20	1.31	0.34	0.20	53	0.011	2.54	26	0.011
30	2.33	6.08	0.28	57	0.023	3.19	29	0.023
40	4.57	1.19	0.38	60	0.048	3.78	32	0.048
50	8.80	2.30	0.56	62	0.10	4.39	35	0.10
60	14.90	3.89	0.89	63	0.22	5.07	38	0.22
70	21.00	5.48	1.56	63	0.46	5.94	41	0.46
	(GPa)	**(GPa)**	**(MPa)**	**(°)**	**(MPa)**	**(°)**	**(MPa)**	**(MPa)**

A set of plots comparing the yield state of the rock mass for the rock mass strengths investigated using both the confining stress dependent GSI Mohr-Coulomb parameters and the generalised GSI Mohr-Coulomb parameters (See Figure 3.10 and Figure 3.11 respectively) show that yielding occurs at all values tested for both sets of rock mass parameters, however the rock masses can be split broadly into two main groups; Those where tensile delamination with failure of the roof strata has occurred (marked by the formation of zones of shear yielding at the end of the individual strata within the roof – see Figure 3.10 parts A to D and Figure 3.11 parts A to C) and those which have purely undergone tensile yielding due to delamination of the roof strata but with limited displacements and where the excavation roof strata are stable (see Figure 3.10 parts E to G and Figure 3.11 parts D to G).

It is readily apparent that the degree of roof strata sagging in the models that have undergone visible deformations increases with decreasing rock mass strength. The height to which the collapse of the strata extends into the rock mass also increases with decreasing rock mass strength with this zone of failure extending only around 0.2 m into the rock mass above the excavation for a rock mass strength equivalent to a GSI MC-Sigma3 of 40 (Figure 3.10 part D) and increasing to approximately 2.5m at the lowest rock mass strength tested (Figure 3.10 part A).

The models that have undergone roof failure as opposed to yielding also share a common feature in terms of the height to which tensile yielding extends into the rock

mass over the new excavation roof. This zone of damage in these cases extends approximately 5 m into the rock mass over the original excavation roof and forms a wedge at an angle of approximately 15-18 degrees from the vertical. This zone of tensile yielding corresponds in this case to the height to which tensile delamination of the bedding has occurred. This is broadly similar for both the models using the GSI MC-Sigma3 and GSI MC-G parameters with some slight differences in the geometry that do not appear to be significant in terms of roof stability. The primary difference appears to be in terms of the shear yielding which is discussed below.

From the above and from observation of the plots there are two significant differences between the results modelled using the confining stress dependent GSI Mohr-Coulomb parameters and the generalised GSI Mohr-Coulomb parameters. This is in the occurrence of shear yielding within the rock mass. As stated earlier, the generalised GSI Mohr-Coulomb failure envelope over estimates the cohesion at low confining stresses. This is reflected in the modelling results (Figure 3.11) whereby although tensile yielding occurs (the models use a tensile cut off which is not linked to confining stress and so is identical in both cases) there is no evidence of shear yielding in the rock mass in those models using the GSI MC-G parameters.

However the lower cohesion values produced by the confining stress dependent GSI Mohr-Coulomb envelope lead to shear failure occurring within the rock at the ends of the roof strata and propagating upwards into the rock mass. In this case this has also led to variations in the height to which failure has occurred within the rock mass, whereby as previously stated, in the rock mass with GSI MC-Sigma3 10 parameters, the failure of the strata has propagated approximately 2.5m into the rock mass above the excavation, whereas in the rock mass using the generalised GSI Mohr-Coulomb parameters, GSI MC-G 10, the failure propagates only 1.2 m into the rock mass.

Further to the above, the two differing methods for estimating the Mohr-Coulomb parameters with their consequent variations in the shear strength properties of the rock mass have lead to roof failure (*i.e.* delamination and significant visible displacements of roof strata) occurring in the model with GSI MC-Sigma3 40 strength parameters, but not occurring in the model using the GSI MC-G 40 strength parameters.

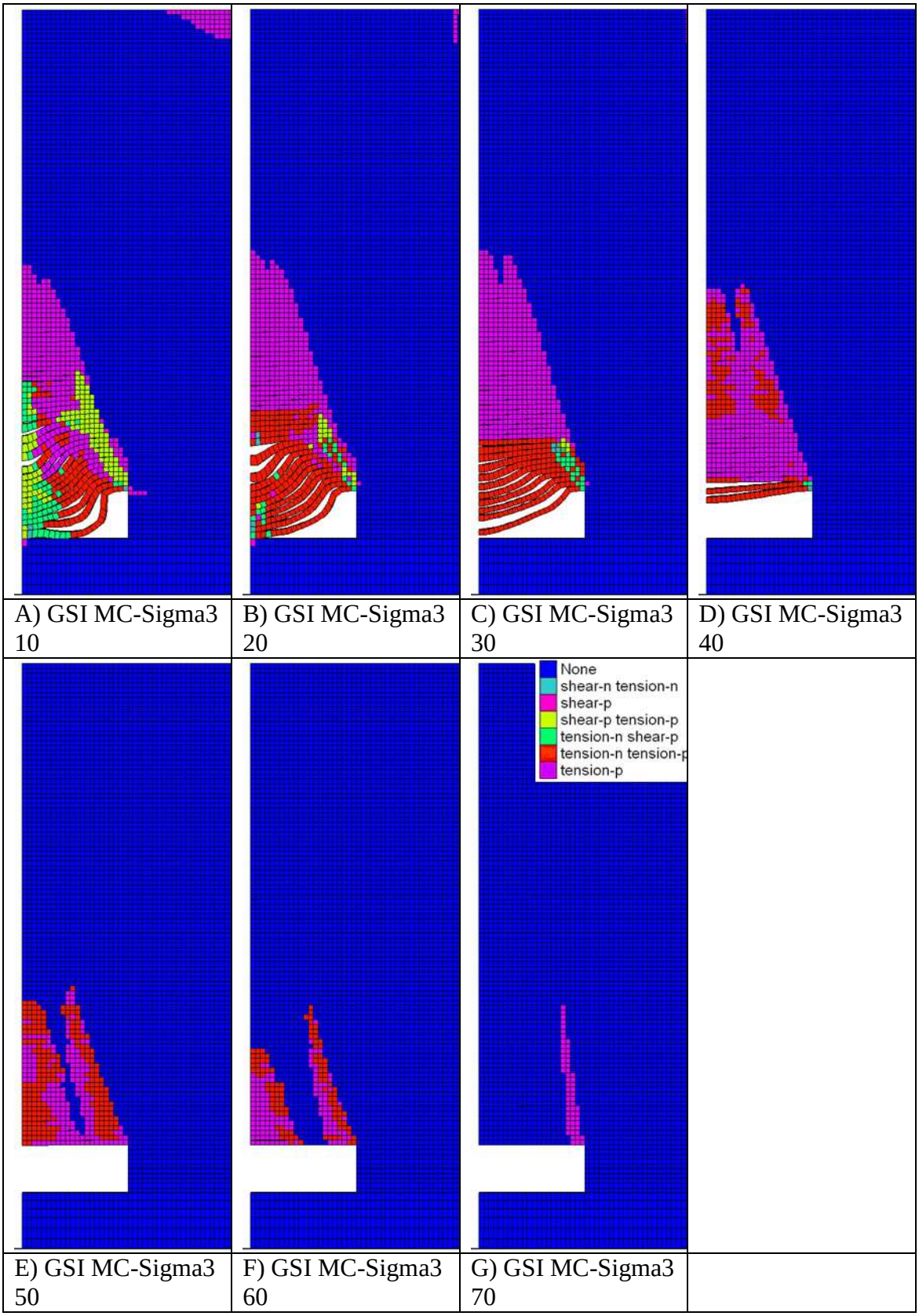

A) GSI MC-Sigma3 10	B) GSI MC-Sigma3 20	C) GSI MC-Sigma3 30	D) GSI MC-Sigma3 40
E) GSI MC-Sigma3 50	F) GSI MC-Sigma3 60	G) GSI MC-Sigma3 70	

Figure 3.10: Yield state plot of the rock mass for varying rock mass strength values using the confining stress dependent GSI Mohr-Coulomb parameters. Excavation width 3m, excavation height 1m. Water table below the excavation.

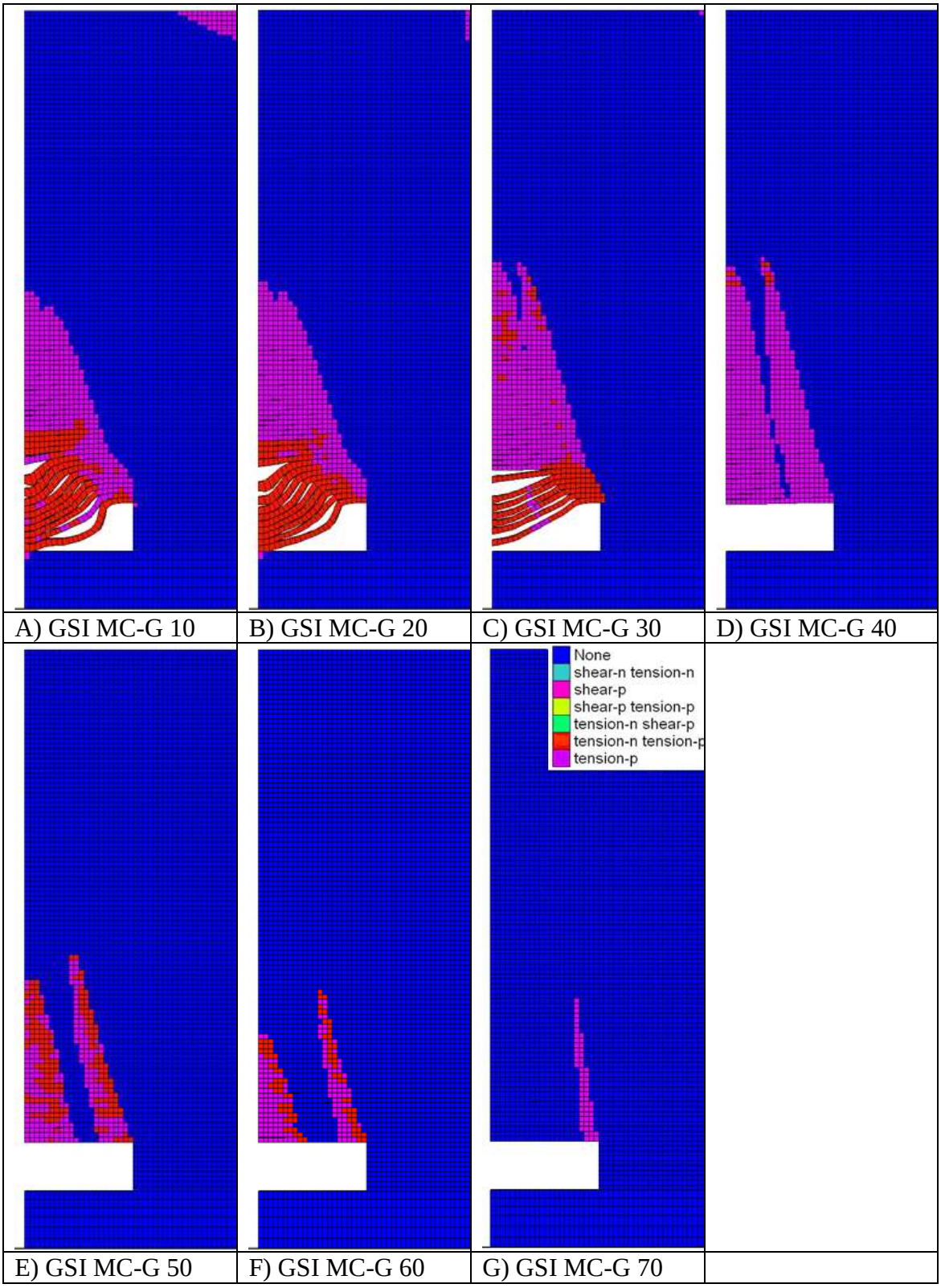

A) GSI MC-G 10	B) GSI MC-G 20	C) GSI MC-G 30	D) GSI MC-G 40
E) GSI MC-G 50	F) GSI MC-G 60	G) GSI MC-G 70	

Figure 3.11: Yield state plot of the rock mass for varying rock mass strength values using the generalised GSI Mohr-Coulomb parameters. Excavation width 3m, excavation height 1m. Water table below the excavation.

3.3.1 Conclusions

This section has demonstrated that there are potentially significant differences in the failure behaviour of the rock mass over the excavation roof when the confining stress dependant Mohr-Coulomb parameters are used in modelling when compared to the results for the generalised Hoek-Brown Mohr-Coulomb parameters. Significantly when the generalised Hoek-Brown Mohr-Coulomb parameters are used there is no occurrence of shear yielding at the roof strata pillar intersection which is the expected failure mechanism during the collapse of roof strata. As the phenomenon of shear yielding / failure in roof strata above the intersection between the excavation and the mine pillar is observed both in laboratory experiments and in the field (Bieniawski, 1984; Healy and Head, 1984; Goodman, 1989) and appears to have a significant impact on stability along with the fact that the GSI MC-Sigma3 failure envelope is a closer fit to the Hoek-Brown failure envelope at low confining pressures representative of the shallow depths encountered in shallow workings, it was decided to use the confining stress dependent GSI Mohr-Coulomb parameters in the modelling undertaken in this thesis.

3.4 Phase 1- Continuum Modelling

3.4.1 Model Discretisation and Boundary Conditions

In all the modelling discussed here, the models are created with a mesh composed of cubic elements 0.1 m^3 in size. Model boundaries are fixed displacement boundaries. The left and right boundaries are free to displace vertically but not horizontally and the model base is fixed in all directions. The grid also extends 10 m below the excavation base. The overlying rock mass is 30 m thick except in the models where the thickness of the overburden was investigated.

3.4.2 Numerical Model Input Parameters

The strength and stiffness properties of coal measures strata were derived using ROCLAB (Rocscience, 2010) which uses the Geological Strength Index (GSI) parameter to estimate rock mass strength and stiffness and the Mohr-Coulomb parameters for use in FLAC. The GSI system was developed to allow reliable rock mass properties to be derived for numerical analysis (Marinos *et al*., 2005).

The system allows the modelling properties to be varied to account for variations in the rock mass which can greatly affect stability. This value is based upon assessment of the

lithology, the rock structure and the condition of joint surfaces in the rock mass. This GSI value is then input into the software along with estimates of intact strength and stiffness properties. Corrected strength and stiffness parameters are then derived to account for variations in the rock mass. The rock forming the overburden was assumed to have the following intact properties: intact uniaxial compressive strength of 75 (this value is chosen as an average UCS for typical coal measures rocks from the range of values quoted by Bell, 1975). The intact elastic modulus was assumed equal to 13.5 GPa taken as an average value for sandstone, shale and siltstone (Zhang, 2005). From this, the values derived for coal measures strata are summarised in Table 3.4.

Table 3.4: Strength and stiffness parameters used in the numerical modelling

GSI	Bulk Modulus	Shear Modulus	Cohesion	Friction Angle	Tensile Strength
10	0.7	0.23	0.11	49.0	0.005
20	1.1	0.35	0.17	55.0	0.011
30	1.9	0.62	0.24	59.0	0.023
40	3.7	1.2	0.33	61.0	0.048
50	7.0	2.4	0.51	63.0	0.1
60	12.0	3.9	0.85	64.0	0.22
70	17.0	5.6	1.5	64.0	0.46
80	20.0	6.7	2.9	64.0	0.98
90	22.0	7.3	5.5	62.0	2.1
100	23.0	7.6	11.0	60.0	4.4
	(GPa)	**(GPa)**	**(MPa)**	**(°)**	**(MPa)**

It is important to note that use of the Mohr-Coulomb model along with the GSI value is applicable to rock masses where failure behaviour is not controlled by steeply dipping joint planes. In cases where there are steeply dipping weakness planes these parameters may over estimate stability and an alternative modelling methodology should be use, for example using the ubiquitous joint model.

3.4.3 Effect of variation in Working Geometry

In the numerical modelling examples in this section, the width of rooms and the pillars have been progressively increased. The strength and stiffness properties of the rock mass, along with the groundwater level / pore pressure in the rock mass and the

overburden load have been kept constant for each example (although the full range of values were used in the tests).

In pillar and stall workings, the relationship between room size and pillar size is described as the extraction ratio (Waltham, 1989).

Pillar and stall workings have variable geometries, however the type most commonly encountered in both England and Scotland (excepting some local variations) are pillar and stall workings with square (in plan) pillars with equal sized rooms (Healy and Head, 1984). See Figure 3.12 for an example.

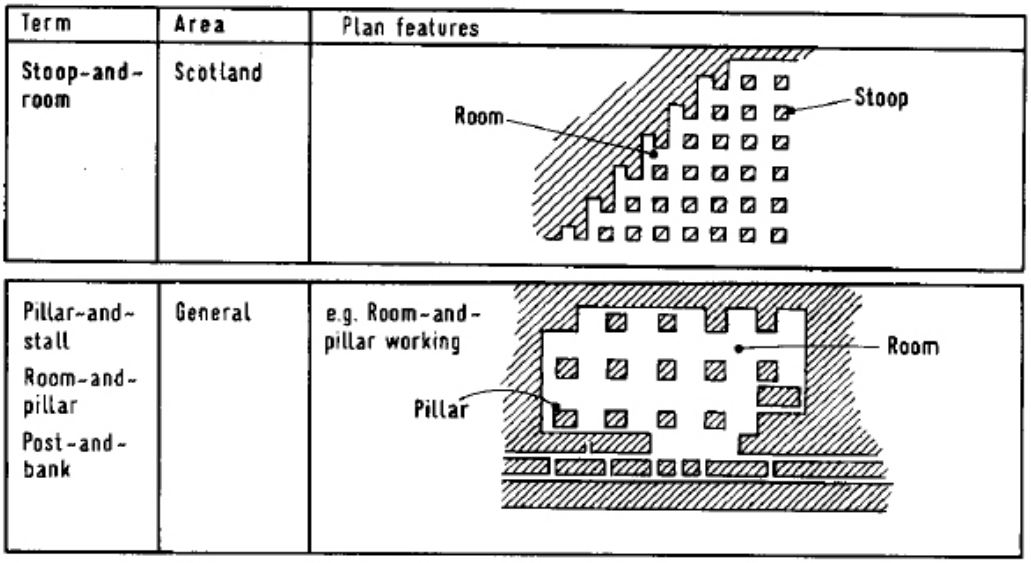

Figure 3.12: Most common geometry of pillar and stall workings found in the UK **(Healy and Head, 1984)**

3.4.4 Effect of Pillar and Room Width on Roof Stability

In the modelling examples in this section, the width of rooms and the pillar widths have been progressively increased. The strength and stiffness properties of the rock mass, along with the groundwater level and overburden load have been kept constant for each example (although the full ranges of values were used in the tests).

In pillar and stall workings where the room and pillar sizes are identical, the increased room width results in an increased tensile stress over the roof of the room, and also an increase in the height to which the tensile stress extends through the overlying strata. In pillar and stall workings, the relationship between room size and pillar size is described as the extraction ratio (Waltham, 1989).

Modern pillar and stall workings have an extraction ratio of 75%. Older workings may have extraction ratios as low 50 - 30%. However pillar robbing on mine abandonment can lead to higher extraction ratios (up to 85%). In the modelling demonstrated here, the range of extraction ratios tested is shown in Table 3.5.

Table 3.5: Pillar and room sizes and the resultant extraction ratios.

Room Width (m)	Pillar Width (m)	Pillar Area (m^2)	Working Area (m^2)	Extraction Ratio
1.0	0.6	0.4	2.3	65%
2.0	1.3	1.6	9.0	65%
3.0	1.9	3.6	20.3	65%
1.0	1.0	1.0	3.0	50%
2.0	2.0	4.0	12.0	50%
3.0	3.0	9.0	27.0	50%
1.0	2.4	5.8	5.8	30%
2.0	4.8	23.0	23.2	30%
3.0	7.2	51.8	52.2	30%

3.4.5 Effect of Variations in Room Width on Excavation Stability

To investigate the effect of variations in the excavation width on initial excavation stability a number of models were created with varying excavation widths and coal pillar widths. Below, the results for the varying excavation widths are presented.

Figure 3.14 represents a 1 m wide room with a 2.4 m wide pillar. The failure plot indicates that there is some limited tensile yielding within the roof. In order to assess the effect on stability of this yielding it is necessary to also examine the displacement history and vertical strain for the roof centreline. During each model change, the record of displacements is set to zero in order to assess the effect on stability of any changes made to the model. For this excavation geometry and with the groundwater below the excavation base, the displacement history is horizontal indicating that there has been virtually no displacement in the roof centreline and that the excavation is stable (displacements in this example are on the order of 1x10-4 m (0.1 mm) which are considered insignificant).

Figure 3.14 and Figure 3.15 display the same data for excavations of 2 m width and 3 m width respectively. It can be seen that with increasing excavation width there is progressively increased yielding within the roof strata. A zone of tensile yielding develops above the roof centreline and a zone of mixed shear and tensile yielding above

the pillar margin, extending upwards into the rock mass above the excavation and away from the coal pillar.

On examination of the displacement and strain plots however it can be seen that the excavation has not undergone significant displacement or strain and that they are ultimately stable. This indicates that although the increase in excavation width causes significant increases in the yield state of the roof material, it does not cause significant displacements that would represent instability for excavations above the water table.

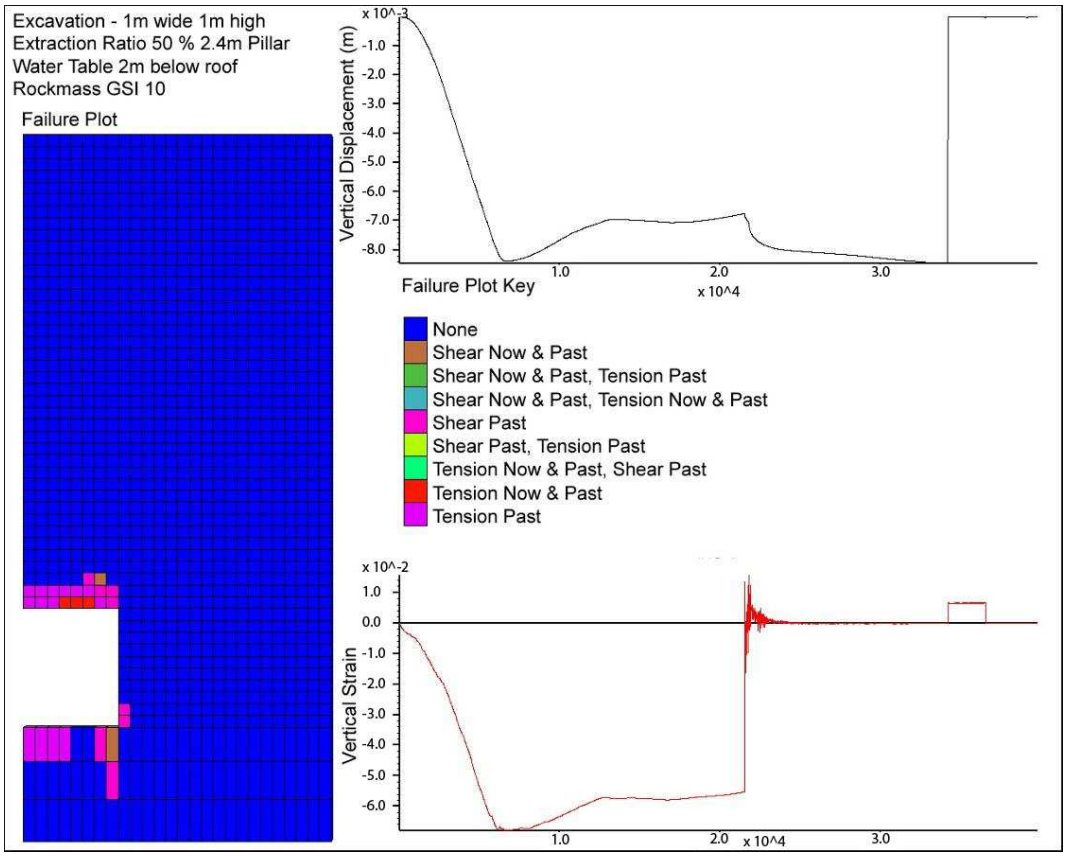

Figure 3.13: Failure plot with vertical displacement and strain in roof centreline for a 1 m wide excavation with an extraction ratio of 30% and water table below the excavation.

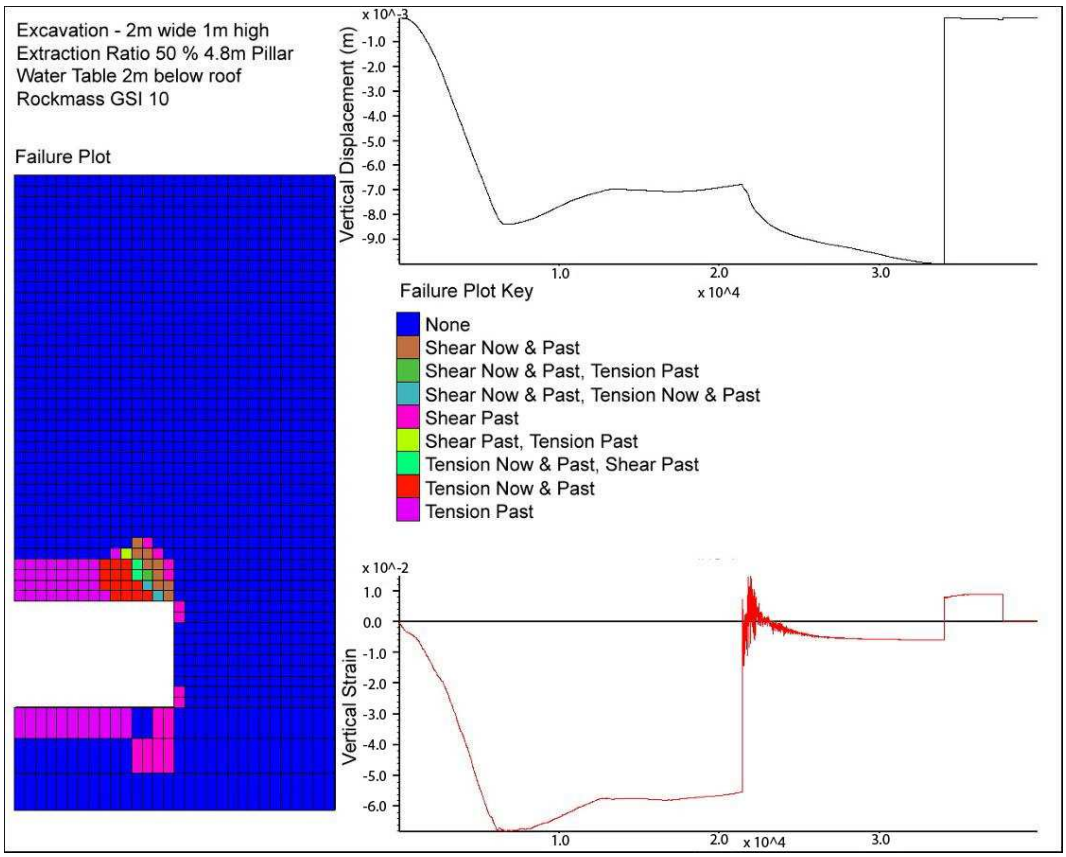

Figure 3.14: Failure plot with vertical displacement and strain in roof centreline for a 2 m wide excavation with an extraction ratio of 30% and water table below the excavation.

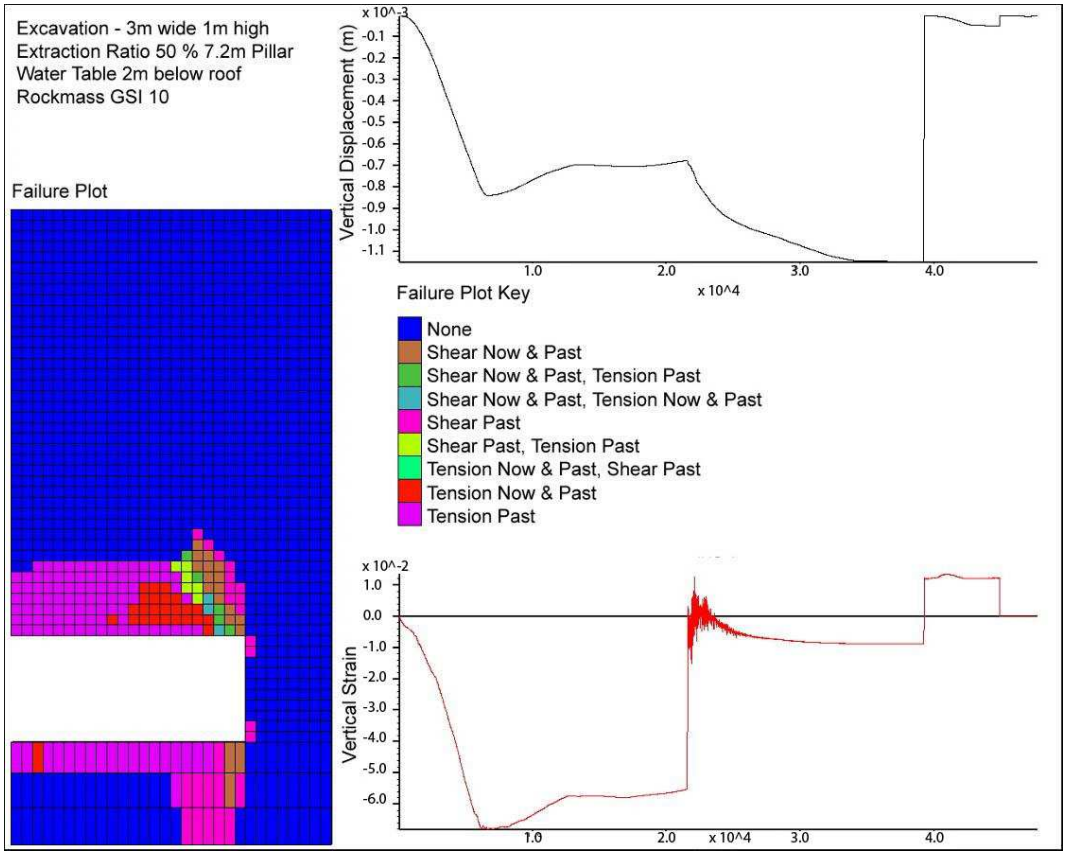

Figure 3.15: Failure plot with vertical displacement and strain in roof centreline for a 3 m wide excavation with an extraction ratio of 30% and water table below the excavation.

3.4.6 Effect of Coal Pillar Width on Excavation Stability

To investigate the effect of variations in the coal pillar width on initial excavation stability a number of models were created with varying extraction ratios.

Figure 3.16 represents an excavation with an overburden thickness of 30 m, an excavation width of 3 m, a rock mass GSI of 10 and an extraction ratio of 50% and Figure 3.17 represent an excavation with the same parameters as Figure 3.16 but with an extraction ratio of 65%.

The failure plots for both figures appear very similar to that of Figure 3.15 (extraction ratio of 30%) where the shear band that forms at the intersection of the coal pillar and the roof strata extends to the same height into the rock mass in all cases (a vertical distance of approximately 0.7 m). It can also be seen that the tensile yielding over the excavation is virtually identical in all three cases again extending to a height of approximately 0.7 m into the rock mass. When the plots of history of displacement are reviewed, it can be seen that there is virtually no vertical displacement in the roof centreline. This indicates that variations in the extraction ratio for excavations above the water table have very limited effect on the stability of the excavation roof.

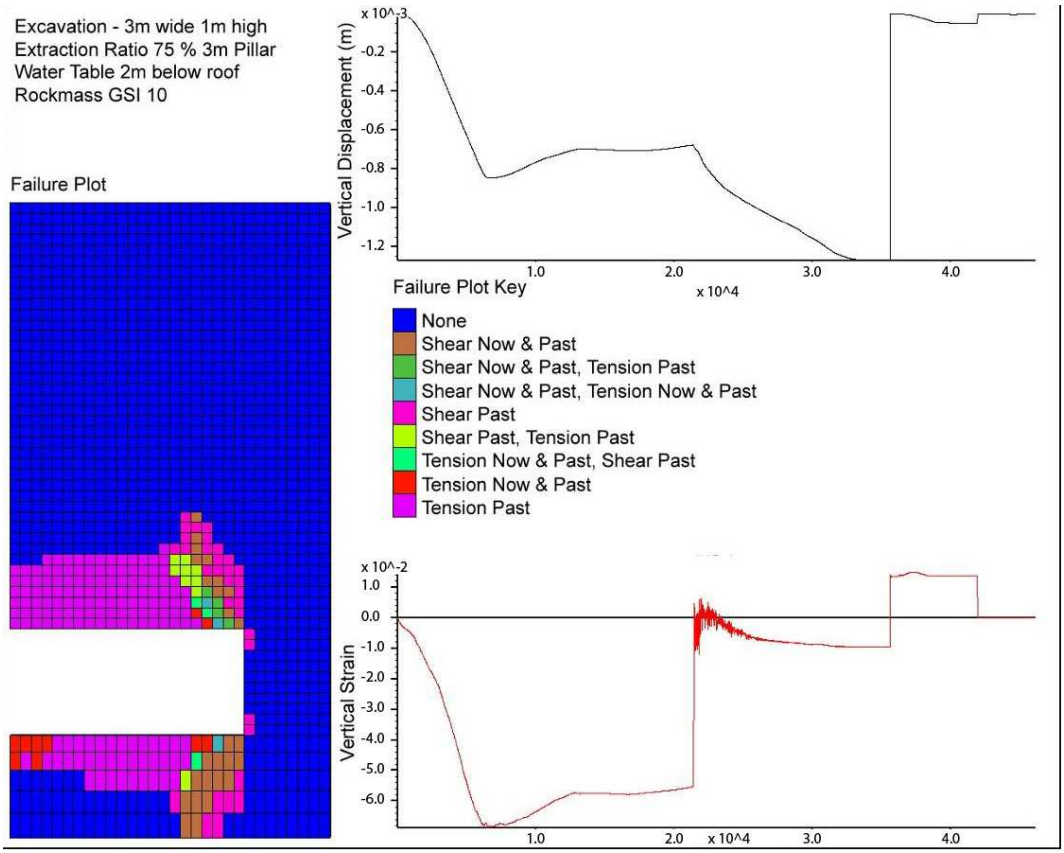

Figure 3.16: Failure plot with vertical displacement and strain in roof centreline for a 3 m wide excavation with an extraction ratio of 50% and water table below the excavation.

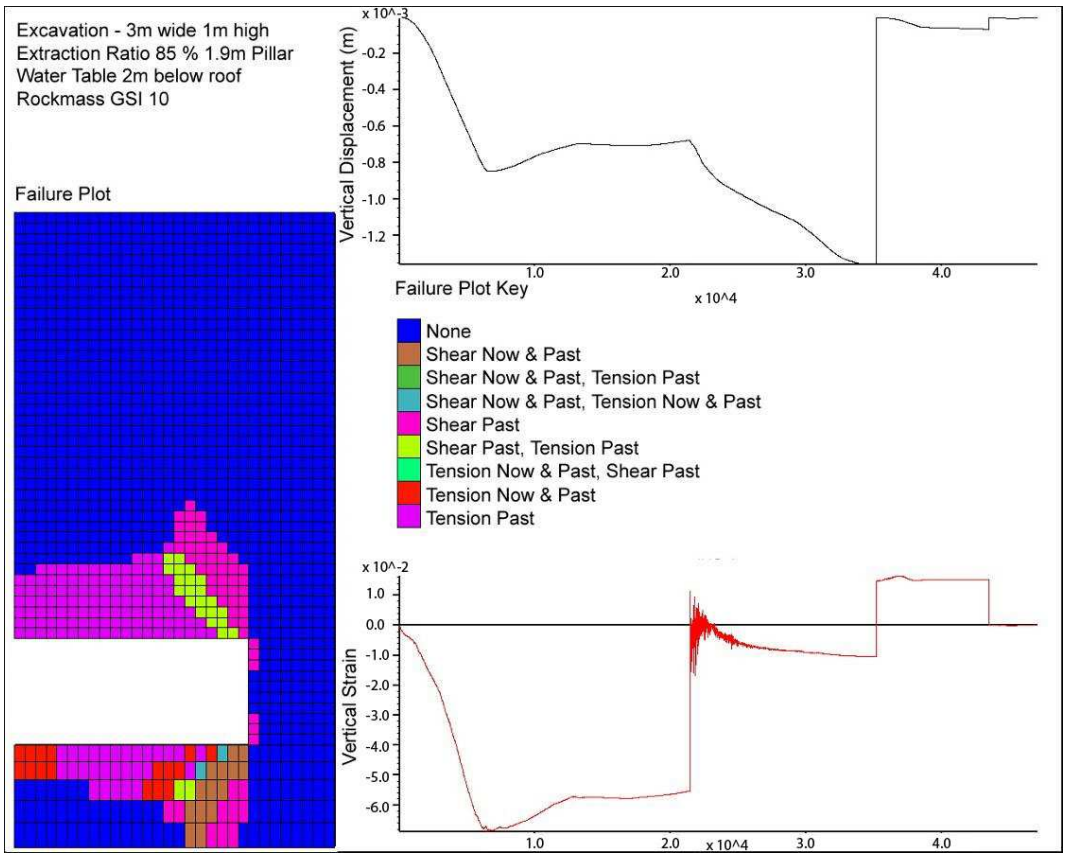

Figure 3.17: Failure plot with vertical displacement and strain in roof centreline for a 3 m wide excavation with an extraction ratio of 65% and water table below the excavation.

The above results for variations in the coal pillar width suggest that even at the lowest rock mass strength tested the excavations above the water table will be stable.

3.4.7 Effect of Underlying Rock Mass and Coal Pillar Strength on Excavation Stability

In order to investigate the effect of variations in the strength of the rock mass underlying the excavation; along with the strength of the coal pillar; a number of models were run with varying underlying rock mass, overburden rock mass and coal pillar strength values.

In each case the models used were composed of a 1 m wide excavation with an extraction ratio of 30% and overburden loads of 30 m. For each of the models, upon excavation of the mined void, the water table was raised to the ground surface to represent an absolute worst case. The history of vertical displacements in the excavation roof centreline and the pillar margin were recorded to allow an assessment to be made of the stability of the excavation.

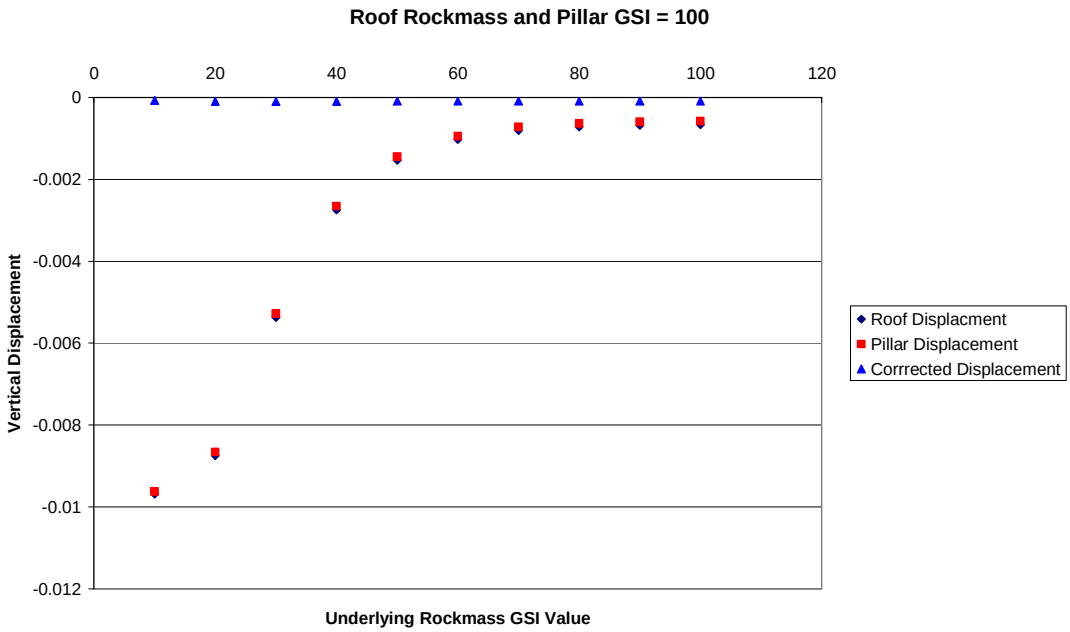

Figure 3.18: Variation in vertical displacements due to variations in underlying rock mass strength

Figure 3.18 shows the vertical displacements in the roof centreline and coal pillar for variations in the underlying rock mass. The coal pillar and roof strata were given the maximum strength value of 100 GSI. The roof displacement and the coal pillar displacement are identical. This indicates that the rock mass is undergoing rigid body motion. The corrected roof centreline displacements (*i.e.* roof centreline minus coal pillar which is essentially an indication of differential movement within the rock mass indicative that the roof may be unstable) values are essentially zero for all GSI values of underlying rock mass. At the minimum strength value, there is only approximately 10 mm of displacement. This suggests that the underlying rock mass strength is not directly significant in the stability of the excavation roof; however it is more broadly significant in terms of general subsidence as it contributes to the phenomenon of sag or areal subsidence which can occur as a result of the coal pillar punching through the weaker underlying rock mass.

Figure 3.19 displays similar data for variations in the rock mass strength of the coal pillar. The displacements within the roof and the pillar are again almost identical. The maximum vertical displacement occurs at the lowest strength value. In this case where the roof rock mass and the underlying rock mass strength are significantly higher than the strength of the coal, shear failure occurs within the pillar. This would lead to pillar crushing rather than roof collapse and ultimately would lead to sag subsidence rather than void migration.

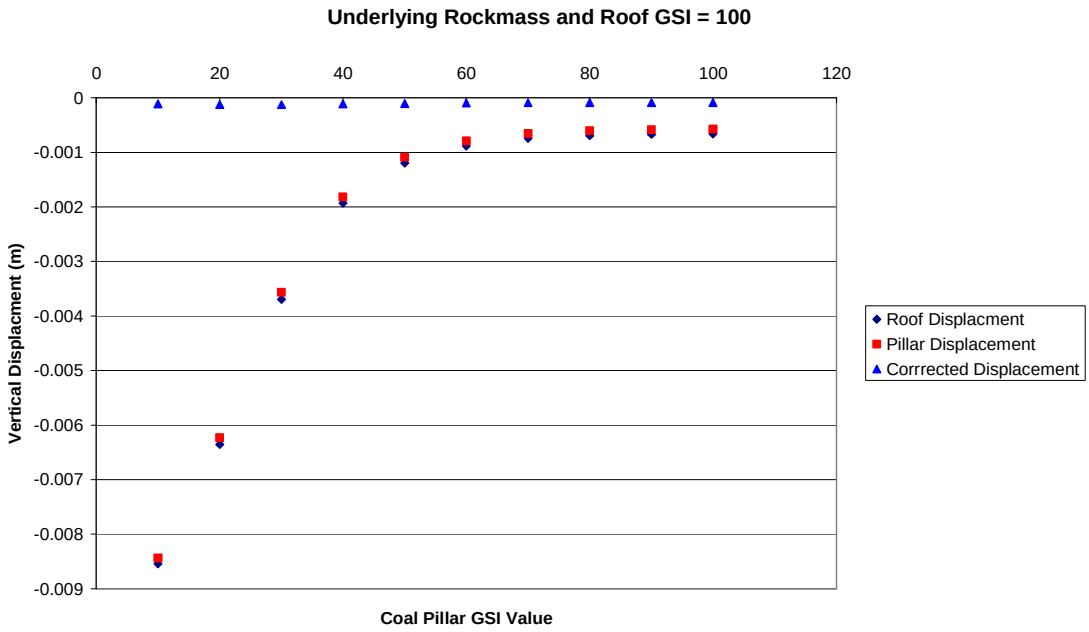

Figure 3.19: Variation in vertical displacements due to variations in coal pillar rock mass strength.

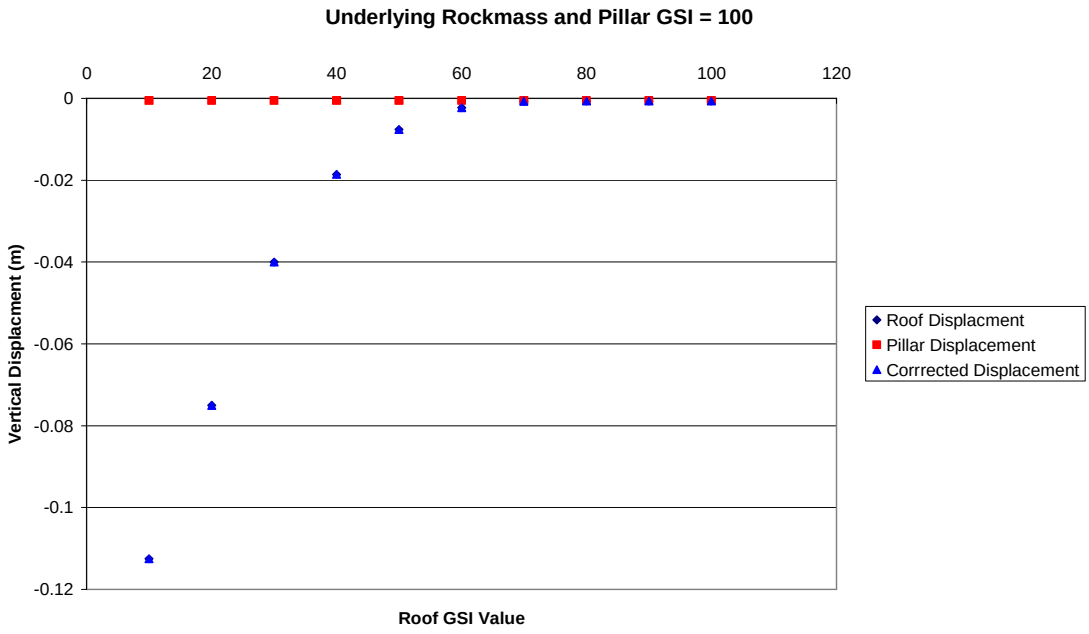

Figure 3.20: Variation in vertical displacements due to variations in roof rock mass strength.

Figure 3.20 shows the variation in displacements as the roof rock mass strength is varied. The measured and corrected displacements here are identical. It can be seen in the figure that roof rock mass values below a GSI of 60 display significantly increased displacements. Rock Mass strength values above GSI 60 produce a very stable roof.

To rule out the possibility that the high strength values used for the sections of the model not being tested were influencing the results, a second set of data is plotted below. In this set of results, the rock mass strength of the model zones which were not

of interest are given minimum strength and stiffness values and compared to a range of values for the area of interest.

In Figure 3.21 the roof and coal pillar are given a minimum GSI value and the underlying rock mass GSI value is varied. It can be seen that the roof and pillar displacements both decrease by an equal amount as the GSI of the underlying rock mass decreases. This indicates once more that the model is undergoing rigid body motion and confirms that the underlying rock mass is not significant in roof stability under these conditions.

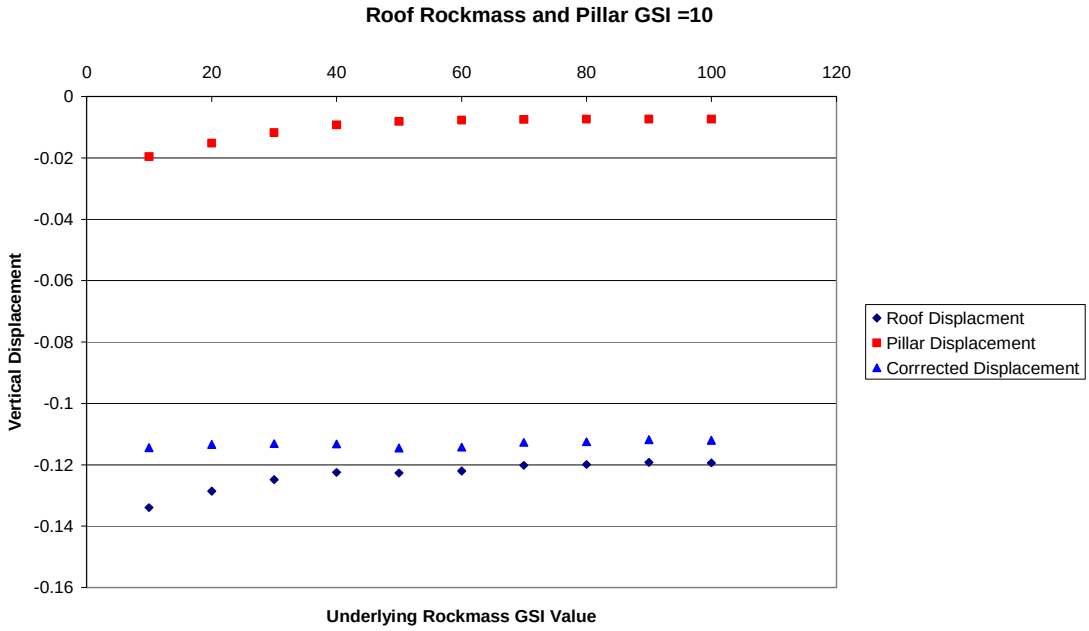

Figure 3.21: Variation in vertical displacements due to variations in underlying rock mass strength with minimum rock mass strengths for coal pillar and roof.

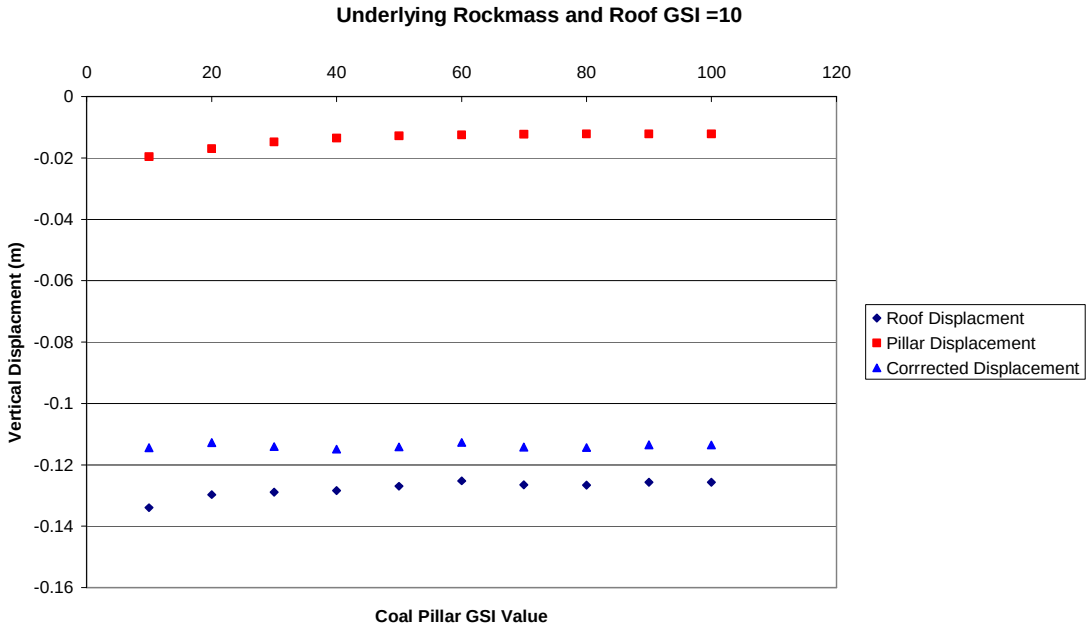

Figure 3.22: Variation in vertical displacements due to variations in coal pillar strength with minimum rock mass strengths for the underlying material and roof.

Figure 3.22 is a plot of the data for the variation in the coal pillar strength with the roof and underlying rock mass GSI set to 10. The plot of corrected displacement values for the roof centreline again indicates rigid body motion as opposed to the roof flexing and failing. Figure 3.23 confirms that the variations in displacements due to alterations in the roof rock mass strength are the cause of the displacements in the roof centreline and are the controlling factor in excavation roof stability.

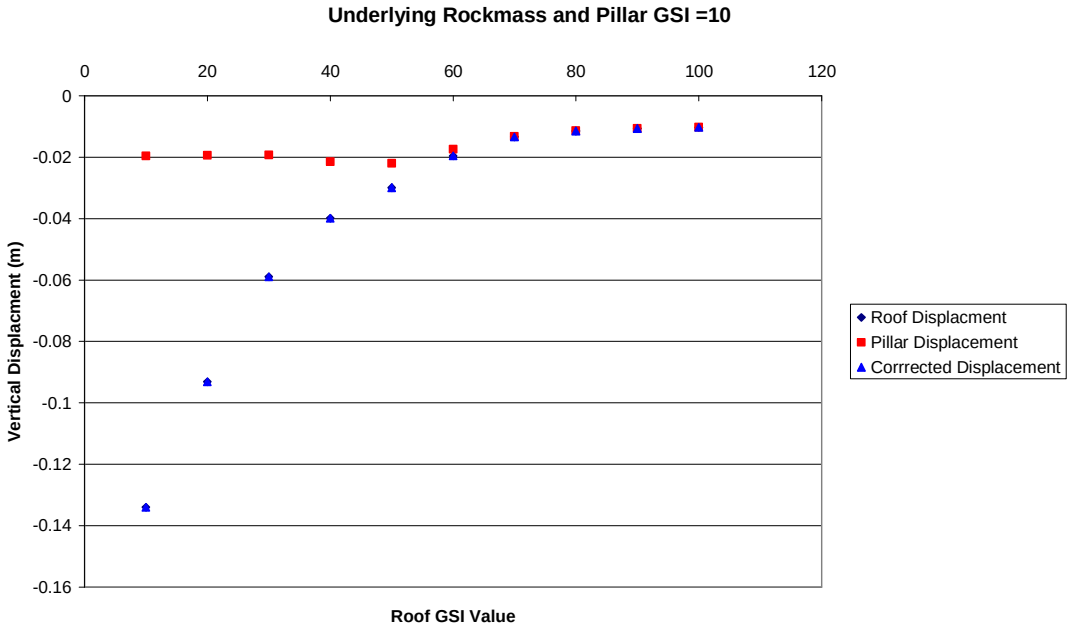

Figure 3.23: Variation in vertical displacements due to variations in roof rock mass strength with minimum rock mass strengths for coal pillar and underlying material.

3.4.8 Conclusions

The comparison between the roof displacement and the pillar margin displacements as seen in the graphs above suggest the following:

- The strength of the overburden material has the most significant impact on roof stability and displacements. Predictably the lower the value, the greater the yielding and displacement. The rock mass strength of the roof material is most significant in roof collapse and void migration.
- Rock mass strength values with a GSI above 60 show virtually no yielding and very low displacements. If the overburden / roof material is of this strength or above, the excavation will be extremely stable under any of the conditions tested here.
- The effect of decreasing underlying rock mass strength leads to a uniform increase in both the pillar vertical displacements and the roof centreline displacements. It is not indicative of roof failure or collapse that would lead to

void migration. The yielding within the underlying rock mass beneath the pillar suggests this may represent the coal pillar punching into the underlying material. This is most significant when the strength of the coal pillar and overlying rock mass are significantly higher than that of the underlying rock mass.

- The strength of the coal pillar can have a significant impact on the type of subsidence that will occur. Where the coal pillar strength is low compared to those of the overlying and underlying rock mass, significant shear yielding can occur along with large horizontal displacements within the pillar and pillar margins. This represents pillar crushing which although significant in the occurrence of sag subsidence has not contributed to the instability of the roof centreline and is unlikely to lead to void migration in the model shown here but where a single weak pillar fails, this may cause a localised loss of support which could increase roof stresses and lead to a roof collapse however such behaviour is not captured by the modelling undertaken here.

3.4.9 Effect on Stability of Variations in the Overburden Load and Overburden Thickness

The overburden load on the roof of an excavation is the sum of the bulk density and thickness of overburden.

Coal measures strata are typically composed of interbedded sandstone, siltstones and shales. Dry densities of the theses materials can vary from around 1800 kgm^{-3} up to 2650 kgm^{-3} and with porosity values from 0.05 to 0.3 (Bell, 1992).

For stress calculations in material above the water table, FLAC makes use of dry density. For material below the water table the bulk density is used. This is calculated using the following (Itasca, 2005):

$$\rho = \rho_d + (n \times S_w \times \rho_w) \qquad 3.21$$

Where

ρ = Bulk density (kgm^{-3})

ρ_d = Dry density (kgm^{-3})

n = Porosity

S_w = Saturation

ρ_w = Fluid density (kgm^{-3})

The parameters used are detailed below where the suggested values are sourced from the literature:

- Porosity values: 0.05 - 0.3 = 5 – 30% (Zhang, 2005).
- Saturation: assumed to be one below water table and zero above.
- Dry density: 2000 – 3000 kgm^{-3} (Bell, 1975; Bell, 1992; Zhang, 2005)
- Resultant bulk density range: 2050 – 3300 kgm^{-3}

In order to investigate the effect of overburden load, a number of numerical models were run using varying overburden thicknesses, densities and hence resulting in varying overburden loads.

The modelling procedure for these investigations differed slightly from the other modelling runs in that the displacements were not reset to zero with every model change, so displacements plots represent cumulative displacements as model changes are made.

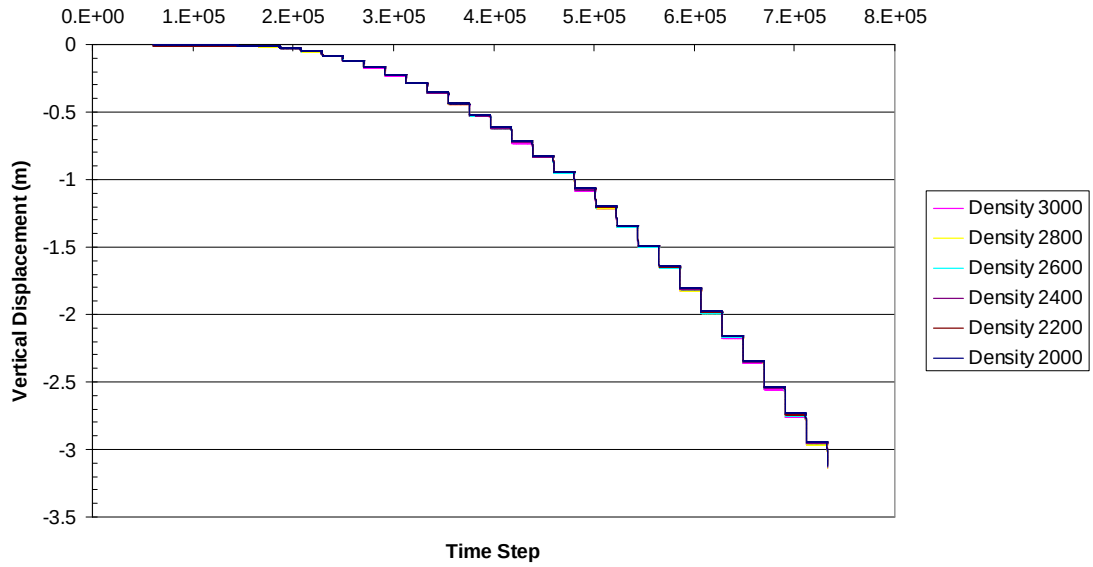

Figure 3.24: Plot of vertical roof displacements for varying density values of overburden material.

Figure 3.24 shows the variations of vertical displacement within the excavation roof for progressively increasing pore water pressure. Each step in the displacement plot represents a 1 m increase in the pore pressure head. The roof displacement for a range of density values is plotted. The variation in displacements for the range of densities is very low at all groundwater levels. At a GSI of 10 (the lowest rock mass strength tested), the maximum variation occurs at the highest level of groundwater table, where the difference in displacements from an overburden density of 2000 to 3000 kgm^{-3} was

equal to 4×10^{-2} m (40mm). This is around 1% of the total displacement. At higher strengths the variations in displacements for differing densities are even lower (around 1×10^{-3} m – 10 mm) As such the overburden density is not considered to have a significant influence on excavation stability at such shallow depths.

Figure 3.25 shows the variations in roof displacements for a range of rock mass strength values with increasing overburden thickness. Excavations with lowered groundwater display uniform displacement within the roof centerline at ranges of rock mass strength from 100 down to 60 GSI and at all overburden thicknesses. At GSI values below 60, progressively increased displacements are observed as the overburden thickness increases.

At GSI values between 40 and 10, it can be seen that the initial 4 to 6 m of additional overburden increases the displacement within the roof strata for a given rock mass strength. However additional increases in overburden beyond the first 6 m do not effect roof displacements. The one exception to this is for the rock mass with a GSI of 10 where there is a sudden change in displacements at around 16m. This corresponds with a limited occurrence of tensile yielding within the models.

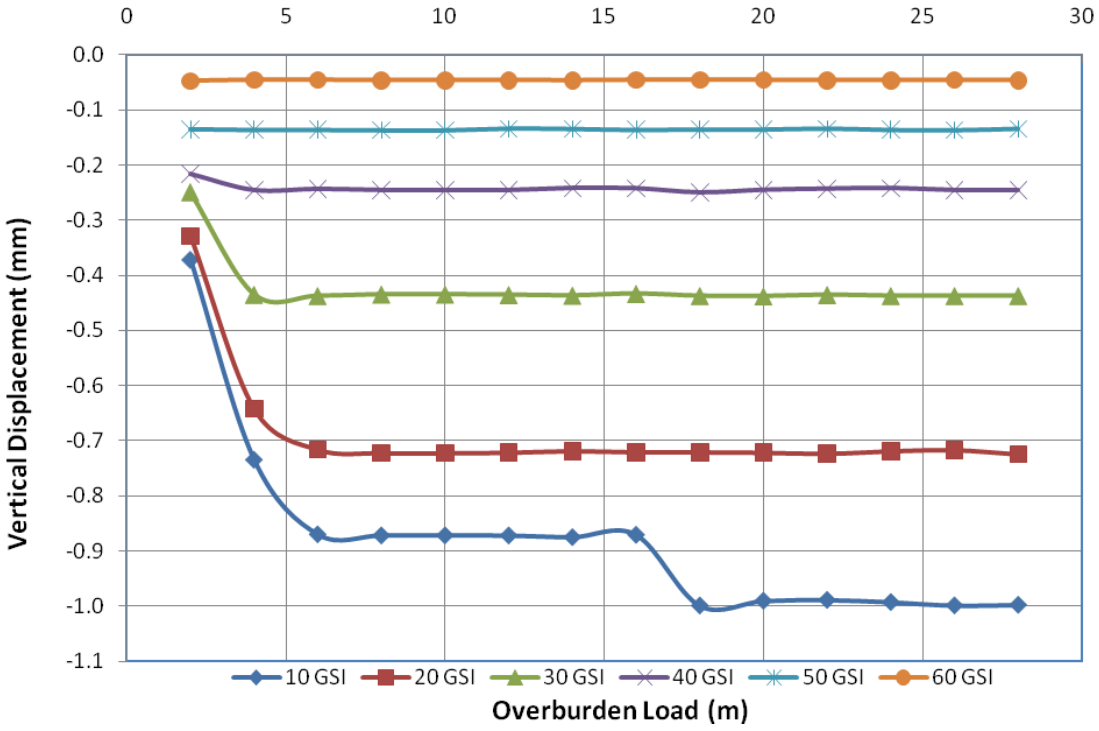

Figure 3.25: Roof centreline displacement for varying rock mass strength values and increasing overburden thickness

Figure 3.25 indicates that overburden thickness has virtually no effect on excavation stability above a GSI value of 60. Below this value the influence of overburden load increases progressively as the strength of the rock mass decreases, but only the first 6 m have any effect. Even at the lowest value of rock mass strength tested, the overburden thickness has a limited effect on excavation stability with very low excavation roof displacements ranging from 0.36 mm (2 m overburden) up to 1 mm (28 m overburden). It is doubtful that such small displacements would contribute significantly to roof failure or collapse.

3.4.10 Effect of Groundwater on Stability at Varying Rock Mass Strengths

In order to assess the effect of a rising groundwater table on the rock mass, a hydrostatic pore water pressure was applied to the model in one metre increments from 1 m below the base of the excavation to the upper boundary of the model grid representing the surface. The density of the zones was also increased to account for the body forces generated by the weight of the water. This was repeated for varying rock mass strengths (GSI 10 to 100) and for varying thicknesses of overburden material (2 to 30 m).

Failure Criterion

In order to establish a point where the roof has become unstable, a function was written using the inbuilt programming language within FLAC to asses the vertical displacement within the roof centreline and to calculate the strain of these elements. In the following modelling it is assumed that the roof has failed when the immediate roof elements have undergone 100% vertical tensile strain.

Modelling Results

It rapidly became apparent that rock masses with a GSI greater than 60 were stable at all the conditions tested here.

This can be seen in Figure 3.26 which represents a 3 m wide excavation with an extraction ratio of 50% and an excavation height of 3 m. The water table has been brought up to the ground surface (30 m above the excavation roof). From the failure plot it is clear that there is virtually no yielding within the roof strata and the displacement plots indicate that there has been virtually no displacement (vertical

displacement values are in the 10^{-4} m range (0.1 mm), this is interpreted as the elastic response to excavation and are considered to be insignificant).

Another factor apparent from the failure plot is that at high rock mass strength values, the coal pillar will yield before the roof of the excavation. This is likely to result in pillar failure / crushing and sag subsidence rather than void migration.

Rock mass strengths below this value all displayed initial stability when the water table was below the excavation as seen in section 3.4.4. However as the water table level increases, in all cases the roof material became unstable based on the criterion described above.

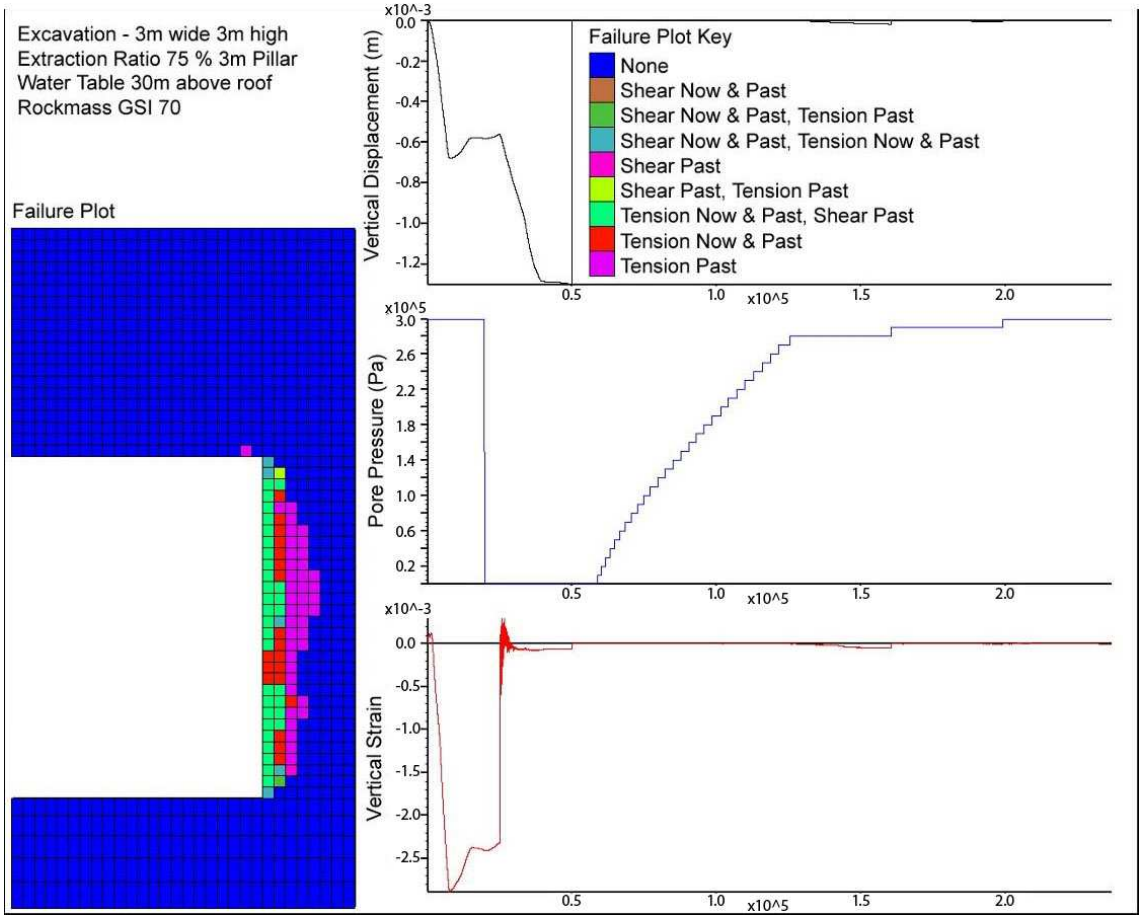

Figure 3.26: Plot with vertical displacement and strain in roof centreline for 3 m wide excavation, extraction ratio of 50%, rock mass GSI of 70 and water table 30 m above the excavation.

Modelling Results for Effect of Groundwater Variation on Excavation Stability with Varying Excavation and Pillar Widths

In the following modelling examples, the width of excavation has been increased and the water table varied to assess the effect, if any, on roof stability. For each change in model state (*i.e.* increase in water table or extraction of material), the models were

stepped to equilibrium to ensure that the roof was stable. If a model was unable to step to an equilibrium condition, this was used as in indicator of instability. This combined with the strain criterion described previously is a good indicator that the roof has become unstable and collapse initiation has occurred.

Excavation Width 1 to 3 m - 50% Extraction GSI 10

The following models all have a rock mass GSI of 10. In each case the water table was increased in 1 m increments until roof yield occurred and the strain criterion was exceeded.

Figure 3.27, Figure 3.28 and Figure 3.29 display the failure plot and displacement and strain data for increasing excavation width with an extraction ratio of 30%. Figure 3.27 (the 1 m excavation) shows that the excavation is stable until the 1st increment of groundwater increase over the excavation roof (the 1st step in the pore pressure graph). At this point there is some initial instability as demonstrated by the deflection in the displacement and strain curves. However the model ultimately comes to equilibrium and the displacement curve can be seen to return to horizontal.

The groundwater level is again increased and an attempt is made to step the model to equilibrium. At this point however the vertical displacement begins to “run away” the gradient of the line can be seen to steepen indicating that the instability is progressively worsening. This continues until the strain criterion is exceeded and the model is reset. The yield plot indicates that there is current tensile yielding in the roof (zones indicated as failure in Tension Now & Past). This represents a failure of the roof and an initiation of void migration. Figure 3.28 and Figure 3.29 show a similar trend to the 1 m wide excavation, with an initially stable excavation until the groundwater level increases above the excavation. The main difference in this case is that the collapse initiates at a groundwater level 1 m above the excavation roof rather than 2 m.

As the excavation width is increased, the height that the yield zone extends into the rock mass increases (from 0.4 m in the 1 m model, to 0.7 m in the 3 m wide excavation) as demonstrated in the failure plots for the 3 models. However the overall yield pattern is virtually identical with a zone of tensile failure above the roof centreline and a region of mixed shear and tensile failure near the pillar margin.

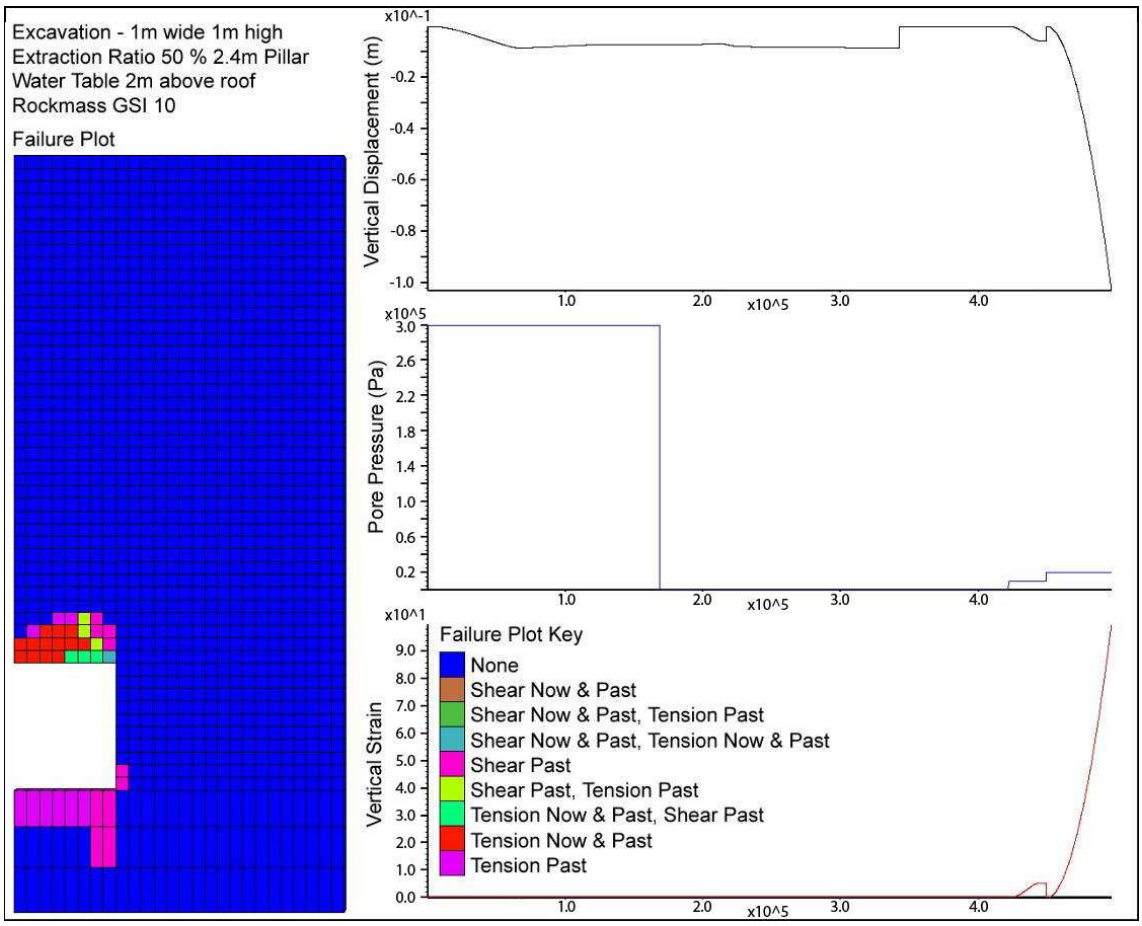

Figure 3.27: Plot with vertical displacement and strain in roof centreline for 1 m wide excavation, extraction ratio of 30%, rock mass GSI of 10 and water table 2 m above the excavation roof.

The above indicates that excavations may be initially stable, but small increases in the groundwater table can initiate roof instability and void migration. Figure 3.28 and Figure 3.29 also show that an increase in excavation width will lead to instability at lower groundwater levels.

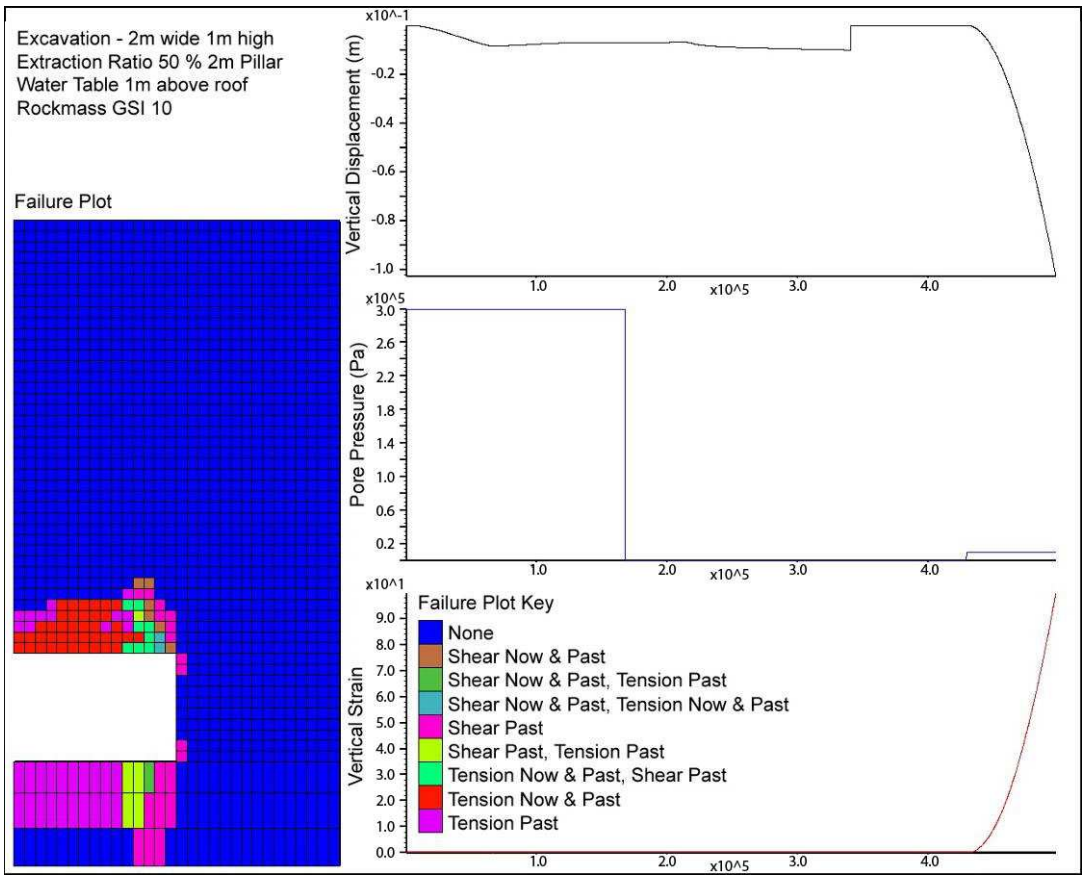

Figure 3.28: Plot with vertical displacement and strain in roof centreline for 2 m wide excavation, extraction ratio of 30%, rock mass GSI of 10, water table 1 m above the excavation Roof.

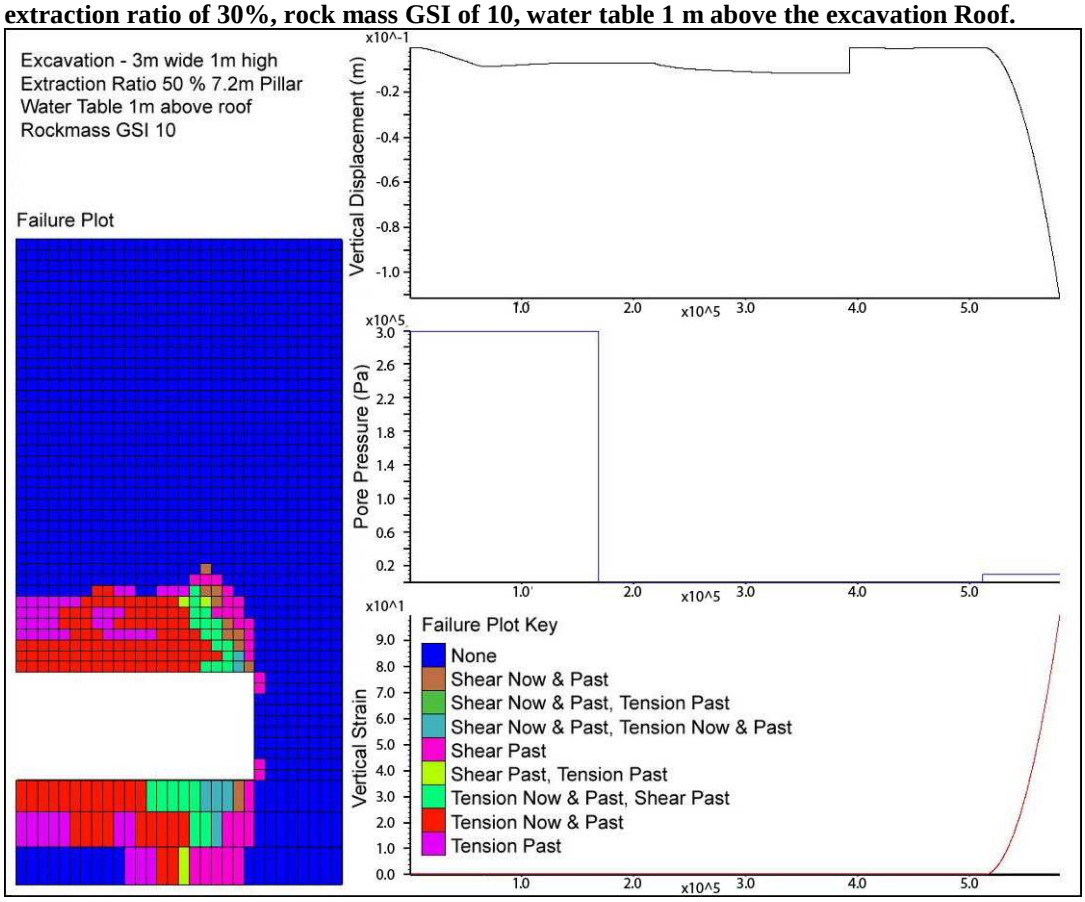

Figure 3.29: Plot with vertical displacement and strain in roof centreline for 3 m wide excavation, extraction ratio of 30%, rock mass GSI of 10 and water table 1 m above the excavation roof.

Excavation Width 1 to 3 m - 75% Extraction GSI 10

The following models all have a rock mass GSI of 10. In each case the water table was increased in 1 m increments until roof yield occurred and the strain criterion was exceeded.

Figure 3.30, Figure 3.31 and Figure 3.32 display the failure plot and displacement and strain data for increasing excavation width with an extraction ratio of 50%. The results show a similar trend to those for the 30% extraction ratio, with an initially stable excavation until the groundwater level increases above the excavation. The water table leads to failure at the same level for the same width of extraction regardless of the reduced pillar thickness due to the increase in extraction ratio.

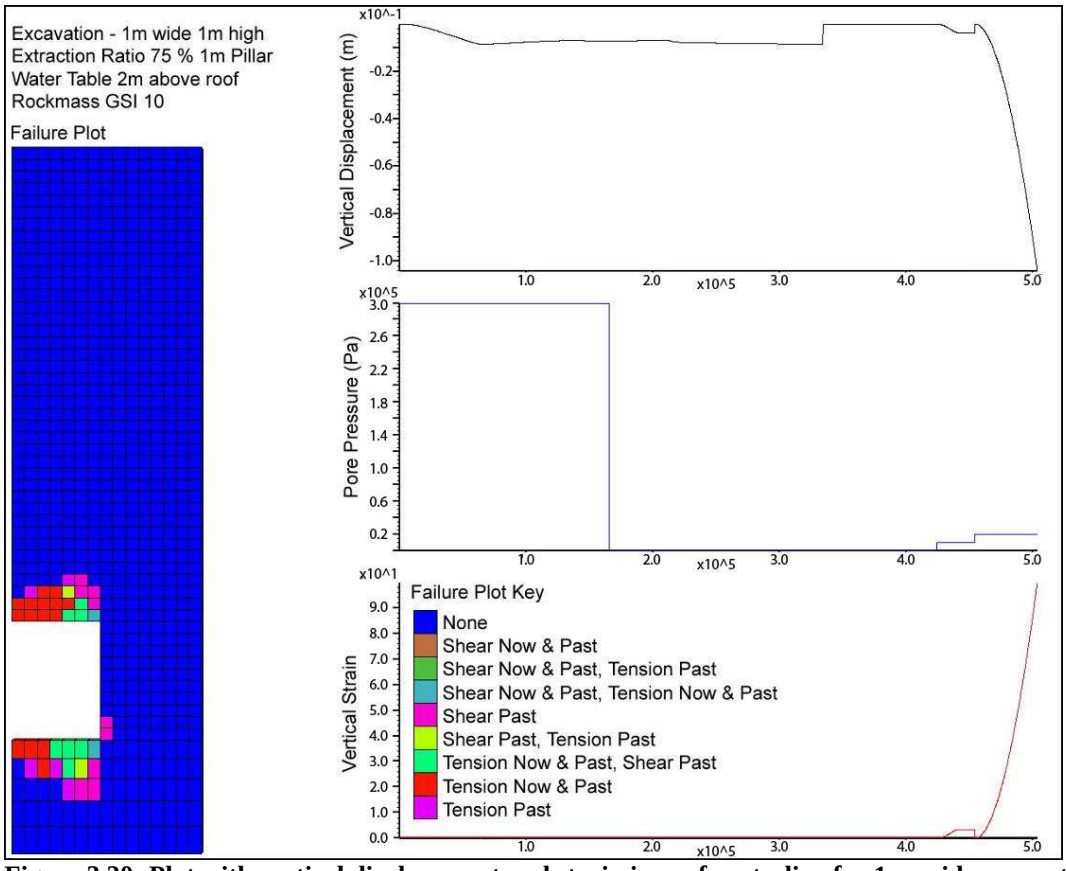

Figure 3.30: Plot with vertical displacement and strain in roof centreline for 1 m wide excavation, extraction ratio of 50%, rock mass GSI of 10 and water table 2 m above the excavation roof.

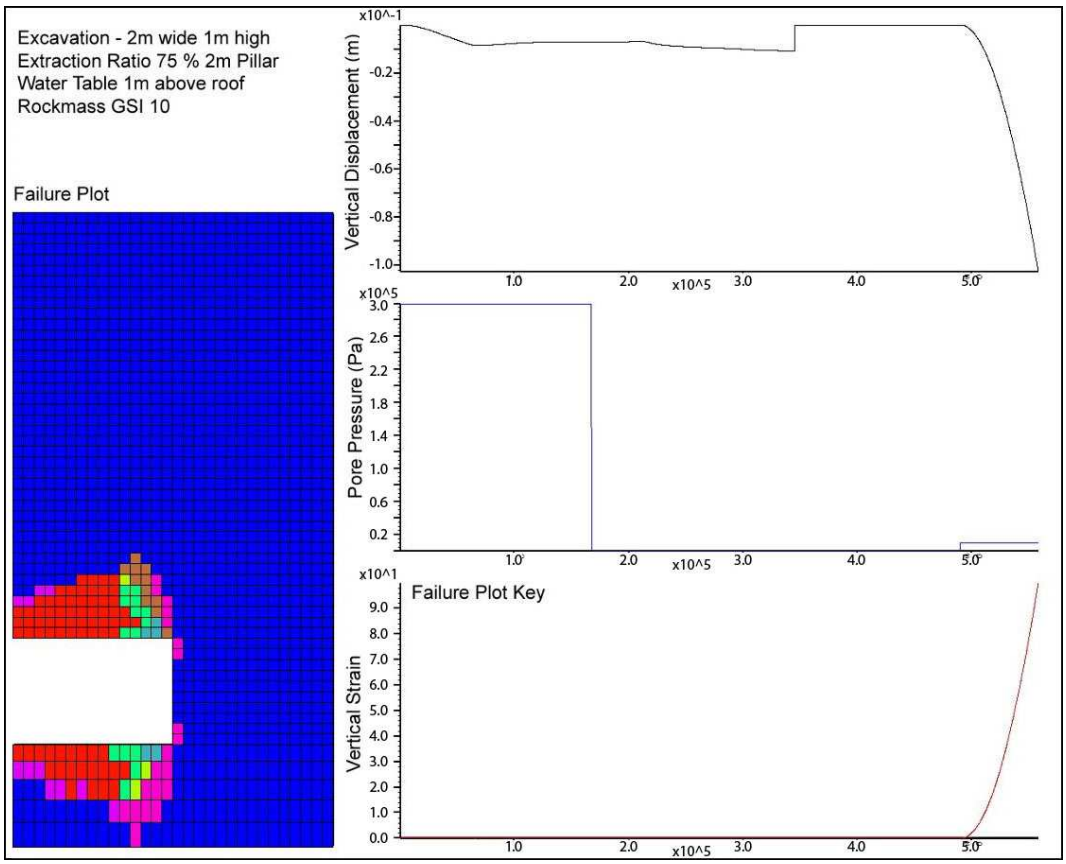

Figure 3.31: Plot with vertical displacement and strain in roof centreline for 2 m wide excavation, extraction ratio of 50%, rock mass GSI of 10 and water table 1 m above the excavation roof.

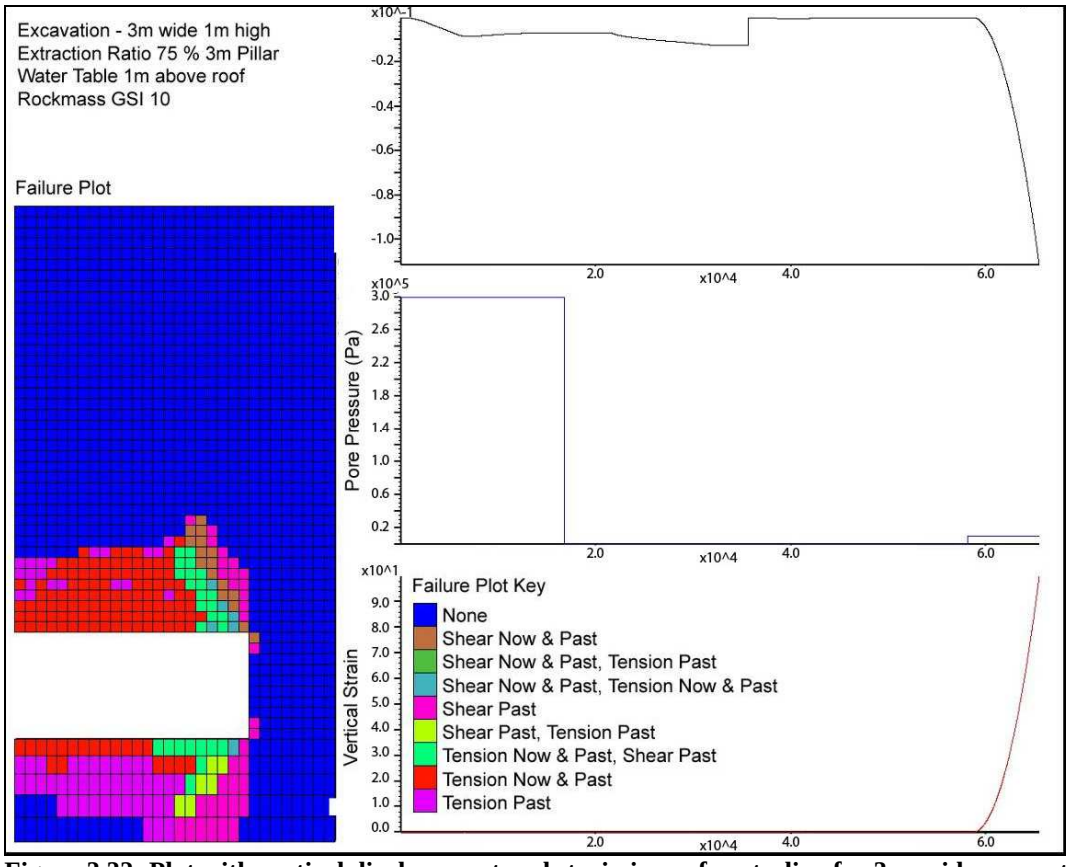

Figure 3.32: Plot with vertical displacement and strain in roof centreline for 3 m wide excavation, extraction ratio of 50%, rock mass GSI of 10 and water table 1 m above the excavation roof.

Excavation Width 1 to 3 m - 85% Extraction GSI 10

The following models all have a rock mass GSI of 10. In each case the water table was increased in 1 m increments until roof yield occurred and the strain criterion was exceeded.

Figure 3.33, Figure 3.34 and Figure 3.35 display the failure plot and displacement and strain data for increasing excavation width with an extraction ratio of 65%. Again the results are very similar to those for the 30% and 50% extraction ratios, with an initially stable excavation until the groundwater level increases above the excavation roof. The trend seen for the previous extraction ratios is followed here where the water table leads to failure at the same level for the same width of extraction regardless of the reduced pillar thickness due to the increase in extraction ratio.

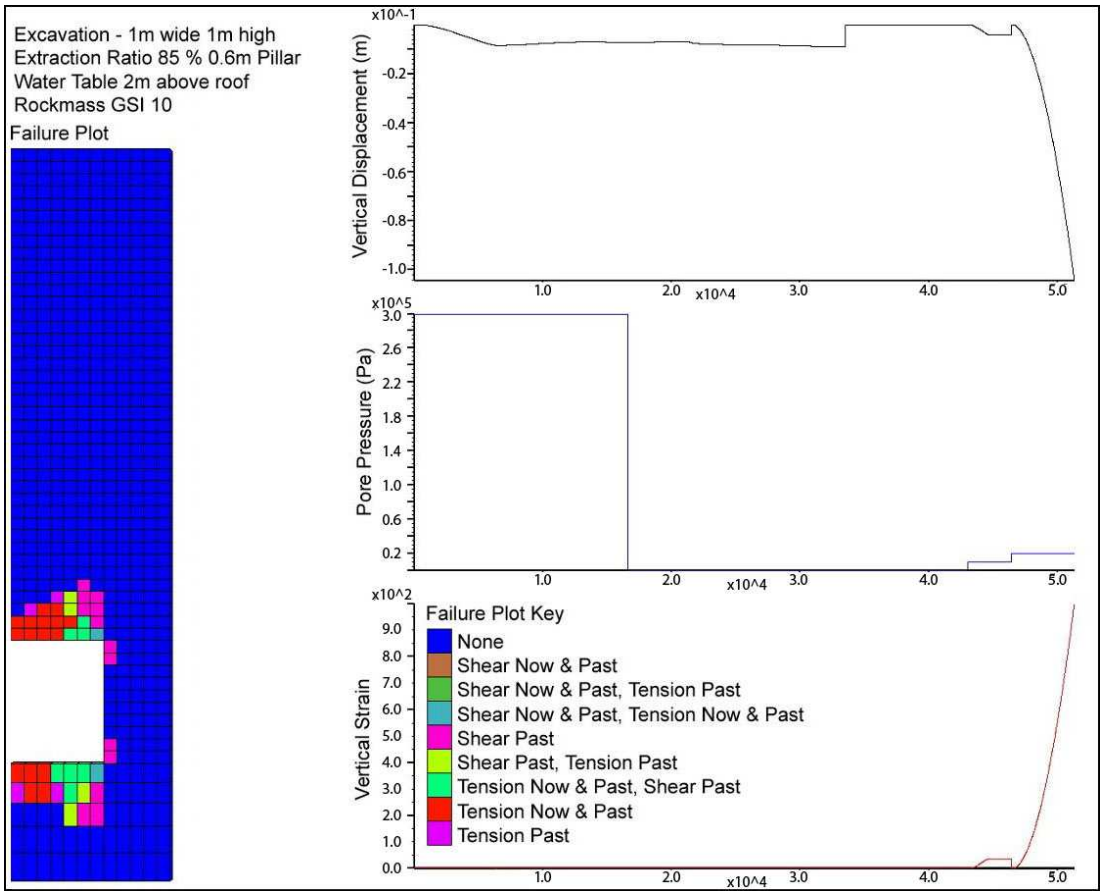

Figure 3.33: Plot with vertical displacement and strain in roof centreline for 1 m wide excavation, extraction ratio of 65%, rock mass GSI of 10 and water table 1 m above the excavation roof.

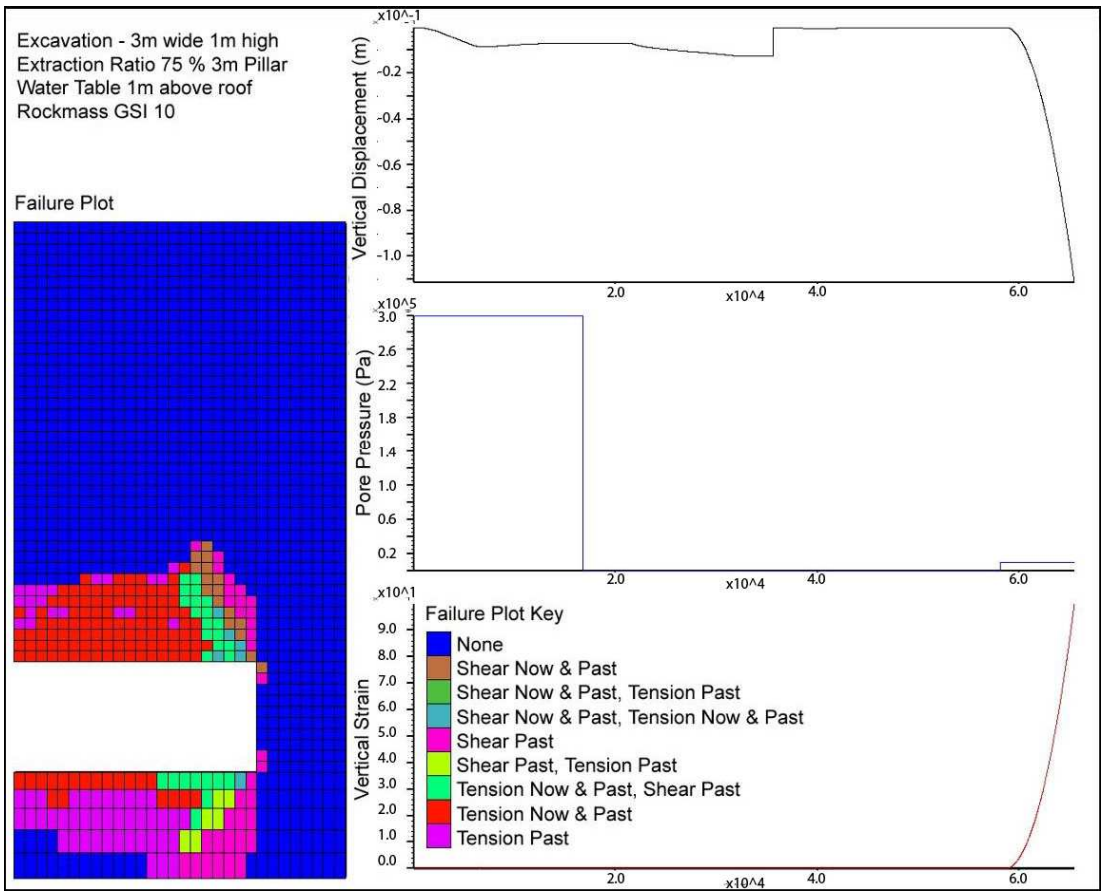

Figure 3.34: Plot with vertical displacement and strain in roof centreline for 2 m wide excavation, extraction ratio of 65%, rock mass GSI of 10 and water table 1 m above the excavation roof.

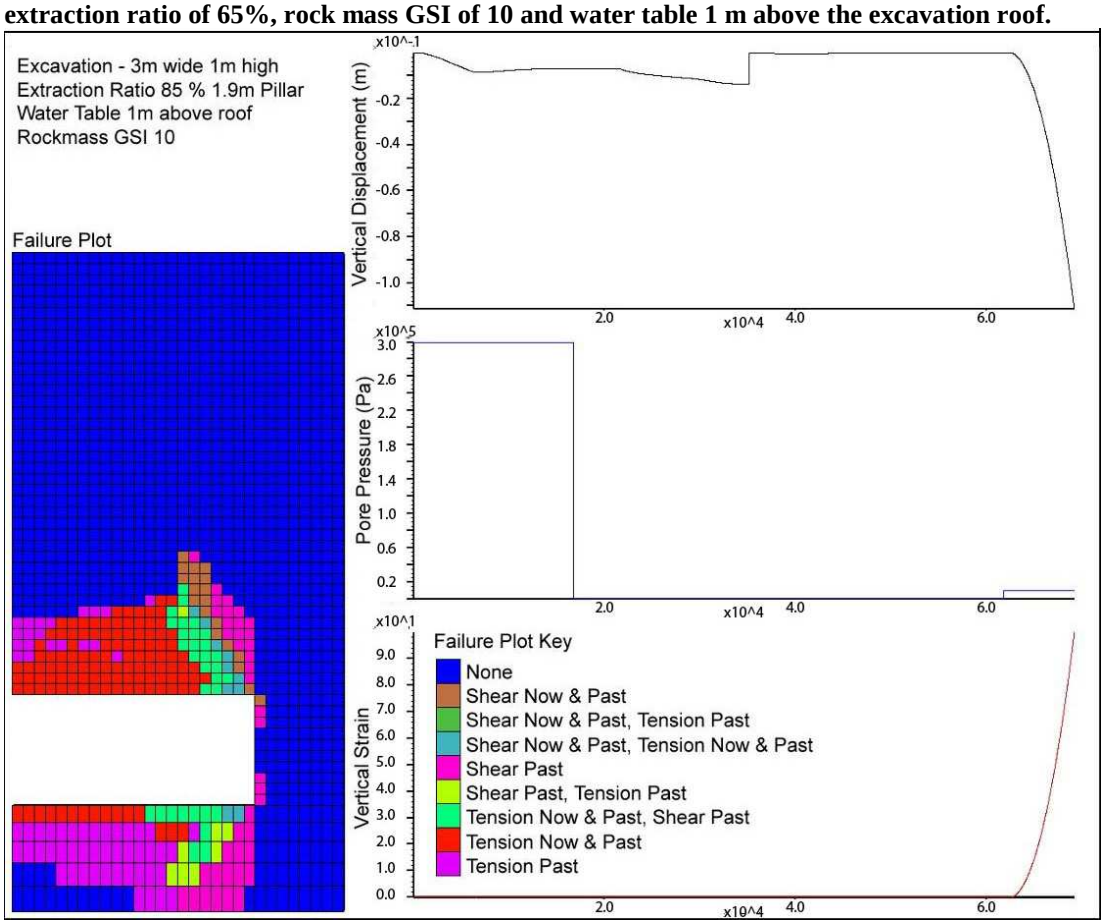

Figure 3.35: Plot with vertical displacement and strain in roof centreline for 3 m wide excavation, extraction ratio of 65%, rock mass GSI of 10 and water table 1 m above the excavation roof.

3.4.11 Effect of Groundwater Variation on Excavation Stability with Varying Rock Mass Strength

The following models have rock mass GSI values varying from 10 to 60. In each case the water table was increased in 1 m increments until roof yield occurred and the strain criterion was exceeded. Each model represents a 2 m wide excavation with a 2 m thick coal seam and an extraction ratio of 50%

Figure 3.36 shows the yield state and displacement in the excavation roof for a rock mass GSI of 10. This represents the lowest strength rock mass tested.

At this rock mass strength the excavation is initially stable, however as the water table level increases, the pore pressure increase results in a reduction in the effective stress within the rock mass. This ultimately exceeds the tensile strength of the rock mass leading to failure and vertical displacement. The roof collapse criterion is exceeded at a water table level 1 m above the excavation roof.

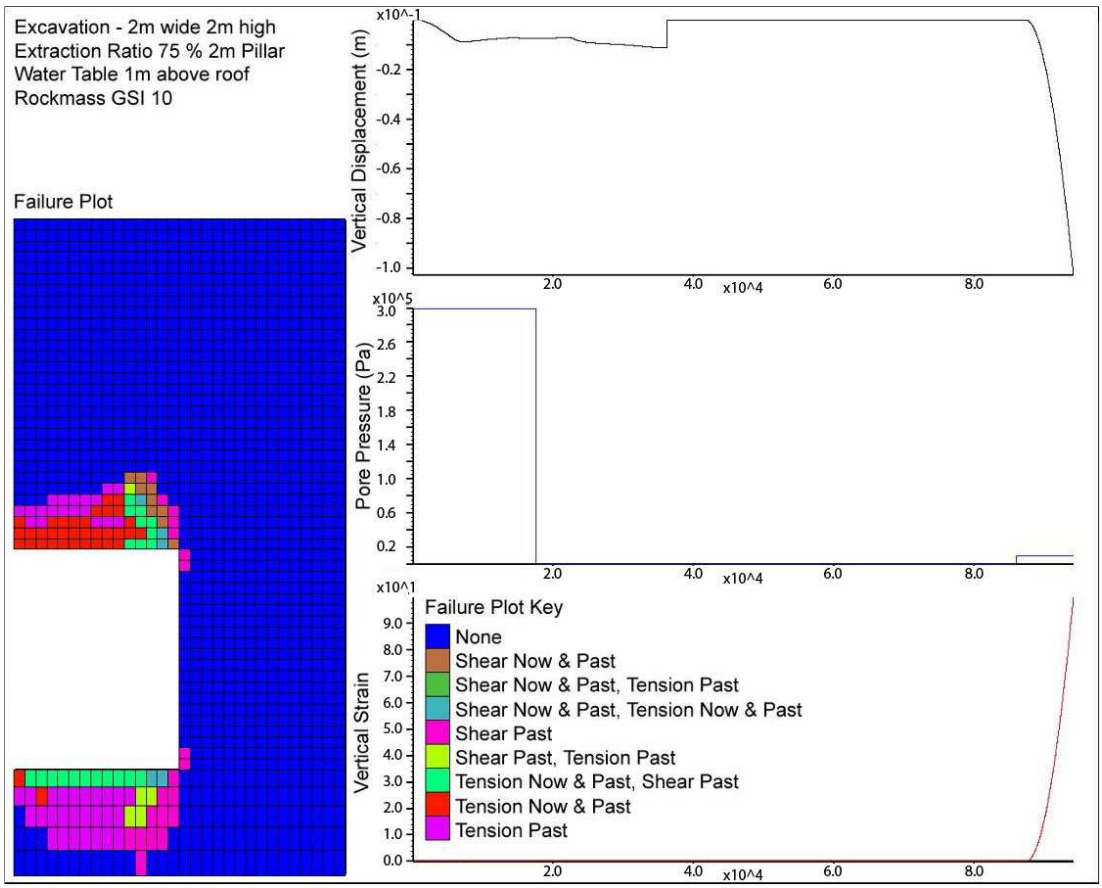

Figure 3.36: Failure plot with vertical displacement and strain in roof centreline for 2 m wide excavation, extraction ratio of 50%, rock mass GSI of 10 and water table 1 m above the excavation roof.

Excavations in rock masses with a GSI of 10 or below are highly susceptible to small fluctuations in the groundwater level. At a rock mass GSI of 20, the level of water table required to cause significant yielding within the roof which leads to collapse is increased by 1 m. The pattern of yielding within the rock mass shown in Figure 3.37 is similar to that for the lower strength rock mass but the zone of shear failure above the pillar margin has decreased. This trend of decreased shear yielding above the pillar margin continues as the rock mass GSI is increased. The increase in GSI also leads to an increase in the level of water table required to initiate roof failure. At a GSI of 30, the water table must reach a level of 3 m above the excavation to initiate roof collapse as shown in Figure 3.38. For values of GSI above 30 the water table increases required to initiate failure start to increase. In Figure 3.39 where the rock mass has a GSI of 40, the water table increase required to initiate failure has doubled to 6 m over the excavation roof. This trend continues through a GSI of 50 (requiring a water level of 12 m over the excavation roof to cause failure as shown in Figure 3.40) and for a GSI value of 60 (Figure 3.41) which is stable until the water level is 23 m over the excavation roof.

Another point of note is that the rock masses with GSI of 30 or below display a sudden failure upon increase in the water table with virtually no displacements in the rock mass before the increase in water table that leads to failure. However the rock masses with GSI from 40 to 60 undergo a preceding yield event with displacements ranging from 10 to 50 mm.

This sudden failure with a small increase in groundwater level suggests that even relatively high strength rock masses (GSI 50 to 60) may be at risk from roof failure if the water table is at a point where stability is marginal. This may be exacerbated by superposition of an unseasonably high rainfall event or other extreme events that may affect the groundwater regime.

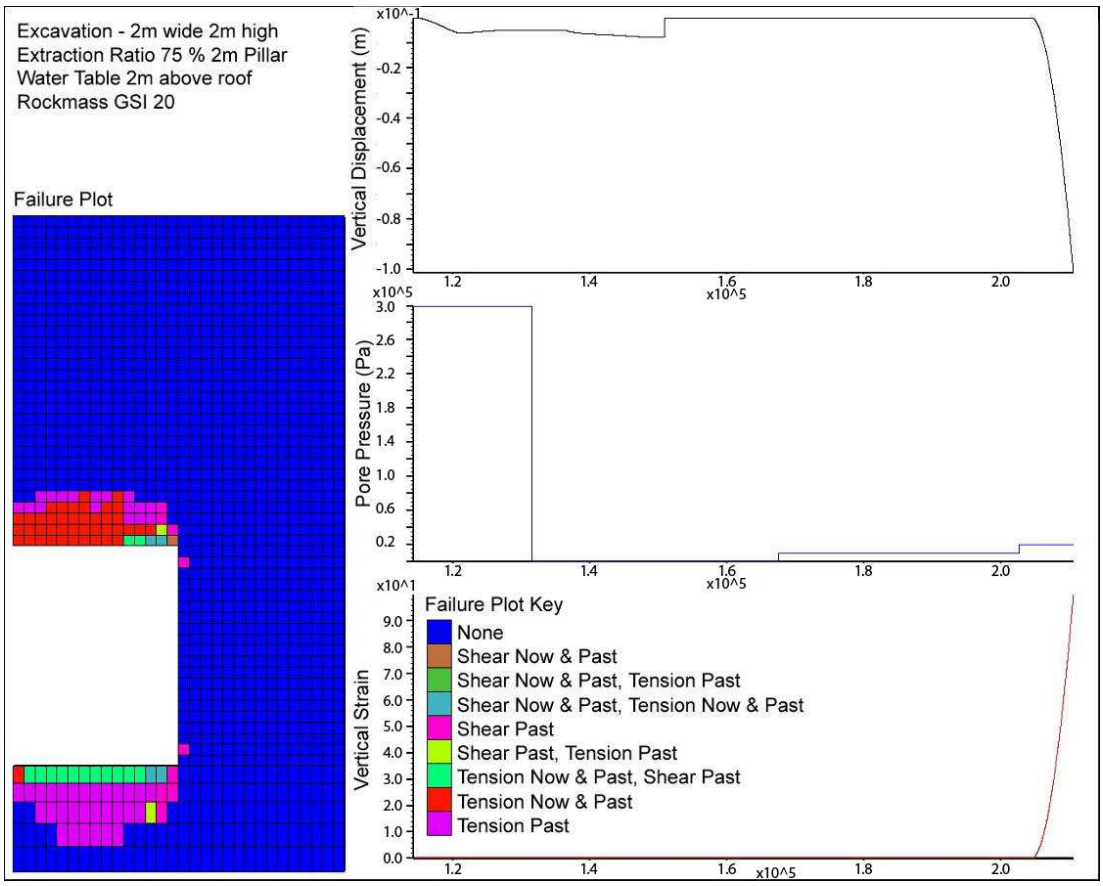

Figure 3.37: Plot of vertical displacement and strain in roof centreline for 2 m wide excavation, extraction ratio of 50%, rock mass GSI of 20 and water table 2 m above the excavation roof.

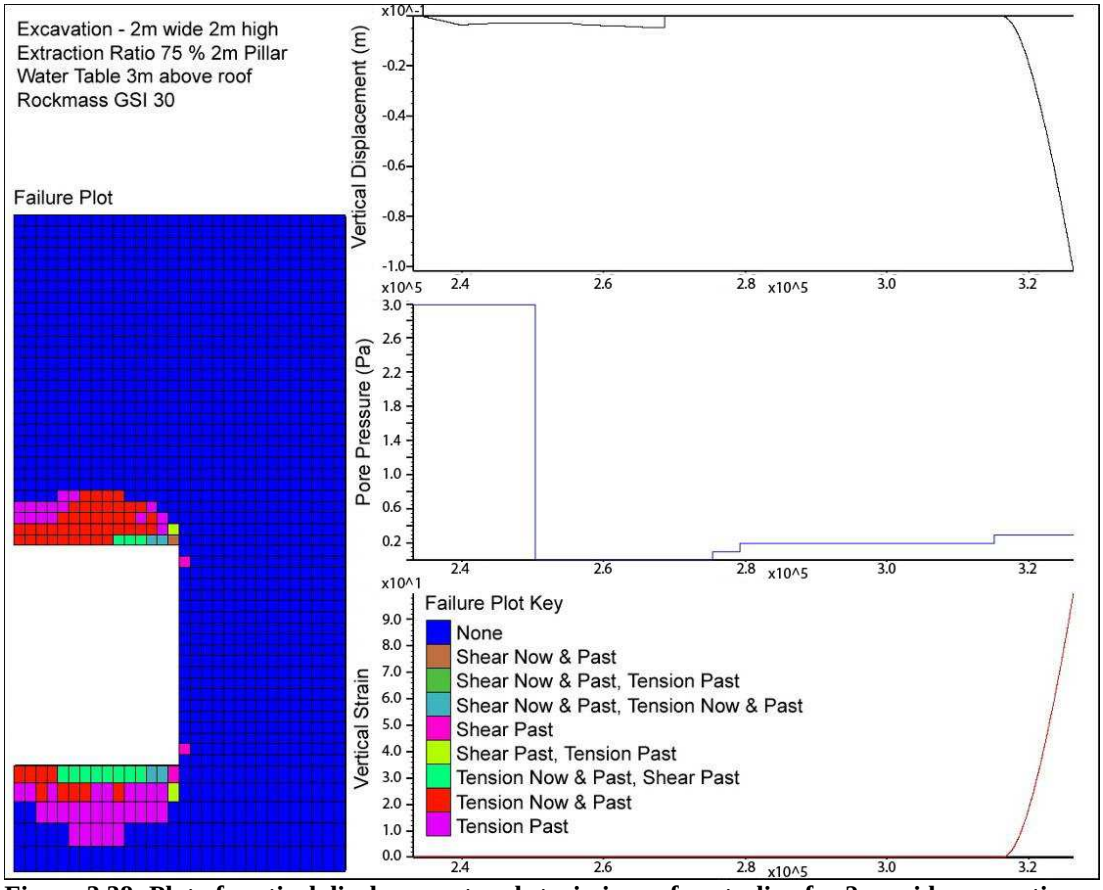

Figure 3.38: Plot of vertical displacement and strain in roof centreline for 2 m wide excavation, extraction ratio of 50%, rock mass GSI of 30 and water table 3 m above the excavation roof.

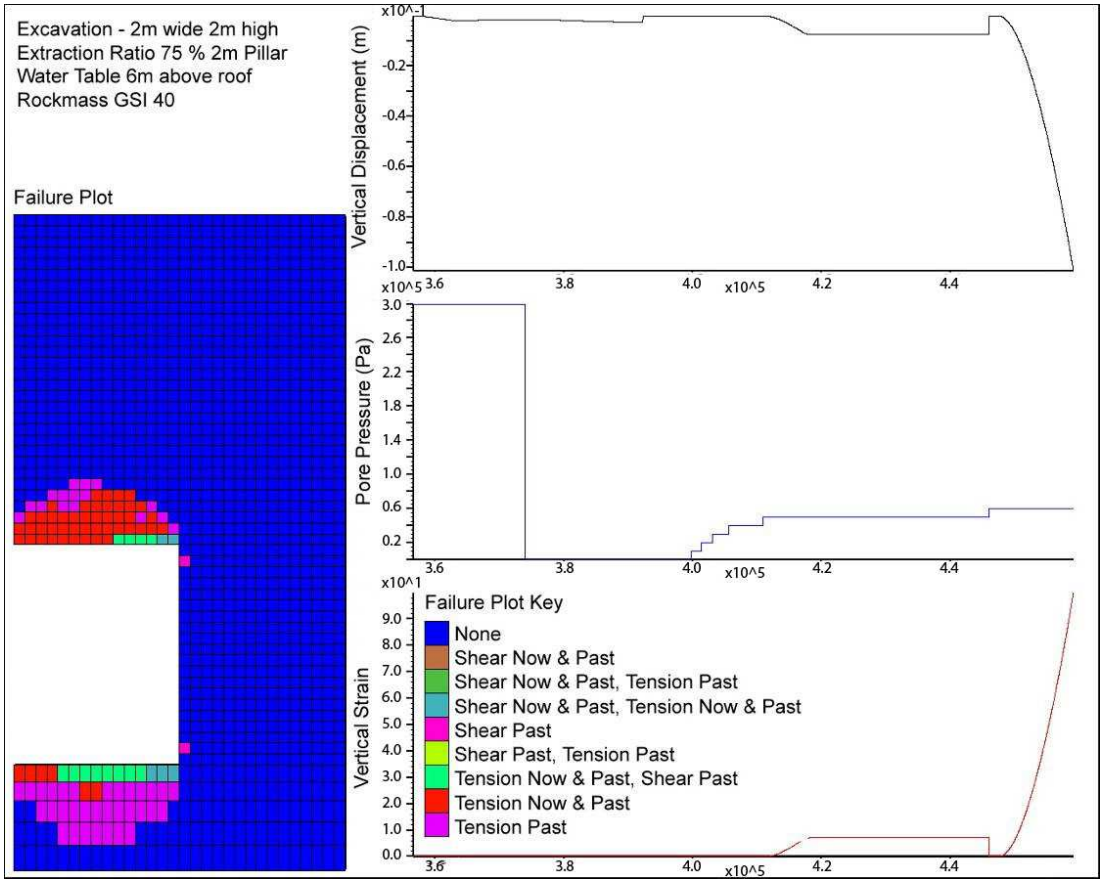

Figure 3.39: Plot of vertical displacement and strain in roof centreline for 2 m wide excavation, extraction ratio of 50%, rock mass GSI of 40 and water table 6 m above the excavation roof.

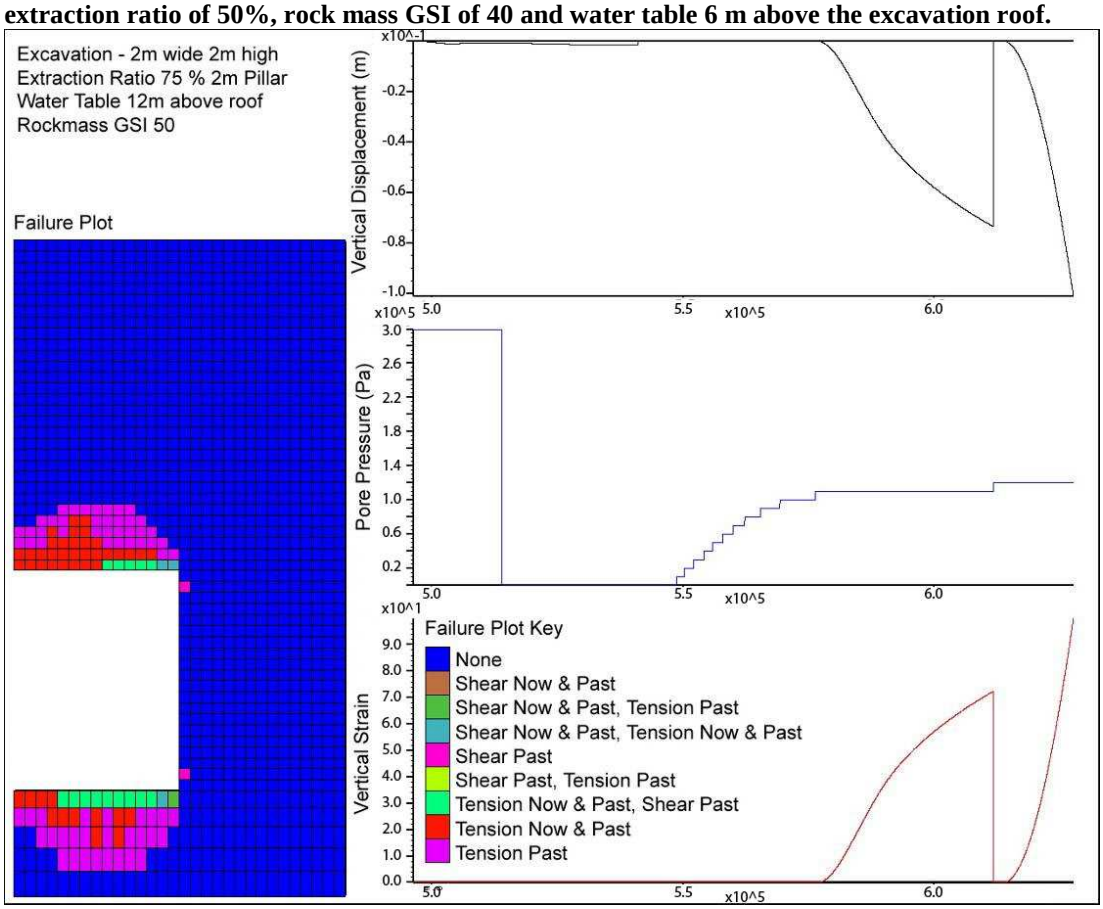

Figure 3.40: Plot of vertical displacement and strain in roof centreline for 2 m wide excavation, extraction ratio of 50%, rock mass GSI of 50 and water table 12 m above the excavation roof.

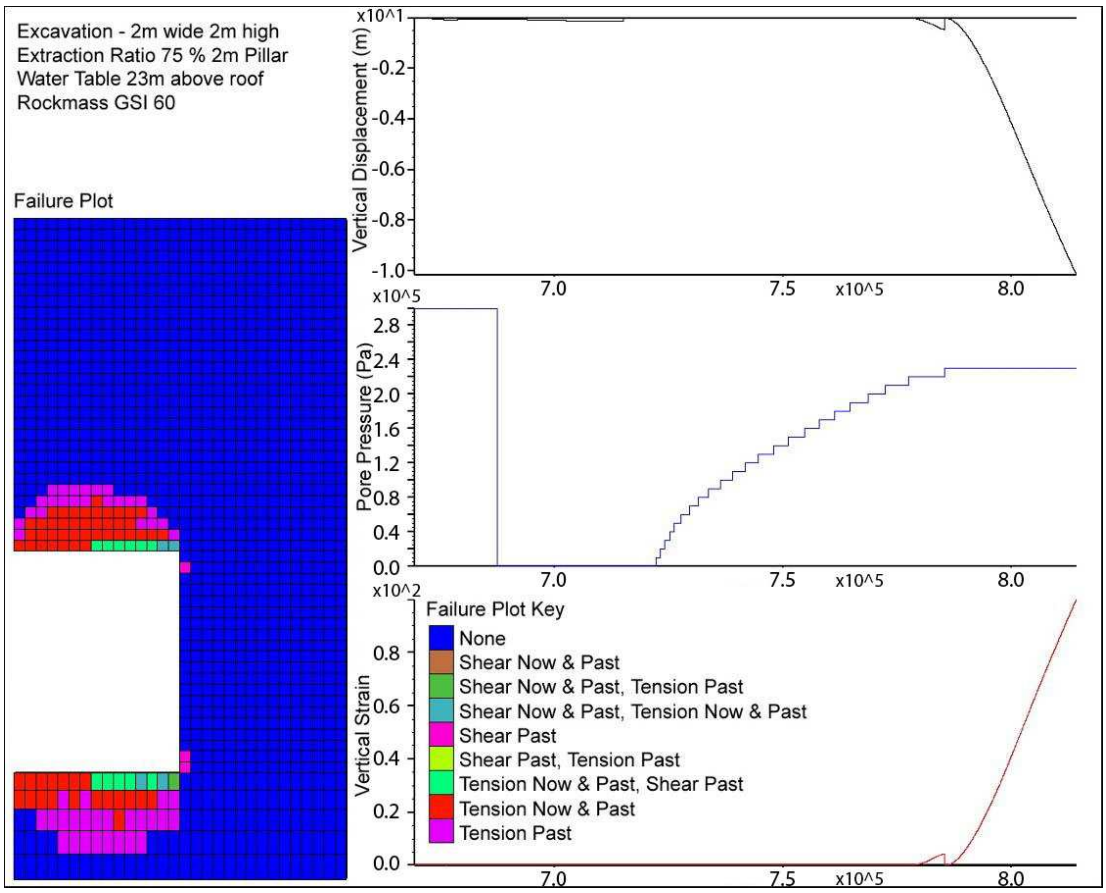

Figure 3.41: Plot of vertical displacement and strain in roof centreline for 2 m wide excavation, extraction ratio of 50%, rock mass GSI of 60 and water table 23 m above the excavation roof.

3.5 Phase 1 Conclusions

Summary of conclusions:

- The overburden density and thickness in the ranges tested appear to be insignificant in terms of excavation roof stability.
- Increased excavation width in shallow workings increases the extent of yielding within the rock mass above the excavation. However in dry conditions where the excavation is above the water table the excavations are ultimately stable, even at the lowest rock mass strength tested.
- Changes in the coal pillar width (extraction ratio) appear to have little effect on the stability of the excavation roof when the water table is below the level of the excavation.
- Variations in the height of extraction appear to be insignificant in terms of excavation stability.
- The rock mass strength of the coal pillars and the under burden seem to be insignificant in terms of excavation roof stability.

- The presence of ground water greatly reduces the stability of abandoned workings. Excavations that are initially stable at rock mass strengths between 10 and 60 will fail if the water table rises beyond a critical level. This level is predominantly affected by the rock mass strength and to a much lesser extent the excavation width.

Initial studies were undertaken using a linear elastic perfectly plastic model to investigate the effects of geometry in terms of excavation width as well as pillar width on the stability of excavations. Using the continuum assumption and a Mohr-Coulomb plasticity model indicated that the width of the excavation affected the degree of yielding that occurred within the rock mass but had no effect on the ultimate stability at even the lowest rock mass strength and stiffness properties at all excavation widths when the water table was below the excavation. However the fact that it was demonstrated to have an effect on the yield state of the rock mass meant that it was deemed worthy of further investigation in the more in depth modelling undertaken in the second phases.

Variations in the width of the coal pillar were shown to have virtually no effect on the stability of the roof with yielding occurring to the same extent for a given excavation width and rock mass strength in all cases. As such this was deemed to be an insignificant parameter in the stability of the excavation roof and was not investigated further.

The initial investigation into the effect of the roof material rock mass strength and stiffness properties indicated that this parameter had a significant impact on the yielding that occurred within the roof of the excavation although the results indicated that excavations at all geometries were stable when using a Mohr-Coulomb model. As this parameter was clearly significant it is intended to investigate this further in the second phase of modelling using the more sophisticated constitutive models available.

Variations in the strength of the underlying rock mass were shown to effect the displacements in the roof strata, whereby a decrease in strength led to increased vertical displacements in the roof centreline. However it was observed that these were also occurring in the coal pillar with exactly the same magnitude so it was interpreted that this represented rigid body motion and was not indicative of roof failure or collapse that

would lead to void migration. The strength of the underlying rock mass was not deemed significant in terms of its effect on excavation stability in this case (although it is recognised that this would not be the case in multi seam mining which is not investigated here).

The effect of variations in the coal pillar strength were shown to be minimal in terms of the stability of the roof strata, with decreasing strength of the coal pillar relative to the under and over burden rock mass leading to increasing yielding within the pillar and ultimately pillar failure. However this did not lead to differential displacements in the roof centre line as the overlying material deformed uniformly as a rigid body and so was not observed to affect the stability of the excavation roof. As such the effects of variations in the strength of the coal pillar will not be investigated in any greater detail in the second numerical modelling phase of the study.

The modelling undertaken to investigate the effect of overburden thickness on excavation stability was surprising as it demonstrated that it has virtually no effect on excavation stability above a GSI value of 60 and a very limited effect below this, where the influence of overburden load increases progressively as the strength of the rock mass decreases, but only the first 6 m of overburden appeared to have any effect. Even at the lowest value of rock mass strength tested, the overburden thickness has a limited effect on excavation stability with very low excavation roof displacements ranging from 0.1 mm (2 m overburden) up to 1 mm (at an overburden thickness of 28 m). It is doubtful that such small displacements would contribute significantly to roof failure or collapse. As such it was assumed that the overburden thickness did not play a significant role on the initiation of roof instability (however it is recognised that it is clearly a very significant parameter in terms of the potential height to which void migration may occur). As such the effects of variations in over burden thickness will not be investigated any further in the second numerical modelling phase of the study. However it is recognised that this parameter is significant in post failure and void migration behaviour which is discussed in Chapter 6.

Chapter

4

Parametric Study Phase 2 Part A – Use of Advanced Constitutive Continuum Models

4 Parametric Study Phase 2 Part A – Use of Advanced Constitutive Continuum Models

In this section of the modelling work, the parameters identified from phase one as being significant in the stability of the roof strata are investigated in greater detail. Use is made of more complex constitutive models that allow anisotropic materials to be modelled along with the post failure variation in strength behaviour. Initially modelling is undertaken using the strain softening Mohr-Coulomb model to investigate the effect of post failure strain dependant strength reductyion on the stability of shallow mine workings. Following this, use is made of the strain softening ubiquitous joint Mohr-Coulomb model to investigate the effect of variations on the dip angle of a weakness plane on the model.

4.1 Effect of the Use of the Strain Softening Mohr-Coulomb Model Compared to the Standard Mohr-Coulomb Model

To this point the modelling work within FLAC has made use of the Mohr–Coulomb constitutive model. This is the recommended model for making initial investigations into geomechanics problems where yielding or failure is possible, but the post failure response of the material is less important and for problems with limited lab test or site investigation derived strength parameters (Itasca, 2005). Although, this is well suited for modelling the conditions leading to initial failure (*i.e.* collapse initiation), it is not ideally suited for modelling the post failure response of the system (*i.e.* caving).

This is because the standard Mohr-Coulomb model within FLAC assumes that when the strength of the material has been exceeded, it yields in a ductile fashion rather than a brittle manner. As such, the material in the model has maintained cohesion (in a continuum model) and is still able to support a stress equal to the failure strength. This is adequate for initial sagging of roof strata, but not for ultimate collapse. In reality, the roof material upon failure would lose cohesion once discrete fractures have formed. This would result in a drop in shear strength and a total loss of tensile strength.

This problem is partly negated in discrete modelling where interface elements have been included as the roof strata are physically able to sag and as such will lose contact with the strata above them and therefore no longer offer support. A conceptual diagram to explain the Strain Softening model is shown below.

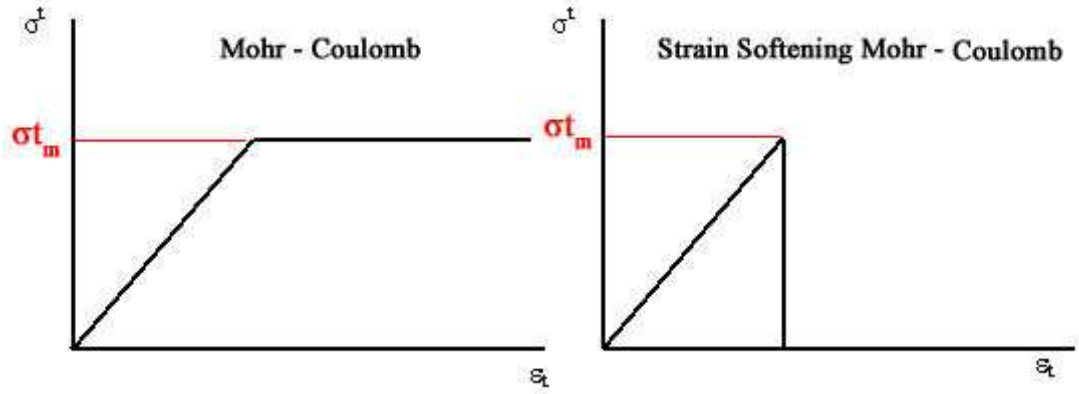

Figure 4.1: Stress strain relationships for the Mohr-Coulomb and strain-softening models

Figure 4.1 shows the stress-strain relationships for an element under an increasing tensile stress that ultimately exceeds the failure strength of the material. In both cases the tensile failure strength (σ^t)of the material is identical but the post failure responses are different. In the Mohr-Coulomb model the strain continues to increase with no further increase in tensile stress. However, the element is still supporting a proportion of the stress, which should realistically have been transferred to the surrounding zones. It is possible therefore that the Mohr-Coulomb model would underestimate the height of collapse over the workings.

In the strain-softening model the user can define the post failure strength of the material at varying increments of strain. In the example shown here, representative of brittle failure and a total loss of tensile strength, the post failure strength drops immediately to zero and the element is no longer able to support any tensile load. Softening parameters can also be applied to vary the cohesion and frictional properties of the material at varying strains. In this section it is intended to investigate the effect of applying a strain softening model to the rock mass as compared to a Mohr-Coulomb model.

4.1.1 Mesh Dependency and Localisation

When using a strain-softening constitutive model, continuum mechanics codes are subject to mesh dependency and in turn localisation whereby once yielding has occurred, the size of the element mesh can affect the degree of plastic strain that occurs and its location (Alehossein and Korinets, 2000). This stems from the fact that, in a grid with mesh sizes that vary, for a given stress gradient, the finer the mesh, the higher the average stress in a given element in the region nearer to the zone of maximum stress when compared to a single or fewer larger elements as the larger mesh element which spans a greater range of the stress contours ultimately has a lower average stress.

As yield criteria in FLAC are calculated based on the averaging of subzone stresses, it is apparent that the smaller zones near the region of highest stress are more likely to lie in a region where the stress exceeds their yield criterion compared to those at a greater distance. Therefore as the mesh becomes finer, the location of the boundary between the region where yielding occurs and the region where it does not becomes more accurate. Conversely it is also possible that the lower average stress within a larger zone in a more coarse mesh applied to the same problem domain may actually result in the yield criterion not being exceeded. As such in these cases the mesh density has affected the results of the model, hence the term mesh dependency / mesh dependent plasticity.

This then leads onto the issue of mesh dependency affecting localisation in strain-softening constitutive models. Localisation occurs where an element that has yielded begins to soften (where the softening is governed by the value of plastic tensile and shear strain within the element which is linked to a user defined variation in the tensile strength, cohesion and friction angle of the material). As this element is now weaker than those surrounding it, any further deformation will concentrate in the softened region or zone.

It should be noted that localisation isn't a problem in and of itself, and in fact it does occur in reality (a good example would be the "necking" of a steel bar in uniaxial tension) however care must be taken to ensure that any localisation of strain occurring within the model is as a result of the problem being modelled leading to high stress concentrations in turn initiating yielding as opposed to mesh dependent yielding leading to high strains causing softening leading to localisation. In order to minimise the impact of mesh dependency and localisation, the mesh discretisation within the grid is maintained at a uniform size and shape.

4.1.2 Strain Softening Parameters

Ideally the parameters used for strain softening would be derived from laboratory testing of coal measures strata where the peak and residual strength values and the strains at which these occur could be derived. However as this information was not available it was necessary to estimate parameters based on information available in the literature.

As such the post peak strength and friction properties are derived based on the recommendations in a number of rock mechanics and rock mass engineering property text books (Goodman, 1989; Brady and Brown, 1993; and Zhang, 2005) along with the methodology suggested by Cai *et al.*, (2007) where the residual strength of a rock mass can be estimated based on the minimum value of GSI which occurs when a rock mass has underdone significant fracturing and a significant reduction in block size and the quality of the discontinuity surfaces has become "poor" In other words, the residual strength of a rock mass is assumed to be equal to the lowest possible GSI value . As such this assumption allows the GSI value to be scaled to find the residual strength properties of the rock mass.

The strains at which softening due to tensile and cohesive strength as well as that at which friction angle reduction occurs, are derived based on a review of parameters used for the modelling of similar problems in the literature in work by Esterhuizen and Karacan (2005); Badr *et al.*, (2003) and Singh and Singh (2009) as well as a laboratory investigation and back analysis undertaken in a South African mine (Roberts *et al.*, 2005), all using values in the range of 10-50 millstrains (1 to 5% strain). Work undertaken on the numerical modelling of deep long wall mine workings using strain softening parameters was also reported by Zipf (2005; 2006). In this work it was assumed that the tensile strength dropped to zero at 1 millistrain (0.1% strain). This lower value is in broad agreement with the laboratory results reported for various rock types by Okubo and Fukui (1996), who for a series of intact rocks derive values equal to between 0.25 and 0.75 millistrains (0.025 - 0.075%) at which tensile strength loss occurs. See Figure 4.2. However the strain behaviour of a delaminating excavation roof with tensile failure along the bedding planes may not be identical to that of an intact rock specimen. As such there is the potential for over estimating the strain dependent strength reduction of the rock mass.

Because of this potential for over estimating the strain softening behaviour and based on the published work where tensile strength reduction occurs at around 10 millistrain (1%) and compressive strength at around 40-50 millistrain (4 to 5%), the residual cohesion and friction properties are assumed to drop to the minimum values equivalent to a GSI of 5 for the rock mass, at a plastic shear strain of 0.05 (50 millistrain or 5% strain) and the tensile strength falls to a residual value of zero at a plastic tensile strain of 0.01 (10 millistrain or 1% strain).

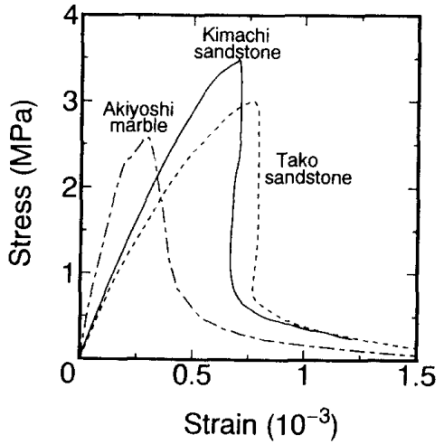

Figure 4.2: Complete stress-strain curves for various rock types in uniaxial tension (Okubo and Fukui, 1996).

See Table 4.1 for the parameters as used in the modelling comparing the effect on stability of the use of the Strain-Softening Mohr-Coulomb constitutive model, with that of the standard Mohr Coulomb model.

Table 4.1: Strain softening parameters showing peak and residual strength values.

GSI	Cohesion	Internal Friction Angle	Tensile Strength	Cohesion at 5% strain	Internal Friction Angle at 5% strain	Tensile Strength at 1% strain
10	0.13	49.0	0.005	0.05	46.0	0.0
20	0.17	55.0	0.011	0.05	46.0	0.0
30	0.24	59.0	0.023	0.05	46.0	0.0
40	0.33	61.0	0.048	0.048	46.0	0.0
50	0.51	63.0	0.1	0.18	46.0	0.0
60	0.85	64.0	0.22	0.118	46.0	0.0
	(MPa)	**(°)**	**(MPa)**	**(MPa)**	**(°)**	**(MPa)**

Based on the discussion above, it is recognised that there is some variability in the softening parameters which are derived for intact rock specimens in the laboratory (0.1 to 5 millistrain of post peak strain before strength loss – 0.01 to 0.5%) and the parameters used in modelling (10 to 50 millistrain – 1 to 5%). As such a parametric study was undertaken to investigate the effect of varying softening post peak strain values on the stability of an excavation at values of post failure tensile strain (ε^{pt}) from 0.005 to 0.01 (0.5 to 1% strain) and post failure shear strain (ε^{ps}) from 0.025 to 0.05 (2.5 to 5% strain).

4.1.3 Model Geometry and Mesh Discretisation

These models all represent a void of uniform height (1 m) and width (3 m) at 10 m below surface, with 10 m of underlying rock mass material and square numerical zones. To observe the relative effect of variations in the input parameters on the models they were each run for a uniform number of time steps as opposed to being stepped to a state of uniform equilibrium ratio. The results are presented below.

4.1.4 Results of Strain Softening Parameter Investigation

When the plots of yield state are observed (Figure 4.3) it can be seen that the results for the range of parameters are broadly similar with the height of the shear failure zone that propagates upwards from the roof pillar intersection extending at the same angle to the same height into the rock mass in all models. The same thing is true (excluding one exception) for the zone of tensile failure which extends above the shear zone forming a column reaching the surface. This is associated with tensile delamination of the strata which is represented by the normal failure of the interface elements (Figure 4.4). There is however one exception. In the $\varepsilon^{pt} = 0.005$ $\varepsilon^{ps} = 0.025$ model, the zone of tensile yielding over the excavation extends approximately 8 m into the rock mass where as for the other parameters in all cases it extends to the surface. This is thought to be related to the increased magnitude of shear (Figure 4.5) and volumetric strains (Figure 4.6) that occur at a lower height over the excavation in this model as the strains concentrate in this region due to the softening that is occurring, this in turn has affected the stress distribution resulting in lower tensile stresses and tensile delamination extending to a greater height.

Further observation of the shear and volumetric strain plots reveals that the maximum magnitude of shear and volumetric strain decreases as the plastic softening parameters increase which is to be expected as the material will soften less rapidly.

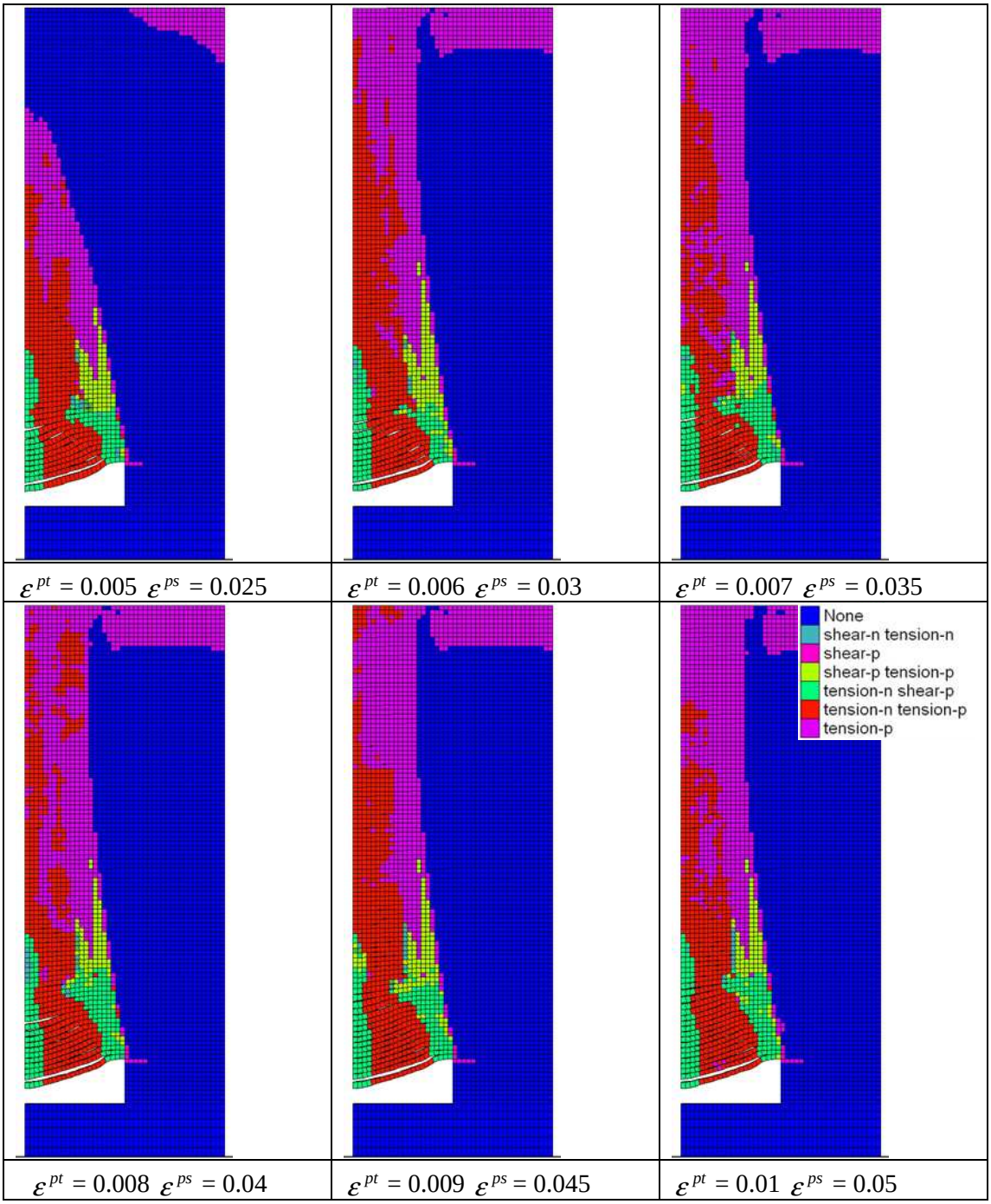

Figure 4.3: Plot of the yield state of the rock mass at varying post peak softening levels.

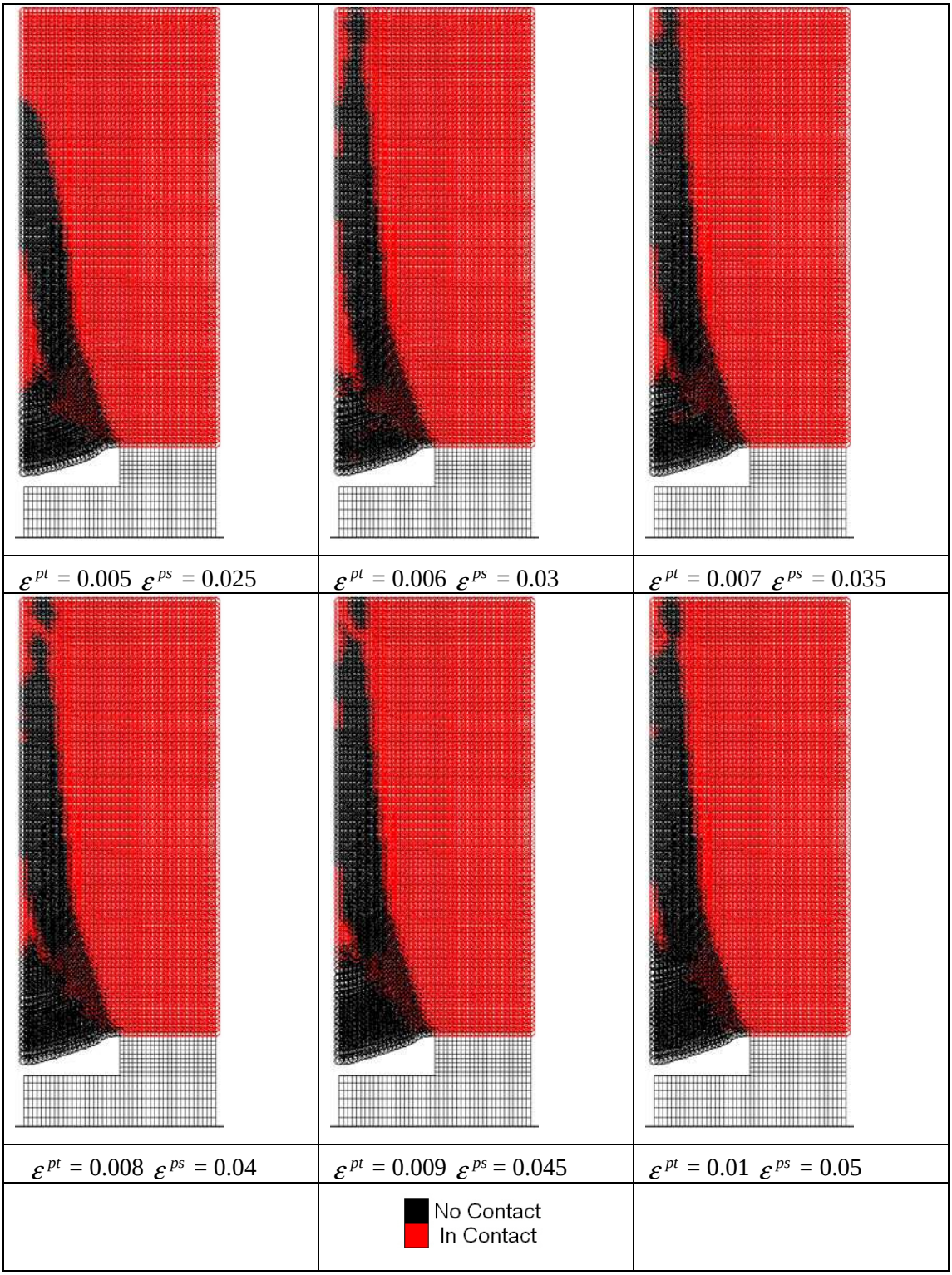

Figure 4.4: Plot of delamination of the rock mass at varying post peak softening levels.

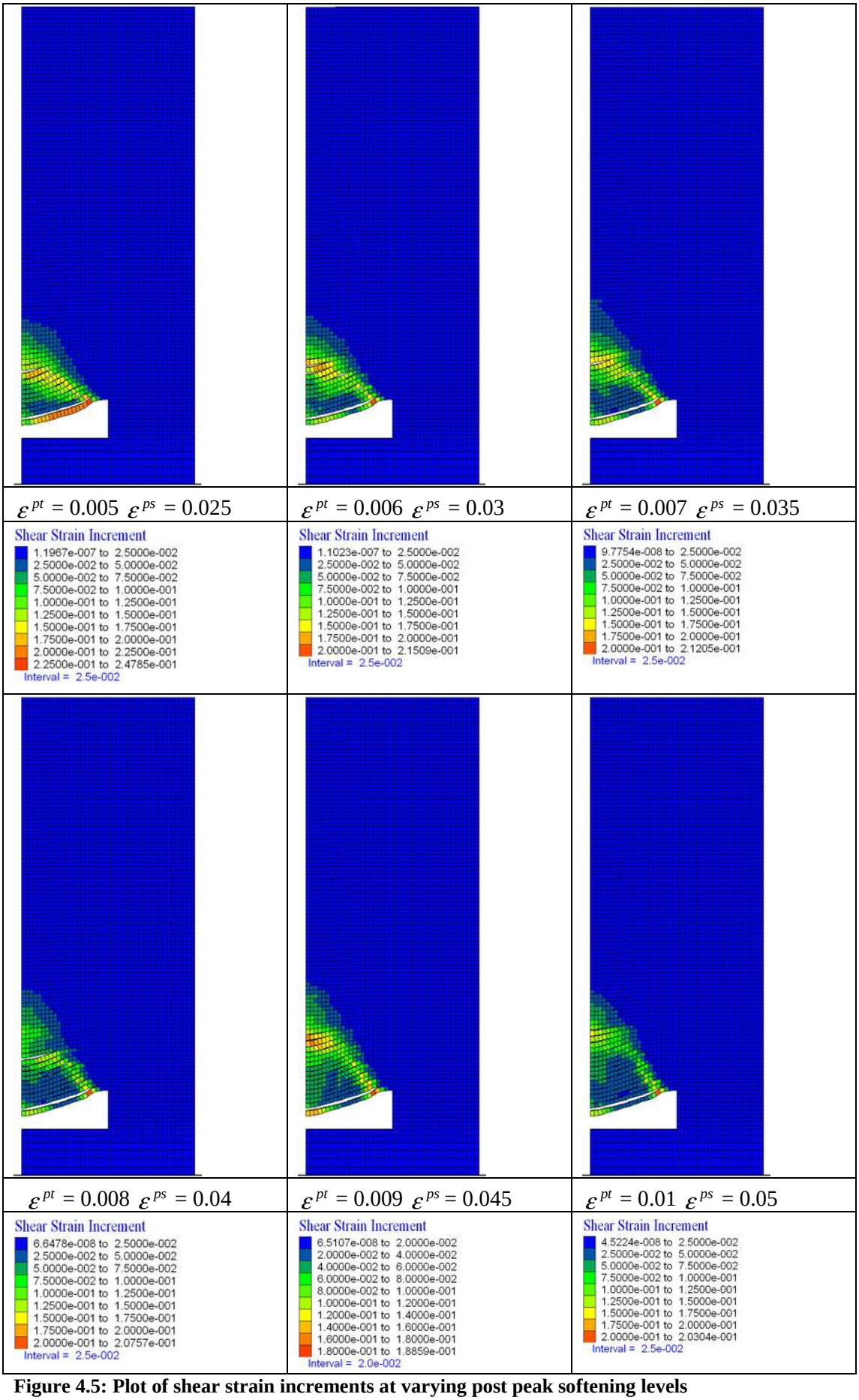

Figure 4.5: Plot of shear strain increments at varying post peak softening levels

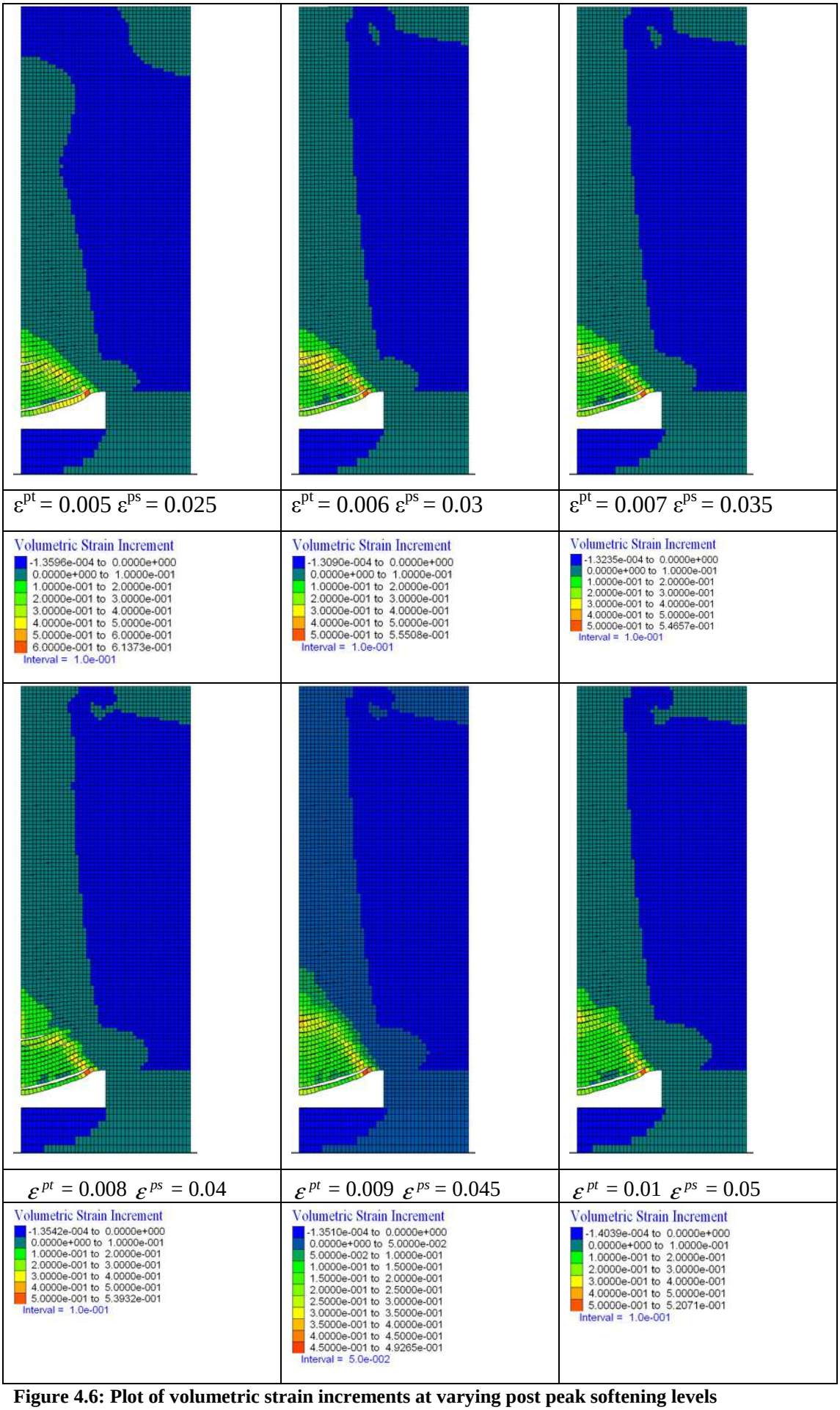

Figure 4.6: Plot of volumetric strain increments at varying post peak softening levels

4.2 Comparison of the Mohr-Coulomb and Strain Softening Models

In the modelling presented here it is intended to identify any significant differences between the Mohr-Coulomb and Strain Softening results.

4.2.1 Model Geometry and Mesh Discretisation

These models all represent a void of uniform height (1 m) and width (3 m) at 10 m below surface, with 10 m of underlying rock mass material and square numerical zones. To observe the relative effect of variations in the input parameters on the models they were each run for a uniform number of time steps as opposed to being stepped to a state of uniform equilibrium ratio. The results are presented below.

4.2.2 Results of Comparisons of Strain Softening and Mohr-Coulomb Modelling

Figure 4.8 is a yield state plot of the rock mass for four different rock mass strengths (from 10 to 40 GSI) where the Mohr-Coulomb results can be compared directly with those for the strain softening model. The main difference that can be observed within the two models is that the height to which tensile yield occurs within the rock mass is greater for the strain softening models than for the problems modelled using the Mohr-Coulomb model. This is related to tensile softening that is occurring in the rock mass in the yield zones above the excavation roof. This in turn reduces the tensile strength of these strata and allows tensile delamination to occur to a greater height as shown in Figure 4.7.

This increased yielding is also related to a reduction in tensile stress within the rock mass over the excavation which drops from a maximum of approximately 9.9 kPa in the Mohr-Coulomb model to a value of 8 kPa in the strain softening model and which can be seen when comparing the plots of maximum principal stress contours in Figure 4.9. One other feature visible on the maximum principal stress plot for both constitutive models is the zone of increased compressive stress which occurs in the rock mass over the pillar centre, underlain by a region of tensile stress within the pillar. This is assumed to be caused by cantilevering of the roof strata over the excavation which are able to pivot at the roof pillar intersection and are being forced upwards into the overlying strata which is causing the compressive stress concentration seen within the rock mass over the pillar.

Another difference between the results for the two constitutive models can be seen in the extent of roof strata failure that occurs with the associated shearing which would

lead to failure of the individual roof stratum. In the models with rock mass strength equivalent to 20 GSI, in both cases shear yielding has commenced within the rock mass over the excavation roof / mine pillar intersection, however the degree to which it has extended into the rock mass is larger in the strain softening model than of that which occurs in the Mohr-Coulomb model again due to softening of the rock mass, allowing the immediate roof strata to fail, whereas in the Mohr-Coulomb model, the shear yielding has not yet resulted in failure of that strata but stability would be marginal.

This increased yielding results in compressive stress reduction in the zone of softening within the model which can be seen in the plots of minimum principal stress (See Figure 4.10) where for the strain softening model the maximum compressive stress at the roof pillar intersection is approximately 1 MPa as opposed to 1.5 MPa for the Mohr-Coulomb model.

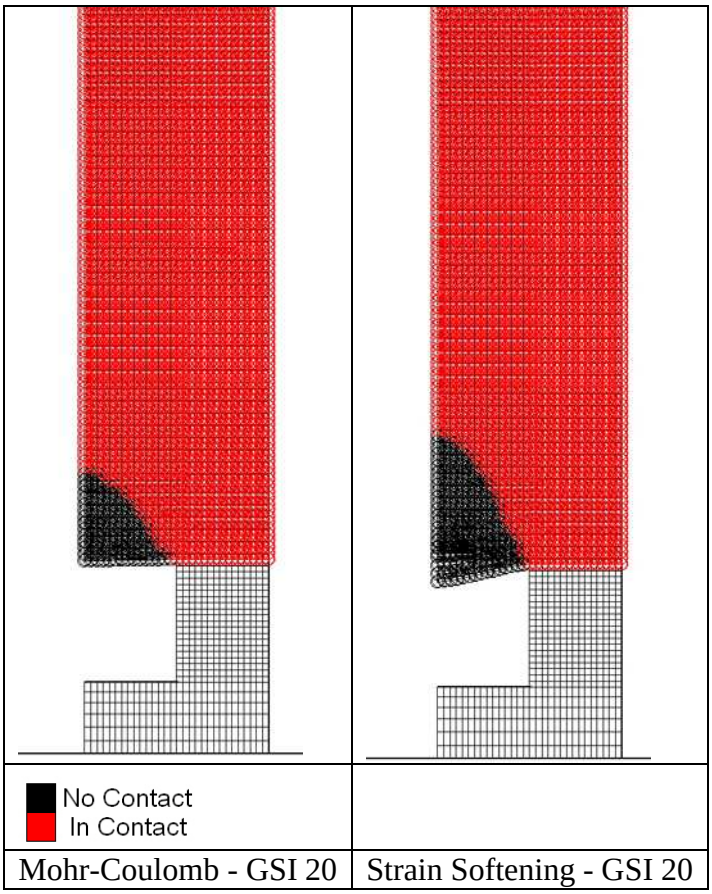

Figure 4.7: Interface normal failure plot for two identical model geometries and rock mass strengths but with varying constitutive models.

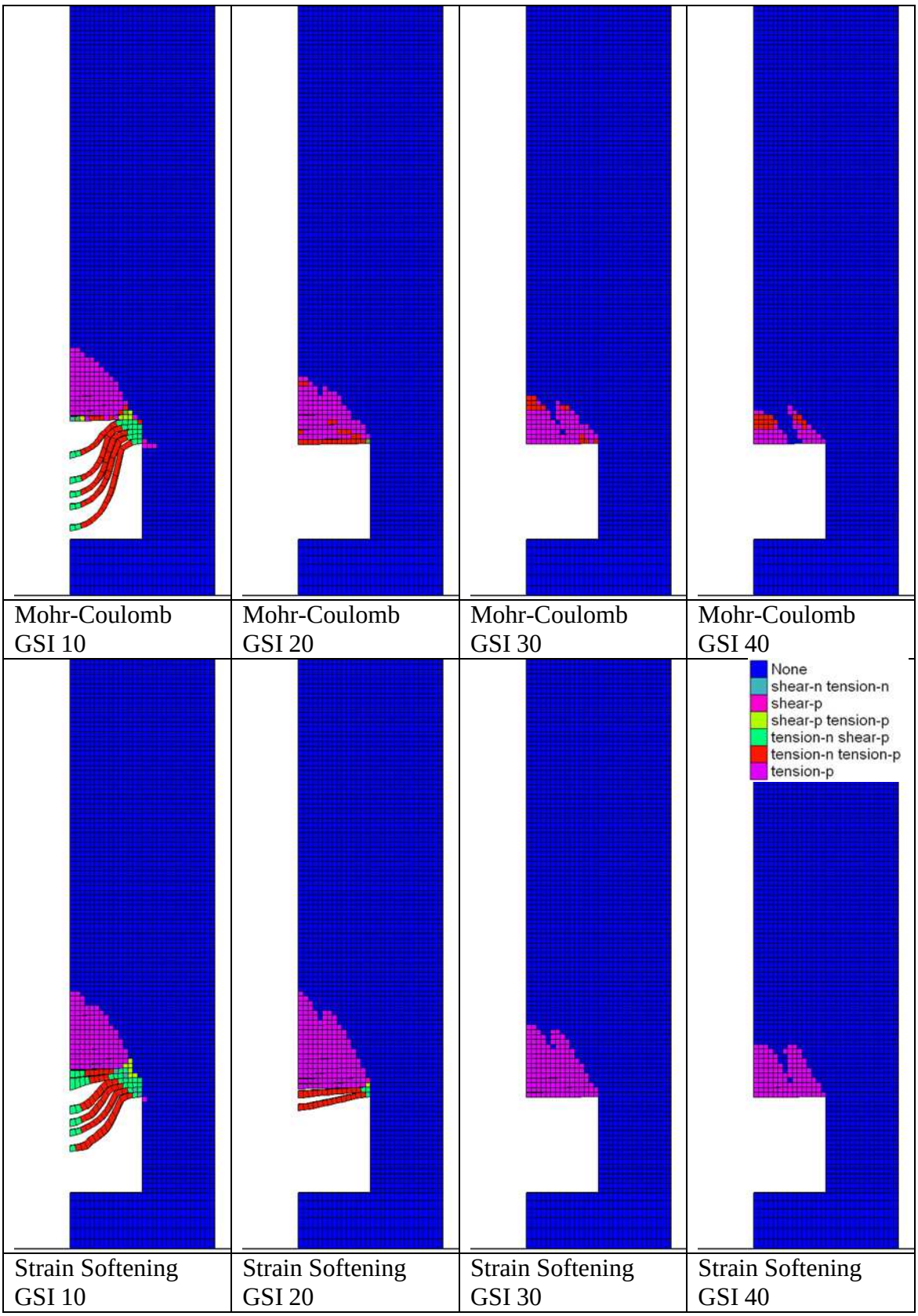

Figure 4.8: Yield state plot for varying rock mass strength values for both the Mohr-Coulomb and Strain-Softening constitutive models.

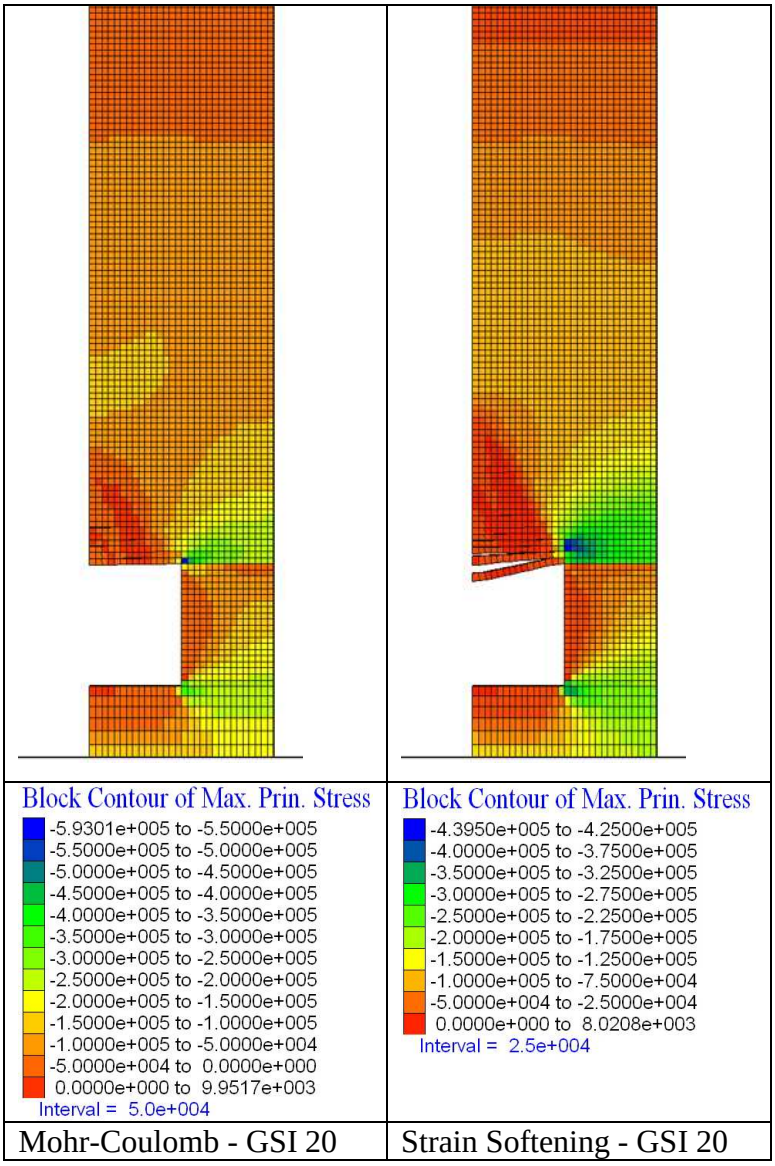

Figure 4.9: Maximum principal stress contours (Sigma 3) within the model. Excavation 2 m wide, 2 m high, bedding plane spacing, 0.1 m, GSI 20.

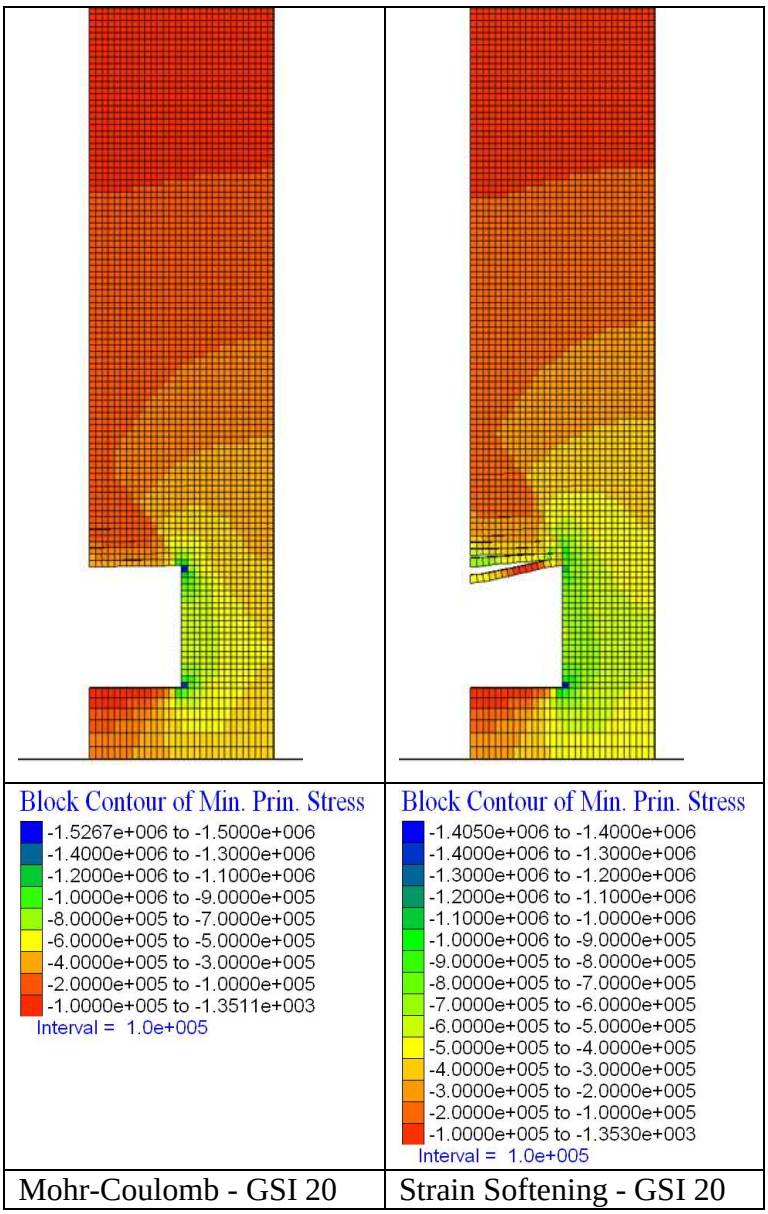

Figure 4.10: Minimum principal stress contours (Sigma 1) within the model. Excavation 2 m wide, 2 m high, bedding plane spacing, 0.1 m, GSI 20.

4.3 Conclusions from Strain Softening Model Testing

An analysis of the effect of varying the post peak strain values used in the stability analysis was undertaken (see section 4.1.4,) and it was found that although there were decreases in the magnitudes of shear and volumetric strains that developed within the model as the post peak plastic strain value (ε^{ps}) was increased, there was not a significant effect on the resultant roof deformations and yield state. Based on this finding, the softening parameters presented in the literature related to modelling (Esterhuizen and Karacan, 2005; Badr *et al.*, 2003; Singh and Singh, 2009 and Roberts *et al.*, 2005) are used for the modelling work undertaken from this point forward.

The results of the modelling undertaken to compare the results achieved using the standard Mohr-Coulomb and Strain-Softening models were presented in section 4.2.2. Here it could be seen that the strain-softening model causes an increase in the height of yielding into the rock mass and an increase of the extent to which failure of roof strata occurs. However it is also worth noting that the broad trends are similar (*i.e.* the height to which roof failure propagates into the overlying rock mass decreases with increased rock mass strength as per continuum and discontinuum modelling whether using a Mohr-Coulomb or Strain Softening constitutive model).

This is significant as it indicates that it is possible to use a consistent set of modelling results (be they Mohr-Coulomb or Strain softening) to identify the key parameters in instability and their relative importance, as it is this information on their relative importance and effect on excavation stability and not necessarily their absolute value that is of interest. However strain softening behaviour is generally assumed to be more representative of post failure behaviour and as such it is intended to use the strain softening model in the modelling from here on.

4.4 Effect of Variations in the Orientation of Discontinuity Planes within the Rock Mass on the Stability Behaviour of Shallow Mine Workings

4.4.1 Introduction

Numerical investigations into rock mass problems are commonly conducted using an "equivalent continuum" approach whereby the strength and stiffness variations that occur due to the presence of varying discontinuities in a rock mass are accounted for by the use of strength reduction parameters such as the GSI system used in this work and the various other rock mass strength assessment systems discussed in section 2.3.3. However in situations where the rock mass behaviour is dominated by a specific structural feature such as a fault, joint set or other discontinuity surface this may not always accurately capture the system behaviour. Coal measures are sedimentary rock formations with broadly horizontal bedding but which may potentially have been affected by variations in the regional stress field after their formation. These variations can lead to the formation of joints in the rock mass. Joints are discontinuity fracture surfaces along which there has been no visible displacement (Twiss and Moores, 1992). Joints are regarded as one of the most common and also most geotechnically significant structural features in rock (Brady and Brown, 1993). The orientation of these features (both strike and dip) at formation is dependent on the regional stress field and may be very variable ranging from (sub)horizontal to vertical. Post formational tectonic disturbance of the rock mass can also alter their orientation and as such their orientation may be very variable.

The above factors mean that joint planes tend to be one of the major structural features in sedimentary rocks and certainly the literature (Bell, 1975; Brady and Brown, 1993; Whittles *et al.,* 2007) suggests that failure of the rock mass due to movement or sliding along joint surfaces especially those with a destabilising orientation (*e.g.* steeply dipping joint sets that intersect or "daylight" into the excavation) with respect to any excavation is a potential failure mechanism both in subsurface excavations generally and more specifically in shallow mine working roof collapse and the initiation of void migration. For more information on this see section 2.2.3.

4.5 Effect of Joint Dip Angle on the Stability of Shallow Excavations

In the following sections the modelling methodology used to investigate the effect of joint dip on excavation stability as well as the results and discussion are presented.

4.5.1 Model Geometry and Mesh Discretisation

These models all represent a void of 1 m height and variable width at 10 m below surface, with 10 m of underlying rock mass material and square numerical zones. The geometry parameters are outlined in Table 4.2.

Table 4.2: Numerical model geometry parameters

Parameter	Value
Excavation Width	3.0 m
Excavation Height	1.0 m
Pillar Width	3.0 m
Zone Size	0.1 m^2
Dip Angle of Joint*	0° - 90° in 10° increments

***The dip angle rotates from horizontal (0°) to vertical (90°) in a clockwise direction.**

The modelling work undertaken previously took advantage of the symmetrical nature of the problem geometry to allow a half section of the excavation and pillar to be modelled. However the modelling to account for variations in the joint dip angle is not a symmetrical problem if the joint dip angle is greater than 0° and lower then 90°. To illustrate this point see Figure 4.11.

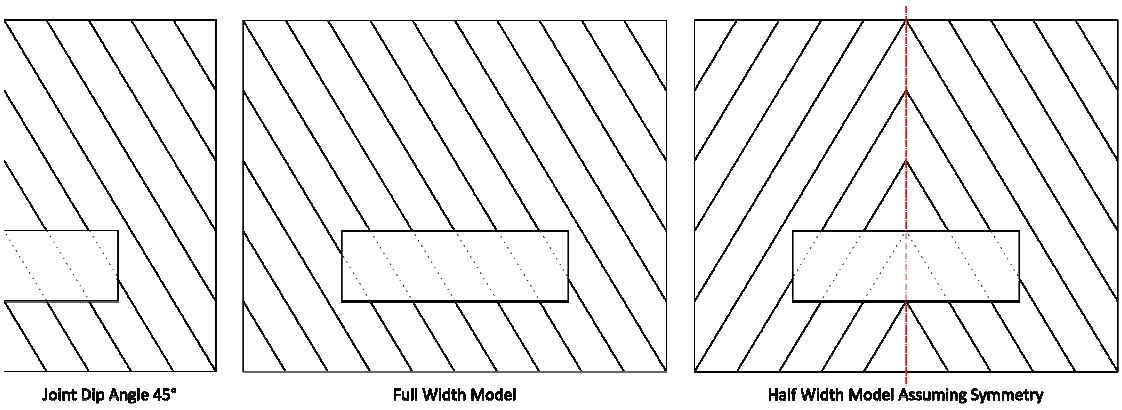

Figure 4.11: Plot demonstrating that the assumption of symmetry appears to be invalid for anisotropic materials where the angle of the plane of anisotropy is less than 90° and greater than 0°

The model geometry and mesh discretisation with the excavated mine void for the full width model is illustrated in Figure 4.12 and that of the half width model in Figure 4.13.

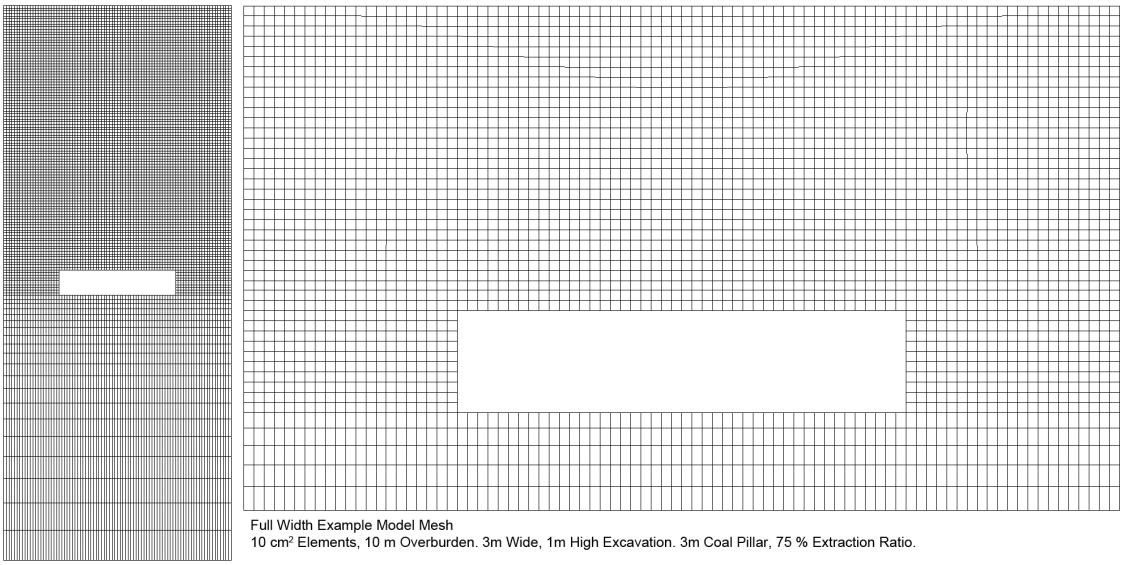

Figure 4.12: Plot showing the full width model geometry, detail view of excavation and mesh discretisation.

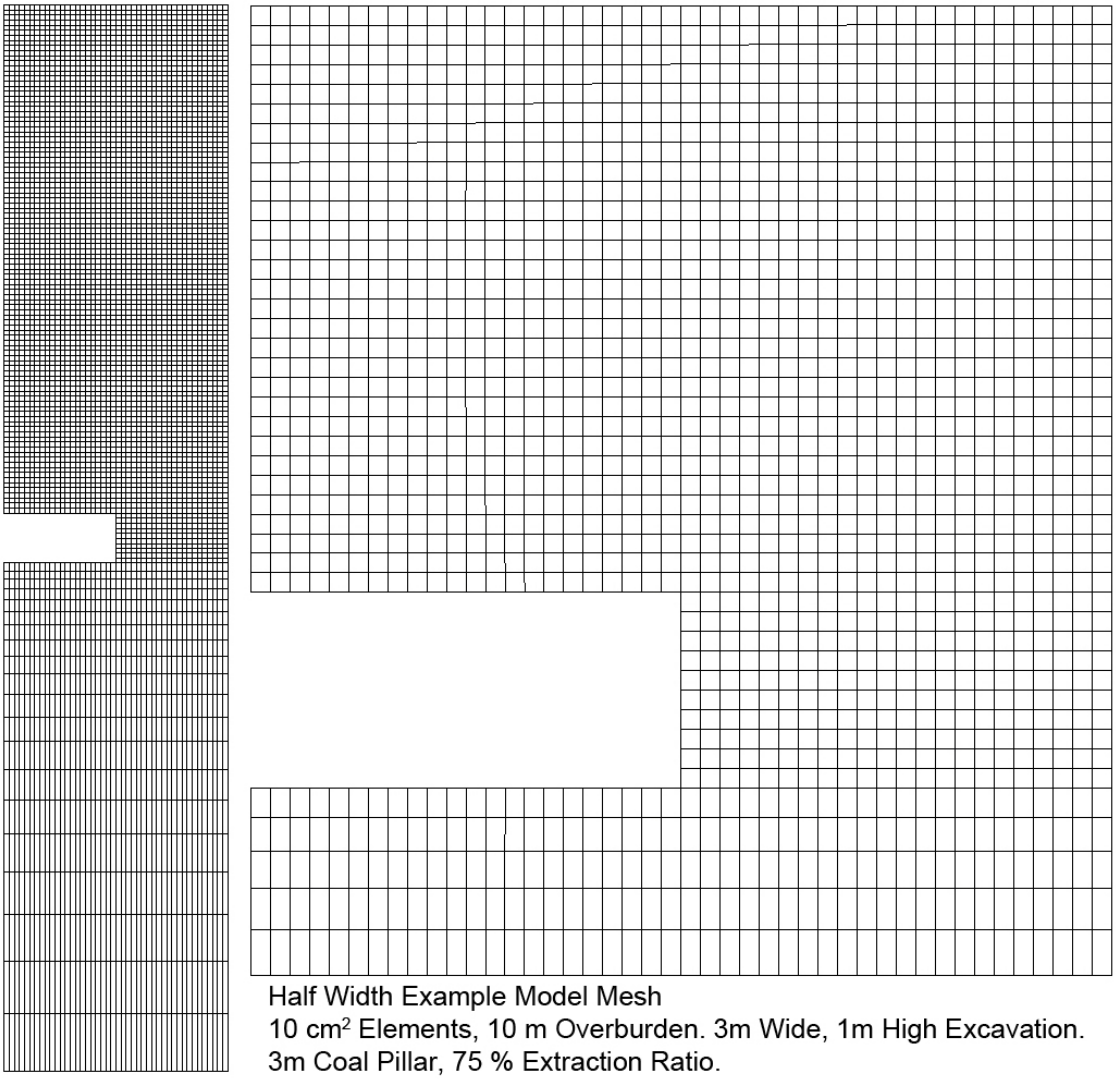

Figure 4.13: Plot showing the half width model geometry, detail view of excavation and mesh discretisation.

4.5.2 Rock Mass Properties

As there is the potential for the rock mass strength to be effected by discontinuities other than the primary joint sets and also to account for the presence of potentially highly fissile material such as shale within Coal Measures strata, it was decided that rather than using the intact strength and stiffness properties of coal measures rocks for the rock mass matrix strength, that instead a range of values would be used as per the previous modelling to avoid the potential for over estimating stability and to account for the variable nature of Coal Measures rocks.

As previous continuum modelling had demonstrated that rock masses with a GSI value greater than 60 were stable at all states (maximum excavation width, overburden load and maximum pore water pressure) it was decided that in this study to concentrate on the effect of the orientation of the discontinuity surface in this investigation. As such modelling was undertaken on a single rock mass strength equivalent to a GSI value of 10 for a rock with an intact uniaxial compressive strength of 75 (this value is chosen as an average UCS for typical coal measures rocks from the range of values quoted by Bell, 1975). The intact elastic modulus was assumed equal to 13.5 GPa taken as an average value for sandstones, shale and siltstones (Zhang, 2005).

However it was also necessary to derive the joint properties and as such, guidance from the literature was sought on joint discontinuity strength properties (cohesion, friction). Joints can be very variable, and their strength properties depend on their surface roughness (related to the presence of asperities on the joint surfaces) and their cohesion. These values can also be strongly affected by the presence of fill materials within the joints which may also significantly affect the joint strength (Goodman, 1989; Brady and Brown, 1993 and Zhang, 2005).

Zhang (2005) summarising work undertaken by Hoek and Bray which suggests that a common value for joint cohesion of coal measures rocks is approximately 0.012 MPa. Tensile strength parameters for joints are set to a value equal to zero. Friction angles for joints in varying rock types and varying common joint fills range from values as low as 7.5° for sheared clay fills up to 38° for rough joints in quartz rich rocks (*e.g.* quartz rich sandstones - Brady and Brown, 1993; Zhang, 2005).

As there are such a wide variety of friction angle properties for joints in rock masses and these properties are effected by deformation (peak vs residual strength values - Goodman, 1989; Brady and Brown, 1993 and Zhang, 2005) and weathering which will also effect the rock mass as a whole it was deemed sensible to scale the joint friction angles relative to the rock mass matrix friction angles whereby it is assumed that the rock mass with the lowest strength matrix friction angle (47°) at a GSI of 10 would have a joint friction angle of 20° (an average value assumed from the lowest common peak friction angles in sedimentary rocks as summarised by Zhang, 2005) and the high strength GSI values (60 – 100, which from the description of the GSI system suggests a rock mass with rough, relatively fresh, unweathered joint surfaces) with matrix friction angles of approximately 63° would have joints with a friction angle equivalent to the maximum peak values for quartz rich sedimentary rocks with rough unfilled, closely spaced joint surfaces (38°) as suggested by Hoek and Bray (see Zhang, 2005). This represents a drop in friction angle of approximately 22° between the matrix friction angle and that of the joint for a given rock mass strength. The intermediate rock mass joint frictional properties for GSI values between 10 and 60 are then scaled accordingly based on their matrix friction angles. A plot of the matrix friction angles derived using the maximum confining stress dependent GSI Mohr-Coulomb parameters as described in section 3.3 and the joint friction angles derived using the friction angle reduction value of 22° as described above are shown in Figure 4.14 and the strength and stiffness properties used in the modelling of the effect of variably dipping joints are summarised in Table 4.3 and Table 4.4.

Table 4.3: Rock mass matrix and joint strength and stiffness parameters

GSI	K	G	Matrix Cohesion	Matrix Friction Angle	Matrix Tensile Strength	Joint Fric. Angle	Joint Cohesion	Joint Tensile Strength
10	0.87	0.28	0.128	47.0	0.005	20.0	0.126	0.0
	(GPa)	**(GPa)**	**(MPa)**	**(°)**	**(MPa)**	**(°)**	**(MPa)**	**(MPa)**

Table 4.4: Strain softening parameters showing peak and residual strength values.

GSI	Matrix Cohesion at 5% Strain	Matrix Friction Angle at 5% Strain	Tensile Strength at 1% Strain	Joint Friction Angle at 5% Strain	Joint Cohesion at 5% Strain
10	0.092	46.0	0.0	16.0	0.092
	(MPa)	**(°)**	**(MPa)**	**(°)**	**(MPa)**

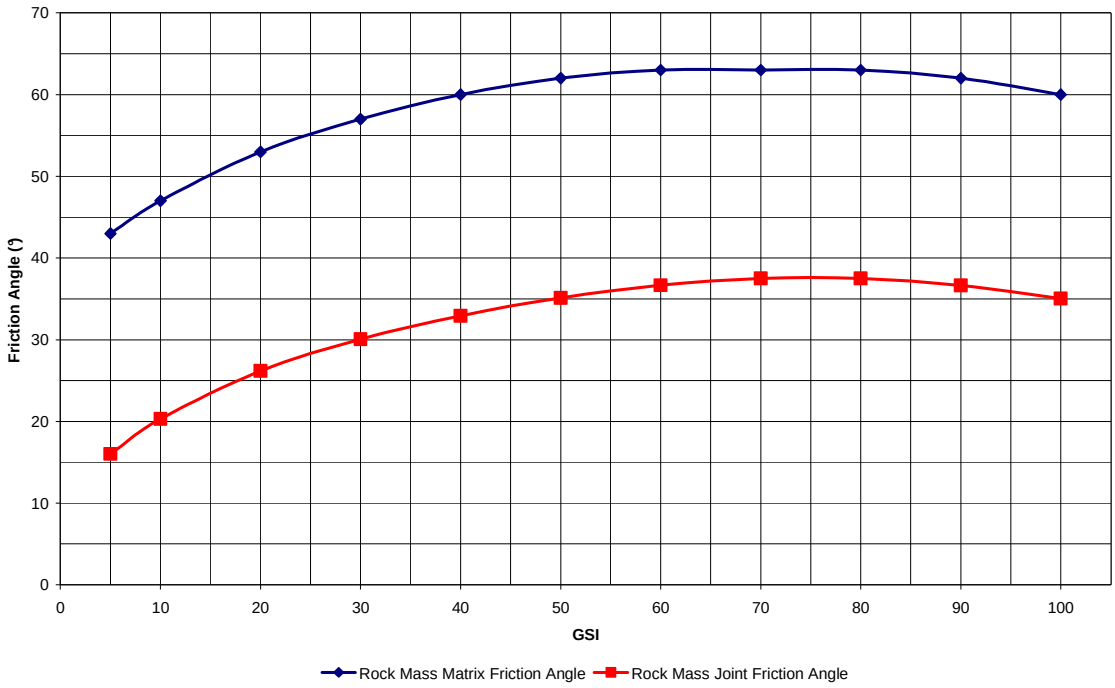

Figure 4.14: Rock mass matrix and joint friction angle properties at varying GSI values.

Joints are commonly described in terms of their persistence. This in simple terms is a description of the uninterrupted length of a joint through the rock mass. The degree of persistence can have a significant impact on the shear strength of rock masses (Brady and Brown, 1993; Zhang, 2005). It should be noted that the ubiquitous joint model assumes that the weakness planes that are modelled are persistent and have an uninterrupted span across the modelled region. This is a conservative assumption as it is the least stable case possible for a given joint or discontinuity orientation and strength (Itasca, 2005).

Further to this, the joint properties vary depending on the degree of shear strain that occurs on the joint whereby deformation will remove asperities on the joint surface making it smoother and so reducing the frictional properties resulting in peak and residual friction values. As such both the matrix and the joints undergo strain softening behaviour and as such the strain softening ubiquitous joint constitutive model is used in this modelling work.

The post peak strength and friction strain softening parameters are derived based on the methodology outlined in section 4.1 and the same assumptions apply here. See Table 4.1 for the parameters as used in this modelling.

As the initial modelling undertaken in section 3.2 indicated that the strength of the coal pillar and the rock mass underlying the excavation were not significant in the stability of the roof (rather they were important in the phenomena of pillar crushing leading to areal or sag subsidence or punching failure of the pillars into the softer underlying rock mass), the strength of the coal and the underlying rock mass were scaled to an intermediate value whereby the coal was assumed to have a uniaxial compressive strength (UCS) of approximately 15 MPa (Bell, 1975) and the underlying rock UCS was assumed to have the following intact properties: intact uniaxial compressive strength of 75 (this value is chosen as an average UCS for typical coal measures rocks from the range of values quoted by Bell, 1975). The intact elastic modulus was assumed equal to 13.5 GPa taken as an average value for sandstone, shale and siltstone (Zhang, 2005). The Mohr-Coulomb parameters were then estimated using the Hoek-Brown method as applied by ROCLAB (Rocscience, 2010). See Table 4.5.

Table 4.5: Strength and stiffness properties as used for the coal and underlying rock mass.

Rock Type	Bulk Modulus	Shear Modulus	Cohesion	Friction Angle	Tensile Strength
Coal	1.47	0.38	0.498	49	0.26
Underlying Rock Mass	9.39	2.45	1.21	51	0.651
	(GPa)	**(GPa)**	**(MPa)**	**(°)**	**(MPa)**

An approximation for the bulk density of coal measures sandstone strata was selected from the literature and based on the previous modelling undertaken in section 3.2.8. In this case from the literature a bulk density of 2700 kg/m^3 (Bell, 1992; Thomlinson, 2001; Zhang, 2005). It is acknowledged that this value may be considered somewhat higher than that quoted as an average for coal measures strata (*e.g.*2240 kg/m^3 in Bell, 1975) however this is a conservative assumption and so should avoid underestimating potential instability.

4.6 Modelling Methodology

In order to investigate the effect of asymmetry on the model a series of full width and half width models were run at varying joint dip angles at a uniform rock mass strength.

4.6.1 Comparison of Full Width and Half Width Symmetry Models

In this section the yield results from a series of modelling runs with uniform strength and stiffness properties (GSI 10 see Table 4.3), overburden height (10 m) and excavation width (3 m) parameters for both the full and half width symmetry models

will be very briefly summarised and compared. The yield plots for the models with joint dip from 0° to 50° can be seen in Figure 4.15 and from 60° to 90° in Figure 4.16. Here it can be seen that there are significant differences in the results of the half and full width models at varying dip angles. It can also be seen that the only pair of half width and full width models which match perfectly are the 0° and 90° models. These are the models with perfect mirror symmetry along the boundary forming the roof centre line occurs. From this it is clear that to study the effect of joint dip at angles between 0° and 90° a full width model must be used as the assumption of symmetry clearly breaks down.

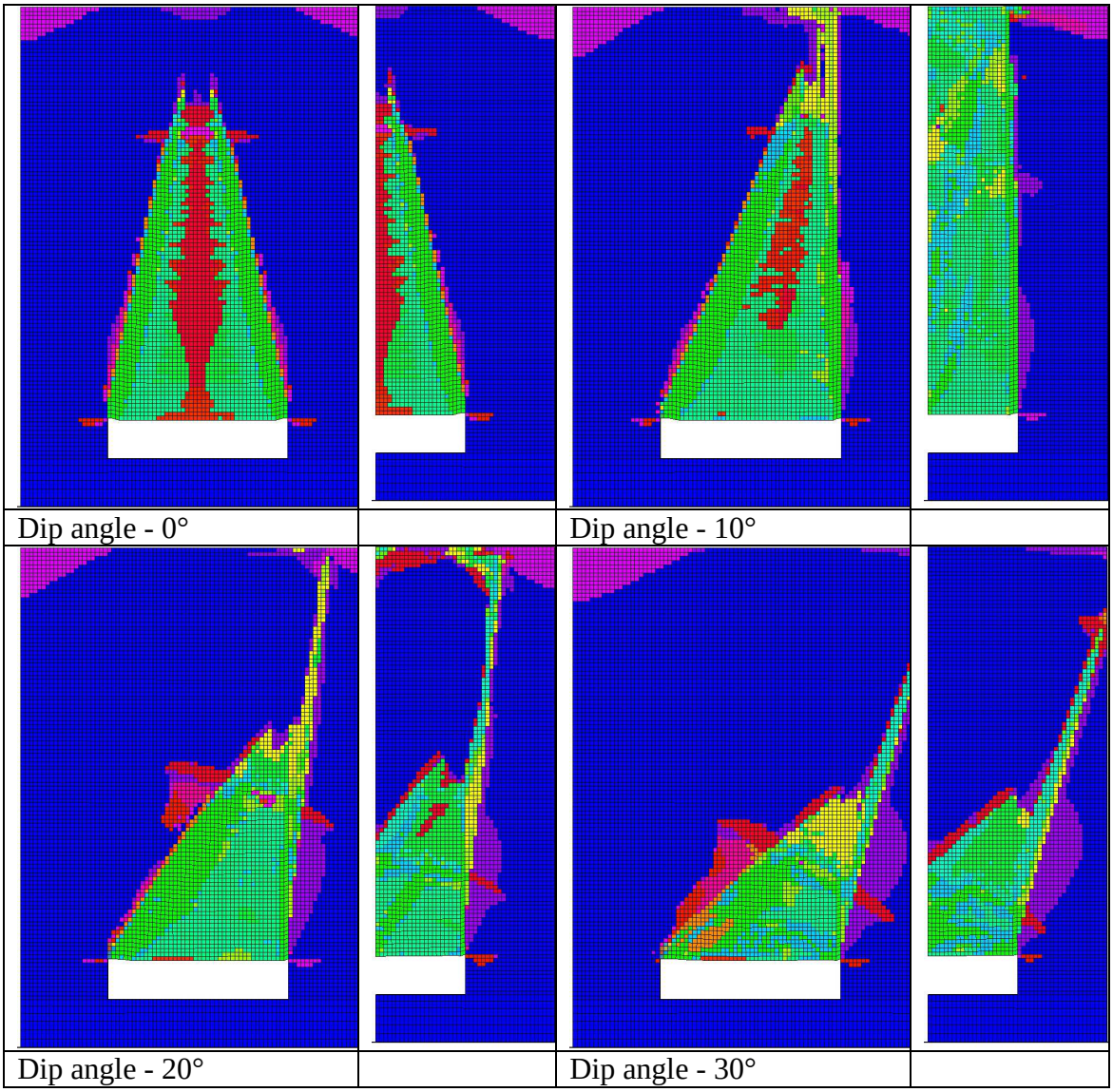

Figure 4.15: Yields states for half and full width models at varying dip angle from 0 to 50°

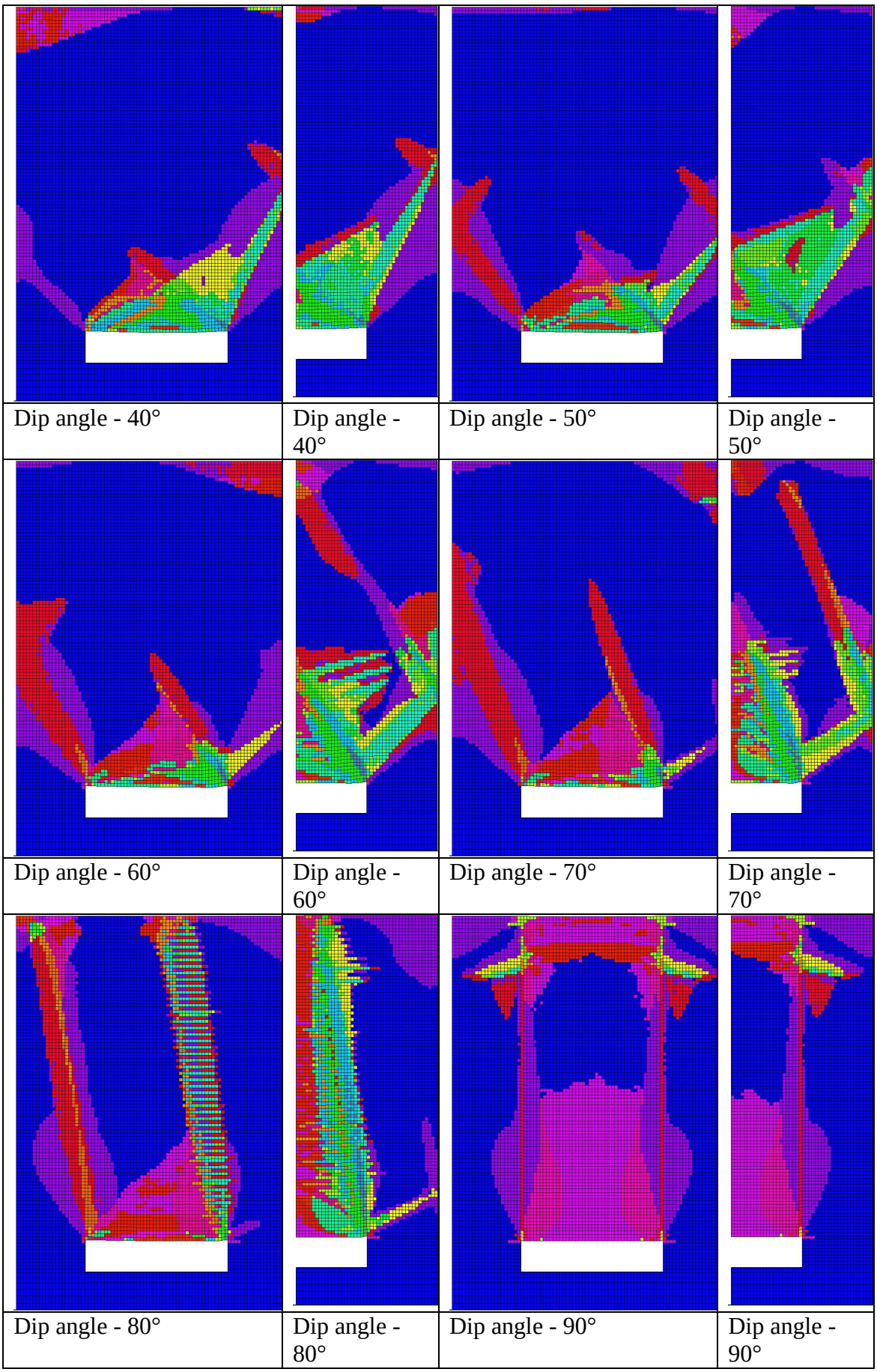

Figure 4.16: Yields states for half and full width models at varying dip angle from 40 to 90°

4.6.2 Parametric Study of the Effect of Joint Dip on Excavation Stability

The parametric study to investigate the effect of joint dip angle on the stability of shallow abandoned mine workings was run using an automated FISH routine which varied the geometry and strength of the model automatically while stepping to either static equilibrium (a stable solution without collapse) or to a prescribed uniform step limit (equal to 10,000 steps after an excavation equilibrium state has been achieved and the Strain Softening Ubiquitous Joint Mohr-Coulomb parameters have been applied) if the model is unstable and roof collapse is occurring to aid comparison of the results. The full modelling process is described in more detail below:

The initial geometry was generated which represented a two dimensional section through a shallow mine excavation. The point chosen was the intersection between two roadways or rooms as this represents the largest span and so the highest stresses within the roof strata and the greatest potential for instability. The resultant two-dimensional model geometry can be seen in Figure 4.12 and Figure 4.13 for the half width and full width models respectively. The model uses fixity conditions at the boundaries. As in the previous modelling conducted, the base is fixed in the z-axis so that no vertical movement can occur and the side boundaries are fixed in the x-axis to prevent horizontal movement.

Once an initial geometry is selected, the elastic constitutive model, bulk density and elastic properties are applied to the mesh. The model is then brought to equilibrium under gravity. In this case (as in all the modelling undertaken in this thesis) the force ratio limit for equilibrium was set to 1×10^{-5}. This helps to ensure unbalanced forces do not influence the results.

Once initial equilibrium is achieved the mine void is excavated by nulling zones within the model. The model is again stepped to equilibrium to remove excess unbalanced forces caused by the sudden excavation as recommended in the FLAC manual (Itasca, 2005) and then the Strain Softening Ubiquitous Joint Mohr-Coulomb (SS-UBJ-MC) constitutive model and associated parameters are applied.

Once a solve cycle has been completed for a given joint dip angle, the joint dip angle is increased by an increment of 10° and the model cycled again from an excavation equilibrium state. This is repeated for a given rock mass strength until all joint dip

angles have been tested (joint dip varies from horizontal (0°) to vertical (90°)). More detail on specific sections of the modelling methodology is described below.

4.6.3 Monitoring of the Model Run

A number of parameters are monitored during the model run. These primarily include the vertical displacement in the centre line of the roof strata, the vertical strain of the strata in the roof centre line, the ratio of unbalanced force and maximum unbalanced force within the model (which allow the user to identify if the model has reached a stable state or if failure and steady state plastic flow are occurring).

4.7 Effect of Joint Dip Angle on the Yielding and Failure of the Rock Mass Over Mined Voids

In this section the results from a series of modelling runs with uniform strength, stiffness and geometry parameters will be summarised and discussed. The results will highlight the effect of joint dip angles on the stability of mine voids. The following models all have uniform excavation heights (1 m), overburden thicknesses (10 m) and rock mass strength and stiffness properties (GSI 10). The full width (3 m) of the excavation as well as the half width of both coal pillars has been modelled. The joint dip angle varies from 0° to 90° in 10° increments. It should also be noted that in FLAC, the sign convention for compressive stresses is negative so that in plots of stress state, compression is negative and tension is positive and that as such, the maximum principal stress plot is the least negative stress Sigma 3 rather then Sigma 1 and vice versa for a minimum principal stress contour plot.

In all cases it is anticipated that roof failure will occur due to the low strength of the strata modelled, however in this instance it is intended to investigate the effect of varying dip angles on failure geometry. All angles will be described relative to the following axis unless stated otherwise. This matches the convention used to describe the angle of dip. See Figure 4.17.

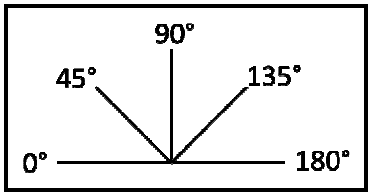

Figure 4.17: Datum for angular measurement

4.7.1 Full Width Model with Horizontal (0°) Joints, 3 m Excavation Width, 1 m Excavation Height, GSI 10

From observation of the yield state plot shown in Figure 4.18A it is clear that significant yielding has occurred within the rock mass over the excavation, in this case both within the rock mass matrix and along the joint planes. The shear strength of the rock mass matrix (Cohesion = 0.128 MPa and friction angle = 47°) is apparently too high to allow significant shear yielding to occur (see Figure 4.18B) except at the roof pillar intersections where the highest magnitudes of maximum and minimum principal stress occurs (Figure 4.19) suggesting that the differential stress and hence the shear stress will be very high which is assumed to be the cause of the small degree of shear yielding observed within the model at this location.

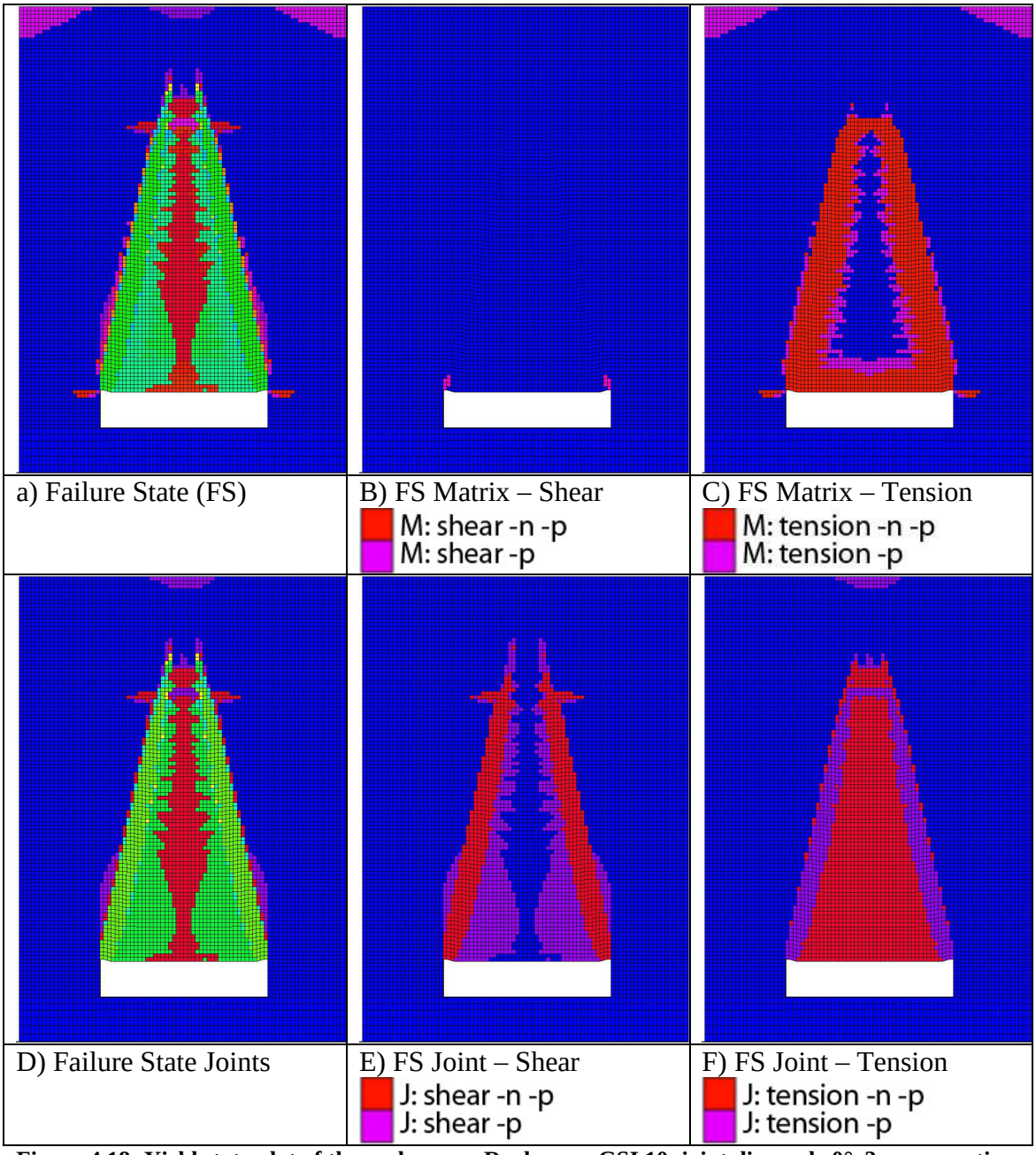

Figure 4.18: Yield state plot of the rock mass. Rock mass GSI 10, joint dip angle 0°, 3 m excavation width, 1 m excavation height

The rock mass matrix material has however failed in tension (see Figure 4.18C), forming a triangular geometry above the excavation roof. When the plots of joint yielding (see Figure 4.18D,E,F) are viewed, it can be seen that the majority of shear and tensile yielding within the rock mass is predominantly occurring within the rock mass joints. Shear failure of the joints in the rock mass originates at the point of maximum differential stress (Sigma3 – Sigma 1) in the rock mass above the pillar roof intersection and propagates upwards at an angle into the rock mass over the excavation roof (see Figure 4.18E). When compared with the maximum and minimum stress plots, it can be seen that the bands of shear failure follow the outer boundaries of a wedge shaped zone of tensile stress within the rock mass over the excavation. The joint tensile strength is zero and as such, the joints within the region of tensile stress in the rock mass above the excavation have failed in tension, forming a filled wedge or triangular geometry with a truncated top (a frustum).

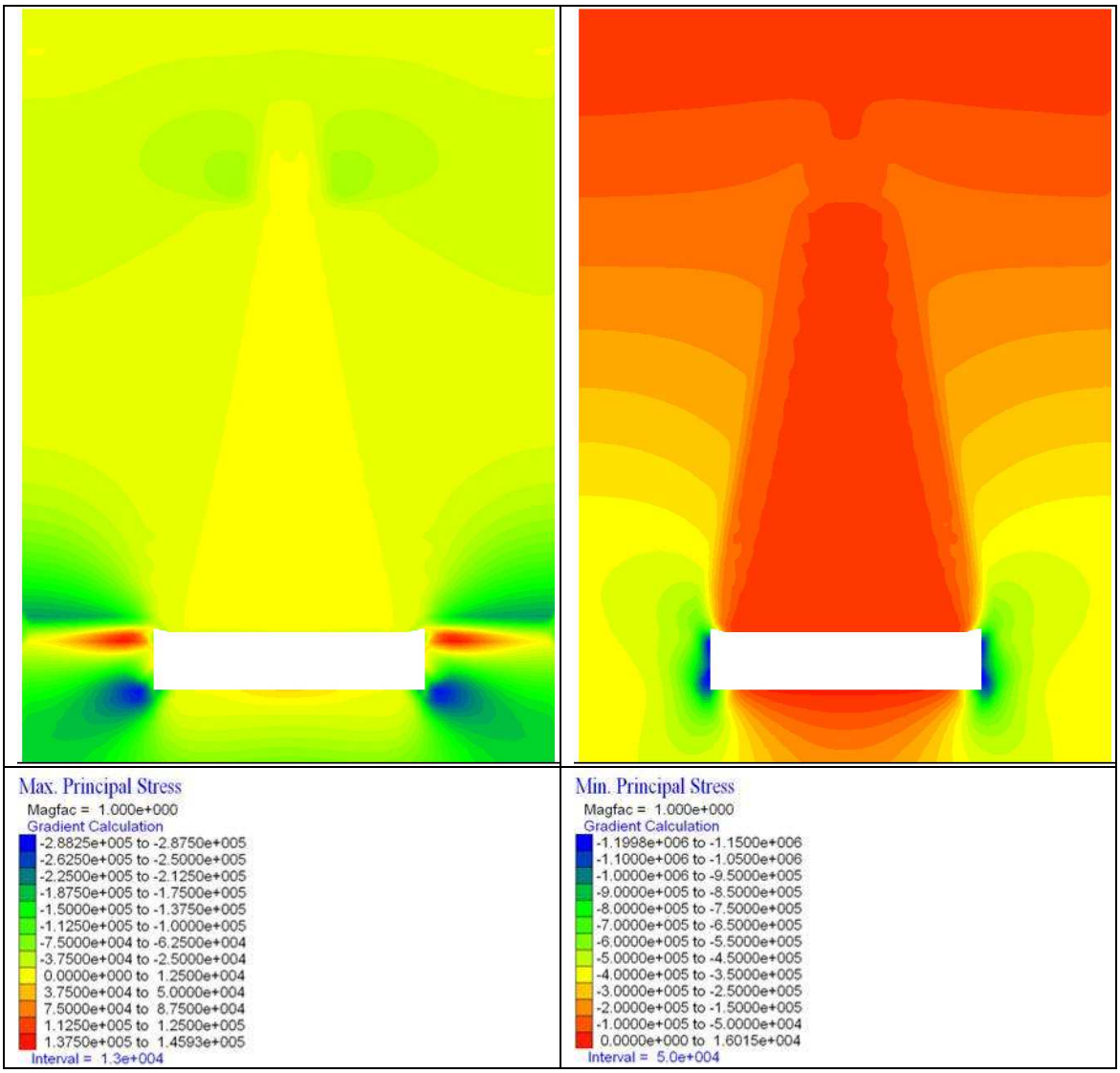

Figure 4.19: Maximum (Sigma 3) and minimum (Sigma 1) principal stress state of the rock mass. Rock mass GSI 10, joint dip angle 0°, 3 m excavation width, 1 m excavation height

When the plots of shear and volumetric strains are observed (Figure 4.20) it can be seen that the shear failure along the joints has caused a band of shear strain to form with the maximum shearing occurring immediately above the excavation (shear strain increment 8%) which as the location where shear failure will have initiated seems reasonable, and decreases with increased height above the excavation / length along the shear plane, reaching a minimum (of 3-4%) at the vertical extent of the shear band.

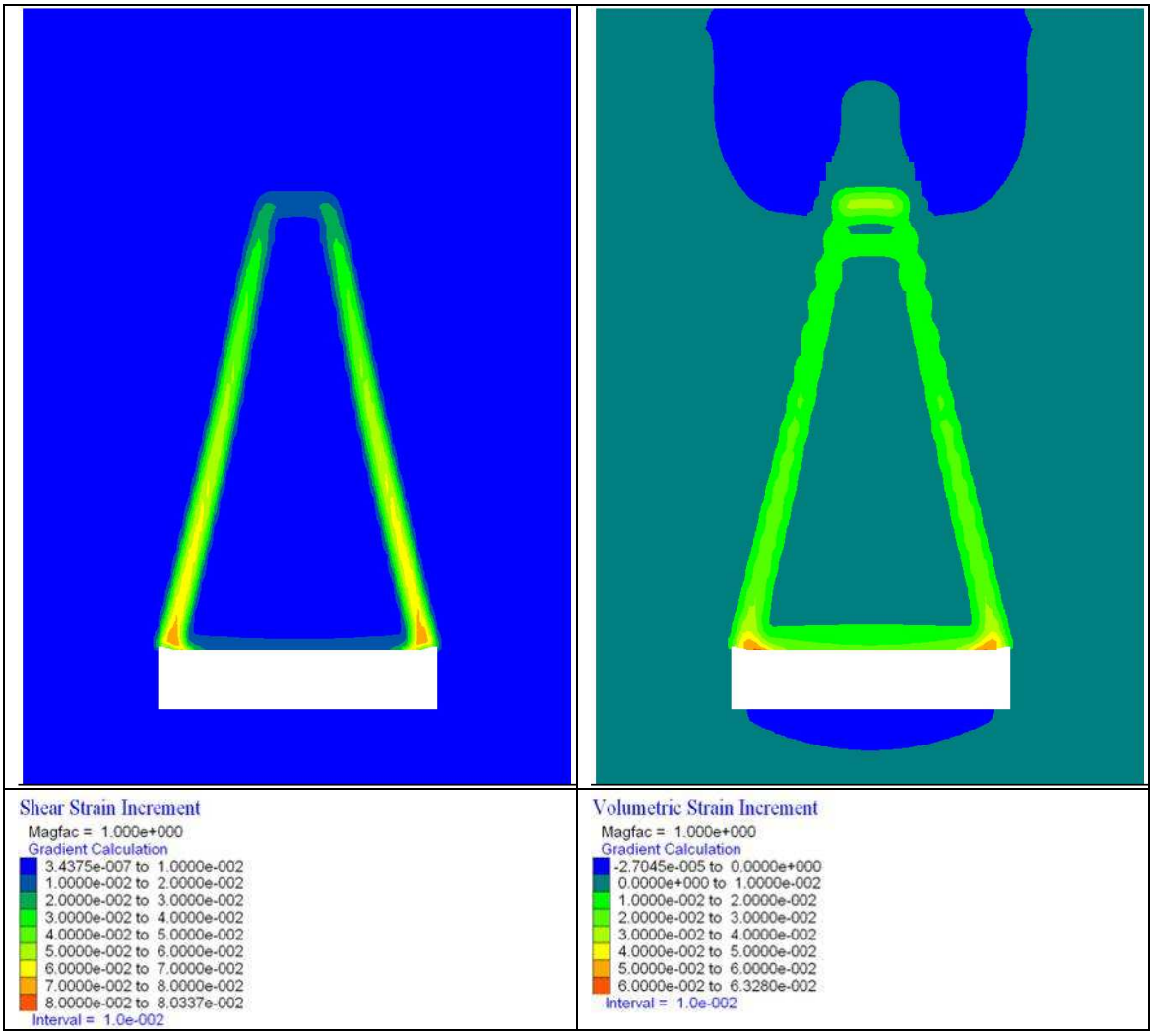

Figure 4.20: Shear and volumetric strains within the rock mass. Rock mass GSI 10, joint dip angle 0°, 3 m excavation width, 1 m excavation height.

The contour plot of displacements as a result of this deformation can be seen in Figure 4.22, where it can be seen that the wedge bounded by the shear bands is undergoing vertical movement down into the excavation and appears to be deforming predominantly as a rigid body with the sliding occurring along the shear surfaces. This appears to very closely match the failure mechanism outlined by Whittles *et al.*, (2007) specifically that which is described as shear failure of the roof beds with the failure initiating from the roadway corners. See section 2.2.3.

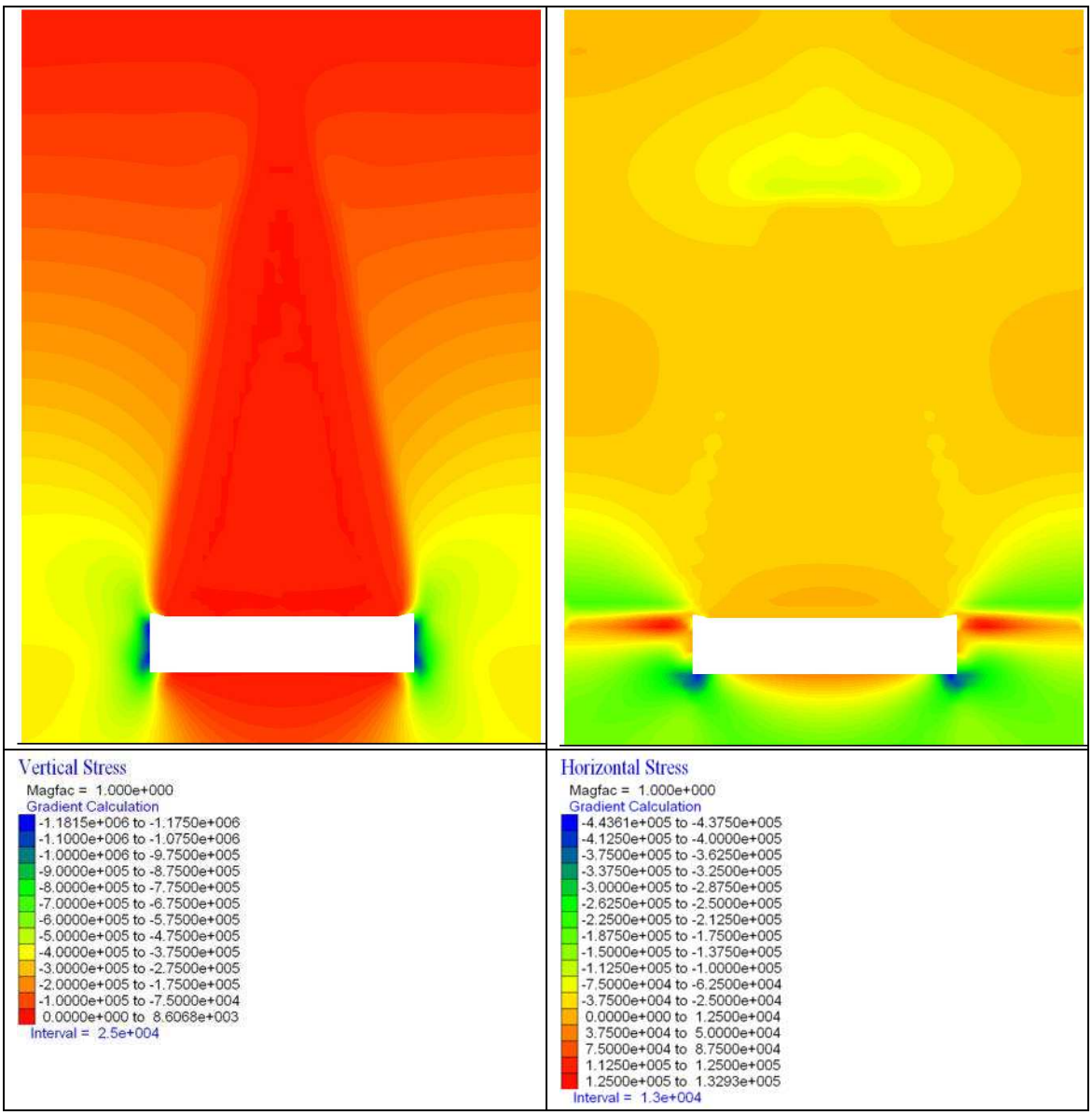

Figure 4.21: Vertical and horizontal stress state of the rock mass. Rock mass GSI 10, joint dip angle 0°, 3 m excavation width, 1 m excavation height.

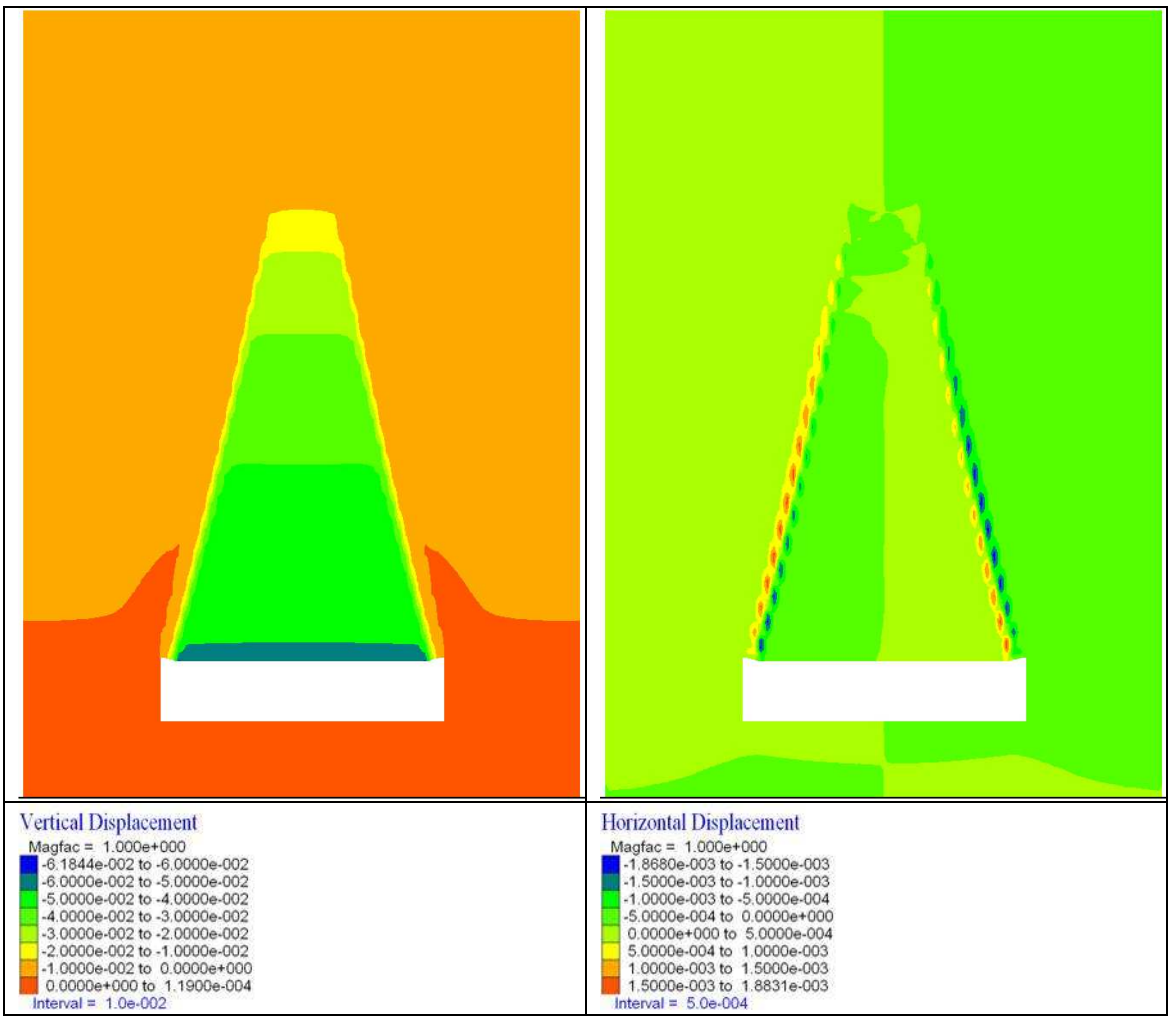

Figure 4.22: Vertical and horizontal displacements within the rock mass. Rock mass GSI 10, joint dip angle 0°, 3 m excavation width, 1 m excavation height.

In this case the failure geometry appears to have been controlled by the rock mass friction angle, whereby the joints have softened after undergoing plastic shear strains and reached their residual friction angle of 16°. The angle of the failure wedge to the vertical in this case is approximately equal to the friction angle of the rock mass joints. This can be seen in Figure 4.23, in which the left hand boundary has formed at an angle of 106°. The sense of dip of the right hand side of the failure zone is equal to 74°.

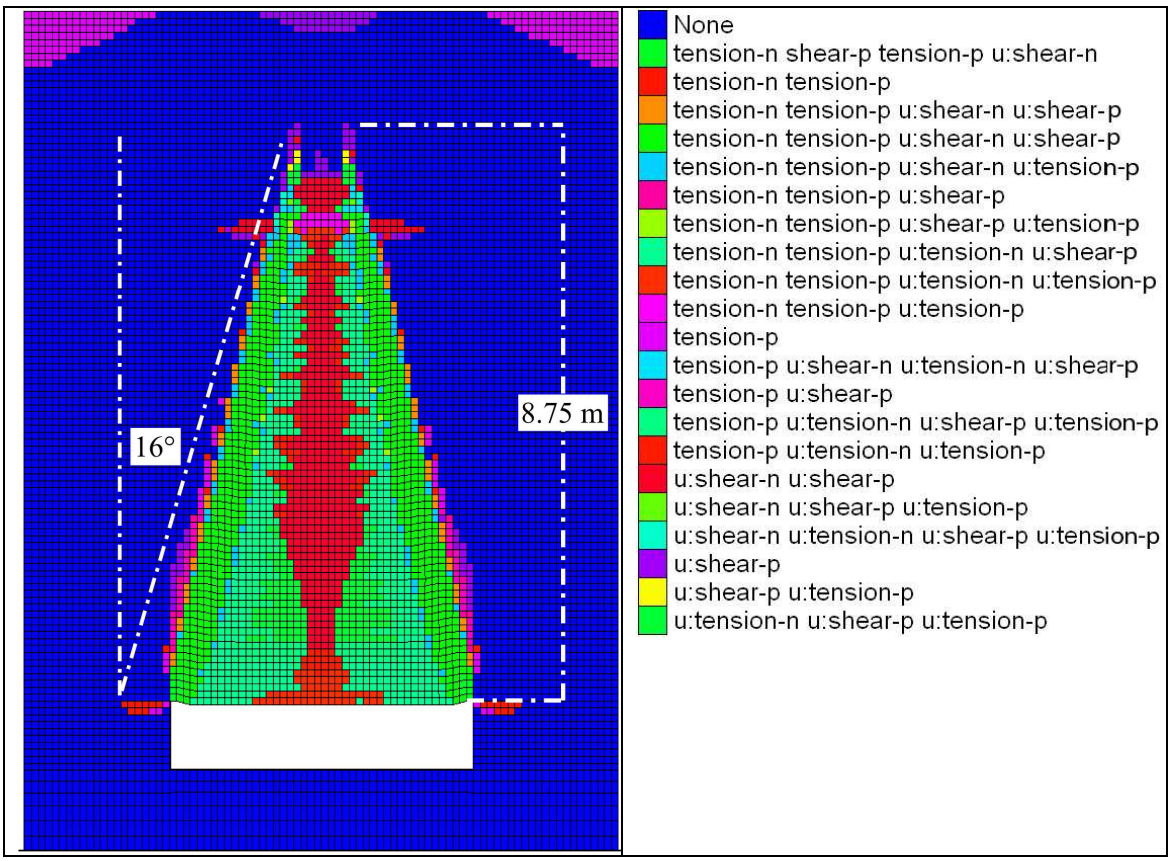

Figure 4.23: Failure angle of the rock mass relative to vertical and height of total yielding for joint dip of 0°.

4.7.2 Full Width Model with Subhorizontal (10°) Joints, 3 m Excavation Width, 1 m Excavation Height, GSI 10

As the dip angle increases from horizontal to 10° it can be seen that the failure geometry within the rock mass over the excavation roof changes as the failure wedge becomes less steep on the left hand (up-dip) side and has a vertical boundary on the right hand (down-dip) side, directly above the roof pillar intersection. Once again the majority of the shear yielding is occurring within the joints due to their lower shear strength parameters when compared to the rock mass matrix strength (compare Figure 4.24B and E), although significant tensile yielding of the rock mass matrix has also occurred (see Figure 4.24C). The joints within the failure wedge have all failed in tension (see Figure 4.24E) while the shear yielding has occurred as two distinct bands approximately forming a right angle triangle with the base formed by the excavation roof (see Figure 4.24E).

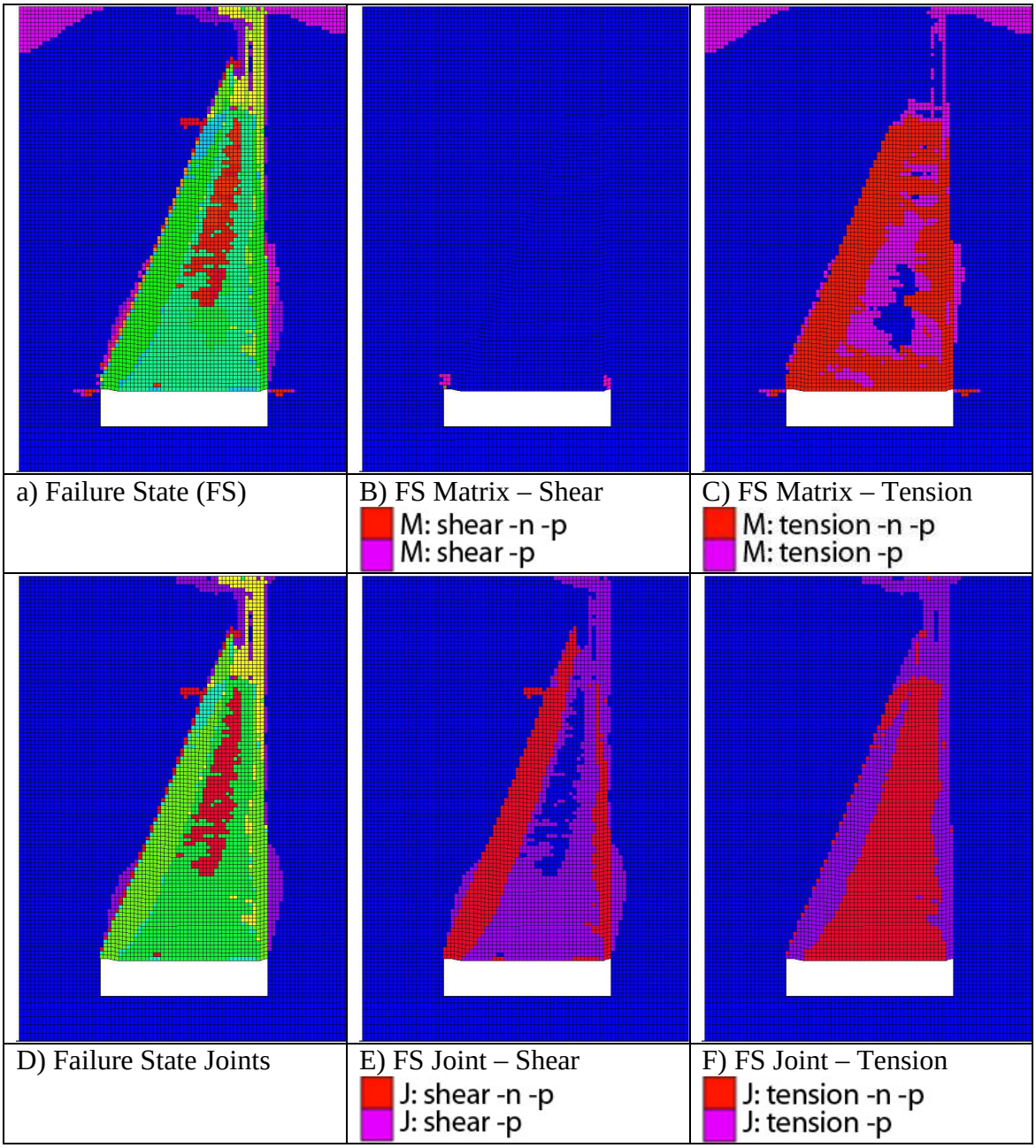

Figure 4.24: Yield state plot of the rock mass. Rock mass GSI 10, joint dip angle 10°, 3 m excavation width, 1 m excavation height

The adjustment in the orientation of the planes of weakness has also resulted in a rotation of the principal stresses. The rotation of the region of tensile stress over the excavation (reaching a magnitude of 12-15 kPa) can be seen on both the plot of maximum and minimum principal stress (see Figure 4.25). This has also resulted in significant anisotropy of the stresses within the pillars to the left and right of the excavation with the compressive stresses shown to be significantly higher on the up dip side of the excavation (the left – *N.B.* strata dip down from the left to the right with the sense of dip as shown in Figure 4.11) than on the down dip side (1.5 MPa vs 1.1 MPa – see the minimum principal stress plot in Figure 4.25).

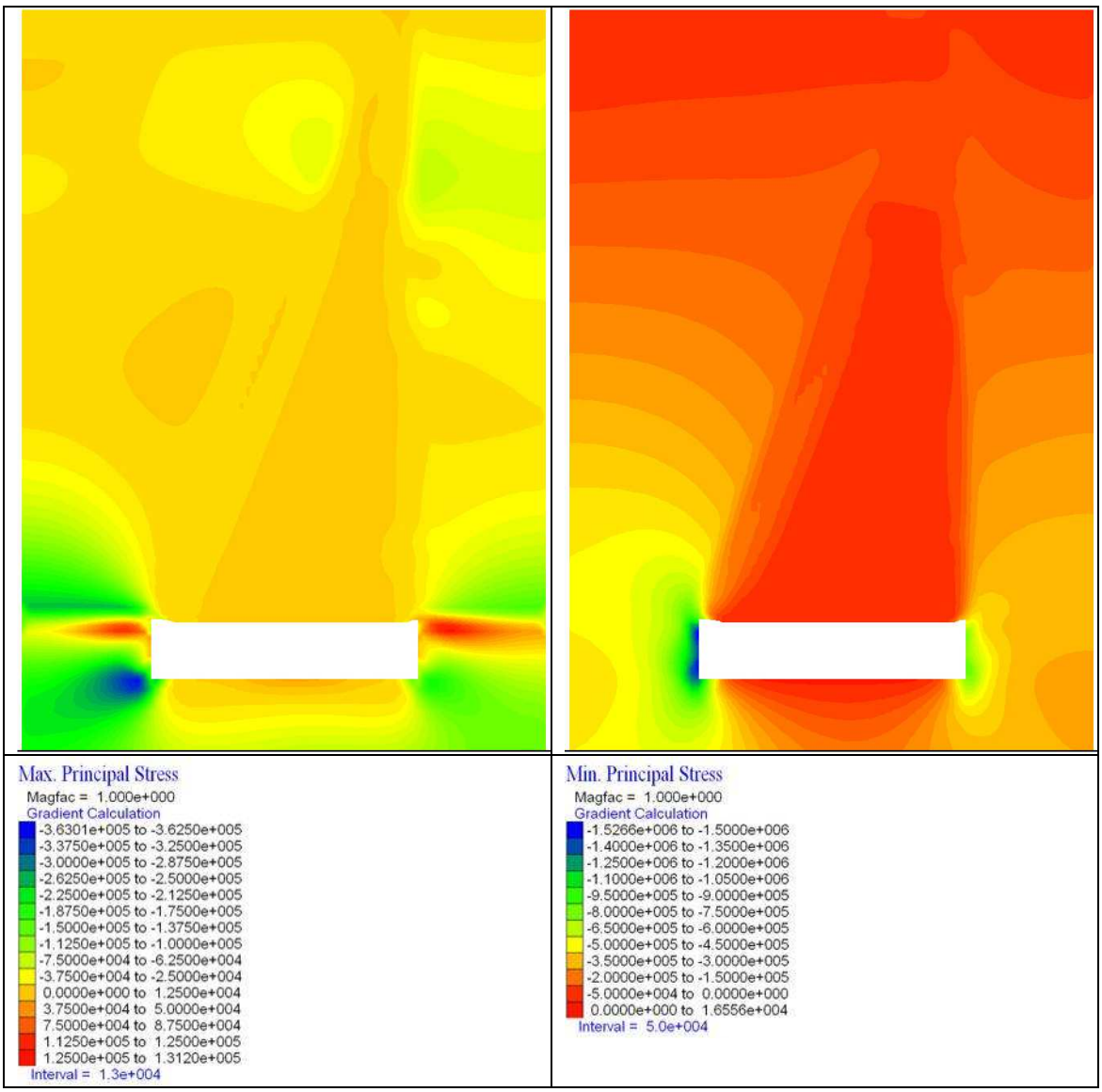

Figure 4.25: Maximum (Sigma 3) and minimum (Sigma 1) principal stress state of the rock mass. Rock mass GSI 10, joint dip angle 10°, 3 m excavation width, 1 m excavation height.

The yielding of the rock mass has once again resulted in deformation with both volumetric and shear strains occurring within the rock mass (see Figure 4.26). The shear bands once again propagate upwards into the rock mass from the excavation roof / pillar intersection however they are rotated to match the principal stress field and failure plots. Of some interest is the initiation of a band of volumetric strain immediately above the right hand pillar margin which appears to be following the joint dip at approximately 10°. This may indicate the initiation of tensile failure along the joint plane potentially leading to the separation of the failure wedge into two. The flat upper surface of the volumetric strain wedge shape also appears to follow the trend of the joint dip.

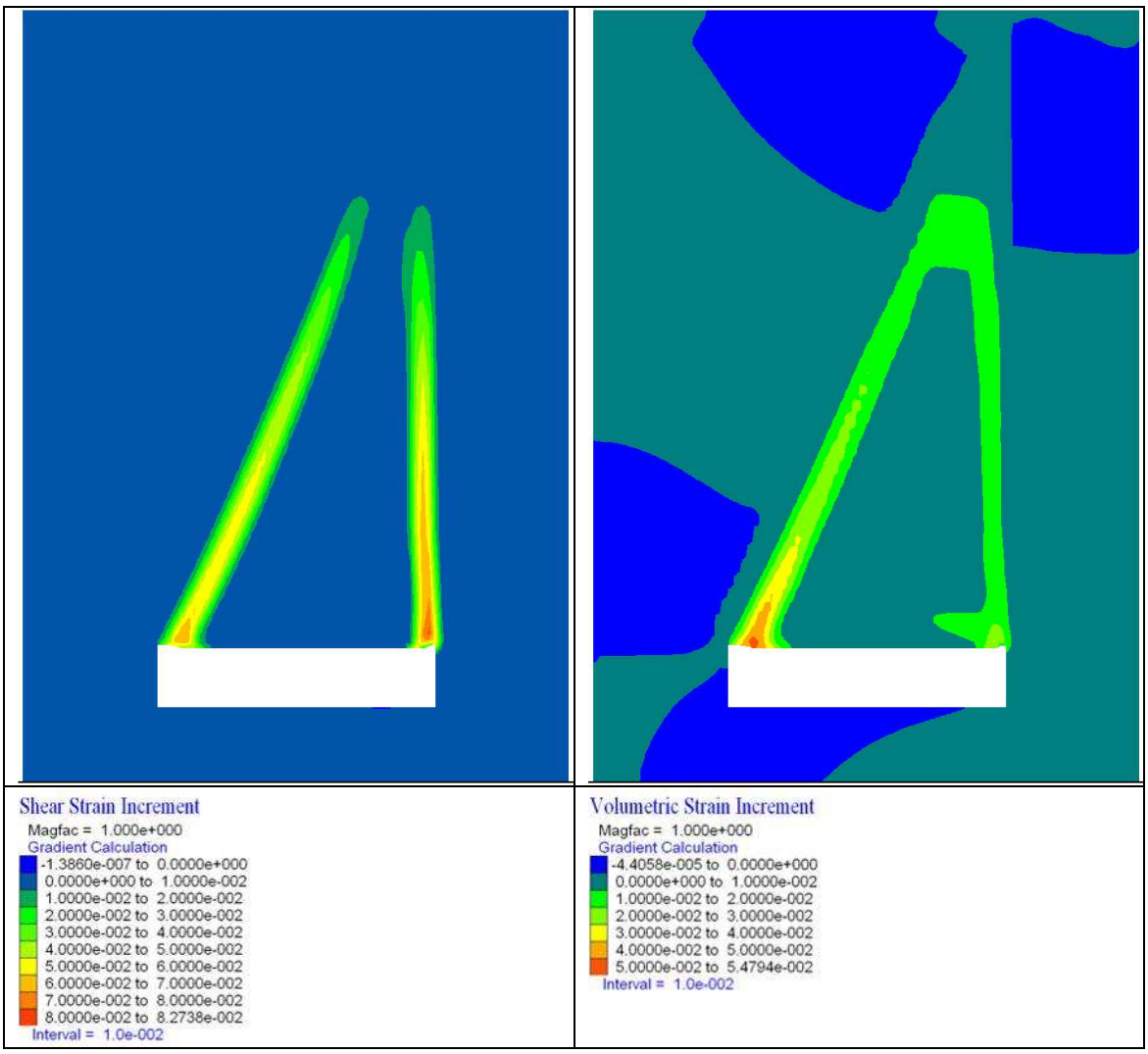

Figure 4.26: Shear and volumetric strains within the rock mass. Rock mass GSI 10, joint dip angle 10°, 3 m excavation width, 1 m excavation height.

As for the results of the previous dip angle, the rock mass above the excavation appears to be failing as a relatively rigid body with the deformation being accommodated by the discrete shear bands that have formed within the model as seen in Figure 4.26. The resultant unstable wedge can be seen displacing in Figure 4.27. As the failure geometry has rotated around the vertical axis, there is now an increased horizontal component to the displacements that would not occur in (and was not demonstrated by) the model with horizontal bedding (compare Figure 4.27 with Figure 4.22) however this is of very low magnitude (mm scale).

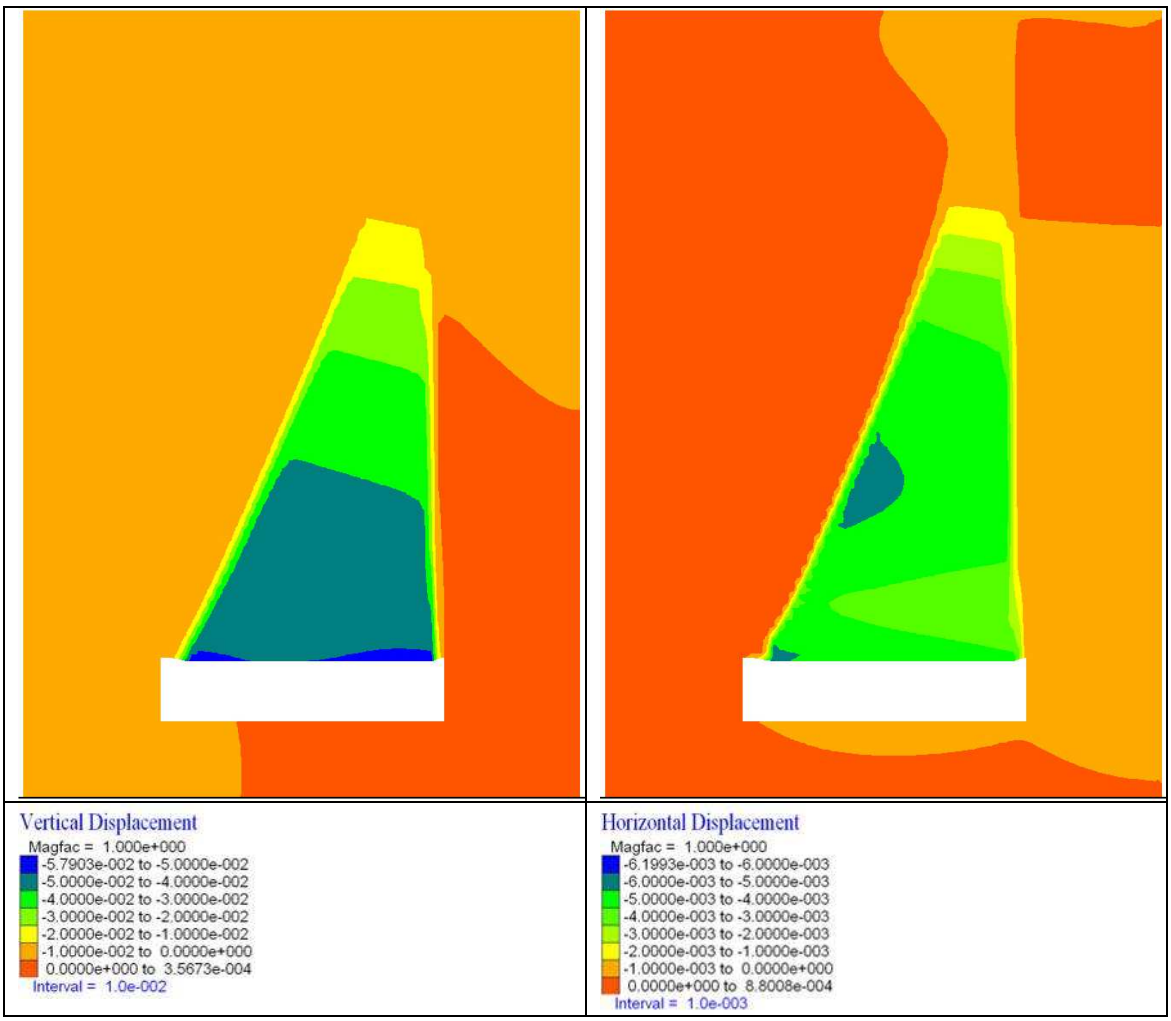

Figure 4.27: Vertical and horizontal displacements within the rock mass. Rock mass GSI 10, joint dip angle 10°, 3 m excavation width, 1 m excavation height.

The angles formed by the left and right hand margin of the failure wedge are again related to the friction angle of the rock joints and significantly the dip angle of the bedding plane, whereby the failure angle from vertical for the left hand side is equal to the residual friction angle of the joints + angle of joint dip (angle = 116°, new angle from vertical = 26°), which indicates that the angle of failure has rotated 10° as the angle of dip has increased by the same amount. The same phenomenon appears to have occurred for the right hand / down dip boundary whereby the failure angle has rotated from 74° to approximately vertical (84-86°). The disparity in angles (a 12° rotation) is thought to be due to the fact that the joints on the right hand side of the wedge in the regions of shear failure have not softened to the same extent as the left hand boundary as the displacements are vertical (or very nearly so) and as such there is a very limited component of plastic strain occurring along the joint plane (when compared to the much shallower dipping left hand boundary). Instead it is occurring approximately normal to the dip and so it would seem that this shear zone has a slightly higher friction angle. As such the new angle is equal to the original dip angle + 10° + 2° (based on this it is

estimated that he friction angle is approximately 18°). The angle from vertical of the left hand margin is illustrated in Figure 4.28.

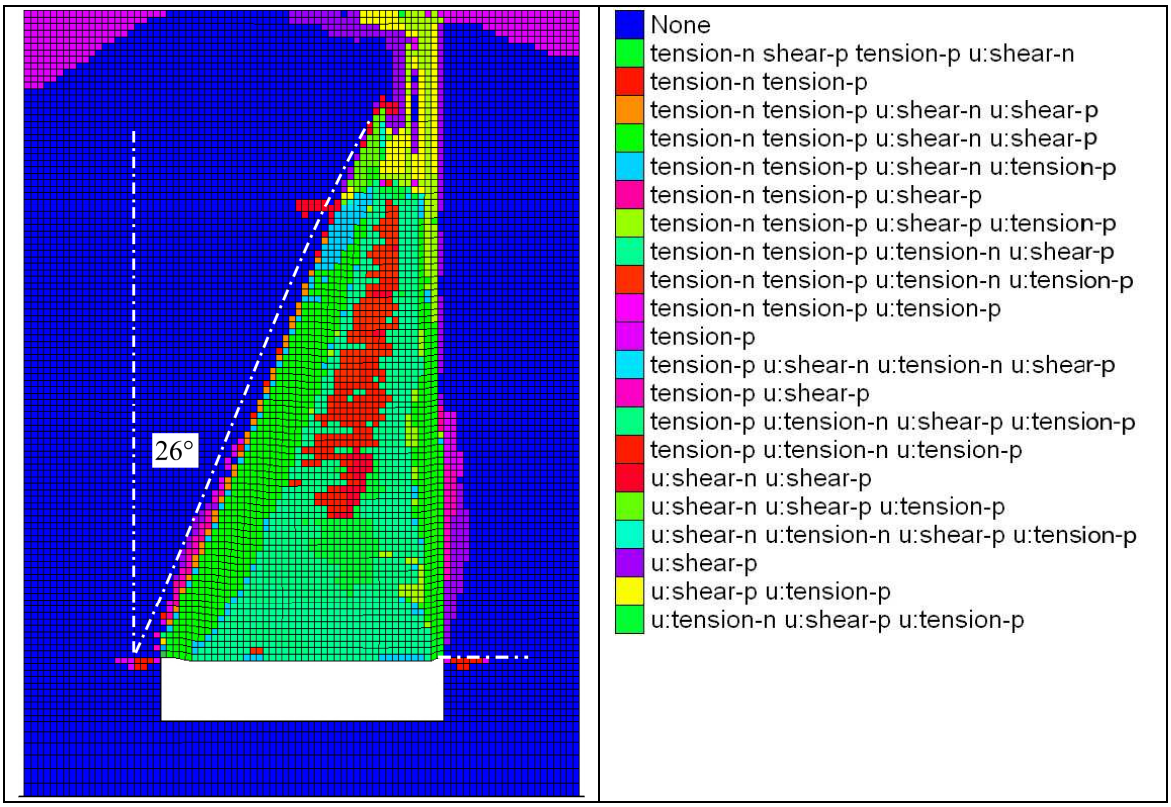

Figure 4.28. Angle of failure surface on up dip side of excavation for joint dip of 10°.

4.7.3 Full Width Model with Subhorizontal (20°) Joints, 3 m Excavation Width, 1 m Excavation Height, GSI 10

As the dip angle increases further it can be seen that the trend of rotation of the failure geometry around the vertical axis continues. Once again, the angle formed by the left hand margin of the failure wedge is related to the friction angle of the rock joints and the dip angle of the bedding plane, whereby the failure angle from vertical is equal to the residual friction angle of the joints plus angle of joint dip (in total equal to 36° from the vertical) causing it to dip at 126°. This is illustrated in Figure 4.29. The right hand margin of the failure wedge is again marked by the rotation caused by the increased dip angle which has now formed at an angle of approximately 96°. 20° steeper than the initial failure angle in the 0° dip model.

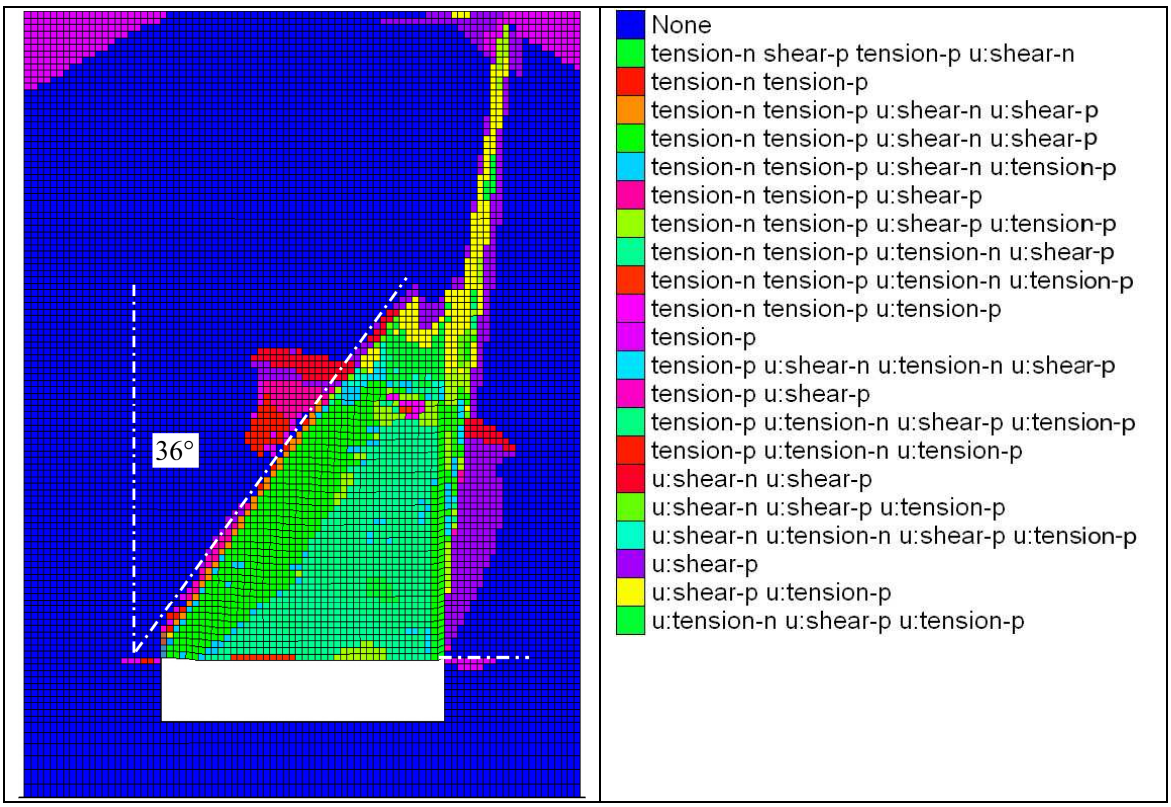

Figure 4.29: Angle of failure surface on up dip side of excavation for joint dip of 20°.

When the failure state plots of the rock mass are examined, it can be seen that a region of joint shear failure has started to develop forming a band parallel to the joint dip and cross cutting the upper portion of the failure wedge. This is most clearly visible on the plot of shear failure state for the joints in Figure 4.30E. This has occurred at an angle of dip equal to the joint friction angle hence there is the potential for frictional sliding to occur on these joints if they soften to a friction angle less than 20°. The formation of this band of shear failure also appears to be linked to the formation of a region of tensile failure of the rock mass matrix outside the boundaries of the main failure wedge. This corresponds with a region on the maximum principal stress plot (Figure 4.31) where the stress state to the left of the primary failure wedge has become tensile. Above this is a region of compressive stress and the boundary between the two is the location of the shear plane that has developed. These regions have been marked on Figure 4.31. The approximate lateral extent of the shear failure surface has been marked on the minimum principal stress plot in Figure 4.31 along with approximate geometry of the regions of maximum and minimum stresses within the model which appear to broadly mark the location of the failure wedge. Another feature worthy of note is the change in geometry of the failure wedge above the down dip (right hand side) side of the model. Where previously (10° dip angle) it was subvertical, it has now rotated in a clock wise direction past vertical by approximately 8-10° following the trend outlined earlier where the

angles forming the boundaries of this wedge are controlled by the dip angle of joints and the friction angle. These relations are summaried below:

$$((90 + \phi_r) + \text{joint dip angle}) \quad 4.1$$

Angle of failure surface at dip angles below the joint friction angle on down dip side of excavation:

$$((90 - \phi_r) + \text{joint dip angle}) \quad 4.2$$

Where the angle of failure has the same sense of rotation as that described in Figure 4.17

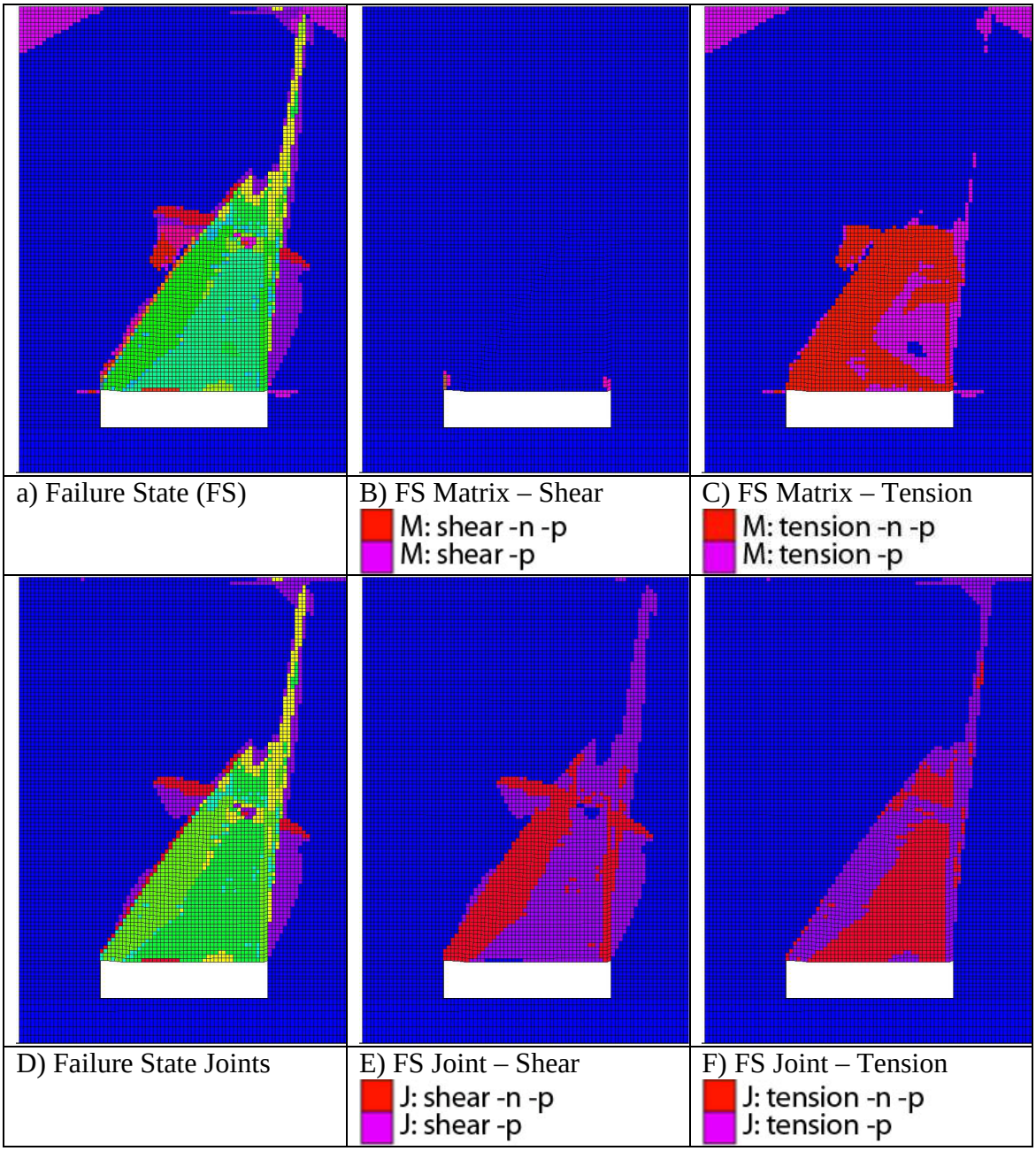

Figure 4.30: Yield state plot of the rock mass. Rock mass GSI 10, joint dip angle 20°, 3 m excavation width, 1 m excavation height

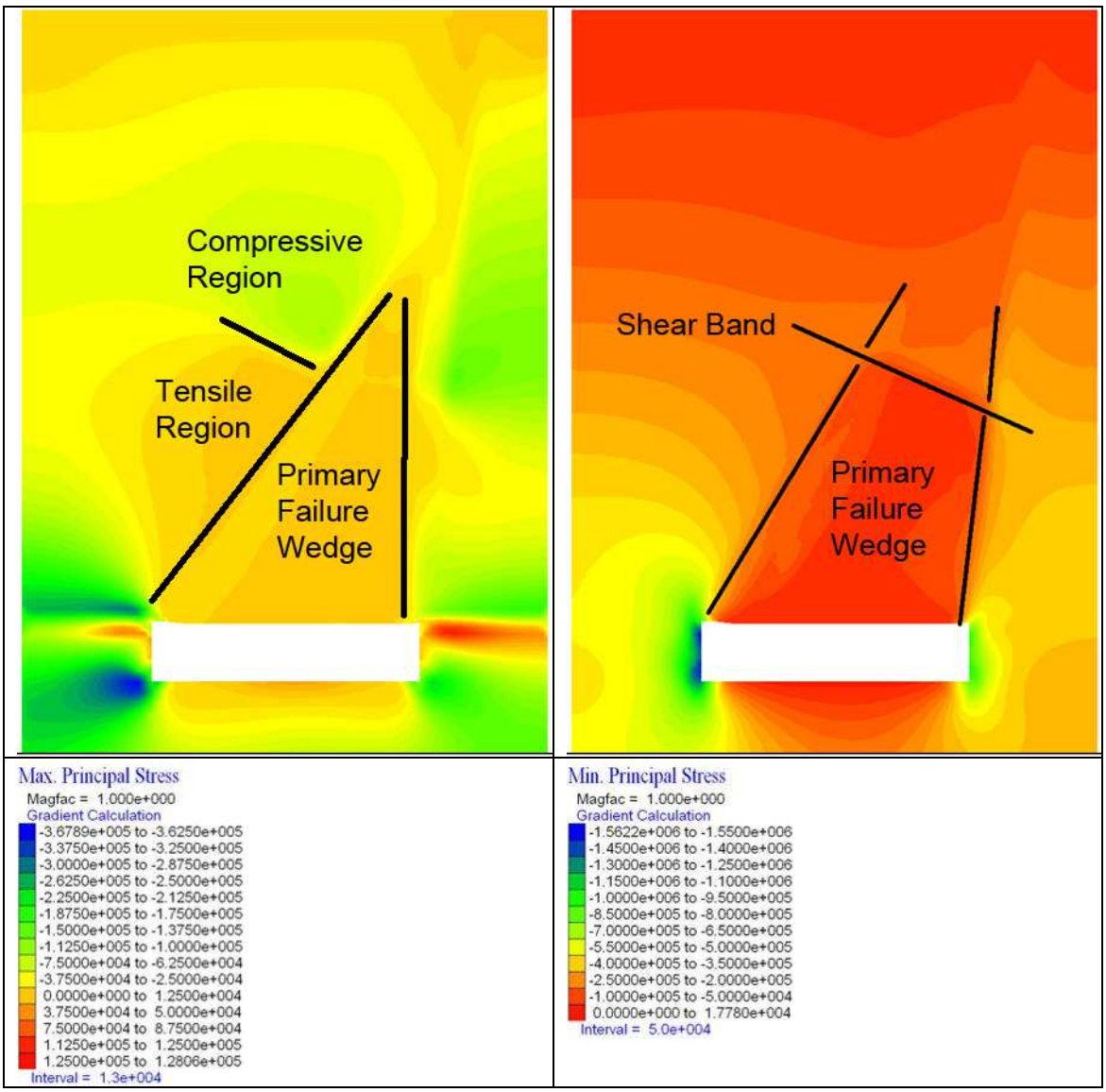

Figure 4.31: Maximum (Sigma 3) and minimum (Sigma 1) principal stress state of the rock mass. Rock mass GSI 10, joint dip angle 20°, 3 m excavation width, 1 m excavation height.

The increased dip angle and alteration in failure geometry and stress distribution has had a corresponding effect on both the volumetric and shear strains occurring within the rock mass (see Figure 4.32). The shear bands once again propagate upwards into the rock mass from the excavation roof / pillar intersection however they are rotated to match the principal stress field and failure plots. It also can be seen that the flat upper surface of the shear and volumetric strain wedge shape is once again oriented parallel to the joint dip. The region of shear failure described above however has not resulted in significant movement within the rock mass as it does not appear to have undergone significant shear strains, however it does correspond to a zone of volumetric strain so it is possible that the shear failure occurred along the joints due to a reduction in the normal stress acting on the joint surface in this region (which would correspond with the zone of tensile stress below the region where the shear failure occurred).

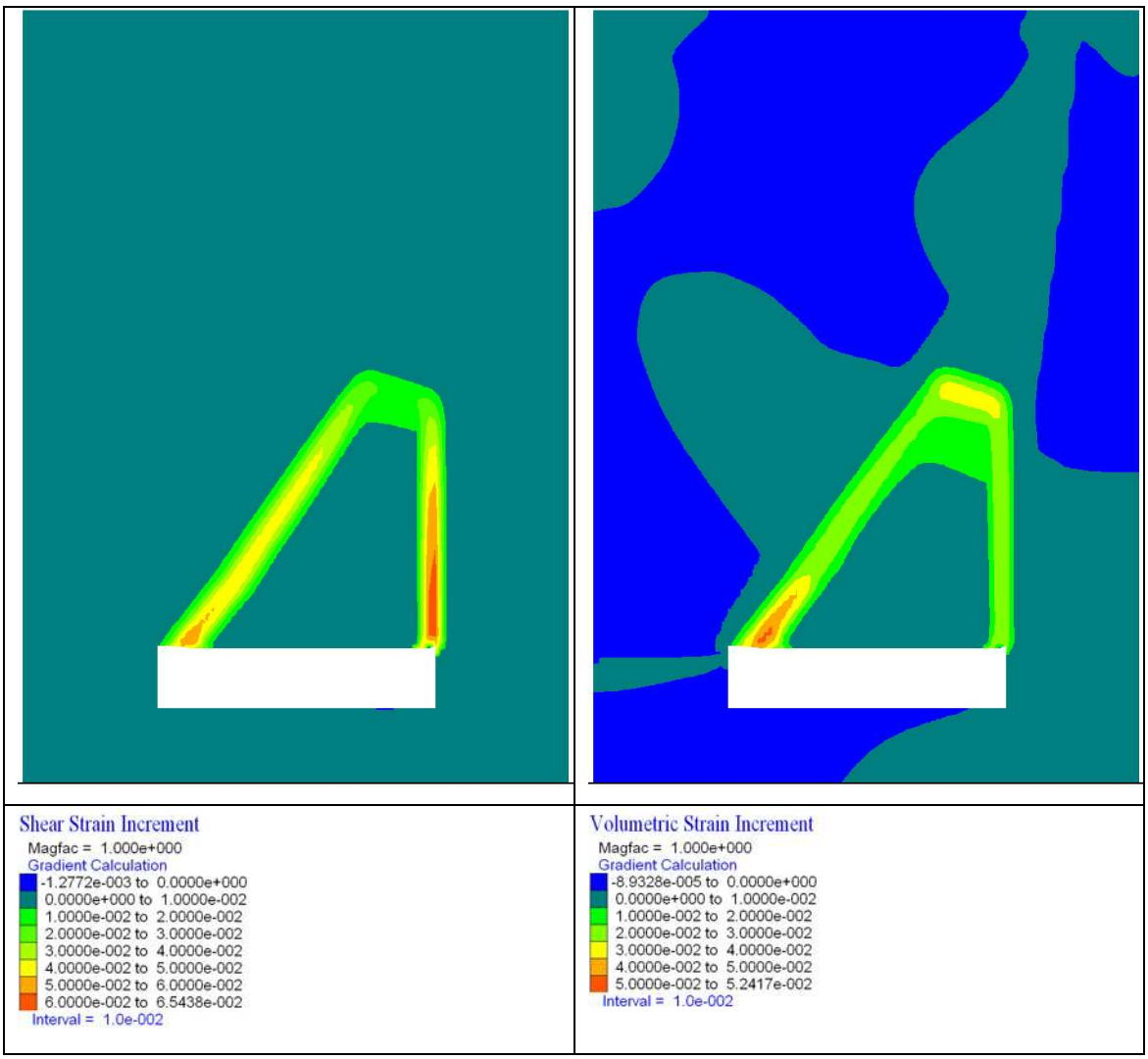

Figure 4.32: Shear and volumetric strains within the rock mass. Rock mass GSI 10, joint dip angle 20°, 3 m excavation width, 1 m excavation height.

As the failure geometry has rotated further around the vertical axis, there is an even greater horizontal component to the displacements than in the lower dip angle models with an order of magnitude increase in maximum horizontal displacements (mm scale) which can be seen in Figure 4.33. This however has lead to a decrease in the vertical displacements (from 48 mm to 58 mm) as the horizontal component of the displacement increases.

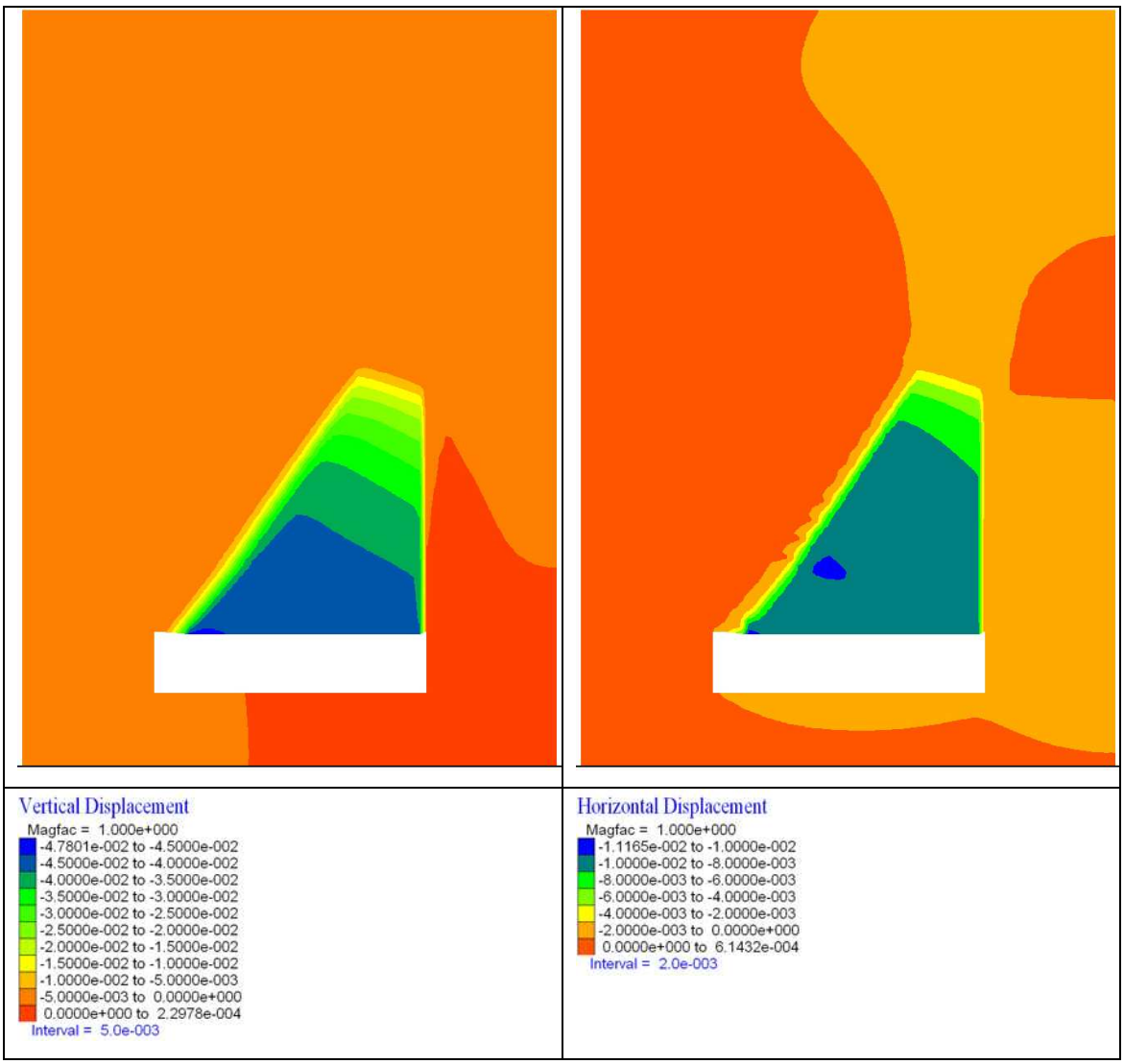

Figure 4.33: Vertical and horizontal displacements within the rock mass. Rock mass GSI 10, joint dip angle 20°, 3 m excavation width, 1 m excavation height.

4.7.4 Full Width Model with Subhorizontal (30°) Joints, 3 m Excavation Width, 1 m Excavation Height, GSI 10

As the dip angle of the joint planes increases beyond their friction angle, there is increased shear yielding parallel to the joint set within the rock mass. This shear band is of greater lateral extent and forms lower within the rock mass (*i.e.* closer to the excavation roof) than the one observed at the shallower dip angle (20°). This can be seen clearly in the plot of joint failure in Figure 4.35E. As per the previous models, the failure angle of the up-dip boundary of the region of joint failure is once again roughly equal to the joint dip angle + residual friction angle of the joint planes (a dip angle of 136°). This can be seen in Figure 4.34. The down dip angle forming the right hand margin of the failure zone dips at an angle equal to the initial failure angle at 0° dip + joint dip (*i.e.* (90 - ϕ_r) + joint dip angle)). In this case this is equal to 104°.

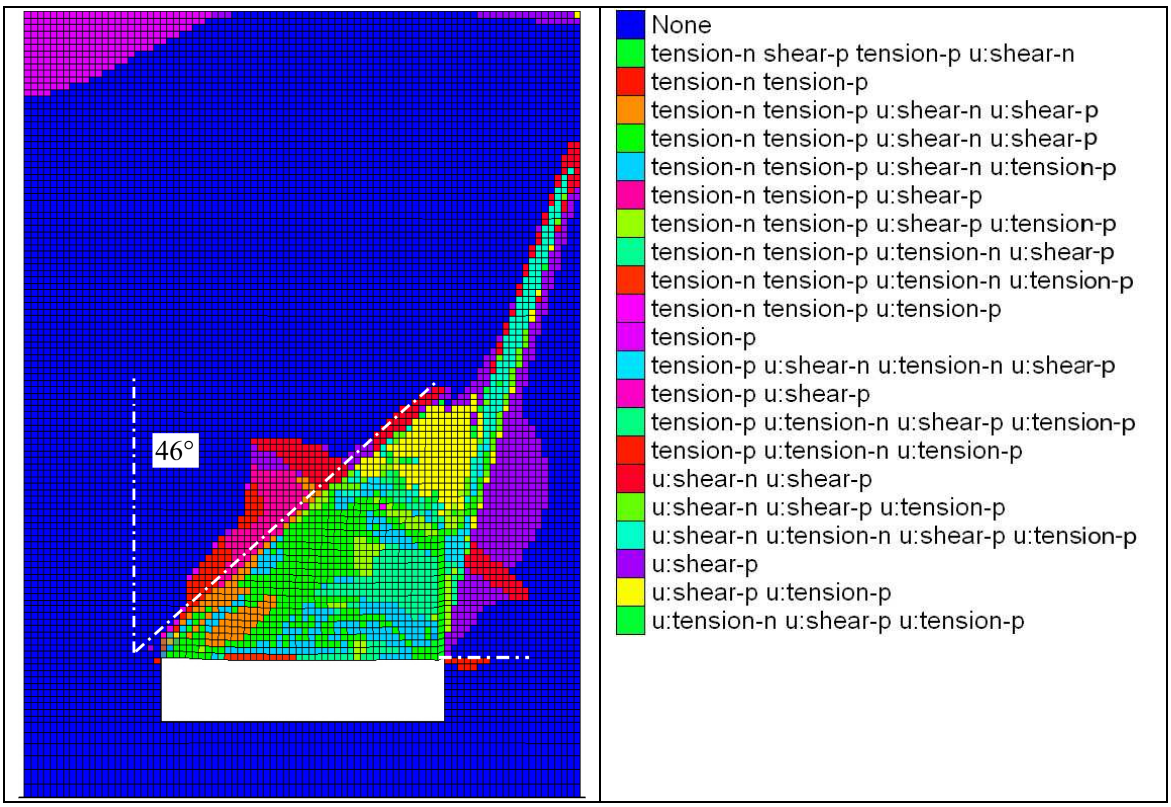

Figure 4.34: Angle of failure surface on up dip side of excavation for joint dip of 30°.

Another feature of note is the change in tensile yield state of the rock mass matrix. As the dip angle has increased, the size of tensile failure / yielding relating to the joints has decreased while the size of the zone of tensile failure / yielding related to the rock mass matrix has also decreased but to a lesser extent. In the previous modelling at shallower dip angles, the tensile failure of the matrix and joints had broadly the same geometry and were bounded within a single failure wedge marked by the region of maximum tensile stress within the rock mass overlying the excavation. However comparison of the tensile failure plots for the matrix and joints (Figure 4.35C and F respectively) shows that the tensile failure of the matrix material extends to a greater extent into the rock mass to the left of this zone. The relation of the two tensile failure geometries to the maximum principal stress is described below.

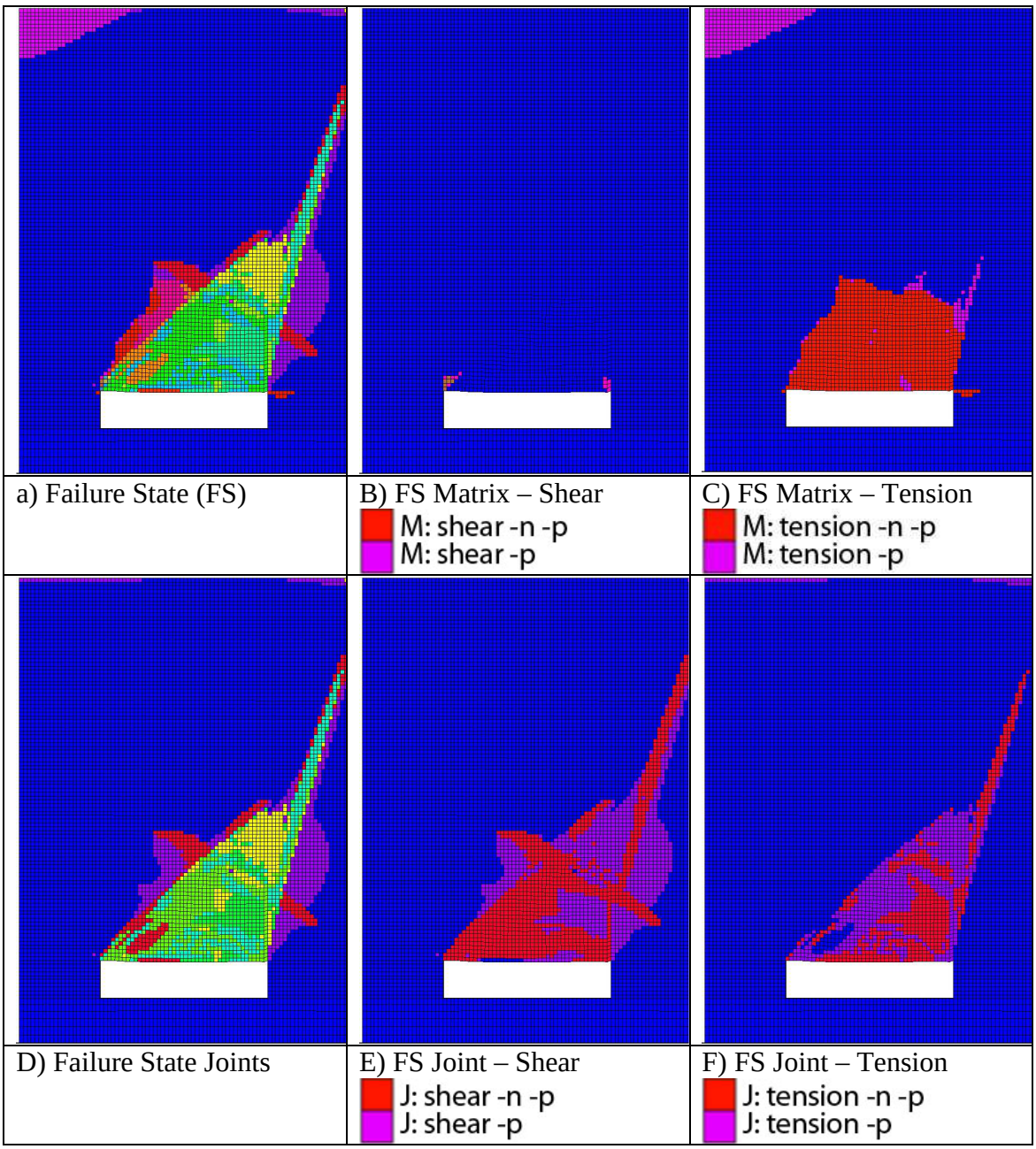

Figure 4.35: Yield state plot of the rock mass. Rock mass GSI 10, joint dip angle 30°, 3 m excavation width, 1 m excavation height.

Examination of the maximum principal stress plot (Figure 4.36) shows that two discrete regions of tensile stress concentration have developed within the rock mass over the excavation, one that appears to be related to the joint tensile failure and in which the boundary geometry is controlled by the joint dip angle and rock mass joint friction angle and the second which is related to the rock mass matrix tensile failure. These two regions are highlighted in the plot and have maximum tensile stresses on the order of 12 kPa. The region of tensile stress related to joint yielding is bisected by a band of shearing which has occurred in the rock mass in the immediate roof of the excavation and is related to a band of compressive stress within the otherwise tensile zone within the roof strata and reaches a peak value of approximately 0.15 MPa that can be seen in

the plot of minimum principal stress running at an angle parallel to the joint dip into the rock mass above the excavation and initiating at the pillar roof intersection.

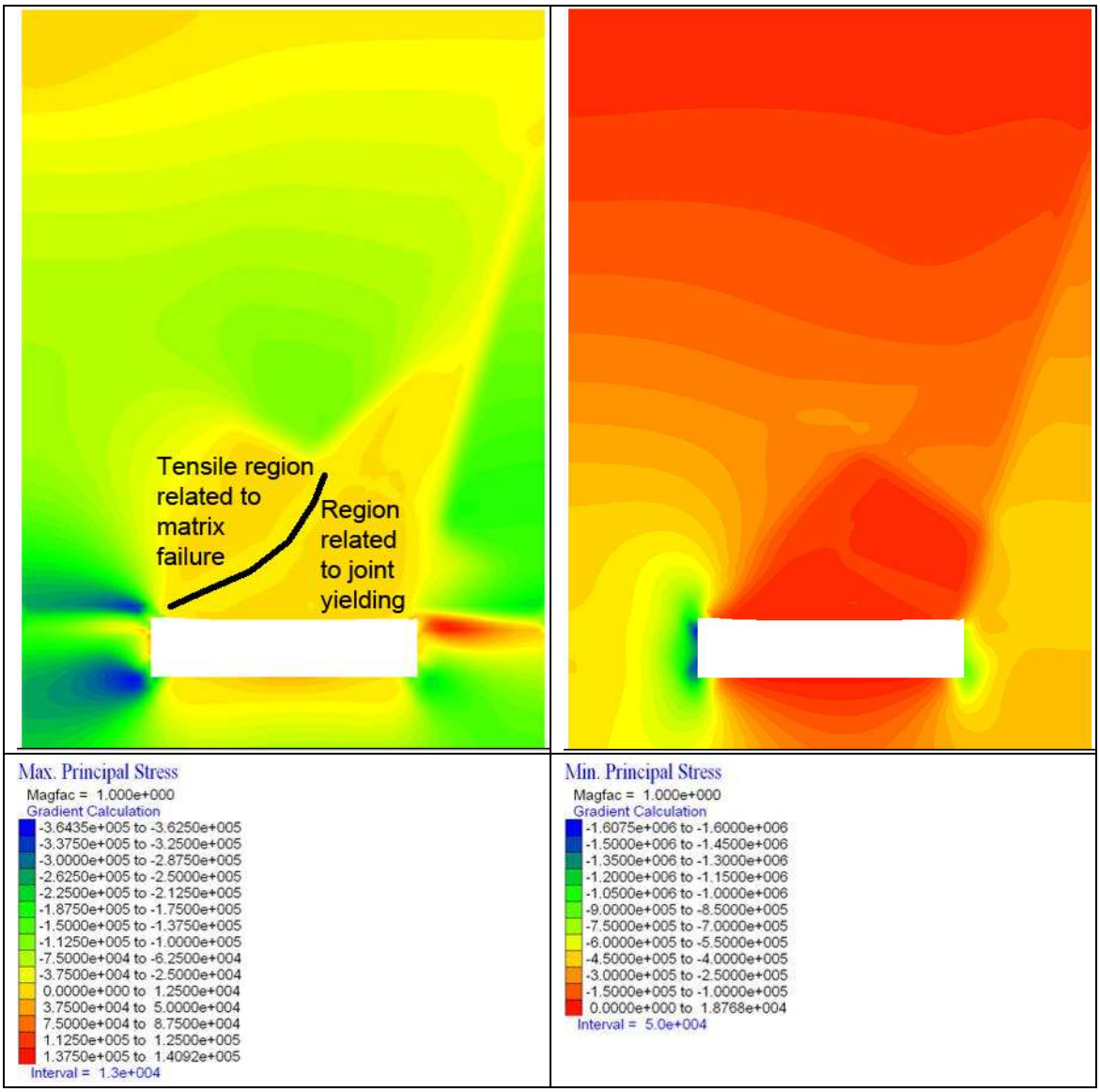

Figure 4.36: Maximum (Sigma 3) and minimum (Sigma 1) principal stress state of the rock mass. Rock mass GSI 10, joint dip angle 30°, 3 m excavation width, 1 m excavation height.

The shear failure within the immediate roof strata appears to be related to the formation of a secondary failure wedge within the roof. The initial development of this feature can be seen in the plots of shear and volumetric strain Figure 4.37. In both cases a shear band appears to be forming parallel to the joint dip and linking the left hand boundary of the failure surface to the excavation roof / pillar intersection on the right hand side of the excavation. The increased extensional volumetric strain highlighted in the plot is indicative of tensile delamination along the shear failure surface that has formed which cross cuts the joints and the initiation of the formation of a second failure wedge / unstable block within the roof.

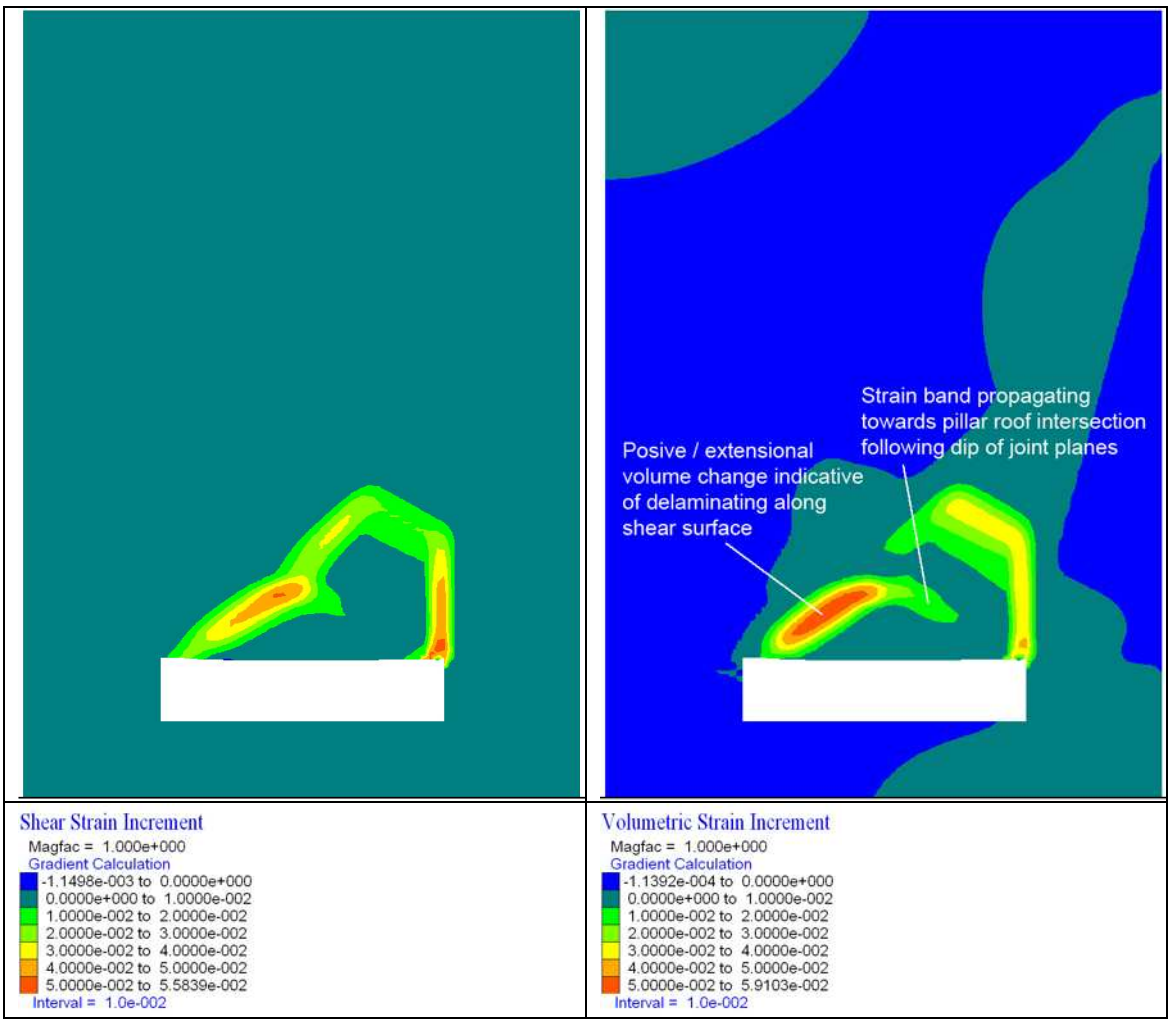

Figure 4.37: Shear and volumetric strains within the rock mass. Rock mass GSI 10, joint dip angle 30°, 3 m excavation width, 1 m excavation height.

Observation of the plots of horizontal and vertical displacements indicate that the two regions appear to be undergoing differing vectors of displacement with the lower "block" or "wedge" displacing vertically to a greater extent than the upper wedge and the upper wedge displaying significantly higher horizontal displacements. Based on the above it is interpreted that the lower block has begun to yield and is moving from the roof down into the void and this displacement has resulted due to a loss of support due to the formation of the region of shear yielding between the lower and upper blocks within the roof. This shearing is assumed to be the cause of the creation of this separate block and the loss of support leading to instability.

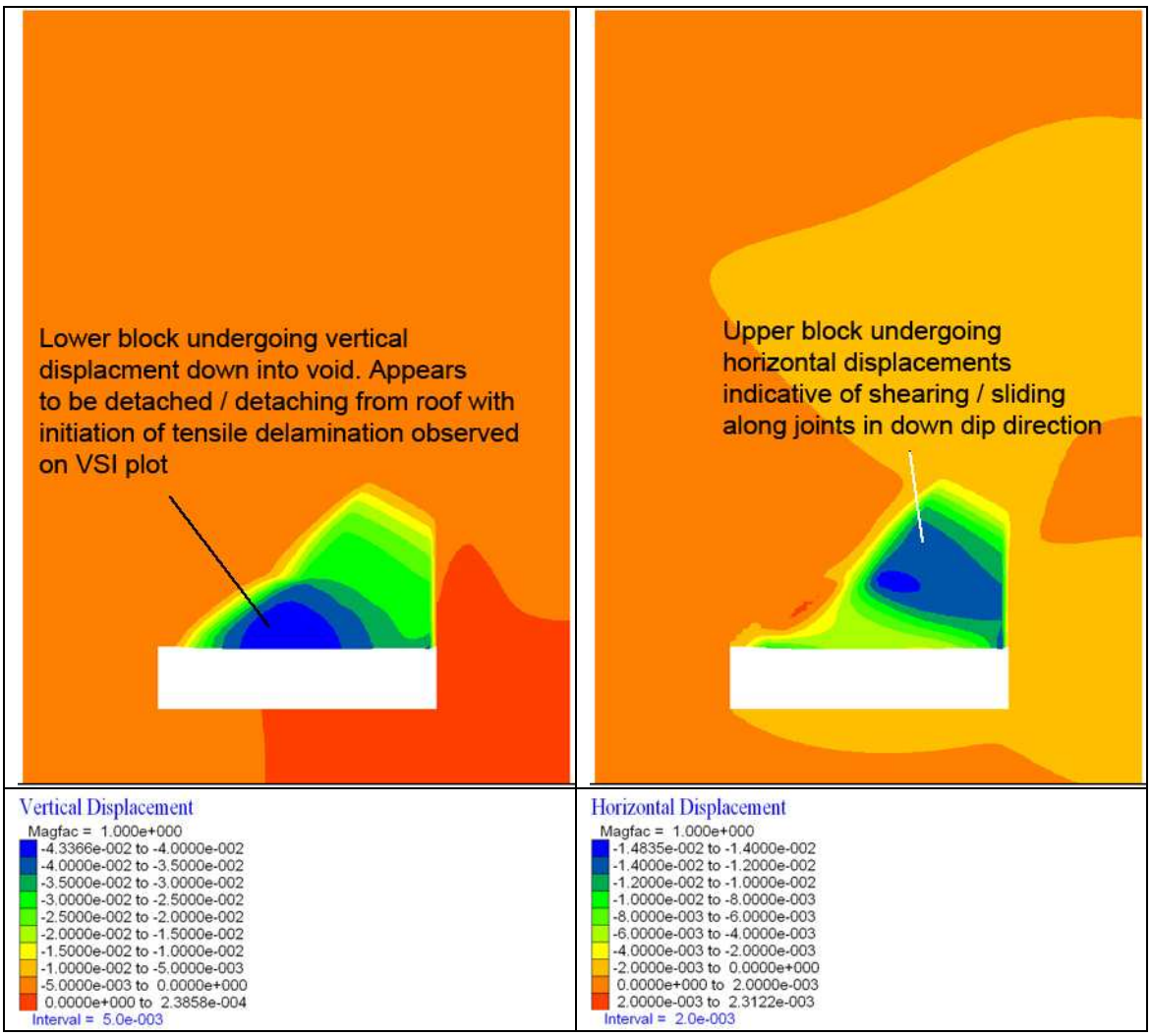

Figure 4.38: Vertical and horizontal displacements within the rock mass. Rock mass GSI 10, joint dip angle 30°, 3 m excavation width, 1 m excavation height.

The unstable nature of this model is confirmed by observation of the plots of unbalanced force and force ratio (see Figure 4.39). Significantly both the maximum unbalanced force (0.4 kPa) and the unbalanced force ratio ($4x10^{-4}$) have stabilised at a non zero value / value significantly higher than the normal ratio limit for stability which is strongly indicative of continued failure (for clarity, the closer the maximum unbalanced force is to zero, the more stable the model. A uniform non zero value is indicative of plastic flow – observation of the displacement and yield plots appears to confirm this to be occurring).

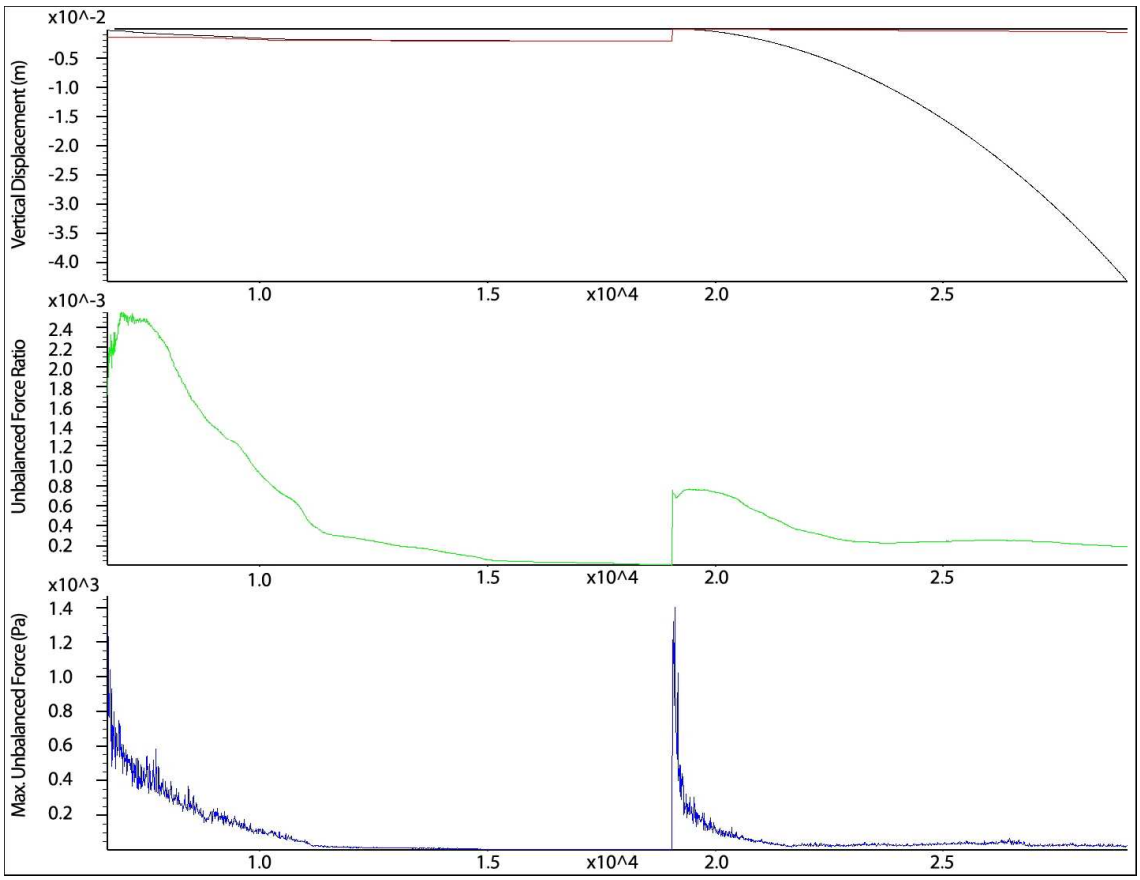

Figure 4.39: Plot of vertical displacement in the excavation roof centreline along with the unbalanced force ratio and maximum unbalanced force. Rock mass GSI 10, joint dip angle 30°, 3 m excavation width, 1 m excavation height.

4.7.5 Full Width Model with Dipping (40°) Joints, 3 m Excavation Width, 1 m Excavation Height, GSI 10

The continued increase in the angle of dip leads to further variation in the geometry of yielding. Broadly summarised, the angle of the zone of tensile yielding (seen in Figure 4.40F) of the joints continues to follow the pattern described for the previous modelling at lower dip angles whereby it is related to the joint dip and friction angle. See Figure 4.41. However the shear yield plot is affected by the occurrence of shear failure along the joint planes which propagates upwards into the rock mass from the pillar roof intersection on the down dip (right hand) side of the excavation (see Figure 4.40E). A band of shear failure has also developed from the left hand side of the excavation toward the boundary of the model again following joint dip.

The matrix tensile yielding geometry in this example appears to be controlled by the friction angle of the rock mass matrix and the dip angle of the joints, where the left hand boundary has formed at an angle of approximately 47° relative to the excavation roof with an anti clockwise sense of rotation (133° when compared to the axes used for dip measurement) whereas the right hand side dips at an angle approximately equal to the

joint dip angle at 40° and appears to be bounded by the band of shearing that has formed along the joint planes (see Figure 4.40C and Figure 4.41B).

As the dip angle has increased the importance of tensile yielding of the joint planes has decreased as their orientation diverges from that of the excavation roof (*i.e.* the roof and joint plane orientation become increasingly less parallel).

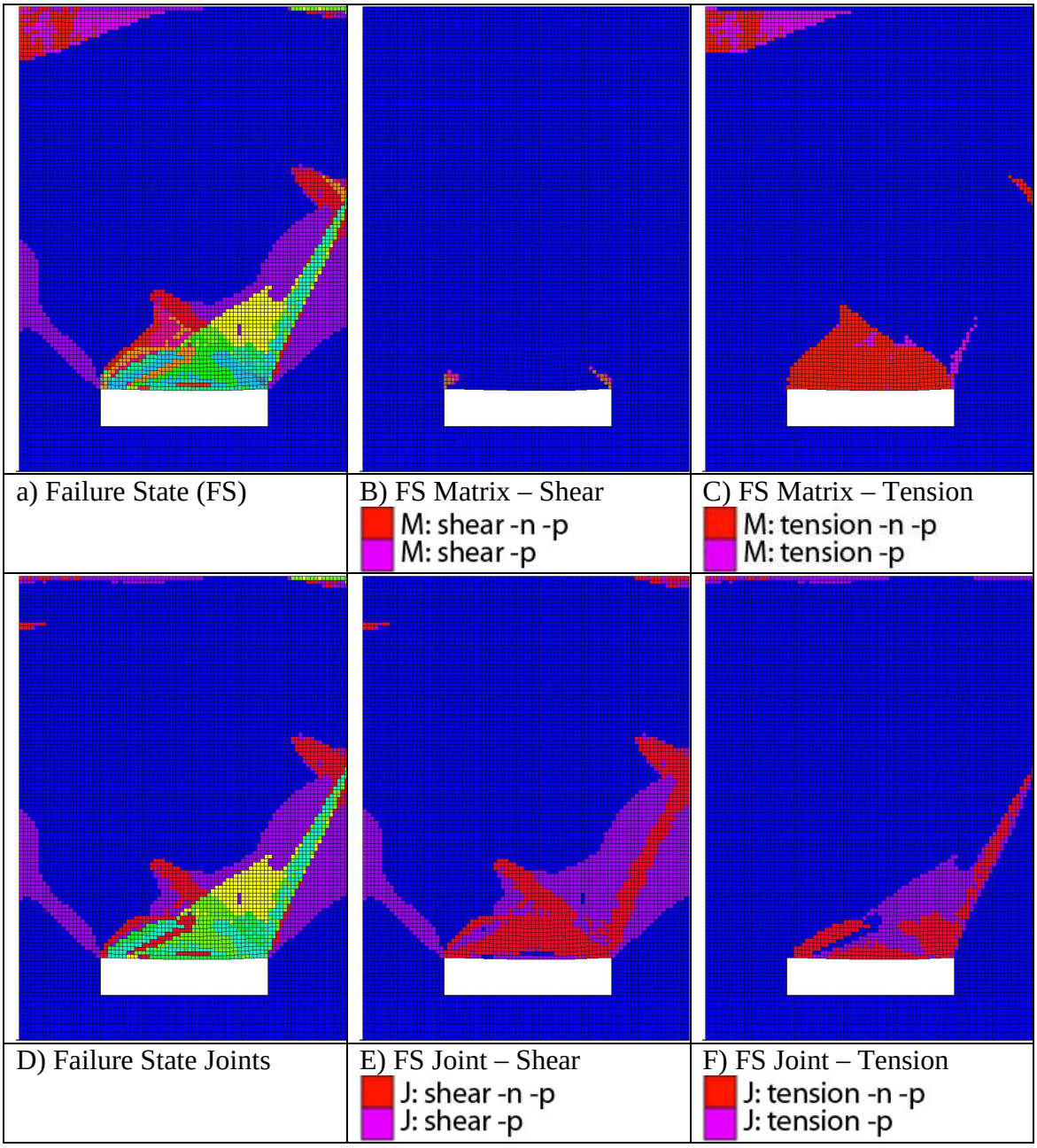

Figure 4.40: Yield state plot of the rock mass. Rock mass GSI 10, joint dip angle 40°, 3 m excavation width, 1 m excavation height.

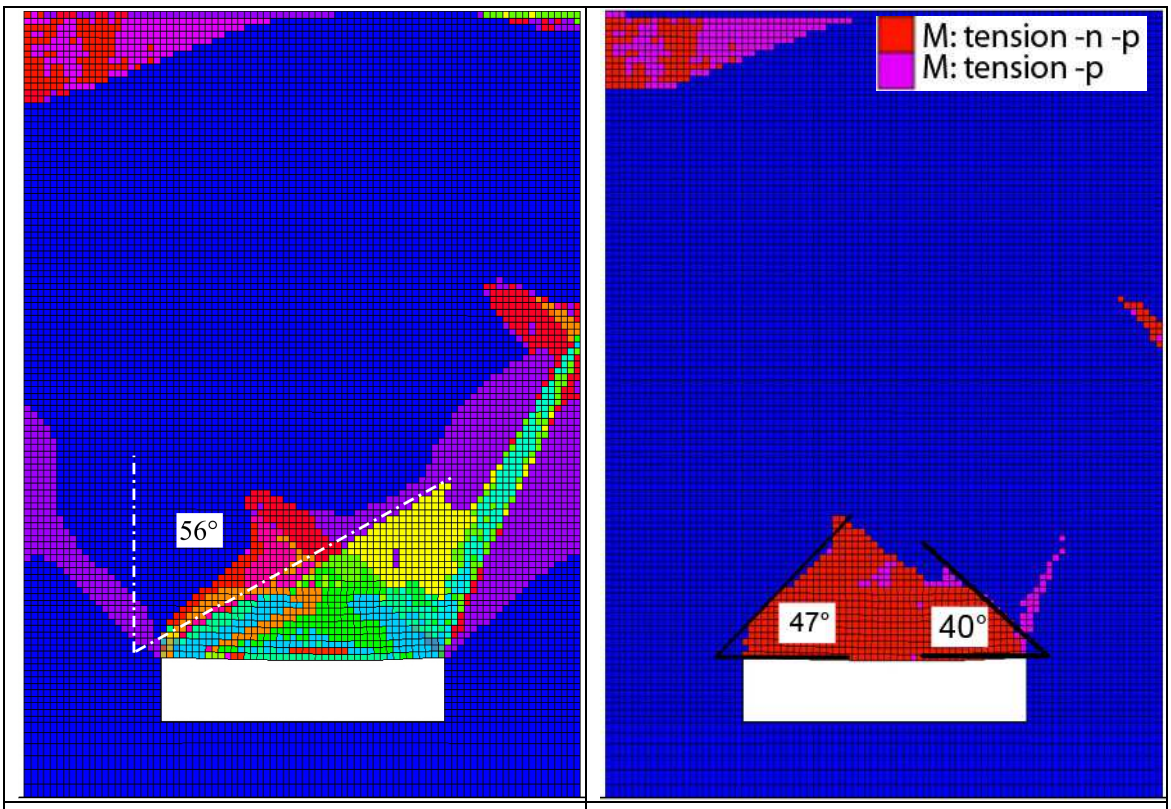

a) Failure State Plot | b) FS Matrix – Tension Plot

Figure 4.41: Angle of joint tensile failure surface on up dip side of excavation for joint dip of 40°.

The geometry of the matrix tensile failure and the joint tensile failure appear to closely match the region of high tensile stresses in the maximum principal stress plot which can be seen overlaid in Figure 4.42.

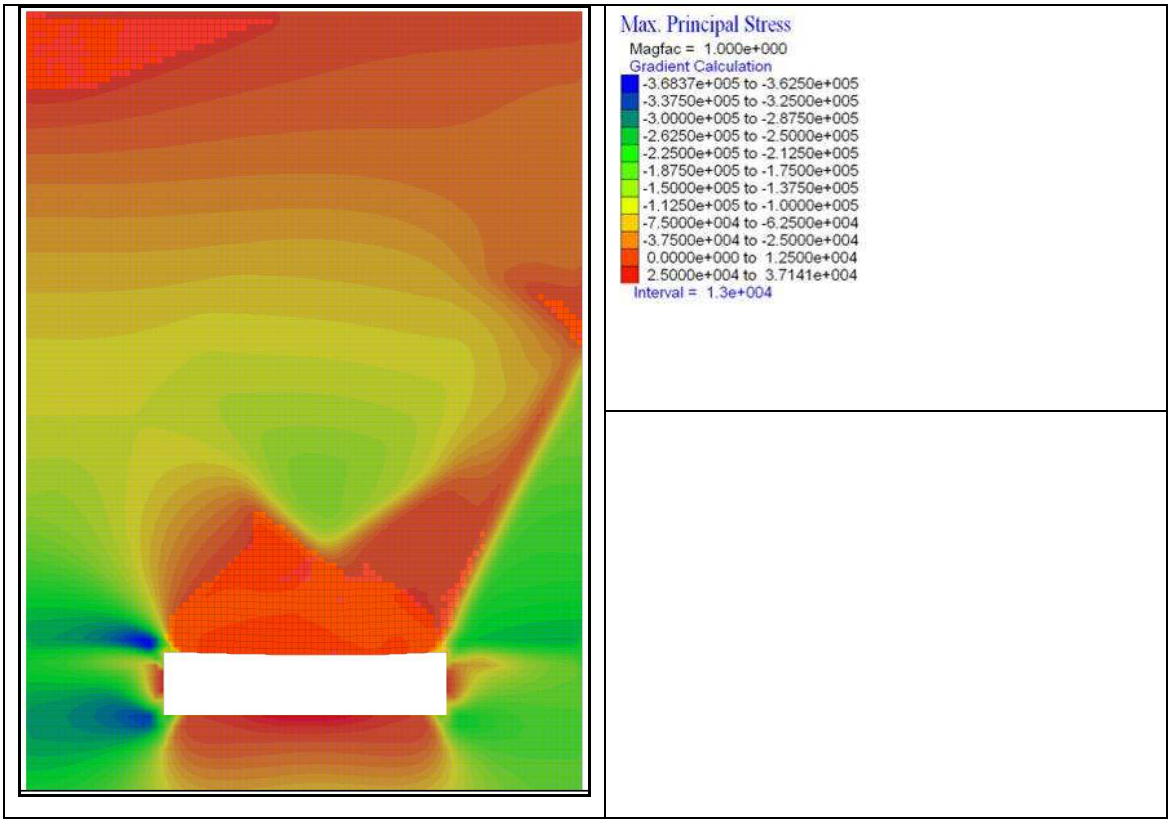

Figure 4.42: Plot of maximum principal stress overlain with matrix tensile failure plot.

The contour plot of minimum principal stress (Figure 4.43) shows a region of tension in the immediate roof above the excavation that is bounded to the right hand side by a zone of compressive stress that is protruding from the pillar roof intersection into the rock mass. The contour spacing here is very dense and there is a large contrast between the magnitudes of the tensile and compressive stress. This zone appears to correlate closely with the formation of the band of shearing on the joint failure state plot that propagates upwards into the rock mass from the right hand coal pillar roof intersection.

Observation of the shear and volumetric strain plots for this model (see Figure 4.44) indicate that the primary region of deformation occurs within the immediate roof of the excavation. It would appear this extends to only a limited extent within the rock mass. This is further confirmed by the plots of vertical and horizontal displacements (Figure 4.46). Another feature of note in the displacement plots is the significant difference in vertical displacements across the excavation roof which is at a maximum to the right hand side of the roof centreline. Also the roof strata are undergoing differing directions of horizontal displacement to the right and left hand sides of the excavation roof.

It is also of note that the degree of strain and the displacements are larger in this region than for that which occurred in the failed regions in previous models. This suggests that although the initial region of failure does not appear to extend as far into the rock mass, the immediate roof will undergo greater deformations than that seen in the models with lower dip angles. As per the previous models, from the plot of unbalanced force and force ratio the rock mass is currently unstable as the unbalanced force ratio is significantly higher than $1x10^{-5}$ (see Figure 4.45).

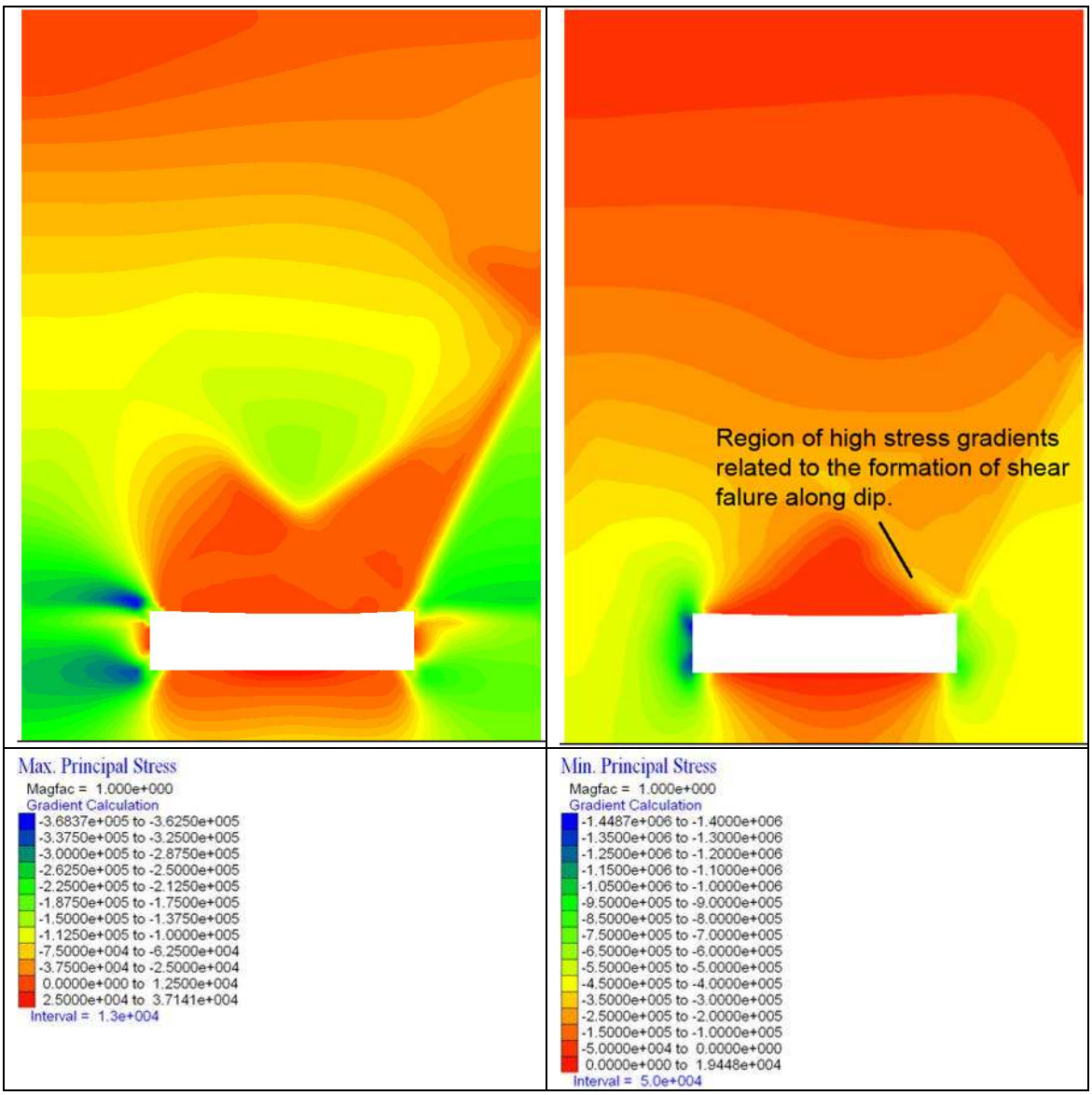

Figure 4.43: Maximum (Sigma 3) and minimum (Sigma 1) principal stress state of the rock mass. Rock mass GSI 10, joint dip angle 40°, 3 m excavation width, 1 m excavation height.

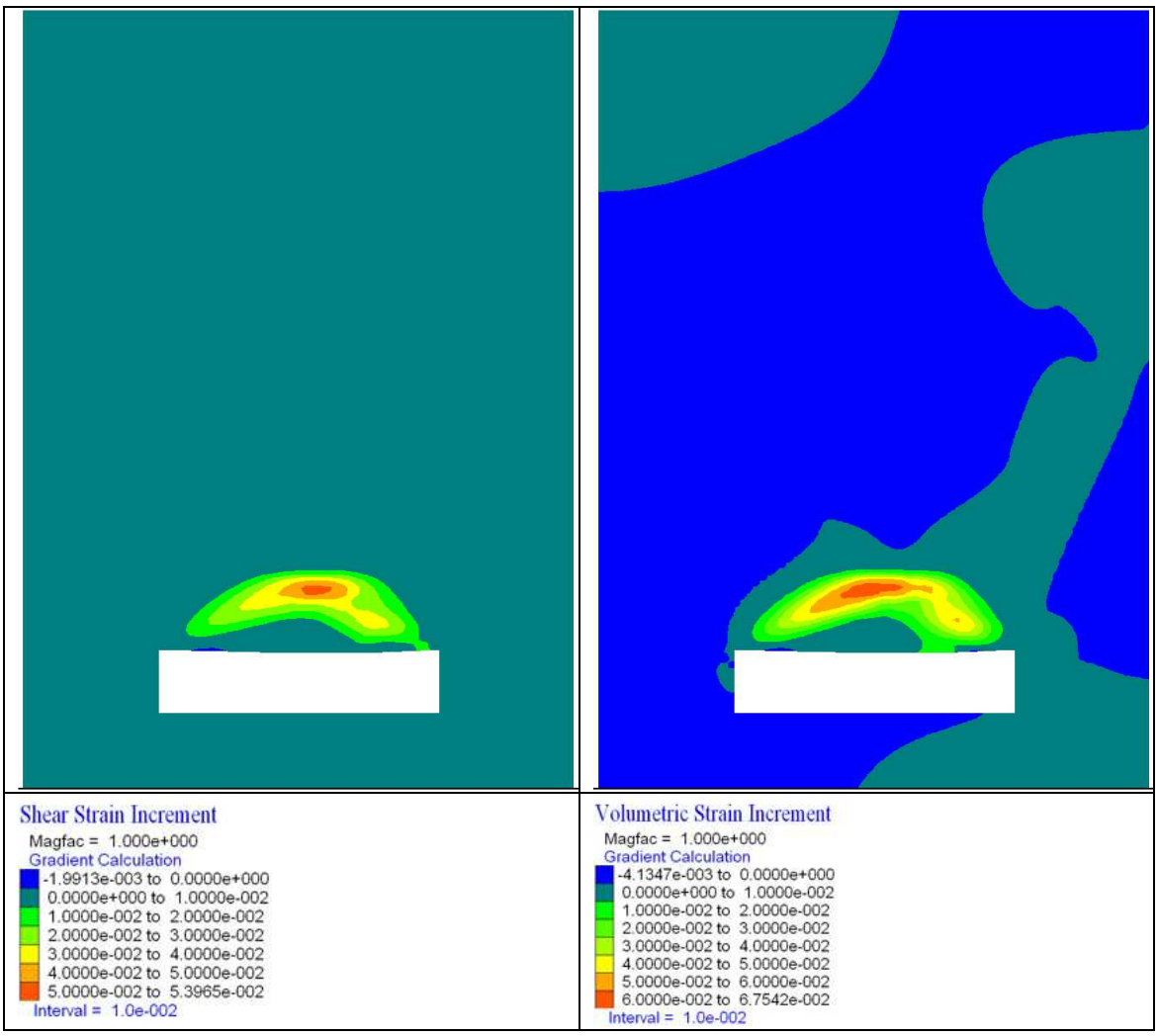

Figure 4.44: Shear and volumetric strains within the rock mass. Rock mass GSI 10, joint dip angle 40°, 3 m excavation width, 1 m excavation height.

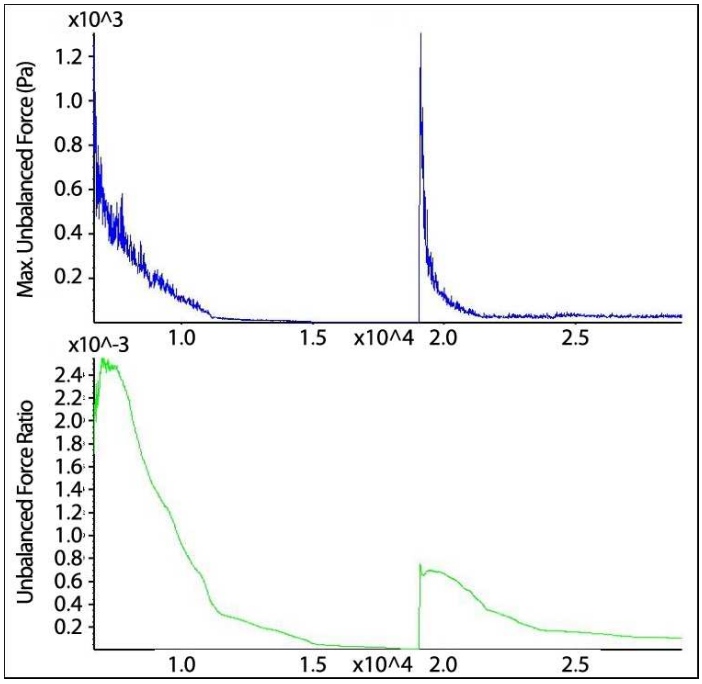

Figure 4.45: Plot showing unbalanced force ratio and maximum unbalanced force. Rock mass GSI 10, joint dip angle 40°, 3 m excavation width, 1 m excavation height.

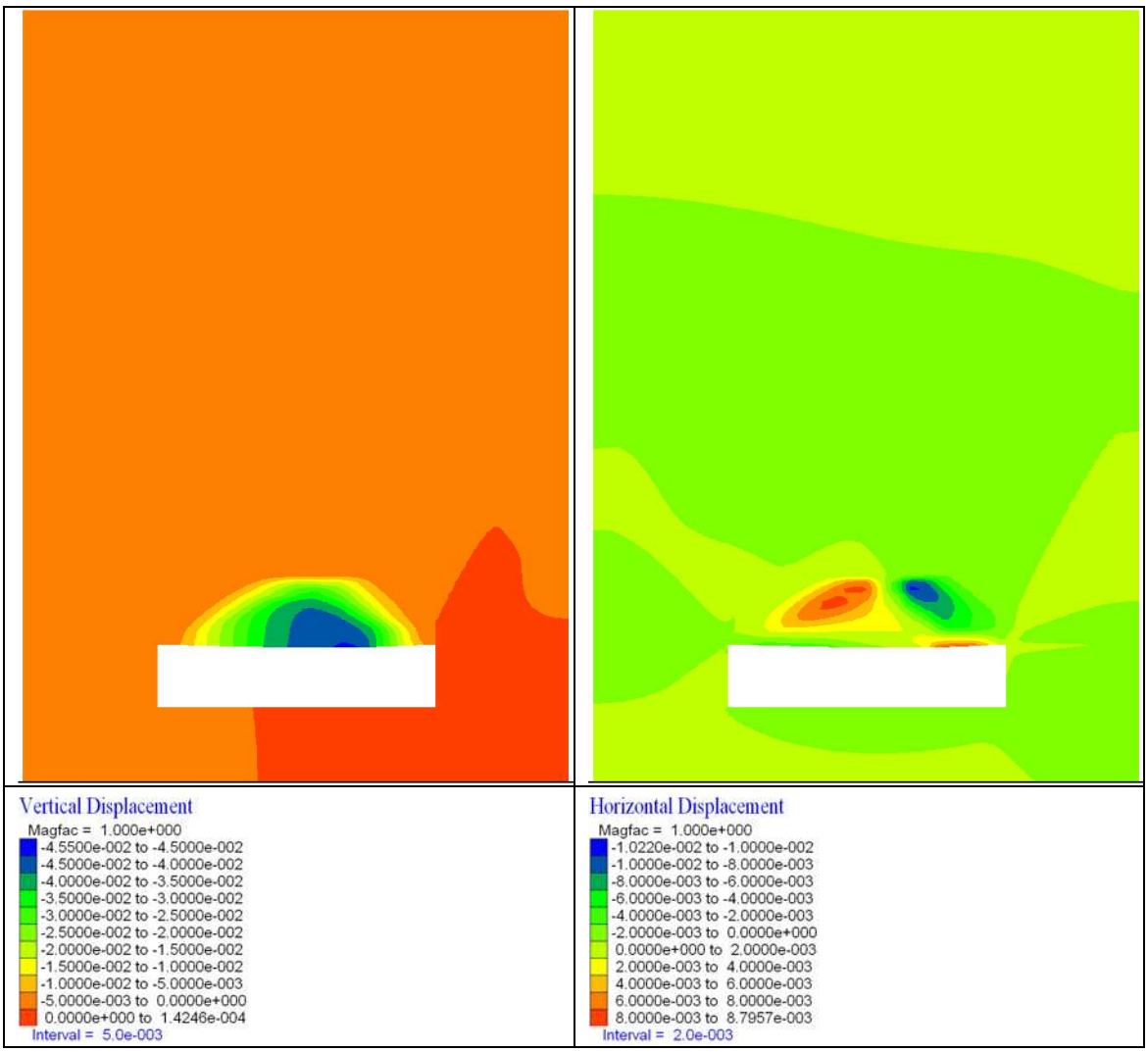

Figure 4.46: Vertical and horizontal displacements within the rock mass. Rock mass GSI 10, joint dip angle 40°, 3 m excavation width, 1 m excavation height.

4.7.6 Full Width Model with Steeply Dipping (60°) Joints, 3 m Excavation Width, 1 m Excavation Height, GSI 10

At a dip angle of 60° it is immediately apparent that significant levels of shear failure are occurring along the joint planes within the rock mass. Tensile failure of the joint planes is relatively insignificant whereas the rock mass matrix is undergoing quite significant yielding in tension. See Figure 4.47. The geometry of the tensile failure zone of the rock mass is again controlled by the rock mass matrix friction angle on the up dip side and by the joint dip angle on the down dip (right hand) side.

The principal stresses have continued to rotate and the orientation of the joint dip is now very clearly defined in the plot of maximum principal stress (Figure 4.48). The height of the upper boundary of the zone of tensile yielding over the excavation extends to a greater level over the right hand, down dip side of the excavation due to the relationship between failure geometry, dip angle and friction angle outlined previously and this is

reflected most clearly in the minimum principal stress plot whereby the tensile stresses in the rock mass extend to a greater height to the down dip (right hand) side of the excavation

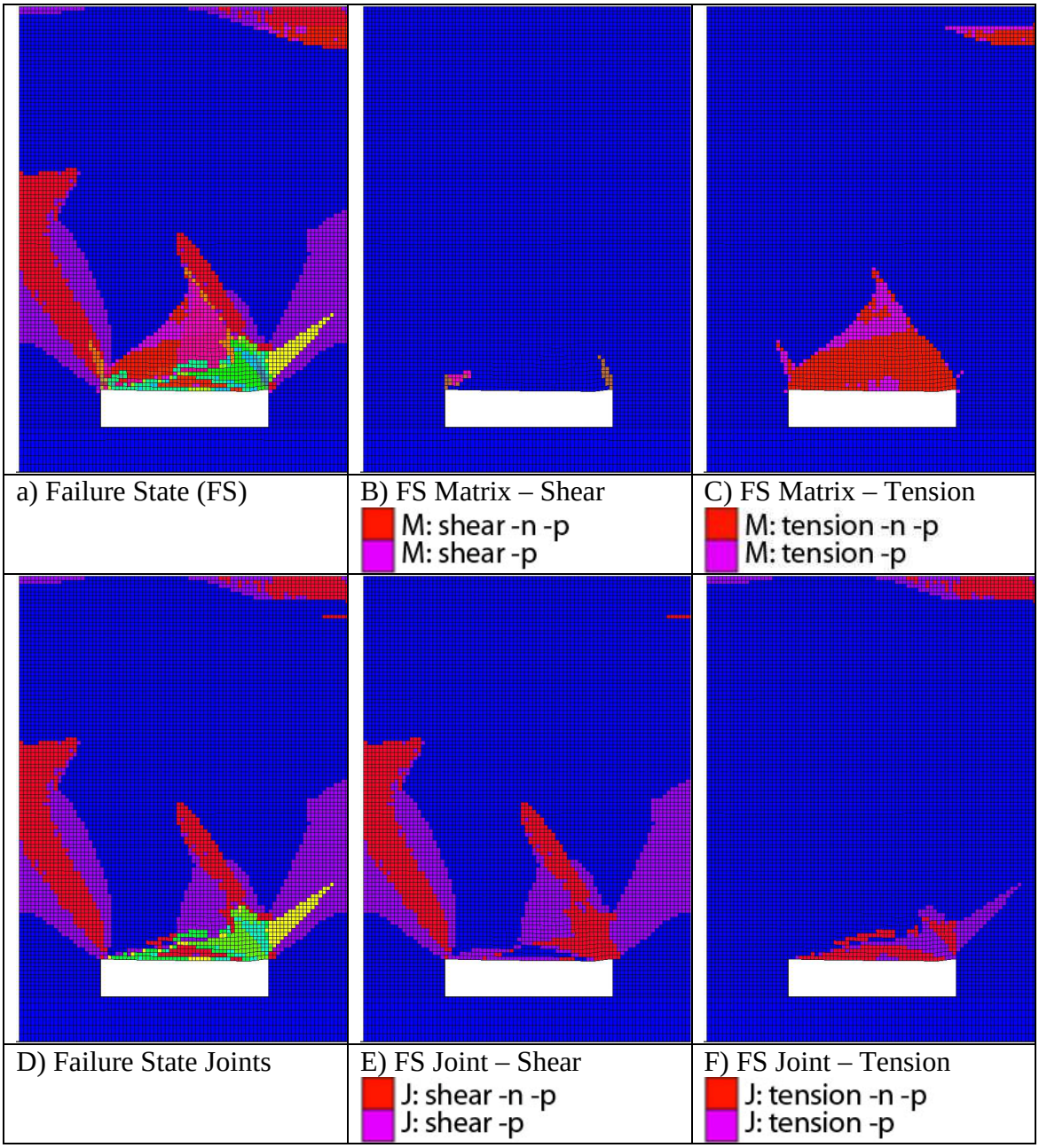

Figure 4.47: Yield state plot of the rock mass. Rock mass GSI 10, joint dip angle 60°, 3 m excavation width, 1 m excavation height.

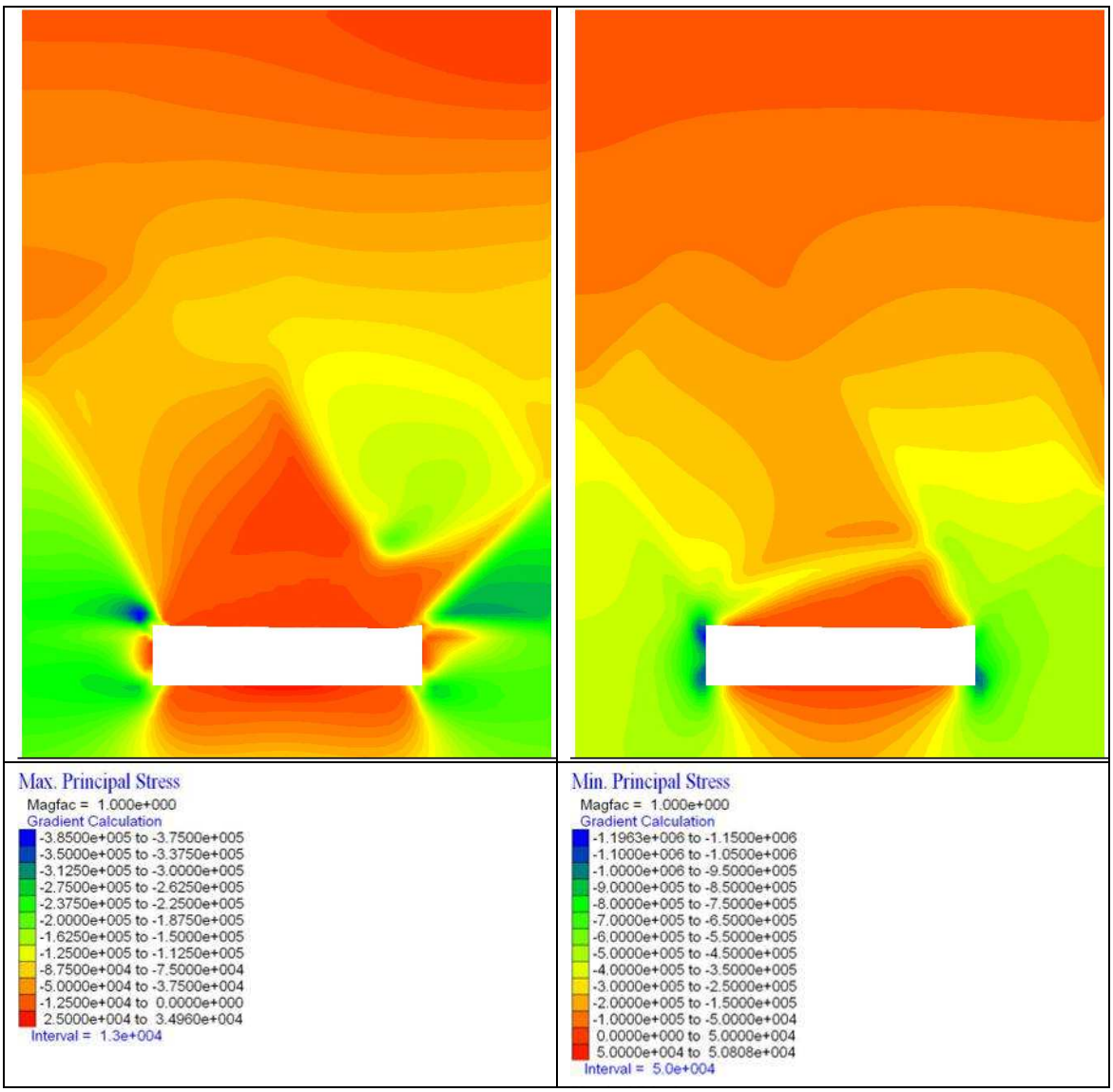

Figure 4.48: Maximum (Sigma 3) and minimum (Sigma 1) principal stress state of the rock mass. Rock mass GSI 10, joint dip angle 60°, 3 m excavation width, 1 m excavation height.

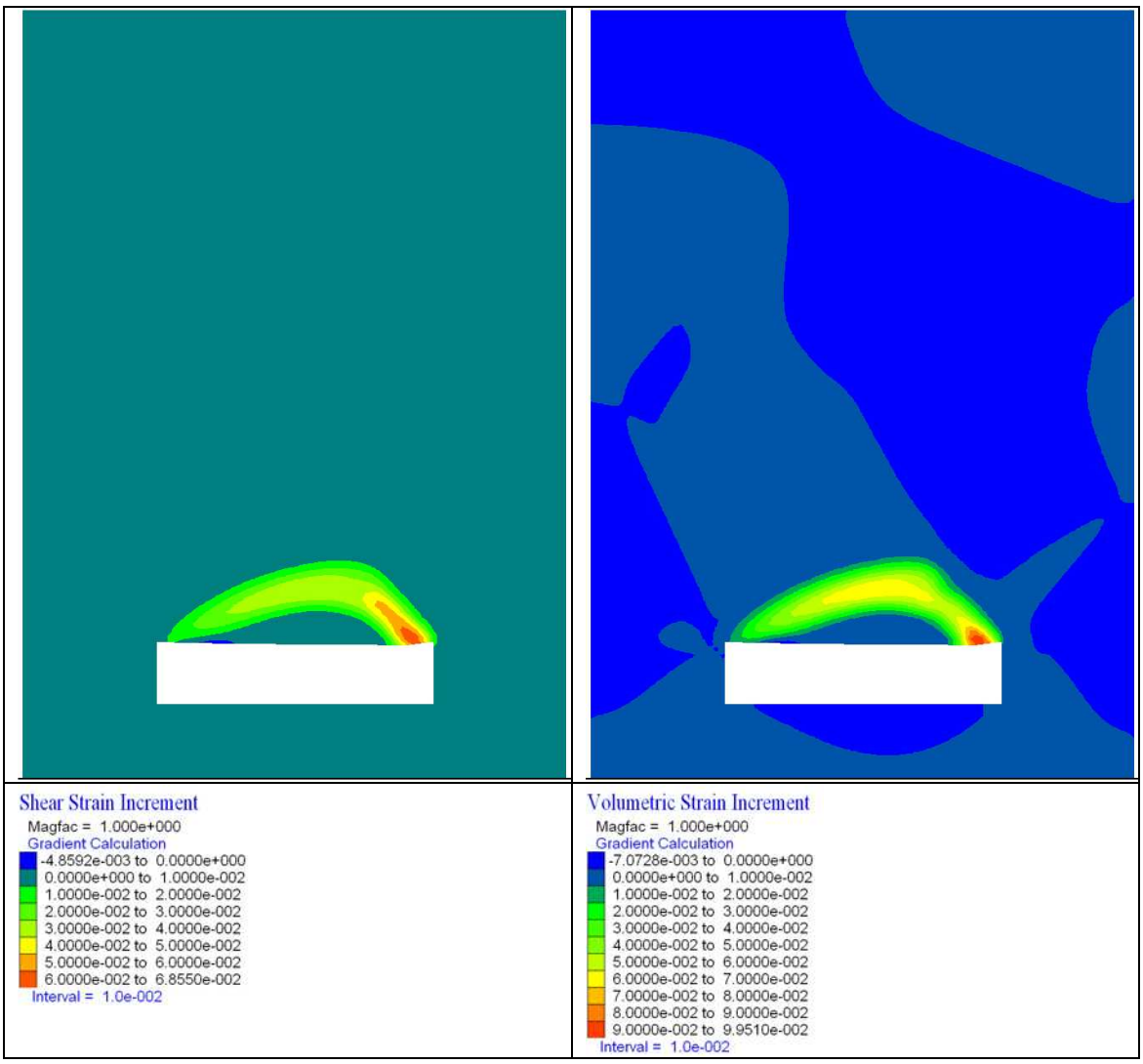

Figure 4.49: Shear and volumetric strains within the rock mass. Rock mass GSI 10, joint dip angle 60°, 3 m excavation width, 1 m excavation height.

The region of shear and volumetric strain is concentrated within the immediate excavation roof to a height of approximately 1 m (see Figure 4.49) and the geometry of the shear and volumetric strain bands correlate very closely to the boundary of the region of maximum tensile stress in the roof strata that can be seen in the plots of maximum and minimum principal stress. Roof displacements are highly anisotropic in this model with the maximum vertical displacement occurring at the far right hand side / down dip side of the excavation. The region of maximum horizontal displacements overlies this. This can be seen in Figure 4.50.

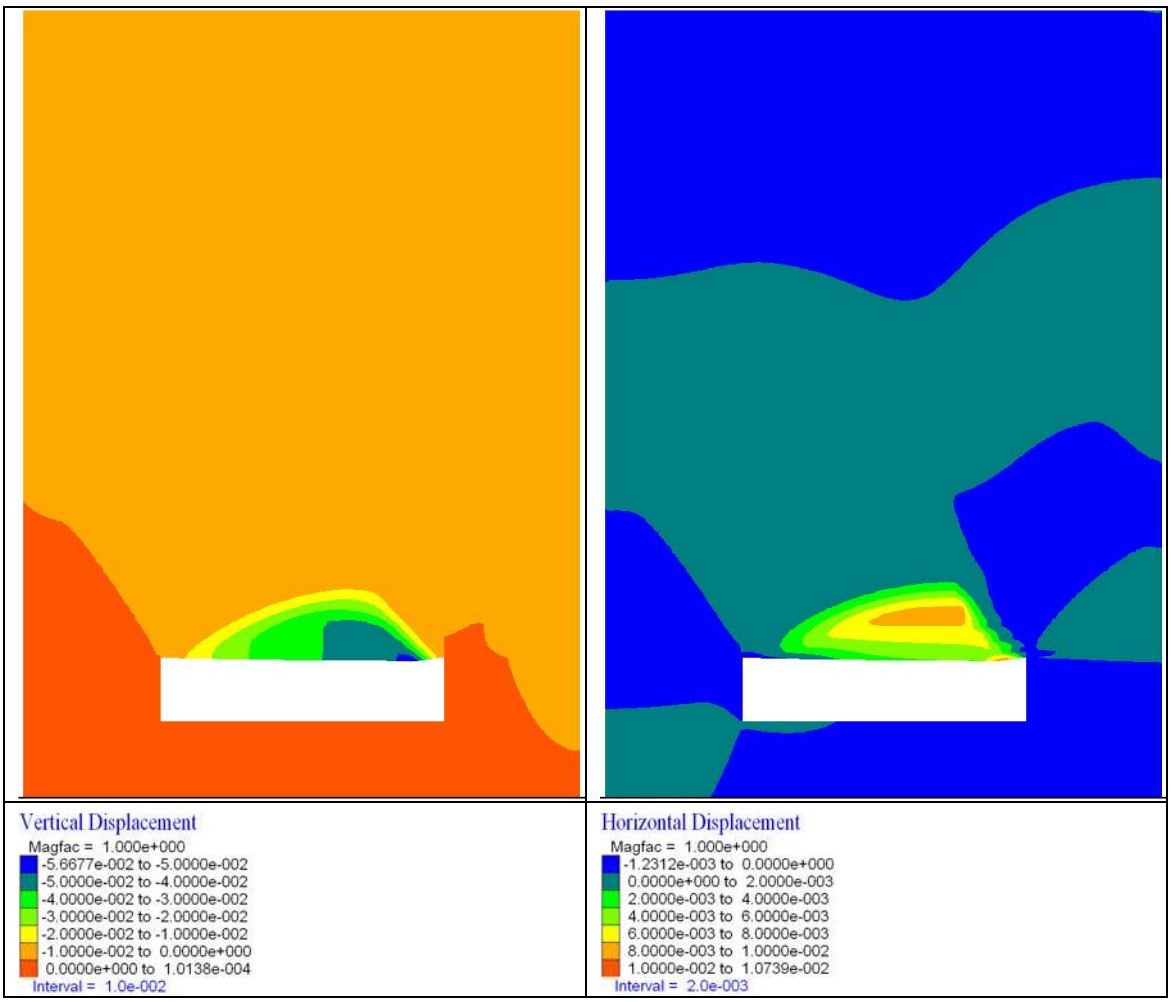

Figure 4.50: Vertical and horizontal displacements within the rock mass. Rock mass GSI 10, joint dip angle 60°, 3 m excavation width, 1 m excavation height.

4.7.7 Full Width Model with Subvertical (80°) Joints, 3 m Excavation Width, 1 m Excavation Height, GSI 10

The continued increase in joint dip to an angle of 80° has caused joint shear failure to occur in bands which propagate from the pillar roof boundaries at the edges of the excavation to the upper boundaries of the model. This has caused a complex mixture of failure types to occur within the model particularly above the right hand side of the excavation, whereby both joint shear and tensile failure along with matrix tensile failure have all occurred in a band along the dip of the joints as shown in Figure 4.51.

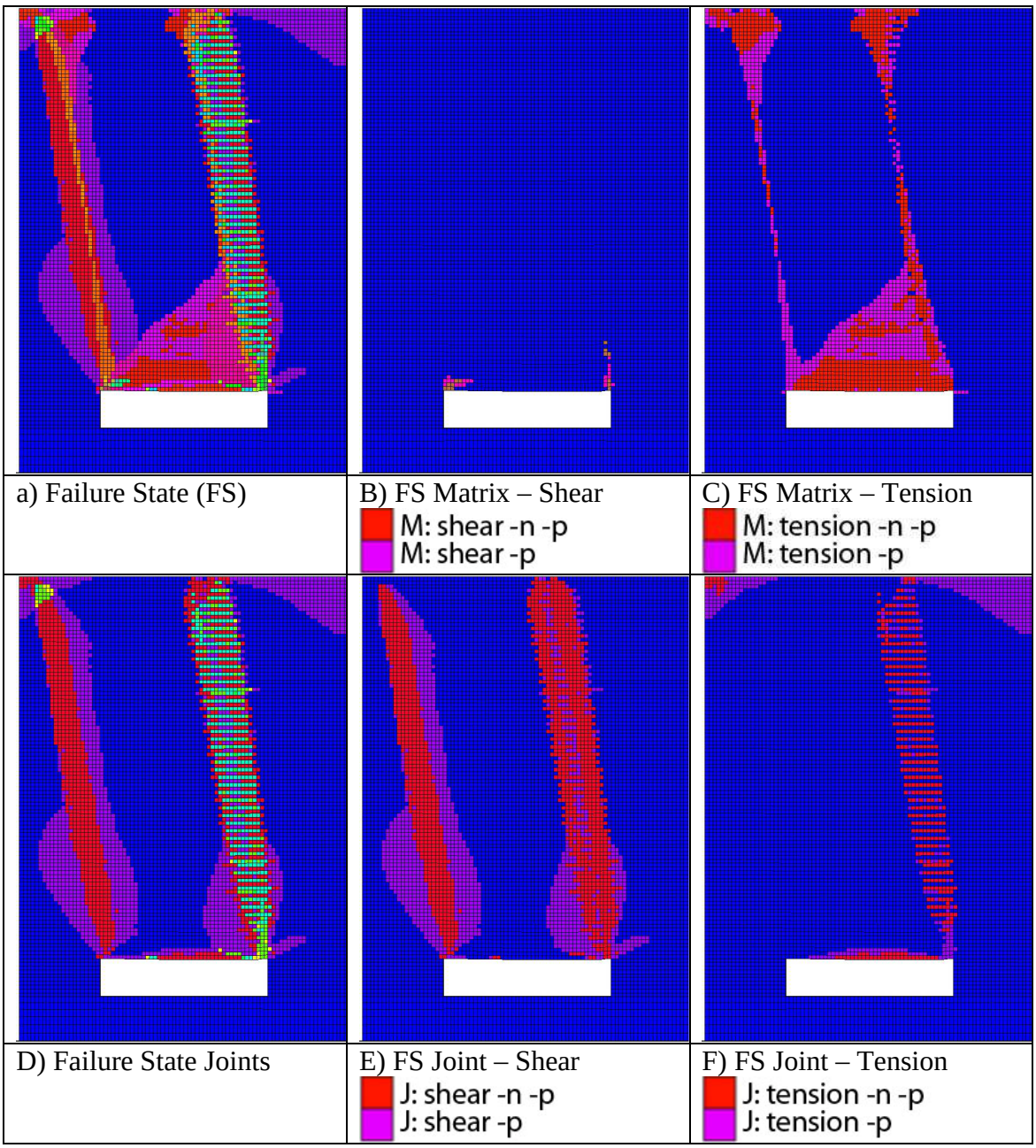

Figure 4.51: Yield state plot of the rock mass. Rock mass GSI 10, joint dip angle 80°, 3 m excavation width, 1 m excavation height.

As in the previous examples the stress field has rotated to account for the change in dip angle and this can be seen for the maximum and minimum principal stresses in Figure 4.52. The unusual nature of the failure geometry in the rock mass over the right hand boundary is reflected within the maximum principal stress plot whereby there are "notches" in the right hand side of the column of low compressive stress where low stress regions extend into the higher compressive stress regions next to the boundaries.

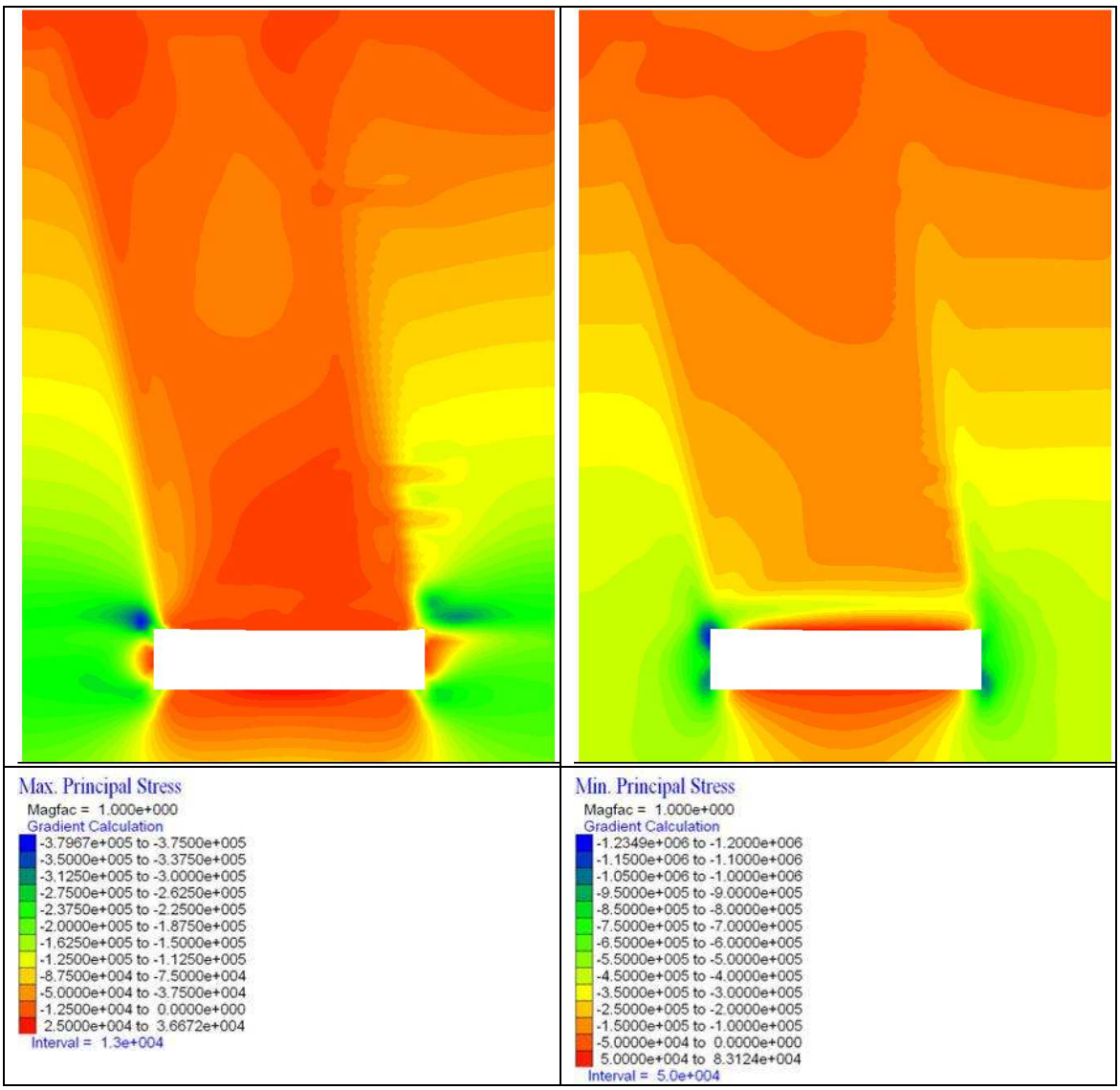

Figure 4.52: Maximum (Sigma 3) and minimum (Sigma 1) principal stress state of the rock mass. Rock mass GSI 10, joint dip angle 80°, 3 m excavation width, 1 m excavation height.

When the block contour plot of maximum principal stress is observed it can be seen that there are alternating bands of compressive and tensile stress (see Figure 4.53). It is not readily apparent what has caused thus phenomenon but it may be a function of the orientation of the model mesh in relation to the orientation of the joint dip angle and it's relation to friction angle rather than an accurate representation of the rock mass behaviour. As such this is assumed to be a numerical modelling artefact / anomaly; however the broad pattern of shear failure extending along joint planes to the upper boundary is a realistic result. The plots of unbalanced force and force ratio in this figure also indicate that the model is unstable and movement is occurring (Figure 4.53).

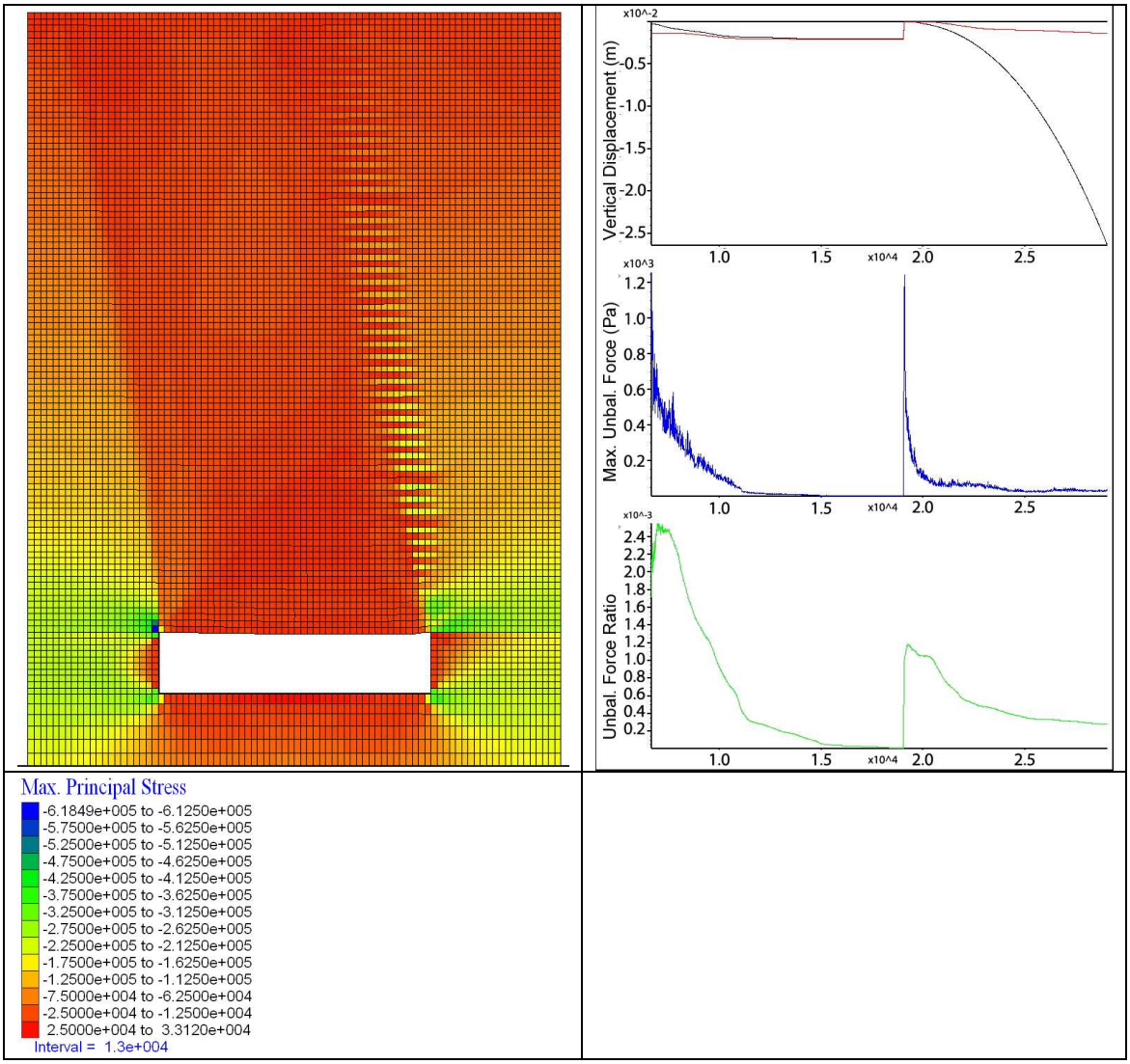

Figure 4.53: Block contour plot of maximum principal stress (principal stresses are average for a zone rather than interpolated from the surrounding zones).

Observation of the shear strain increment plot (Figure 4.54) indicates that the majority of deformation is concentrated within the immediate roof of the excavation reaching a height of approximately 0.75m within the zones of joint and matrix tensile yielding that have occurred there which correlates very clearly with a the base of a band of increased compressive stress that cuts through the region of tension overlying the excavation roof and can be seen clearly in the minimum principal stress plot in Figure 4.52. The plot of volumetric strain increment reveals that there is also a small but significant uniform block of extensional volumetric strain forming a column over the full width of the excavation with the sides following the trend of the dip of the joints. The lack of symmetry in the plots of strain is reflected in the displacement plots whereby displacements are off set to the right hand side of the excavation.

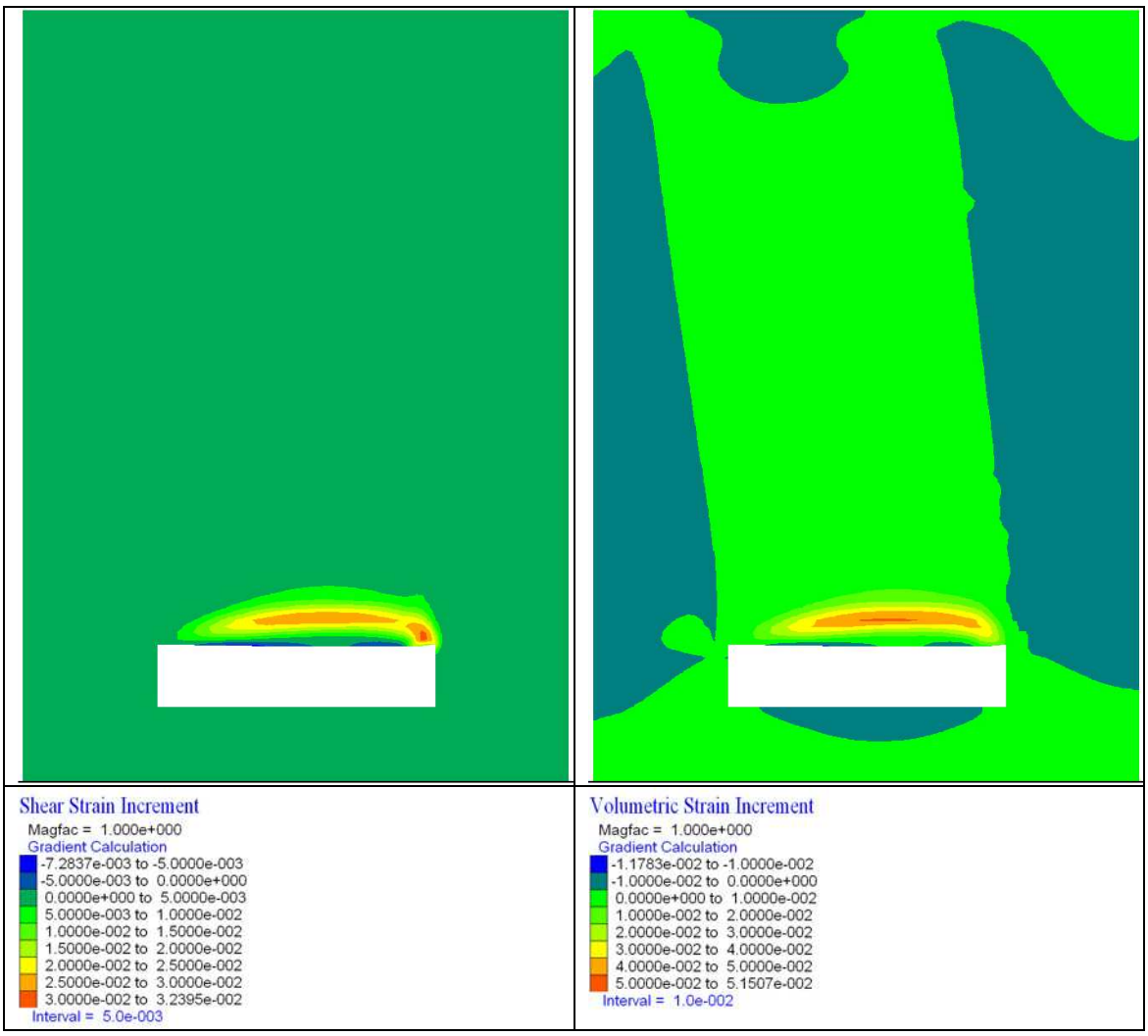

Figure 4.54: Shear and volumetric strains within the rock mass. Rock mass GSI 10, joint dip angle 80°, 3 m excavation width, 1 m excavation height.

4.7.8 Full Width Model with Vertically Dipping (90°) Joints, 3 m Excavation Width, 1 m Excavation Height, GSI 10

Once the joint dip angle reaches 90° there is virtually no tensile failure within the joint planes as all strains are accommodated by shear failure along the joint planes. This has led to the formation of a pair of vertical shear failure surfaces that extend from the roof pillar intersection at both ends of the excavation, nearly to the upper boundary of the model. This can be seen very clearly by comparing the plots of joint shear and tensile failure. See Figure 4.55E, F. Significant tensile failure of the rock mass matrix has also occurred forming a column, broadly constrained to left and right by the vertical zones of joint shear failure.

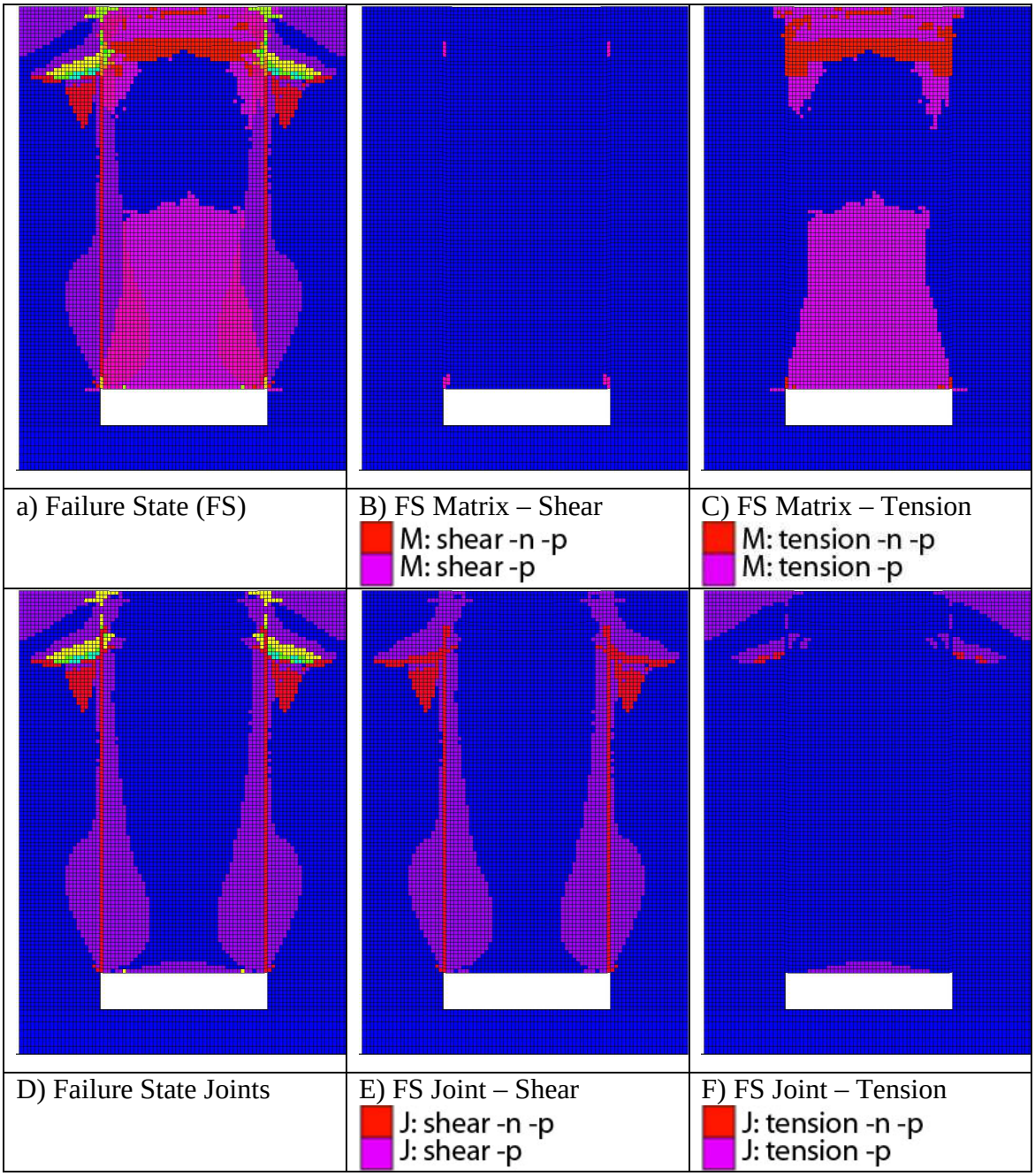

Figure 4.55: Yield state plot of the rock mass. Rock mass GSI 10, joint dip angle 90°, 3 m excavation width, 1 m excavation height.

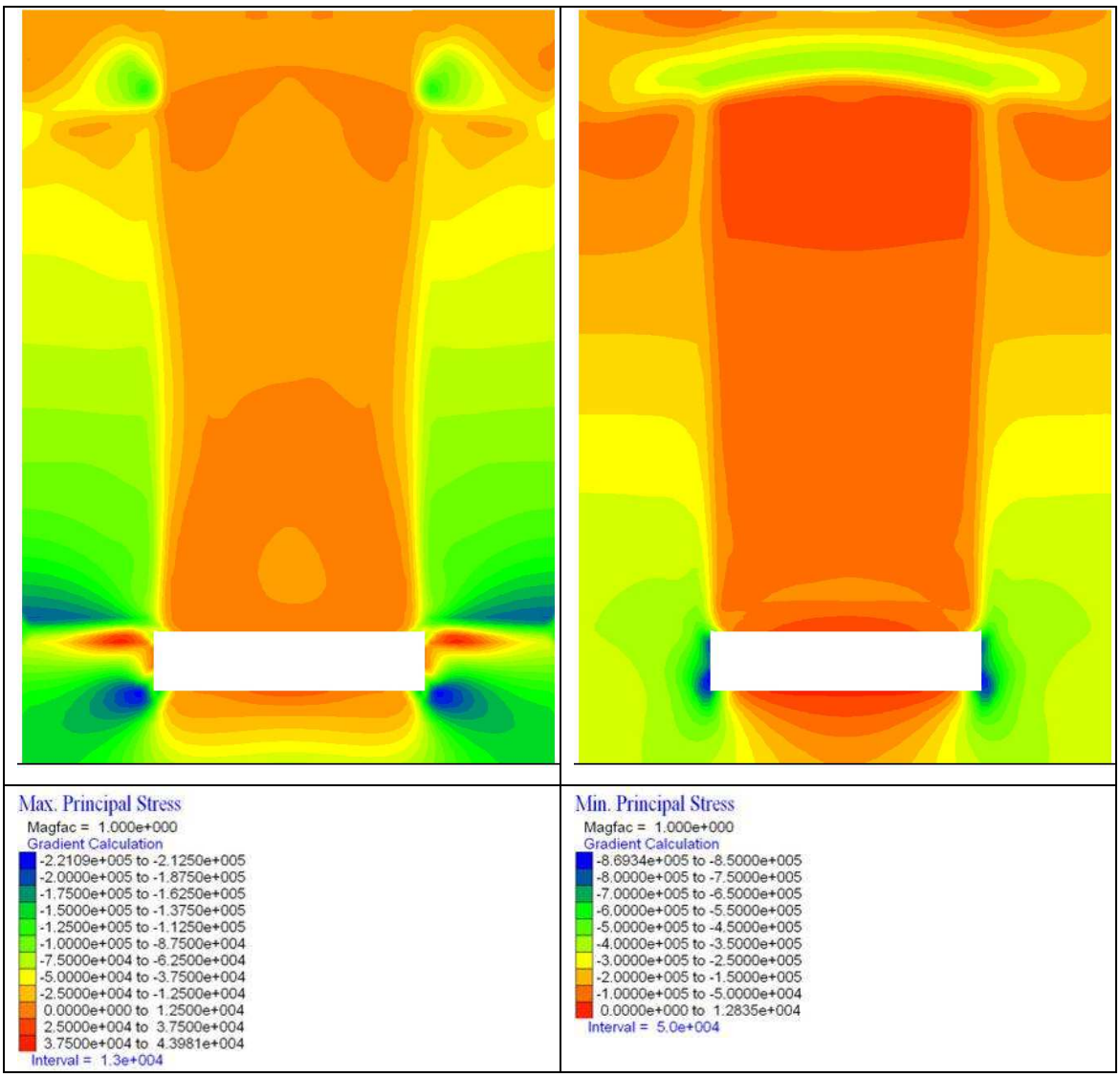

Figure 4.56: Maximum (Sigma 3) and minimum (Sigma 1) principal stress state of the rock mass. Rock mass GSI 10, joint dip angle 90°, 3 m excavation width, 1 m excavation height.

These regions are also very clearly defined in the plots of maximum and minimum stress (Figure 4.56), whereby the zone of matrix tensile failure correlates very strongly to a zone of tensile stress on the maximum principal stress plot and the vertical shear failure bands along the joint surfaces follow the boundary of the region of tensile or low compressive stress that forms a column upwards from the excavation roof towards the upper boundary of the model.

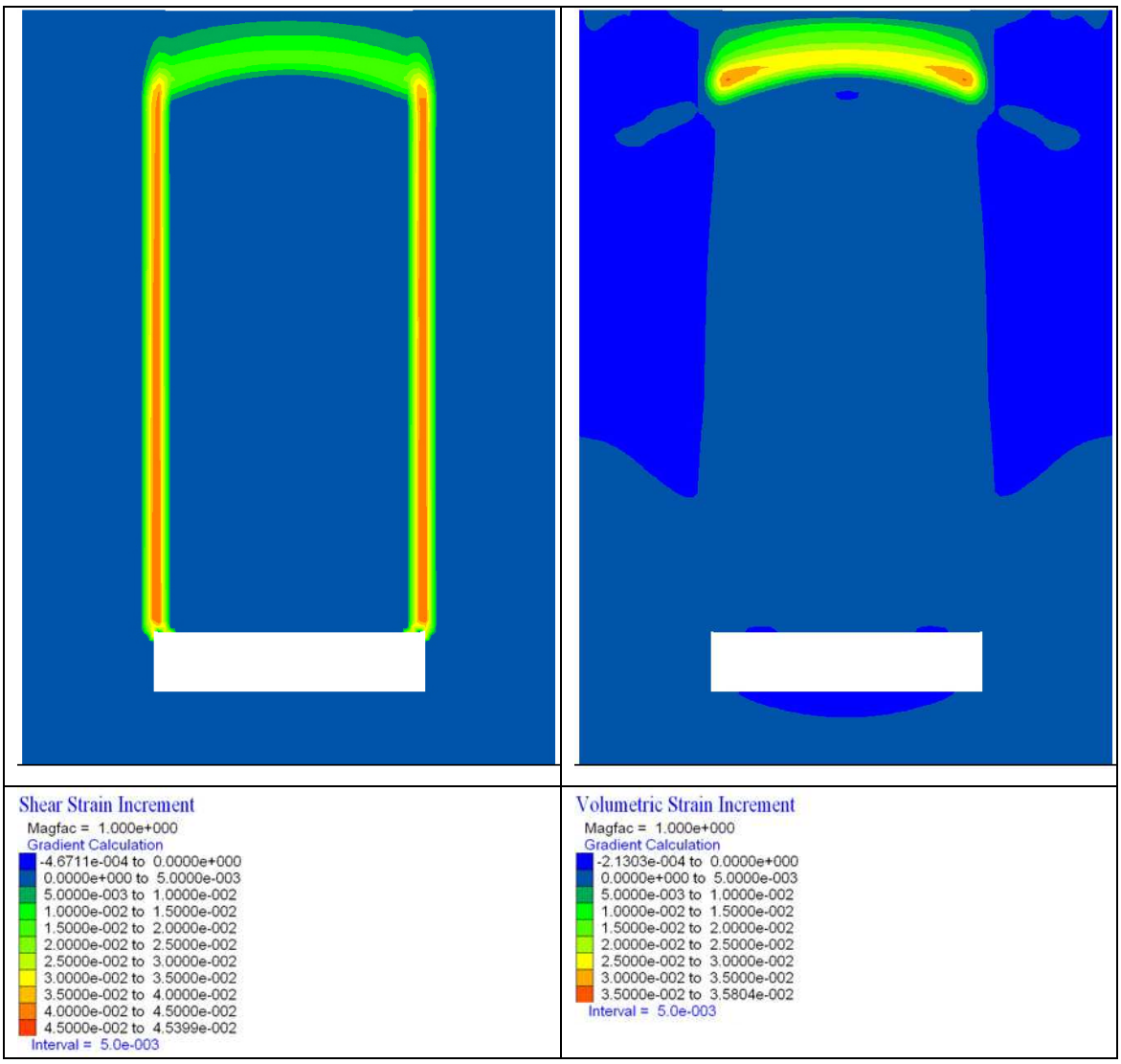

Figure 4.57: Shear and volumetric strains within the rock mass. Rock mass GSI 10, joint dip angle 90°, 3 m excavation width, 1 m excavation height.

Observation of the plots of the shear and volumetric strain (Figure 4.57), show that the vertical failure planes have undergone shear deformation forming very clear and well defined shear bands within the model extending upwards from the pillar roof intersection on both sides of the excavation roof. However they have not reached the surface (the collapse is progressive). The region at the top of the model is marked by significant positive (extensional) volumetric strain showing that the underlying rigid block of material is translating downwards as a rigid mass.

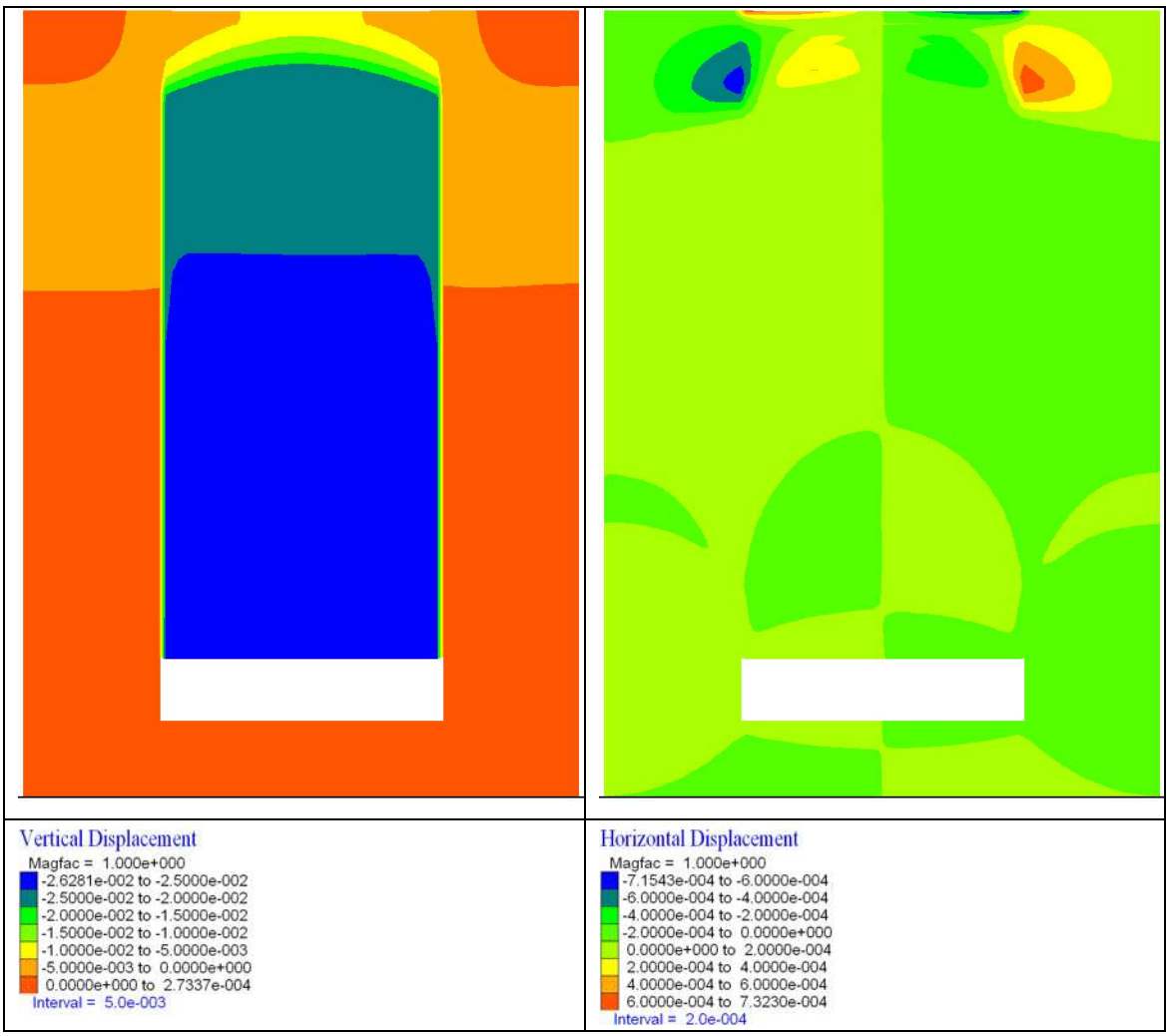

Figure 4.58: Vertical and horizontal displacements within the rock mass. Rock mass GSI 10, joint dip angle 90°, 3 m excavation width, 1 m excavation height.

The interpretation of rigid body motion appears to be confirmed by the plot of vertical displacements in Figure 4.59 where it can be seen that the rock mass between the two vertical bands of shear strain are displacing downwards as a broadly uniform block, as highlighted by the uniformity of the contour plot. The horizontal displacement plot (in Figure 4.59) indicates that there is virtually no horizontal component to displacements within this model, except for that which occurs near the upper boundary of the model and appears to be related to the horizontal compressive stress field.

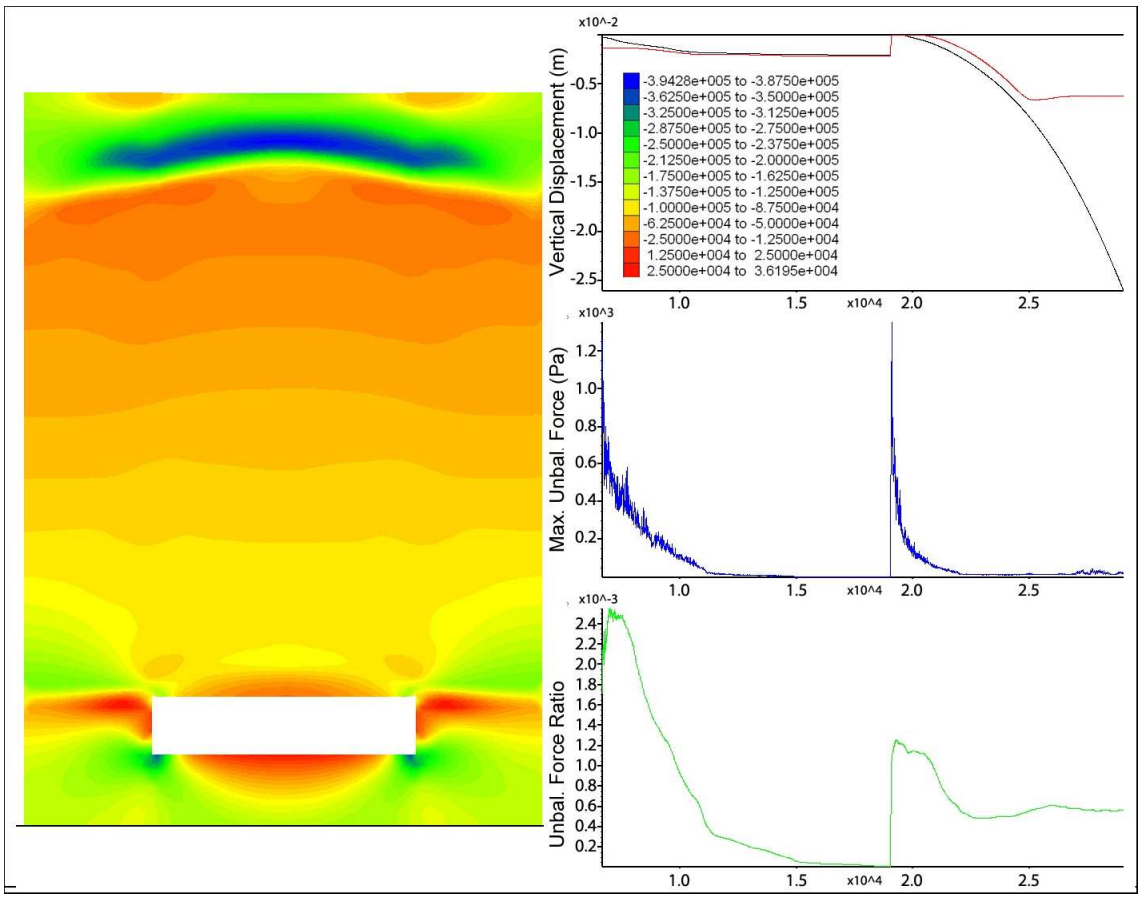

Figure 4.59: Horizontal stress plot along with displacements in the roof centreline and centre of the upper boundary of the model along with history pots of the maximum unbalanced force and the unbalanced force ratio.

Confirmation of the orientation of the stress field is provided by the plot of horizontal stress (see Figure 4.59) where it can be observed that the value of compressive stress in this region reached approximately 0.49 MPa which is as high as the compressive stress at the pillar roof intersection. This compression arch appears to be unstable as the high compressive stresses are already causing shear failure of the rock mass. This will ultimately result in stress relaxation and in turn reduce the normal stress on the vertical joints reducing their shear strength and cause shear yielding to occur again. That the model is unstable in its current state is confirmed by observation of the plots of unbalanced force and force ratio (see Figure 4.59). Significantly both the maximum unbalanced force (0.2 kPa) and the unbalanced force ratio ($6x10^{-4}$) have stabilised at a non zero value / value significantly higher than the normal ratio limit for stability which is strongly indicative of continued failure.

4.8 Conclusions from Parametric Study on the Effect of Joint Dip Angle on the Stability of Shallow Excavations

In this chapter a numerical modelling parametric study was undertaken to investigate the effects of various parameters on the stability of excavations using more sophisticated constitutive models including the strain softening Mohr-Coulomb model and the strain softening ubiquitous joint model which allows the anisotropic behaviour of a rock mass with a persistent joint set, in which the joint dip angle and the joint properties can be varied from that of the rock mass as a whole to be captured. Post yield behaviour is also more realistic as the model allows the post yield values of cohesion, friction and tensile strength to be varied which more accurately captures the failure behaviour of rock masses

An analysis of the effect of varying the post peak strength reduction values used in the stability analysis was undertaken (see section 4.1.4,) and it was found that although there were decreases in the magnitudes of shear and volumetric strains that developed within the model as the post peak plastic strain value (ε^{ps}) was increased, there was not a significant effect on the resultant roof deformations and yield state. Based on this finding, the softening parameters presented in the literature related to modelling (Esterhuizen and Karacan, 2005; Badr *et al.*, 2003; Singh and Singh, 2009 and Roberts *et al.*, 2005) are used for the modelling work undertaken from this point forward.

The results of the modelling undertaken to compare the results achieved using the standard Mohr-Coulomb and Strain-Softening models were presented in section 4.2.2. Here it could be seen that the strain-softening model causes an increase in the height of yielding into the rock mass and an increase of the extent to which failure of roof strata occurs.

The modelling of an anisotropic rock mass using the ubiquitous joint model has demonstrated that the variation in the angle of dip of a weak plane or discontinuity set has a strong impact on the stress state within the rock mass and also on the extent of yielding above the excavation. The modelling of an anisotropic rock mass using the ubiquitous joint model has demonstrated that the variation in the angle of dip of a weak plane or discontinuity set has a strong impact on the stress state within the rock mass and also on the extent of yielding above the excavation.

At shallow dip angles, (*i.e.* those below the friction angle of the joints) the boundary of the zone of yielding is controlled by the joint friction angle and joint dip. Matrix tensile yield occurs within the bounds of the zone defined by joint shear and tensile yielding. In this region this zone is defined as a straight line extending from the pillar roof intersection into the rock mass at an angle defined by:

Angle of failure surface at dip angles below the joint friction angle on up dip side of excavation:

$$((90 + \phi_r) + \text{joint dip angle}) \quad 4.3$$

Angle of failure surface at dip angles below the joint friction angle on down dip side of excavation:

$$((90 - \phi_r) + \text{joint dip angle}) \quad 4.4$$

Where the angle of failure has the same sense of rotation as that described in Figure 4.17.

However as the dip angle increases past the friction angle of the joint planes, the tensile failure boundary begins to be defined to the up-dip side by the rock mass matrix friction angle, the upper boundary by the joint dip and the down-dip side as by the joint friction angle of the rock mass and the joint dip. This forms a broadly trapezoidal shape and can be seen most clearly in Figure 4.35C. As the dip angle increases even further, the matrix tensile yield zone forms a wedge geometry over the excavation (*e.g.* in the 40 degree dip example) whereby the up dip side is controlled by the rock matrix friction angle and the down dip portion by the angle of dip of the bedding or joints. This trend continues for increasing joint dip angles until the joint sets are vertical where the matrix tensile stress forms a square with the left and right hand sides parallel to the joint dip.

The geometry of the joint tensile yield zone follows the relationship outlined earlier in Equation 4.3 and Equation 4.4 whereby the failure angle from vertical for the left hand side of the joint tensile failure region of the model is equal to the residual friction angle of the joints + angle of joint dip and for the right hand side equal to the residual friction angle of the joints - angle of joint dip. This creates a broadly wedge shaped geometry, however the top is truncated at an angle equal to the dip of the joint planes.

As the dip angle of the weak plane increases beyond the angle of friction of the joints, the dominant mode of joint failure changes from tension to shear. Joint shear failure becomes progressively more dominant as a failure mechanism as the dip angle increases reaching a maximum when the angle of dip is at 90°. Conversely at angles of dip below the angle of friction of the joint planes, tensile yielding along the joint planes becomes a

much more significant failure mechanism and is at a maximum when the joint dip is parallel to the free boundary of the excavation (in this case horizontal).

Broadly the magnitudes of the stresses within the immediate roof strata and overlying rock mass do not change significantly between models with differing dip angles with peak tensile stresses of approximately 12.5 kPa within the immediate roof but the distribution of the stress is clearly significantly affected. The magnitudes of the pillar stress are also significantly affected by the dip angle. The pillars on the up dip side of excavations typically have higher compressive stress magnitudes than those on the down dip side with values ranging from 1.2 to 1.6 MPa on the up dip side and 0.75 to 1.2 MPa on the down dip side. The highest contrast between the up dip and down dip pillar stresses occurs for a joint dip angle of 30 where on the up dip side the maximum compressive stress reaches 1.61 MPa and on the down dip side it reaches 0.8 MPa. The key feature here in stability terms, appears to be the fact that the orientation of the joints and the joint strength properties within the rock mass control stability and the angle of failure rather than the rock matrix friction angle. As such, in strata with steeply dipping or vertical joints that are also persistent there is the potential for significant shear failure along these planes leading to progressive roof failure without any arching of the roof strata occurring. This can significantly increase the potential height of collapse before halting of void migration.

Chapter

5

Parametric Study Phase 2 Part B - Effect of Discontinuous / Discrete Behaviour in the Modelling of Shallow Mine Workings

5 Parametric Study Phase 2 Part B - Effect of Discontinuous / Discrete Behaviour in the Modelling of Shallow Mine Workings

5.1 Introduction

In the preious chapter (4) the effect of the strain softening and ubiquitous joint models on stability were investigated. In this chapter use is made of the strain softening Mohr-Coulomb model with embedded interfaces intended to allow discontinuous behaviour and simulate bedding planes. An explanation for the choice of this methodology is given below:

Numerical investigations into rock mass problems are commonly conducted using an "equivalent continuum" approach where the discontinuous nature of a rock mass is accounted for by the use of strength reduction parameters such as the GSI system used in this work and the various other parameters discussed in section 2.4.2. This approach was used to make the initial investigations into the effects of varying parameters on stability in section 3.2 using the Mohr-Coulomb model. However in situations where the rock mass behaviour is dominated by a specific structural feature such as a fault, joint set or other discontinuity surface this may not always accurately capture the system behaviour, particularly the failure mechanisms themselves (as opposed to the conditions or stress state that lead to failure).

Coal measures are sedimentary rock formations that tend to be composed of horizontal to sub horizontal strata, where a stratum is considered to be a discrete layer of rock with broadly consistent internal features that enable it to be distinguished from other layers or stratum (Duff, 1993). These strata (commonly known as "beds" and the structure as "bedding") form with strong planer discontinuity features known as bedding planes (which may also be described as "bedding joints"; Brady and Brown, 1993). In summary, these features form when changes in the depositional environment alter the clast size or nature of the material deposited to form the rock. They may also mark a disconformity which is a surface separating two parallel strata that marks a period of erosion or the halting of deposition (Duff, 1993).

To further reinforce the importance of bedding spacing and strength on the stability of shallow mine workings and subsurface excavations in general it was observed in a large parametric study undertaken by Whittles *et al.,* (2007) that the strength and spacing of

the bedding discontinuities could be shown to account for 26% of potential (in)stability. As such bedding planes tend to be one of the major structural features in sedimentary rocks and certainly the literature suggests that failure of individual stratum separated by bedding surfaces is a common failure mechanism in shallow mine working roof collapse and the initiation of void migration (Healy and Head, 1984; Whittles *et al*., 2007). For more information on this see section 2.2.3.

5.2 Model Geometry and Mesh Discretisation

These models all represent a void of varying height and width at 10 m below surface, with 10 m of underlying rock mass material and square numerical zones. The geometry parameters are outlined in Table 5.1 below:

Table 5.1: Numerical model geometry parameters

Parameter	Value
Excavation Width	1, 2 and 3 m
Excavation Height	1, 2 and 3 m
Pillar Width	1, 2 and 3 m
Zone Size	0.1 m^2
Number of Discrete Strata	20, 50, 100
Discontinuity Spacing	0.5, 0.2 and 0.1 m

The discontinuity spacing values chosen above broadly correspond to the thin, medium and thick descriptors used in BS5930:1999 for the description of bedding plane thickness (while allowing for the constraints imposed by the discretisation of the model).

The model geometry and mesh discretisation with the excavated mine void and interfaces representing bedding planes is illustrated in Figure 5.1.

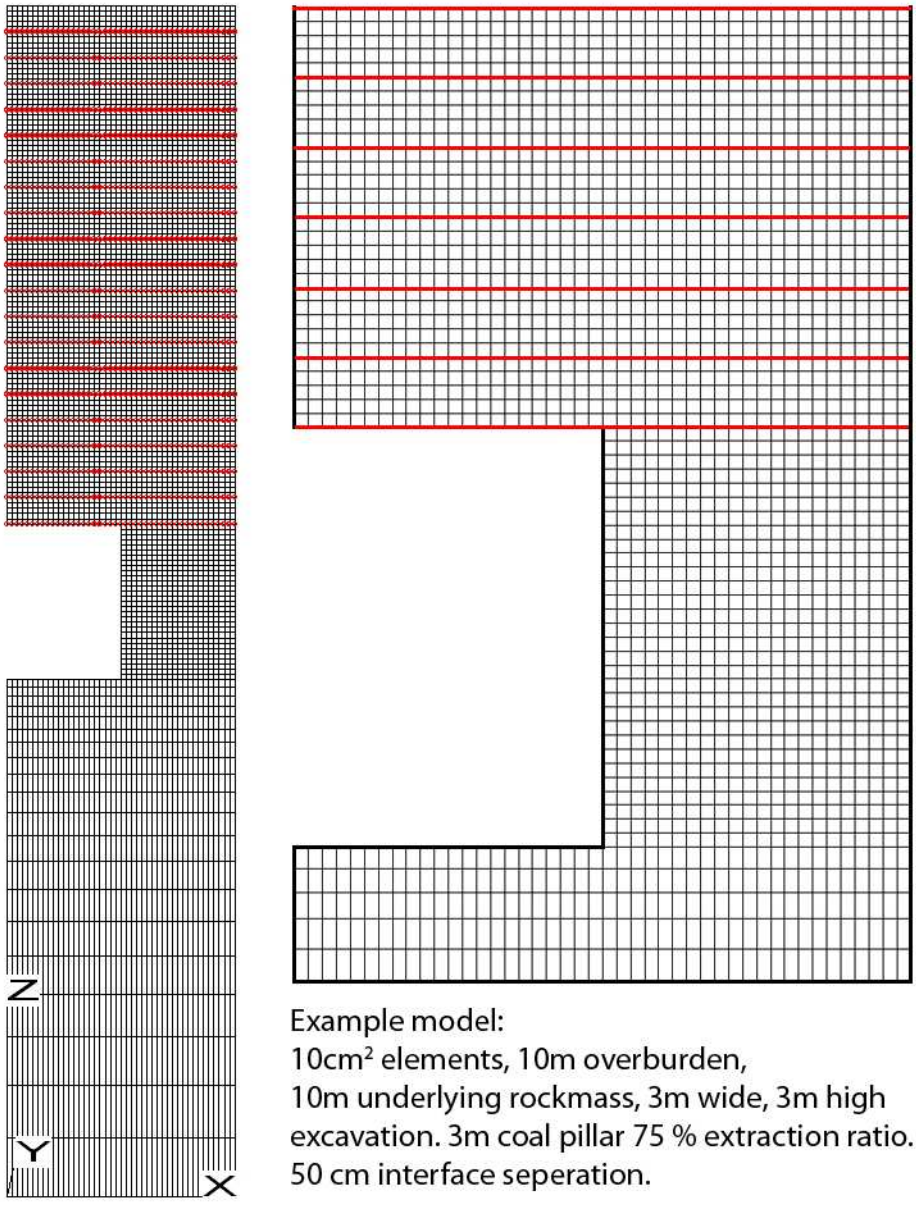

Figure 5.1: Full model geometry and detail view of excavation, mesh discretisation and interface spacing.

5.3 Strength and Stiffness Properties

5.3.1 Rock Mass Properties

As there is the potential for the rock mass strength to be affected by discontinuities other than the bedding planes and also to account for the presence of potentially highly fissile material such as shale within Coal Measures strata, it was decided that rather than using the intact strength and stiffness properties of coal measures rocks for the bedding, instead a range of values would be used as per the previous modelling to avoid the potential for over estimating stability for a given thickness of strata and to account for

the variable nature of Coal Measures rocks. The rock was once again assumed to have the following intact properties: intact uniaxial compressive strength of 75 (this value is chosen as an average UCS for typical coal measures rocks from the range of values quoted by Bell, 1975). The intact elastic modulus was assumed equal to 13.5 GPa taken as an average value for sandstone, shale and siltstone (Zhang, 2005).

Although previous modelling had been undertaken to investigate the effect of strength and stiffness properties, that work was undertaken using an equivalent continuum linear elastic perfectly plastic model. It was unclear what effect the presence of material discontinuities may have and as such, the strength testing was repeated here. As previous modelling had demonstrated that rock masses with a GSI value greater than 60 were stable in all states (maximum excavation width, overburden load and maximum pore water pressure) it was decided that the upper limit of the rock mass strength would be set at a GSI value of 70. The strength and stiffness properties used in the modelling are shown in Table 5.2.

Table 5.2: Rock mass strength and stiffness parameters

GSI	Bulk Modulus	Shear Modulus	Cohesion	Friction Angle	Tensile Strength
10	0.7	0.23	0.11	49	0.005
20	1.1	0.35	0.17	55	0.011
30	1.9	0.62	0.24	59	0.023
40	3.7	1.2	0.33	61	0.048
50	7.0	2.4	0.51	63	0.1
60	12	3.9	0.85	64	0.22
70	21	5.4	1.56	63	0.45
	(GPa)	**(GPa)**	**(MPa)**	**(°)**	**(MPa)**

As the initial modelling undertaken in section 3.2 indicated that the strength of the coal pillar and the rock mass underlying the excavation were not significant in the stability of the roof (rather they were important in the phenomena of pillar crushing leading to areal or sag subsidence or punching failure of the pillars into the softer underlying rock mass), the strength of the coal and the underlying rock mass were scaled to an intermediate value whereby the coal was assumed to have a uniaxial compressive strength (UCS) of approximately 15 MPa (Bell, 1975) and the underlying rock was assumed to have the same intact properties as the overlying rock mass but scaled to a

level which would not cause the initiation of failure. The Mohr-Coulomb parameters were then estimated using the Hoek-Brown method as applied by ROCLAB (Rocscience, 2010). See Table 5.3.

Table 5.3: Strength and stiffness properties as used for the coal and underlying rock mass

Rock Type	Bulk Modulus	Shear Modulus	Cohesion	Friction Angle	Tensile Strength
Coal	1.47	0.38	0.498	49	0.26
Underlying Rock Mass	9.39	2.45	1.21	51	0.651
	(GPa)	**(GPa)**	**(MPa)**	**(°)**	**(MPa)**

An approximation for the dry density and porosity of coal measures strata was selected from the literature (Bell, 1992; Thomlinson, 2001; Zhang, 2005). A bulk density of 2700 kg/m^3 and a porosity of 20% were selected yielding a dry density of 2500 kg/m^3

In material above the water table, FLAC makes use of dry density, whereas for material below the water table the bulk density is used. This is calculated using the following (Cundall, 2003):

$$\rho = \rho_d + (n \times S_w \times \rho_w) \qquad 5.1$$

Where

ρ = Bulk density (kgm^{-3})

ρ_d = Dry density (kgm^{-3})

n = Porosity

S_w = Saturation

ρ_w = Fluid Density (kgm^{-3})

5.3.2 Discontinuity Properties

The normal and shear stiffness of the interface elements used to represent the bedding planes within the model is calculated based on the recommendations in the FLAC manual (ITASCA, 2005) and summarised in section 3.1.4. The function also checks that the calculated stiffness values do not violate the maximum equivalent stiffness.

This process is automated within the model using a FISH function that calculates the effective stiffness based on the rock mass stiffness properties in the surrounding zones. For this study, the bedding planes were initially assumed to have frictional properties equal to those used for the rock mass, however the effect of varying frictional properties is investigated in the following section (see section 5.13). The cohesion of the interface was assumed from Zhang (2005) which suggests that a common value for discontinuity cohesion in coal measures rocks is approximately 0.012 MPa.

As the roof of an excavation is (at least initially) stable due to the strata acting as a compression arch and ultimately failure occurs due to the collapse of the strata forming the arch it was assumed that the bedding planes offered no tensile support to the rock mass and that their shear strength was purely developed from normal stresses and the friction angle. For completeness the stiffness values as calculated are shown in the table below:

Table 5.4: Interface / bedding plane properties.

Spacing	GSI	Intact Bulk Modulus	Intact Shear Modulus	Interface Normal Stiffness	Interface Shear Stiffness	Interface Cohesion	Friction Angle
0.1 m	10	28.50	7.43	6.4	2.3	12.0	49.0
	20	28.50	7.43	10.0	3.5	12.0	55.0
	30	28.50	7.43	18.3	6.3	12.0	59.0
	40	28.50	7.43	38.6	12.5	12.0	61.0
	50	28.50	7.43	94.3	26.2	12.0	63.0
	60	28.50	7.43	217.5	45.2	12.0	64.0
0.2 m	10	28.50	7.43	3.2	1.2	12.0	49.0
	20	28.50	7.43	5.0	1.8	12.0	55.0
	30	28.50	7.43	9.1	3.2	12.0	59.0
	40	28.50	7.43	19.3	6.3	12.0	61.0
	50	28.50	7.43	47.2	13.1	12.0	63.0
	60	28.50	7.43	108.8	22.6	12.0	64.0
0.5 m	10	28.50	7.43	1.3	0.5	12.0	49.0
	20	28.50	7.43	2.0	0.7	12.0	55.0
	30	28.50	7.43	3.7	1.3	12.0	59.0
	40	28.50	7.43	7.7	2.5	12.0	61.0
	50	28.50	7.43	18.9	5.2	12.0	63.0
	60	28.50	7.43	43.5	9.0	12.0	64.0
		(GPa)	**(GPa)**	**($GPam^{-1}$)**	**($GPam^{-1}$)**	**(kPa)**	**(°)**

5.3.3 Strain Softening Parameters

As per the modelling undertaken to investigate the effect of joint dip on excavation stability using the ubiquitous joint model, the rock mass will behave as a strain softening material so the strain softening Mohr-Coulomb constitutive model is used in this investigation. It should be noted however that unlike in the strain softening ubiquitous joint Mohr-Coulomb model there is no facility to allow softening of the interface elements within FLAC and so these values remain at their peak strength throughout. The post peak strength and friction strain softening parameters are derived based on the methodology described previously and the same assumptions apply here. See Table 5.5 for the parameters as used in this modelling.

Table 5.5: Strain softening parameters showing peak and residual strength values.

GSI	Cohesion	Friction Angle	Tensile Strength	Cohesion at 5% Strain	Friction Angle at 5% Strain	Tensile Strength at 1% Strain
10	0.13	49.0	0.005	0.05	46.0	0.0
20	0.17	55.0	0.011	0.05	46.0	0.0
30	0.24	59.0	0.023	0.05	46.0	0.0
40	0.33	61.0	0.048	0.05	46.0	0.0
50	0.51	63.0	0.1	0.05	46.0	0.0
60	0.85	64.0	0.22	0.05	46.0	0.0
70	1.56	63.0	0.45	0.05	46.0	0.0
	(MPa)	**(°)**	**(MPa)**	**(MPa)**	**(°)**	**(MPa)**

5.4 Modelling Methodology

The parametric study to investigate the effect of discontinuity spacing / bedding thickness on the stability of shallow abandoned mine workings was run using an automated FISH routine which varied the geometry and strength of the model automatically while stepping to either static equilibrium (a stable solution without collapse) or to an unstable state where a prescribed level of plastic strain within the roof strata was used as a cut off to represent roof instability. The full modelling process is described in more detail below:

The initial geometry was generated which represented a two-dimensional section through a shallow mine excavation. The point chosen was the intersection between two roadways or rooms as this represents the largest span and so the highest stresses within

the roof strata and the greatest potential for instability as discussed in section 2.2.3. See Figure 5.2 for a graphical representation of the selected section through the abandoned workings.

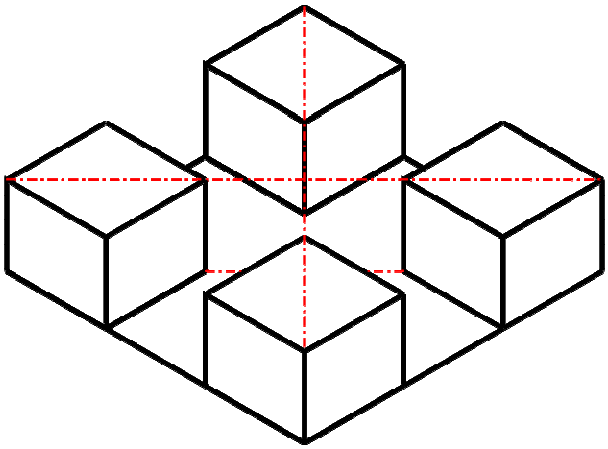

Figure 5.2: Selected section through the abandoned workings.

The resultant two-dimensional model geometry can be seen in **Figure 5.1**. The model uses fixity conditions at the boundaries. As in the previous modelling conducted, the base is fixed in the z-axis so that no vertical movement can occur and the side boundaries are fixed in the x-axis to prevent horizontal movement.

Once an initial geometry is selected, the elastic constitutive model, bulk density and elastic properties are applied to the mesh. The model is also spilt into discrete layers representing the individual strata or bedding using a custom FISH function so that it is no longer a continuum but a discrete series of beds. Interface elements are then placed on the upper and lower sides of the beds to represent the bedding planes within the rock mass. These interfaces are initially given cohesion and tension properties equal to that of the surrounding rock mass and the model is brought to equilibrium under gravity. In this case (as in all the modelling undertaken in this thesis) the force ratio limit for equilibrium was set to 1×10^{-5}. This helps to ensure unbalanced forces do not influence the results. As the potential for large strains was anticipated due to the potential for failure of the roof strata in the model, each model was run in large strain mode, where the mesh changes shape as deformation occurs (gridpoint coordinates are updated at each step according to computed displacements – Itasca, 2005). This is a slower process than small strain mode, but more accurately captures large strain behaviour.

Once initial equilibrium is achieved the mine void is excavated by nulling zones within the model. The model is again stepped to equilibrium to remove excess unbalanced forces caused by the sudden excavation as recommended in the FLAC manual (Itasca,

2005) and then the strain softening Mohr-Coulomb constitutive model applied. Following this the ground water table is progressively increased in 1 m increments from below the level of the excavation to the surface. Strain softening Mohr-Coulomb properties are applied during excavation phases and elastic properties are reapplied during model changes (such as increasing groundwater level) and the model brought back to an equilibrium state to prevent unbalanced forces, due to model changes, initiating failure.

Once a cycle of increasing water table for a given rock mass strength and stiffness (*i.e.* a specific GSI value) is completed, the process is repeated with increasing rock mass strength and stiffness parameters until all the selected GSI values have been tested. The above process is then repeated for the next selected geometry and this continues until the model has iterated through all the other parameters selected to be varied (in this case increasing excavation width, excavation height and variable bedding plane spacing). More detail on specific sections of the modelling methodology is described below.

5.4.1 Iterations of the Parametric Study

The parametric study is undertaken using an automated model and parameter generation system coded by the user in FISH. This function controls the modelling run and iterates through a series of nested loop commands. The loop command uses an integer counter and the command takes the form: Variable (expression 1; expression 2) where variable is given the value of expression 1 initially, and is incremented by one at the end of each loop execution until it obtains the value of expression 2. In this parametric study the set of loops which control the model run are nested as shown below:

A. Bedding thickness (0.1, 0.2, 0.5)
    B. Excavation width (1, 2, 3)
        C. Excavation height (1, 2, 3)
            D. Rock mass strength and Stiffness (10, 20, 30, 40, 50, 60)
                E. Rising water table (base of excavation to surface)
                    F. Roof stability criteria

Whereby for one iteration of a given loop to occur the iterations of the loops following it must all be fully completed. *E.g.* for loop D to iterate from 10 to 20 the water table must rise fully to the surface within the model and for loop C to iterate from 1 to 2, loop D must iterate fully from 10 to 60 and in turn each single increment of loop D would require a full iteration of loop E and so on. Ultimately this results in this case in 162 model runs (3 x 3 x 3 x 6).

5.4.2 Total Stress Adjustment

In the modelling undertaken here pore water pressures are used by the constitutive models for effective stress calculations to check if the yield criteria have been exceeded and if plastic flow / failure in an element will occur. However the presence of an applied pore water pressure does not affect the total stress (unlike in FLAC 2D where the "adjust total stress" command can be used). As such the total stress must be adjusted manually as the pore water pressure (and water table) varies. There are a number of methods for achieving this in FLAC3D when the fluid flow module is not active, the simplest being to increase the density of the material below the water table as it increases. As each 1 m increase in the water table occurs, the material below the phreatic surface is assumed to be 100% saturated whereby a FISH function adjusts the density from dry to bulk to account for the self weight of the water in the rock mass pore spaces using Equation 5.2.

It should also be noted that as the model is not fluid-mechanically coupled, no adjustment is made to the pore water pressures due to the deformation of the rock mass.

However the deformation caused by a new distribution of pore water pressure (for example when raising the water table) is accounted for using a stress-correction technique which is applied as recommended in the FLAC3D manual (Itasca, 2005). This technique consists of:

1) Subtracting the pore water pressure increment in the zones affected by the change from the total normal stresses in those zones
2) Adjusting the input material density to the bulk value, below the new phreatic surface and to the dry density value above this surface (only applicable to a lowered water table)
3) The model is stepped to mechanical equilibrium.

The above corrections are made automatically in this case again using a user coded FISH function.

One other consequence of the way FLAC models body forces is that the nulled zones of the excavation can have a pore water pressure, but as already stated, this is only used in the calculation of the yield criterion within the constitutive model. It is not a body force and so applies no support to the surfaces of the excavation. As the method of stress

correction above requires that the density of the material below the water table be increased to account for the mass of the water in the pore spaces and the water pressure is assumed to be hydrostatic, then the water in the excavation would support the column of water above it. As such a normal stress equal to, but of opposite sign to the vertical stress due to the self weight of the overlying column of water is applied to the excavation roof. To simulate the column of water acting on the floor, the normal stress is again calculated but applied with the opposite sign. A normal stress gradient is also applied to the excavation wall from the maximum value calculated for the floor to the minimum value calculated for the roof.

Whereby the roof normal stress σ_n is calculated as follows:

$$\sigma_n = \left(n \times S_w \times \rho_w \times h_{wt} \times g\right) \qquad 5.2$$

Where:

n = Porosity (0.2)

S_w = Saturation (equal to 1)

ρ_w = Fluid density (kgm^{-3})

h_{wt} = height of water table over excavation roof

g = gravitational acceleration (9.81 ms^{-2})

And the normal stress applied to the floor is as above, but the height of the water column is equal to h_{wt} + excavation height. The above process is also automated using a FISH function during the modelling runs.

5.4.3 Monitoring of the Model Run

A number of parameters are monitored during the model run. These include the vertical displacement in the centre line of the roof strata, the vertical strain of the strata in the roof centre line and the pore water pressure within the immediate roof of the excavation. The vertical strain within the roof is actually more correctly the vertical axial strain of the zones forming the excavation roof centreline. It is calculated by measuring the vertical displacement of the gridpoints at the base and the top of the first row of elements within the excavation roof centreline. The difference between these two values is the extension, which is then divided by the original pre-deformation element height. These monitored parameters are all recorded as history files of the specific parameter vs. model timestep.

5.4.4 Strain Measurement and Yield Criteria

When modelling a problem in FLAC, the solve command is used to step a model until a prescribed criterion or series of criteria are met. This is based on the ratio between the average unbalanced mechanical force magnitude for all gridpoints within a model and the average applied force magnitudes at gridpoints. Once this ratio falls below a prescribed limit (default equals $1x10^{-5}$) the model run is halted.

However in this modelling work it is anticipated that failure of the roof strata within the model will occur. As such if this roof failure occurs, the model will not reach equilibrium and the default solve function based around the unbalanced force ratio alone would not be appropriate as in instances of instability the model would continue to run indefinitely. To account for this a tiered system of criteria were selected to check for either failure of the excavation roof (a strain and yield cut off), or if failure does not occur the model stepping will continue until an equilibrium ratio is reached and the next iteration of the parameter study would begin.

As the initial roof failure is predominantly caused by tensile failure either of the elements forming the roof beam or a combination of the roof beam and the interface / bedding plane, it was initially considered that the presence of yielded elements in the roof of the excavation may be a reasonable criteria for assuming roof failure. However the previous modelling had demonstrated that the yield criteria could be exceeded without significant deformation occurring and as such the roof strata may have been damaged but they had not been damaged to an extant where the roof would start to collapse. It was decided based on this reasoning and based on the previous experience of modelling in FLAC during the initial investigations into the effect of geometry and pore water pressure on the excavation stability that as well as tensile yielding in the roof being detected, significant deformation should also occur. In mine roof design a limiting value corresponding to a midspan deflection of 10% of the beam thickness is commonly recommended as the limit of stability for voussoir arches (Hutchinson and Diederichs, 1996; Diederichs and Kaiser, 1999; Swart and Handley, 2005) however in order to ensure that deformation and yielding were significant a minimum cut off value of 100% vertical tensile strain within the excavation roof was selected as a criterion for failure (ten times the recommended maximum limit for stability).

This means that the model would run during a solve phase until either the equilibrium ratio indicating stability was reached for a given stress state, or tensile failure with vertical tensile strain greater than 100% was detected in the elements forming the excavation roof. Either outcome would result in an end to the solve stage and then model iterating onto the next parameter.

5.5 Effect of Bedding Spacing

Bedding spacing is observed to be a significant parameter on the stability of excavation roof strata (Goodman, 1989; Brady and Brown, 1993, Whittles *et al.*, 2007). It has also been shown to be a significant factor in halting the migration of voids from collapsed strata (Healy and Head, 1984; Attewell and Taylor, 1984; Walthem, 1989).

In order to investigate the effect of bedding thickness / discontinuity spacing on the initial stability of shallow excavations it was necessary to allow slip and separation of discrete strata to occur. As such it was necessary to separate the model grid into discrete sections and then "wrap" upper and lower boundary of each individual section of the model with an interface element, which is able to detect contact with other interfaces as well as allowing slip and separation to occur.

5.5.1 Effect of Variable Bedding Thickness on the Stability of Mine Voids

That the variation in excavation roof strength and stiffness properties has implications for the stability of an excavation is shown in the literature and that it has the same effect in a continuum model is demonstrated in the modelling in section 3.2.6 whereby for a given model geometry and a given stress state (affected by pore water pressure and rock mass density) it can be seen that with decreasing strength and stiffness parameters the extent of yielding within the roof strata increases. In this section it is intended to demonstrate the effect of discrete / discontinuous behaviour on the model by varying bedding thickness / bedding plane separation on roof stability through the use of interface elements.

The following models all have uniform excavation heights (1m), overburden thicknesses (10m) and rock mass strength and stiffness properties (GSI 10) with the groundwater table set below the level of the excavation (at 9 m above the base of the model which is equal to 1 m below the excavation floor). The bedding plane separation

varies using the following values 0.1 m, 0.2 m and 0.5 m. It should also be noted that FLAC uses a compressive stress is negative sign convention so that in plots of stress state compression is negative and that the maximum principal stress plot is the least negative stress Sigma 3 rather then Sigma 1 and vice versa for a minimum principal stress contour plot.

5.5.2 Model: 0.5 m Bedding Plane Spacing, 3 m Excavation Width, 1 m Excavation Height, GSI 10

The plots of maximum (Figure 5.3) and minimum principal stress (Figure 5.4) show that the maximum compressive stress is concentrated within the roof strata above the point where they meet the pillar reaching a maximum compressive stress of approximately 1.9 MPa. Compressive stresses are also elevated within the mine pillar. See (Figure 5.4). This is due to the decreased cross sectional area supporting the over burden load. The maximum tensile stress occurs within the roof strata above the excavation reaching a value of approximately 40.5 kPa.

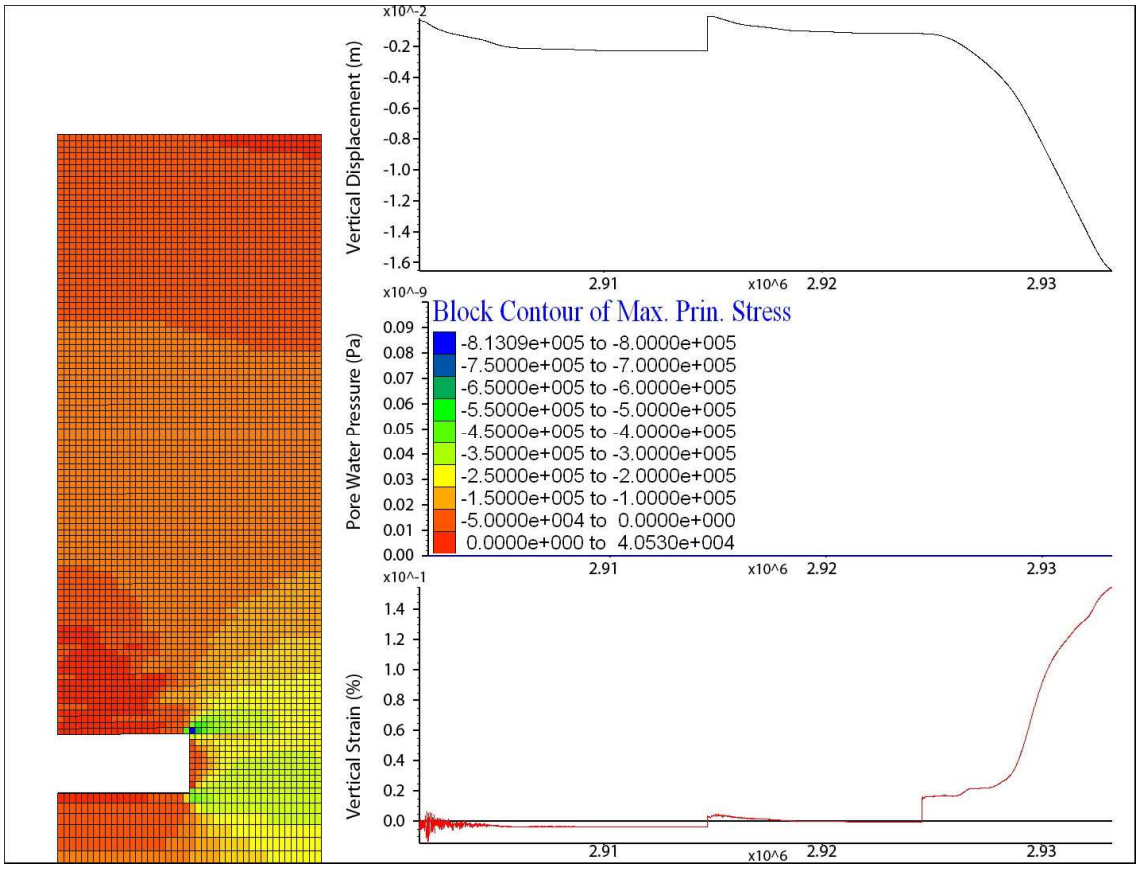

Figure 5.3: Maximum principal stress contours (Sigma 3) within the model for a bedding plane spacing of 0.5 m. Model parameters - Excavation 3 m wide, 1 m high; GSI 10.

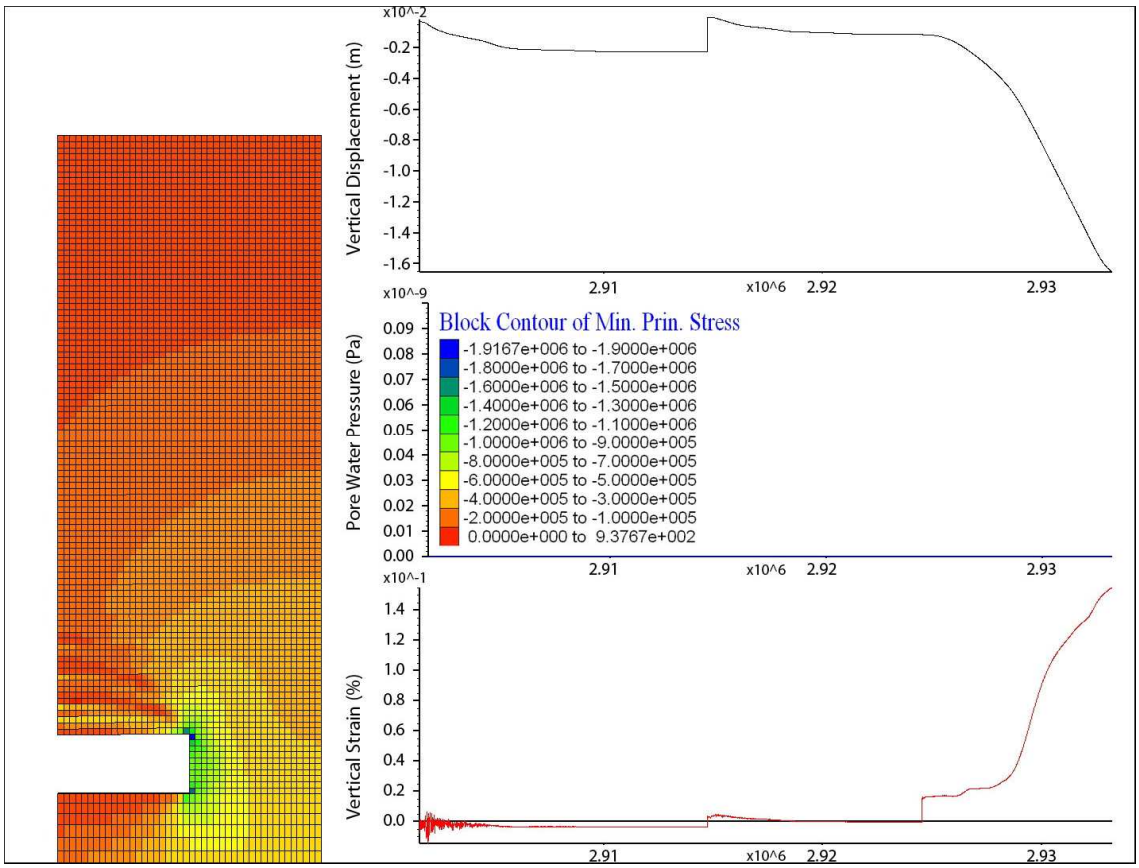

Figure 5.4: Minimum Principal stress contours (Sigma 1) within the model for a bedding plane spacing of 0.5 m. Model parameters - Excavation 3 m wide, 1 m high; GSI 10.

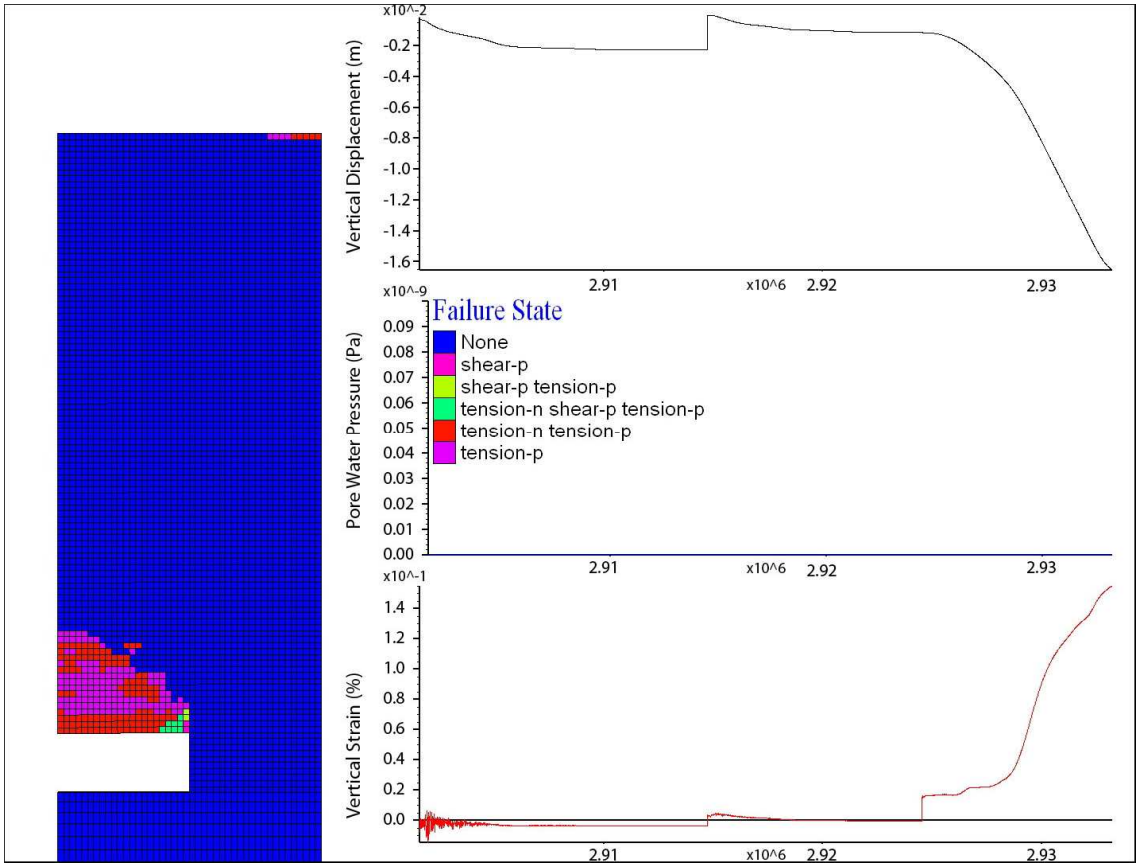

Figure 5.5: Failure state within the model for a bedding plane spacing of 0.5 m. Model parameters - Excavation 3 m wide, 1 m high; GSI 10.

In Figure 5.5 it can be seen that the excavation has caused significant tensile yielding within the rock mass above the excavation roof. Shear failure has also occurred within the elements forming the immediate roof bedding plane directly above the coal pillar. This is linked to failure of the interface elements representing the bedding planes which can be seen in Figure 5.6 and Figure 5.7 and in turn corresponds to the zones of maximum compressive stress in the model at the roof / pillar intersection as seen in Figure 5.4 (causing the shear yielding) and the maximum tensile stress within the roof strata as shown in Figure 5.3 which is associated with the tensile failure of the roof strata and the interface normal failure representing tensile delamination.

It is worth noting that this yield mechanism with the tensile delamination of bedding planes (as represented by the interface element separation as seen in Figure 5.7) along with the shear failure of the strata forming the immediate roof layer, over the excavation at the point where the roof strata meets the pillar is a very close match to that described by Diederichs and Kaiser (1999) in their observations of sub surface excavations workings and in their theoretical work on subsurface excavation stability. It also matches experimental laboratory work undertaken by a number of researchers as summarised by Bieniawski (1984) and Goodman (1989).

It would appear that this represents the initial tensile delamination of the strata as the mesh failure state plot and the plot of interface normal failure demonstrate that tensile failure is occurring within the rock mass and that bedding separation / delamination has occurred, however the rock mass roof is stable (although this stability appears to be marginal) as the model came to equilibrium with only limited vertical movement occurring within the immediate roof as shown in the history of vertical displacement in Figure 5.6 which is equal to approximately 16 mm.

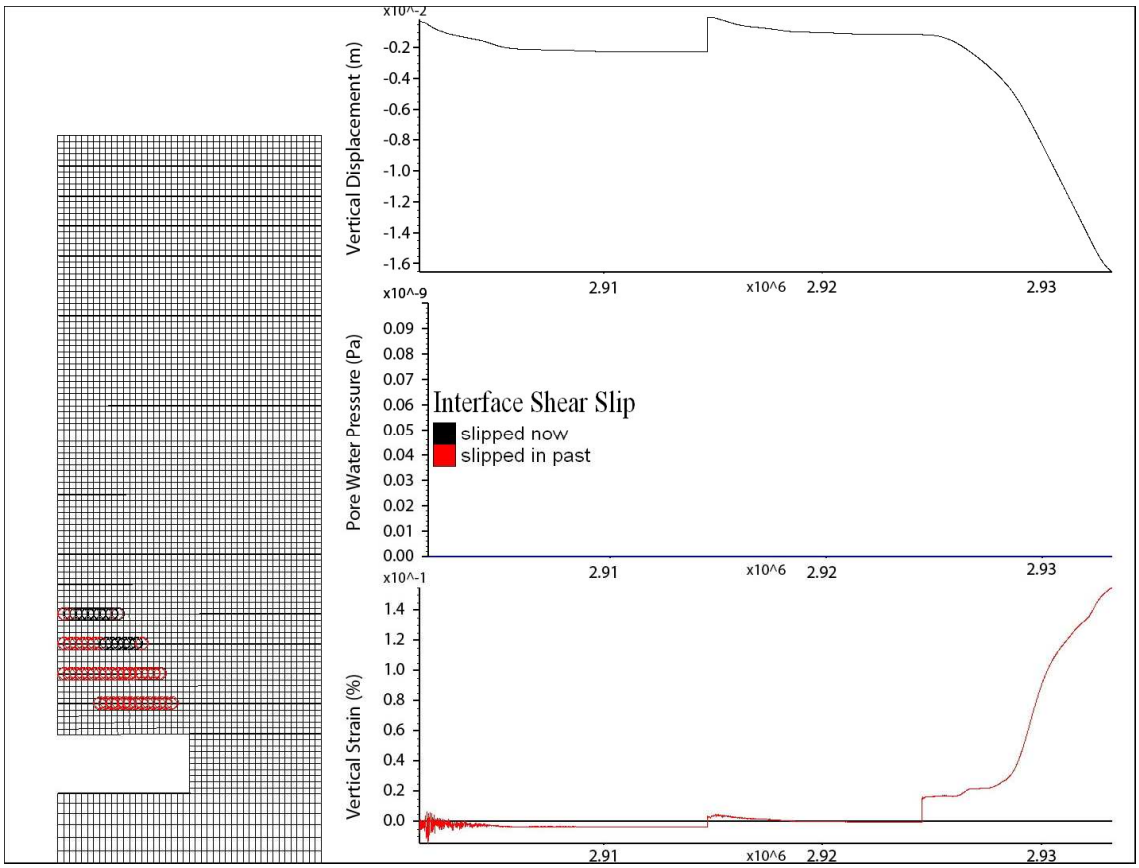

Figure 5.6: Interface shear failure within the model for a bedding plane spacing of 0.5 m. Model parameters - Excavation 3 m wide, 1 m high; GSI 10.

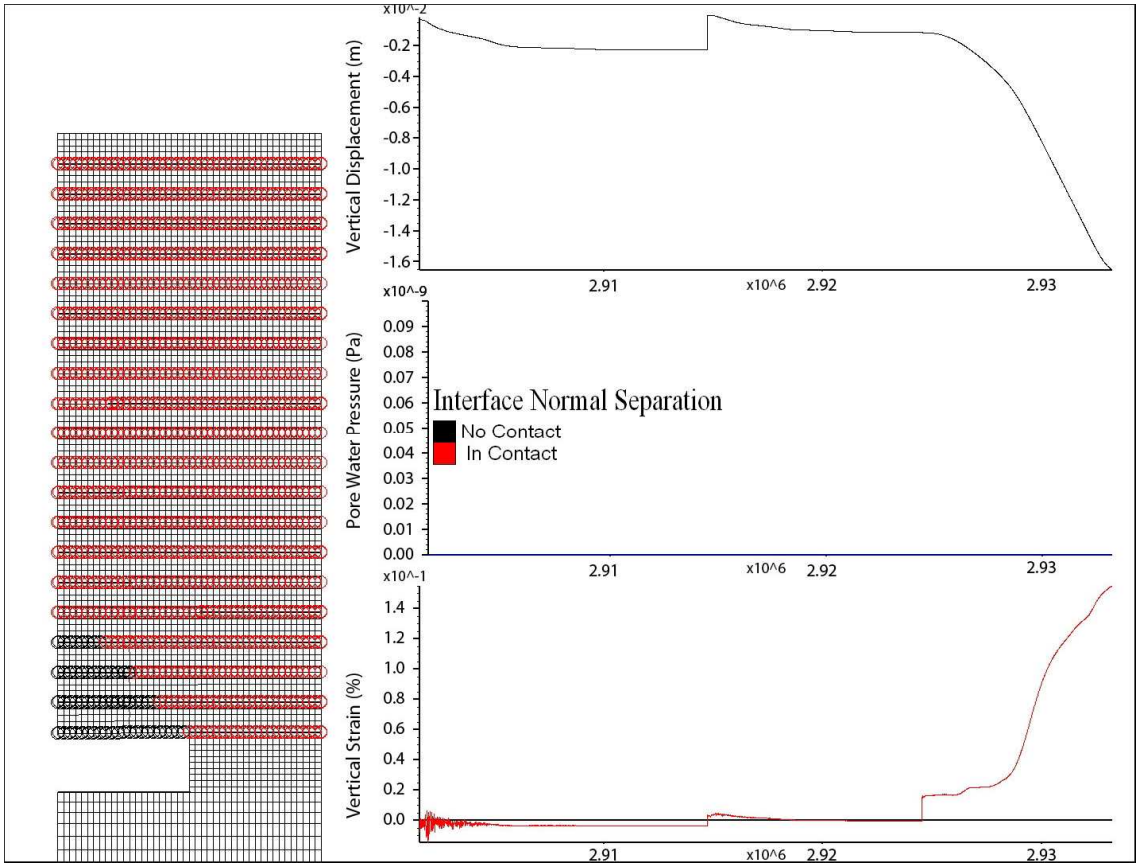

Figure 5.7: Interface separation / tensile failure within the model for a bedding plane spacing of 0.5 m. Model parameters - Excavation 3 m wide, 1 m high; GSI 10.

5.5.3 Model: 0.2 m Bedding Plane Spacing, 3 m Excavation Width, 1 m Excavation Height, GSI 10

In the following model, the excavation width, height and rock mass strength properties have been kept constant; however the bedding surface spacing has been reduced from 0.5 to 0.2 m .

These models were run in large strain mode and so the plots show the grid deformation that has occurred within the model. The plots of maximum (Figure 5.8) and minimum principal stress (Figure 5.9) again show that the maximum compressive stress is concentrated within the roof strata above the point where they meet the mine pillar reaching a maximum compressive stress of approximately 1.5 MPa. Compressive stresses are also elevated within the mine pillar. See (Figure 5.9). This is due to the decreased cross sectional area supporting the over burden load. The maximum tensile stress occurs within the roof strata above the excavation reaching a value of approximately 22.6 kPa. However the most significant detail that can be observed here is that the roof strata have collapsed into the mine void. It is assumed that this collapse is responsible for the reduction in stress in the model. This corresponds to a roof centreline vertical displacement of 1 m (*i.e.* it has reached the excavation floor). Another difference between this model and the previous one is that the zone of tensile stress extends higher into the rock mass (approximately 5 m above the original roof position as opposed to approximately 3 m in the previous model as seen in Figure 5.3). The plot of minimum and maximum principal stress (Figure 5.8 and Figure 5.9) also shows "banding" of the stress contours within this zone of tension, which help delineate the individual roof strata, as their lower half is in a lower compressive stress (or in tension depending on the plot) state than their upper portion. It is likely that this represents the formation of stress arching within the strata whereby the downward flexing of the roof centreline creates tensile stress in the lower half of the beam / strata and compressive stress in the upper half as described in section 2.2.3. This phenomenon can also be observed in the previous model in the plot of minimum stress (see Figure 5.4), however in this case the extra thickness of the roof strata meant that it successfully spanned the initial excavation whereas in the current model approximately five bedding planes collapsed into the void before the effective narrowing of the span created by the abutments of the failed strata allowed a stable compression arch to form in the sixth roof stratum approximately halving the stable span.

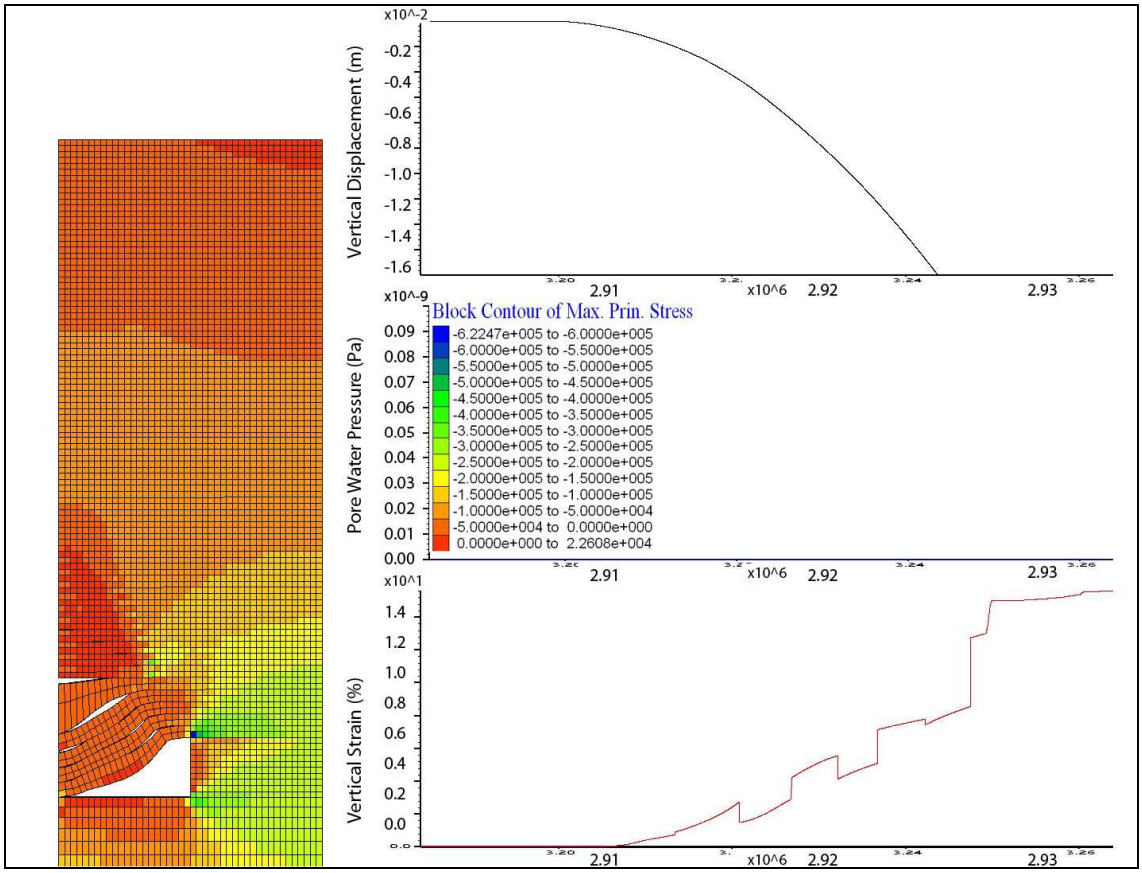

Figure 5.8: Maximum principal stress contours (Sigma 3) within the model for a bedding plane spacing of 0.2 m. Model parameters - Excavation 3 m wide, 1 m high; GSI 10

The zone of tensile failure and the height it extends into the rock mass above the excavation can also be seen in the failure state plot (Figure 5.10). Of significant interest is the zone of shear failure that occurs within the strata at the roof / pillar interface which has propagated to a greater extent upwards into the rock mass, diagonally away from the mine pillar. In reality this would represent a discrete fracture or series of fractures where the roof beam would lose cohesion and collapse into the void while leaving part of the remaining strata on the pillar side of the failure surface to form a pair of cantilevers which reduce the overall span of the excavation and would act as an abutment supporting the overlying strata. This is almost identical to the behaviour observed in the field and in laboratory experiments as reported by Bieniawski (1989) and Goodman (1989).

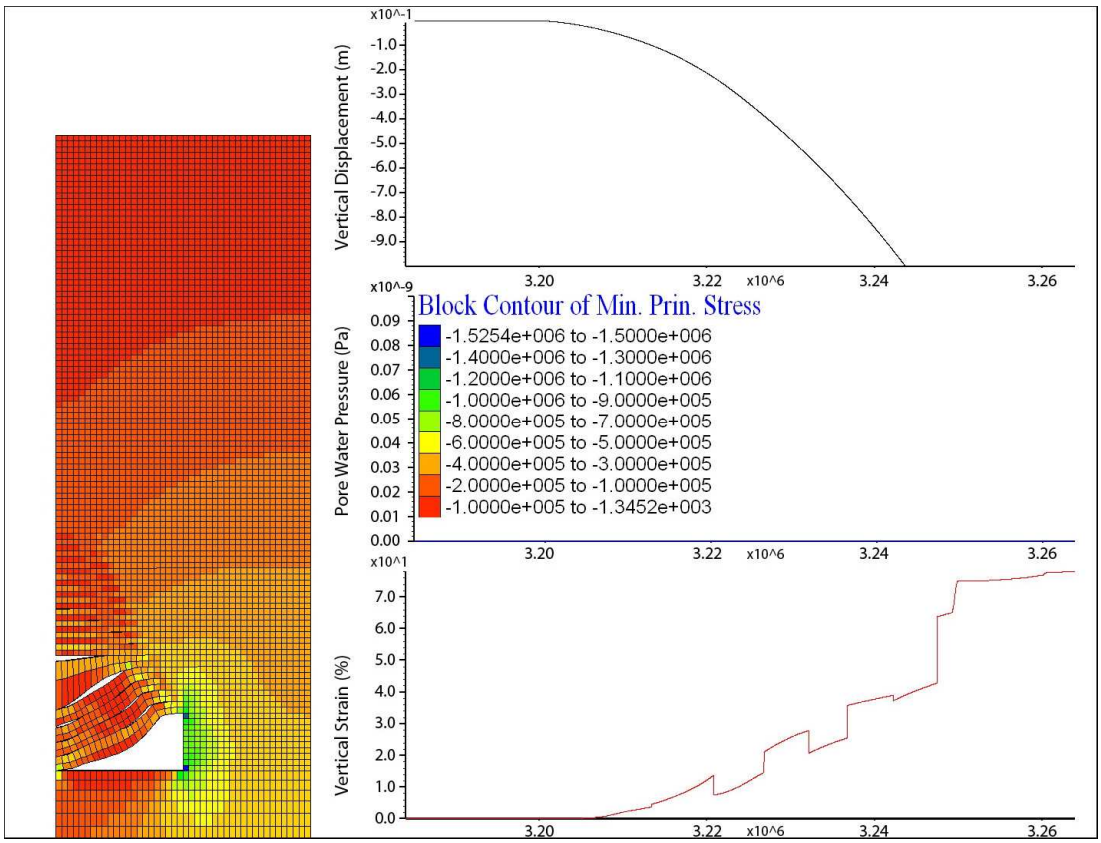

Figure 5.9: Minimum principal stress contours (Sigma 1) within the model for a bedding plane spacing of 0.2 m. Model parameters - Excavation 3 m wide, 1 m high; GSI 10

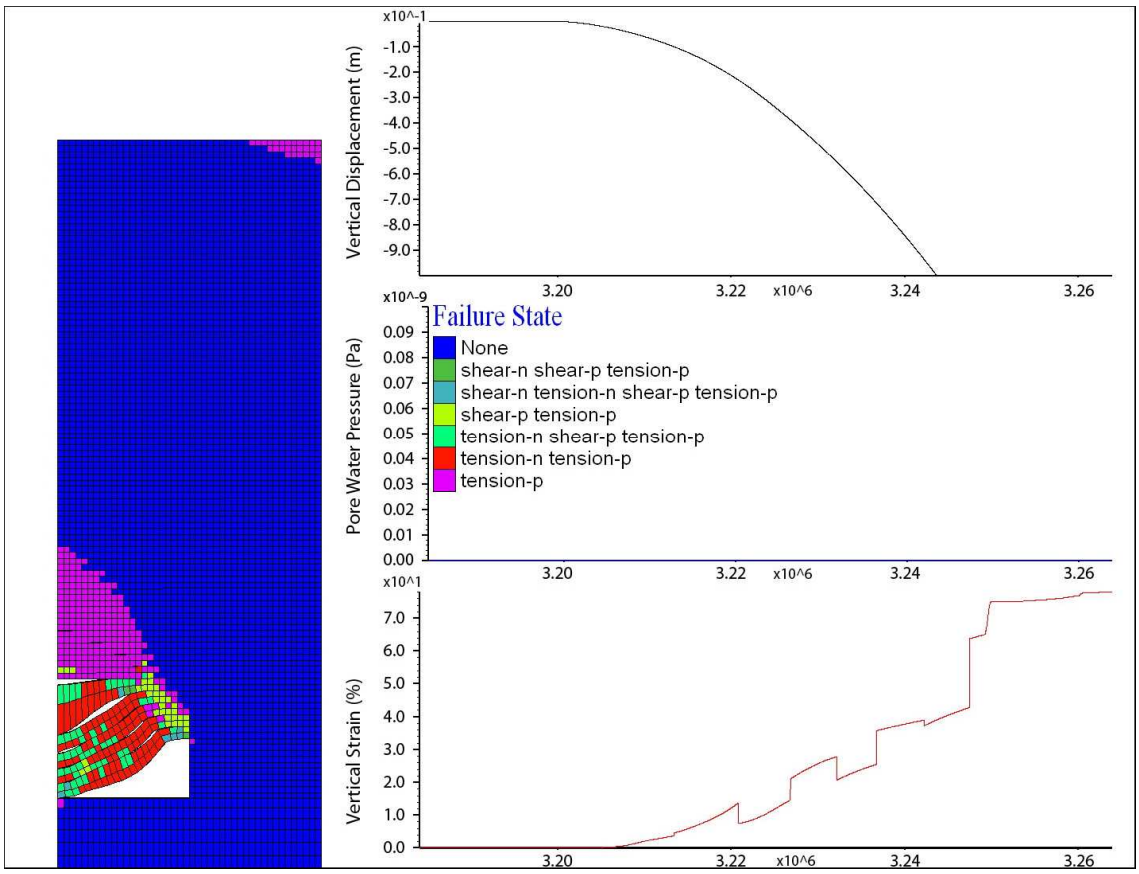

Figure 5.10 : Failure state within the model for a bedding plane spacing of 0.2 m. Model parameters (3 m wide excavation, 1 m high excavation, GSI 10).

Further evidence for the formation of a stress arch(s) within the currently stable strata above the failed layers is shown on the interface normal failure plot (Figure 5.11) where the zone of tensile failure corresponds to a region where the interface elements on the upper and lower surfaces of the bedding planes in the model are no longer in contact. As such they are not being supported directly from below by the underlying strata but instead must be acting as individual simply supported beams. This combined with the observed stress state within the strata where the upper half is in compression and the lower half is in tension in the region over the span. The compressive stress concentration can also be seen to decrease within the strata as the height over the excavation width and hence the effective unsupported span width decreases.

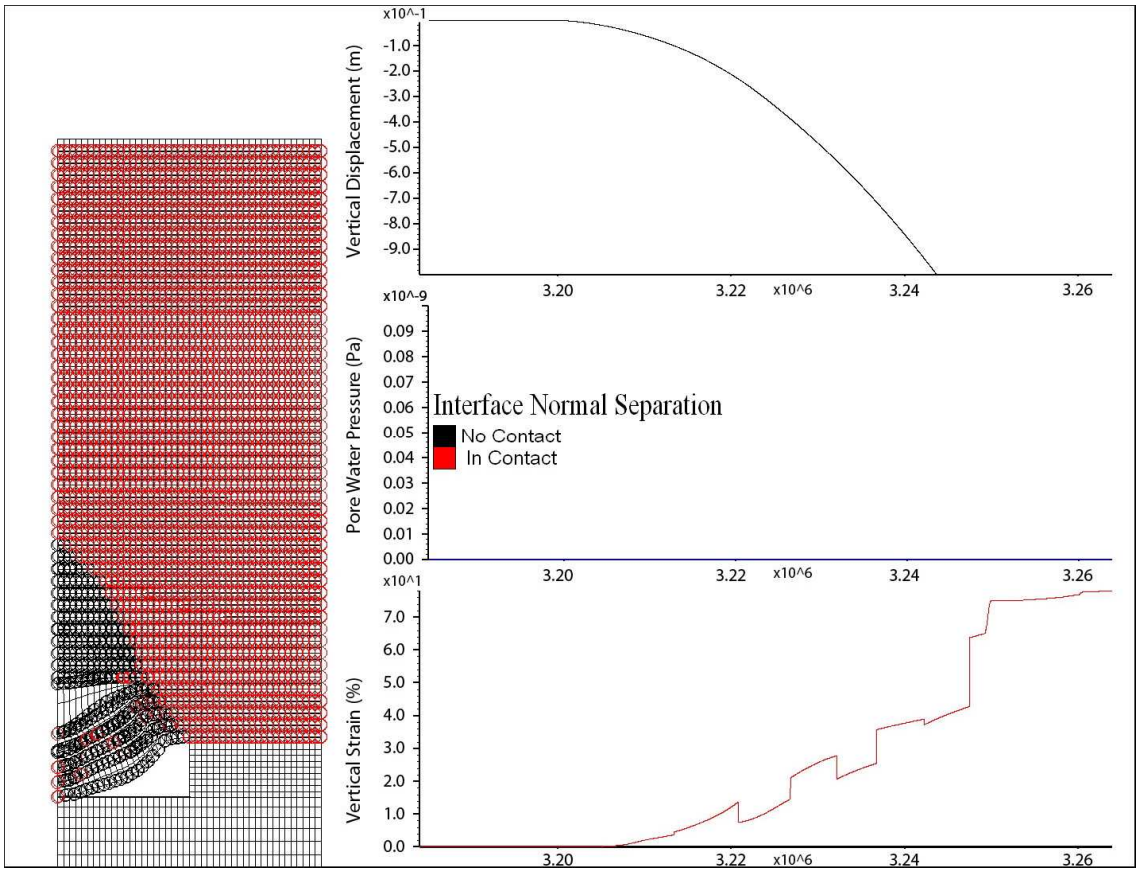

Figure 5.11: Interface separation / tensile failure within the model for a bedding plane spacing of 0.2 m. Model parameters - Excavation 3 m wide, 1 m high; GSI 10.

5.5.4 Model: 0.1 m Bedding Plane Spacing, 3 m Excavation Width, 1 m Excavation Height, GSI 10

In the following model, the excavation width, height and rock mass strength properties have been kept constant, however the bedding surface spacing has been further reduced from 0.2 to 0.1 m.

The plots of maximum (Figure 5.12) and minimum principal stress (Figure 5.13) again show that the maximum compressive stress is concentrated within the roof strata above the point where they meet the mine pillar reaching a maximum compressive stress of approximately 1.6 MPa. Compressive stresses are also elevated within the mine pillar and it is possible that this would result to some degree in spalling however based on the previous modelling in section 3.2 pillar failure and deformation does not seem to significantly effect roof stability, rather it results in a differing subsidence mechanism (areal or sag subsidence).

In this model however the maximum tensile stress occurs not within the roof strata above the excavation, but instead above the mine pillar reaching a maximum value of approximately 131.5 kPa. As per the previous model it can be observed here that the roof strata have collapsed into the mine void and have reached the excavation floor, corresponding to a roof centreline vertical displacement of 1m. Also as occurs in the previous model the collapsed strata are in a compressive stress state (as they have failed they are no longer able to support a tensile stress) where as the overlying stable strata above the failed zones are still in a tensile stress state with a magnitude up to 50 kPa. This zone of tensile stress extends approximately 5 m into the rock mass over the centre of the original excavation roof.

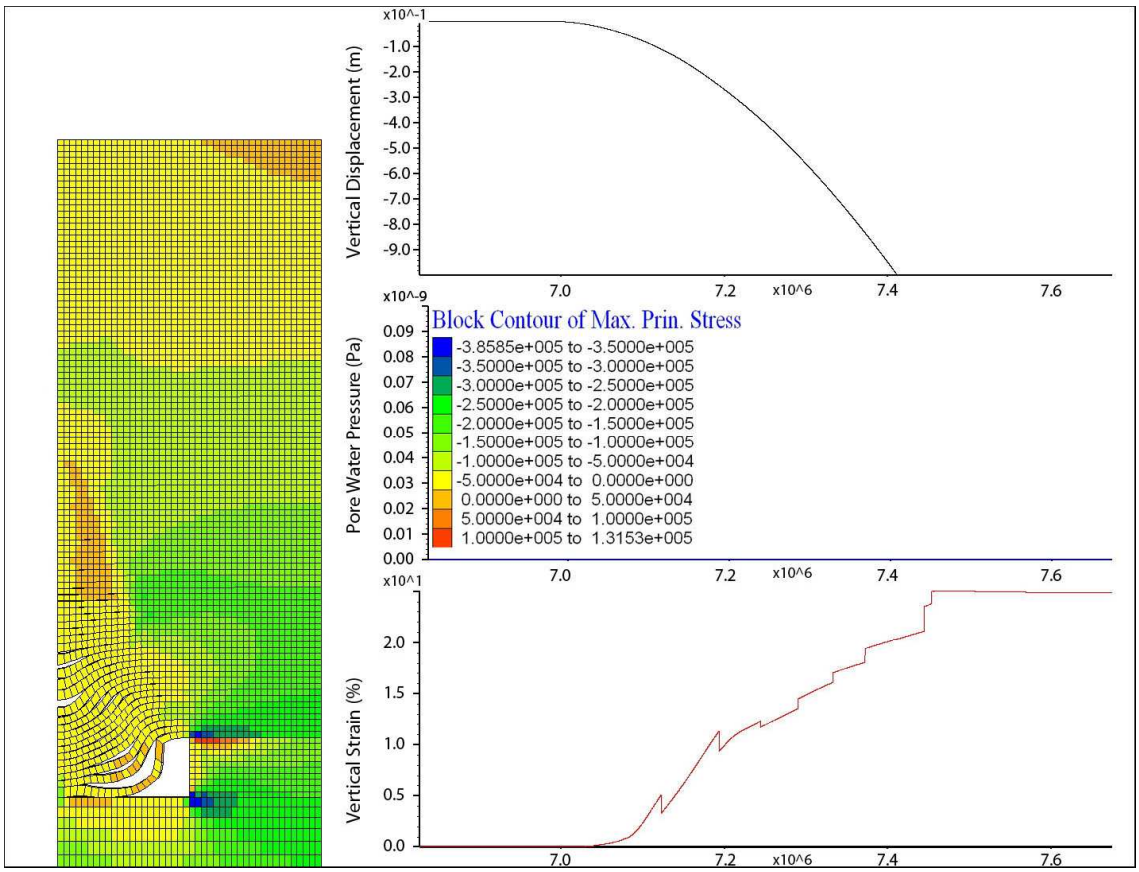

Figure 5.12: Maximum principal stress contours (Sigma 3) within the model for a bedding plane spacing of 0.1 m. Model parameters - Excavation 3 m wide, 1 m high; GSI 10

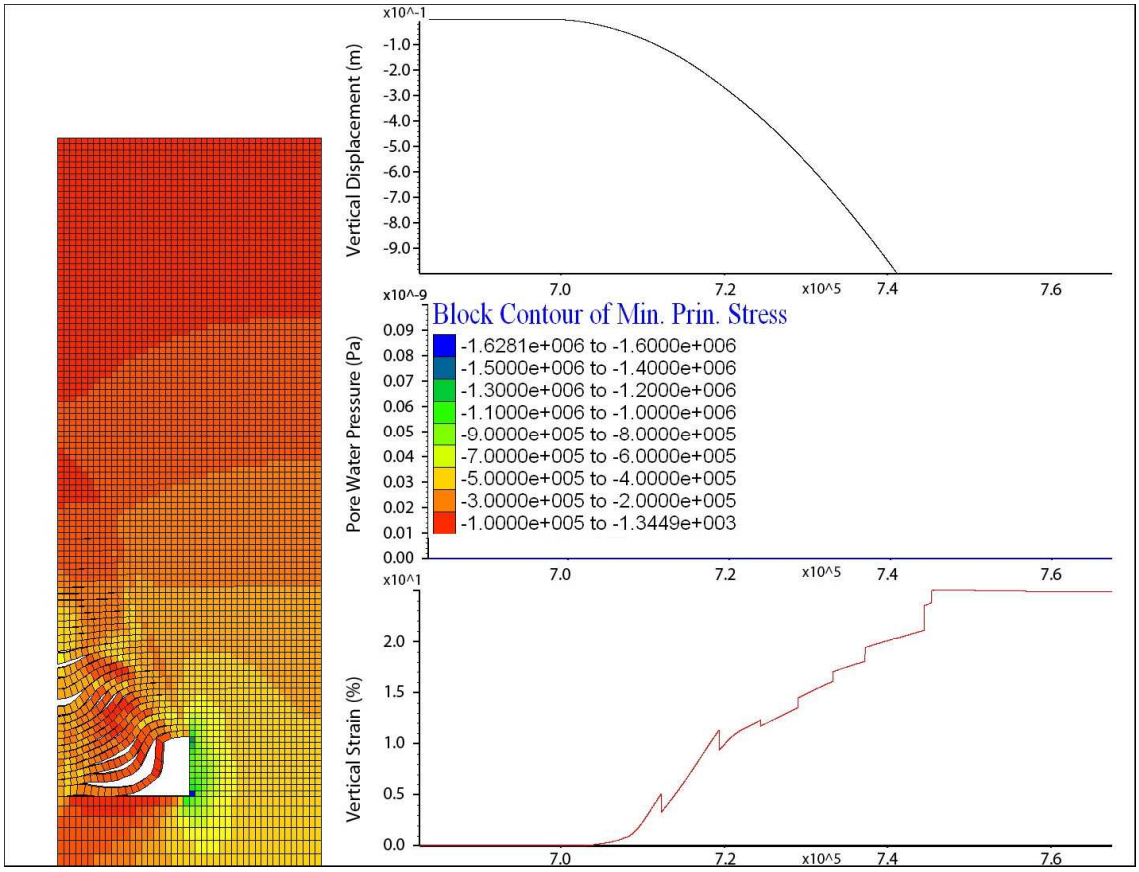

Figure 5.13: Minimum principal stress contours (Sigma 1) within the model for a bedding plane spacing of 0.1 m. Model parameters - Excavation 3 m wide, 1 m high; GSI 10

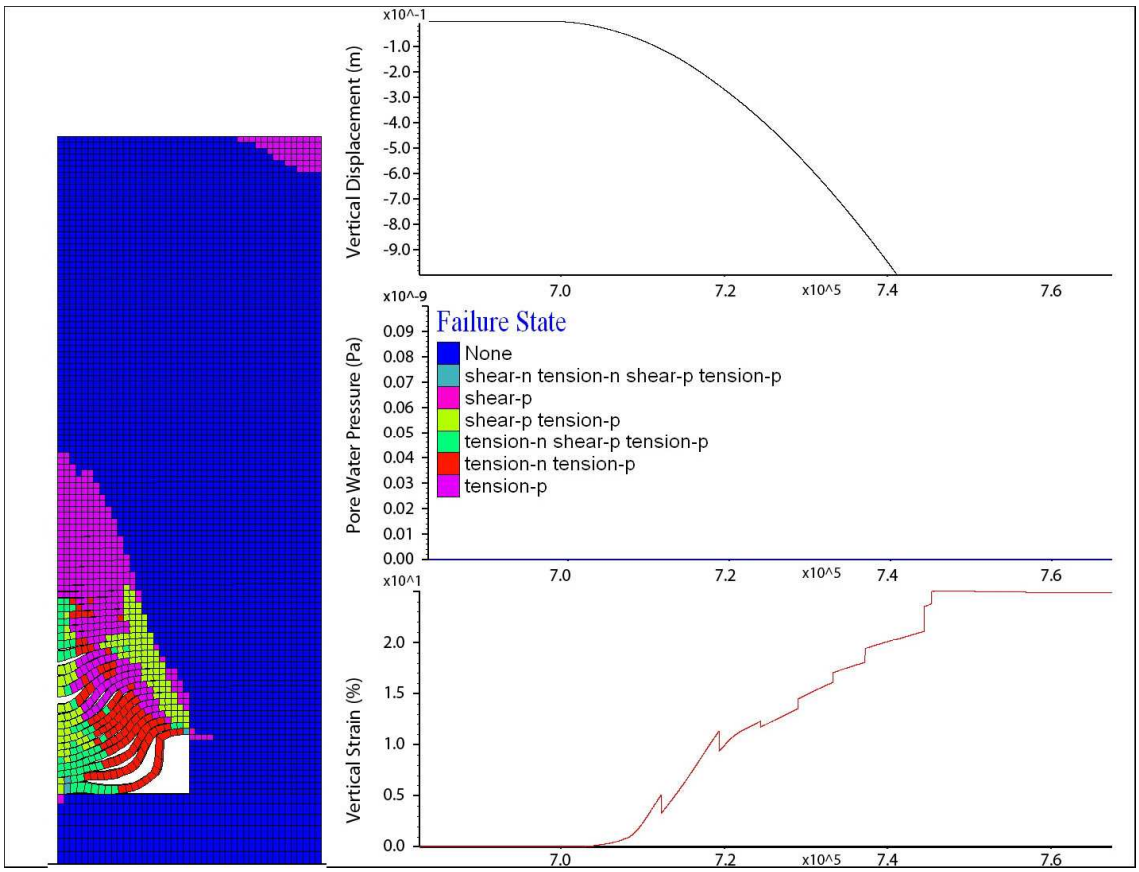

Figure 5.14: Failure state within the model for a bedding plane spacing of 0.1 m. Model parameters (3 m wide excavation, 1 m high excavation, GSI 10).

The zone of tensile stress described previously has resulted in a wedge shaped zone of failure within the model overlying the excavation which in three-dimensions would most likely represent a cone of damage to the rock mass extending above the failed and collapsed strata. Again it would appear that the strata in the failed zone that have not totally collapsed have formed a series of discrete compression arches as the plot of interface normal separation (Figure 5.15) shows that the individual strata are not in contact in this zone and yet are stable and apparently self supporting for the applicable spans. As in the previous model, a zone of shear failure has formed within the strata at the roof / pillar interface which has propagated to an even greater extent (approximately 2.5 metres as opposed to 1 m for the previous model) upwards into the rock mass.

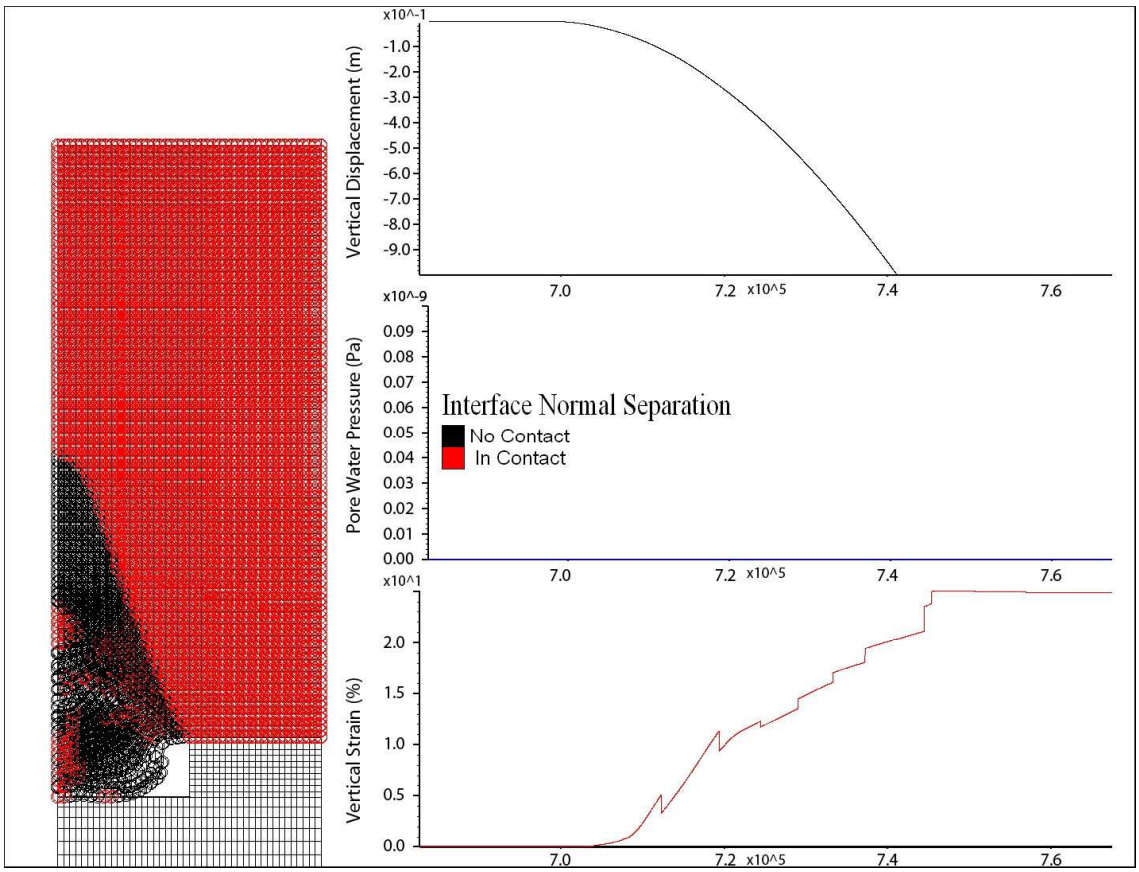

Figure 5.15: Interface separation / tensile failure within the model for a bedding plane spacing of 0.1 m. Model parameters - Excavation 3 m wide, 1 m high; GSI 10.

Compression Arching:

That the individual roof strata form a compression arch has been discussed in the above modelling results. However on the plots shown this was not always clear. As such, in the plots below, a conceptual diagram of a compression arc is shown in Figure 5.16 and detailed plots of the horizontal stress, principal stresses and normal separation and shear slip plots of the immediate roof beams for the 0.5 m bedding spacing model described above (3 m excavation width, 1 m excavation height, strength properties GSI 10) are shown in Figure 5.17 and Figure 5.19:

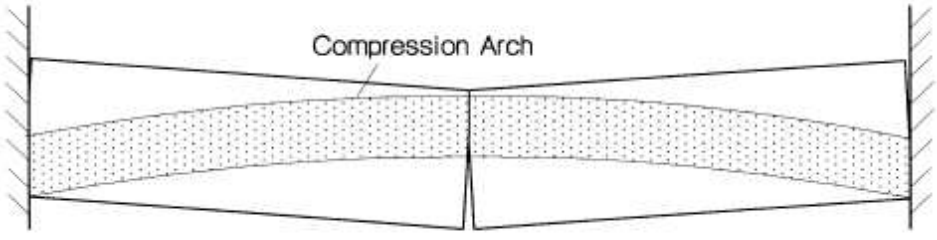

Figure 5.16: Conceptual diagram showing a compression arch in roof bedding planes.

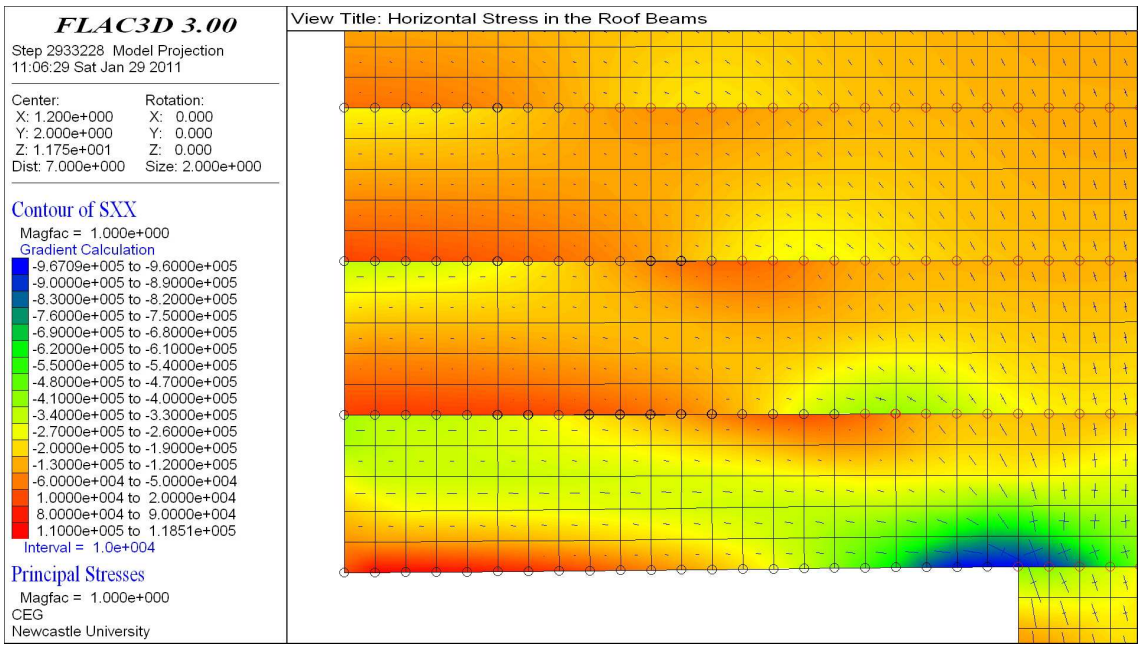

Figure 5.17: Horizontal stresses along with principal stresses and interface separation.

In Figure 5.17 the upper boundary of the immediate roof layer can be seen to have separated from the bedding layer above it (marked by the black circles in this case representing normal interface separation, those in contact are marked in red). The compression arch is most clearly visible in the immediate roof bed. It is marked by the curved band of elevated compressive stress (approximately 0.3 MPa) which passes from the centre of the roof, where it is concentrated in the upper half of the roof beam to the base of the beam at the roof / pillar intersection.

Areas outside the region of compression are in a tensile stress state (*i.e.* below the arch at the roof centreline and above it at the roof pillar intersection, with an intermediate state as the arch passes from the roof centreline to the pillar). This matches closely with the conceptual arch in Figure 5.16. An annotated plot is included – see Figure 5.18.

It can also be seen in Figure 5.18 that the point where bedding plane separation occurs is marked in the layer above by a transition from compression (where the underlying span is still providing support) to tension where support is lost. The phenomenon acts to reduce the effective span width and it can be seen from the plot that this region where tensile delamination occurs and the point of compressive stress where support is provided moves progressively further towards the roof centreline as the height above the roof increases.

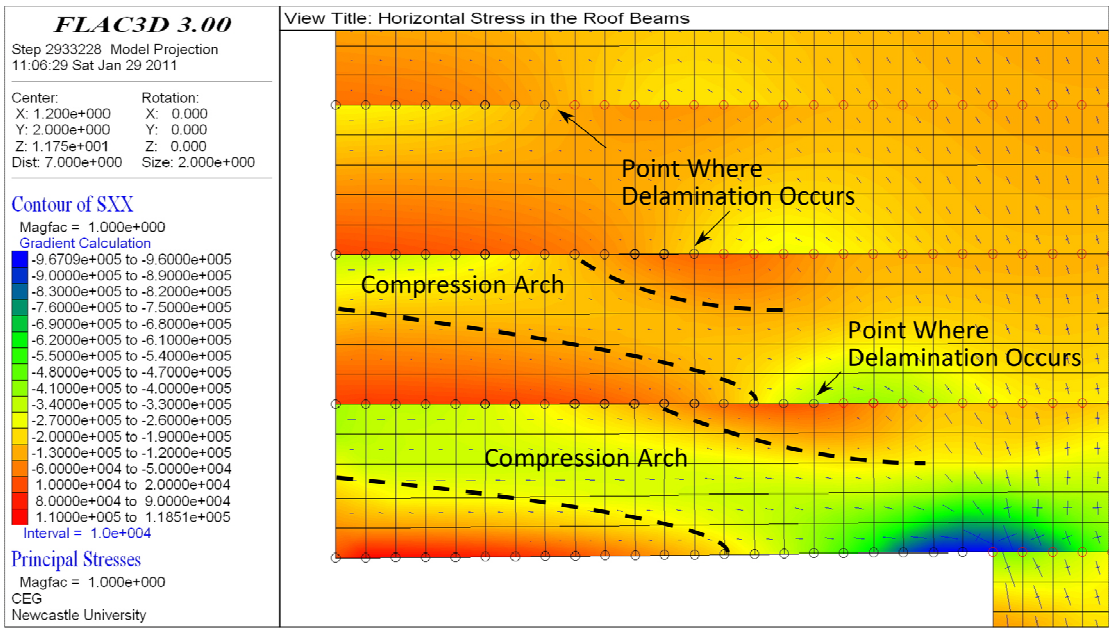

Figure 5.18: Annotated plot of compression arching – schematic – locations are approximate.

This marked contrast in stresses in the layers above and below the interface in this region has also lead to shear slip occurring on the interfaces which can be seen in Figure 5.19: where the red circles mark points where shear slip of the interface has occurred and black circles mark points where it is currently occurring. The movement of the boundary between the region of compressive and tensile stresses at the base of each bed towards the centre of the roof span with increased height over the void also cause the region where bedding plane shear failure to occur to move as seen in Figure 5.19:.

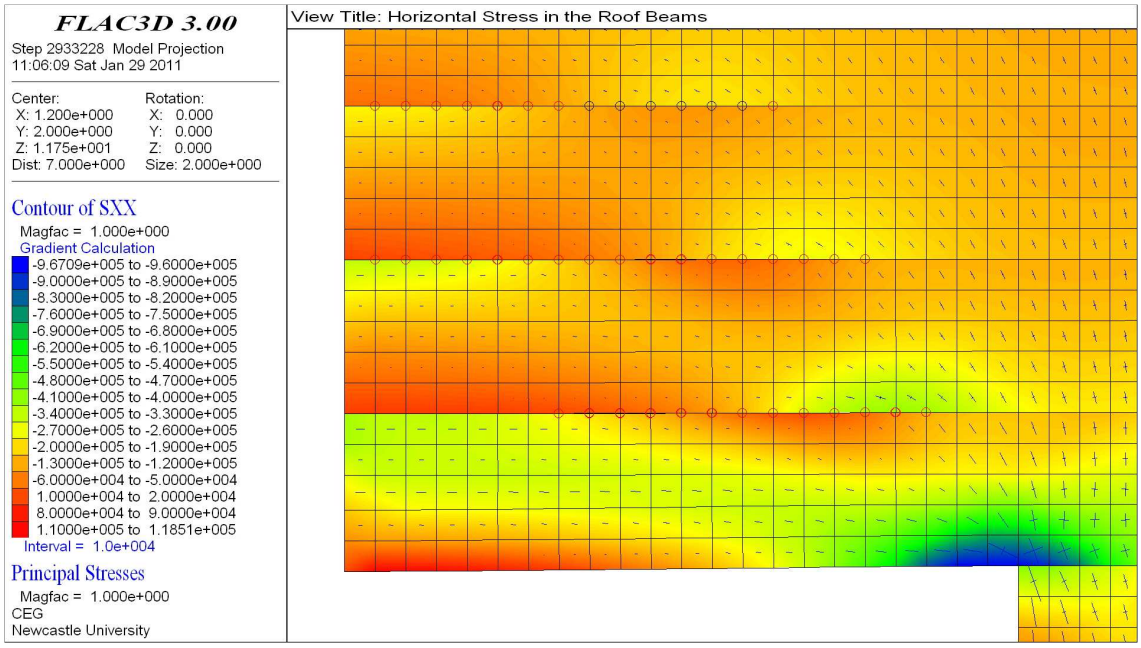

Figure 5.19: Horizontal stresses along with principal stresses and interface slip.

Another interesting observation that can be made about the modelling work undertaken here is related to the transition in failure modes that would occur as bedding thickness increases. Thinly bedded low strength strata commonly undergo self weight sagging along parting or bedding planes (Whittles *et al*., 2007; see Figure 2.24 D) and this behaviour is being captured by FLAC due to the use of interface elements representing the horizontal bedding planes. An example of this occurrence within the modelling can be seen in Figure 5.14.

However at higher thicknesses of bedding this would not be expected to occur. Instead shear failure or shear joint / parting plane failure would be the expected mechanism. It has been observed in the continuum modelling that shear failure occurs in the modelled rock mass extending upwards into the excavation roof over the void (shear failure mechanism C in Figure 2.24). If it crosses the full thickness of a discrete span such as those in the modelling here this would result in shear failure occurring within the bedding planes (shear joint parting plane failure), however the continuum nature of a thick roof beam meant that the shear fractures that would form resulting in the span collapse could not be modelled effectively. This is a fundamental issue with continuum modelling and as such it was necessary to devise an alternative method for modelling the progressive roof collapse in thickly bedded strata dominated by shear joint / parting plane failure.

FLAC was observed to be capable of modelling the self weight sagging of low strength thinly bedded strata directly when use was made of horizontal layered bedding however this failed to totally capture the collapse behaviour in thicker bedded strata (>0.2 m) where shear joint / parting plane failure occurred. It was observed that the shear failure occurred in the rock mass extending upwards into the excavation roof over the void as would be expected, crossing thicker roof spans and this resulted in shear failure occurring within the bedding planes (parting plane failure), however the continuum nature of a thick roof beam meant that the shear fractures that would form resulting in the span collapse could not be modelled effectively. As such it was necessary to devise an alternative method for modelling the progressive roof collapse in thickly bedded strata dominated by shear joint / parting plane failure.

5.6 Conclusions

The variation in bedding plane spacing clearly has an impact on the stability of sub surface excavations. It can be seen that the larger the bedding thickness the greater the excavation stability for a given stress state and the lower the collapse height of roof strata into the rock mass. Also the ability of the model to capture the formation of a stress arch within individual strata has been demonstrated and it has been shown how the variations within the stress field within the beds are linked to shear and tensile failure of the bedding planes. The bedding thickness / bedding plane separation also has a significant effect on the height to which "damage" in the form of tensile yielding and bedding plane delamination propagate upwards into the overlying rock mass, whereby the thicker the bedding / strata, the lower the height that damage extends vertically into the rock mass.

The capability of FLAC to model the self weight sagging of thin roof strata where delamination occurs parallel to the interface element appears to be very good. However it would appear that it does not effectively capture the shear failure expected in thicker roof strata. As such an alternative solution for modelling collapse progression in these scenarios is required. A potential solution is discussed in chapter 4.

5.7 Effect of Variable Excavation Width within a Bedded Rock Mass on the Stability of Mine Voids

That the variation in excavation width and hence the roof span of the mine void has implications for the stability of the excavation is demonstrated in the modelling in section 3.2. whereby for a given set of rock mass strength and stiffness properties and a given stress state (affected by pore water pressure and rock mass density) it can be seen that with increasing width the degree and extent of yielding within the roof strata increases. As the previous section demonstrated clearly that the model behaviour is strongly affected by the inclusion of interface elements to represent bedding planes both in terms of the roof stability within the modelled rock mass and also in terms of the accurate capture of the roof failure mechanism as seen in the field and in laboratory experiments, in this section it is intended to further investigate the effect of varying excavation width on roof stability within a modelled discontinuous rock mass.

The following models all have uniform excavation heights (1m), overburden thicknesses (10m) and rock mass strength and stiffness properties (GSI 10) with the groundwater table set below the level of the excavation (at 9 m above the base of the model which is equal to 1 m below the excavation floor). The excavation width varies from 1 metre to 3 metres in 1 metre increments.

5.7.1 Model: 0.1 m Bedding Plane Spacing, 1 m Excavation Width, 1 m Excavation Height, GSI 10

Figure 5.20 is a plot of the yield state of the rock mass for a 1 meter wide excavation overlain by a rock mass with bedding planes at 0.1 m intervals. It can be seen that some tensile yielding of the elements forming the first 3 roof layers has occurred. The normal separation plot (Figure 5.21) for this model also indicates that the interfaces separating the beds are no longer in contact which suggests that this is the initial stage of tensile delamination of the roof strata. However currently vertical displacements are low (approximately 1.4 mm at the roof centre line as seen in the displacement history plot which is equivalent to approximately 0.15% strain which although potentially large enough to initiate tensile softening within the model is not considered significant) and the model has come to stable equilibrium.

The plots of maximum and minimum principal stress (Figure 5.22 and Figure 5.23) show that the strata at this point are partially in tension and compression which suggests that the tensile yielding / delamination and the vertical movement or sagging has caused some degree of compression arching which has stabilised the excavation roof in this case.

The high stress concentration seen in the pillar roof intersection (maximum value of approximately 1.42 MPa) has resulted in some shear yielding in the first of the roof strata at this point which can be observed in the yield state plot. This is likely to represent the initial formation of shear fractures which would ultimately result in failure of the strata, which is currently stable. However it is possible that this stability is marginal and that even a small change in the stress state would cause further yielding and failure of the roof layer.

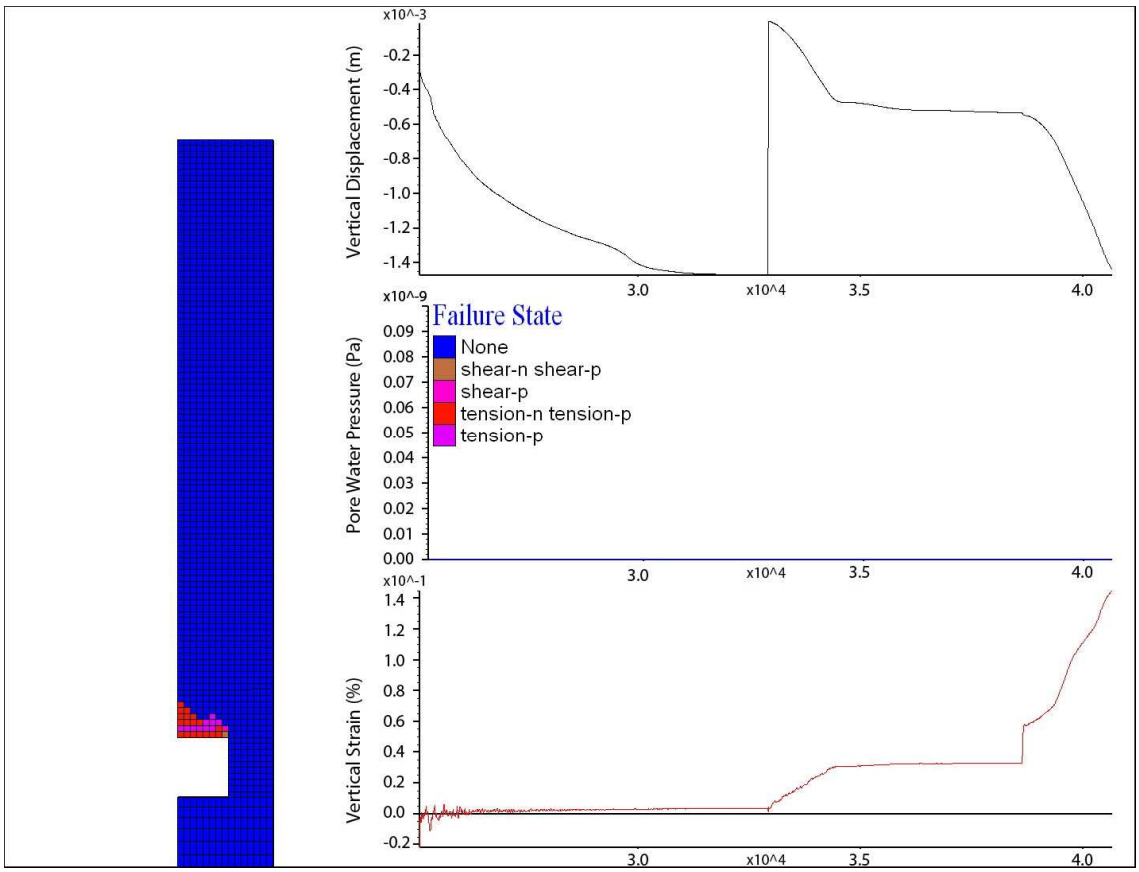

Figure 5.20: Failure state within the model for a bedding plane spacing of 0.1 m. Model parameters (1 m wide excavation, 1 m high excavation, GSI 10).

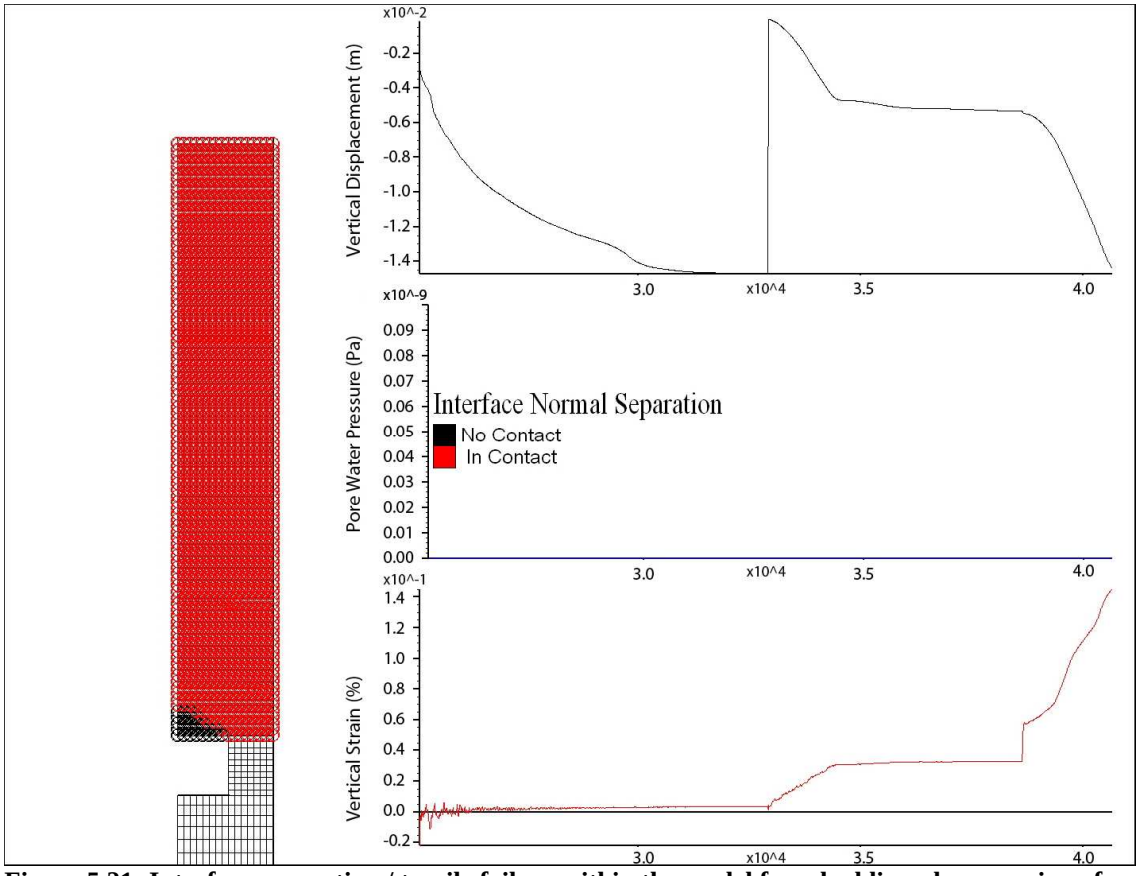

Figure 5.21: Interface separation / tensile failure within the model for a bedding plane spacing of 0.5 m. Model parameters - Excavation 1 m wide, 1 m high; GSI 10.

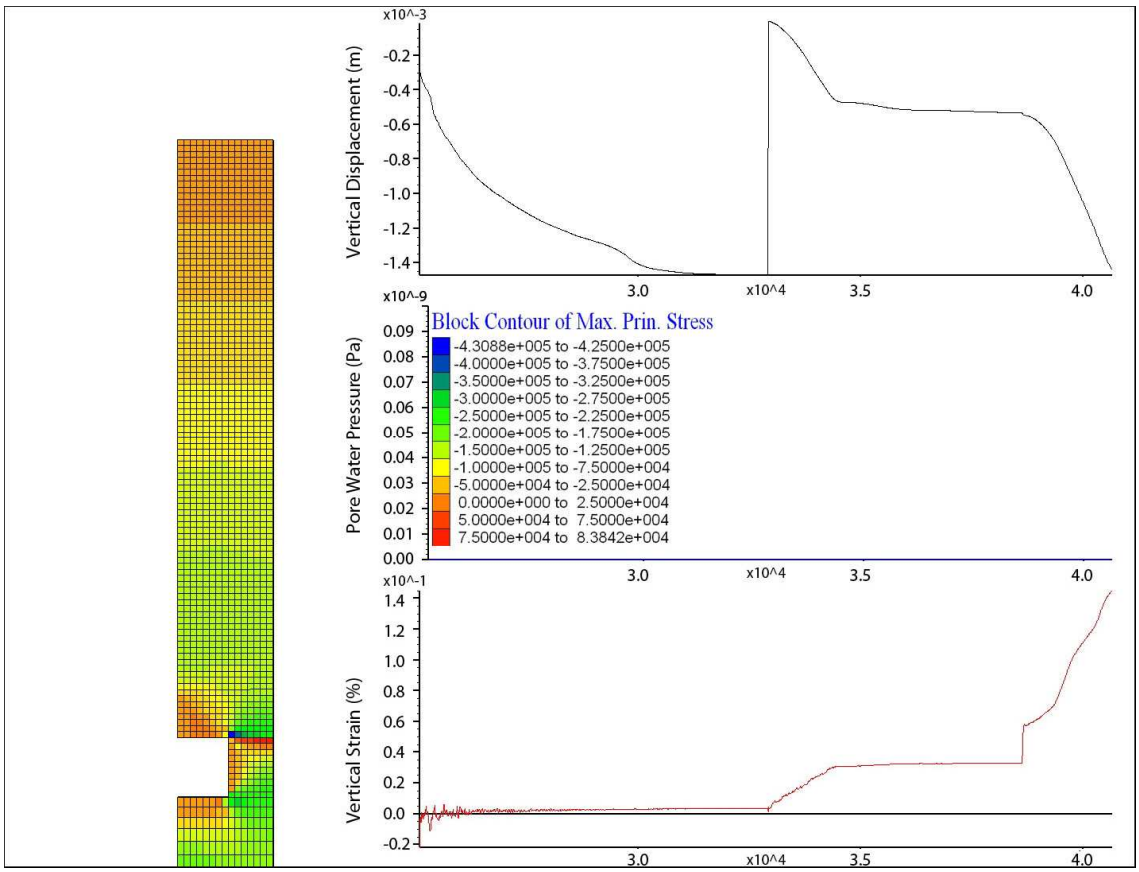

Figure 5.22: Maximum principal stress contours (Sigma 3) within the model for a bedding plane spacing of 0.1 m. Model parameters - Excavation 1 m wide, 1 m high; GSI 10.

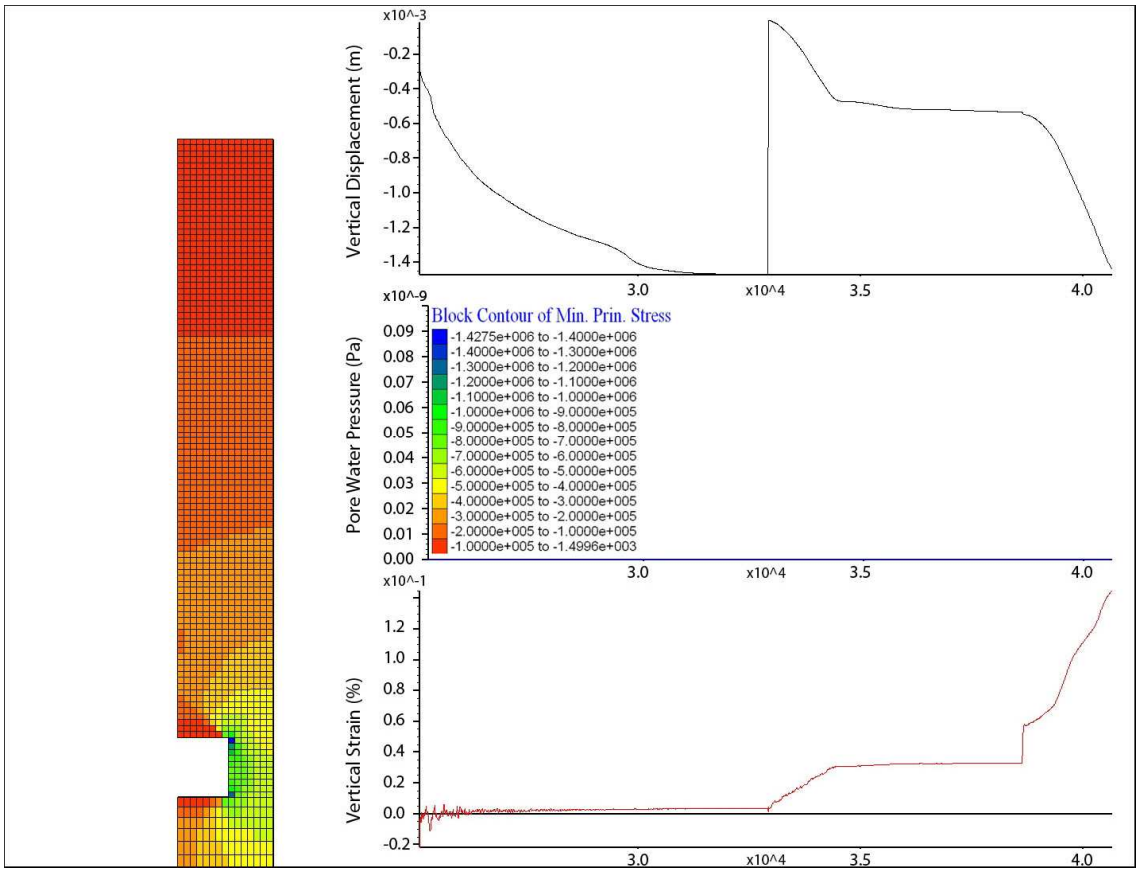

Figure 5.23: Minimum principal stress contours (Sigma 1) within the model for a bedding plane spacing of 0.1 m. Model parameters - Excavation 1 m wide, 1 m high; GSI 10.

5.7.2 Model: 0.1 m Bedding Plane Spacing, 2 m Excavation Width, 1 m Excavation Height, GSI 10

In this model the excavation width has been increased from 1 to 2 metres. All other parameters are identical to the previous model run. Figure 5.24 is a plot of the yield state of the rock mass for the 2 m wide excavation (the rock mass has bedding planes at 0.1 m intervals).

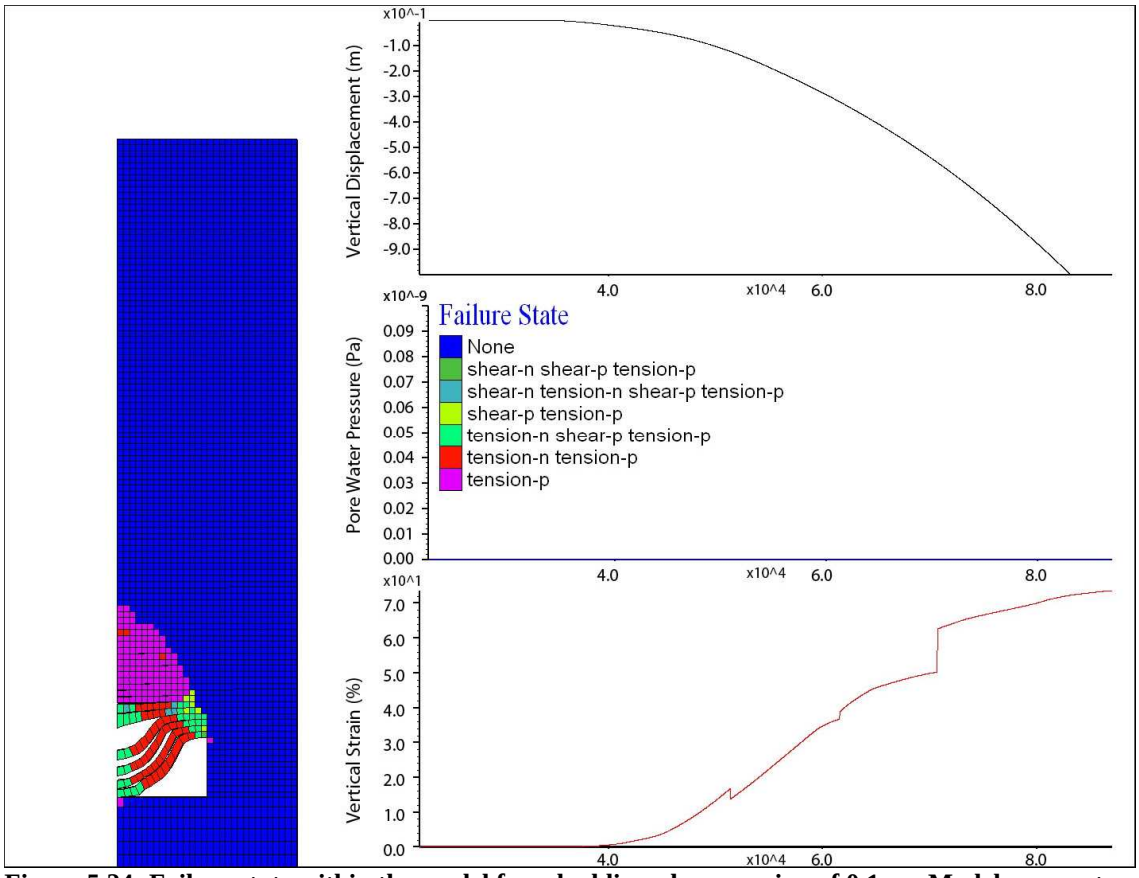

Figure 5.24: Failure state within the model for a bedding plane spacing of 0.1 m. Model parameters (2 m wide excavation, 1 m high excavation, GSI 10).

It can be seen that the increase in excavation width has created a significant decrease in roof strata stability with the collapse of roof strata into the excavation having occurred. In this case the first 4 roof strata overlying the excavation have all failed totally with significant displacements and delamination along their bedding planes and a significant band of shear yielding at their ends nearest to the mine pillar. The 2 roof strata above this are also displaying significant tensile and shear yielding and their stability is likely to be extremely marginal.

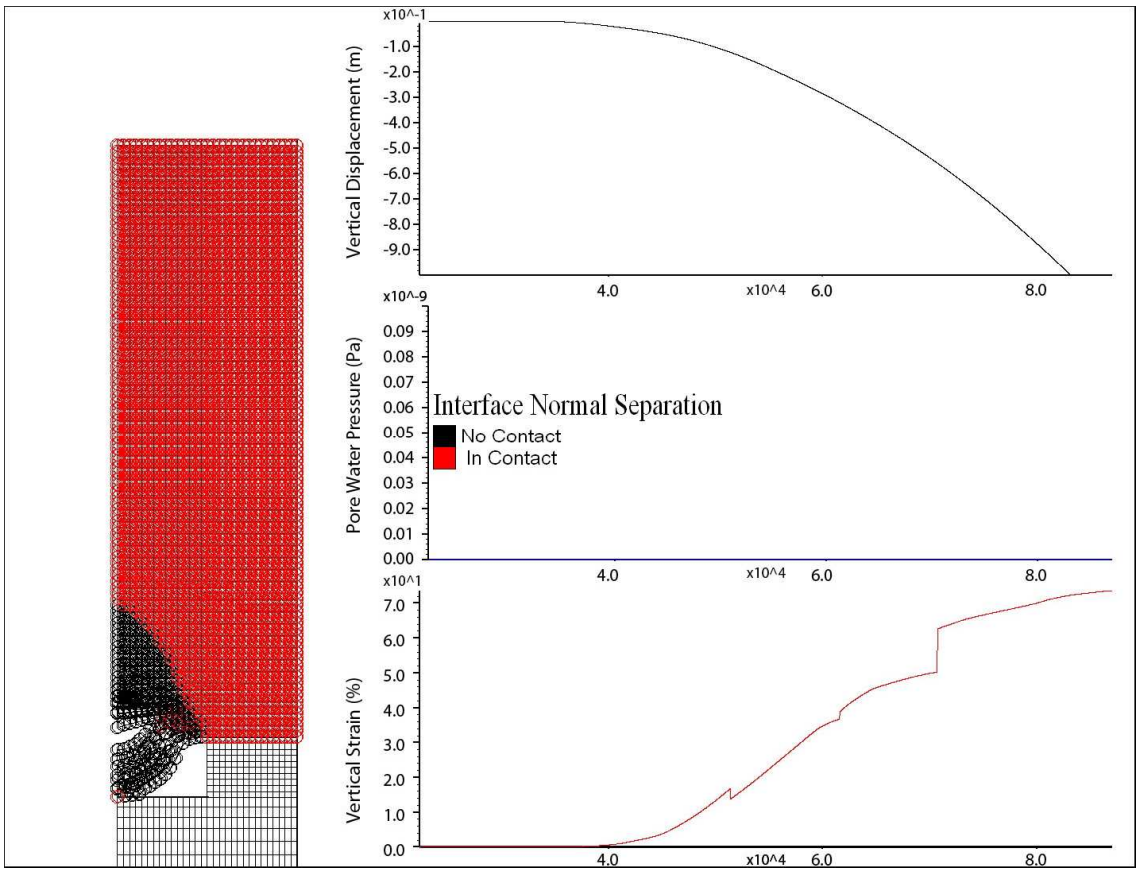

Figure 5.25: Interface separation / tensile failure within the model for a bedding plane spacing of 0.5 m. Model parameters - Excavation 2 m wide, 1 m high; GSI 10.

It can also be observed that there is a zone of tensile yielding that extends above this region higher into the rock mass up to approximately 2 m above the original excavation roof. This is characterised by a zone where delamination of the strata is occurring which can be seen on the normal separation plot (Figure 5.25) for this model as the interfaces separating the beds are no longer in contact even though the displacements are too small to be directly observed on plots of the model mesh. This indicates that as the excavation width increases, so too does the height to which damage in the rock mass occurs (where damage in this case describes tensile yielding of the intact rock and tensile delamination of the bedding planes between the strata). This zone corresponds to a region in a tensile stress state within the rock mass which can be seen in the plot of the maximum principal stress for this model (see Figure 5.26). Conversely the zone of shear yielding forms at the point within the model where there is a very high stress gradient from tensile to compressive stress above the excavation roof / mine pillar intersection.

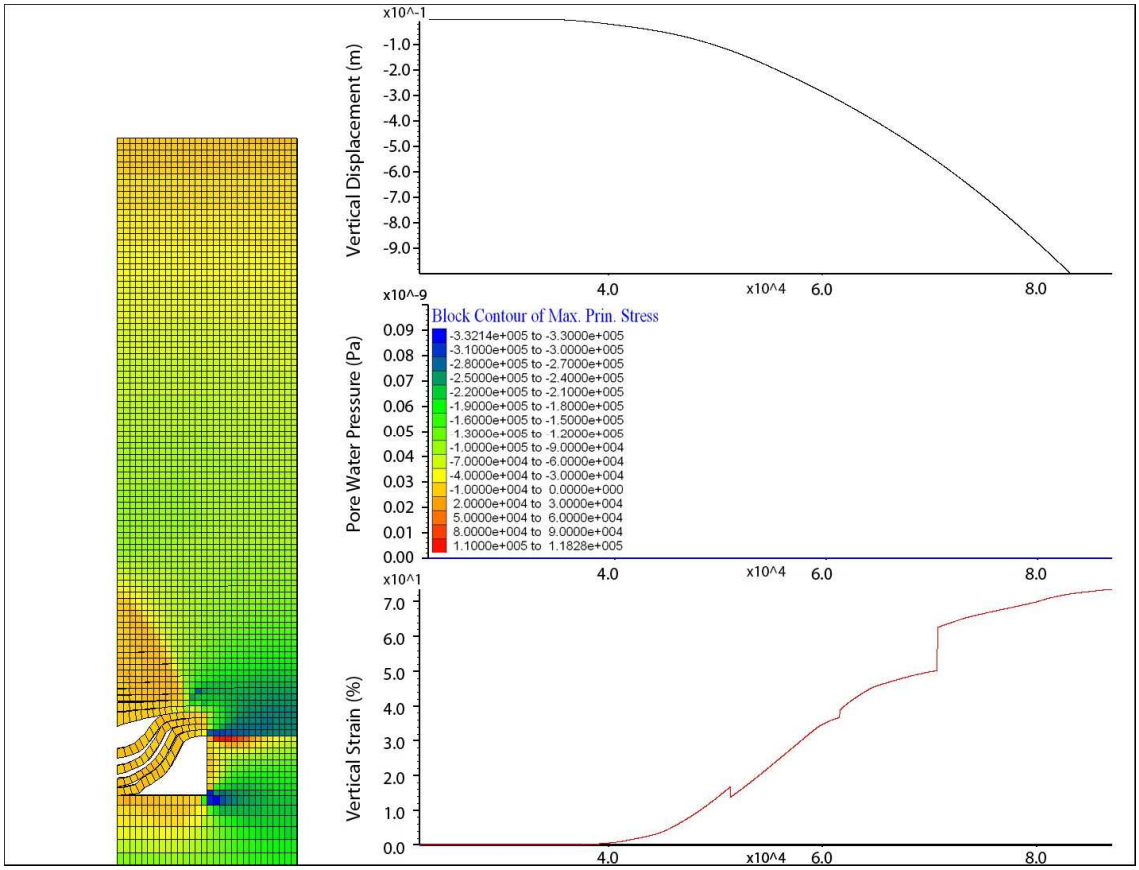

Figure 5.26: Maximum principal stress contours (Sigma 3) within the model for a bedding plane spacing of 0.1 m. Model parameters - Excavation 2 m wide, 1 m high; GSI 10.

In this instance the median principal stress plot (See Figure 5.27) is also of interest as it demonstrates that the deformed but as yet non-collapsed roof strata (the first two strata currently forming the excavation roof) are in a compressive stress state whereas the strata above them are in tension and are undergoing or have undergone tensile delamination. From observation of the interface normal failure plot it can also be seen that the strata in compression are still in contact with the "abutments" of the underlying collapsed strata and it is this which appears to be causing the compressive stress concentrations in these strata in this case. This is significant as these compressive stress concentrations are known to cause the shear failure at the ends of the roof strata leading to roof strata collapse and the progression of failure. This plot appears to capture the stress state that contributes to that mechanism in progress.

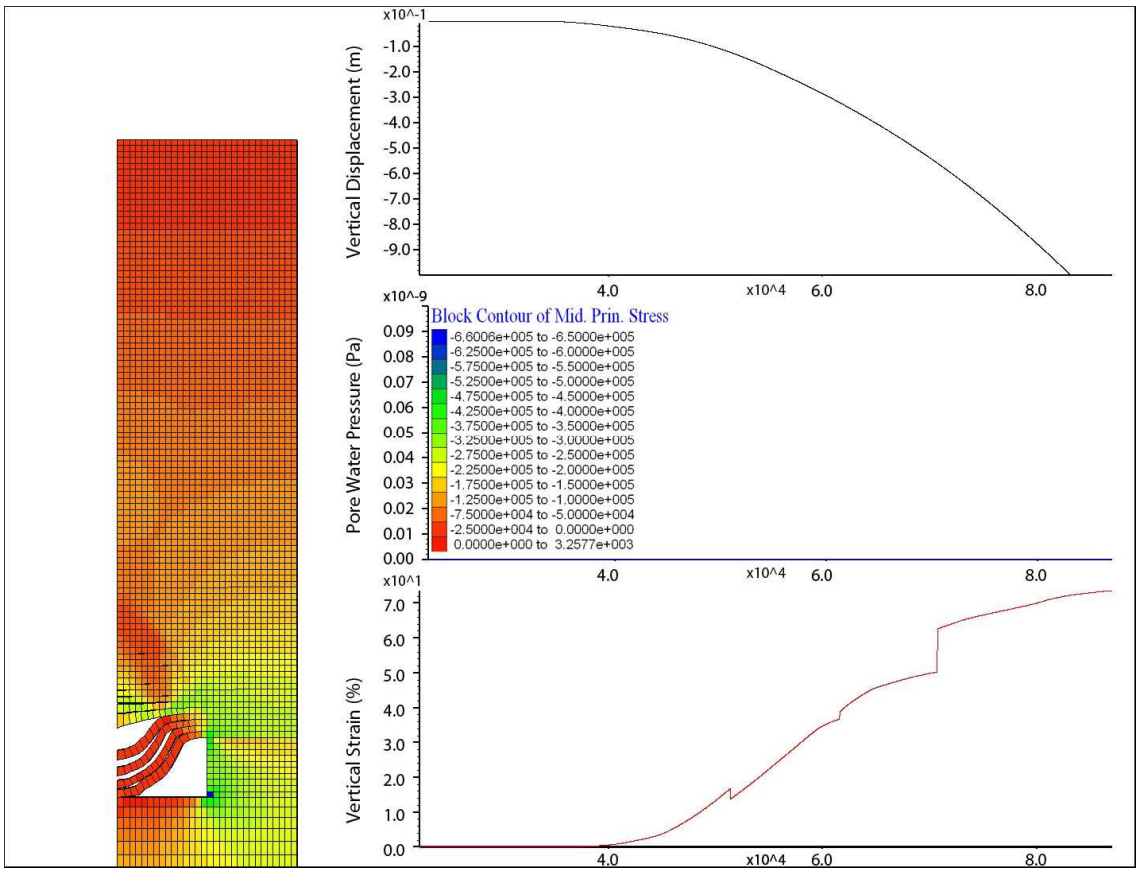

Figure 5.27: Median principal stress contours (Sigma 2) within the model for a bedding plane spacing of 0.1 m. Model parameters - Excavation 2 m wide, 1 m high; GSI 10.

5.7.3 Model: 0.1 m Bedding Plane Spacing, 3 m Excavation Width, 1 m Excavation Height, GSI 10

In the following model, the excavation height and rock mass strength properties have been kept constant, however the width of the excavation has been increased to 3m. The plot of yield state (Figure 5.28) again indicates that significant yielding has occurred and that collapse of roof strata into the void has occurred. In this model the first 15 strata have collapsed into the void and the zone of tensile failure extends vertically approximately 5 m into the rock mass over the excavation centreline (marked by the model boundary). This is approximately 3 m higher than that displayed in the previous model. The zone of shearing marking the failure of the roof strata over the pillar / excavation interface has extended up to 2.5m (measuring the vertical height) into the rock mass. An increase of 1.5m over the 2 m wide model and approximately 2.4 m further than occurred in the 1 m wide excavation model. This collapse has occurred immediately upon excavation and it is clear that neither the 2 m nor 3 m wide excavations would be stable in their current form without significant support.

The plot of median principal stress (Figure 5.29) again captures the point within the model where compressive stress concentrations within the roof strata show the progression from delaminated but stable roof strata to failed collapsed strata below. Again this zone of compressive stress concentration appears to mark the zone where shear failure of the roof strata is actually occurring with those roof strata below this zone already having yielded in shear and those above the upper boundary of this zone (which is a region of tensile stress) having undergone tensile delamination.

As such it would appear that there is a "stress front" that runs vertically through the rock mass above the excavation characterised by an initial zone of tensile stress leading to delamination of the roof strata and associated sagging. As this collapse progresses the tensile stress state is replaced by a zone of compression causing shear failure to occur leading to collapse and the "stress front" then progresses further upwards into the rock mass. It is possible that as the effective span decreases with vertical progression of the yielding and then failure, the tensile and compressive stresses decrease to a point that does not exceed the strength of the rock mass causing a halt in the upward progression of failure.

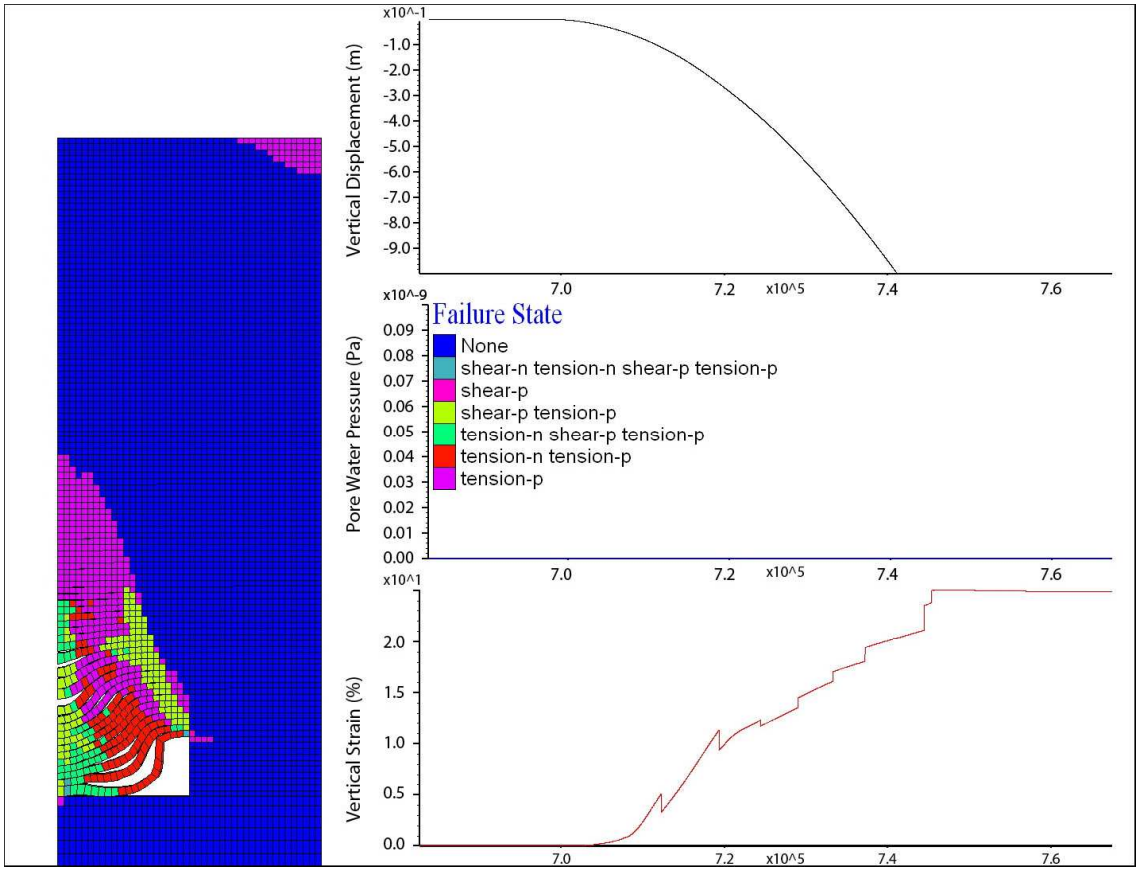

Figure 5.28: Failure state within the model for a bedding plane spacing of 0.1 m. Model parameters (3 m wide excavation, 1 m high excavation, GSI 10).

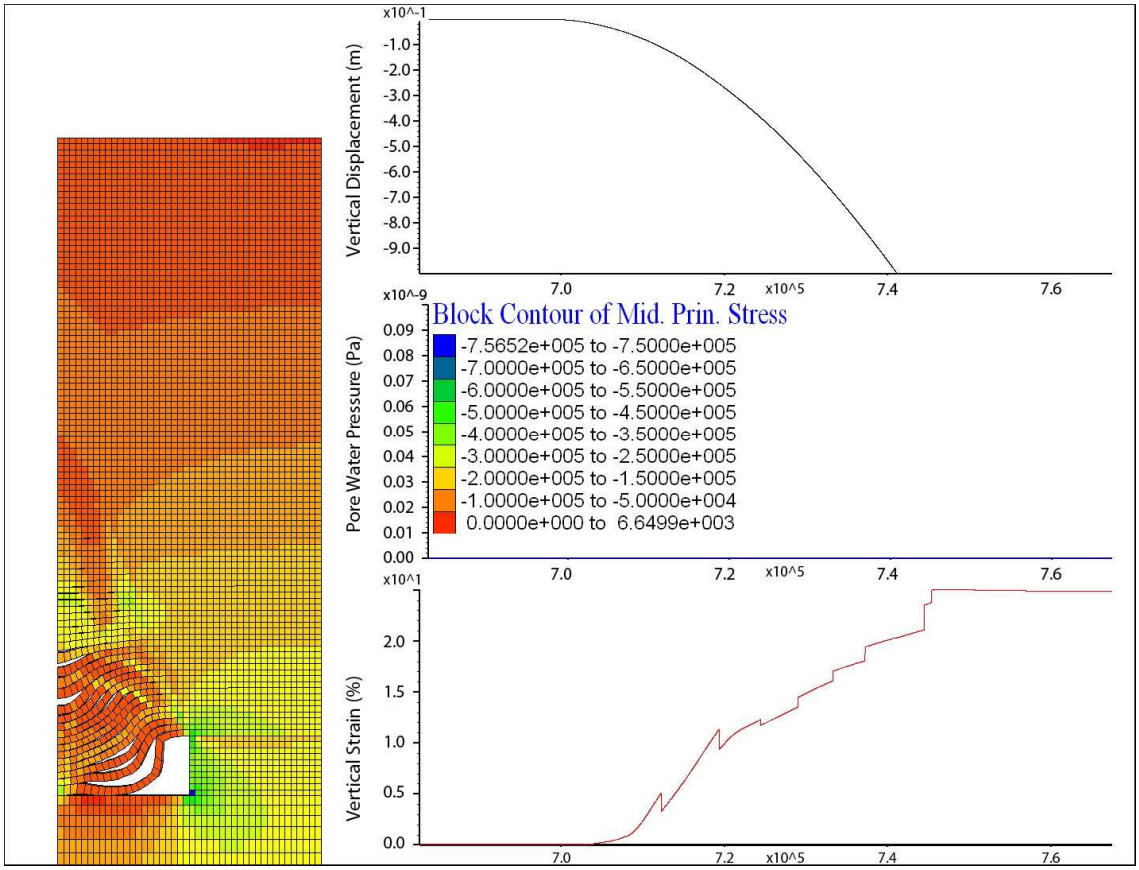

Figure 5.29: Median principal stress contours (Sigma 2) within the model for a bedding plane spacing of 0.1 m. Model parameters - Excavation 3 m wide, 1 m high; GSI 10.

5.7.4 Section Conclusions

The variation in excavation width is shown to have a very significant impact on the stability of the excavation roof, much higher than that which was initially indicated in the phase 1 modelling study. As such it would appear that this is a very significant parameter in excavation stability and also the height to which the failure of the roof strata propagates upwards into the rock mass overlying the excavation.

5.8 Effect of Variable Excavation Height within a Bedded Rock Mass on the Stability of Mine Voids

The variation in excavation height of the mine void potentially has implications for the stability of the excavation as this will affect the distribution of stress within the rock mass. Here it is intended to investigate this potential effect on mine void roof stability for a given set of rock mass strength and stiffness properties, a given stress state (affected by pore water pressure and rock mass density) and for varying bedding thickness / bedding plane separation values. It should be noted that in all examples here the pillar is assumed to be stable as it is the effect on roof stability that is investigated.

Another factor of interest is that empirical methods of estimating the height of void migration are related to the height of the excavation within the seam. This observation is based on empirical data suggesting that voids migrate to a height equal to a maximum of ten times the worked thickness of the coal seam (Bell, 1975; Bell *et al.*, 1988; Healy and Head, 1984). According to some authors (Bell, 1975; Bell *et al.*, 1988; Attewell and Taylor, 1984; Fernando, 1988), this value is overly conservative and they suggest that it is uncommon to find voids migrating to more than 6 times the worked seam thickness, and that a value of 8 times the worked thickness of the seam is a more realistic maximum extent of void migration. It is likely that the primary effect on the height of void migration is due to the increased space within the workings to accept bulked debris; however as stated above, a change in the excavation geometry will alter the stress field within the rock mass which will potentially have implications for stability. In the following modelling examples, the rock mass strength and stiffness is kept constant (GSI value of 10), the excavation width is kept constant at 3 m and the excavation height is varied from 1 to 3 m in 1 m increments.

The yield state of the rock mass above the excavations is shown in Figure 5.30. It can be observed that the pattern of yielding for all three excavation heights is virtually identical forming a wedge of tensile yielding which extends approximately 5 m into the rock mass above the excavation roof. In all cases the zone of tensile failure can be observed to be separated into two regions. Those that are yielding in tension at the present time (zones marked as tension-n) and those that have yielded in tension in the past (tension-p). The region where the zones are currently yielding in tension are associated with roof strata that have undergone delamination and visible sagging as can be seen by the deformation of the mesh and the loss of contact between interfaces as shown in Figure 5.31. It can be seen that this failure is associated with a region where the tensile stress has reduced (Figure 5.32, Figure 5.33) which is assumed to be due to the yielding / deformation causing stress relaxation. The tensile yield zones above this (tension-p) are associated with delamination (which can be seen by observing Figure 5.31), however there is only very limited deformation of the strata and as such they are currently stable. It is within these stable strata that the tensile stress can be seen to be at a maximum within the rock mass over the excavation which reaches a peak value of approximately 50 kPa for all excavation heights shown here. To assist in visualising the relation between yield state of the model and the stress state, a plot combining the yield

state and the plots of maximum, median and minimum principal stress have been combined into a single plot (see Figure 5.33).

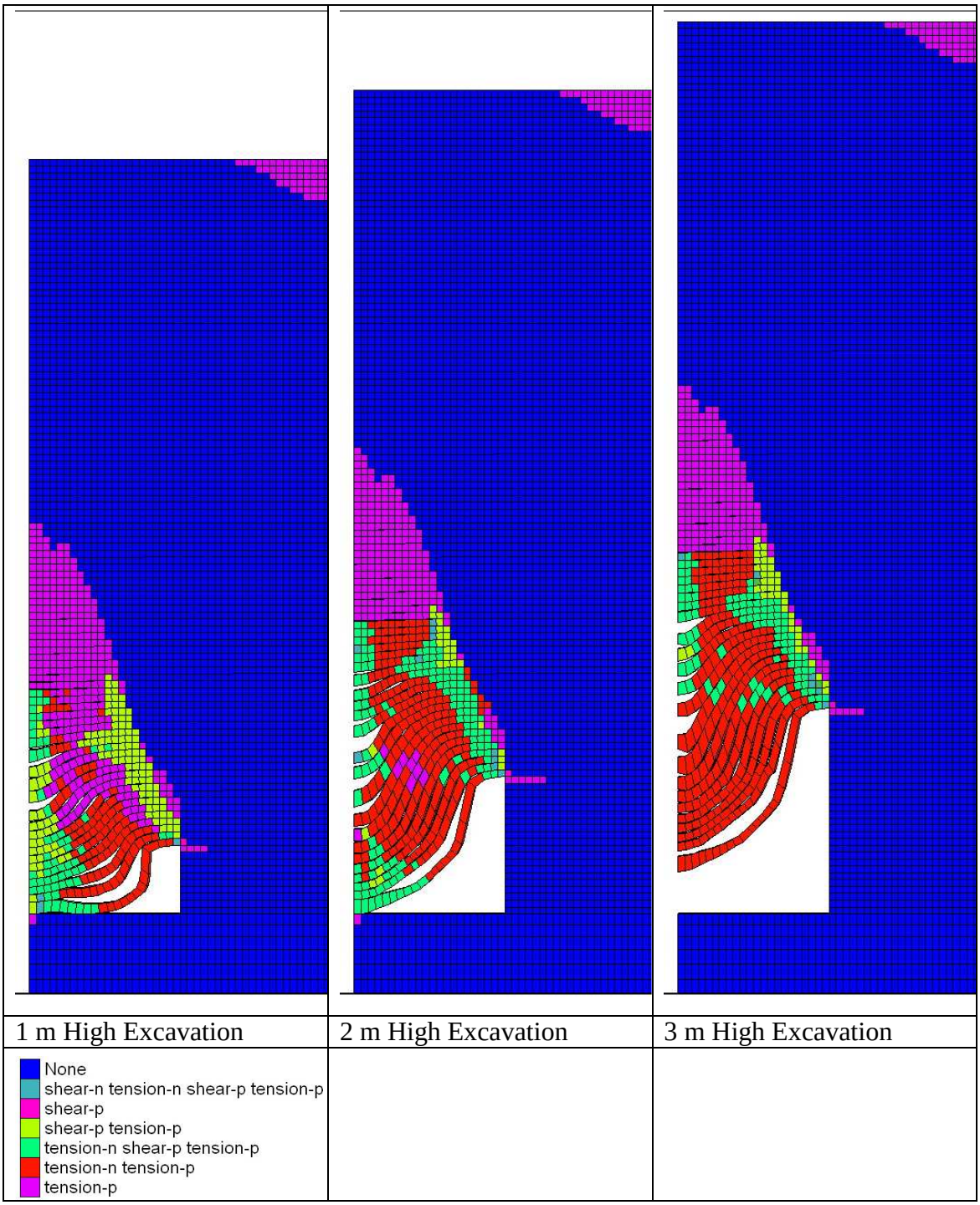

Figure 5.30: Failure state within the model for a bedding plane spacing of 0.1 m. Model parameters (3 m wide excavation, 1 m to 3 m high excavation, GSI 10).

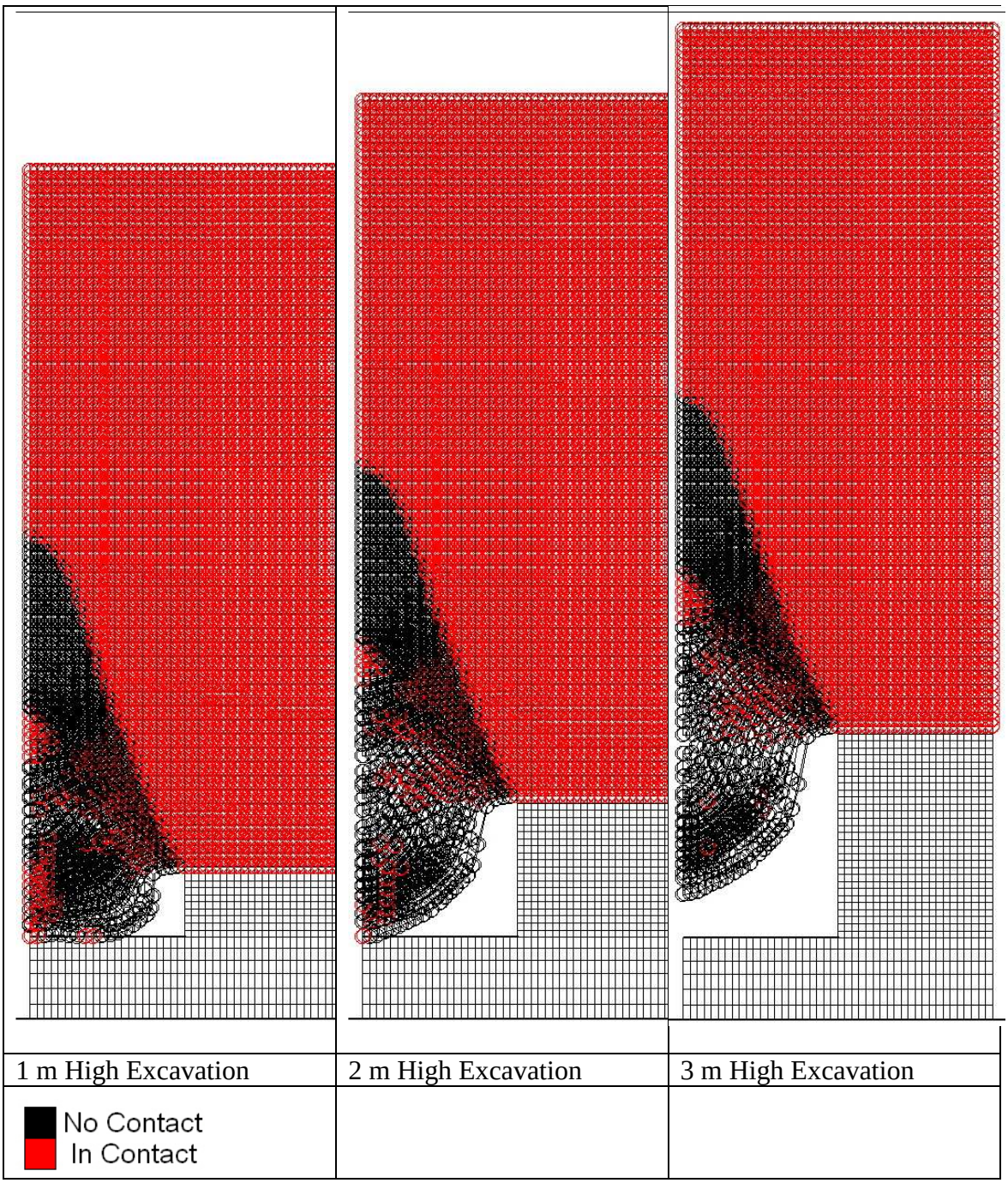

Figure 5.31: Interface separation / tensile failure within the model for a bedding plane spacing of 0.5 m. Model parameters - Excavation 3 m wide, 1 to 3 m high; GSI 10.

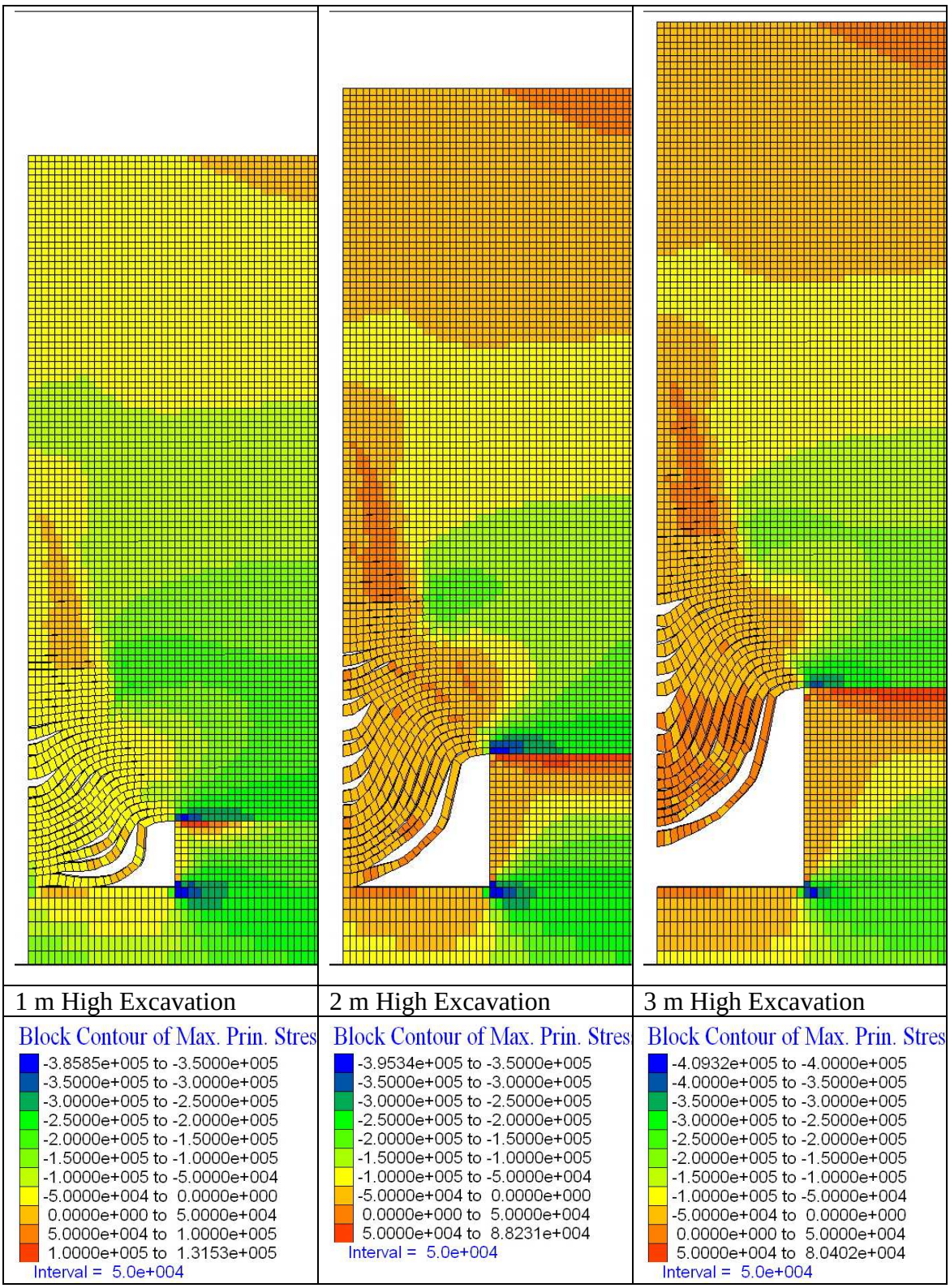

Figure 5.32: Maximum principal stress contours (Sigma 3) within the model for a bedding plane spacing of 0.1 m. Model parameters - Excavation 3 m wide, 1 to 3 m high; GSI 10.

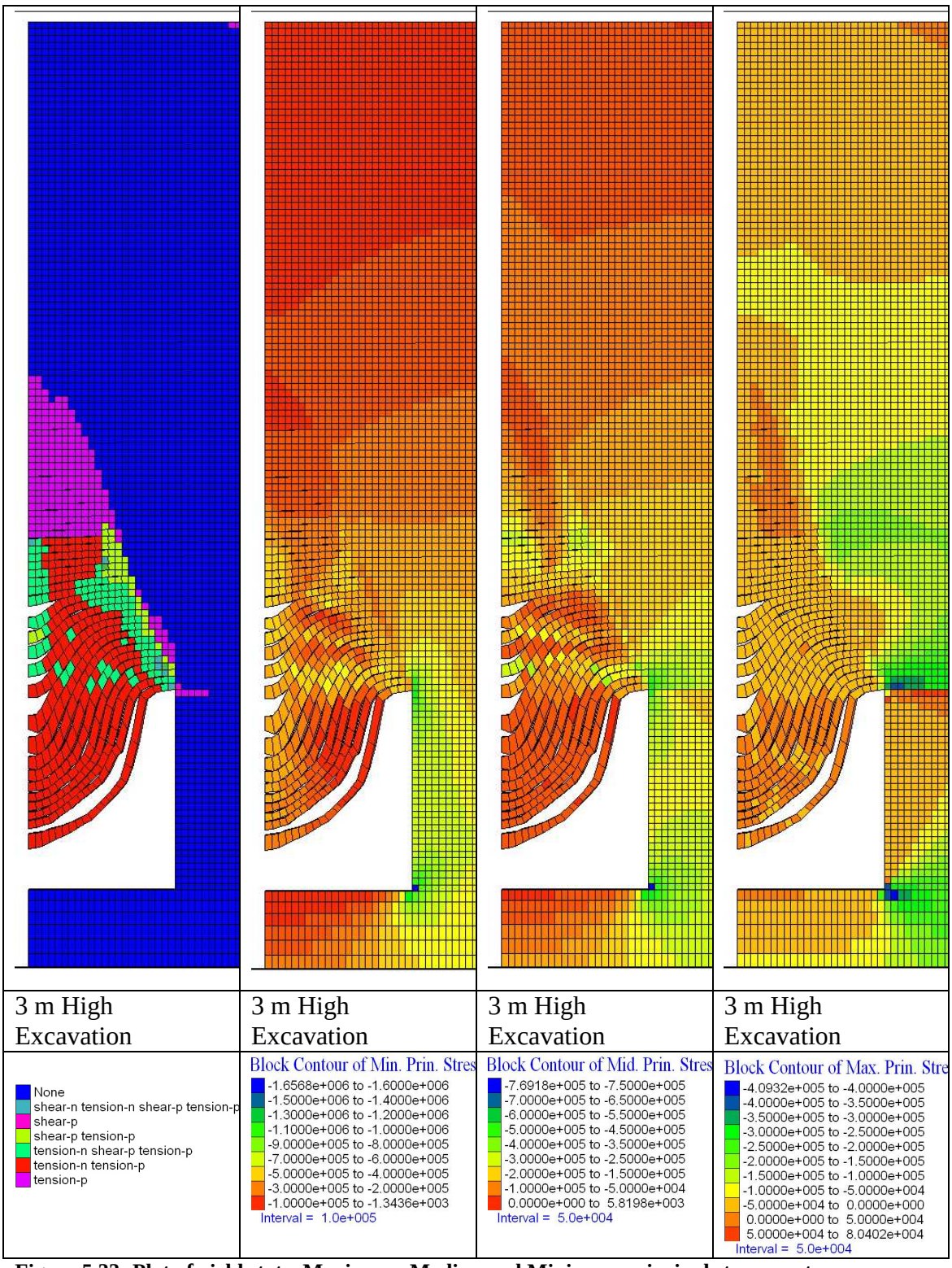

Figure 5.33: Plot of yield state, Maximum, Median and Minimum principal stress contours.

The roof strata that have collapsed are in all cases marked by a band of shear yielding at the point closest to the intersection with the mine pillar. As per previous modelling it is at this point that compressive stresses reach their peak value of approximately 1.6 MPa (see Figure 5.34) so it is unsurprising that shear yielding initiates here. This band of shearing is associated with a thin band of reduced compressive stress which runs diagonally into the rock mass up from the intersection of the roof strata with the mine

pillar which can be seen in the plot of maximum principal stress in Figure 5.34 and its relation to the yield state can be observed in Figure 5.33. It is not readily apparent whether this stress reduction is a result of the yielding or if the presence of this low stress zone acts to increase the stress gradient in the region which in turn is the cause of the shear yielding.

As mentioned in the results relating to variations in excavation width, the upper portion of this zone of shearing is associated with a region of increased compressive stress which is clearly visible in the median stress portion of Figure 5.33 and is a feature of all the model results demonstrated here (see Figure 5.35).

Examination of the yield plot and the interface normal failure plot reveals that for all excavation heights tested the results are similar with virtually identical yield geometry that extends to an equal height into the overlying rock mass. As such it would appear that under the conditions tested here, the height of excavation seems to have very limited effect on the failure of roof strata. It would seem therefore that the main effect of increased excavation height is increasing the volume within the excavation that can accept collapse debris, thus increasing the height to which void migration can occur before bulking would halt it.

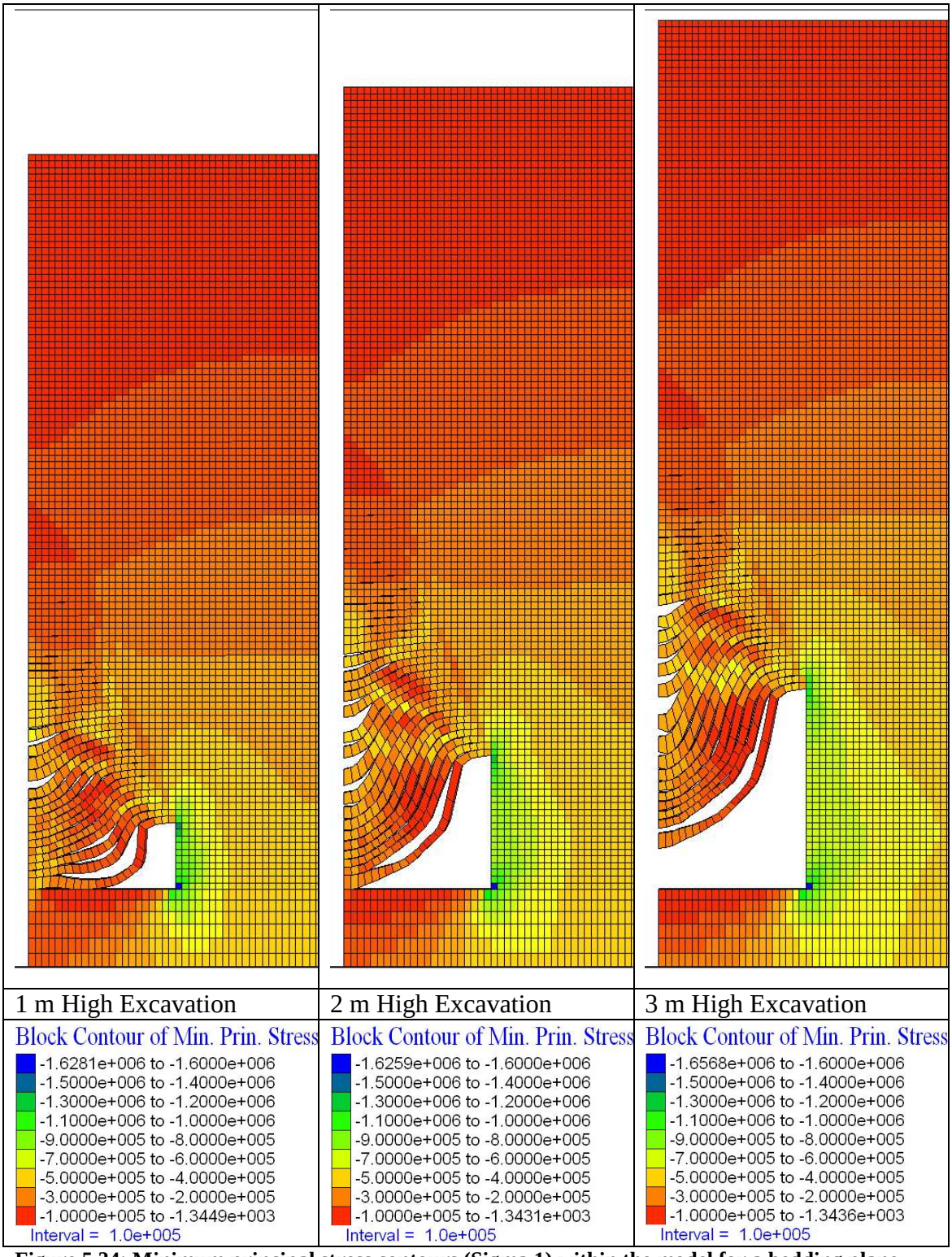

Figure 5.34: Minimum principal stress contours (Sigma 1) within the model for a bedding plane spacing of 0.1 m. Model parameters - Excavation 3 m wide, 1 to 3 m high; GSI 10.

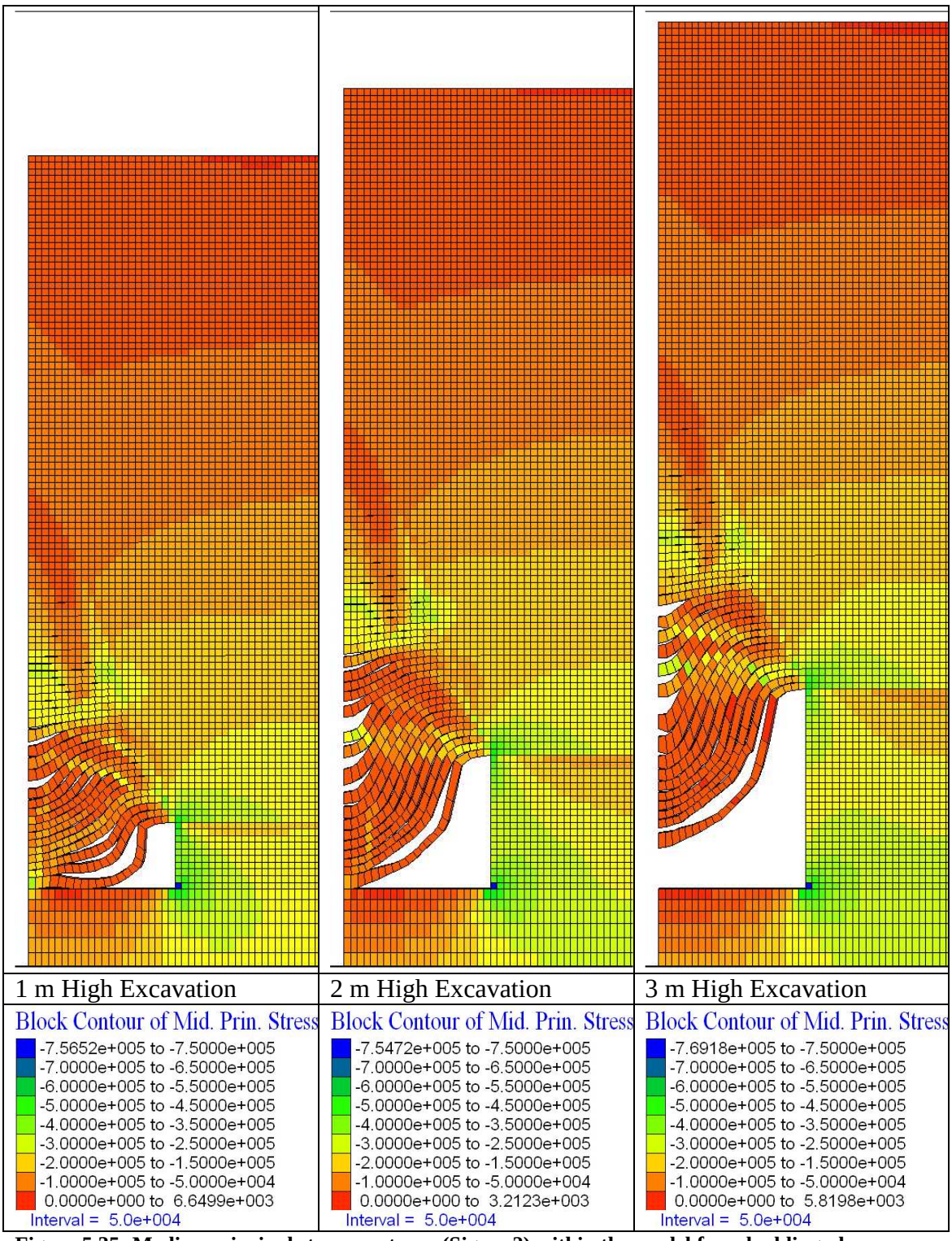

Figure 5.35: Median principal stress contours (Sigma 2) within the model for a bedding plane spacing of 0.1 m. Model parameters - Excavation 3 m wide, 1 to 3 m high; GSI 10.

5.8.1 2 m Excavation Width, Variable Excavation Height

In the following modelling examples, the rock mass strength and stiffness is varied (GSI value from 10 to 60). This variation in the strength and stiffness properties was undertaken in order to identify if there were any effects of the height of excavation on stability that were not observed in the first example above due to the low rock mass

strength leading to the immediate collapse that occurred at all three excavations heights. In these models the excavation width is kept constant at 2 m and the excavation height is varied from 1 to 3 m in 1 m increments. *N.B.* Unlike in the 3 m wide excavation example, in this results section the results are displayed for the level of groundwater table where initial failure occurs within the excavation roof. This allows the effect if any of pore water pressure on the excavation to be observed.

GSI 10

Plots of the minimum and maximum principal stresses are shown in Figure 5.36 and Figure 5.37 where it can be seen that the maximum compressive stress in all cases occurs at the pillar / roof intersection. The maximum compressive stress is approximately the same for all three excavations heights with compressive stresses reaching 1.41, 1.42 and 1.46 MPa in the 1m, 2 m and 3 m high excavations respectively.

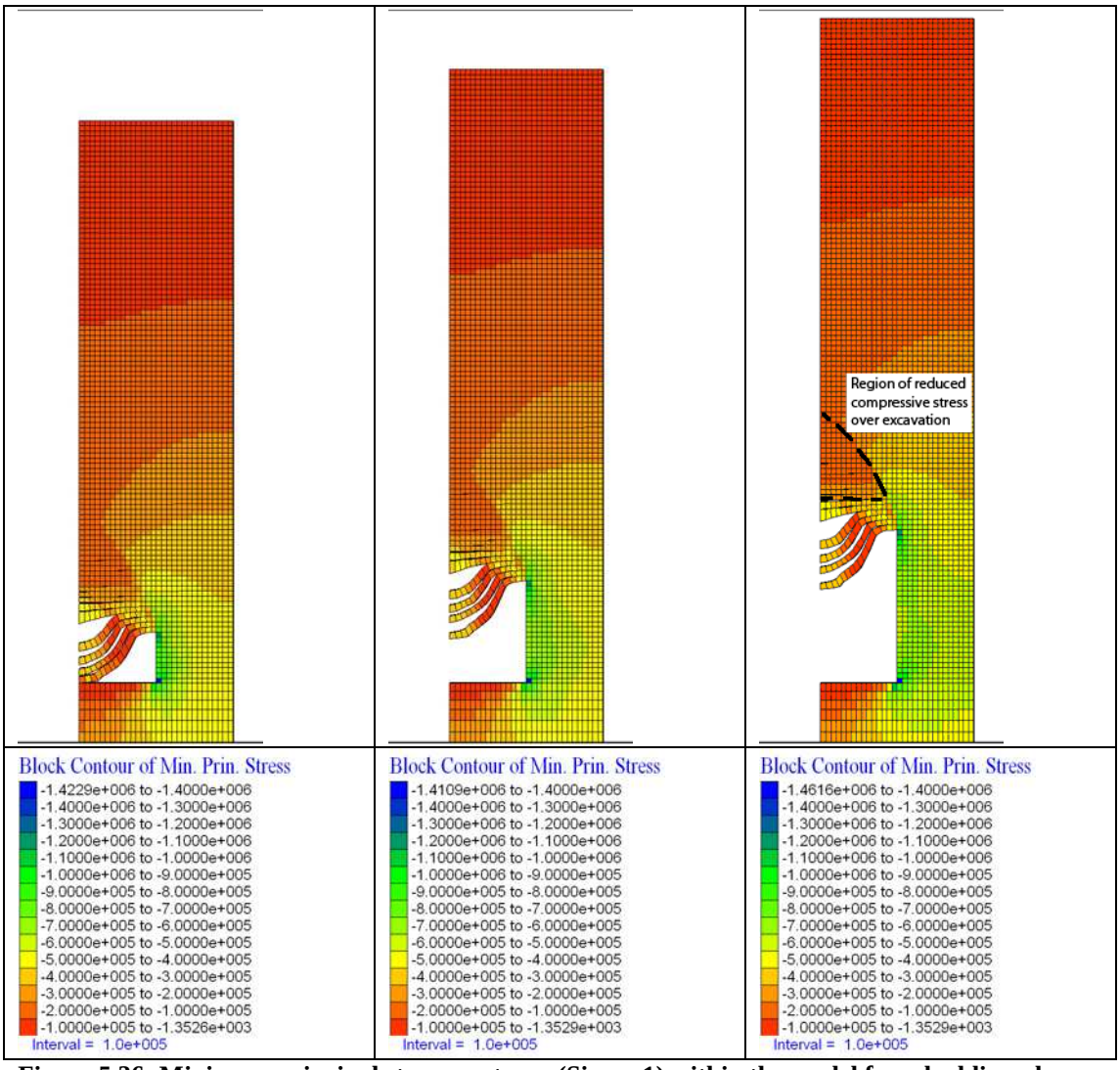

Figure 5.36: Minimum principal stress contours (Sigma 1) within the model for a bedding plane spacing of 0.1 m. Model parameters - Excavation 2 m wide, 1 to 3 m high; GSI 10.

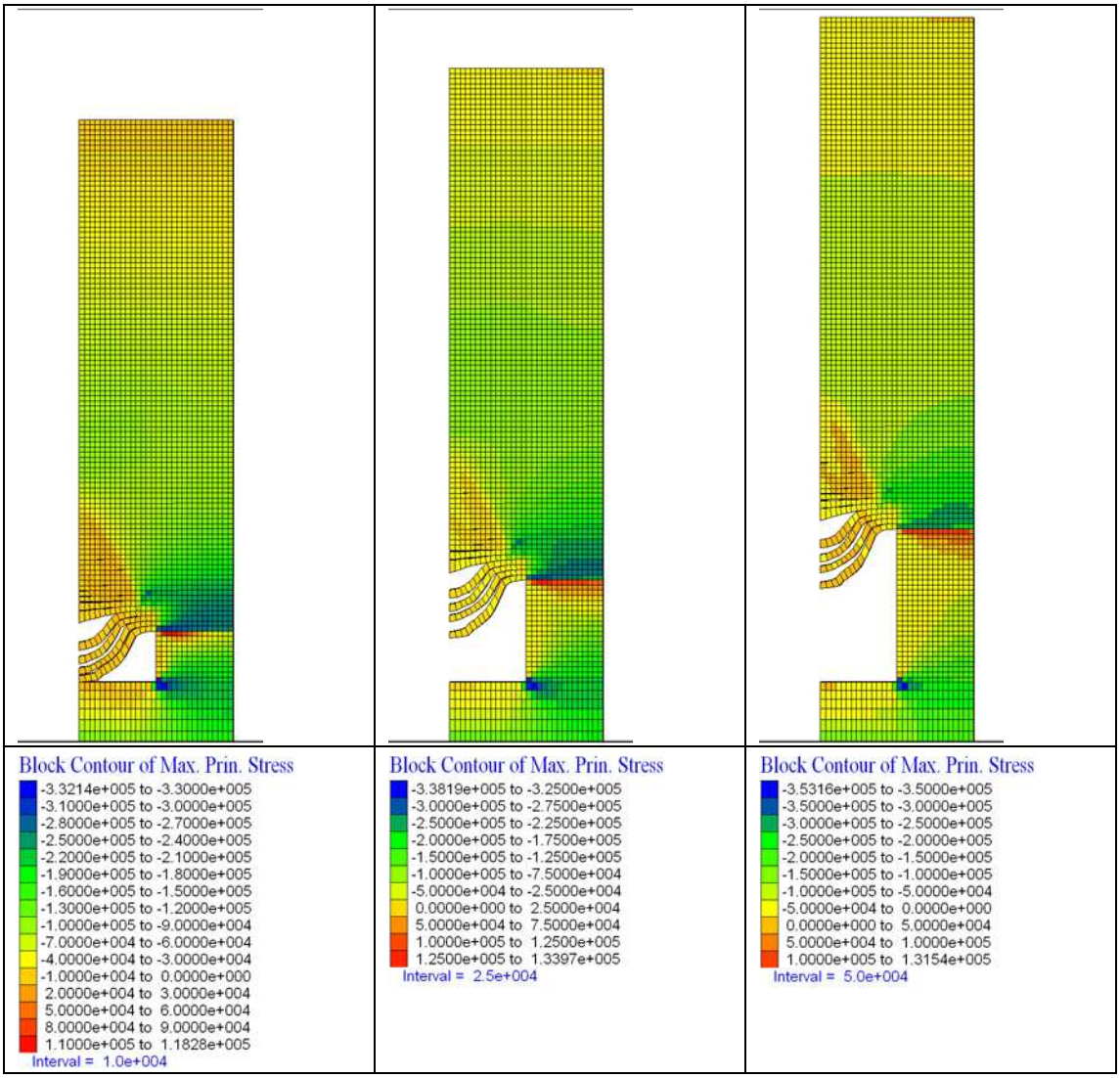

Figure 5.37: Maximum principal stress contours (Sigma 3) within the model for a bedding plane spacing of 0.1 m. Model parameters - Excavation 2 m wide, 1 to 3 m high; GSI 10.

In all three cases it can be seen that compressive stress reduction has occurred over the excavation with the compressive stress lower at a given level within the model for regions over the excavation roof than over the coal pillar. It can be seen that the compressive stress state then increases rapidly at a height level with the excavation within the pillar demonstrated by the high compressive stress gradient in this region indicated by the close spacing of the stress contours. The plot of maximum stress indicates that the region above the excavation roof within the model is in a tensile stress state for all three excavation heights at this rock mass strength with values ranging from approximately 20-50 kPa.

A plot of the yield state of the rock mass above the excavations along with vertical displacement of the roof centre line and pore water pressure in the roof strata is shown in Figure 5.38, Figure 5.39 and Figure 5.40 with heights of 1m, 2 m and 3 m

respectively. In these plots it can be seen that the excavations all show a similar pattern of yielding with a zone of roof failure immediately above the excavation characterised by the tensile delamination and significant visible sagging of the roof strata. This zone is also marked by a zone of shear yielding at the ends of the roof strata within the rock mass above the roof / pillar intersection. Significant shear failure is also occurring within the roof strata at the roof centreline which is likely to represent the formation of a fracture at this point characteristic of snap through failure of the roof strata at this point. The zone of shearing within the roof strata at the excavation / pillar intersection coincides with a region in the maximum stress contour plot where there are very high stress gradients from compression through to tension. For all three excavation heights at this rock mass strength the zone of roof failure extends approximately 0.6 m into the rock mass affecting the first 6 roof strata.

On the yield plot, above the delaminated and sagging roof strata there can be seen a zone of tensile yielding that is not marked by significant visible deformations or shearing which extends approximately 1.5m into the rock mass above the zone of roof failure forming a wedge shape.

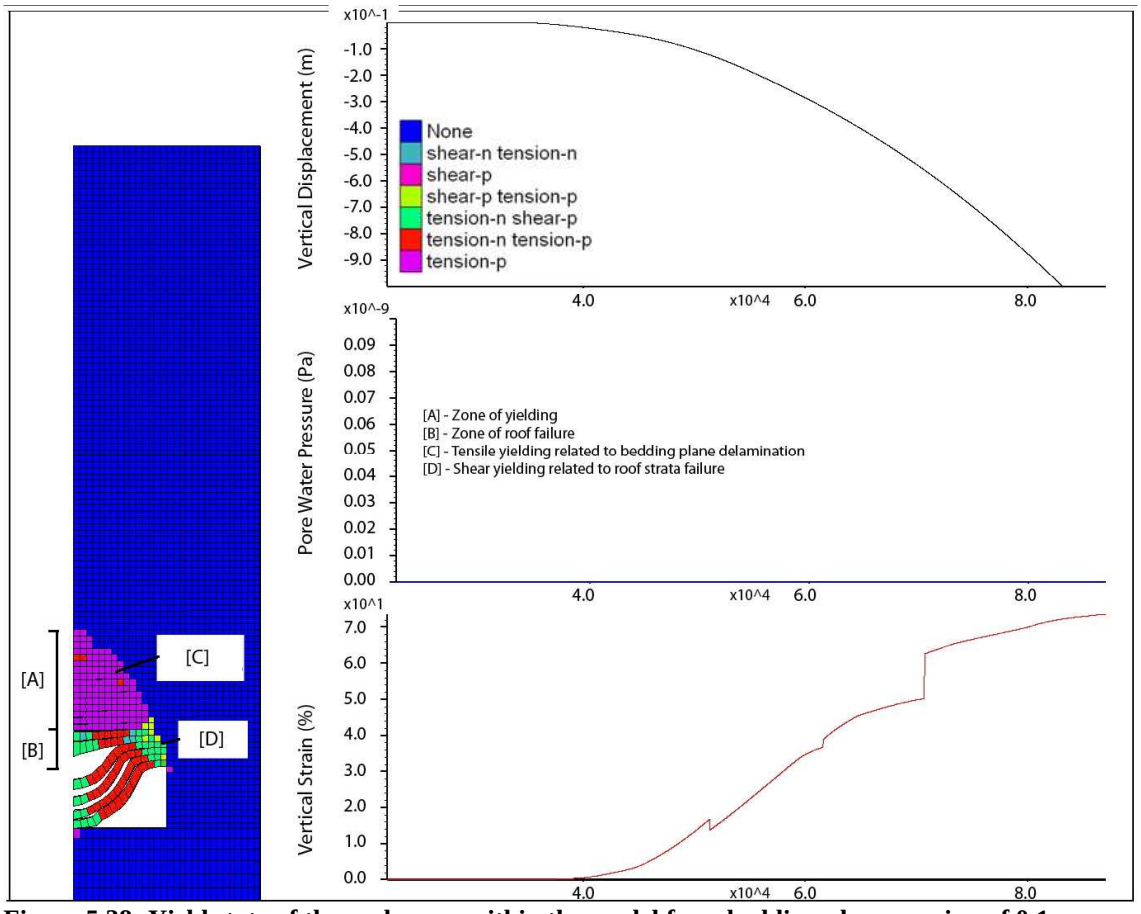

Figure 5.38: Yield state of the rock mass within the model for a bedding plane spacing of 0.1 m. Model parameters - Excavation 2 m wide, 1 m high; GSI 10.

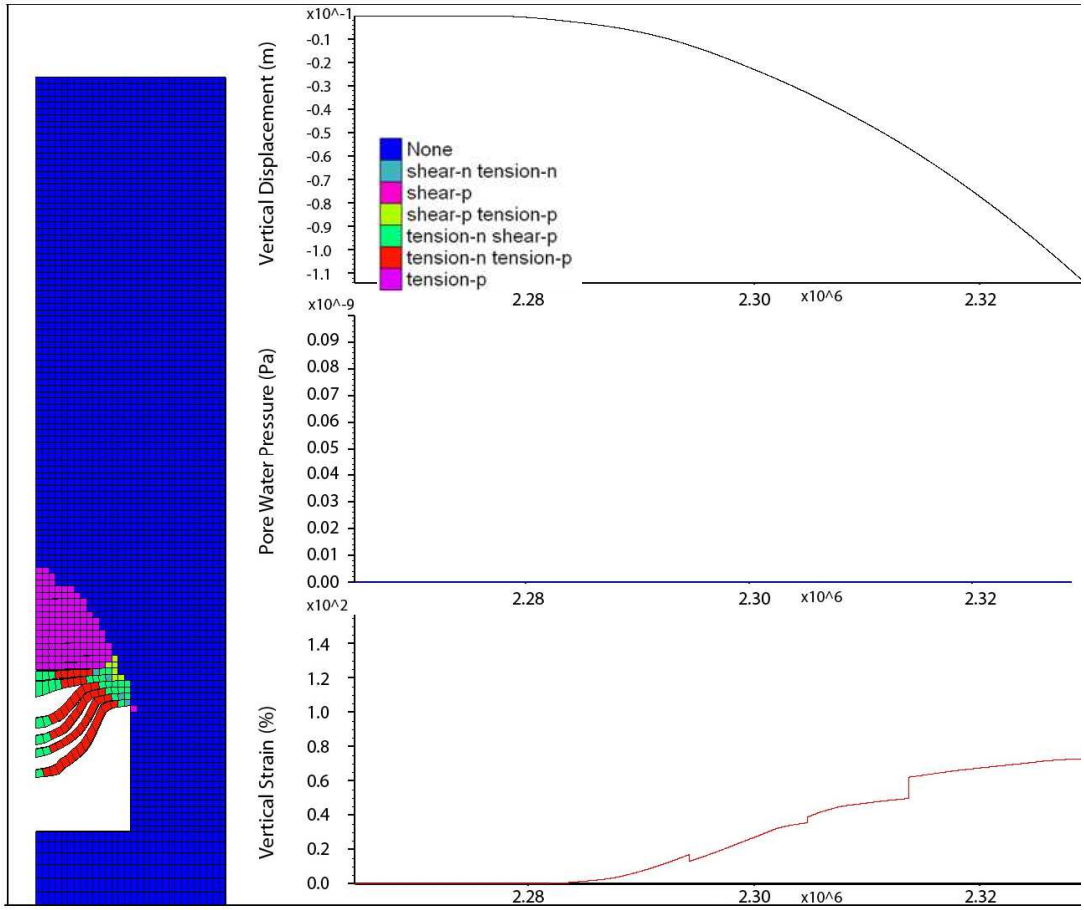

Figure 5.39: Yield state of the rock mass within the model for a bedding plane spacing of 0.1 m. Model parameters - Excavation 2 m wide, 2 m high; GSI 10.

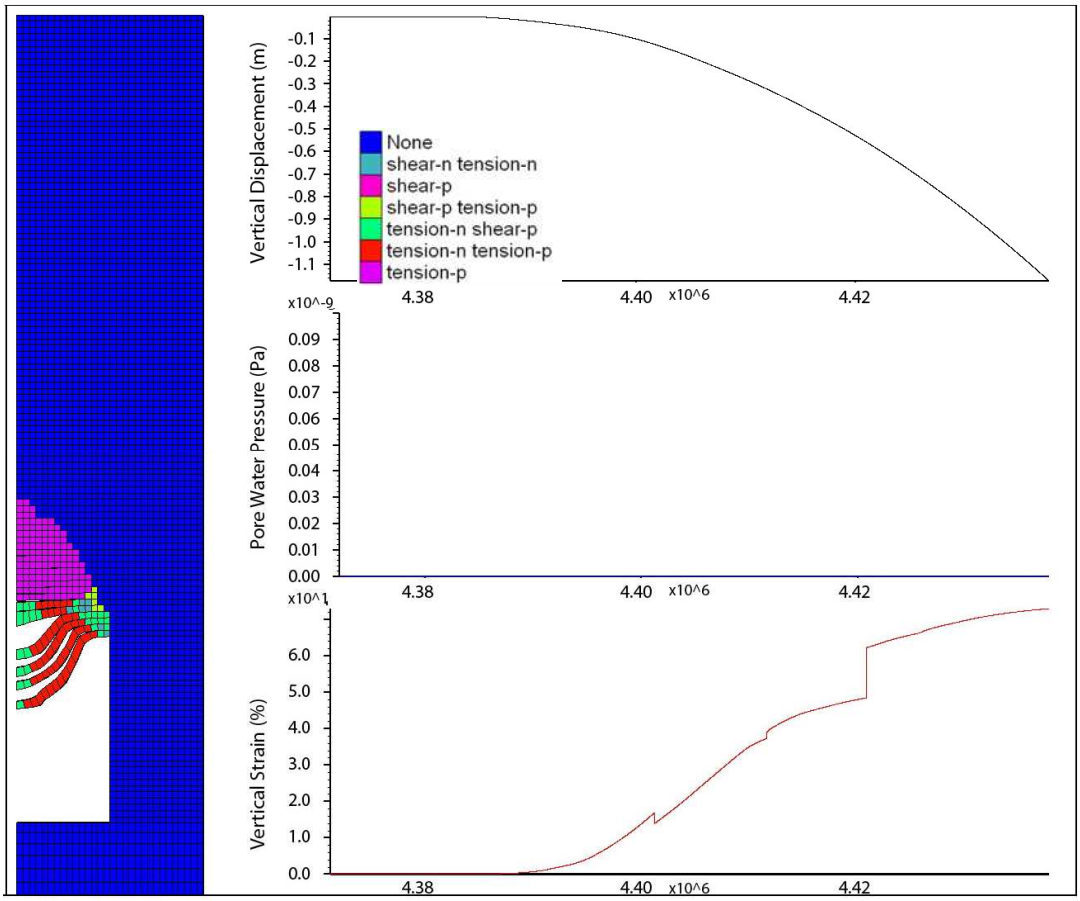

Figure 5.40: Yield state of the rock mass within the model for a bedding plane spacing of 0.1 m. Model parameters - Excavation 2 m wide, 3 m high; GSI 10.

In all three cases it can be observed that the excavation instability is triggered by the excavation of the rock mass before any significant changes in the water table have occurred. As such an excavation with these geometries would have required support to avoid roof failure.

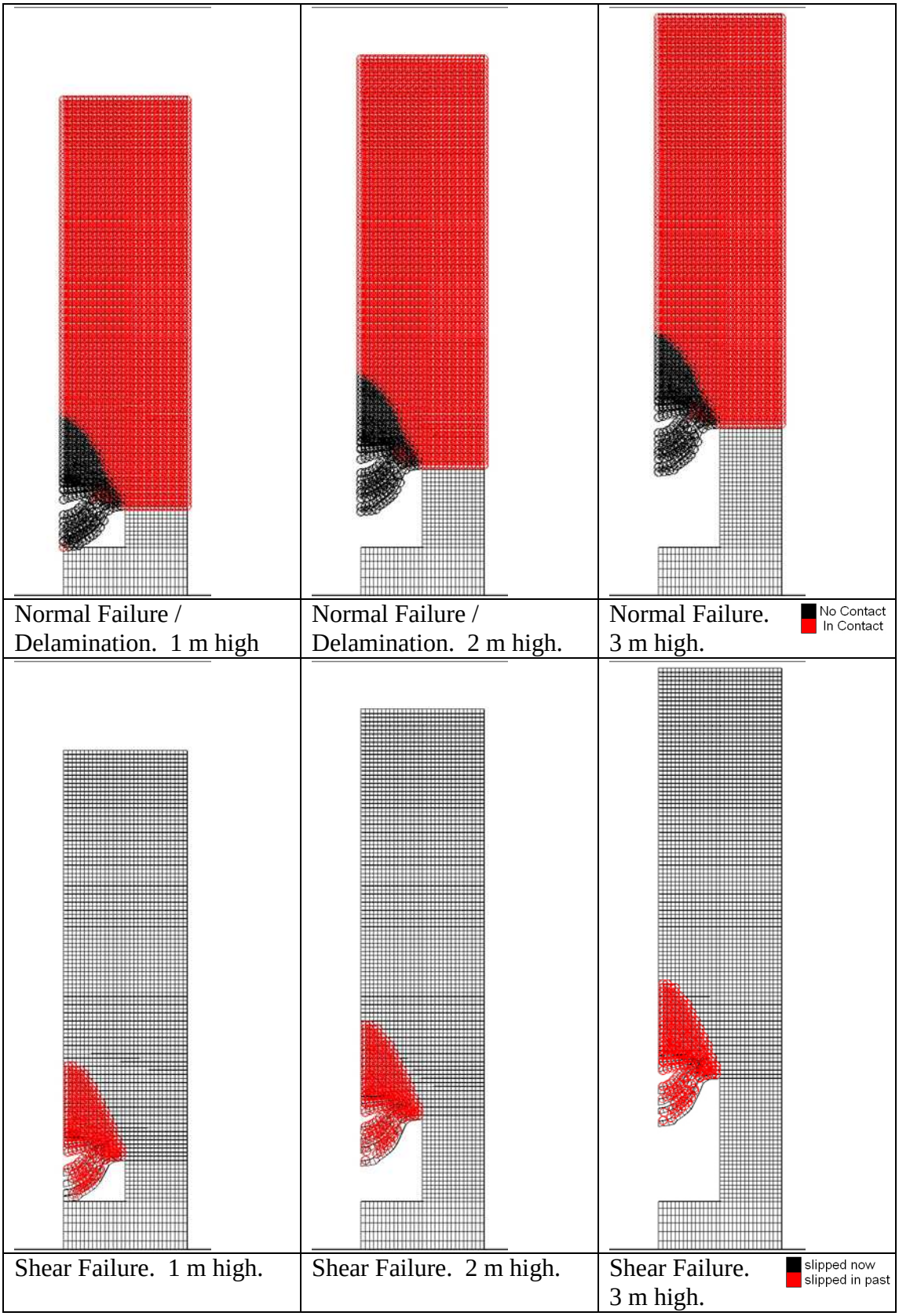

Figure 5.41: Normal and Shear interface failure plots for the rock mass (GSI 10).

Plots of the interface normal and shear failure (see Figure 5.41) show that there is tensile delamination occurring within the rock mass in all of the models which is marked by the loss of contact between interface elements in the plot.

GSI 20

In this results section the rock mass strength has been increased to GSI 20 and as per the previous section, the results are shown at the ground water level where initial failure of the rock mass has occurred. Plots of the minimum and maximum principal stresses are shown in Figure 5.42 and Figure 5.43 where it can be seen that the maximum compressive stress in all cases occurs at the pillar / roof intersection. The maximum compressive stress is approximately the same for all three excavations heights with compressive stresses reaching 1.35, 1.41 and 1.47 MPa in the 1m, 2 m and 3 m high excavations respectively.

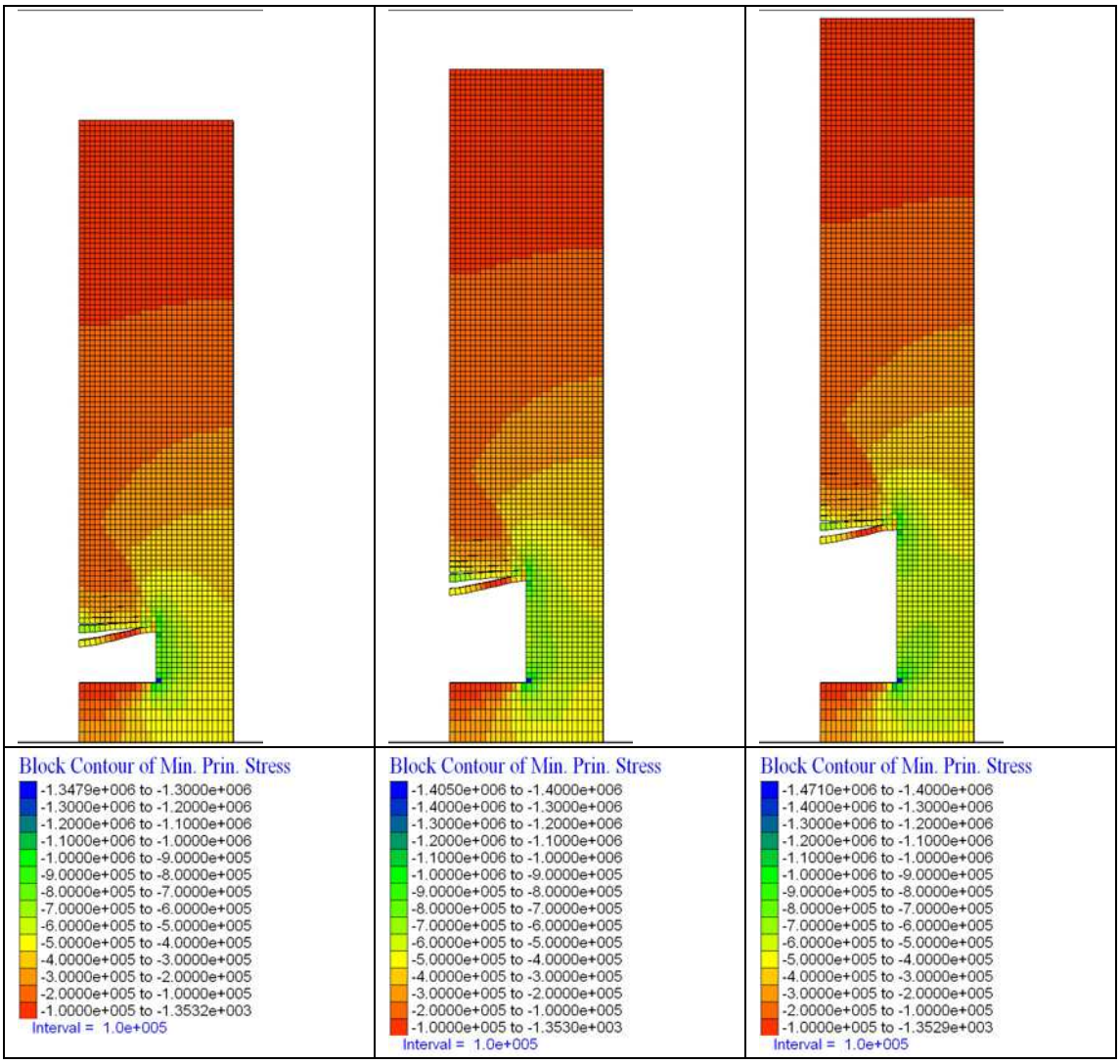

Figure 5.42: Minimum principal stress contours (Sigma 1) within the model for a bedding plane spacing of 0.1 m. Model parameters - Excavation 2 m wide, 1 to 3 m high; GSI 20.

In all three cases it can be seen that compressive stress reduction has occurred over the excavation with the compressive stress lower at a given level within the model for regions over the excavation roof than over the coal pillar and that the width from the roof centreline that this zone extends decreases with increasing height from the excavation roof, essentially forming a wedge of compressive stress relaxation over the excavation. As per the previous modelling at the lower rock mass strength (GSI 10) it can be seen that the compressive stress state then increases rapidly at a height level with the excavation within the pillar demonstrated by the high compressive stress gradient in this region indicated by the close spacing of the stress contours. The plot of maximum stress (Figure 5.43) indicates that the region above the excavation roof within the model is in a tensile stress state for all three excavation heights at this rock mass strength with values ranging from approximately 8-12 kPa. This increase in tensile stress is most likely due to the increase in strength and stiffness properties of the rock mass.

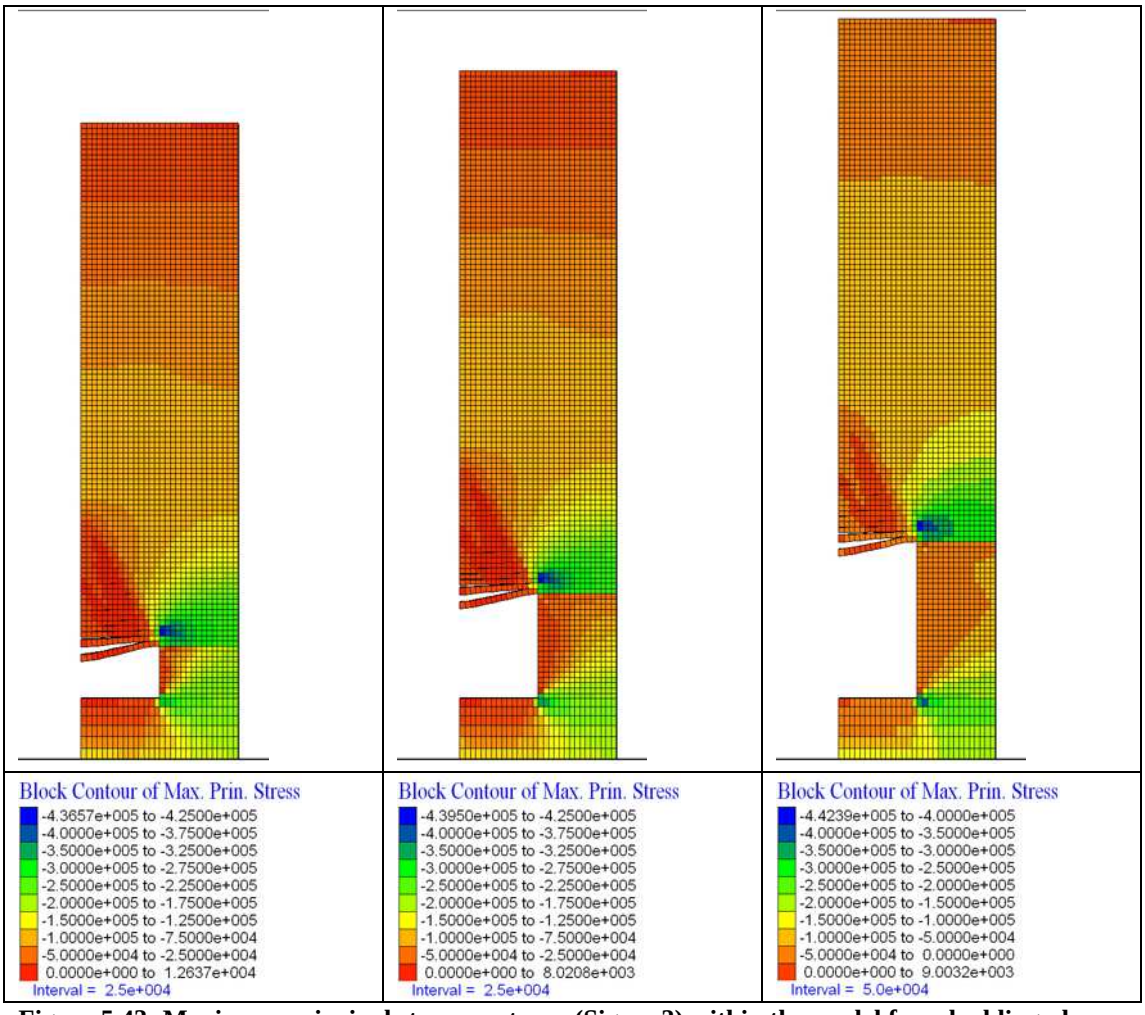

Figure 5.43: Maximum principal stress contours (Sigma 3) within the model for a bedding plane spacing of 0.1 m. Model parameters - Excavation 2 m wide, 1 to 3 m high; GSI 20.

A plot of the yield state of the rock mass above the excavations along with vertical displacement of the roof centre line and pore water pressure in the roof strata is shown in Figure 5.44, Figure 5.45 and Figure 5.46 with heights of 1m, 2 m and 3 m respectively. In these plots it can be seen that the excavations all show a similar pattern of yielding with a zone of roof failure immediately above the excavation characterised by the tensile delamination and significant visible sagging of the roof strata. This zone is also marked by a zone of shear yielding at the ends of the roof strata within the rock mass above the roof / pillar intersection.

Significant shear failure is also occurring within the roof strata at the roof centreline which is likely to represent the formation of a fracture at this point characteristic of snap through failure of the roof strata at this point.
The zone of shearing within the roof strata at the excavation / pillar intersection coincides with a region in the maximum stress contour plot where there are very high stress gradients from compression through to tension. For all three excavation heights at this rock mass strength the zone of roof failure extends approximately 0.2 m into the rock mass affecting the first 3 roof strata, which is a significant decrease on that which occurred for the lower strength rock mass.

On the yield plot, above the delaminated and sagging roof strata there can be seen a zone of tensile yielding that is not marked by significant visible deformations or shearing which extends approximately 1.8m into the rock mass again forming a wedge shaped zone of failure above the excavation. The height of this zone however remains roughly equal to that for the lower rock mass strength.

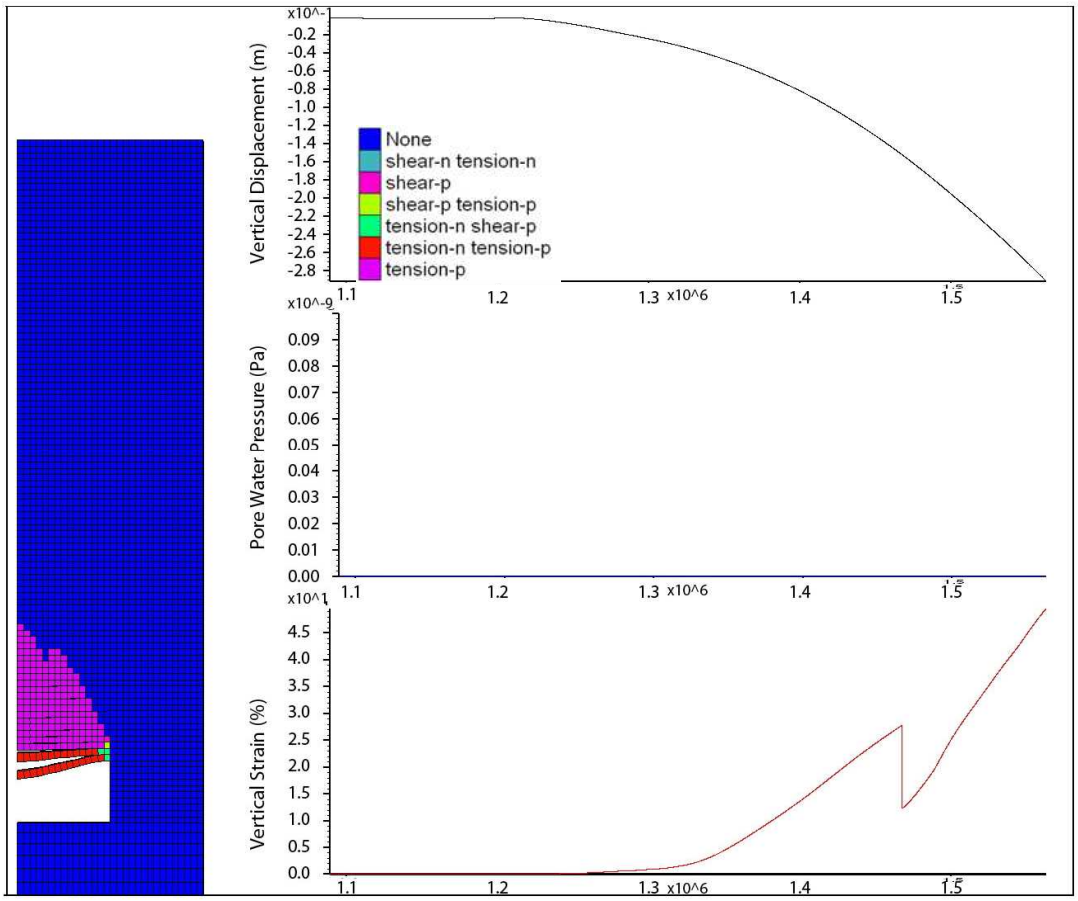

Figure 5.44: Yield state of the rock mass within the model for a bedding plane spacing of 0.1 m. Model parameters - Excavation 2 m wide, 1 m high; GSI 20.

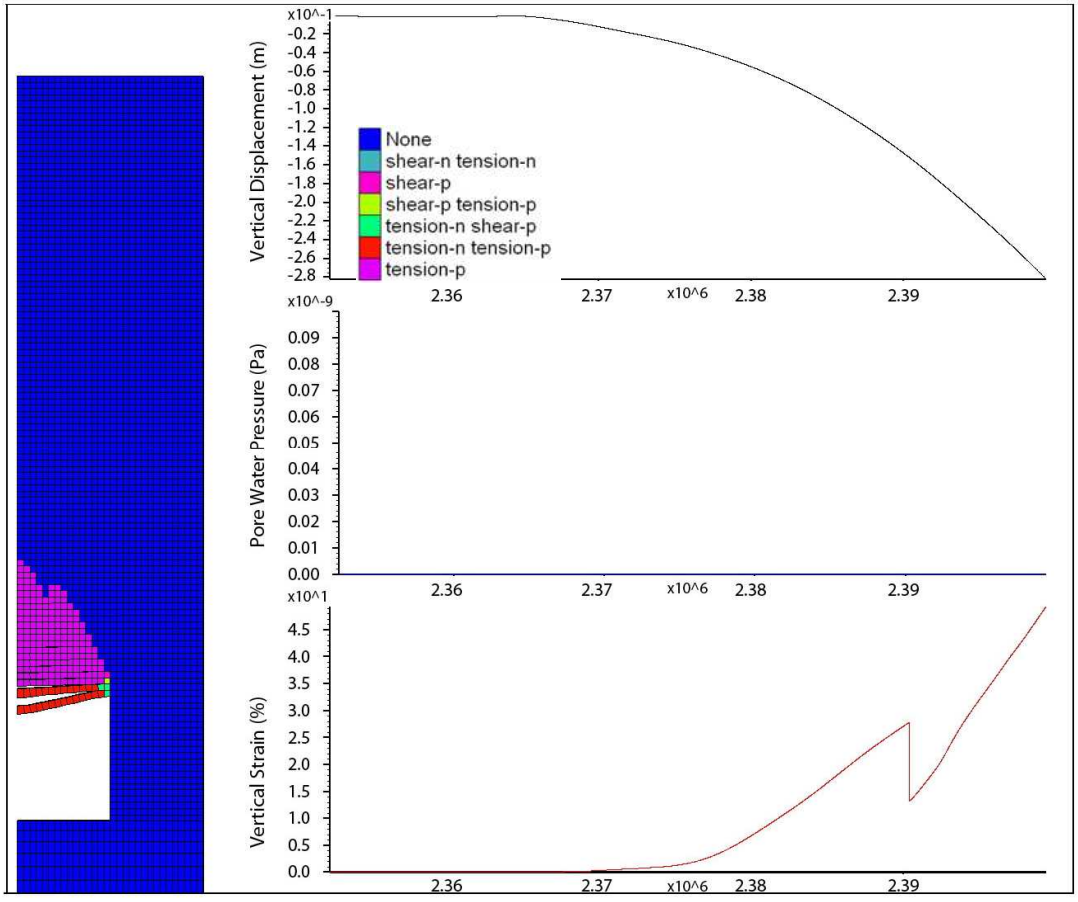

Figure 5.45: Yield state of the rock mass within the model for a bedding plane spacing of 0.1 m. Model parameters - Excavation 2 m wide, 2 m high; GSI 20.

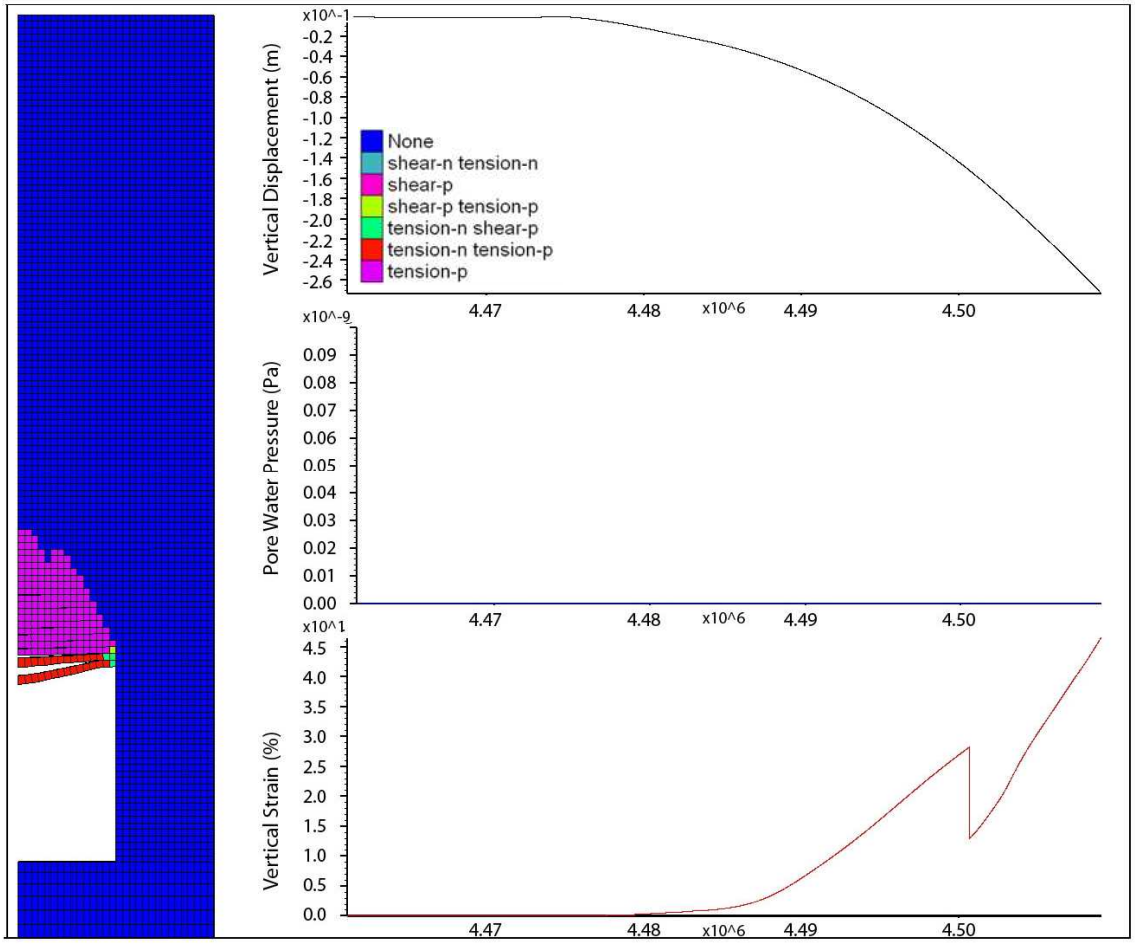

Figure 5.46: Yield state of the rock mass within the model for a bedding plane spacing of 0.1 m. Model parameters - Excavation 2 m wide, 3 m high; GSI 20.

As per the rock mass with a GSI value of 10, in all three cases it can be observed that the excavation instability is triggered by the excavation of the rock mass before any significant changes in the water table have occurred

Plots of the interface normal and shear failure (Figure 5.47) show that there is tensile delamination occurring within the rock mass in all of the models which is marked by the loss of contact between interface elements in the plot.

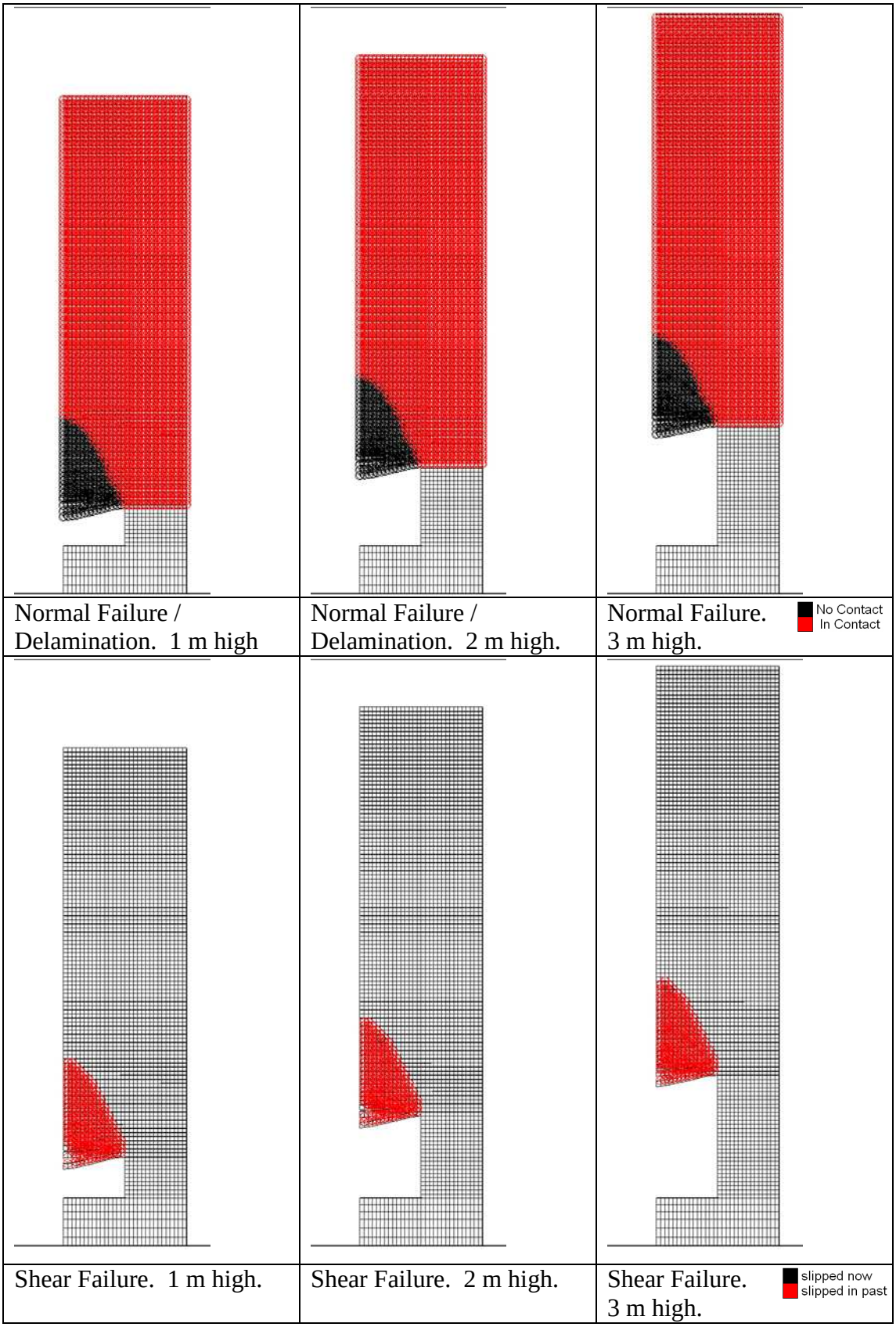

Figure 5.47: Normal and Shear interface failure plots for the rock mass (GSI 20).

GSI 30

In this results section the rock mass strength has been increased to GSI 30 and the results are shown at the ground water level where initial failure of the rock mass has occurred. Plots of the minimum and maximum principal stresses are shown in Figure 5.48 and Figure 5.49 where it can be seen that the maximum compressive stress in all cases occurs at the pillar / roof intersection.

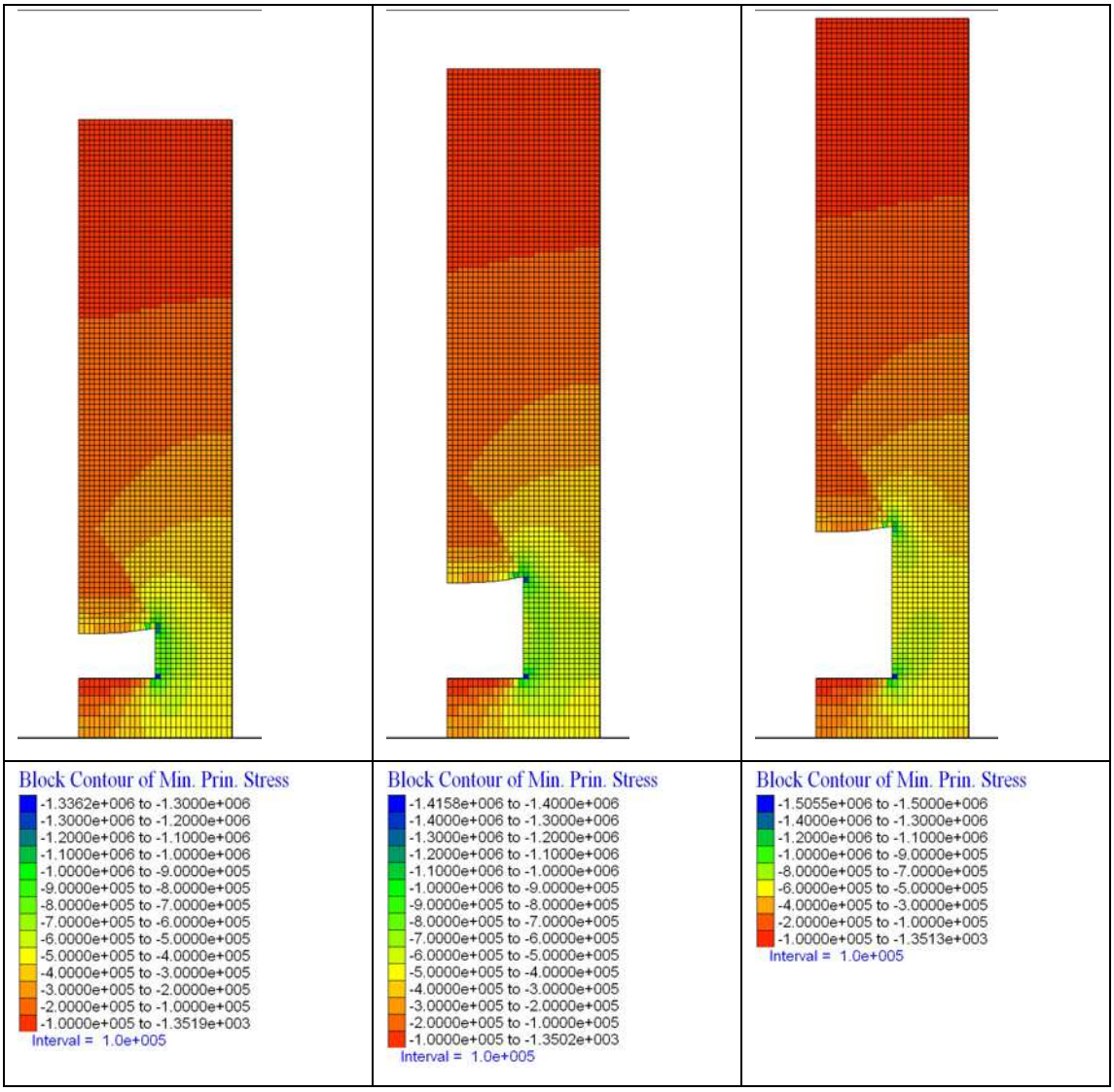

Figure 5.48: Minimum principal stress contours (Sigma 1) within the model for a bedding plane spacing of 0.1 m. Model parameters - Excavation 2 m wide, 1 to 3 m high; GSI 30.

The maximum compressive stress is approximately the same for all three excavations heights with compressive stresses reaching 1.34, 1.42 and 1.51 MPa in the 1m, 2 m and 3 m high excavations respectively which are similar values to those occurring in the lower strength rock mass. In all three cases it can be seen that compressive stress reduction has occurred over the excavation with the magnitude of compressive stress reaching a lower value for a given level within the model for regions over the

excavation roof than over the coal pillar and that the width from the roof centreline that this zone extends decreases with increasing height from the excavation roof, essentially forming a wedge of compressive stress relaxation over the excavation. As per the previous modelling at the lower rock mass strength (GSI 10 and 20) it can be seen that the compressive stress state then increases rapidly at a height level with the excavation within the pillar demonstrated by the high compressive stress gradient in this region indicated by the close spacing of the stress contours. The plot of maximum stress (Figure 5.43) indicates that the region above the excavation roof within the model is in a tensile stress state for all three excavation heights at this rock mass strength with values ranging from approximately 8.5-10 kPa. This tensile stress is approximately the same as that for the GSI 20 modelling.

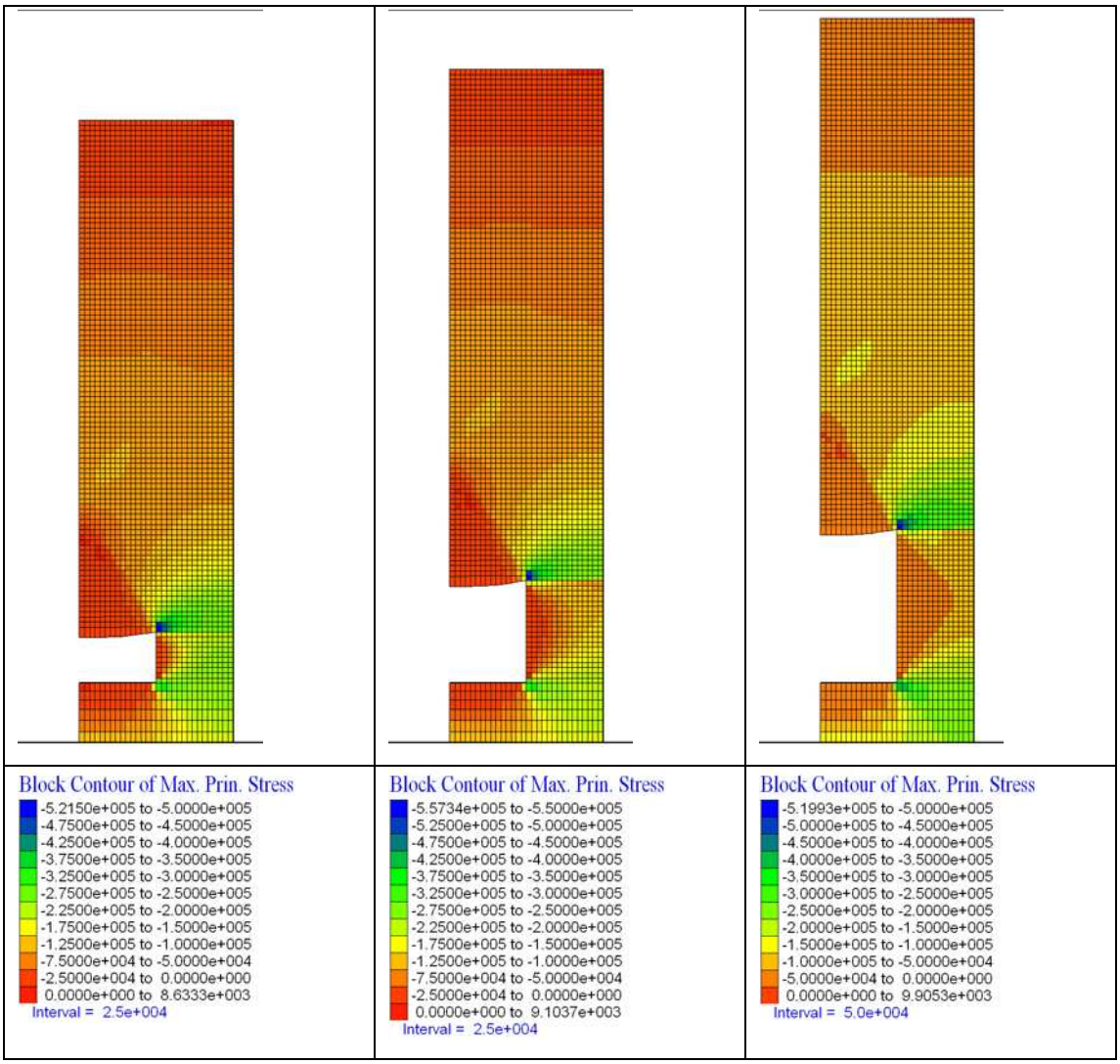

Figure 5.49: Maximum principal stress contours (Sigma 3) within the model for a bedding plane spacing of 0.1 m. Model parameters - Excavation 2 m wide, 1 to 3 m high; GSI 30.

A plot of the yield state of the rock mass above the excavations along with vertical displacement of the roof centre line and pore water pressure in the roof strata is shown in Figure 5.50, Figure 5.51 and Figure 5.52 with heights of 1m, 2 m and 3 m respectively. In these plots it can be seen that the excavations all show a similar pattern of yielding with tensile yielding above the excavation and very limited shear yielding at the pillar roof intersection.

In this case, excavation instability is triggered by the groundwater reaching a specific level above the excavation roof (note the sudden change in gradient of the vertical displacement and vertical strain plots marking the initiation of roof yielding in all three figures), in this case all 3 excavations yield when the water table reaches a level 2 m above the excavation roof which is equal to a pore water pressure within the immediate roof of the excavation of 20 kPa.

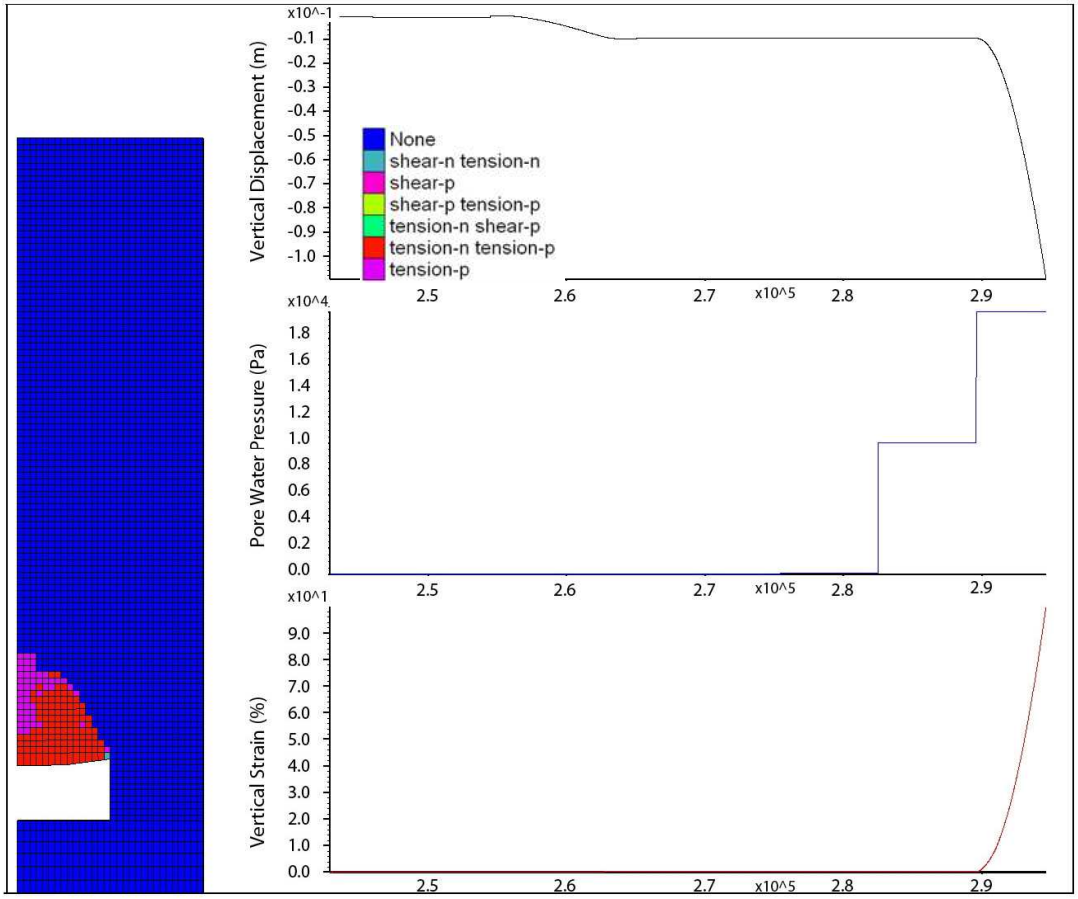

Figure 5.50: Yield state of the rock mass within the model for a bedding plane spacing of 0.1 m. Model parameters - Excavation 2 m wide, 1 m high; GSI 30.

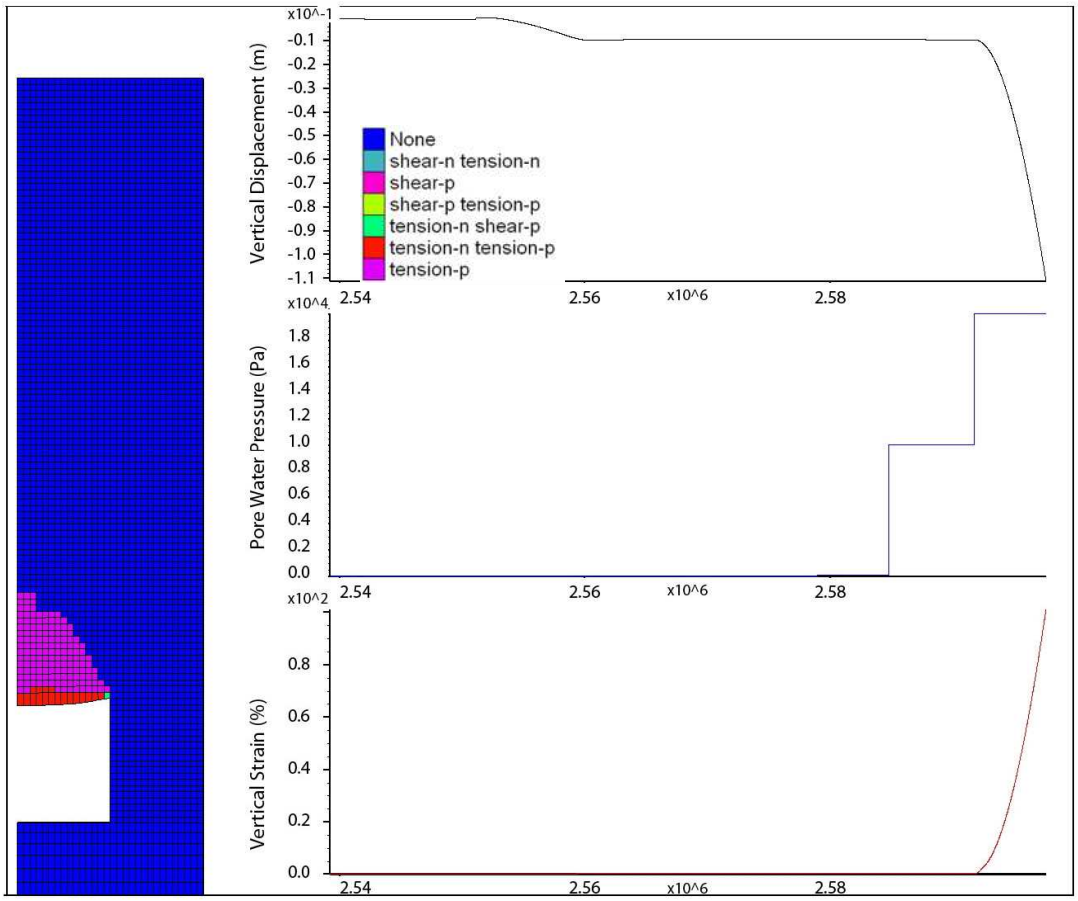

Figure 5.51: Yield state of the rock mass within the model for a bedding plane spacing of 0.1 m. Model parameters - Excavation 2 m wide, 2 m high; GSI 30.

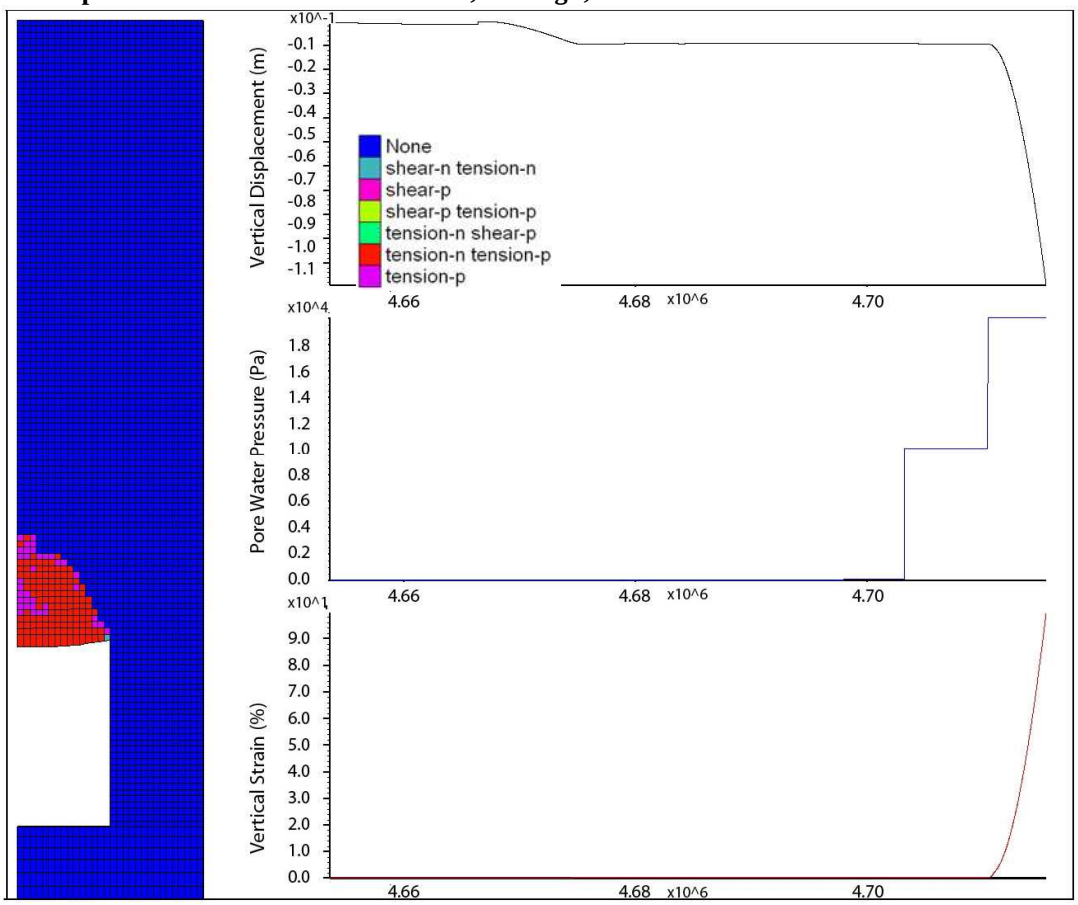

Figure 5.52: Yield state of the rock mass within the model for a bedding plane spacing of 0.1 m. Model parameters - Excavation 2 m wide, 3 m high; GSI 30.

When the yield plot for this rock mass strength is compared to those for GSI values of 10 and 20 it is readily apparent that there are significant differences. The primary difference (other than the yielding being triggered by the increased pore water pressure) is the lack of sagging of roof strata or the formation of a zone of shear yielding above the roof pillar intersection. Instead the majority of deformation seems to be as the result of plastic tensile yielding of the immediate roof strata. The region of tensile yielding extends approximately 1.7 m into the rock mass over the excavation roof which is a lower height than that for the modelling undertaken with lower rock mass strength which is to be expected.

Plots of the interface normal and shear failure (Figure 5.53 and Figure 5.54) show that there is a significant difference in the behaviour of the bedding planes within the models undertaken at GSI 30 as there is only tensile delamination occurring at the upper boundary of the region of tensile failure shown on the yield plot. The interfaces below this are in contact. However all interfaces within the region of tensile yielding are undergoing shear failure.

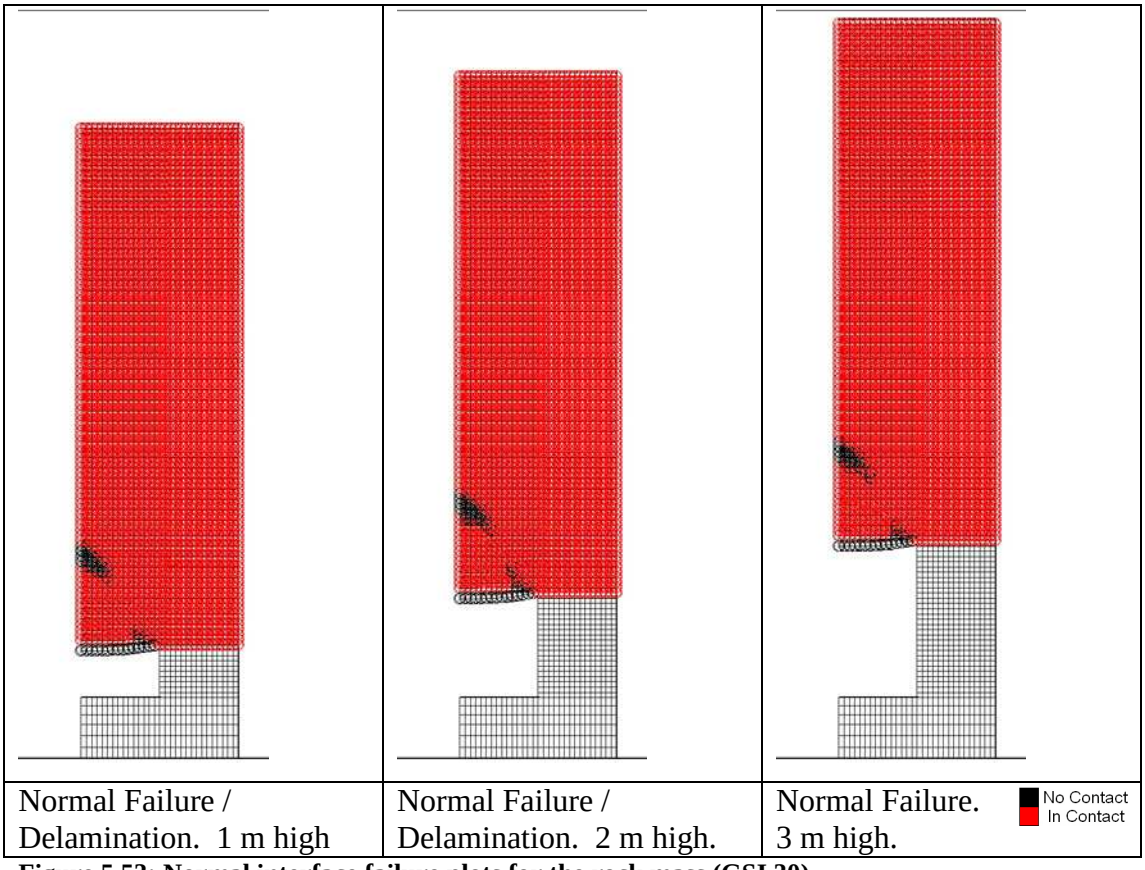

Normal Failure / Delamination. 1 m high	Normal Failure / Delamination. 2 m high.	Normal Failure. 3 m high.

Figure 5.53: Normal interface failure plots for the rock mass (GSI 30).

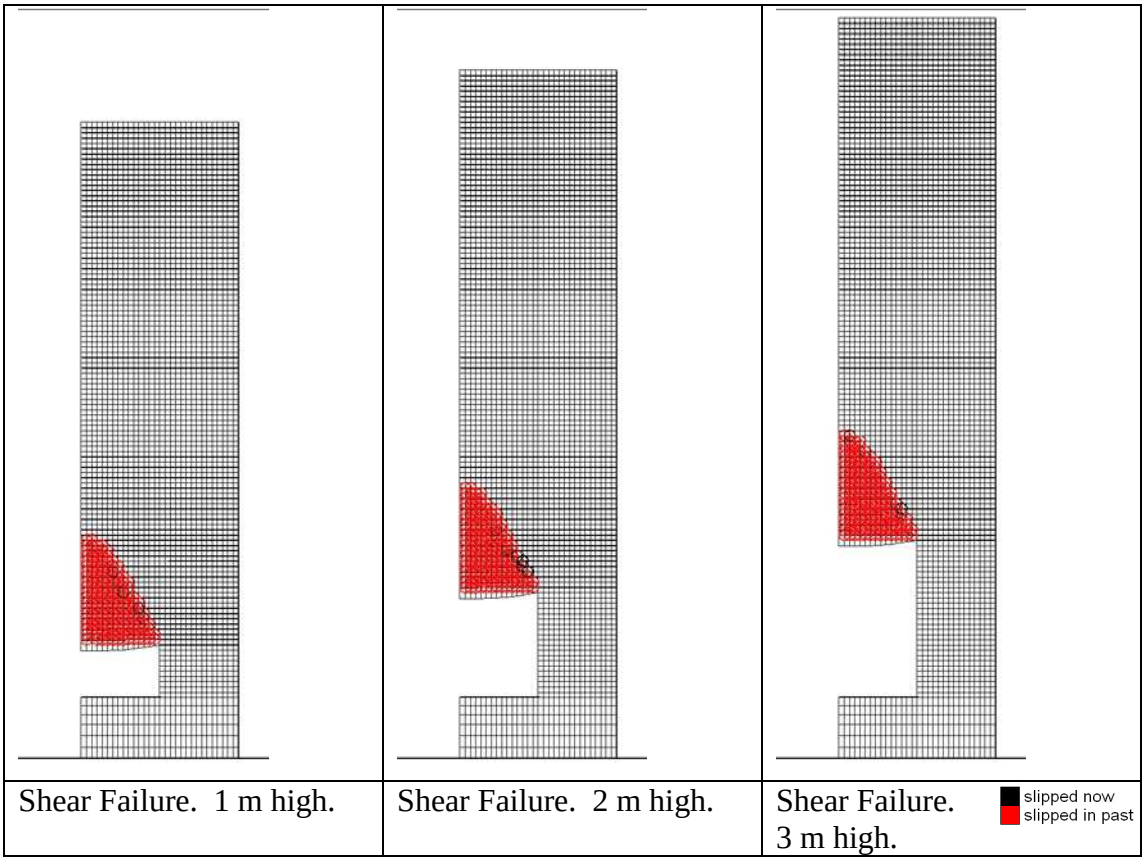

Figure 5.54: Shear interface failure plots for the rock mass (GSI 30).

GSI 40

In this results section the rock mass strength has been increased to GSI 40 and results are shown at the ground water level where initial failure of the rock mass has occurred. Plots of the minimum and maximum principal stresses are shown in Figure 5.55 and Figure 5.56 where it can be seen that the maximum compressive stress in all cases occurs at the pillar / roof intersection. The maximum compressive stress is approximately the same for all three excavations heights with compressive stresses reaching 1.32, 1.42 and 1.52 MPa in the 1m, 2 m and 3 m high excavations respectively which are similar values to those occurring in the lower strength rock mass. Broadly in this case it can be seen that the trends in the minimum principal stress contour behaviour follow that of the previous lower strength modelling. However there is one significant difference in this case. This is where horizontal bands of high compressive stress form within the roof strata over the rock mass in the 2 and 3 m high excavation models with magnitudes approximately equal to 300 kPa.

The plot of maximum stress (Figure 5.56) indicates that there is a region above the excavation roof within the models that is in a tensile stress state for all three excavation

heights at this rock mass strength, however the 2 and 3 m excavation height models show that this region becomes progressively smaller and forms at an increasing height within the region of compressive stress reduction above the excavation roof. Below this region of tensile stress it can be seen that the stress is compressive whereas in previous models at lower rock mass strengths this would remain in tension (this is particularly clear in the plot of maximum principal stress of the 3 m high excavation).

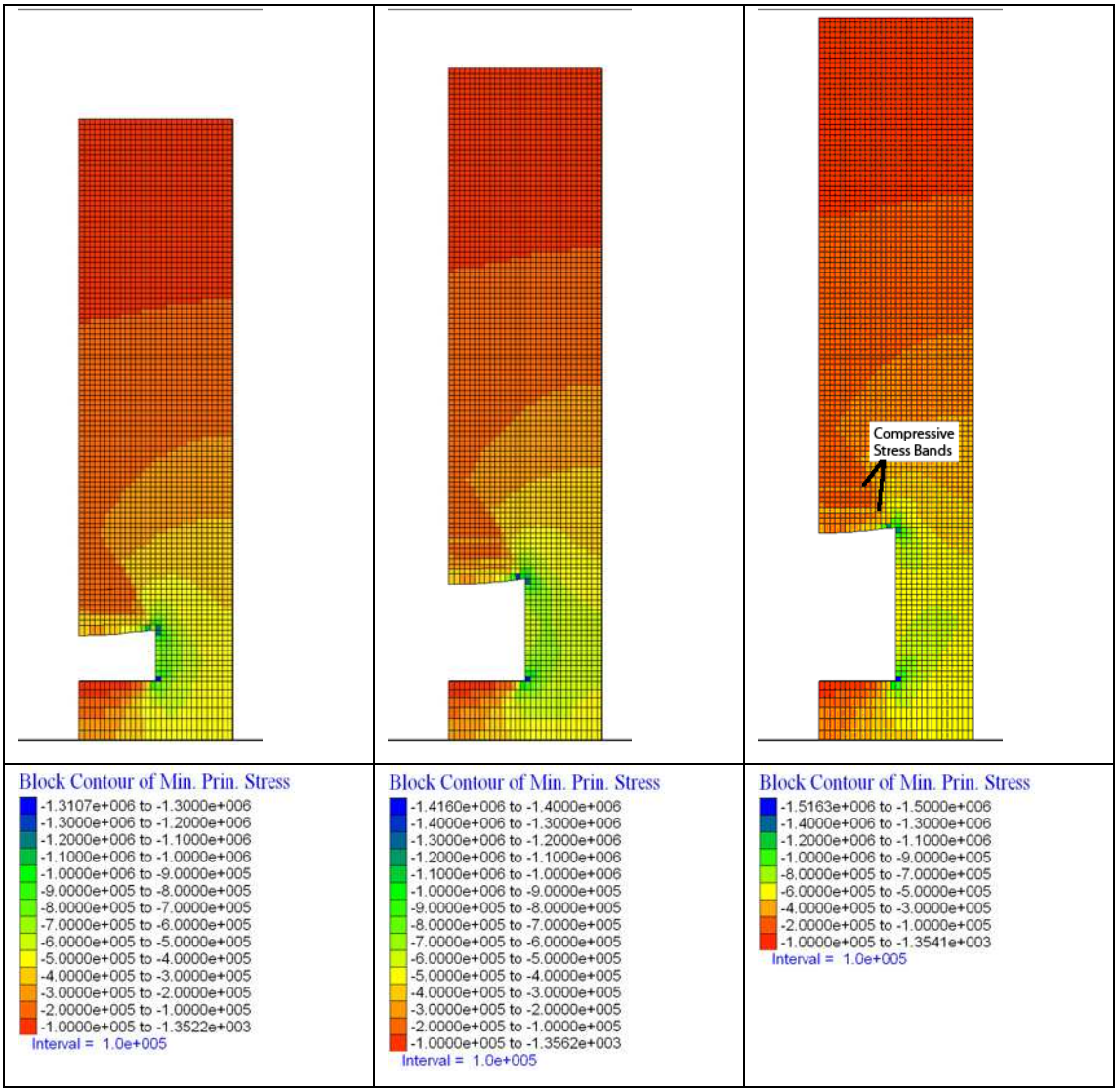

Figure 5.55: Minimum principal stress contours (Sigma 1) within the model for a bedding plane spacing of 0.1 m. Model parameters - Excavation 2 m wide, 1 to 3 m high; GSI 40.

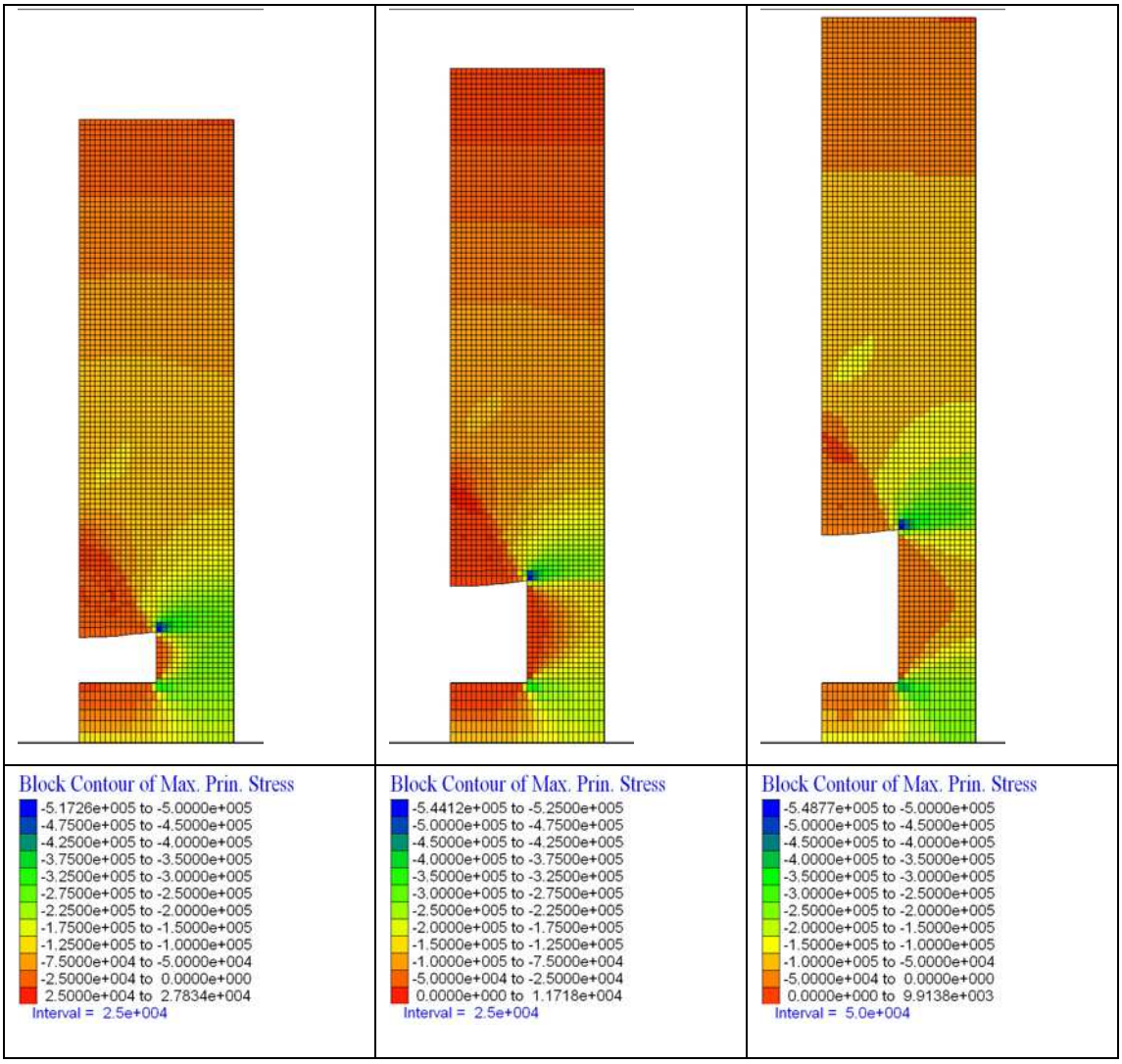

Figure 5.56: Maximum principal stress contours (Sigma 3) within the model for a bedding plane spacing of 0.1 m. Model parameters - Excavation 2 m wide, 1 to 3 m high; GSI 40.

A plot of the yield state of the rock mass above the excavations along with vertical displacement of the roof centre line and pore water pressure in the roof strata is shown in Figure 5.57, Figure 5.58 and Figure 5.59. In these plots it can be seen that the excavations all show a broadly similar type of yielding in that tensile yielding occurs in the rock mass above the excavation and very limited shear yielding at the pillar roof intersection. This pattern is broadly similar to that seen for a rock mass strength of GSI 30. However there is one obvious difference in the 3 yield plots and that is geometry whereby the region of yielding in the 1 m high model appears to have developed with a "notch" in its upper surface whereas the 2 and 3 m models have developed as a trapezoidal geometry with a flat upper surface. It is possible that this change may be accounted for by the variable nature of the stress field above the excavation roof (where it varies from tension to compression) or possibly de due to the varying pore water pressure where yielding occurs.

Another point of note is that the overall geometry of the region of yielding is changing as the rock mass strength increases from that of a wedge to that of a trapezium (with parallel upper and lower boundaries). In three-dimensions this would likely represent a change from a cone to a frustum.

Once again it is apparent form the modelling at this rock mass strength that excavation instability is triggered by the groundwater reaching a specific level above the excavation roof (note the sudden change in gradient of the vertical displacement and vertical strain plots marking the initiation of roof yielding in all three figures), however in this case the 1 m high excavation yields when the water table reaches a level 1 m above the excavation roof (note the change in gradient of both the vertical displacement and vertical strain plots in Figure 5.57 at a pore water pressure of 10 kPa).
Also significant is the fact that in Figure 5.58 and Figure 5.59 it can be seen that yielding occurs when the water table is 2 m over the excavation roof for the 2 and 3 m high excavations. This is the first indication that extraction height may have an impact on the stability of excavations.

Plots of the interface normal and shear failure (Figure 5.60) show that the discontinuity failure behaviour of the bedding planes within the models undertaken at GSI 40 is very similar to that seen for the GSI 30 modelling as there is only tensile delamination occurring at the upper boundary of the region of tensile failure shown on the yield plot. This region where the interfaces are in contact extends from the excavation roof to approximately 0.3 m into the rock mass for the 1 m high excavation (as measured over the roof centreline) and becomes increasingly large for the 2 and 3 m high excavations where it extends approximately 1.5 m into the rock mass over the roof centreline. The presence of this region where the interfaces are in contact correlates well with the bands of high compressive stress that form above the excavation as seen in the minimum principal stress plot and potentially represent the formation of stress arching within the strata forming the roof of the excavation.

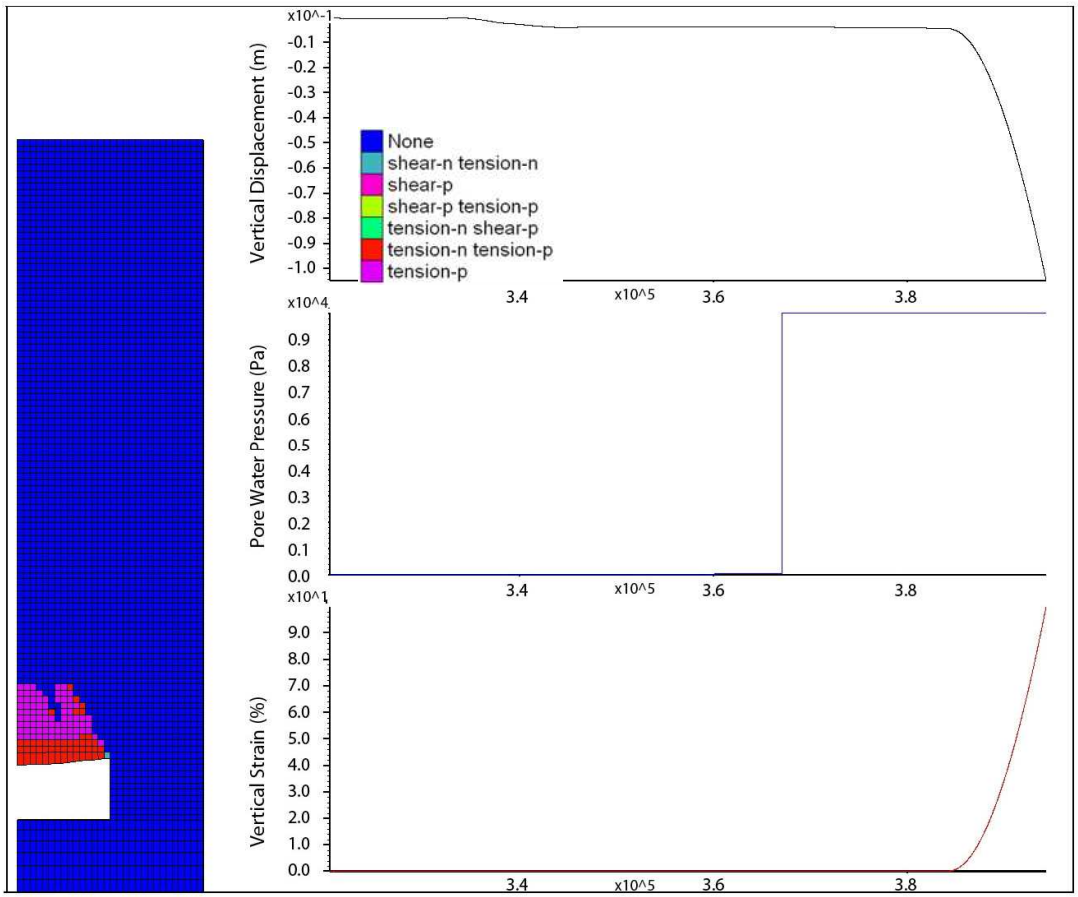

Figure 5.57: Yield state of the rock mass within the model for a bedding plane spacing of 0.1 m. Model parameters - Excavation 2 m wide, 1 m high; GSI 40.

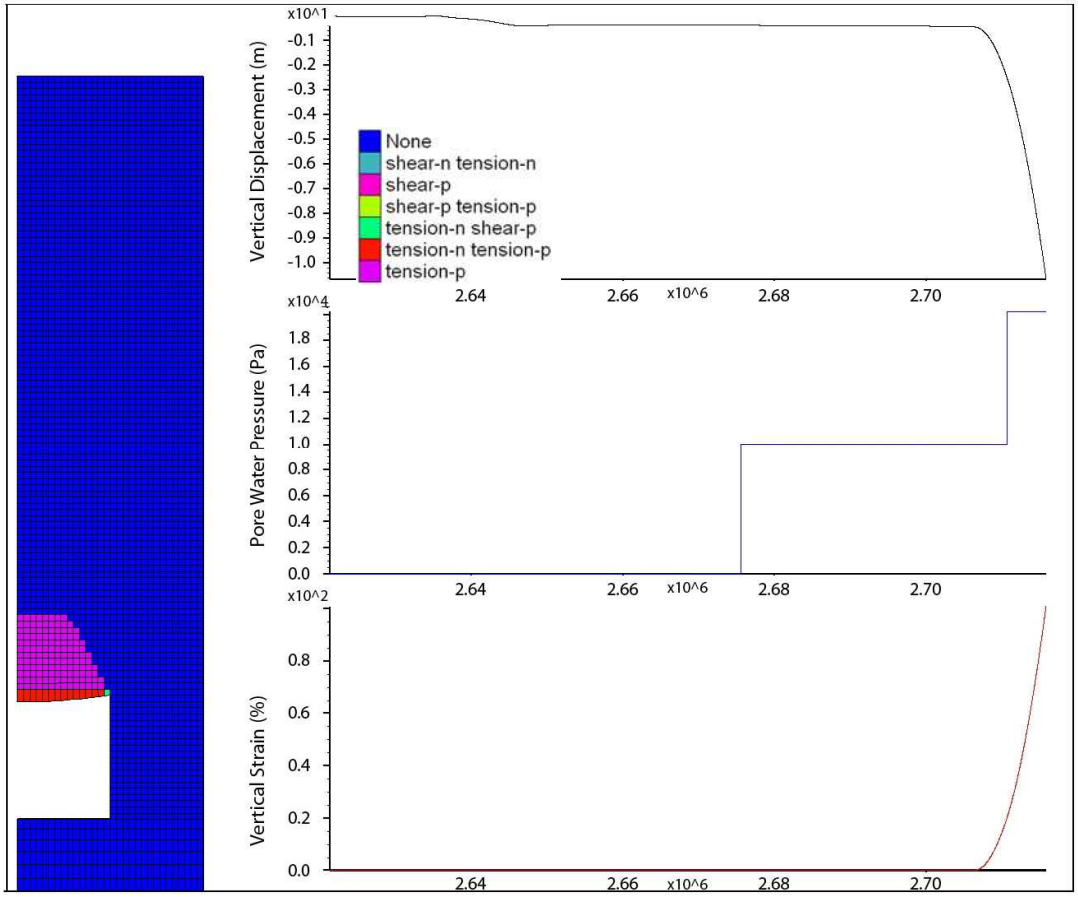

Figure 5.58: Yield state of the rock mass within the model for a bedding plane spacing of 0.1 m. Model parameters - Excavation 2 m wide, 2 m high; GSI 40.

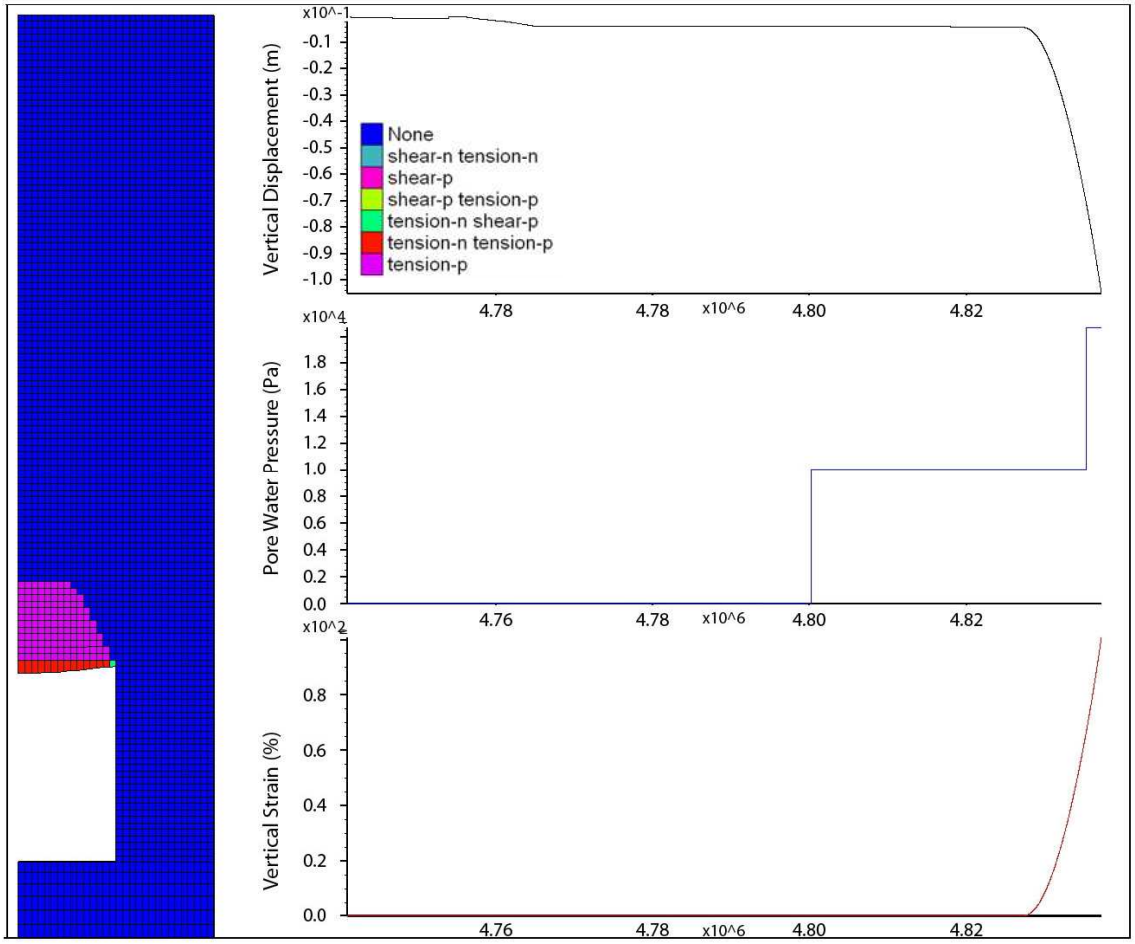

Figure 5.59: Yield state of the rock mass within the model for a bedding plane spacing of 0.1 m. Model parameters - Excavation 2 m wide, 3 m high; GSI 40.

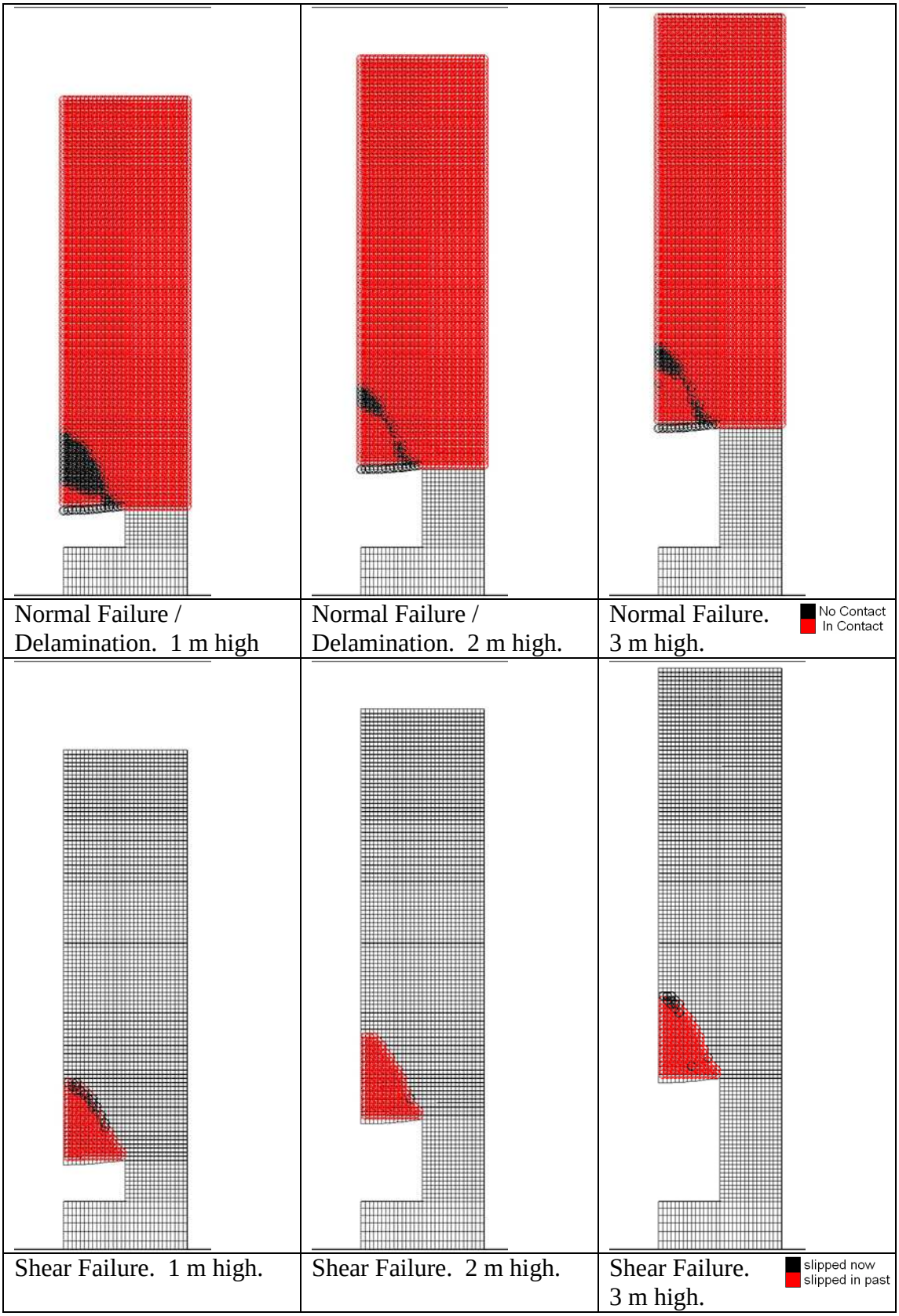

Figure 5.60: Normal and Shear interface failure plots for the rock mass (GSI 40).

GSI 50

In this results section the rock mass strength has been increased to GSI 50 and results are shown at the ground water level where initial failure of the rock mass has occurred. Plots of the minimum and maximum principal stresses are shown in Figure 5.61 and Figure 5.62 where the maximum compressive stress is highest for the 2 and 3 m high excavations (2.0 MPa) whereas the maximum compressive stress in the 1 m excavation is 1.5 MPa

Broadly in this case it can be seen that the trends in the minimum principal stress contour behaviour follow that of the previous lower strength modelling. However as per the modelling at GSI 40, horizontal bands of high compressive stress have formed within the roof strata over the rock mass in the 2 and 3 m high excavation models with magnitudes approximately equal to 300 kPa.

The plot of maximum stress (Figure 5.62) indicates as per the GSI 40 models that there is a region above the excavation roof within the rock mass that is in a tensile stress state for all three excavation heights at this rock mass strength, however In this case all three excavation height models show that this region has become progressively smaller with increasing strength and forms at an increasing height within the region of compressive stress reduction above the excavation roof. Below this region of tensile stress it can be seen that the stress is compressive.

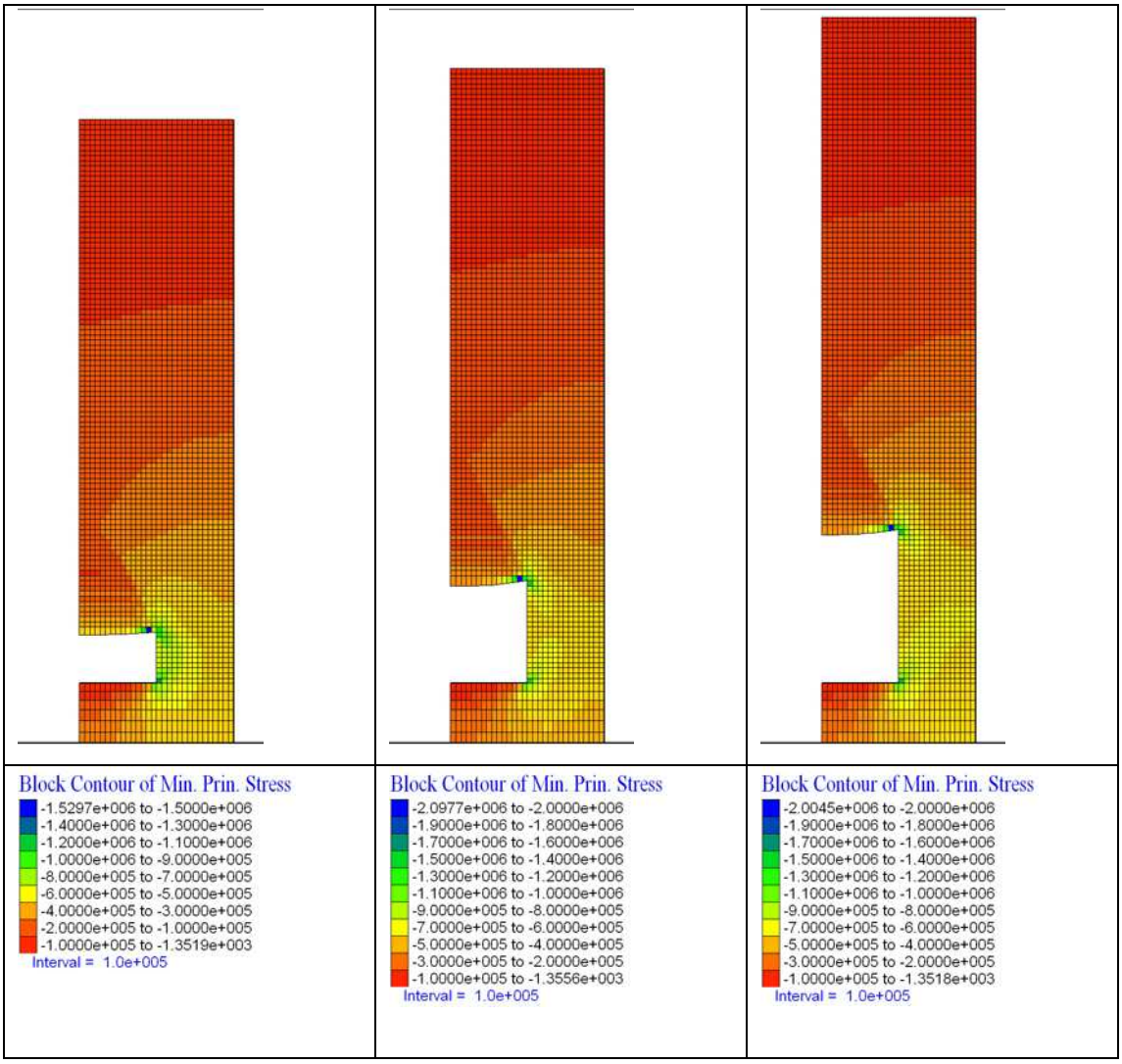

Figure 5.61: Minimum principal stress contours (Sigma 1) within the model for a bedding plane spacing of 0.1 m. Model parameters - Excavation 2 m wide, 1 to 3 m high; GSI 50.

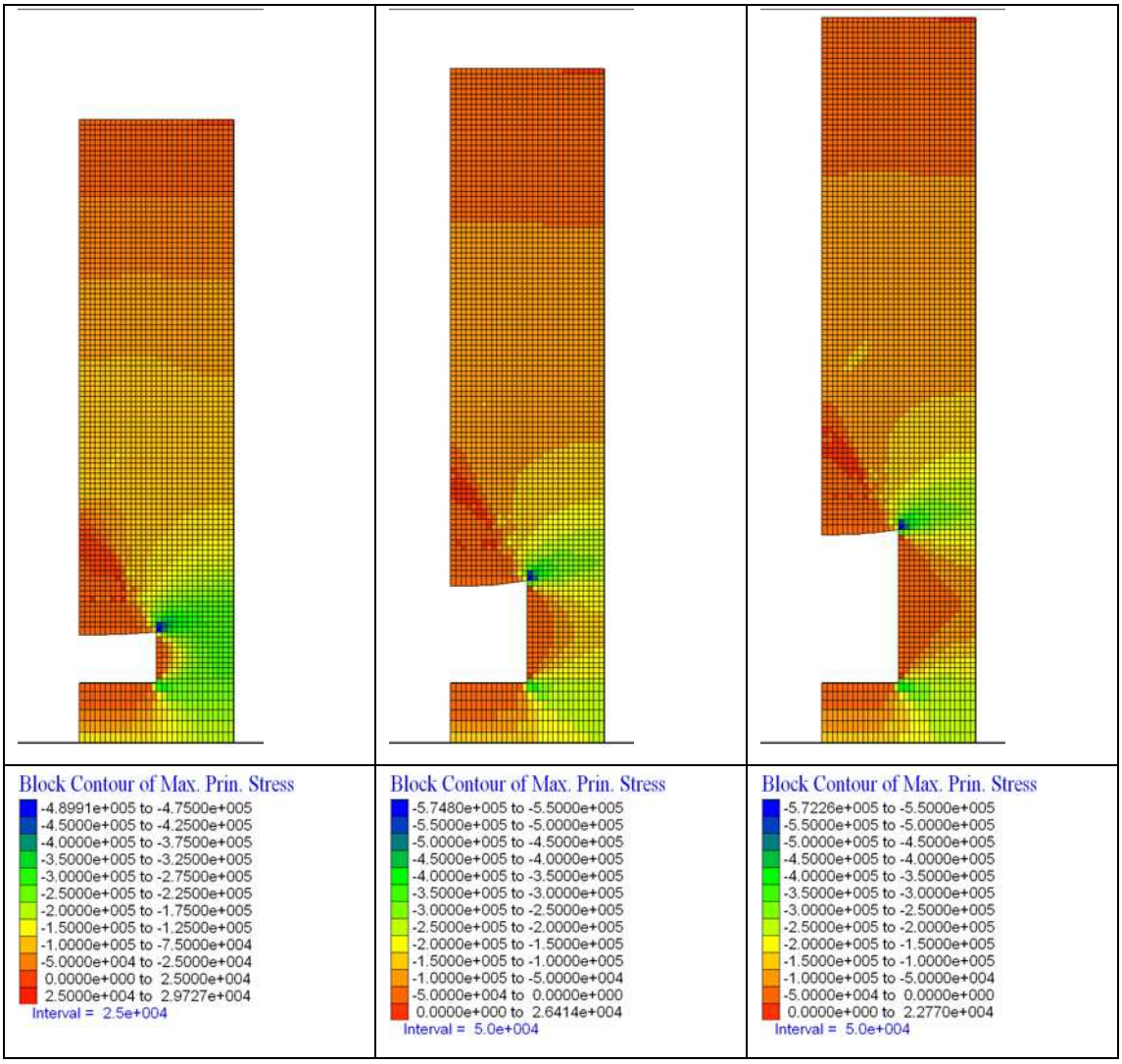

Figure 5.62: Maximum principal stress contours (Sigma 3) within the model for a bedding plane spacing of 0.1 m. Model parameters - Excavation 2 m wide, 1 to 3 m high; GSI 50.

A plot of the yield state of the rock mass above the excavations along with vertical displacement of the roof centre line and pore water pressure in the roof strata is shown in Figure 5.64, Figure 5.65 and Figure 5.65. In these plots it can be seen that the excavations all show a broadly similar pattern of yielding to that seen for rock masses with GSI 30 and 40 where tensile yielding occurs in the rock mass above the excavation and very limited shear yielding occurs at the pillar roof intersection at the point f highest compressive stress. In this case all of the excavation heights modelled at this rock mass strength have developed as a trapezoidal geometry with a flat upper surface. As the rock mass strength has increased, the height to which yielding extends into the rock mass has also decreased from approximately 1.5 m in the GSI 40 model to just 1 m in this modelling.

Once again it is apparent from the modelling at this rock mass strength that excavation instability is triggered by the groundwater reaching a specific level above the excavation roof (note the sudden change in gradient of the vertical displacement and vertical strain plots marking the initiation of roof yielding in all three figures), however in this case the 1 m high excavation yields when the water table reaches a level 2 m above the excavation roof (note the change in gradient of both the vertical displacement and vertical strain plots in Figure 5.63 at a pore water pressure of 20 kPa), a 1 m increase in head compared to the level of water table that initiated failure in the rock mass with strength and stiffness properties equivalent to GSI 40.

Also significant is the fact that in Figure 5.65 and Figure 5.65 it can be seen that yielding occurs when the water table is 3 m over the excavation roof for the 2 and 3 m high excavations. This is evidence that extraction height has an impact on the stability of an excavation roof; however it currently appears to be limited.

Plots of the interface normal and shear failure (Figure 5.66 and Figure 5.67) show that the discontinuity failure behaviour of the bedding planes within the models undertaken at GSI 50 is very similar to that seen for the GSI 40 modelling as there is only tensile delamination occurring in the region where tensile stresses occur within the maximum principal stress plot. The region where the interfaces are in contact extends from the excavation roof to approximately 1.5m into the rock mass for the 1 m high excavation (as measured over the roof centreline) and to a broadly similar extent for the 2 and 3 m high excavations. The presence of the region where the interfaces are in contact again correlates well with the bands of high compressive stress that form above the excavation as seen in the minimum principal stress plot and to the point in the roof where the strata are in compression rather than tension as seen on the maximum principal stress plot and potentially represent the formation of stress arching within the strata forming the roof of the excavation.

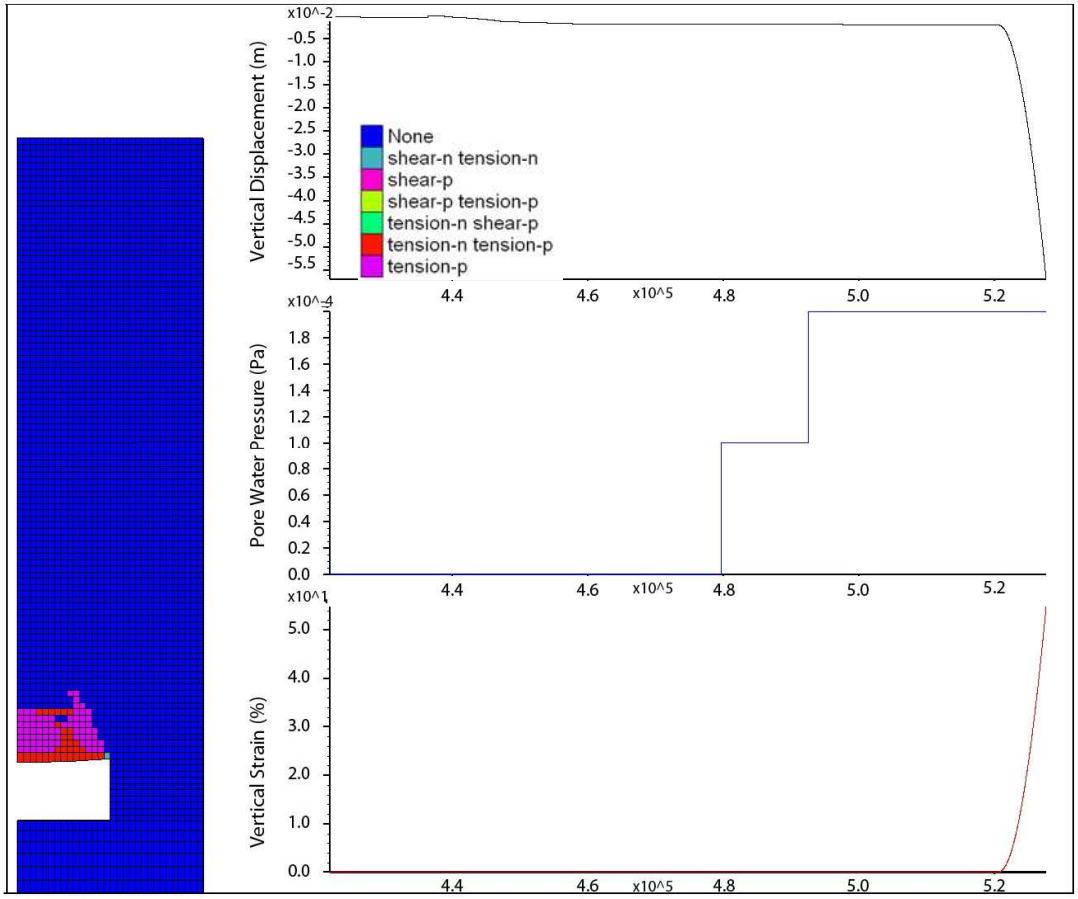

Figure 5.63: Yield state of the rock mass within the model for a bedding plane spacing of 0.1 m. Model parameters - Excavation 2 m wide, 1 m high; GSI 50.

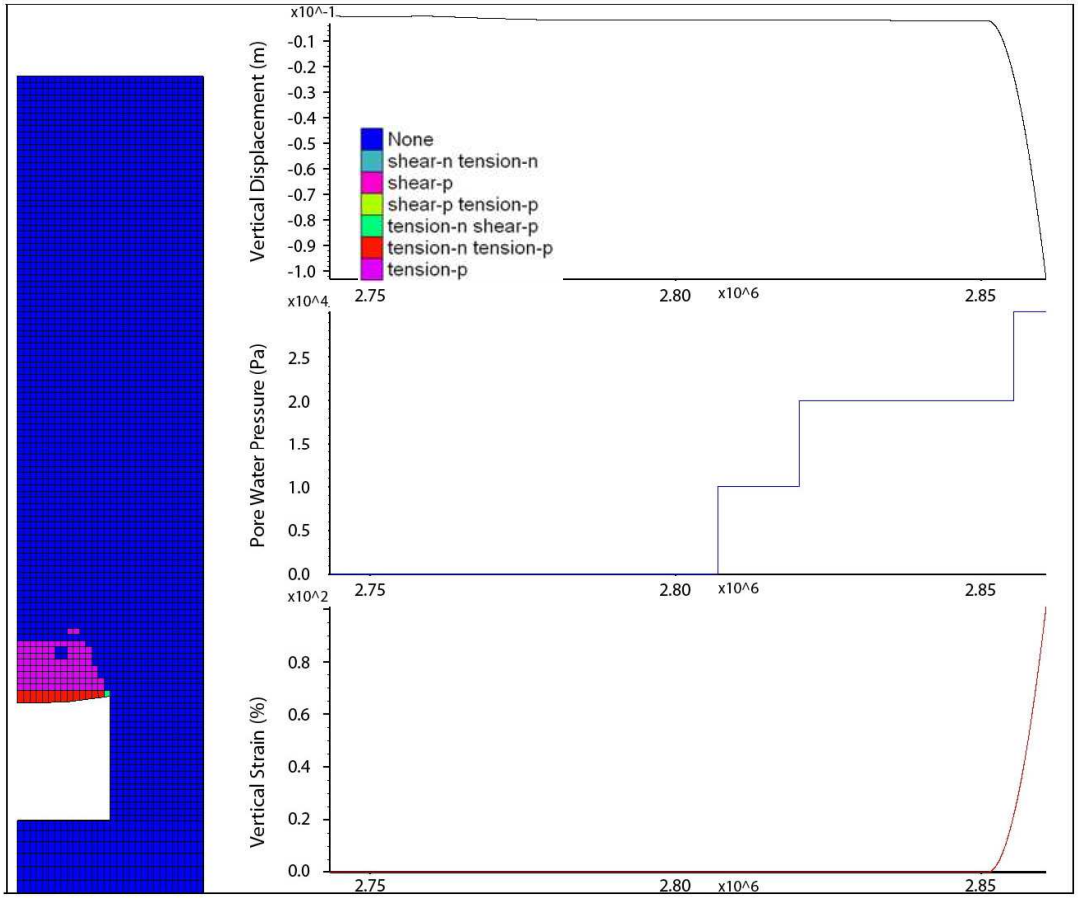

Figure 5.64: Yield state of the rock mass within the model for a bedding plane spacing of 0.1 m. Model parameters - Excavation 2 m wide, 2 m high; GSI 50.

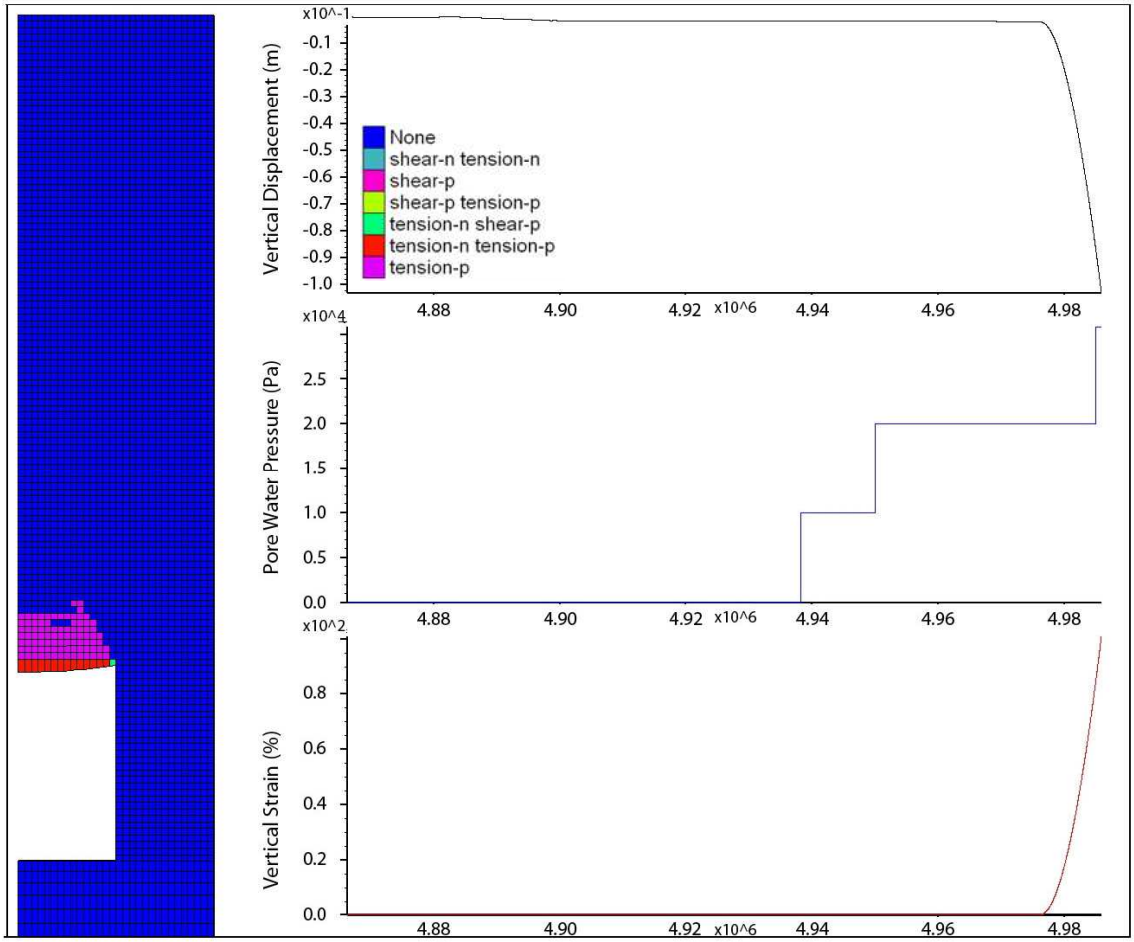

Figure 5.65: Yield state of the rock mass within the model for a bedding plane spacing of 0.1 m. Model parameters - Excavation 2 m wide, 3 m high; GSI 50.

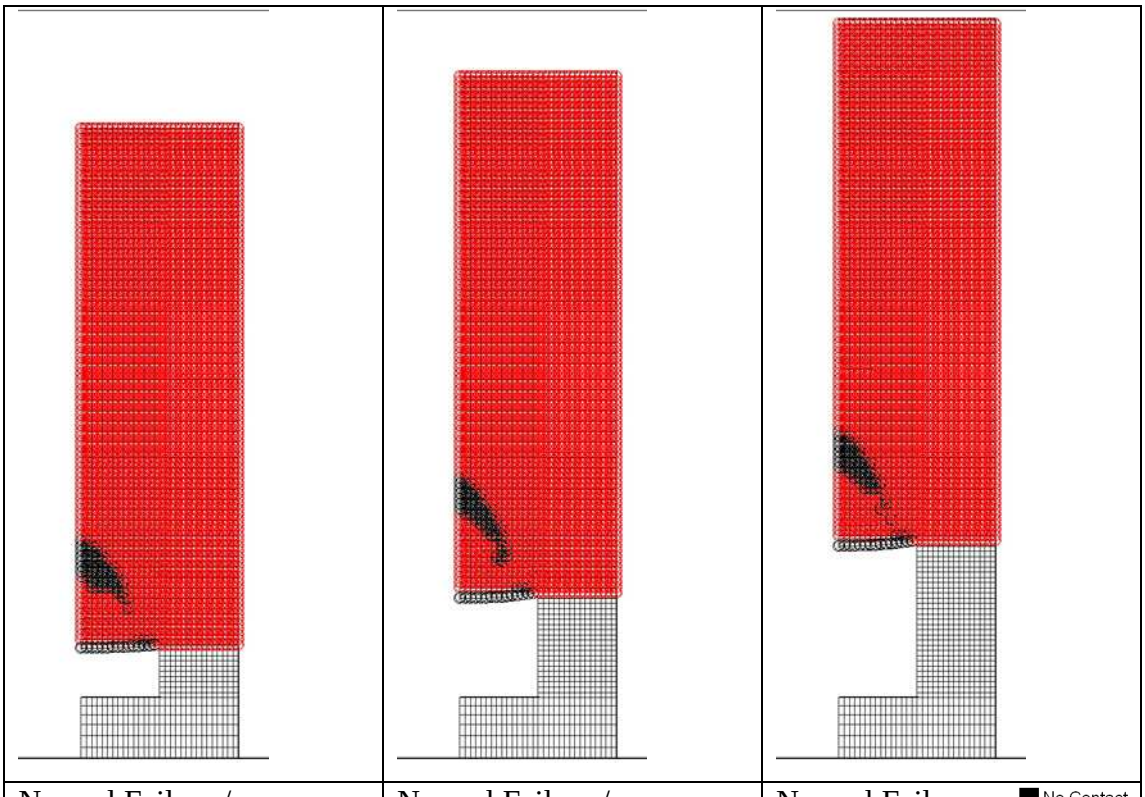

Normal Failure / Delamination. 1 m high	Normal Failure / Delamination. 2 m high.	Normal Failure. 3 m high.

Figure 5.66: Normal interface failure plots for the rock mass (GSI 50).

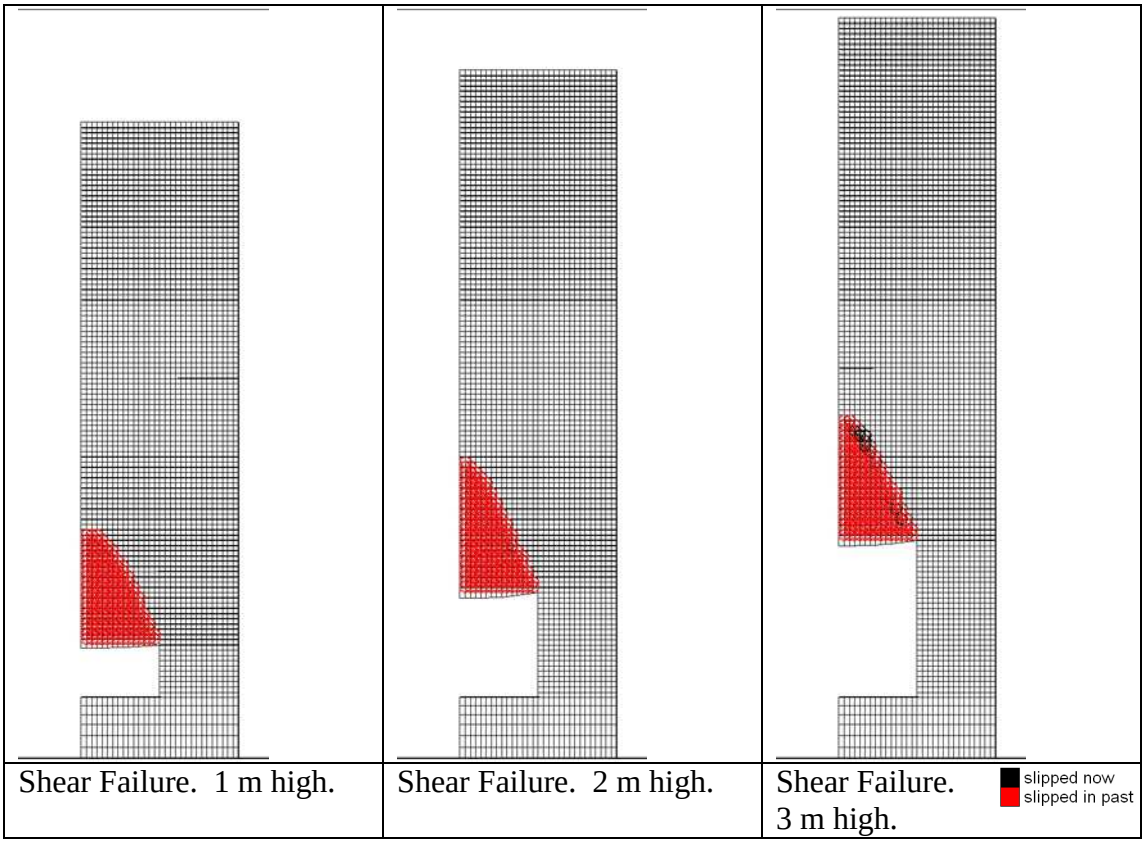

Figure 5.67: Shear interface failure plots for the rock mass (GSI 50).

GSI 60

In this results section the rock mass strength has been increased to a GSI value of 60 and results are shown at the ground water level where initial failure of the rock mass has occurred. Plots of the minimum and maximum principal stresses are shown in Figure 5.68 and Figure 5.69 where it can be seen that the compressive stress reached a maximum value in the coal pillar. It can also be seen in the maximum stress plot, that a large region of tensile stress has formed over the excavation roof in all three cases reaching values of between approximately 73, 71 and 56 kPa respectively. It can also be seen that significant tensile stresses develop within the coal pillar increasing as the height of the excavation increases. It is likely that in reality the pillar would fail under such conditions as the high strength roof strata are likely to result in the maximum stress being transmitted into the pillar and pillar crushing occurring. However the pillar strength in these investigations was kept high in order to investigate the roof stability as it is roof (in)stability which is the cause of void migration.

For all three excavation heights, the zone of tensile stress extends a significant distance into the rock mass forming the excavation roof (approximately 3 m over the roof centreline) when compared to models of lower rock mass strength

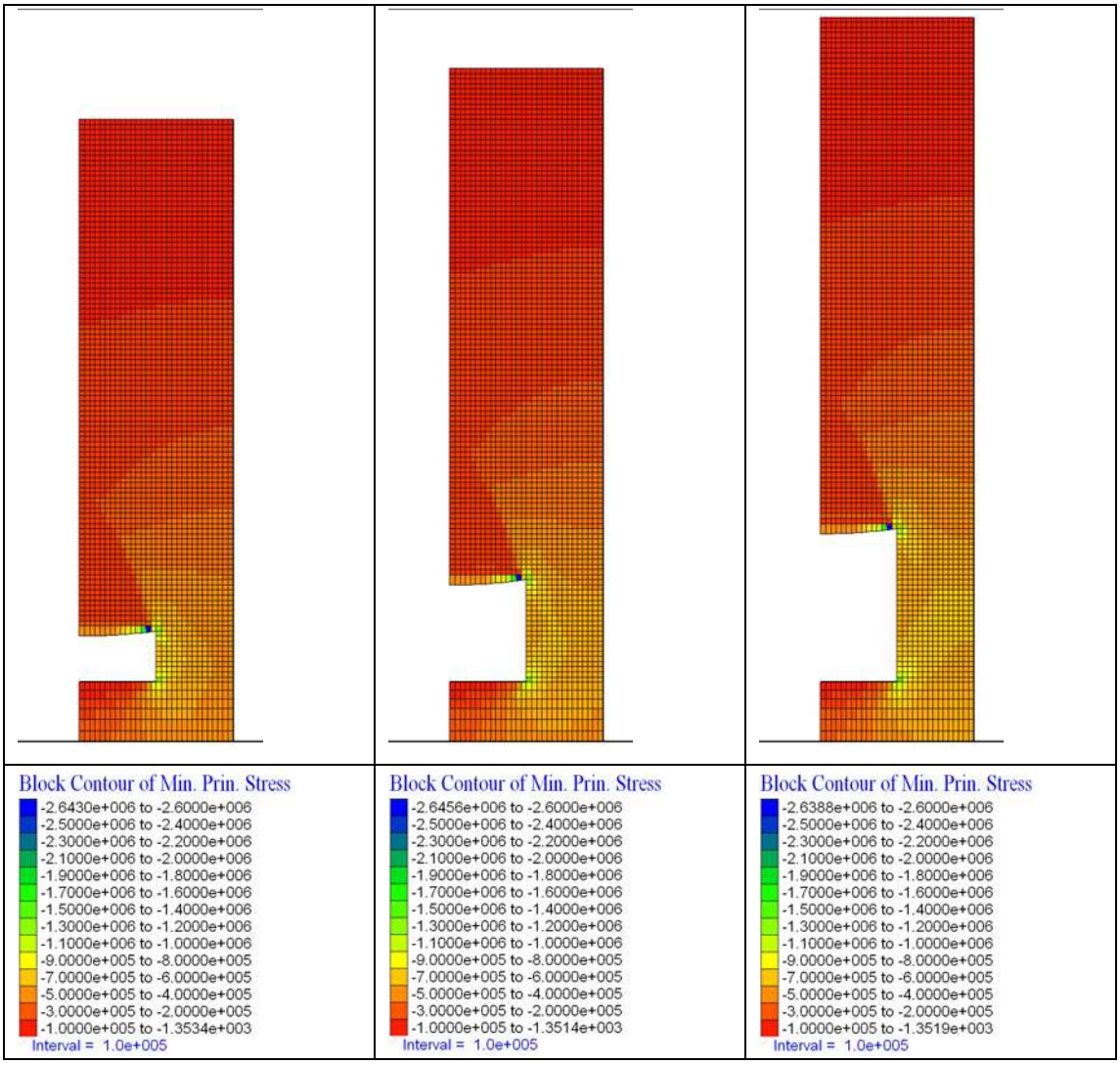

Figure 5.68: Minimum principal stress contours (Sigma 1) within the model for a bedding plane spacing of 0.1 m. Model parameters - Excavation 2 m wide, 1 to 3 m high; GSI 60.

A plot of the yield state of the rock mass above the excavations along with vertical displacement of the roof centre line and pore water pressure in the roof strata is shown in Figure 5.70, Figure 5.71 and Figure 5.72. In these plots it can be seen that the excavation roof in all three cases undergoes yielding of the rock mass but of very limited extent affecting only the immediate roof stratum when compared to the previous modelling at lower rock mass strength.

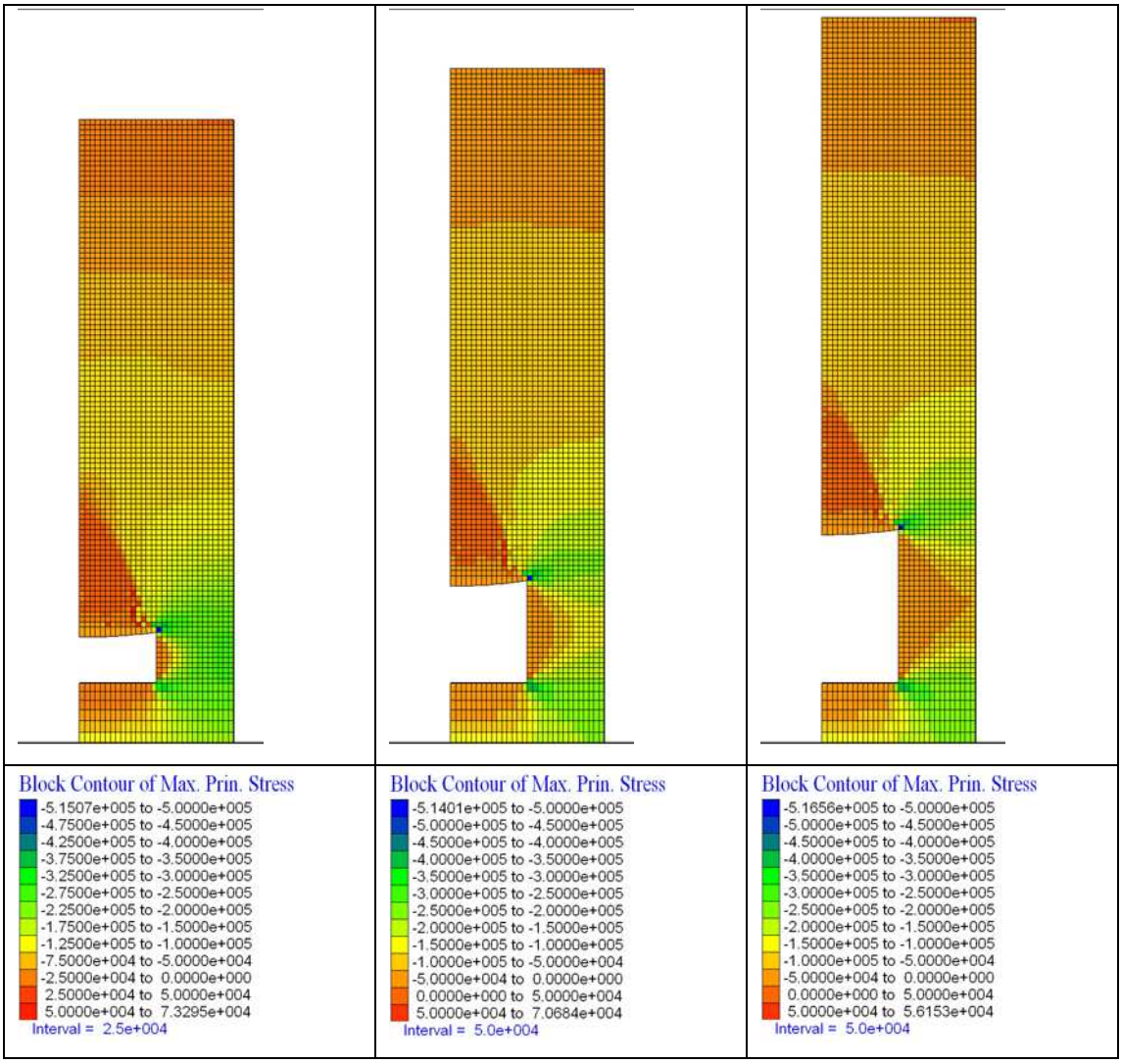

Figure 5.69: Maximum principal stress contours (Sigma 3) within the model for a bedding plane spacing of 0.1 m. Model parameters - Excavation 2 m wide, 1 to 3 m high; GSI 60.

Increases in the groundwater table cause yielding to occur that exceed the yielding criterion at a water table 3 m above the excavation roof at all three excavation heights. The higher strength of the rock mass means that the higher stresses that can develop lead to an increased height of tensile delamination and shearing along bedding planes within the rock mass which can be seen in Figure 5.73 and Figure 5.74 whereby the zone of tensile delamination as marked b y interface failure and the region of interface / bedding plane shear failure extends approximately 3 m into the rock mass over the roof centreline for all three excavation heights.

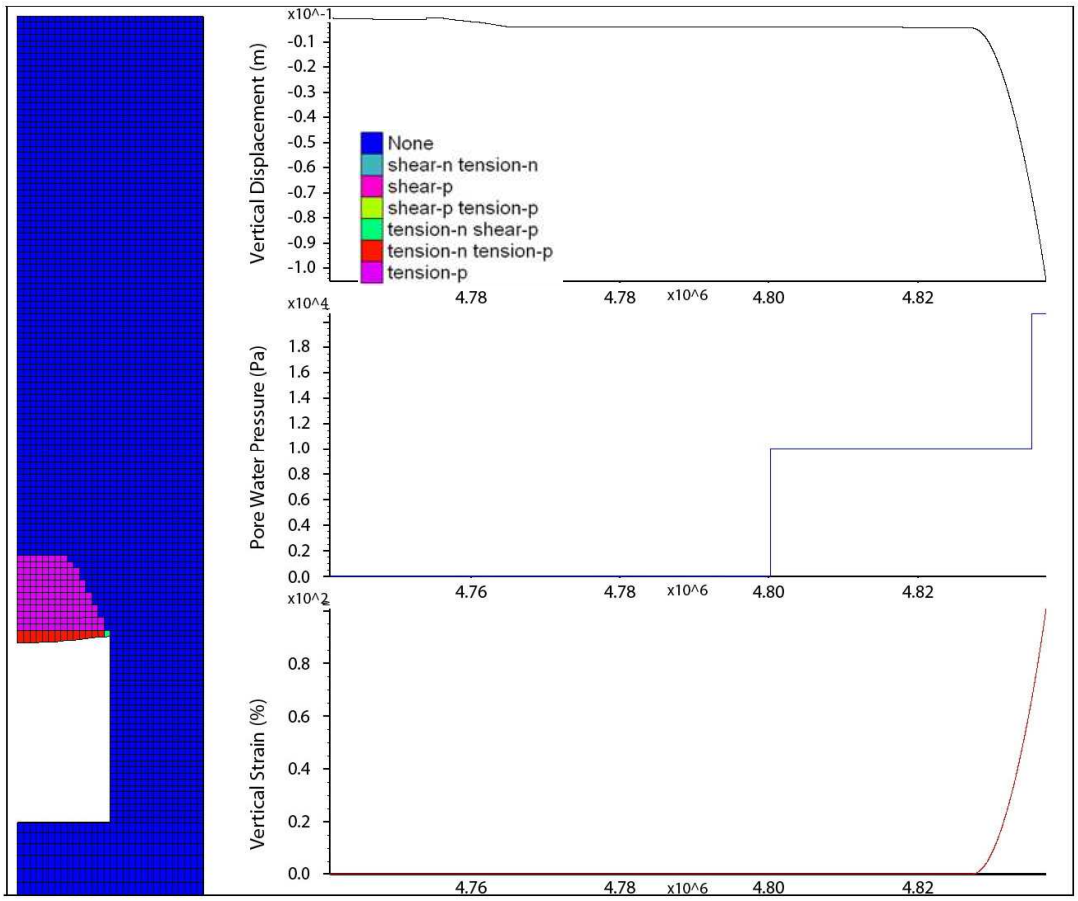

Figure 5.70: Yield state of the rock mass within the model for a bedding plane spacing of 0.1 m. Model parameters - Excavation 2 m wide, 1 m high; GSI 60.

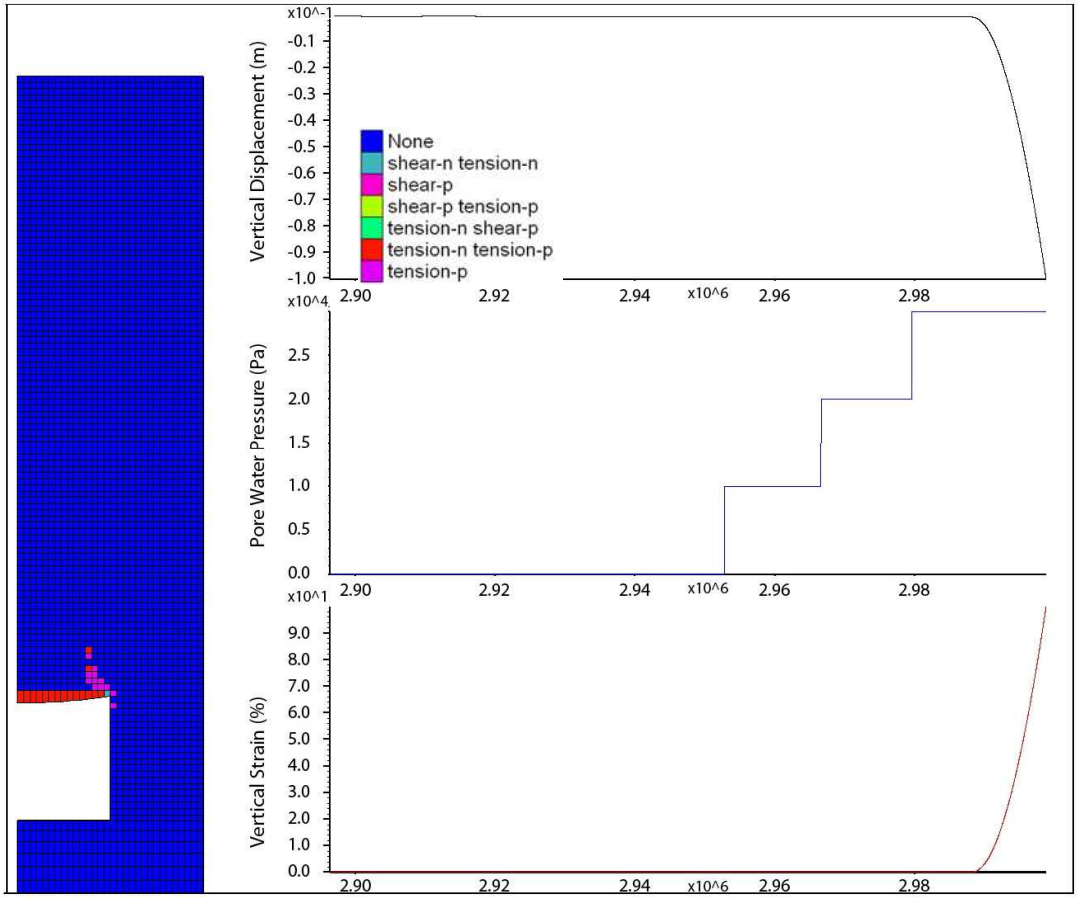

Figure 5.71: Yield state of the rock mass within the model for a bedding plane spacing of 0.1 m. Model parameters - Excavation 2 m wide, 2 m high; GSI 60.

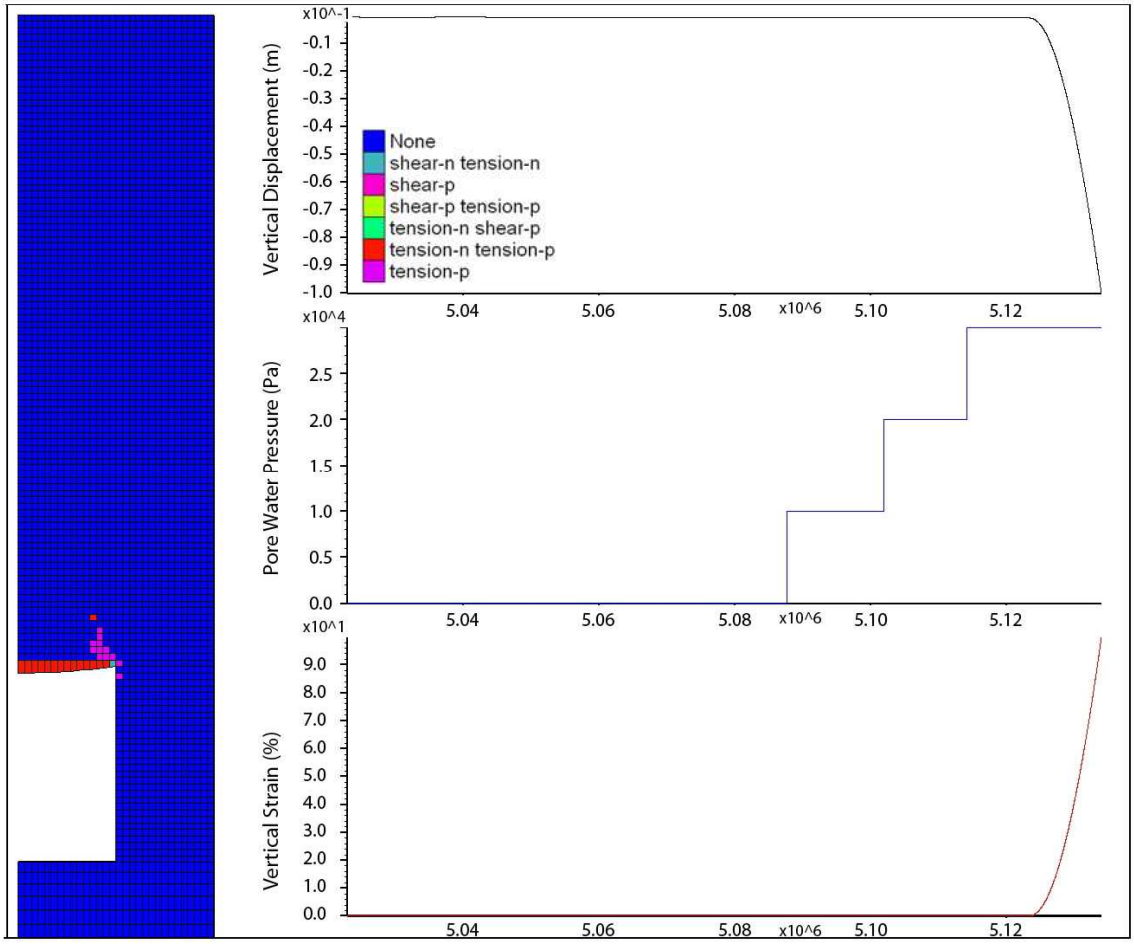

Figure 5.72: Yield state of the rock mass within the model for a bedding plane spacing of 0.1 m. Model parameters - Excavation 2 m wide, 3 m high; GSI 60.

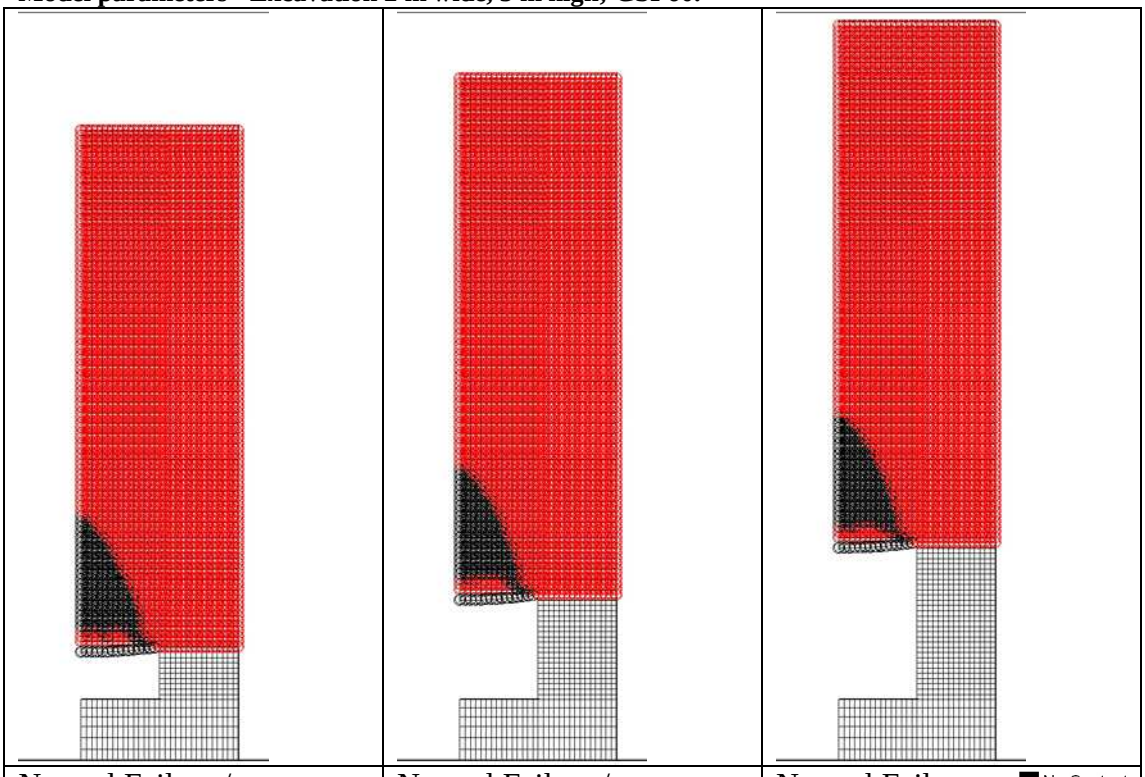

Normal Failure / Delamination. 1 m high	Normal Failure / Delamination. 2 m high.	Normal Failure. 3 m high.

Figure 5.73: Normal interface failure plots for the rock mass (GSI 60).

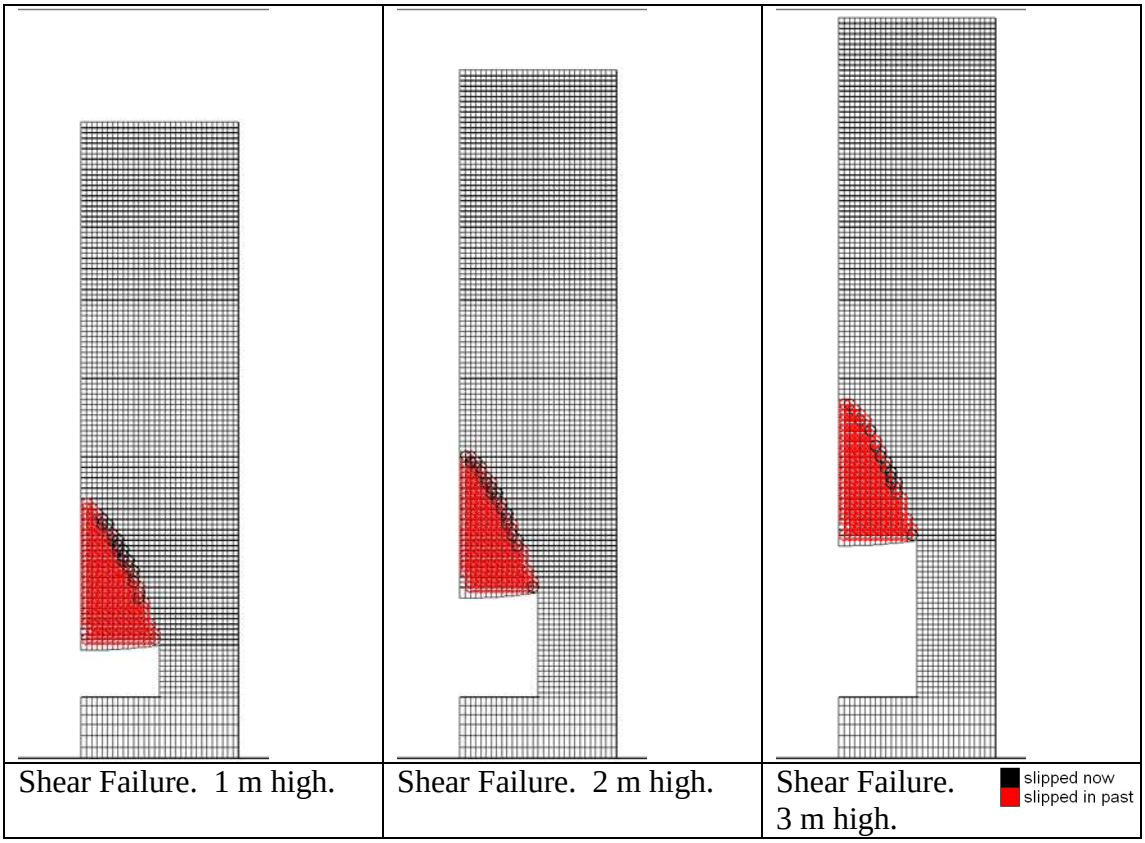

Figure 5.74: Shear interface failure plots for the rock mass (GSI 60).

5.9 Summary of the Full Modelling Results

A significant parametric study was undertaken and some of the results were discussed in detail in the previous sections. A summary of the results for the full range of varying excavation widths, heights, rock mass strengths and bedding plane separations has been created in the form of a series of tables where the level of the groundwater height at which initial instability occurs within the model for the varying parameters is indicated These tables are presented organised in a form where the effect of excavation height on stability is apparent. See Table 5.6 through to Table 5.14.

Table 5.6: Level of water table in which the initiation of yielding occurs for varying excavation heights and rock mass strengths in a 1 m wide excavation at 0.1 m bedding thickness.

Bedding Plane Separation (m)	GSI	Excavation Width (m)	Excavation Height (m)	Hydraulic Head Above Excavation Roof at Instability (m)
0.1	10	1.0	1.0	1.0
0.1	20	1.0	1.0	1.0
0.1	30	1.0	1.0	1.0
0.1	40	1.0	1.0	2.0
0.1	50	1.0	1.0	4.0
0.1	60	1.0	1.0	10.0 - Stable
0.1	10	1.0	2.0	1.0
0.1	20	1.0	2.0	1.0
0.1	30	1.0	2.0	1.0
0.1	40	1.0	2.0	2.0
0.1	50	1.0	2.0	4.0
0.1	60	1.0	2.0	10.0 - Stable
0.1	10	1.0	3.0	1.0
0.1	20	1.0	3.0	1.0
0.1	30	1.0	3.0	1.0
0.1	40	1.0	3.0	3.0
0.1	50	1.0	3.0	4.0
0.1	60	1.0	3.0	10.0 - Stable

Table 5.7 Level of water table in which the initiation of yielding occurs for varying excavation heights and rock mass strengths in a 2 m wide excavation at 0.1 m bedding thickness.

Bedding Plane Separation (m)	GSI	Excavation Width (m)	Excavation Height (m)	Hydraulic Head Above Excavation Roof at Instability (m)
0.1	10	2.0	1.0	0.0
0.1	20	2.0	1.0	0.0
0.1	30	2.0	1.0	1.0
0.1	40	2.0	1.0	1.0
0.1	50	2.0	1.0	2.0
0.1	60	2.0	1.0	3.0
0.1	10	2.0	2.0	0.0
0.1	20	2.0	2.0	0.0
0.1	30	2.0	2.0	2.0
0.1	40	2.0	2.0	2.0
0.1	50	2.0	2.0	3.0
0.1	60	2.0	2.0	3.0
0.1	10	2.0	3.0	0.0
0.1	20	2.0	3.0	0.0
0.1	30	2.0	3.0	2.0
0.1	40	2.0	3.0	2.0
0.1	50	2.0	3.0	3.0
0.1	60	2.0	3.0	3.0

Table 5.8: Level of water table in which the initiation of yielding occurs for varying excavation heights and rock mass strengths in a 3 m wide excavation at 0.1 m bedding thickness.

Bedding Plane Separation (m)	GSI	Excavation Width (m)	Excavation Height (m)	Hydraulic Head Above Excavation Roof at Instability (m)
0.1	10	3.0	1.0	0.0
0.1	20	3.0	1.0	0.0
0.1	30	3.0	1.0	0.0
0.1	40	3.0	1.0	0.0
0.1	50	3.0	1.0	1.0
0.1	60	3.0	1.0	2.0
0.1	10	3.0	2.0	0.0
0.1	20	3.0	2.0	0.0
0.1	30	3.0	2.0	0.0
0.1	40	3.0	2.0	1.0
0.1	50	3.0	2.0	2.0
0.1	60	3.0	2.0	2.0
0.1	10	3.0	3.0	0.0
0.1	20	3.0	3.0	0.0
0.1	30	3.0	3.0	0.0
0.1	40	3.0	3.0	1.0
0.1	50	3.0	3.0	2.0
0.1	60	3.0	3.0	2.0

Table 5.9: Level of water table in which the initiation of yielding occurs for varying excavation heights and rock mass strengths in a 3 m wide excavation at 0.2 m bedding thickness.

Bedding Plane Separation (m)	GSI	Excavation Width (m)	Excavation Height (m)	Hydraulic Head Above Excavation Roof at Instability (m)
0.2	10	1.0	1.0	1.0
0.2	20	1.0	1.0	1.0
0.2	30	1.0	1.0	1.0
0.2	40	1.0	1.0	2.0
0.2	50	1.0	1.0	7.0
0.2	60	1.0	1.0	10.0 - Stable
0.2	10	1.0	2.0	1.0
0.2	20	1.0	2.0	1.0
0.2	30	1.0	2.0	1.0
0.2	40	1.0	2.0	3.0
0.2	50	1.0	2.0	6.0
0.2	60	1.0	2.0	10.0 - Stable
0.2	10	1.0	3.0	1.0
0.2	20	1.0	3.0	1.0
0.2	30	1.0	3.0	1.0
0.2	40	1.0	3.0	2.0
0.2	50	1.0	3.0	7.0
0.2	60	1.0	3.0	10.0 - Stable

Table 5.10: Level of water table in which the initiation of yielding occurs for varying excavation heights and rock mass strengths in a 3 m wide excavation at 0.2 m bedding thickness.

Bedding Plane Separation (m)	GSI	Excavation Width (m)	Excavation Height (m)	Hydraulic Head Above Excavation Roof at Instability (m)
0.2	10	2.0	1.0	1.0
0.2	20	2.0	1.0	1.0
0.2	30	2.0	1.0	1.0
0.2	40	2.0	1.0	2.0
0.2	50	2.0	1.0	2.0
0.2	60	2.0	1.0	10.0 - Stable
0.2	10	2.0	2.0	1.0
0.2	20	2.0	2.0	1.0
0.2	30	2.0	2.0	1.0
0.2	40	2.0	2.0	3.0
0.2	50	2.0	2.0	7.0
0.2	60	2.0	2.0	10.0 - Stable
0.2	10	2.0	3.0	1.0
0.2	20	2.0	3.0	1.0
0.2	30	2.0	3.0	1.0
0.2	40	2.0	3.0	3.0
0.2	50	2.0	3.0	6.0
0.2	60	2.0	3.0	10.0 - Stable

Table 5.11: Level of water table in which the initiation of yielding occurs for varying excavation heights and rock mass strengths in a 3 m wide excavation at 0.2 m bedding thickness

Bedding Plane Separation (m)	GSI	Excavation Width (m)	Excavation Height (m)	Hydraulic Head Above Excavation Roof at Instability (m)
0.2	10	3.0	1.0	0.0
0.2	20	3.0	1.0	0.0
0.2	30	3.0	1.0	2.0
0.2	40	3.0	1.0	1.0
0.2	50	3.0	1.0	2.0
0.2	60	3.0	1.0	4.0
0.2	10	3.0	2.0	0.0
0.2	20	3.0	2.0	0.0
0.2	30	3.0	2.0	1.0
0.2	40	3.0	2.0	1.0
0.2	50	3.0	2.0	2.0
0.2	60	3.0	2.0	3.0
0.2	10	3.0	3.0	0.0
0.2	20	3.0	3.0	0.0
0.2	30	3.0	3.0	1.0
0.2	40	3.0	3.0	1.0
0.2	50	3.0	3.0	2.0
0.2	60	3.0	3.0	3.0

Table 5.12: Level of water table in which the initiation of yielding occurs for varying excavation heights and rock mass strengths in a 3 m wide excavation at 0.5 m bedding thickness

Bedding Plane Separation (m)	GSI	Excavation Width (m)	Excavation Height (m)	Hydraulic Head Above Excavation Roof at Instability (m)
0.5	10	1.0	1.0	1.0
0.5	20	1.0	1.0	1.0
0.5	30	1.0	1.0	1.0
0.5	40	1.0	1.0	3.0
0.5	50	1.0	1.0	5.0
0.5	60	1.0	1.0	10.0 - Stable
0.5	10	1.0	2.0	1.0
0.5	20	1.0	2.0	1.0
0.5	30	1.0	2.0	1.0
0.5	40	1.0	2.0	3.0
0.5	50	1.0	2.0	5.0
0.5	60	1.0	2.0	10.0 - Stable
0.5	10	1.0	3.0	1.0
0.5	20	1.0	3.0	1.0
0.5	30	1.0	3.0	1.0
0.5	40	1.0	3.0	3.0
0.5	50	1.0	3.0	5.0
0.5	60	1.0	3.0	10.0 - Stable

Table 5.13: Level of water table in which the initiation of yielding occurs for varying excavation heights and rock mass strengths in a 3 m wide excavation at 0.5 m bedding thickness

Bedding Plane Separation (m)	GSI	Excavation Width (m)	Excavation Height (m)	Hydraulic Head Above Excavation Roof at Instability (m)
0.5	10	2.0	1.0	1.0
0.5	20	2.0	1.0	1.0
0.5	30	2.0	1.0	1.0
0.5	40	2.0	1.0	2.0
0.5	50	2.0	1.0	5.0
0.5	60	2.0	1.0	10.0 - Stable
0.5	10	2.0	2.0	1.0
0.5	20	2.0	2.0	1.0
0.5	30	2.0	2.0	1.0
0.5	40	2.0	2.0	3.0
0.5	50	2.0	2.0	7.0
0.5	60	2.0	2.0	10.0 - Stable
0.5	10	2.0	3.0	1.0
0.5	20	2.0	3.0	1.0
0.5	30	2.0	3.0	1.0
0.5	40	2.0	3.0	3.0
0.5	50	2.0	3.0	6.0
0.5	60	2.0	3.0	10.0 - Stable

Table 5.14: Level of water table in which the initiation of yielding occurs for varying excavation heights and rock mass strengths in a 3 m wide excavation at 0.5 m bedding thickness

Bedding Plane Separation (m)	GSI	Excavation Width (m)	Excavation Height (m)	Hydraulic Head Above Excavation Roof at Instability (m)
0.5	10	3.0	1.0	1.0
0.5	20	3.0	1.0	2.0
0.5	30	3.0	1.0	3.0
0.5	40	3.0	1.0	5.0
0.5	50	3.0	1.0	10.0 - Stable
0.5	60	3.0	1.0	10.0 - Stable
0.5	10	3.0	2.0	1.0
0.5	20	3.0	2.0	2.0
0.5	30	3.0	2.0	3.0
0.5	40	3.0	2.0	5.0
0.5	50	3.0	2.0	10.0 - Stable
0.5	60	3.0	2.0	10.0 - Stable
0.5	10	3.0	3.0	1.0
0.5	20	3.0	3.0	2.0
0.5	30	3.0	3.0	3.0
0.5	40	3.0	3.0	5.0
0.5	50	3.0	3.0	10.0 - Stable
0.5	60	3.0	3.0	10.0 - Stable

Plotting the data for variations in rock mass strength against the pore water pressure where yielding of the roof occurs for differing excavation heights yields information on the impact of excavation height on stability.

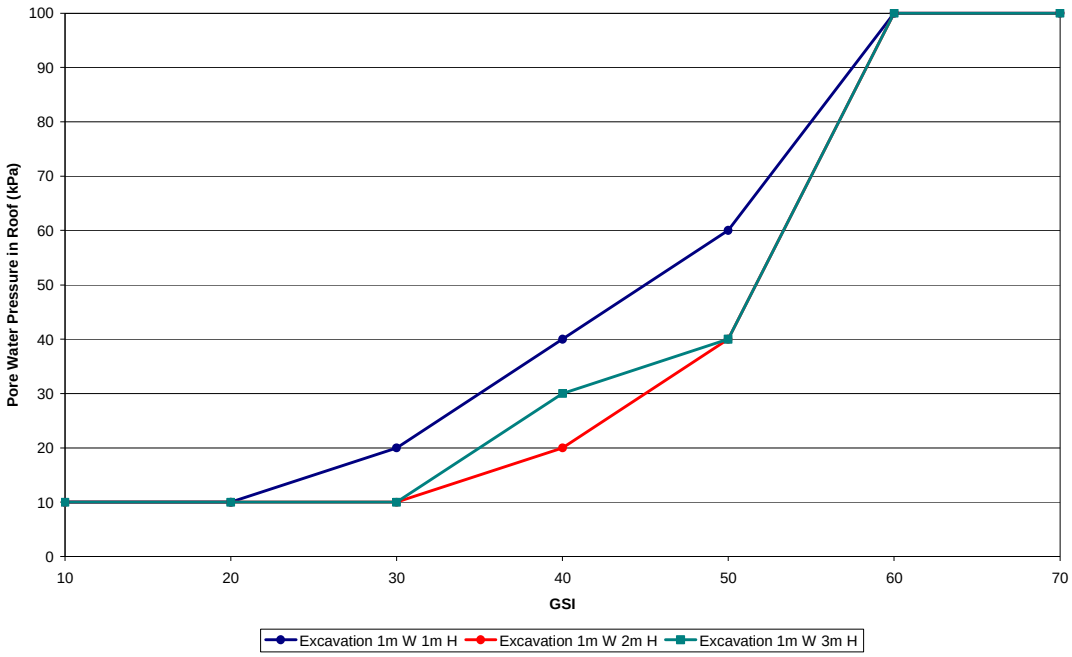

Figure 5.75: Plot of pore water pressure in the excavation roof when yielding exceeds the prescribed criterion at varying rock mass strengths with bedding spacing at 0.1 m, an excavation width of 1 m and for variable excavation heights.

In the modelling results summarised here, the excavation width has been set to 1 m within the model and the results for varying rock mass strengths and excavation heights are discussed. Figure 5.75 is a plot of the pore water pressure in the roof centreline (as derived from the hydraulic head value recorded in Table 5.6) at which yielding within the roof strata exceeds the prescribed yield criterion of 100% vertical strain in the roof strata.

Initially the stability for all three excavation heights is equal in that at a GSI value of 10 they all yield as the pore water pressure reaches 10 kPa equivalent to the water table rising to a point 1 m above the excavation. As the rock mass strength of the models is increased the results remain the same with yielding occurring at 10 kPa in all three cases for a GSI of 20. At GSI 30 the behaviour changes as the model with the lowest excavation height (1 m) yields at a higher pore water pressure (20 kPa) than the 2 and 3 m high excavation models (which are unchanged, once again yielding at 10 kPa) indicating that the 1 m high excavation is more stable. This trend continues as the rock mass strength is increased to GSI 40. The increase in strength results in an increase in stability in all three excavations with the 1 m excavation yielding at 40 kPa compared to

a value of 20 kPa and 30 kPa for the 2 and 3 m high excavations respectively. The difference in stability between the 2 and 3 m high excavations was marginal and yielding commenced in the 3 m high excavation at a roof pore water pressure of 10 kPa which is lower than that recorded in the 2 m high excavation but stabilised and ultimately yielded as the groundwater table increased to 3 m above the excavation roof. This initial deformation representing precursor instability behaviour at a pore water pressure of 10 kPa and then the final yielding of the roof can be seen in the plots of vertical displacement and strain which are plotted against pore water pressure in Figure 5.76.

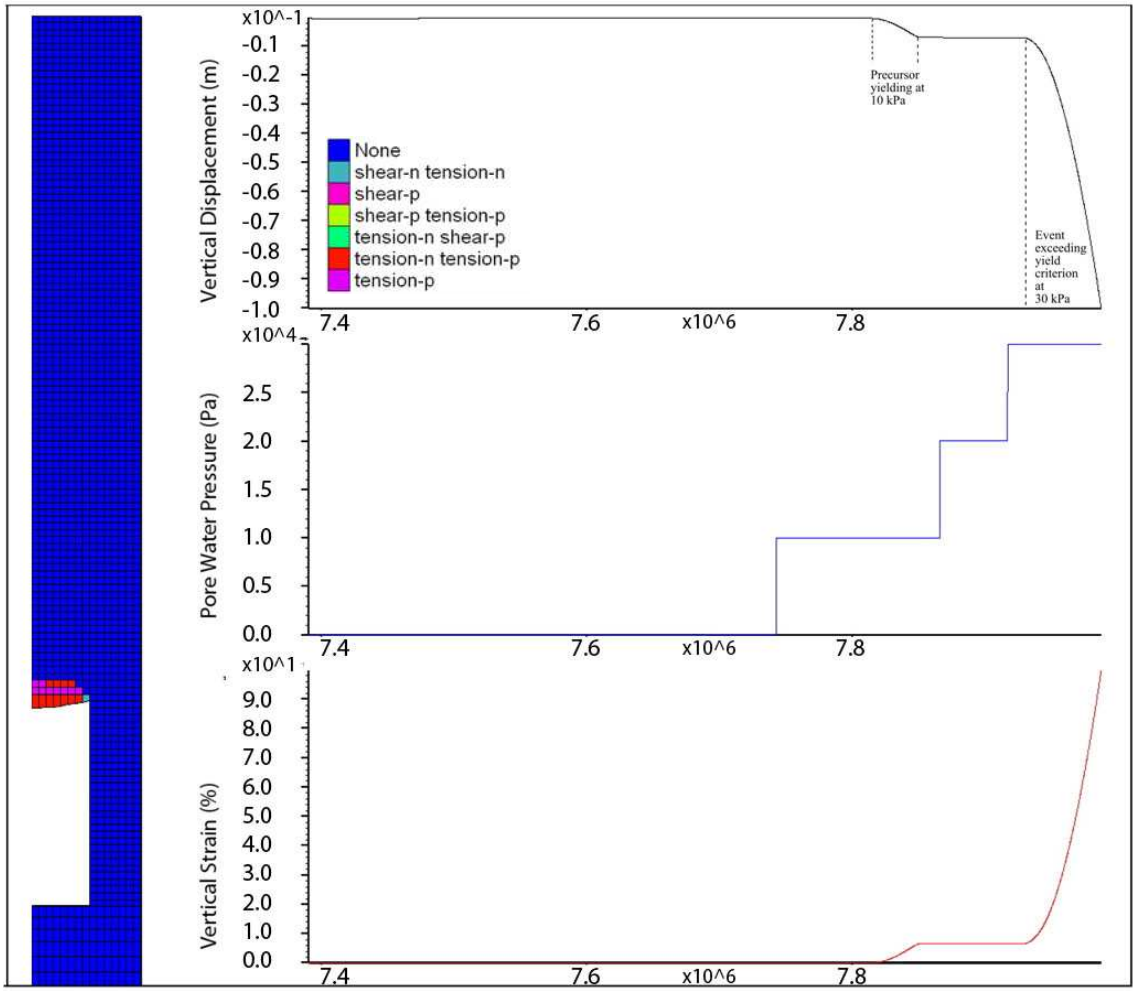

Figure 5.76: Yield state of the rock mass within the model for a bedding plane spacing of 0.1 m. Model parameters - Excavation 1 m wide, 3 m high; GSI 40.

As the rock mass strength increases to GSI 50 the stability of all three excavations increases once again, however the 1 m high excavation remains stable up to a pore water pressure of 60 kPa as opposed to a value of 40 kPa for the 2 and 3 m high excavations. Finally as the rock mass strength is increased again to a GSI value of 60, all three excavations are stable at the maximum pore water pressure recorded here at 100 kPa.

Based on the above, for a 1 m wide excavation, it can be seen that there is broadly a decrease in stability (defined as a decrease in the pore water pressure required to cause yielding of the roof sufficient to exceed the prescribed criterion) as the excavation height increases from 1 m to 2 m at intermediate rock mass strengths (between GSI 30 and 50). The 2 and 3 m high rock masses show broadly equivalent stability.

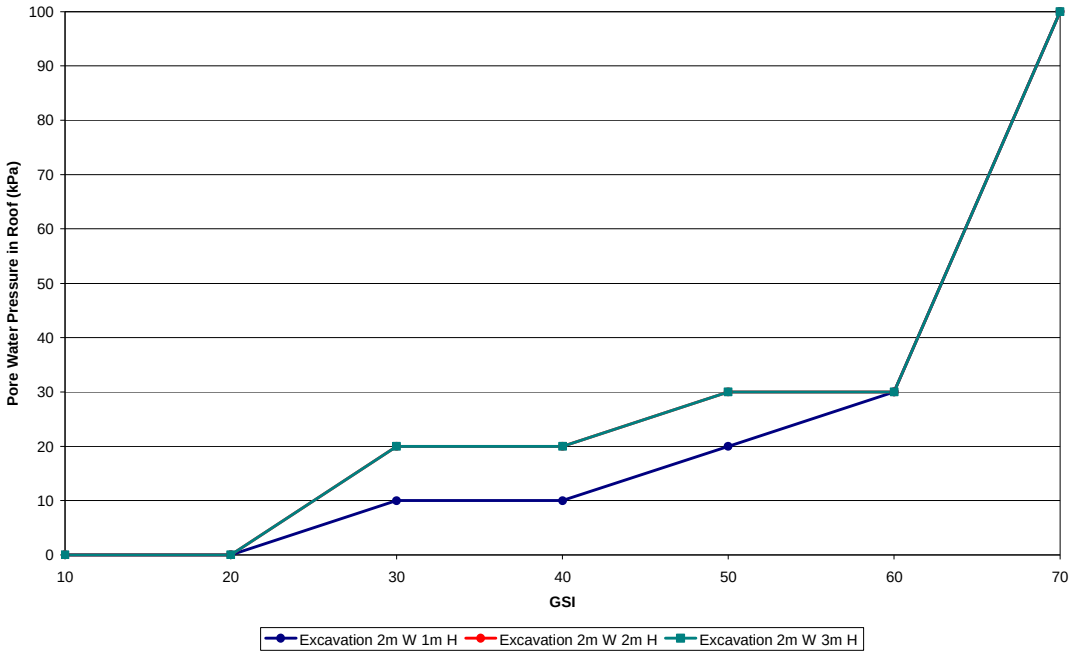

Figure 5.77: Plot of pore water pressure in the excavation roof when yielding exceeds the prescribed criterion at varying rock mass strengths with bedding spacing at 0.1 m, an excavation width of 2 m and for variable excavation heights.

In the modelling results summarised here, the excavation width has been increased to 2 m and the results for varying rock mass strengths and excavation heights are discussed. Figure 5.77 is a plot of the pore water pressure in the roof centreline (as derived from the hydraulic head value recorded in Table 5.7) at which yielding within the roof for excavation heights from 1 to 3 m and for an excavation width of 1 m.

As for the 1 m wide model it can be seen that initially the stability for all three excavation heights is equal. However significantly in all three cases, the excavations are unstable before the water table reaches the base of the excavation. This can be seen in Figure 5.78, Figure 5.79 and Figure 5.80 for the 1, 2 and 3 m excavation height examples respectively.

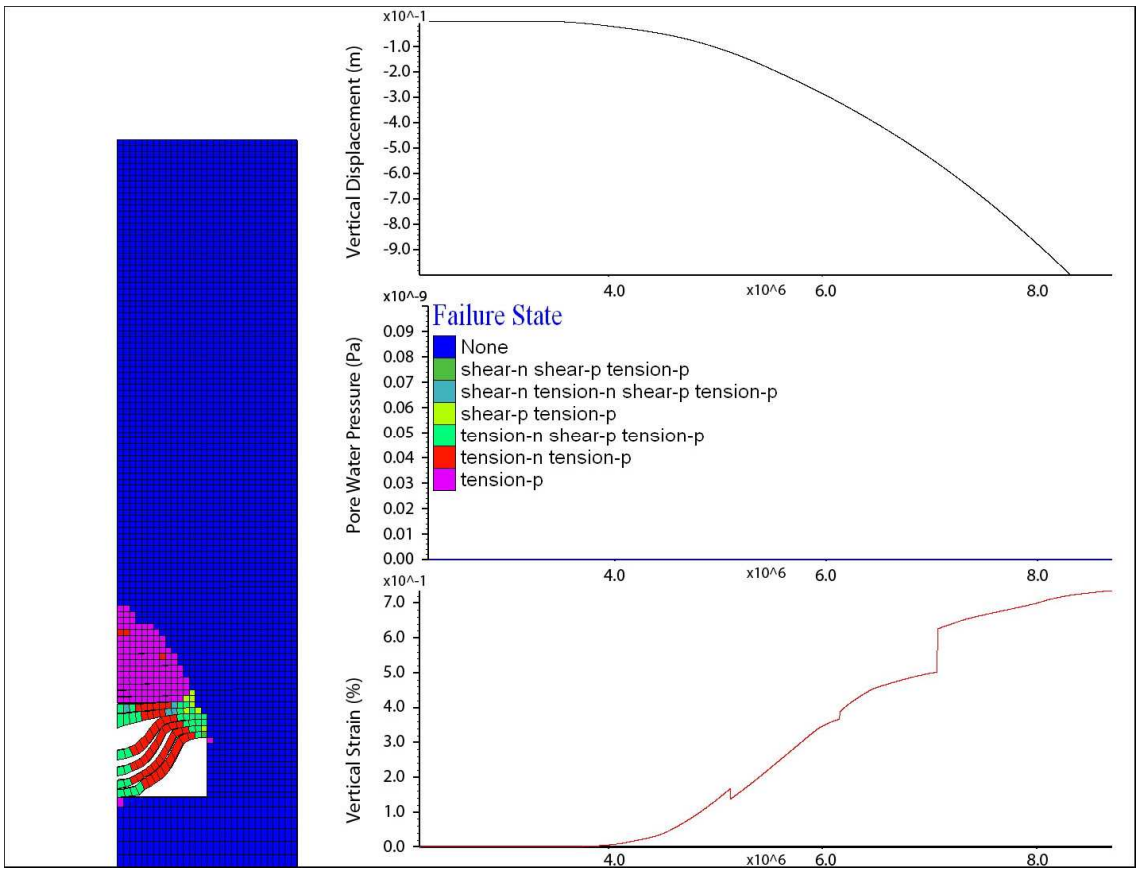

Figure 5.78: Yield state of the rock mass within the model for a bedding plane spacing of 0.1 m. Model parameters - Excavation 2 m wide, 1 m high; GSI 10.

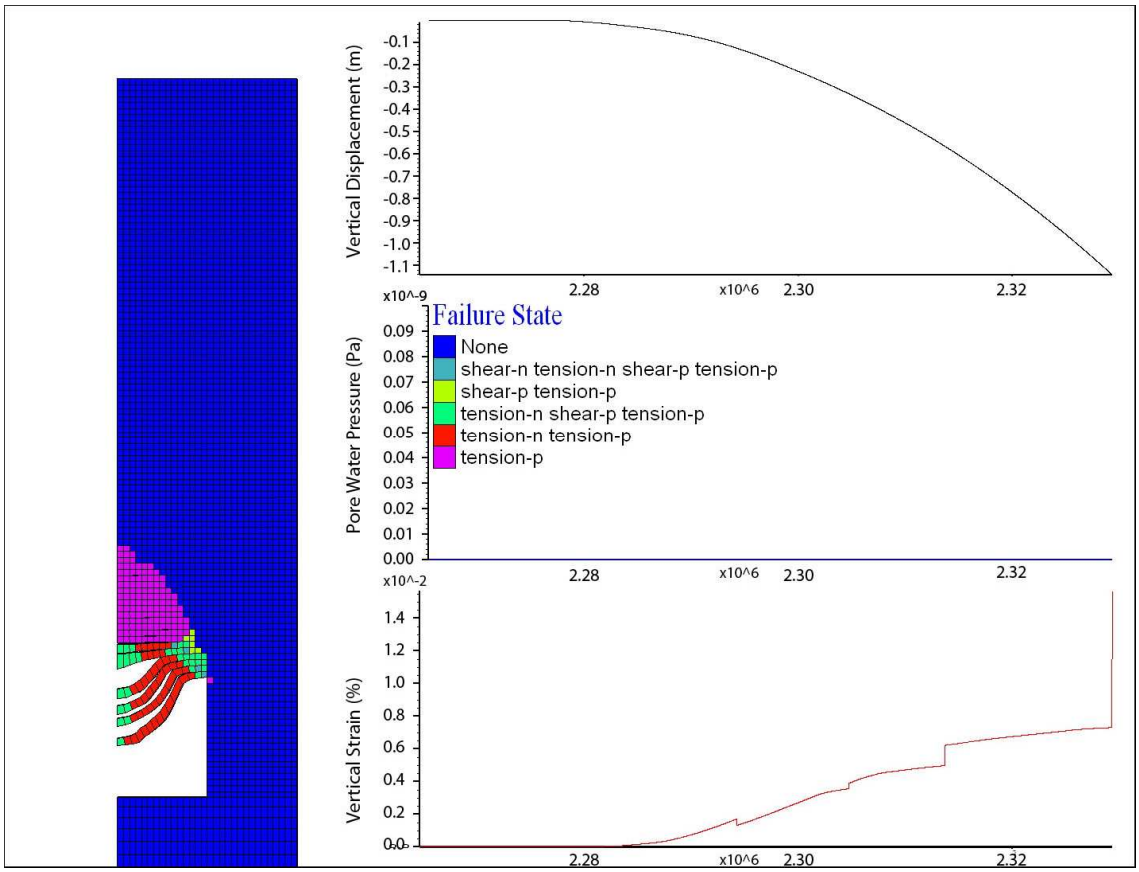

Figure 5.79: Yield state of the rock mass within the model for a bedding plane spacing of 0.1 m. Model parameters - Excavation 2 m wide, 2 m high; GSI 10.

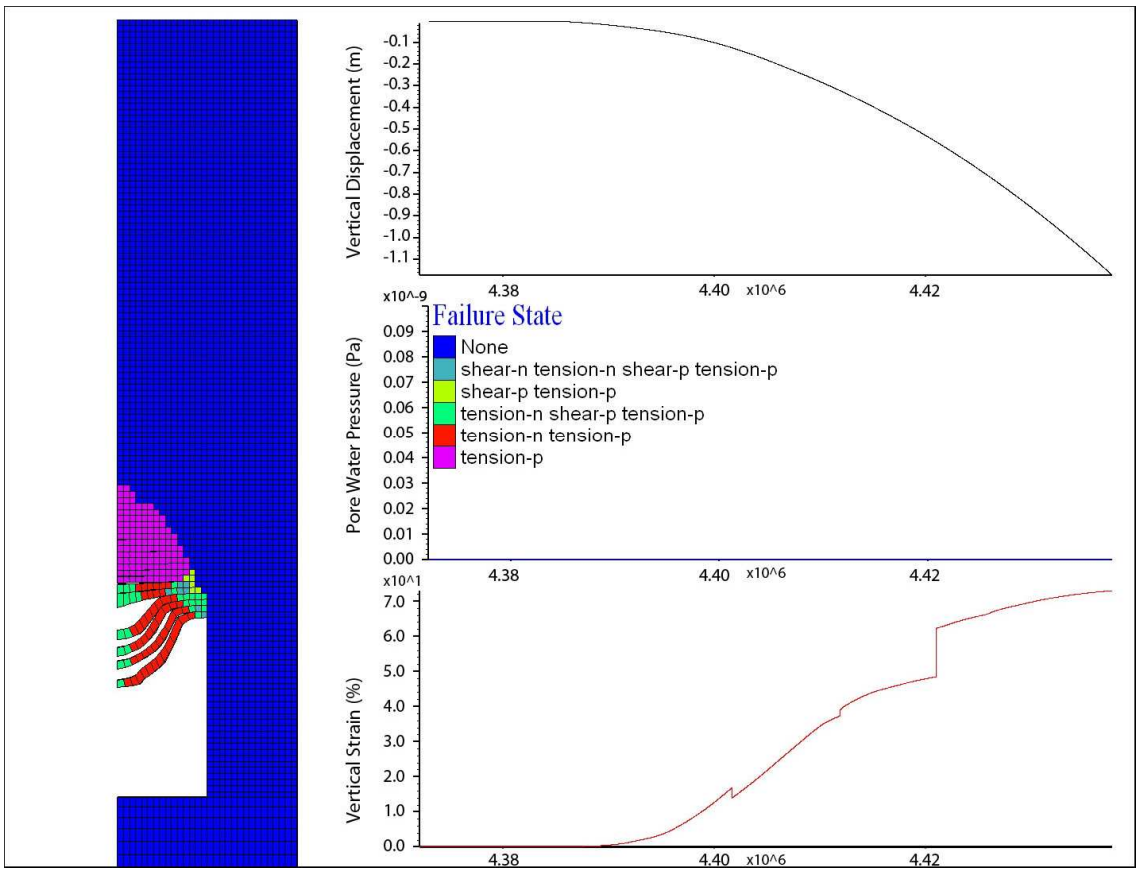

Figure 5.80: Yield state of the rock mass within the model for a bedding plane spacing of 0.1 m. Model parameters - Excavation 2 m wide, 3 m high; GSI 10.

As the rock mass strength of the models is increased the results remain the same with yielding occurring before the water table reached the excavation in all three cases for a GSI of 20. At GSI 30 the behaviour changes as the stability of the roof strata increases with an initially stable excavation where yielding is triggered once the water table and hence pore water pressures exceed a certain value.

For the GSI 30, 2 m width models, it can be seen that the model with the lowest excavation height (1 m) yields at a lower pore water pressure (10 kPa) than the 2 and 3 m high excavation models (which in this case display increased stability compared to the lower excavation). This appears to be a reversal of the trend seen for the 1 m wide excavation models where increased excavation height led to a decrease in stability at this rock mass strength. Another significant change is the progression from roof failure with visible sagging of the roof strata which occurred in the rock masses with GSI values of 10 and 20, through to yielding of the roof mass without visible delamination and sagging of the roof material into the void. This can be seen in a comparison of the yield plots for models with a rock mass GSI of 10, 20 and 30 respectively as seen in Figure 5.81. For this excavation width, roof failure characterised by significant sagging

of roof strata does not occur at rock mass strengths greater than GSI 20, instead plastic yielding occurs.

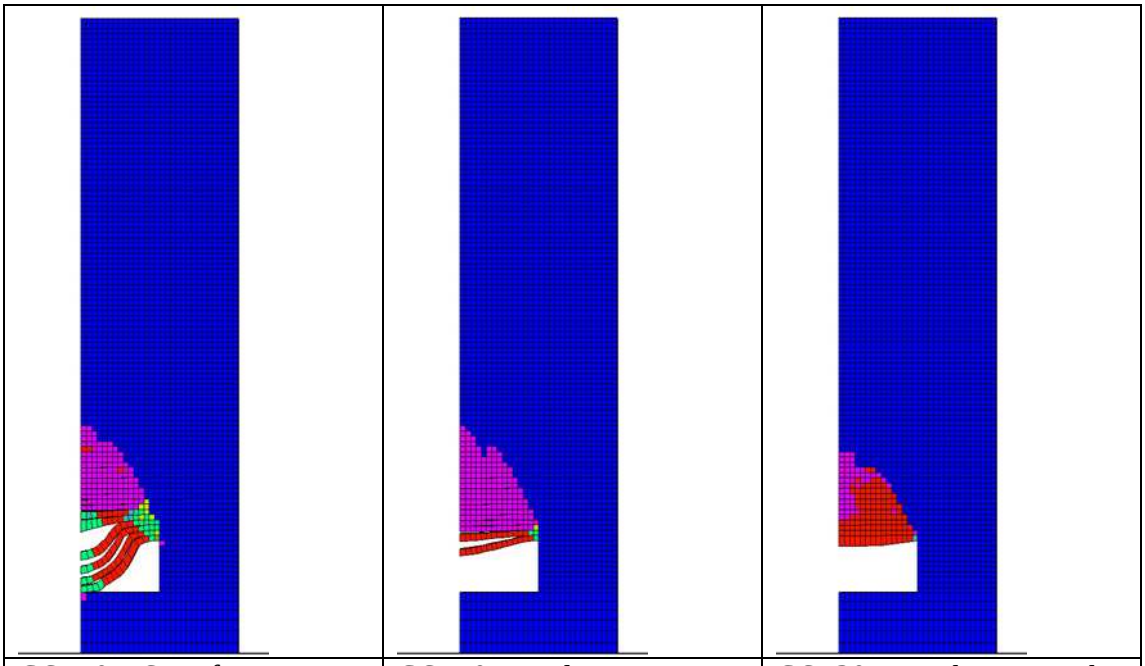

GSI 10 – Significant sagging and delamination	GSI 20 – Reduction in sagging and delamination as strength is increased.	GSI 30 – Further strength increase leads to no visible sagging of strata. Instead roof yields plastically as a continuum.

Figure 5.81: Comparison of yielding within the rock mass within the model for a bedding plane spacing of 0.1 m. Model parameters - Excavation 2 m wide, 1 m high; GSI 10, 20 and 30.

The trend whereby the 2 and 3 m high excavations are more stable than the 1 m high excavation continues as the rock mass strength is increased to GSI 40, with the pore water pressure the initiate instability being equal to that seen at the lower rock mass strength (GSI 30). When compared to the results for the 1 m wide excavation, it can been that the 1 m high excavation is significantly less stable (yielding at a pore water pressure of 10 kPa in the 2 m wide model compared to a value of 40 kPa in the 1 m wide excavation model). The stability of the 2 and 3 m high excavations appears unaffected by the increase in excavation width from 1 to 2 m.

As the rock mass strength is once again increased to a GSI value of 50, the stability of all three excavations increases with a pore water pressure of 20 kPa required to cause yielding of the 1 m high excavation (a reduction of 40 kPa when compared to the 60 kPa value required to cause instability in the 1 m width model) and the 2 and 3 m excavations are stable until a pore water pressure of 30 kPa occurs within the roof strata (a reduction of 10 kPa when compared to the 40 kPa value required to cause instability

in the 1 m width models at his rock mass strength). As the rock mass strength is increased to GSI 60 the stability of the roof strata again increases, requiring a pore water pressure equal to 30 kPa to cause yielding to occur in all three cases.

Finally at GSI 70 all three excavations are stable at all pore water pressures tested here as per the 1 m wide excavation models.

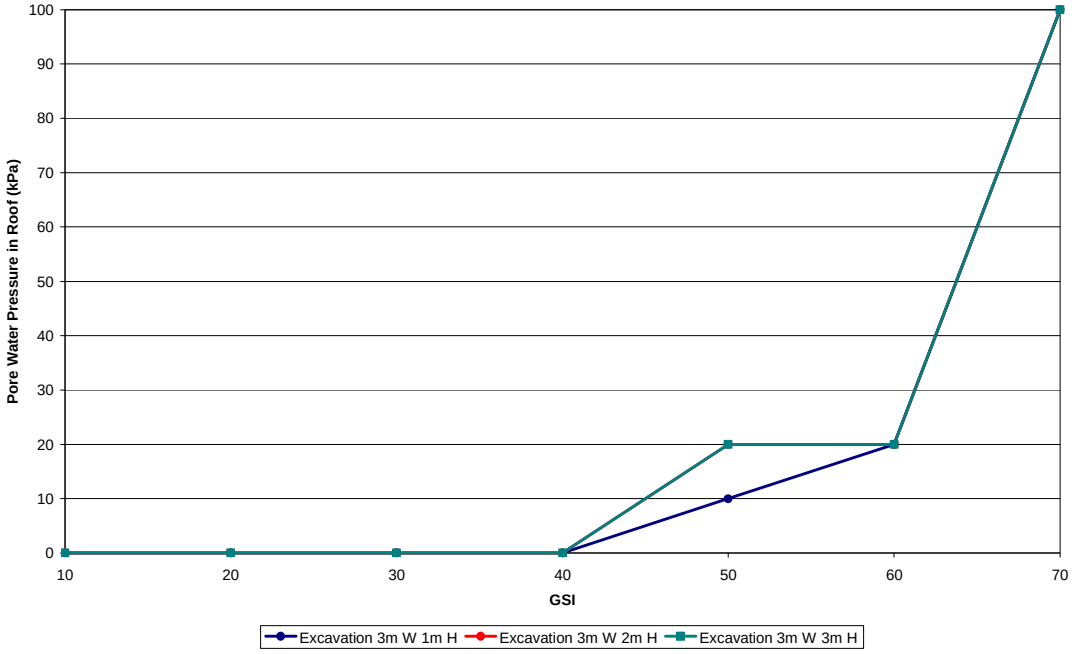

Figure 5.82: Plot of pore water pressure in the excavation roof when yielding exceeds the prescribed criterion at varying rock mass strengths with bedding spacing at 0.1 m, an excavation width of 3 m and for variable excavation heights.

In the modelling results summarised here, the excavation width has been increased to 3 m and the results for varying rock mass strengths and excavation heights are discussed.

Figure 5.82 is a plot of the pore water pressure in the roof centreline (as derived from the hydraulic head value recorded in Table 5.8) at which yielding within the roof strata exceeds the prescribed yield criterion of 100% vertical strain. As for the modelling undertaken with the 1 and 2 m wide excavations it can be seen that initially the stability for all three excavation heights is equal. Again significantly in all three cases, the excavations are unstable before the water table reaches the base of the excavation. As the rock mass strength of the models is increased the results remain the same with yielding occurring before the water table reached the excavation in all three cases for a GSI of 20 as per the 2 m wide modelling. At GSI values of 30 and 40, the rock mass is still unstable before any increase in the pore water pressure occurs, this is a significant

decrease in the stability of the excavation roof when compared to the 1 m and 2 m wide excavation modelling.

At GSI 50 the 2 and 3 m high excavations are initially stable until the pore water pressure reached 20 kPa within the roof of the excavation at which point yielding occurs within the roof, however it can be seen that the model with the lowest excavation height (1 m) yields at a lower pore water pressure (10 kPa). Another significant change at this rock mass strength is the progression from roof failure with visible sagging of the roof strata which occurred in the rock masses with GSI values of 10 through to 40, through to yielding of the roof mass without visible delamination and sagging of the roof material into the void. This also indicates a significant decrease in stability compared to the modelling undertaken with lower excavation width. This can be seen in a comparison of the yield plots for models with a rock mass GSI of 10, 20, 30, 40 and 50 respectively as seen in Figure 5.83. For this excavation width, roof failure characterised by significant sagging of roof strata does not occur at rock mass strengths greater than GSI 40, instead plastic yielding occurs.

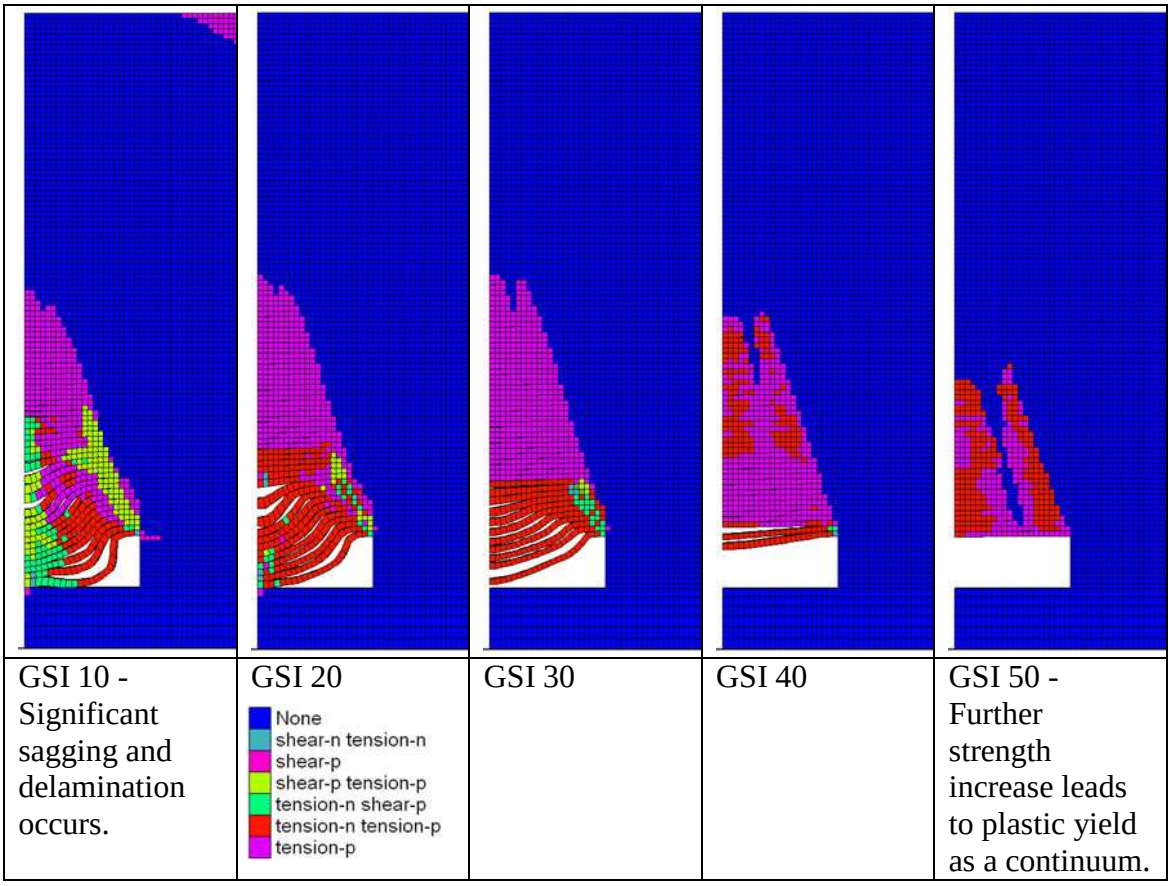

Figure 5.83: Comparison of yielding within the rock mass within the model for a bedding plane spacing of 0.1 m. Model parameters - Excavation 3 m wide, 1 m high; GSI 10 to 50.

As the rock mass strength is increased further to GSI 60 the rock mass for all excavation heights is stable until the water table reaches a height 2 m over the excavation roof (pore water pressure of 20 kPa). This marks a decrease in stability from the 2 m wide model (where a pore water pressure of 30 kPa was required to initiate instability) and a significant decrease on the stability of the 1 m wide excavation.
Excavations with a GSI of 70 were stable at all variations of pore water pressure and excavation geometry.

5.10 Conclusions of Modelling on the Effect of Variations in Excavation Height on Roof Stability

The results of the modelling of varying excavation height indicate that this parameter appears to have a very limited impact on the stability of excavations with the rock mass strength and the height of the groundwater table being far more significant parameters. However it is noted that the excavation height has a limited impact on excavation stability that is related to the ratio of width of excavation to excavation height. Whereby excavation stability increases as the excavation width to height ratio approaches one and decreases as this parameter diverges from 1.
From the results presented here it is clear that the decrease in stability due to increase in height of an excavation for a given rock mass strength cause significantly less instability than increase in excavation width or variations in the water table.

5.11 Effect of Averaged Rock Mass Strength on Excavation Stability

In the modelling results presented below the averaged rock mass strength parameters were varied to investigate its impact on the stability of shallow excavations. In this case the averaged rock mass strength refers to the case here where the friction angle of the discontinuities is assumed to be equal to that of the material forming the bedding planes.

A plot comparing the yield state of the rock mass for the rock mass strengths investigated (see Figure 5.84) shows that some yielding occurs at all values tested however the rock masses can be split broadly into two main groups. Those where tensile delamination with failure of the roof strata has occurred (marked by the formation of zones of shear yielding at the end of the individual strata within the roof – see Figure 5.84 parts A to D) and those which have purely undergone tensile yielding due to delamination of the roof strata but with limited displacements and where the excavation roof strata are stable (see Figure 5.84 parts E to G).

It is readily apparent that the degree of roof strata sagging in the models that have undergone visible deformations increases with decreasing rock mass strength. The height to which the collapse of the strata extends into the rock mass also increases with decreasing rock mass strength with this zone of failure extending only around 0.2 m into the rock mass above the excavation for a rock mass strength equivalent to a GSI of 40 (Figure 5.84 part D) and increasing to approximately 2.5 m at the lowest rock mass strength tested (Figure 5.84 part A).

The models that have undergone roof failure as opposed to yielding also share a common feature in terms of the height to which tensile yielding extends into the rock mass over the new excavation roof. This zone of damage in these cases extends approximately 5 m into the rock mass over the original excavation roof and forms a wedge at an angle of approximately 15-18 degrees from the vertical. This zone of tensile yielding corresponds in this case to the height to which tensile delamination of the bedding has occurred.

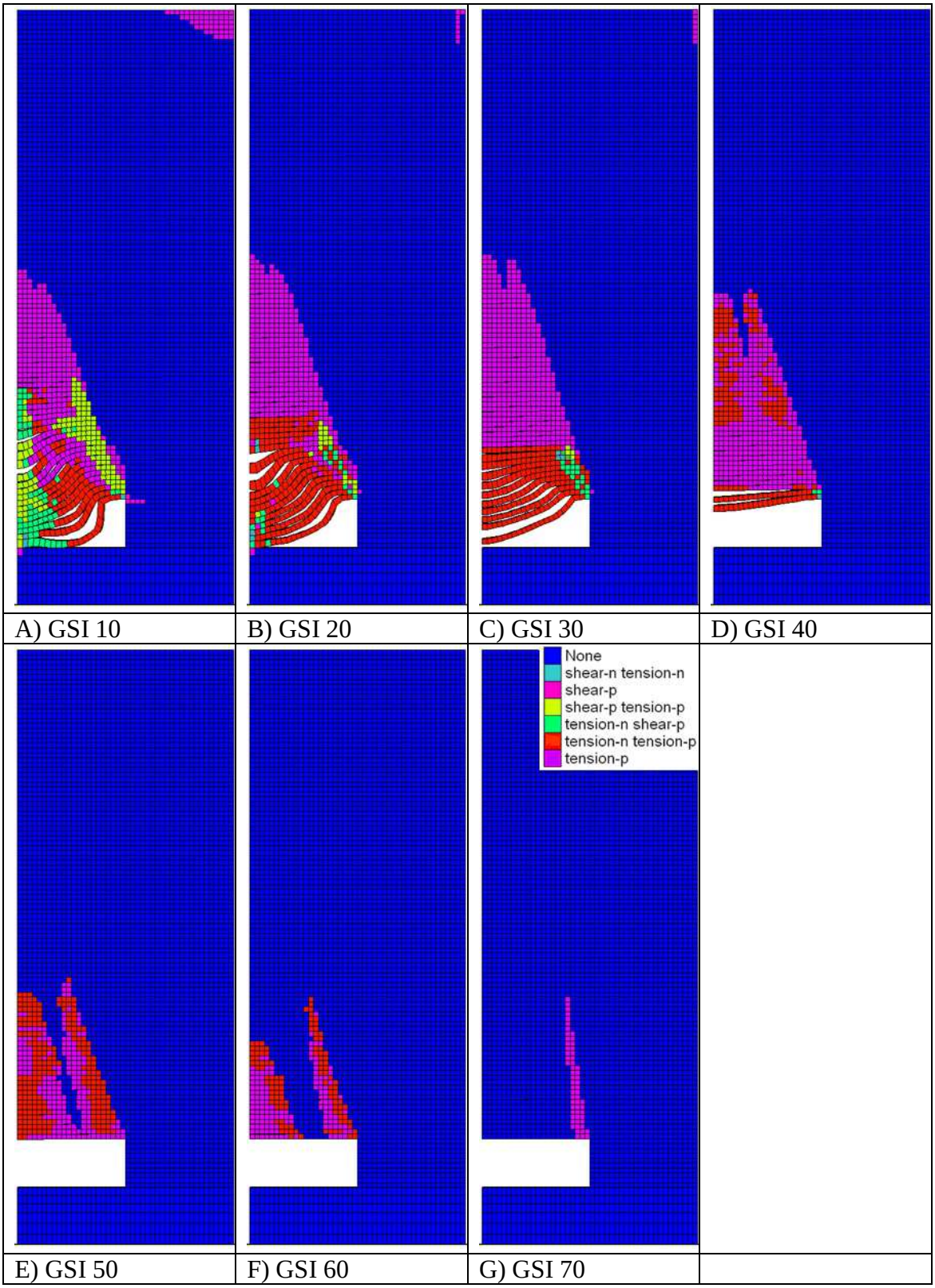

A) GSI 10 | B) GSI 20 | C) GSI 30 | D) GSI 40

E) GSI 50 | F) GSI 60 | G) GSI 70

Figure 5.84: Yield state plot of the rock mass for varying rock mass strength values. Excavation width 3m, excavation height 1m. Water table below the excavation.

5.12 Comparisons of Varying Water Table on the Stability of Excavations with Varying Bedding Surface Friction Angles.

In this section, the effect of increasing pore water pressure / water table level on the stability of excavations in a rock mass with interface elements is investigated. The continuum modelling and the section on the effect on stability of varying excavation height has demonstrated clearly that even small changes in the pore water pressure can trigger initial instability so in this section it is intended to investigate the post failure response of a rock mass where the roof has failed.

In this example, the effect of the water table on a rock mass with a GSI value equal to 10 above a 3 m wide, 1 m high, excavation is demonstrated. Figure 5.85 shows a yield state plot overlain with contours of pore water pressure. In this example the excavation was unstable so collapse occurred instantaneously. Initially the rising groundwater table has a limited effect on the rock mass with the rise through the excavation causing some limited change in the yield state of the rock mass (typically a change from yield in the past to yield in the present). This may prompt further instability however in this case does not seem to cause visible movement of the roof strata.

As the water table continues to rise however, upon reaching the maximum extent of yielding within the rock mass at approximately 6 m above excavation roof (marked by the region where tensile yielding has occurred related to tensile delamination of the bedding plane which in the model is demonstrated by normal and shear failure of the interface elements) the increased pore water pressures begin to cause tensile failure of the rock mass to occur above this zone, with the tensile yielding progressing gradually further upwards into the rock mass until it reaches the surface. On examination of the normal and shear interface element yield plots, a phenomenon was observed whereby the increasing water table causes the interface elements to be forced back into contact with each other which can be observed in the normal interface plot in Figure 5.86.

It can be seen in this plot that the interfaces begin to be forced back together at a point at the base of the zone of tensile delamination and tensile yielding above the zone that is characterised by tensile yielding of bedding along with shear yielding. As the water table continues to rise, the bedding surfaces represented by the interface elements are forced back into contact. However the bedding planes below this boundary are still separated.

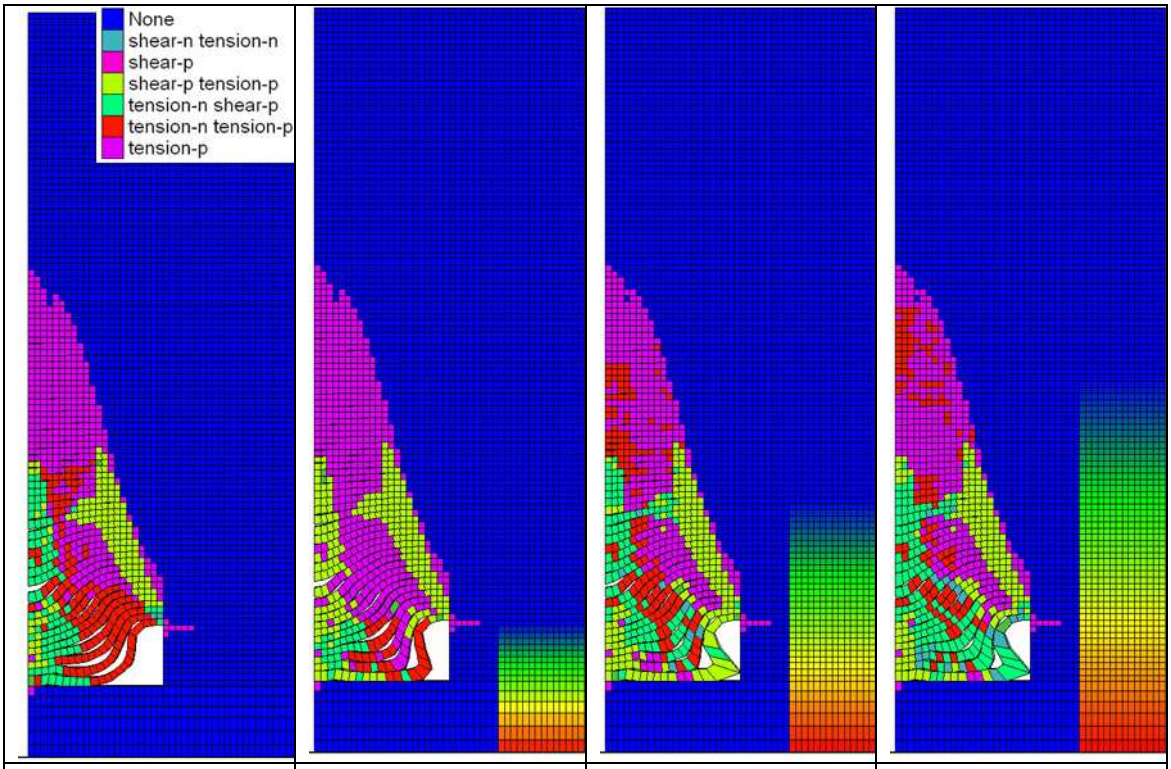

Phreatic surface: 2 m below exc. roof	Phreatic surface level with exc. roof	Phreatic surface: 2 m above exc. roof	Phreatic surface: 4m above exc. roof

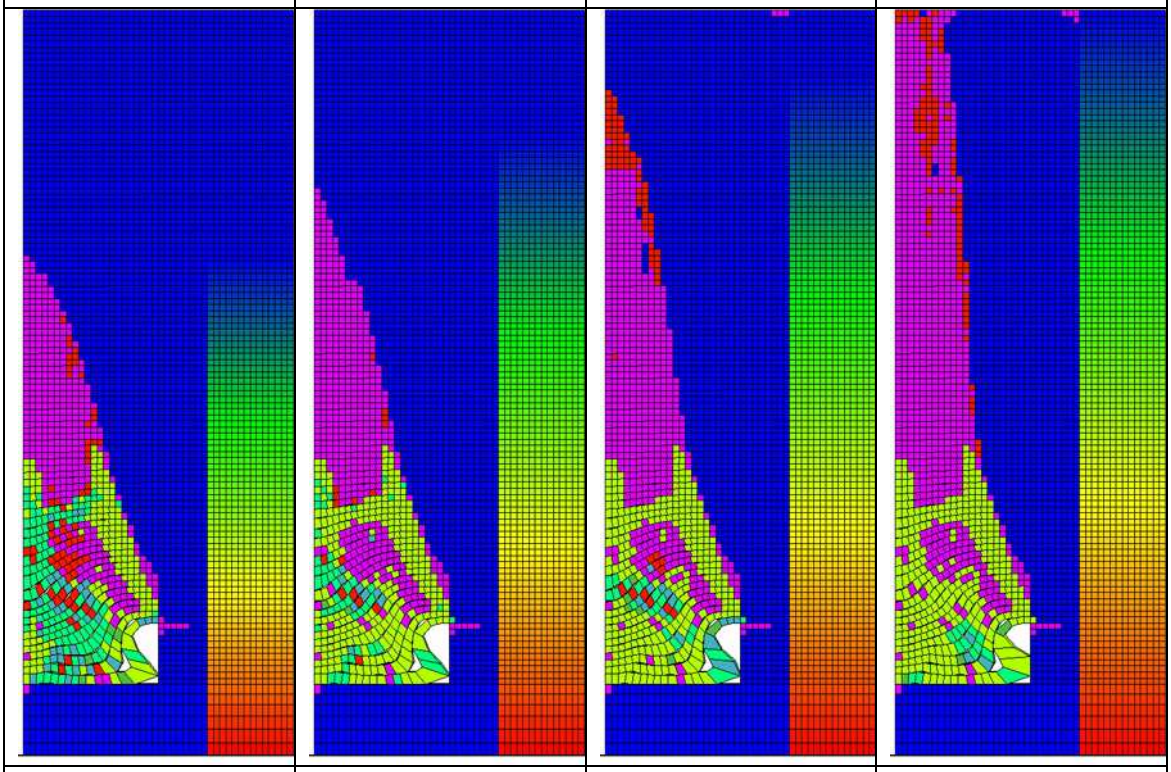

Phreatic surface: 6m above exc. roof	Phreatic surface: 8m above exc. roof	Phreatic surface: 9m above exc roof	Phreatic surface: 10m above exc roof

Figure 5.85: Effect of varying pore water pressure / groundwater table on the rock mass above an excavation. Excavation 3 m wide, 1 m high, GSI 10.

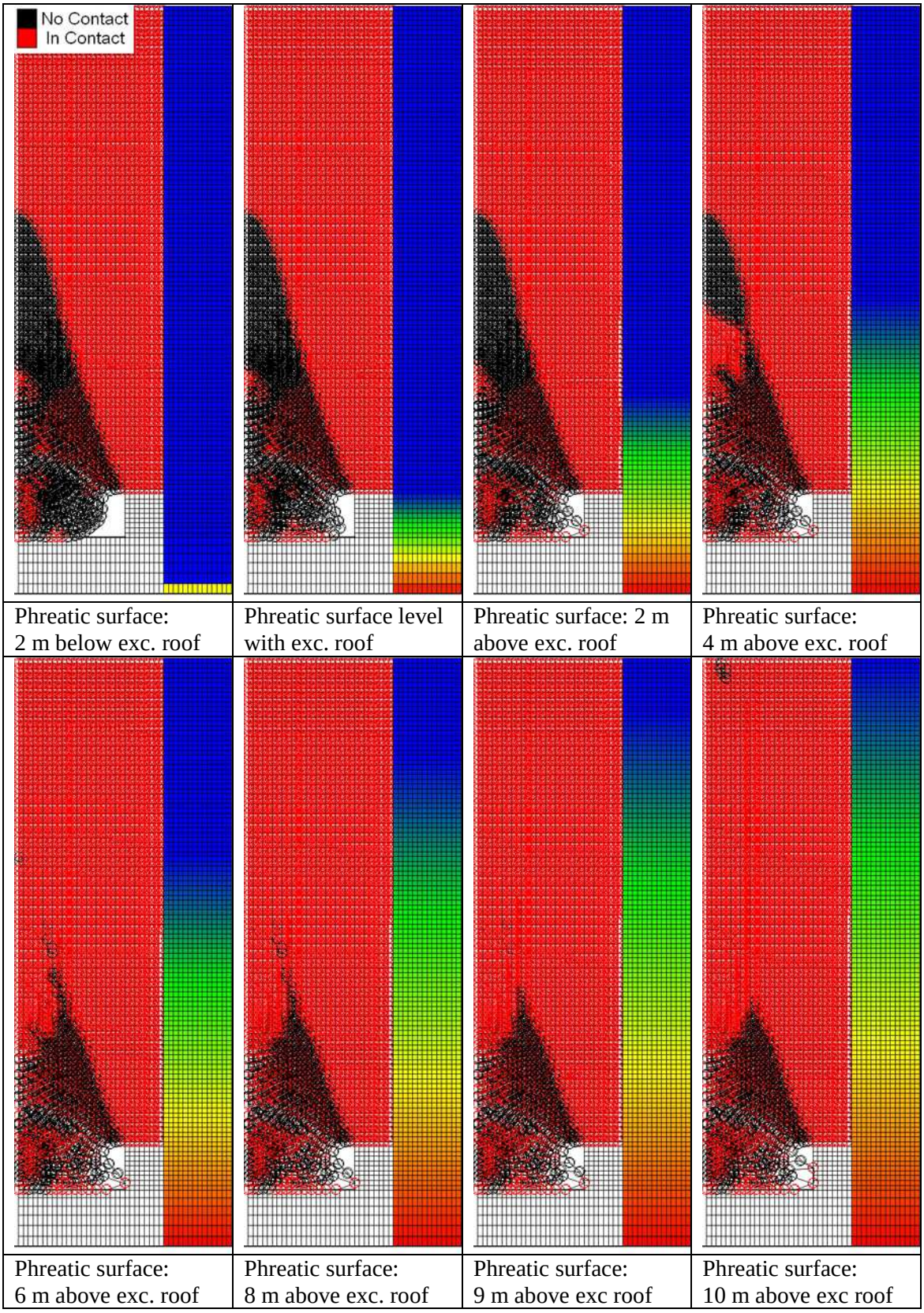

Figure 5.86: Normal failure plot demonstrating variation in tensile delamination of bedding planes within the rock mass as the groundwater level increases.

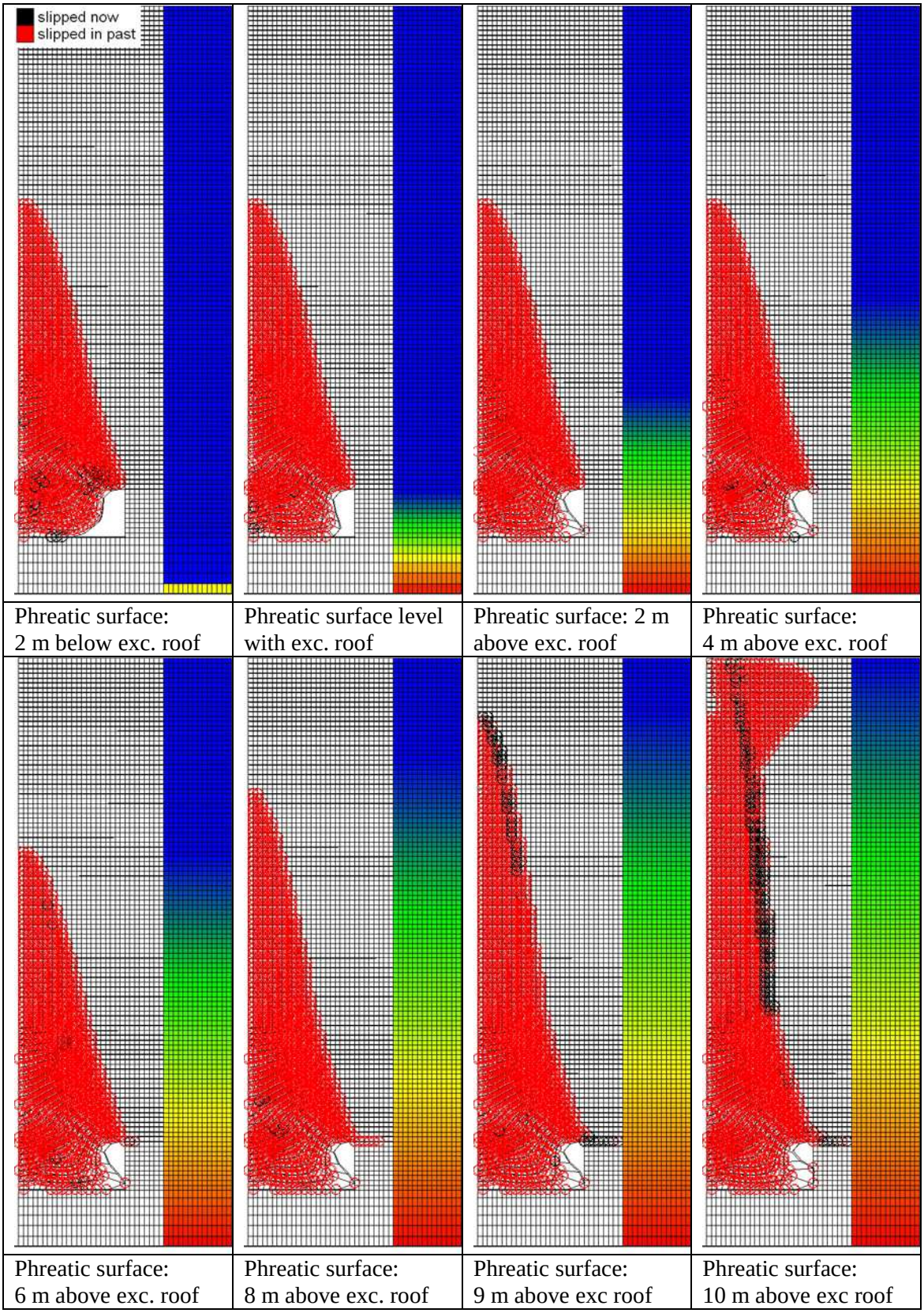

Phreatic surface: 2 m below exc. roof	Phreatic surface level with exc. roof	Phreatic surface: 2 m above exc. roof	Phreatic surface: 4 m above exc. roof
Phreatic surface: 6 m above exc. roof	Phreatic surface: 8 m above exc. roof	Phreatic surface: 9 m above exc roof	Phreatic surface: 10 m above exc roof

Figure 5.87: Interface Shear failure plot demonstrating variation in shear failure of bedding planes within the rock mass as the groundwater level increases.

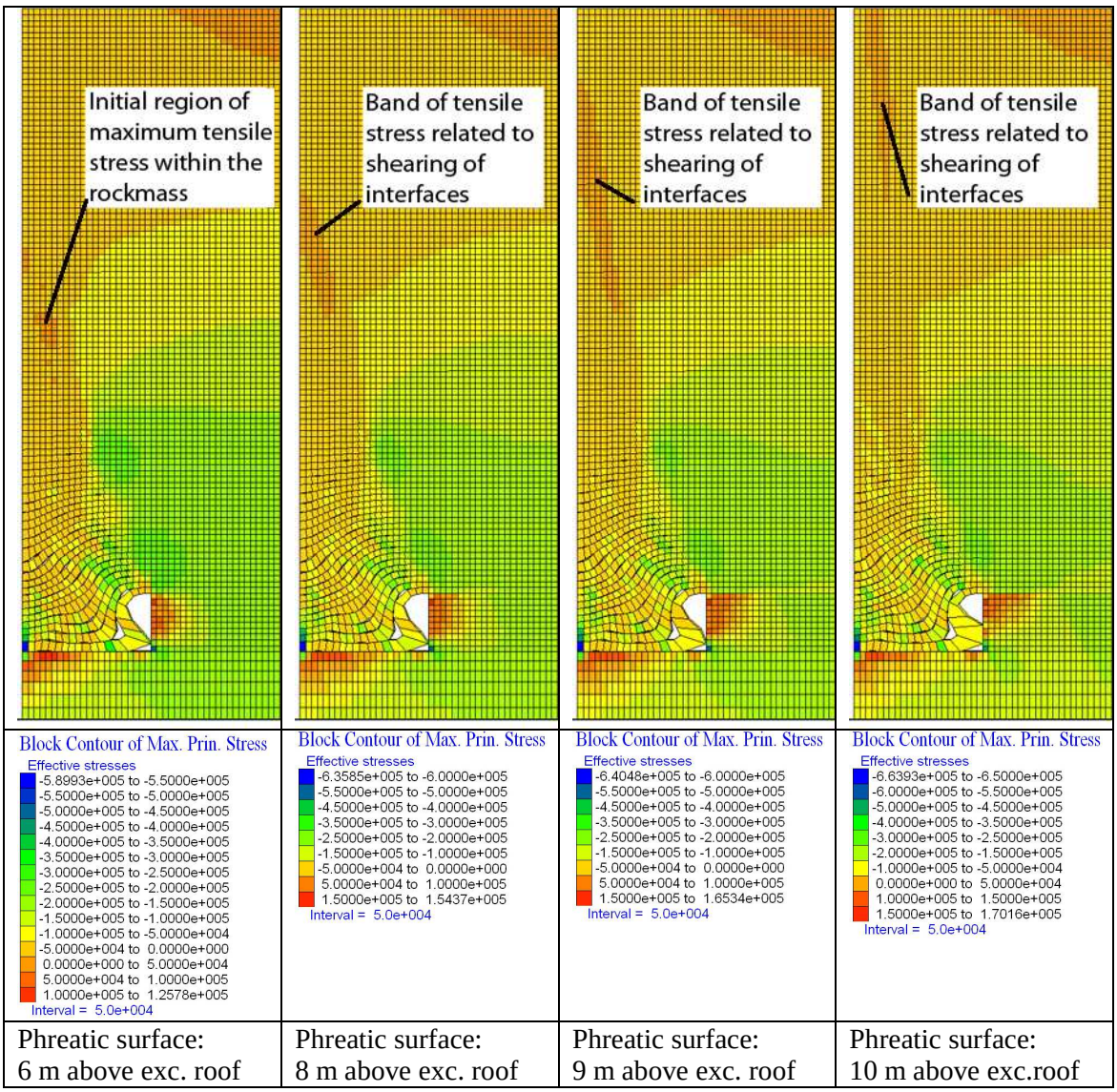

Phreatic surface: 6 m above exc. roof	Phreatic surface: 8 m above exc. roof	Phreatic surface: 9 m above exc. roof	Phreatic surface: 10 m above exc.roof

Figure 5.88: Maximum principal effective stress plot for increasing groundwater table.

The plot of shear yielding along the interfaces (Figure 5.87) demonstrates that this increased tensile yielding within the rock mass is related to shear failure along the interface elements which seems puzzling until a plot of the minimum principal effective stress contours are viewed for this portion of the model (see Figure 5.88) where as the pore water pressure increases a banded region of tensile stress develops above the water table in a region that cuts diagonally upward through a region of compressive stress. The band is oriented at an angle to the bedding surfaces and as such will be creating a component of shear stress along the bedding planes. This tensile stress concentration also is likely to account for the tensile yielding that occurs within the beds / strata at this point as the water table rises.

Another factor that is worthy of note is that the increasing water table does not appear to have any obvious impact on the height to which the zone of shearing extends into the rock mass further reinforcing the fact that the angle of friction is the dominant factor that controls the angle of caving. The increased water table / pore water pressure however has caused some additional shear yielding within the rock mass causing a horizontal shear band to form which connects the zone of shear that propagates diagonally upwards into the rock mass above the excavation roof away from the roof pillar intersection to the vertical zone of shearing that forms within the roof centreline.

The initial modelling of the effect of groundwater strongly demonstrated that the pore water pressure had a significant effect on the initial stability of excavations. As such in this section the effect of a change in the groundwater table on the rock mass above an excavation where roof failure has occurred is investigated. Modelling undertaken in this section indicates that as well as significant impacts on initial stability, the pore water pressure also has a significant impact on the rock mass and the bedding interfaces leading to a significant increase in the height of the zone of tensile failure above the excavation which occurs at a level equal to the height of the groundwater table. It also causes a significant increase in the shearing that occurs along bedding surfaces which has been linked in the previous modelling to the height at which an arch may form within the rock mass. In a real rock mass this would potentially cause a reduction in the shear strength of the joints due to either the removal of surface asperities as shear movements occur acting to reduce bedding joint surface roughness which would potentially also have an impact on the stability of the rock mass overlying an excavation.

5.13 Effect of Variation in Friction Angle of the Bedding Surfaces within a Rock Mass on Excavation Stability

The values of interface friction angle used in the modelling work to this point were set at a value equal to the angle of internal friction of the rock mass. It is recognised that these values are higher than those expected in a "real" rock mass however as the intent was to analyse the *relative* effect of the presence of discontinuities on the failure mechanism in the model (*i.e.* discontinuous behaviour using interface elements to capture the initial collapse of roof strata when compared to a continuum) and the relative as opposed to absolute effects of bedding spacing and other parameters such as excavation size on stability this is not assumed to be unreasonable. However it is also recognised that the frictional properties of discontinuities present in a rock mass are a very important property (Goodman, 1989; Brady and Brown, 1993) in their own right and are likely to impact the stability of an excavation. As such it was decided to investigate the effect of the friction angle of the bedding surfaces on the rock mass behaviour and the stability of shallow workings.

In the modelling undertaken here, both the strength of the elements forming the bedding and also the interface elements forming the bedding planes were given scaled strength properties. Conceptually this can be thought of as separating the rock mass forming the beds (and is still described as a rock mass here as it is likely to contain laminations or joints which reduce the strength of the material and so make the use of intact rock properties inappropriate but which are two irregular or small in scale to model as discrete surfaces using interface elements) from the main discontinuity surfaces (in this case the bedding planes) which will control the failure behaviour of the rock mass. In numerical modelling terms this could be described as a discontinuous equivalent continuum.

In the following modelling the zones forming the roof strata were given a range of strength and stiffness values corresponding to GSI values from 10-30 (Table 5.15). The strain softening properties were as per the previous modelling.

Table 5.15: Strength and stiffness properties.

GSI	Bulk Modulus	Shear Modulus	Cohesion	Friction Angle	Tensile Strength
10	0.7	0.23	0.11	49	0.005
20	1.1	0.35	0.17	55	0.011
30	1.9	0.62	0.24	59	0.023
	(GPa)	**(GPa)**	**(MPa)**	**(°)**	**(MPa)**

The friction angle of the interfaces representing the bedding planes were given frictional properties varying from 5 to 40 degrees in 5 degree increments (based on recommended values of discontinuity friction angle taken from Goodman (1989) and Zhang (2005). A summary of some common rock types and their discontinuity fills and the resultant friction angles of the discontinuity are included in Table 5.16.

Table 5.16: Summary of common discontinuity and discontinuity fill frictional properties (Zhang, 2005).

Rock Type	Fill Types	Peak Discontinuity Friction Angle (ϕ'_j)	Residual Discontinuity Friction Angle (ϕ'_{jr})
Coal Measures Rocks		15°	11-12°
Bentonitic Shale		8.5-29°	8.5°
Clay Shale		32°	19-25°
	Bentonite	12-17°	
	Clays	12-18.5°	10.5-16°
Quartz Rich Rocks	No Fill, Rough joint surface.	36-38°	

The results presented are of a 3 m wide, 1 m high excavation in a rock mass with 0.1 m wide bedding surfaces and with an over burden height of 10 m.

Yield states of the model zones after excavation and initial stepping are presented for GSI 10 with varying interface friction angles in Figure 5.89. Here it can be clearly observed that the friction angle of the primary discontinuity surfaces (the bedding planes in this case) has a very significant effect on the yielding of the rock mass and the height to which the zone of failure extends above the excavation, whereby decreasing friction angle results in increasing instability and height of roof collapse (where the zone of roof collapse is delimited by the height to which the shear zone marking the failure of roof strata extends) and the height to which disturbance within the rock mass extends (as marked by the zones of tensile yielding within strata with associated tensile

delamination but without the shear failure required for collapse). A plot highlighting these two regions can be seen in Figure 5.89 (Friction Angle 35 degrees). A plot of the normal separation of interfaces (Figure 5.90) confirms that for cases where the friction angle is less than 35 degrees, the delamination of strata reaches the surface. This corresponds with the zone of tensile yielding reaching the surface in the yield state plots.

It is also apparent that the shear surface which marks the point where the individual strata have failed is approximately equal to the angle of friction of the interface elements representing the bedding planes. This can effectively be considered the potential angle of caving of the rock mass. This matches results as observed in laboratory experiments and in the field as outlined by Bieniawski (1984) and Goodman (1989). The difference (which is most apparent at low friction angle values) is due to the contrast between the internal friction angle of the material forming the strata (which is relatively high as it represents a relatively intact cohesive mass) and the interface friction angle. In other words the rock mass friction angle is a composite of the discontinuity and "intact" properties. A plot showing the angle of caving overlaid on the yield plot can be seen in Figure 5.91.

Increases in the strength of the material forming the strata causes a reduction in the height to which the band of shear failure propagates into the rock mass over the mine roof / mine pillar intersection for a given value of friction angle for the discontinuity. This is in part due to the increase in the effective rock mass friction angle and also due to the increase in cohesion and tensile strength of the material forming the roof strata. The increase in strata strength parameters consequently leads to a reduction in the shear yielding in that there is a decrease in thickness of the shear zone band that develops above the excavation roof / mine pillar intersection which can be observed for the rock strata with strength and stiffness properties equivalent to GSI 20 and GSI 30 in Figure 5.92 and Figure 5.93 respectively. However the relationship of the angle of friction to the angle of caving remains broadly similar to that observed for the lowest strata strength observed in Figure 5.91. This can be seen in Figure 5.94 Also of note is the fact that at lower bedding plane rock mass friction angles (values less than 30°) the region of tensile yielding within the model extends into the rock mass to the pillar side of the shear zone band and at very low bedding plane rock mass friction angles (values below approximately 20°) it extends into the rock mass over the coal pillar as well as

forming an increasingly wide and steep column above the excavation. This can be seen clearly in Figure 5.89.

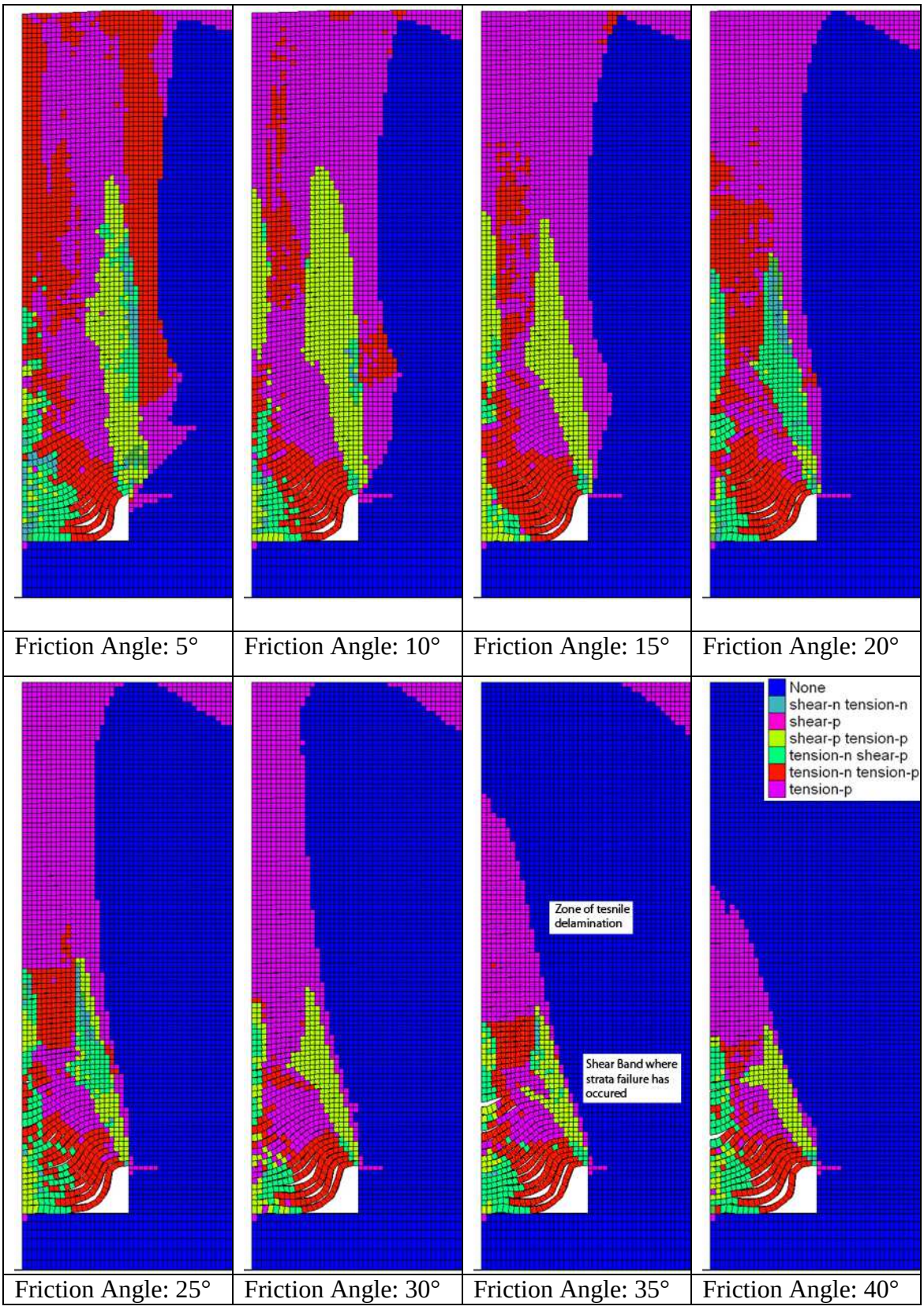

Figure 5.89: Yield state plot for variations in friction angle of the bedding surfaces. Rock mass GSI = 10, Interface spacing 0.1 m, 3 m wide excavation, 1 m high.

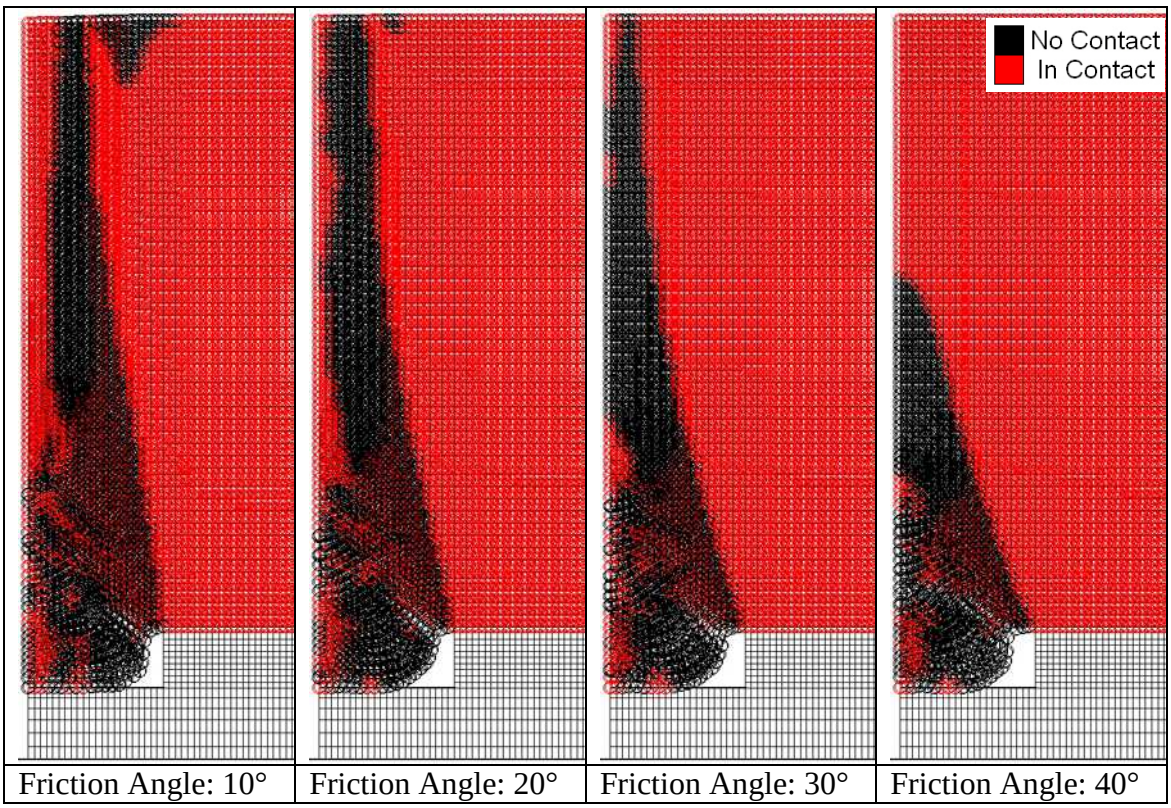

Figure 5.90: Normal separation of interface elements for varying friction angles at GSI 10.

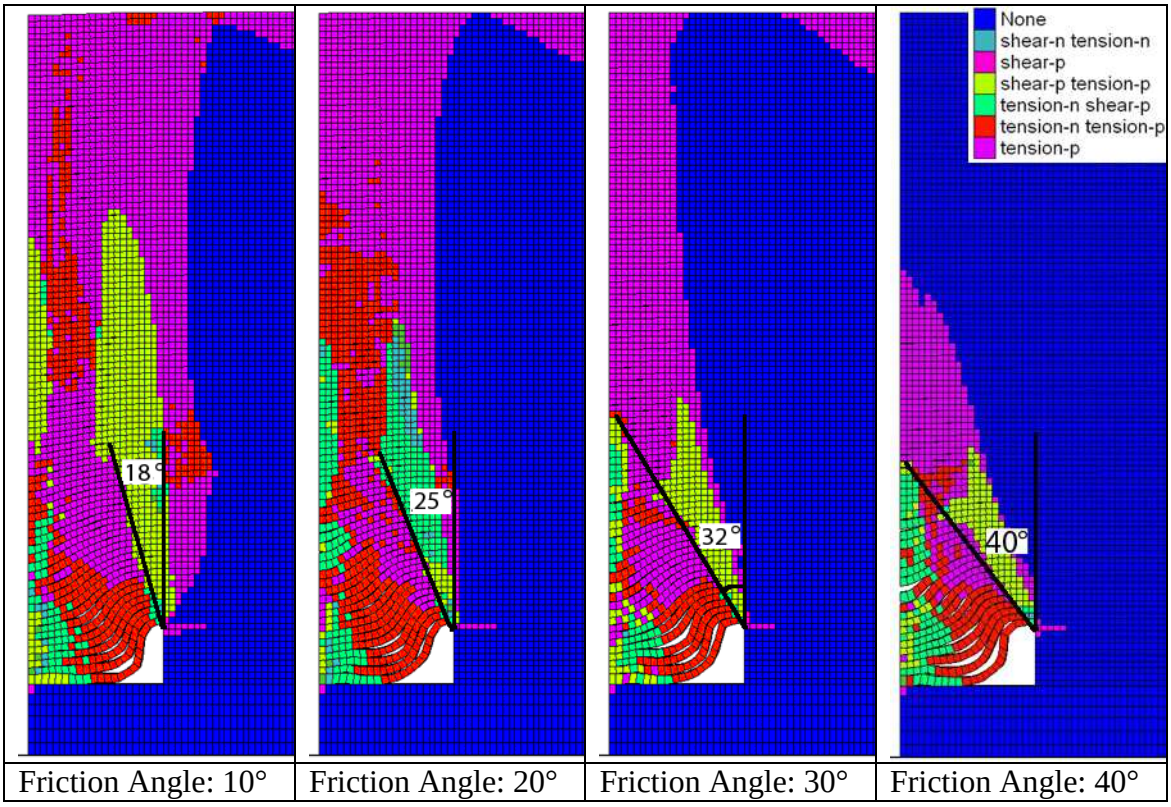

Figure 5.91: Caving angle overlain on the yield state plot for variations in friction angle of the bedding surfaces. Rock mass GSI = 10, Interface spacing 0.1 m, 3 m wide excavation, 1 m high.

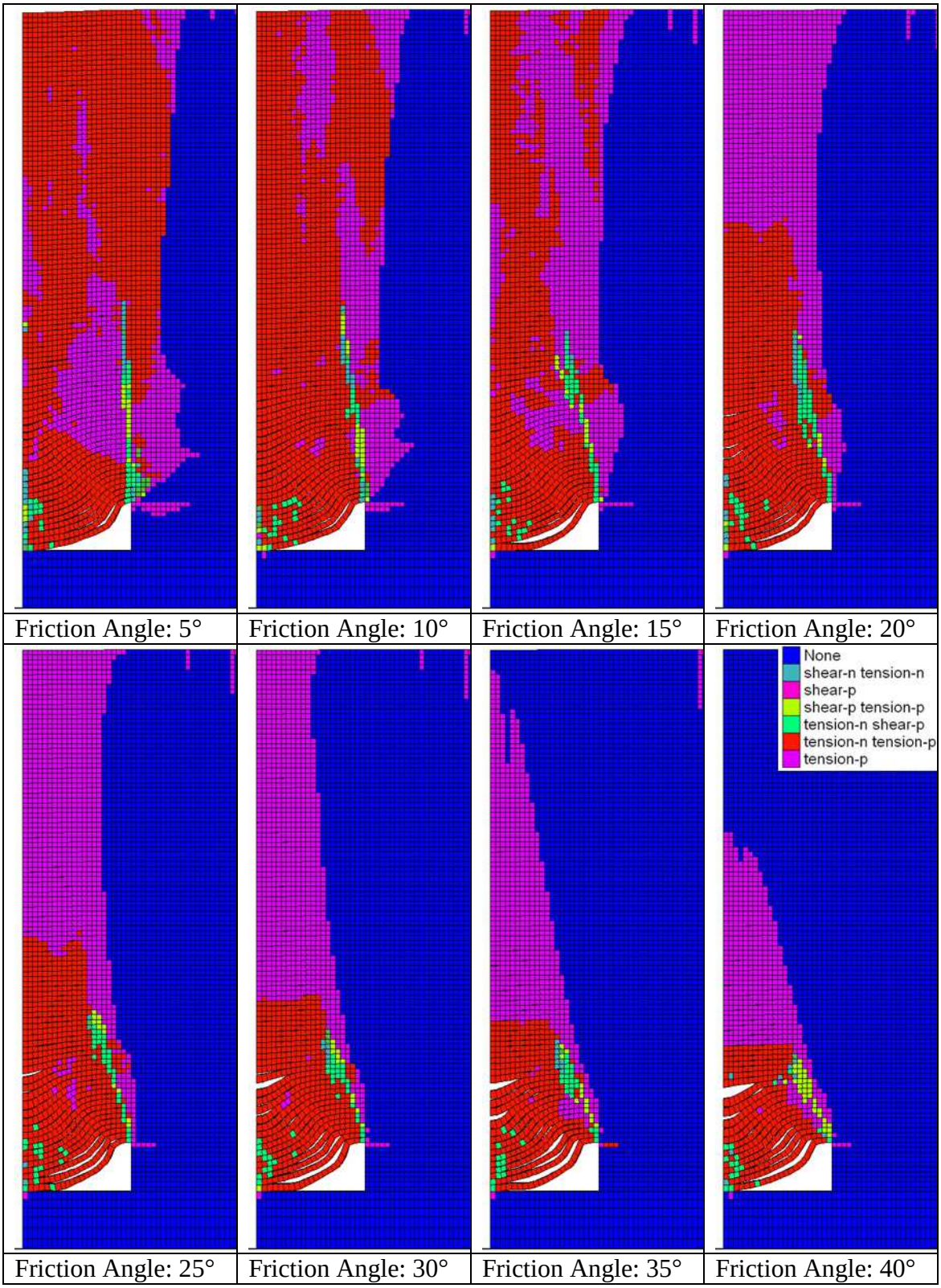

Figure 5.92: Yield state plot for variations in friction angle of the bedding surfaces. Rock mass GSI = 20, Interface spacing 0.1 m, 3 m wide excavation, 1 m high.

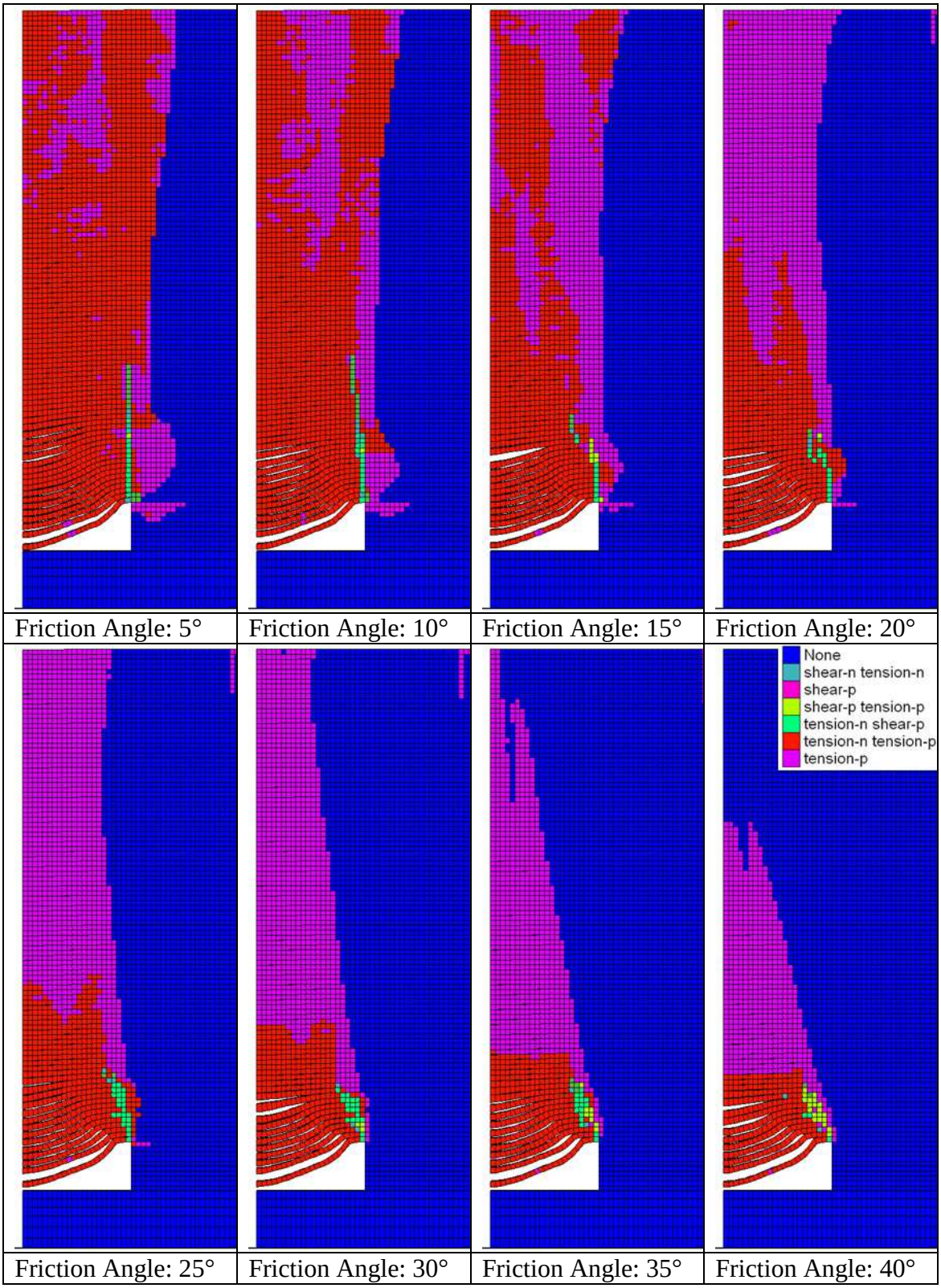

Figure 5.93: Yield state plot for variations in friction angle of the bedding surfaces. Rock mass GSI = 30, Interface spacing 0.1 m, 3 m wide excavation, 1 m high.

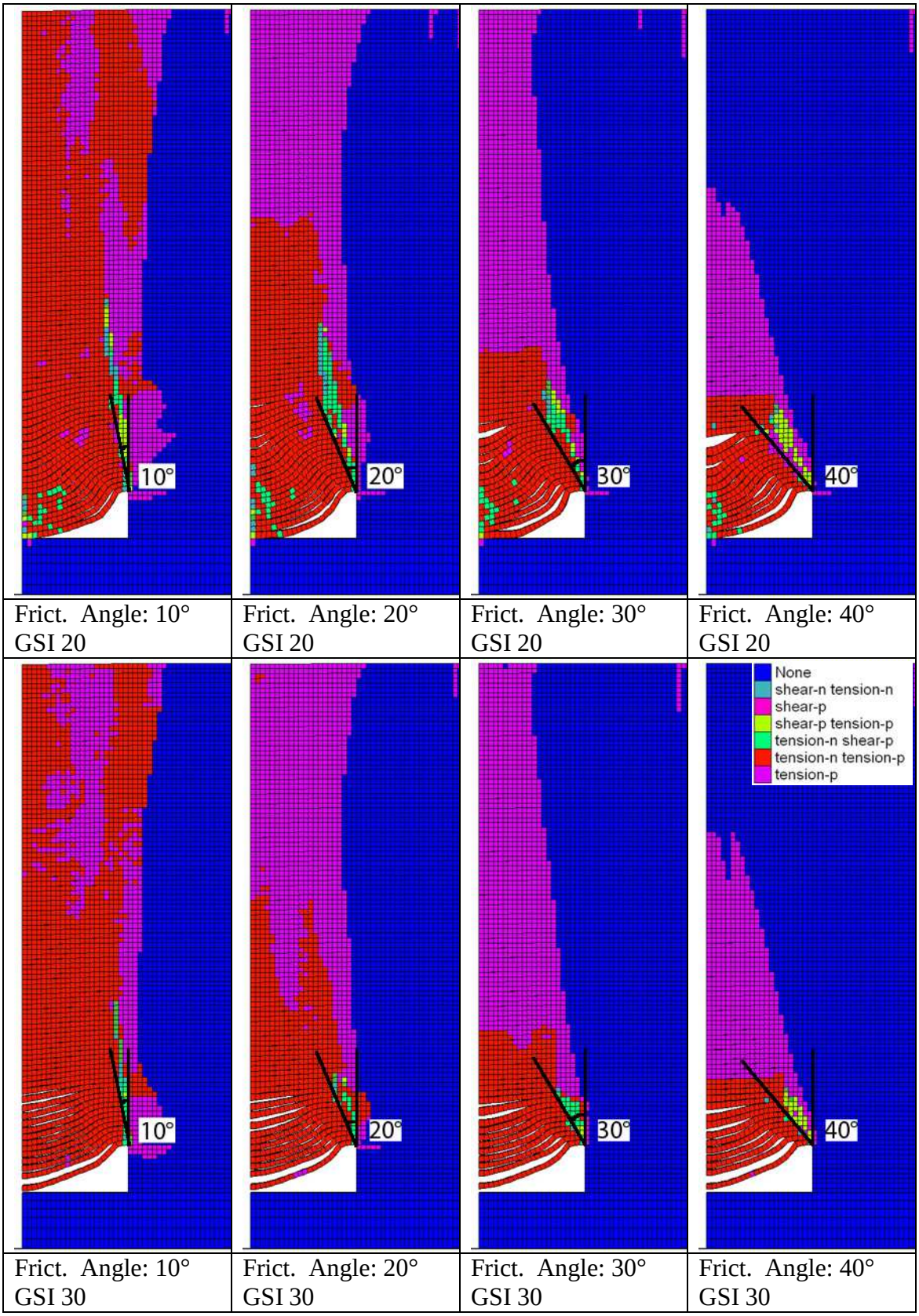

Frict. Angle: 10° GSI 20	Frict. Angle: 20° GSI 20	Frict. Angle: 30° GSI 20	Frict. Angle: 40° GSI 20
Frict. Angle: 10° GSI 30	Frict. Angle: 20° GSI 30	Frict. Angle: 30° GSI 30	Frict. Angle: 40° GSI 30

Figure 5.94: Caving angle overlain on the yield state plot for variations in friction angle of the bedding surfaces. Rock mass GSI = 20-30, Interface spacing 0.1 m, 3 m wide excavation, 1 m high.

Another significant detail in the above modelling is the link between rock mass strength and the maximum stable span. It is the maximum stable span width that is the limiting factor in controlling the height to which void migration can occur before arching

(usually by the formation of a compression arch within an over lying roof stratum). As the collapse of the roof strata migrates upwards the rate that the roof span decreases with increased caving height is dependant on the caving angle which is in turn controlled by the angle of friction of the rock mass. However from viewing the plots of uniform strata strength versus variations in the discontinuity friction angle it can be seen that although the height of roof instability decreases with increases in the friction angle, the width of the stable span is always the same for a given rock mass strength.

In this instance, the yield state plots of a 3 m wide 1 m high excavation are included in Figure 5.95 with the maximum height of shear failure which represents failed roof strata and hence caving height before arching has occurred within the rock mass. It can be seen that as the friction angle of the rock mass increases, the angle of caving decreases resulting in a smaller height of potential void migration before the halting of movement by arching.

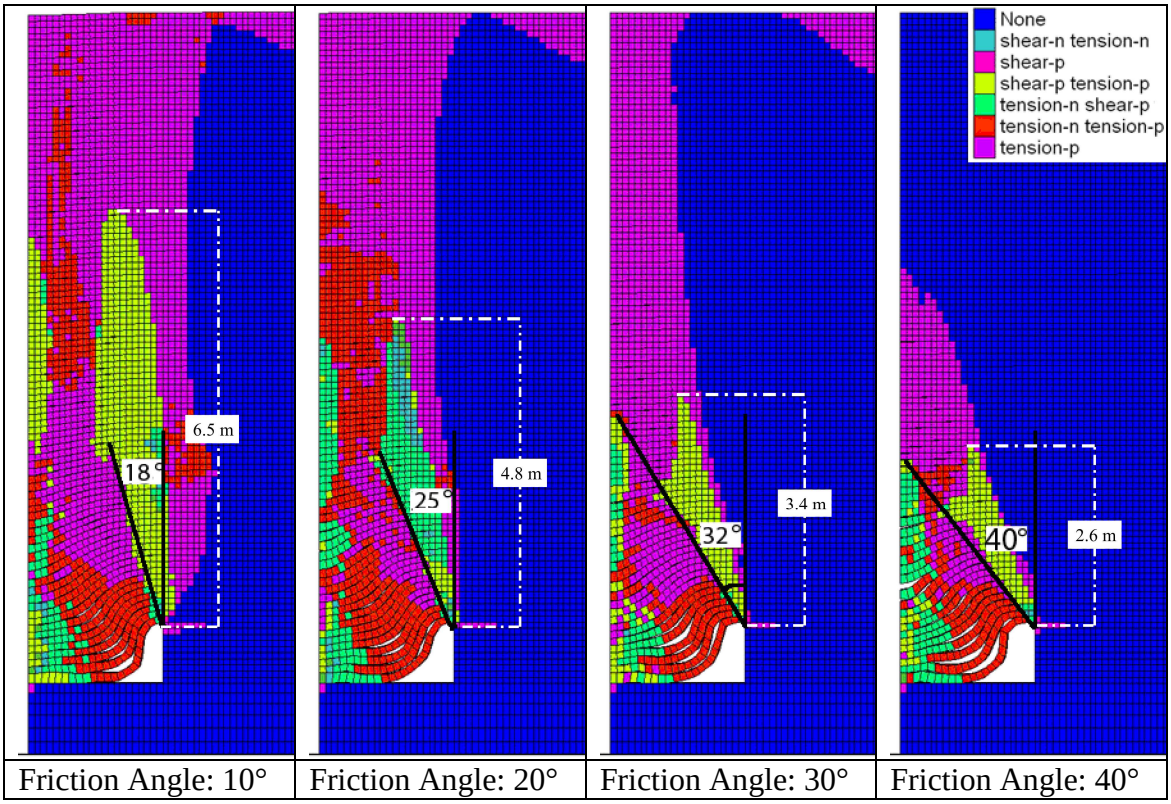

Figure 5.95: Height of extent of roof failure through shear yielding that would allow collapse to occur at four different rock mass friction angle values. 3 m wide, 1 m high excavation, rock mass GSI 10, bedding spacing 0.1 m.

As the strength of the rock mass (*i.e.* the GSI value of the strata forming the rock mass) increases, the height to which roof collapse extends before being halted by the formation of an arch decreases. As stated earlier this appears to coincide with an increase in the stable roof width that can form.

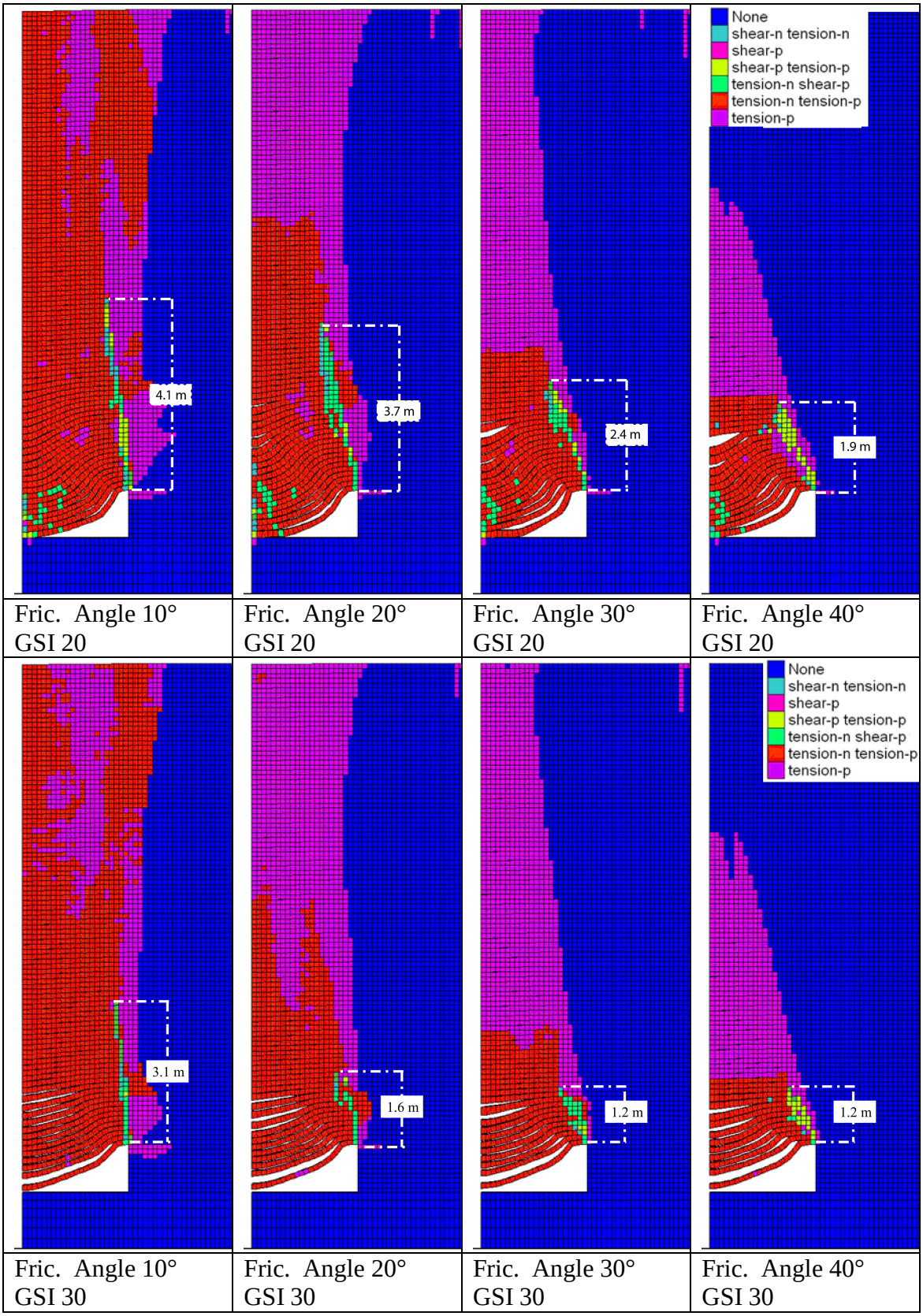

Fric. Angle 10° GSI 20	Fric. Angle 20° GSI 20	Fric. Angle 30° GSI 20	Fric. Angle 40° GSI 20
Fric. Angle 10° GSI 30	Fric. Angle 20° GSI 30	Fric. Angle 30° GSI 30	Fric. Angle 40° GSI 30

Figure 5.96: Height of extent of roof failure through shear yielding that would allow collapse to occur at four different rock mass friction angle values. 3 m wide, 1 m high excavation, rock mass GSI 20, bedding spacing 0.1 m.

As the rock mass strength increases the caving angle remains equal to 90° minus the angle of rock mass friction however the width of the stable span increases and so the height of collapse decreases.

This forms a flat upper boundary to the region of roof collapse forming a frustum geometry of collapse with the frustum having a decreasing height as the rock mass strength increases. Also apparent from the above is the fact that for a given rock mass strength the minimum stable span width is the same for all variations in friction angle which suggests that this variable is controlled by the tensile strength or cohesion of the strata rather than the discontinuity properties. The frustum geometry can be seen most clearly in the 30° and 40° friction angle plots for a rock mass strength of GSI 20 and 30 in Figure 5.96 which is highlighted in detail in Figure 5.97. In this plot it can be seen that the upper boundary of the frustum is formed at the point where the roof strata are no longer undergoing shear failure and so a stable roof has formed.

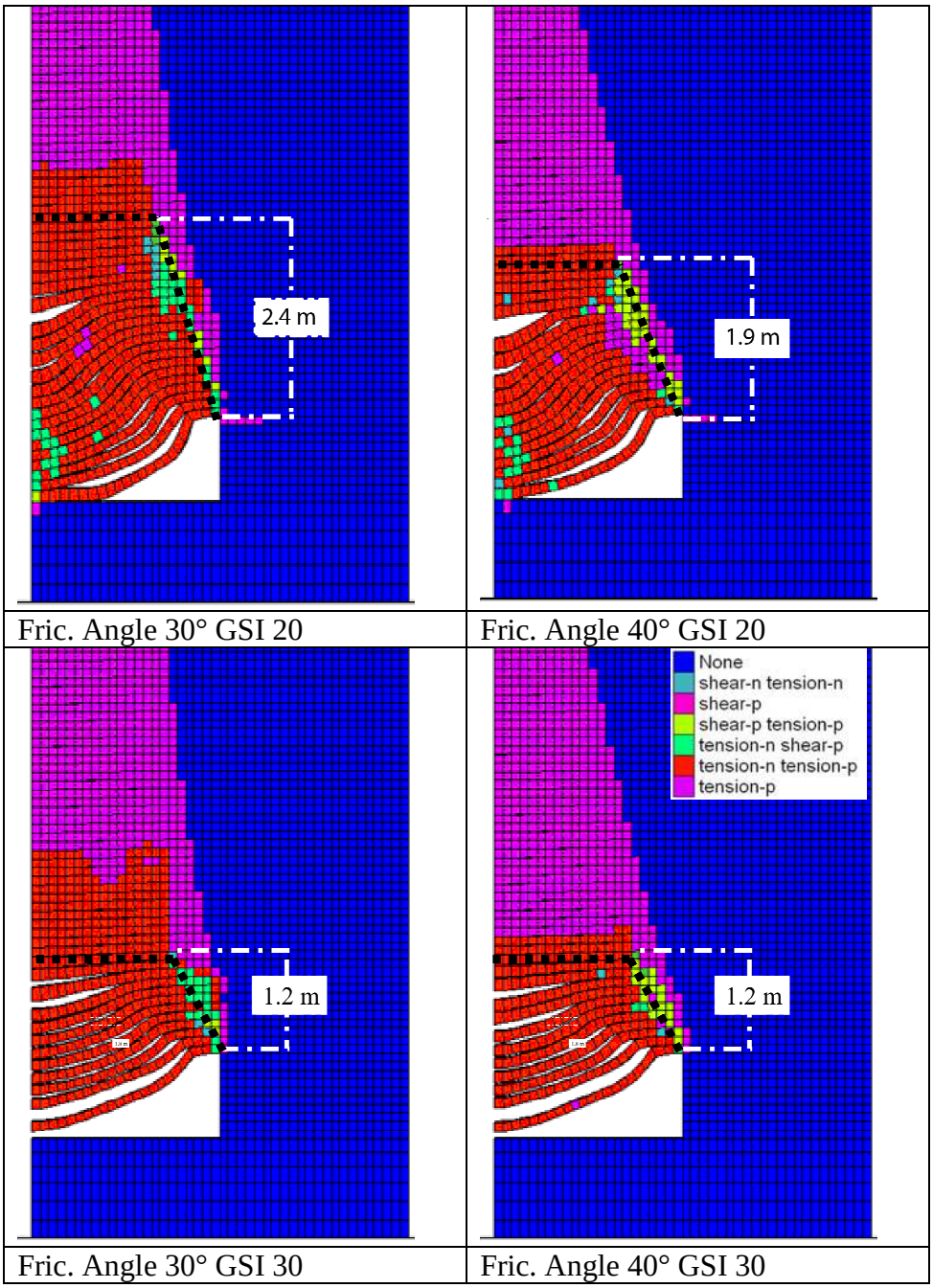

Fric. Angle 30° GSI 20	Fric. Angle 40° GSI 20
Fric. Angle 30° GSI 30	Fric. Angle 40° GSI 30

Figure 5.97: Plot showing broadly frustum shaped geometry of the collapsing roof strata.

The uniform span width for a given rock mass strength at varying interface / discontinuity friction angles can be seen in Figure 5.98. From this it seems clear that the geometry of the collapse frustum is defined by the angle of friction which controls the angle that the edge of the frustum forms to the vertical and the strength of the strata control the diameter of the top of the frustum by affecting the maximum roof span width.

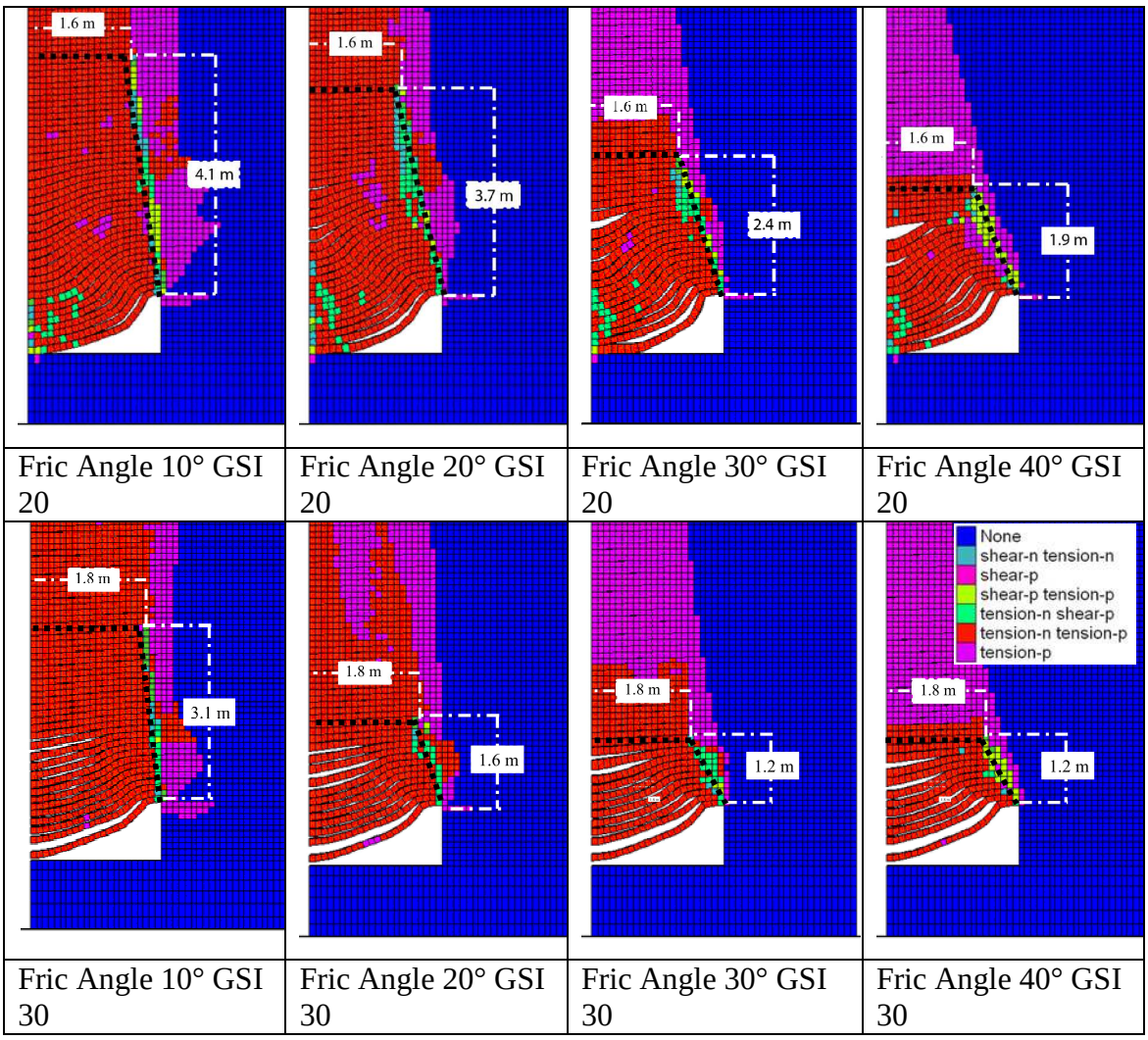

Fric Angle 10° GSI 20	Fric Angle 20° GSI 20	Fric Angle 30° GSI 20	Fric Angle 40° GSI 20
Fric Angle 10° GSI 30	Fric Angle 20° GSI 30	Fric Angle 30° GSI 30	Fric Angle 40° GSI 30

Figure 5.98: Effect of varying parameters on the geometry of the collapse frustum.

5.13.1 Conclusions

In this section it was demonstrated that the friction angle of a discontinuous rock mass has a very significant impact on the stability of an excavation and the degree to which failure propagates upwards through the rock mass (both in terms of the height to which tensile delamination appears to extend into the rock mass and in terms of the shear failure of strata at the roof pillar intersection leading to sagging and collapse).

It is also apparent that the friction angle is a significant parameter in controlling the failure geometry as was initially demonstrated in the modelling undertaken in section 4.4 using the ubiquitous joint model. The close relation of the friction angle to the angle of failure of the bedding planes within the rock mass potentially allows estimates to be made of the maximum likely level that roof instability may propagate into the rock mass and hence the level of void migration that may occur before the formation of a stable arch within a rock mass halts the void migration process.

5.14 Chapter Conclusions

In this chapter a significant numerical modelling parametric study was undertaken to investigate the effects of various parameters on the stability of excavations

This phase of the modelling work was undertaken using more sophisticated constitutive models including the strain softening model which allows post yield behaviour to be captured in a more realistic manner as the model allows the post yield values of cohesion, friction and tensile strength to be varied which more accurately captures the failure behaviour of rock masses. The standard strain softening Mohr-Coulomb model was also used combined with the use of interface elements to capture the discontinuous behaviour seen in stratified rock masses where tensile delamination and sagging of the bedding planes forming the overburden rock mass can occur.

Broadly it can be observed from the modelling results that a number of parameters all influence the stability of shallow excavations. These include the variation in strength properties of the rock mass, the discontinuity spacing, the excavation geometry (specifically the excavation width) and the pore water pressure / ground water table. More detail on the conclusions of the phase two study are given below.

The variation in bedding plane spacing was shown to have a significant impact on the stability of sub surface excavations, where the larger the bedding thickness the greater the excavation stability for a given stress state and the lower the collapse height of roof strata into the rock mass.

The discrete modelling of the type undertaken here has also allowed the model to capture the formation of a stress arch within individual strata as well as sagging of thinner strata leading to the formation of a progressively narrower span as the collapse migrates upwards into the rock mass over the excavation.

The bedding thickness / bedding plane separation also has a significant effect on the height to which tensile yielding and bedding plane delamination propagate upwards into the overlying rock mass, whereby the thicker the bedding / strata, the lower the height that damage extends vertically into the rock mass.

The variation in excavation width is shown to have a very significant impact on the stability of the excavation roof, much higher than that which was initially indicated in the phase 1 modelling study. As such it would appear that this is a very significant parameter in excavation stability and also the height to which the failure of the roof strata propagates upwards into the rock mass overlying the excavation.

The results of the modelling of varying excavation height indicate that this parameter appears to have a limited impact on the stability of excavations with the rock mass strength and the height of the groundwater table being far more significant parameters. It is however observed that the excavation height has an impact on excavation stability that is related to the ratio of width of excavation to excavation height. Whereby excavation stability increases as the excavation width to height ratio approaches one and decreases as this parameter diverges from 1.

However from the results it was determined that the decrease in stability due to variations in height of an excavation for a given rock mass strength caused significantly less instability than increases in excavation width.

The initial modelling of the effect of groundwater demonstrated that the pore water pressure had a significant effect on the initial stability of excavations. Modelling undertaken in this section confirms the findings of phase one whereby small changes in the pore water pressure can trigger yielding of the rock mass. It was also observed that as well as significant impacts on initial stability, the pore water pressure also has an effect on the rock mass over a failed excavation where it causes tensile delamination of the bedding planes and the bedding interfaces leading to a significant increase in the height of the zone of tensile failure above the excavation which occurs at a level equal to the height of the groundwater table. It also causes a significant increase in the shearing that occurs along bedding surfaces which has been linked in the previous modelling to the height at which an arch may form within the rock mass. In a real rock mass this would potentially cause a reduction in the shear strength of the joints due to either the removal of surface asperities as shear movements occur acting to reduce bedding joint surface roughness which would potentially also have an impact on the stability of the rock mass overlying an excavation.

The use of the strain softening Mohr-Coulomb model and the presence of interfaces to more accurately capture the failure behaviour of the roof strata demonstrated that roof strata of low strength may fail when the excavation width is increased and that excavation width is a significant parameter in the stability of shallow workings.

The modelling work undertaken here has demonstrated that the friction angle of a discontinuous rock mass has a significant impact on the stability of an excavation and the degree to which failure propagates upwards through the rock mass (both in terms of the height to which tensile delamination appears to extend into the rock mass and in terms of the shear failure of strata at the roof pillar intersection leading to sagging and collapse), where the geometry of the collapse frustum is defined by the angle of friction$_r$ which controls the angle that the edge of the frustum forms to the vertical ($90 \pm \phi'$) and the strength of the strata control the diameter of the top of the frustum by affecting the maximum roof span width. The close relation of the caving angle to the friction angle of the rock mass potentially allows estimates to be made of the maximum likely level of void migration that may occur before the formation of a stable arch within the rock mass halts the void migration process.

Chapter

6

Tools to Estimate the Height of Void Migration

6 Tools to Estimate the Height of Void Migration

This section is split broadly into two main parts. The first section (section 6.1) introduces a pair of empirical tools which have been developed based on relations observed in the literature and on the numerical modelling undertaken during this work. They were initially used to investigate the parameters that may be of significance in controlling the height to which void migration may occur before arching or bulking of a layered rock mass can halt the movement.

The second section (Section 0) discusses the development and initial trial of an automated FISH function that allows the removal of failed elements in the FLAC model to simulate the progressive collapse of roof strata to be undertaken to allow the model to successfully capture the failure mechanism occurring in thicker roof strata (shear joint / parting plane failure).

6.1 Void Migration

Void migration is normally halted by one of three processes.

1. Choking of the void by rubble
2. Natural arching
3. Spanning of the void by a competent layer

It has also been demonstrated that a number of factors affect the degree of stability of shallow excavations including the excavation width (see section 5.7), the rock mass strength (see section 5.5) and the level of groundwater table. It has also been demonstrated that the geometry of collapse is strongly affected by the friction angle of the rock mass (see section 5.13).

It is the first two processes, choking and arching, that are dealt with in this section. The methodologies are both derived from empirical relations found in the literature and based on the results of the modelling work undertaken on excavation stability in section 4. In both cases the only parameters required are estimates of the unconfined compressive strength of the strata overlying the workings or void, the maximum span of the void and the extraction height. These can either be assumed as the worst case values, or constrained ever more tightly as more information regarding the geologic profile, material and geometric (*i.e.* working dimensions) parameters become available.

6.1.1 Choking of the Void by Rubble

The height to which a void will migrate before it is halted by bulking is dependent on the bulking factor of the material, the volume available within the workings to store the bulked debris, the geometry of collapse and the angle of repose of the debris pile. These vary depending on the rock mass properties of the strata in question. Palchik (2002) identified the following relationship between the uniaxial compressive strength (UCS) of coal measures strata and the bulking factor:

$$BF_R = 1 + \alpha_{BF}\sqrt{\sigma_{ci}} \qquad 6.1$$

Where:

BF_R = bulking factor

σ_{ci} = uniaxial compressive strength of rock (MPa)

α_{BF} = empirical constant dependent on local geology (≈ 0.05)

Das (2000) identified a relationship between the uniaxial compressive strength (UCS) of coal measures strata and their caving angle. This relation can be seen in Table 6.1. Using Palchik's relation and the caving angle derived from Table 6.1 on the following page, it is possible to estimate the height to which a void will migrate before it is choked by the bulking of collapse debris. The methodology is simple to implement within a simple spreadsheet that can be used to estimate maximum heights of collapse before bulking will choke the void for a given stratigraphy and for varying working dimensions.

6.1.2 Natural Arching

The height to which a void will migrate before it is halted by arching is dependant on the caving angle of the material. As stated above, Das (2000) identified a relationship between the uniaxial compressive strength (UCS) of coal measures strata and their caving angle, where an increase in the UCS of the rock mass is linked to a decrease in the caving angle. As such the height of collapse before an arch is formed will decrease. The caving angle can be estimated either from an engineering description of the rock or from UCS as seen in Table 6.1 below.

Table 6.1: Relation between strata formations, caving angle and UCS1 (Das, 2000).

Strata formation	Caving angle	Mean compressive strength (kgf/cm^2)
Extremely weak strata including very weak composite layer, very weak sandstone layer, etc., for example, extremely cavable strata.	> 81–85°	Less than 100
Very weak sandstone, weak and soft carbonaceous shale, very soft and fractured intercalation, etc., for example, highly cavable strata	> 75–81°	> 100–200
Most of the type of shale, shale sandstone, weak sandstone, intercalated shale and sandstone, etc., for example, moderately stronger very good cavable strata	> 65–75°	> 200–300
Hard, grey shale, medium strength sandstone, etc., for example, for good cavable strata.	> 50–65°	> 300–450
Quite strong sandstone, medium strength massive sandstone, etc., for example, for poorly cavable strata.	> 35–50°	> 450–600
Very thick massive sandstone, very strong sandy shale, competent fine grained sandstone with shale lamination i.e., example, for highly uncavable strata.	> 30–35°	> 600–800
Very thick strong massive sandstone i.e., for extremely uncavable strata.	≤ 30°	> 800

The modelling work undertaken in section 5.13 indicates that the caving angle is also strongly dependent on the friction angle of the rock mass. It is worth noting that from UCS tests the intrinsic deformability properties of the material can be derived (Goodman, 1989) as well as an estimate of the bulking factor and angle of caving as seen above in Equation 6.1 and Table 6.1. Some authors (e.g Mohammad *et al.,* (1997) and Whittles *et al.,* (2007) have suggested empirical links based on rock mass classification schemes between the UCS of a rock and its tensile strength, cohesion and friction angle, however it is more common to derive cohesion and friction angles from triaxial test data and the tensile strength from a Brazilian disc test.

Other authors have suggested empirical relations between the intact UCS of the rock and a rock mass UCS as summarised in Zhang (2005) which in turn can be used to derive the angle of friction of the rock mass for example using the Hoek-Brown criterion (Hoek, 2004) to derive the rock mass friction angle which has been shown to be representative of the caving angle as demonstrated by the results of the modelling work summarised in section 5.13.

6.2 Parametric Study using Empirical Tools

6.2.1 Effect of Variation in Bulking Factor on Height of Void Migration

In this phase of the study it is intended to test the importance of bulking factors and rock debris slope angles on the choking of voids from workings of varying dimensions and with differing heights of extraction. This is done using a spread sheet to calculate the available void space compared to the volume of bulked collapse debris. This data is then used to calculate the maximum extent to which a void could migrate before being halted by bulking.

It is intended to identify how sensitive the height of void migration is to the bulking factor and ultimately to attempt to quantify its importance when compared with other parameters to enable a decision to be made on the importance of derivation of this parameter from SI or lab tests. It should be noted that the mechanisms of failure initiation and progression cannot be investigated using this technique. Only the height that a void may reach before bulking occurs.

6.2.2 Assumptions

A number of assumptions are made within each parametric study phase. They are based on either literature information or data that is consistent with known field data and engineering judgment.

1. The workings will fail through roof collapse at a tunnel intersection.
    - Tunnel intersections have the largest spans and so the greatest concentrations of tensile stress (Attewell and Taylor, 1984)
2. The workings are horizontal (no dipping seams).
3. The collapse will take the form of one of two geometric shapes
    - Cone – typical collapse geometry over a roadway intersection in a uniform material (Attewell and Taylor, 1984)
    - Frustrum - typical collapse geometry over a roadway intersection in a stratified material (Attewell and Taylor, 1984)
4. It is possible for any fraction of the intersection roof to collapse, however where the collapse is less than 100% the centre of collapse will occur in the centre of the intersection.
    - The centre of the intersection is where the tensile stress concentration will be highest (Diederichs, 1999). Also this is the worst case in terms of available working volume to receive collapse debris.
5. The collapse will only be halted by choking of the void, not by natural arching (which will be investigated in Phase 1b).

6.2.3 Hypotheses

1. Materials with higher UCS values will have larger bulking factors. This will lead to earlier choking of the void (Palchik, 2002)

- As the bulking factor increases the bulked volume of the collapse debris increases. Therefore a smaller collapse height will produce sufficient debris volume to choke the void

2. Increasing excavation height will increase the height of void migration.
   - This will increase the volume of free space which the collapse rock can fill before choking occurs

6.2.4 Methodology

This phase of the parameter study makes use of the solver function within common spread sheet packages such as EXCEL. The methodology involves the comparison of the volume of bulked collapse material with the available volume within the workings and the volume created by collapse. When these two volumes are equal, it is assumed that the void migration has halted whereby:

$$V_s = (V_w + V_c) - V_b \qquad 6.2$$

V_w = Volume of workings which can be filled (m^3)

V_c = Volume of free space created by collapse (m^3)

V_b = Volume of bulked collapse debris (m^3)

V_s = Summation of the volumes (m^3)

If V_s = 0 the void has choked.

The volume of workings (V_w) is assumed to be the volume of a cone directly below the intersection roof, minus the intrusion of the square pillars into the cone.

Using the solver function in Excel it is possible to find the height of collapse (Hc) that satisfies the condition where V_s = 0 and the void has choked. As such it is intended to investigate how the following parameters affect the height of collapse before choking of the void can occur:

- Tunnel height (0.5 - 3.5m), Healy and Head (1984) suggest that maximum thickness of the coal seams in the UK ≈ 3 m. Accepted convention (again from Healy and Head suggests that the maximum height of void migration is 10 time worked thickness, even small increases in the extraction height may potentially add significantly to the collapse height.
- Bulking factor (1.3 - 1.5) - Healy and Head (1984)

6.2.5 Results and Discussion for Parametric Study Effect of Variation in Bulking Factor on Height of Void Migration

Before discussing the results of the bulking factor parametric study and a discussion of it's implications, it is necessary to consider the results obtained to estimate the height of void migration by using common pre-existing methods such as those proposed by Tincelin (in Bell, 1975) and the widely used relation derived by Wardell and Eynon (in Healy and Head, 1984; Bell, 1988).

Tincelin proposed a relation based on the average density of colliery waste (approximately 2000 kg/m^3 – where the colliery spoil is considered representative of broken roof strata) compared to the intact density of coal measures strata (Approximately 2240 kg/m^3). Using these density contrasts a relation was proposed between collapse height (H_C) and thickness of coal seam (T_C).

$$H_C = T_C \left[\frac{\rho_C}{\rho_I} \Big/ 1 - \frac{\rho_C}{\rho_I} \right] \qquad 6.3$$

Where:

ρ_C = Bulk density of collapse debris

ρ_I = Bulk density of intact rock

The density ratio in this case indicates a bulking factor of 1.12 (112%) which is lower than that commonly used in coal measures strata of 1.3-1.5 (130-150%).

Wardell and Eynon (Bell, 1975) proposed the following relation based on the cone geometry of a collapse and the bulking factor of the rock mass:

$$H_C = \frac{3 \times T_C}{BF_R} \qquad 6.4$$

Where:

BF_R = bulking factor as a ratio (normally quoted as between 1.3 and 1.5 for coal measures strata).

The heights of void migration estimated for varying excavation heights from these relations is shown in Figure 6.1.

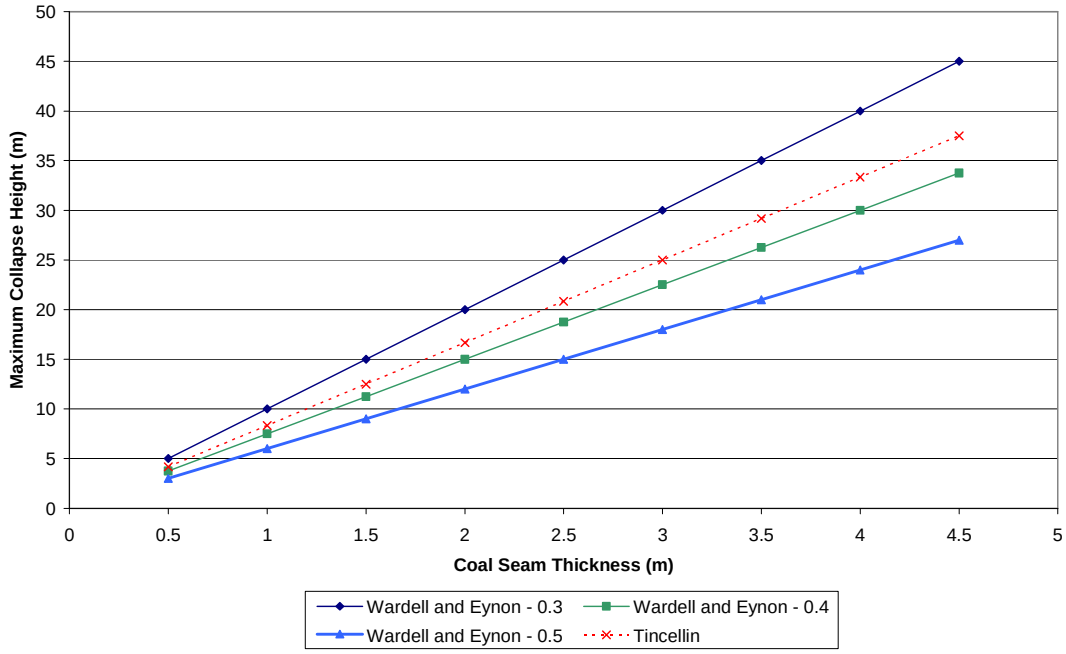

Figure 6.1: Estimated height of migration of a void before bulking of the void by collapse debris occurs based on the methods proposed by Tincelin and by Wardell and Eynon.

Observation of the plot reveals that the maximum height of void migration is given by Wardell and Eynon's method at a bulking factor of 1.3 where void migration is equal to 10 times the worked seam thickness; whereas Tincelin's method produces a collapse height approximately 8 times worked thickness before bulking halts void migration.

The results using the methodology employed here where the failure is assumed to be a cone and the volume of the workings immediately below the collapse along with the cone itself are considered is seen in comparison with those of Tincelin (Bell, 1975) and those of Wardell and Eynon (Healy and Head, 1984) in Figure 6.2. Here it can be seen that there is broad agreement although the values derived using this methodology may be considered somewhat conservative compared to those of Tincelin and Wardell and Eynon.

From Figure 6.2 it can be seen that in all cases, as the excavation height increases, so to does the height of void migration and the inverse relationship is true for the bulking factors, whereby as it increases, the height of collapse decreases. It is intended to combine this height estimation tool with a relation to estimate caving angle that will allow an automated spread sheet tool to be created that can estimate the potential height of collapse that may occur before either arching or bulking will halt the migration of the void.

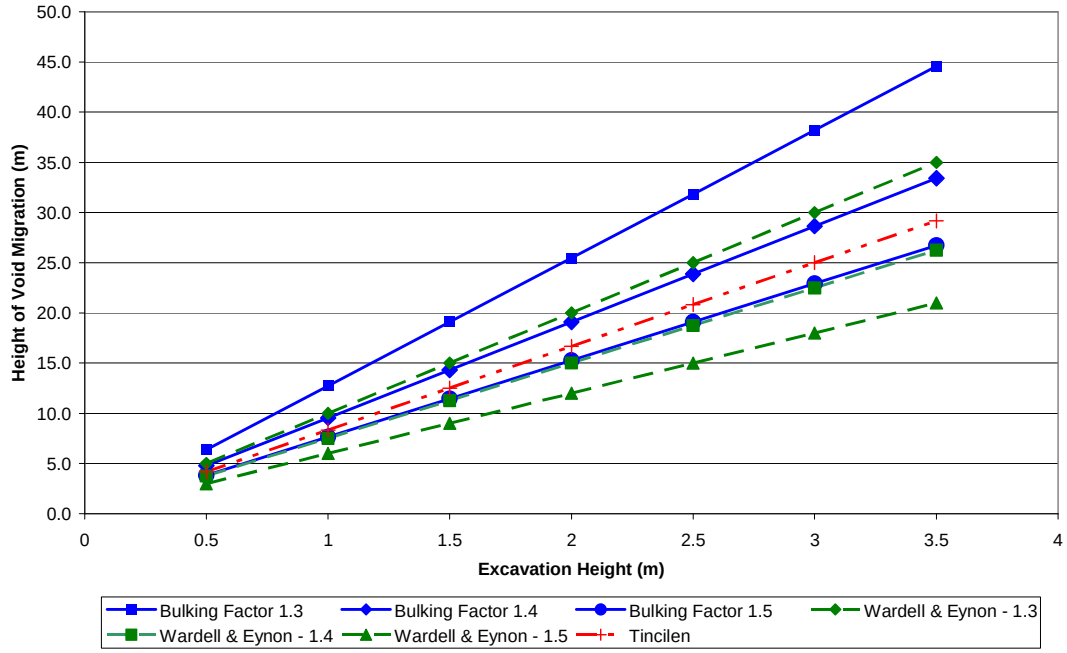

Figure 6.2: Comparison of the bulking height results for the methodology employed in this work with those of Tincelin and by Wardell and Eynon.

6.3 Effect of Variation in Caving Angle on Height of Void Migration

In this phase of the study it is intended to test the importance of the caving angle on the halting of void migration due to natural arching when compared with the heights for bulking factors above. It is intended to identify how sensitive the height of void migration is to the caving angle with differing strata and ultimately to attempt to quantify its importance when compared with other parameters to enable a decision to be made on the importance of derivation of this parameter from site investigation or laboratory tests.

It should be noted that the mechanisms of failure initiation and progression cannot be investigated using this technique. Only the height that a void may reach before arching occurs whereby the calculation of collapse height is done using a spread sheet to calculate the changing shape of the collapse chimney depending on caving angle and stratum thickness.

6.3.1 Assumptions

As per study phase 1a with the following exception:

The collapse will only be halted by natural arching, not by bulking.

6.3.2 Hypotheses

1. Increasing the caving angle of the material will increase the height of void migration.

- Caving angle is related to UCS of the rock as described previously therefore the lower the UCS the higher the caving angle, the steeper the sides of the collapse chimney and the greater the collapse height. Depending on the strata thickness, a very shallow angle of collapse may arch in a relatively thin strong layer (long before bulking), whereas for high angles of caving it is possible that even within a very thick layer or series of layers, that the void may reach superficial deposits without an arch being formed – in this case bulking may prove more significant.

2. Increased overburden thickness will allow arching to successfully halt void migration in weaker strata and or with wider excavation widths
3. Increasing excavation width will increase the height of void migration.

- For a given caving angle, the cone or frustum formed will have a larger base diameter for a wider excavation width. This will result in a greater height of collapse before arching occurs

6.3.3 Methodology

Height of collapse in uniform material (collapse geometry forms a cone):

$$H_C = \frac{q_r}{\tan(90 - \beta)} \qquad 6.5$$

Where:

H_C = height of collapse (m)

q_r = radius of roof collapse (m)

β = Caving angle (°)

In a stratified material if the height of collapse in a given stratum exceeds the stratum thickness then the collapse geometry forms a series of frustums. As such it is intended to investigate how the following parameters affect the height of collapse before choking of the void can occur:

- Tunnel width (0.5 - 3.5m) – Typical values for UK shallow workings (Attewell and Taylor, 1984).
- Caving angle (5 - 35°) – These represent the typical ranges of values suggested by Das (2000) and the range of joint friciton angles that may be found in a rock mass (Goodman, 1980; Brady and Brown, 1992, Zhang, 2005).
- Overburden rock mass – in this empirical investigation it is assumed that the overburden rock mass is a uniform material and that therefore a uniform cone will be formed, rather than a series of frustums which would form in a stratified material.

The results from these studies are then compared with the numerical modelling results.

6.3.4 Results and Discussion for Parametric Study of Variation in Caving Angle on Height of Void Migration

A plot of the maximum collapse height which will occur before formation of an arch in a rock mass with horizontally bedded strata and for a given excavation width is shown in Figure 6.3.

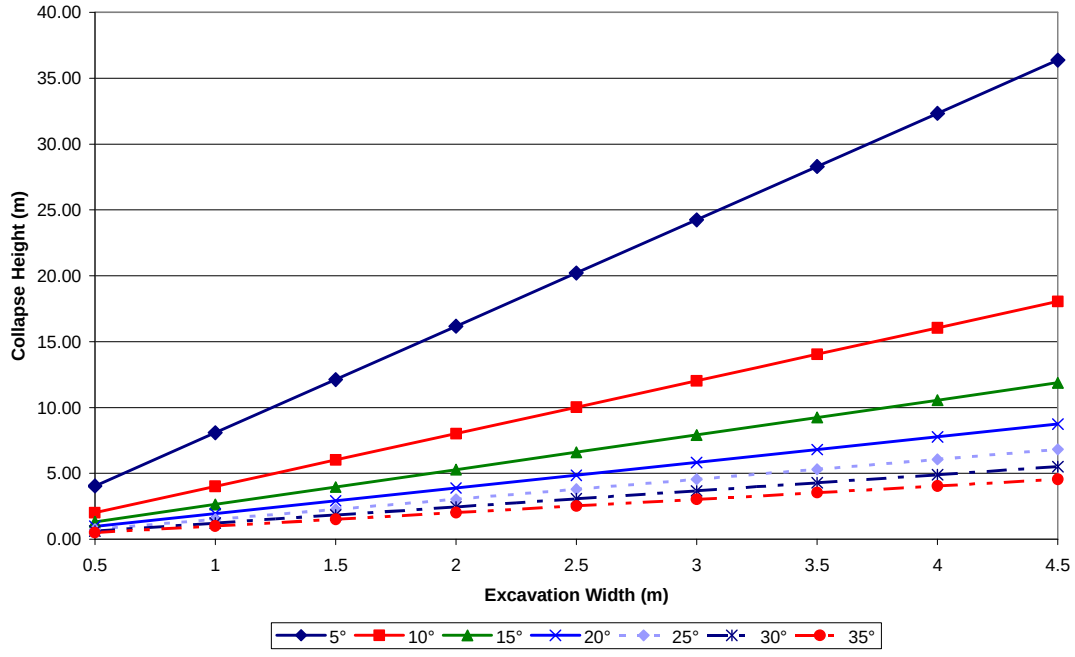

Figure 6.3: Plot showing relationship between the excavation width and height of maximum void migration before arching can occur at varying friction angle values.

It is readily apparent from the plot that the friction angle of the rock mass and the width of the excavation both have a significant effect on the maximum height of void migration that can occur before arching halts upwards migration. Whereby decreases in rock mass friction angle and increases in excavation width lead to increases in the height of void migration.

It is also apparent that the relationship between caving height and excavation width is linear with collapse height being equal to the caving angle in radians multiplied by the excavation width. However it can also be seen that the relationship between collapse height and angle of friction is more complex as at lower angles of friction (which result in steeper caving angles) the rate of change of collapse height with respect to varying friction angle increases.

This relationship is clearer if a plot of the varying collapse height is plotted against friction angle of the rock mass as seen in Figure 6.4. Here it can also be seen that at friction angles below 20 degrees, the height to which void migration can occur before arching increases significantly compared to higher angles of friction.

Here the height of maximum void migration is related to the friction angle of the rock mass by a power law whereby height of migration (H_m):

$$H_m = (61.21 \times Span_{Max}) \phi'^{-1.1773} \qquad 4.6$$

Where:

$Span_{Max}$ = Maximum excavation span (m)

ϕ' = Friction angle of rock mass (°)

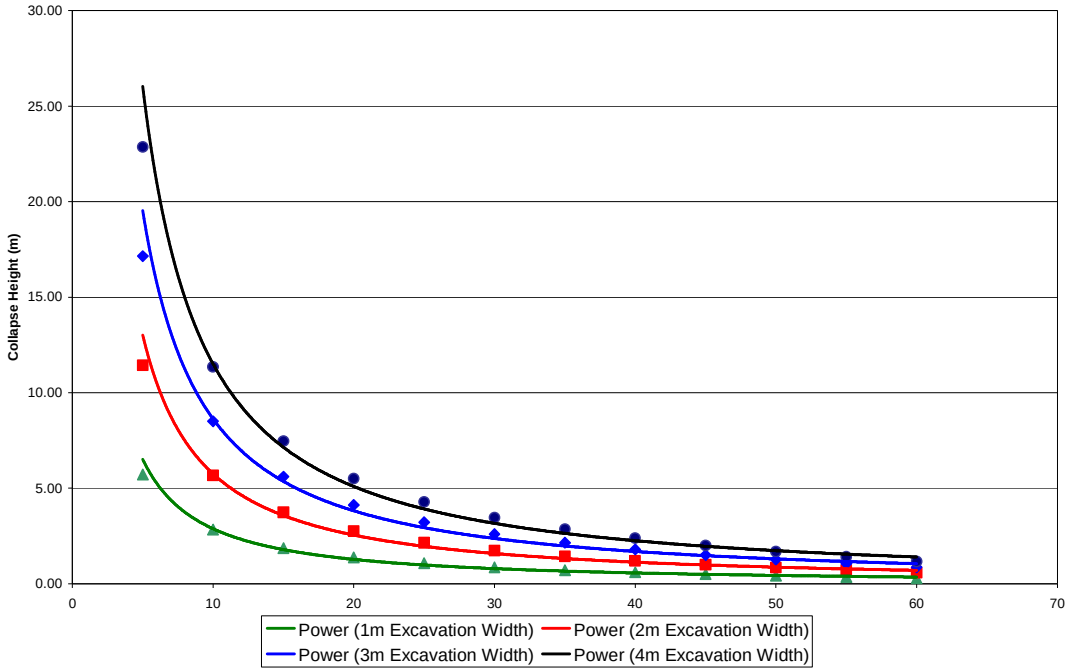

Figure 6.4: Plot showing relationship between rock mass friction angle and height of maximum void migration for varying excavation widths before arching can occur.

Ackenheil and Dougherty (in Bell, 1975) proposed a height of approximately twice the distance between pillars as being the level within the rock mass where an arch will successfully develop. This would be approximately equal to a caving angle of 15° from the vertical, which is perhaps most significantly equivalent to the angle of friction quoted for coal measures rocks with clay infilled joints of 16° (Zhang, 2005) and which based on the numerical modelling work undertaken in the previous section demonstrating that the friction angle is the key factor in controlling failure geometry appears to be a very reasonable estimate of the caving height. It is also of more general interest as it is indicative that it may be possible to estimate a generalised caving angle or range of potential caving angles for use in the initial assessment of the potential for void migration to reach the surface.

6.4 Comparison of Empirical to Numerical Results

In order to validate the empirical tool it is necessary to compare the maximum height of caving seen in the numerical modelling results for rock masses with varying friction angles as discussed in chapter 5 to the equivalent results for the estimated height of caving using the empirical spreadsheet tool and the relation outlined in section 6.3.3 in 6.5.

In this instance, the yield state plots of a 3 m wide 1 m high excavation are included in Figure 6.5 with the maximum height of shear failure which represents failed roof strata and hence caving height before arching has occurred within the rock mass. As stated in the section summarising the numerical modelling results for variable discontinuity frictional properties (Section 5.13) it can be seen that as the friction angle of the rock mass increases the angle of caving decreased resulting in a smaller height of potential void migration before the halting of movement by arching.

Table 6.2 shows a comparison between the maximum collapse heights as derived by the numerical model compared to those estimated using the empirical relationship. It can be seen that the numerical model values for collapse height are larger than those estimated by the empirical tool by approximately 0.2 to 0.3 m.

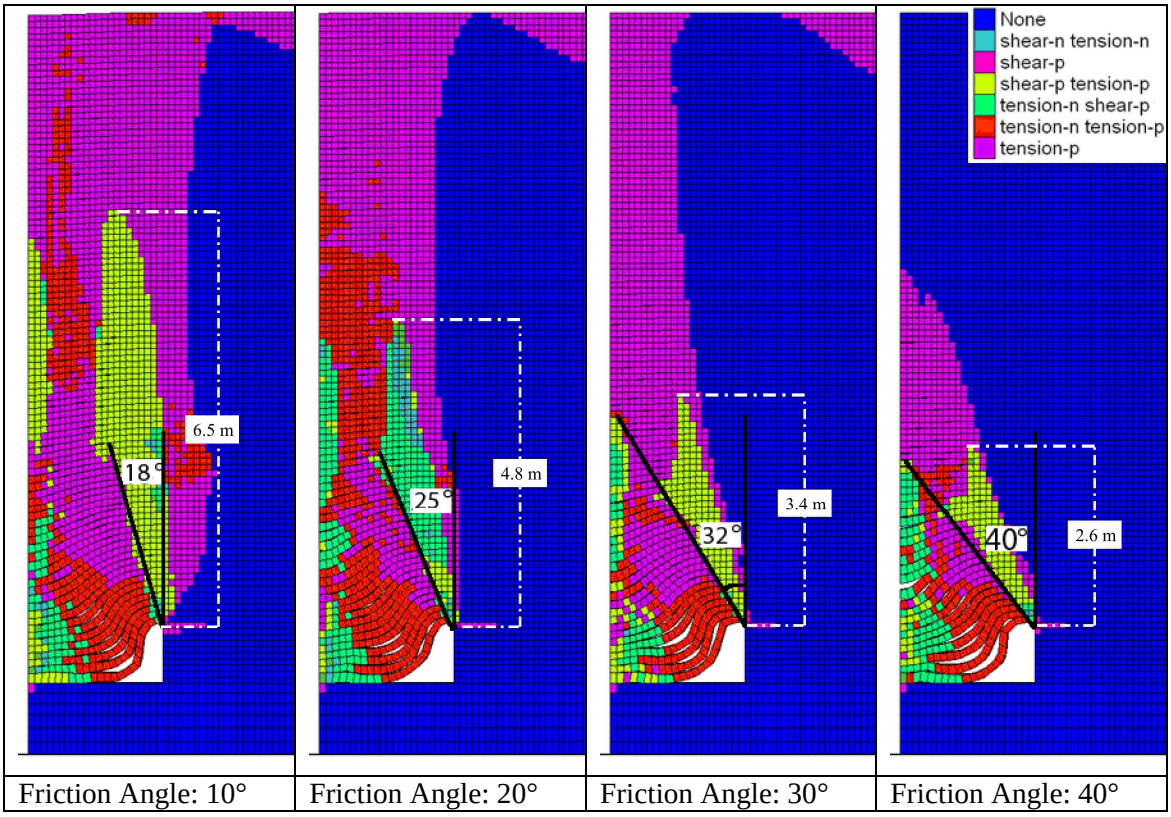

Friction Angle: 10°	Friction Angle: 20°	Friction Angle: 30°	Friction Angle: 40°

Figure 6.5: Height of extent of roof failure through shear yielding that would allow collapse to occur at four different rock mass friction angle values. 3 m wide, 1 m high excavation, rock mass GSI 10, bedding spacing 0.1 m.

Table 6.2: Comparison of numerical and empirical estimates of maximum height of void migration before arching occurs.

Interface Friction Angle (°)	Rock Mass Friction Angle (°)	Caving Angle (°)	Excavation Width (m)*	Height of Collapse Before Arching Occurs (m)	
				Empirical Value	Numerical Modelling Value
40.0	40.0	50.0	3.0	2.5	2.6
35.0	36.5	53.5	3.0	2.9	3.1
30.0	32.2	57.8	3.0	3.4	3.4
25.0	28.5	61.5	3.0	3.9	4.2
20.0	25.0	65.0	3.0	4.5	4.8
15.0	20.5	69.5	3.0	5.7	6.0
10.0	18.0	72.0	3.0	6.5	6.5

*Note that the excavation width in this case is the width of the room. The maximum span is the hypotenuse of a right angled triangle with sides equal in size to the excavation width.

Another important detail is that as it has been established that increases in the strength of the rock mass (*i.e.* the GSI value of the strata forming the bedding planes) will lead to a decrease in the height to which the collapse of the roof will extend into the rock mass before being halted by arching which in turn coincides with an increase in the stable roof width that can form, it would appear that the empirically derived heights of caving presented in Table 6.2 represent a worst case for this failure mechanism where the

strength of the rock mass is at a lowest value and so empirical estimations of the collapse height may also be considered a worst case.

This suggests that the height to which collapse of the roof strata extends into the rock mass would be significantly over estimated by the empirical tool as the estimated height is based on the assumption that the collapse geometry will form a cone in three dimensions. However as the rock mass strength increases the caving angle remains equal to 90° – angle of rock mass friction but the width of the stable span increases and so the height of collapse decreases forming a flattened top to the cone which in three dimensions takes the form of a frustum whose upper diameter increases and height from base to top decreases as the rock mass strength increases. This occurrence can be seen in Figure 6.6.

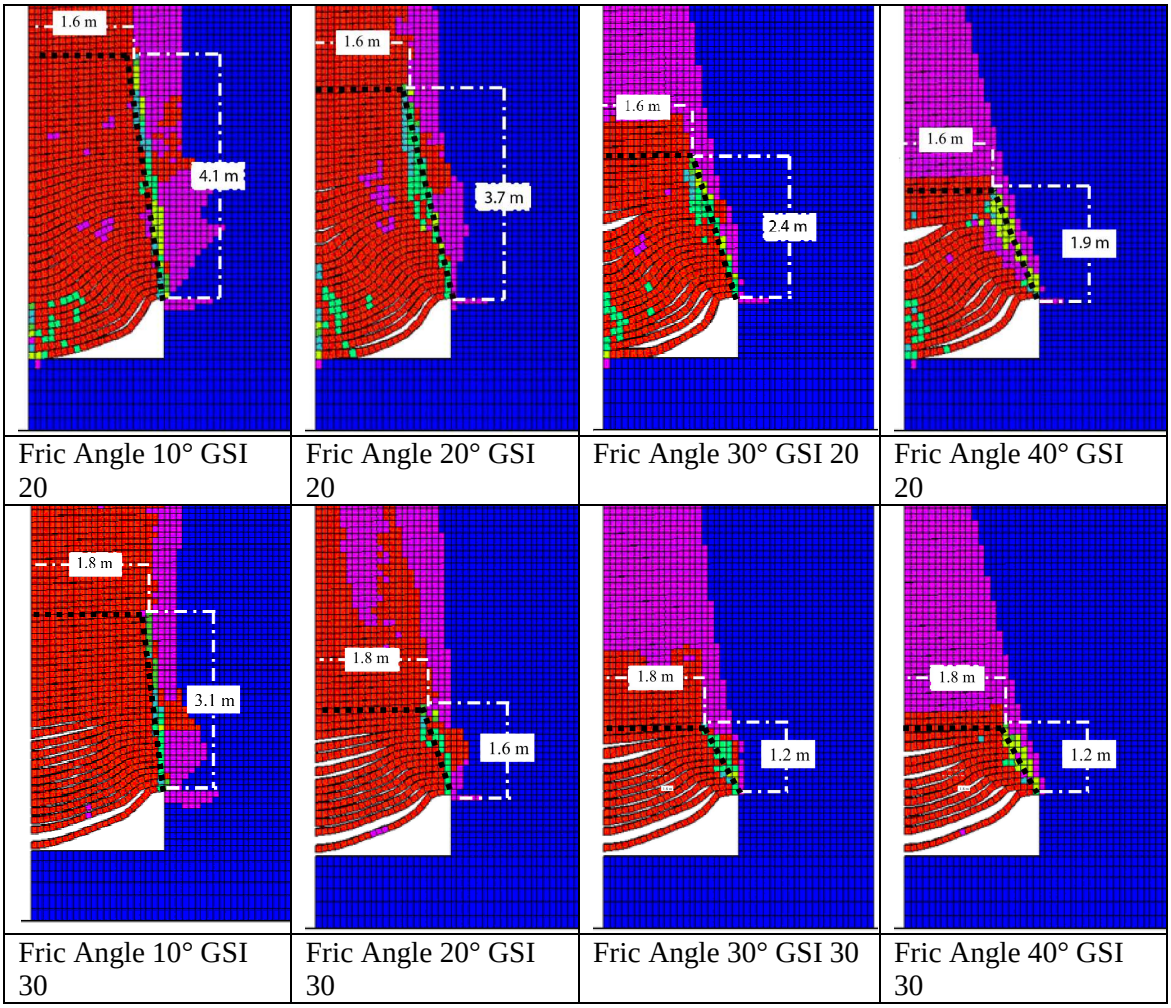

Fric Angle 10° GSI 20	Fric Angle 20° GSI 20	Fric Angle 30° GSI 20	Fric Angle 40° GSI 20
Fric Angle 10° GSI 30	Fric Angle 20° GSI 30	Fric Angle 30° GSI 30	Fric Angle 40° GSI 30

Figure 6.6: Height of extent of roof failure through shear yielding that would allow collapse to occur at four different rock mass friction angle values. Also shown is the width of stable roof span. Excavation 3 m wide, 1 m high, rock mass GSI 20 and 30, bedding spacing 0.1 m.

6.5 Extension of the Empirical Relations to Apply to Layered Strata.

From the modelling results it seems apparent as stated previously that the geometry of the collapse frustum is defined by the angle of friction of the rock mass which controls the angle that the edge of the frustum forms to the vertical and the strength of the strata control the diameter of the top of the frustum. An expression has been derived to allow estimation of the maximum stable span length of a roof beam using the following equation (Bell, 1975):

$$L_S = \sqrt{\frac{2\sigma_t T_S}{\gamma}} \qquad 6.6$$

Where:

L_S = span length (m)

σ_t = tensile strength of rock stratum

γ = bulk density of the rock mass

T_S = thickness of intact stratum (m)

This and similar estimates of stable span should be viewed with caution however as this assumes that there are no joint sets along which failure can occur within the rock mass. Also an estimate of the tensile strength of the roof beam must be made which will require scaling from a measured laboratory value.

As such it may be sensible to assume a worst case and that the collapse height will form a perfect cone.

Another point of note which was mentioned above, is the fact that coal measures strata are typically composed of layers of varying materials with variable properties. As such it is necessary to attempt to factor this variability into the empirical tools used to estimate the height of collapse before arching or bulking occurs. In order to account for the presence of strata with differing properties, the following methodology is applied:

The total volume available for the bulked debris includes the space within the excavation and also includes the total volume of the collapse zone (above the workings). This zone can be modelled as a cone (or a series of frustums in varying strata).

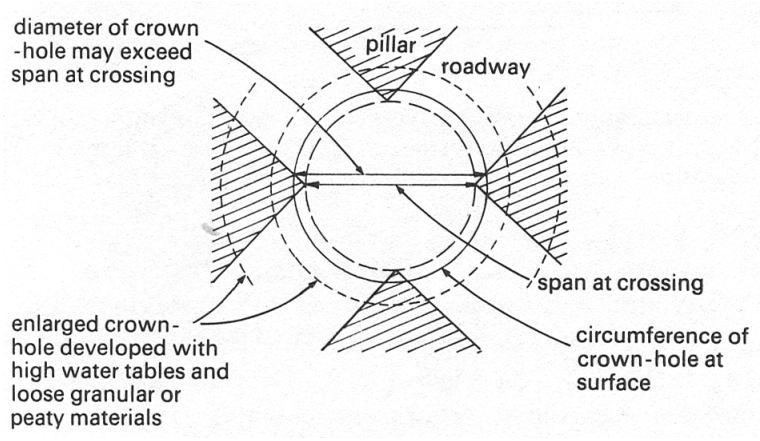

Figure 6.7: Failure most commonly occurs at roadway intersections due to increased span (after Attewell and Taylor, 1984).

Figure 6.7 shows that the most common failure location within workings is at room intersections. These roof failures produce conical failure geometry in the strata above the working (Attewell and Taylor, 1984).

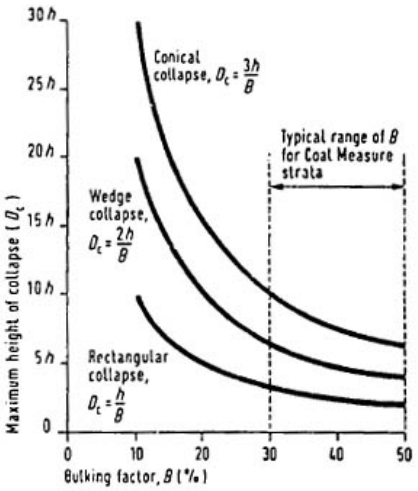

Figure 6.8: Heights of collapse for varying collapse geometries (Healy and Head, 1984).

Wedge failures may occur along roadways however it has been shown that cone shaped failures produce the highest degree of collapse height and as such a conical collapse above tunnel intersections represents the worst case. See Figure 6.8.

In order to calculate the additional volume made available due to the collapse it is first necessary to determine the height of collapse in the first stratum.

$$\text{Height}_{\text{Collapse}} = \frac{q}{\tan(90 - \beta)} \qquad 6.7$$

Where:

q = radius of roof collapse.

β = Caving angle °

If the height of collapse is less than the stratum thickness then collapse geometry can be represented as a cone

$$\text{Vol}_{\text{CollapseCone}} = \frac{1}{3}\pi q^2 h \qquad 6.8$$

Where:

h = $\text{Height}_{\text{Collapse}}$ (m)

If however the height of collapse would exceed the stratum thickness, it is necessary to represent the collapse geometry as a series of overlying frustums. In order to visualise this, see Figure 6.9. D_{RC} represents the roof collapse diameter (m), t_1 is the thickness of the first strata (m) overlying the workings and β is the caving angle for the strata.

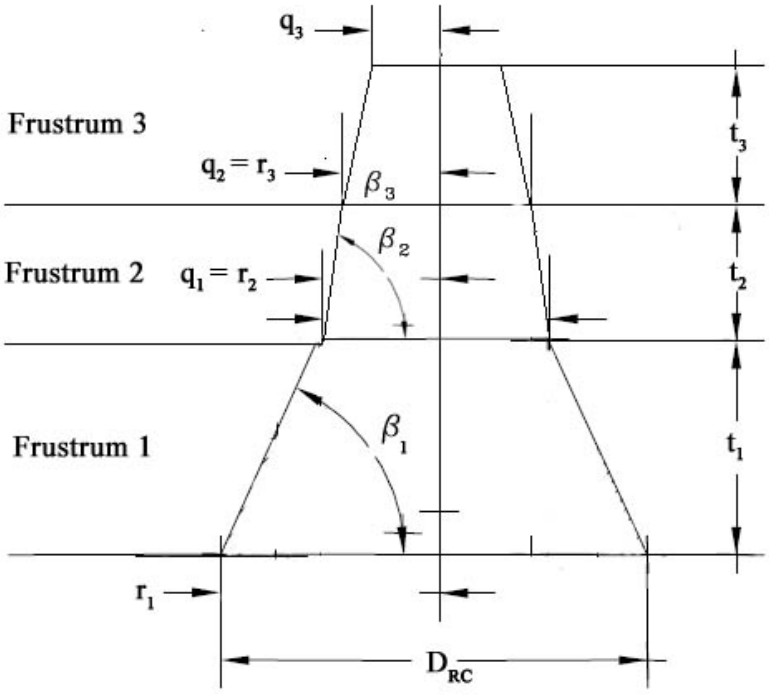

r_1 r_2 r_3 = base radii of the frustrums, q_1 q_2 q_3 = upper radii of frustrums
β_1 β_2 β_3 = Caving angle of stratum

Figure 6.9: Geometry of collapse in a layered material with varying caving angles.

The volume of a frustum:

$$\text{Vol}_{\text{CollapseFrustrum}} = \frac{\pi t_1}{3}\left(r_1^{\,2} + (q_1 \times r_1) + q_1^{\,2}\right) \qquad 6.9$$

Where:

r_1 = D_{RC} / 2

q_1 = radius of top of any Frustrum (m) = $r_1 - \left(\text{Tan}(90 - \beta_1) \times t_1\right)$

This process is then repeated for the overlying strata until either the collapse height exceeds the height to rock head or until the void is fully choked by bulked debris and migration halts.

To provide a better understating of this, a simple example is given below based on the parameters from Figure 6.9:

Volume of space to receive debris ($\mathrm{Vol}_{\mathrm{Debris}}$) :

$$\mathrm{Vol}_{\mathrm{Debris}} = \mathrm{Vol.\,workings} + \mathrm{Vol.\,Frus\,1} + \mathrm{Vol.\,Frus\,2} + \mathrm{Vol.\,Frus\,3} \qquad 6.10$$

The total volume available for debris rock is therefore equal to the volume of the collapse zones plus the volume of the debris pile in the workings.

The volume of the debris rock ($\mathrm{Vol}_{\mathrm{BulkDebris}}$) is equal to the collapse volume multiplied by the bulking factor (k). This can be estimated for rock according to Equation **6.11** (Palchik (2002)):

$$BF_R = 1 + \alpha_{BF}\sqrt{\sigma_{ci}} \qquad 6.11$$

Where:

BF_R = bulking factor

σ_{ci} = uniaxial compressive strength of rock (MPa)

α_{BF} = empirical constant dependent on local geology (≈ 0.05)

This relation only holds for rocks with UCS in the ranges 35 – 100 MPa. Coal measures rocks with UCS below 35MPa are assumed to have a bulking factor of 1.3 and rocks over 100 MPa a value equal to 1.5 based on the typical range of values quoted in the literature (Healy and Head, 1984)

The void can be assumed to have choked when:

$$0 = \left(\mathrm{Vol}_{\mathrm{CollapseFrustrum}} + \mathrm{Volume}_{\mathrm{DebrisWorkings}}\right) - \mathrm{Vol}_{\mathrm{BulkDebris}} \qquad 6.12$$

This is done most simply by incorporating the above equations into a spreadsheet which calculates the volumes of the frustums in each layer and multiplies each of these individual volumes by the appropriate bulking factor to find the debris volume. The total volumes of the frustums and the available volume within the workings are then added to find the total volume available to receive debris.

As described in Equation 6.12, once these two volumes are equal, the void has been choked. In order to find the height of the last frustum and to find the overall height of collapse it is necessary to use the solver function to vary the height and upper radius of the final frustum (when Equation 6.12 is approaching 0) until Equation 6.12 = 0.

Numerical Modelling of Void Migration

In the modelling undertaken in chapter 5, the height to which the roof collapse propagates into the rock mass is being assessed subjectively by observation of the yield state plot and the height to which shearing which represents the failure of the strata over the excavation roof / pillar intersection propagates into the rock mass. In other words, the user has to display engineering judgement. In order to remove the subjectivity from the interpretation of the height to which roof failure propagates and to model the migration of the void it is necessary to create an automated system that will remove elements from the mesh that represent "failed" roof strata that are collapsing into the void. In order to do this it is necessary to use a custom FISH function.

6.5.1 FISH Collapse Function

This function identifies zones within the model grid that have failed in tension and shear (incorporating a minimum strain parameter by measuring in built zone strain variables) and then removes these from the model.

In more detail, this function scans through the list of zones to identify those elements which have failed either in tension or shear. Once a zone which has failed has been located, the function then examines the volumetric strain increment values of the model zone and compares this to a prescribed cut off value. If the strain increment as measured within the element exceeds the prescribed cut off, then the element group name is changed which in turn allows the element to be nulled from the mesh and the function carries on scanning through the list of zones. In order to correctly locate the zone to be nulled it is necessary to manipulate grid point parameters as well as zone parameters. Whereby, FLAC uses a number of primitive zone shapes to create mesh geometries. The most common and the type used in the modelling undertaken in this thesis are cube shaped zones (see Figure 6.10 where a diagrammatic representation of a cube or brick zone primitive can be seen). This is composed of 8 grid points (located at the vertices of the brick) and 6 planer faces forming the surface of the zone.

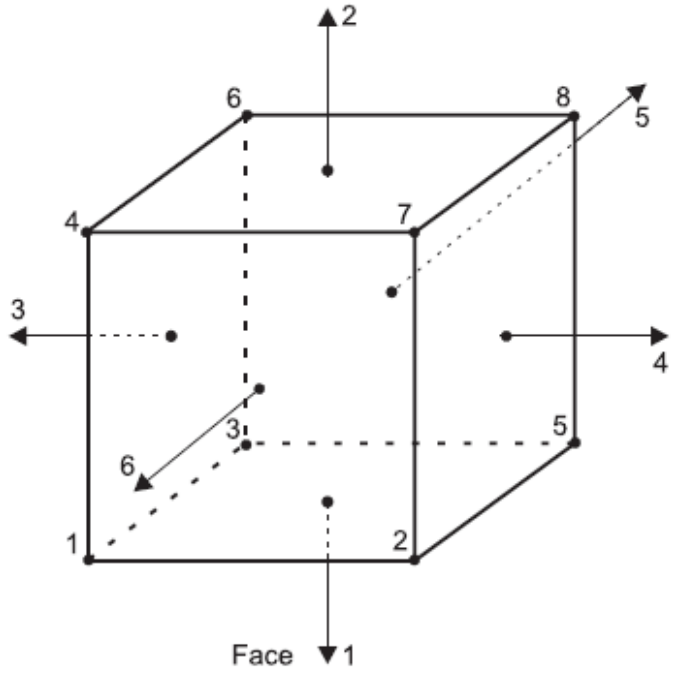

Figure 6.10: Zone primitive showing vertices and faces.

In order to identify and manipulate the zone geometry using grid point parameters at least four grid points must be identified; grid points 1, 2, 3 and 4. Grid points 1, 2 and 3 define the X and Y co-ordinates and widths of the base of the zone, and grid point 4 defines the z co-ordinate and height of the zone. If the interior angles of the zone are all orthogonal (as in the diagram) then these four points are sufficient to define the zone that is to be removed. In this function the decisions are made in a series of logic tests using the IF command logic in FLAC which takes the form:

IF expr1 test expr2 THEN
Commands
ELSE
Alternate Commands
ENDIF

Where expr1 and expr2 are any valid algebraic expression and test makes use of any of the following operators: = - equal to; # - not equal to; > - greater than; < - less than. As such, if the test evaluates as true, then the statement(s) immediately following IF are executed until ELSE or ENDIF are encountered. If the test is false, the statements between ELSE and ENDIF are executed if the ELSE statement exists; otherwise, control jumps to the line after ENDIF (Itasca, 2005). The decision process involved in the collapse height void migration tool is illustrated in a flow chart. See Figure 6.11.

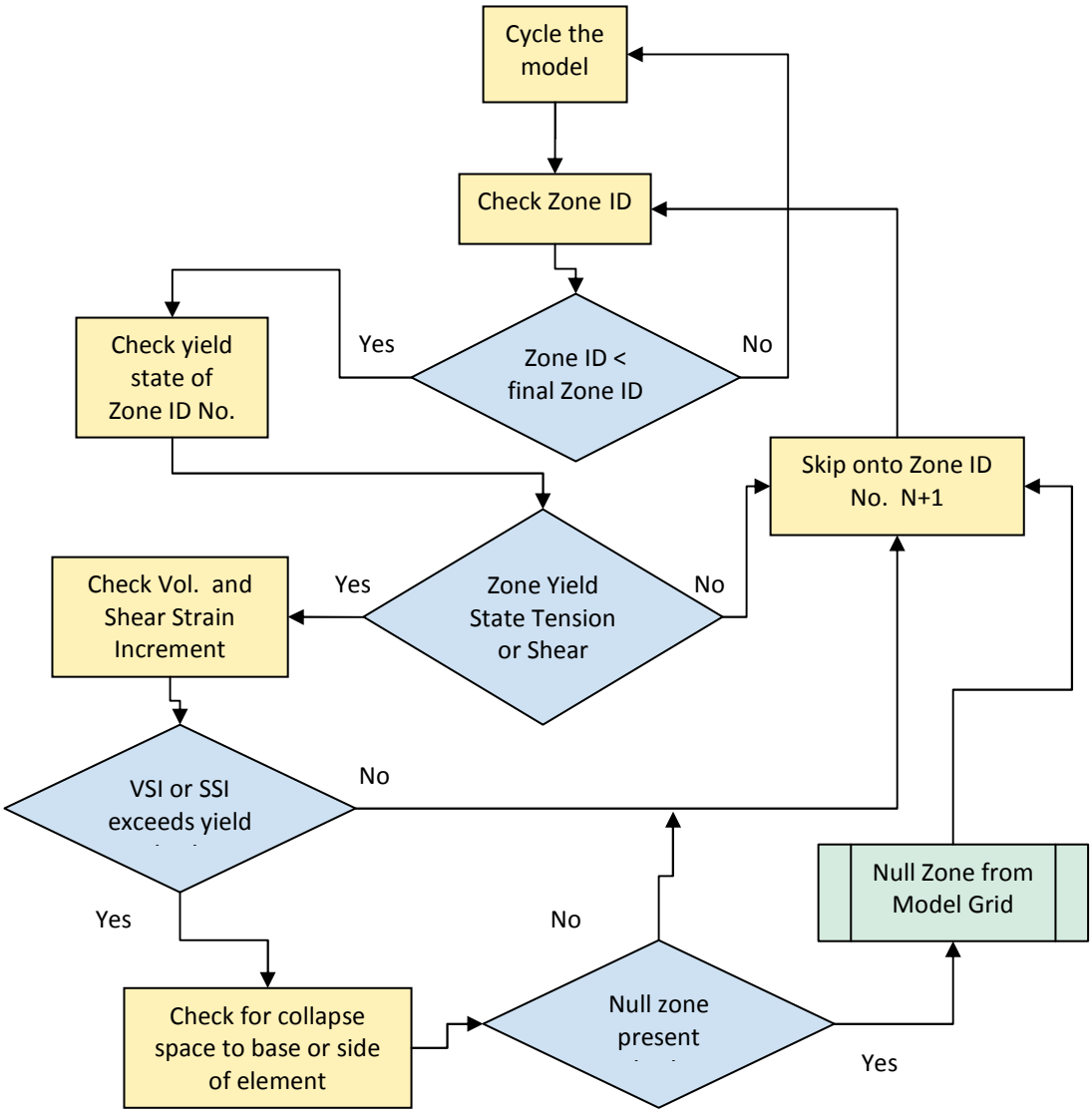

Figure 6.11: Flow chart summarising the process used to remove elements from the model.

A simple FISH function was also written that would examine the grid for the presence of detached blocks and remove them from the model. This tool took advantage of the model symmetry and the method used to separate the grid into layers, whereby a function had been written to automatically number the strata sequentially from the base upwards so as to allow the automation of separation of the grid and also to automate the insertion of interface elements. As such the FISH function would search for elements that had a null zone to their right hand side and then if found, check the zone to identify its group number. This would then be compared to the group number of the element above it. If the group numbers of the zones matched it was assumed to be supported from above. If they did not match then the element was nulled.

In order to use the element removal tool it was necessary to calibrate the volumetric strain increment used as the cut off criterion.

A model was selected with uniform properties (3 m excavation width, 1 m excavation height, rock mass GSI 10 and interface separation of 0.1 m) where failure of the roof strata were known to occur due to self weight sagging in order to allow a comparison of the final result from the element removal tool with that caused by the collapse of the strata due to self weight. This acted to validate the methodology employed. Initially the element removal function was run repeatedly with a range of volumetric strain increment cut off values in order to constrain a value that most accurately captured the expected void migration geometry. It should be noted that initially the element removal tool was run after the model had been stepped to failure; as such the elements that exceeded the criterion were all removed in one step at the end of modelling and as such it is possible that if this occurred while the model was running, further instability and collapse may have occurred. However this approach was taken initially as running the element removal tool while stepping the model was exceptionally computationally expensive and hence very time consuming.

The volumetric strain increment cut off value was initially varied from 0.1 to 0.01. The resultant roof collapse geometries that are produced by each of these values are shown in Figure 6.12 where it can be seen that as the volumetric strain cut off value is decreased, the height to which void migration occurs increases.

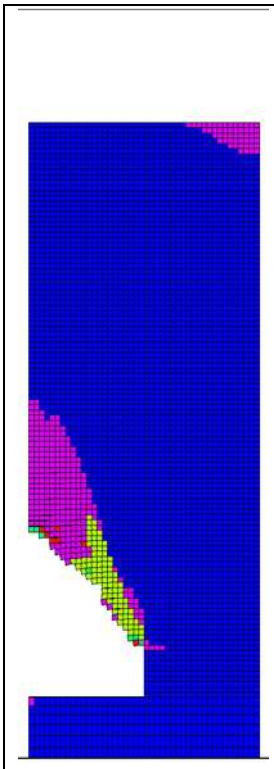	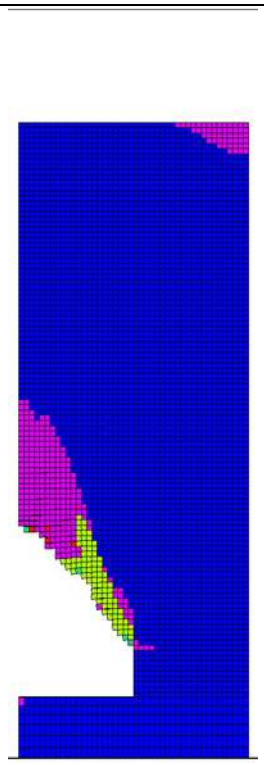	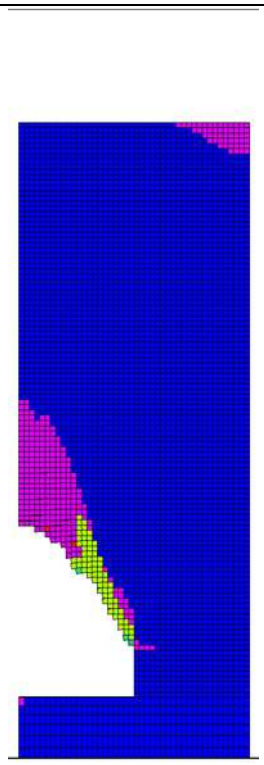
VSI Criterion 10%	VSI Criterion 7.5%	VSI Criterion 5%
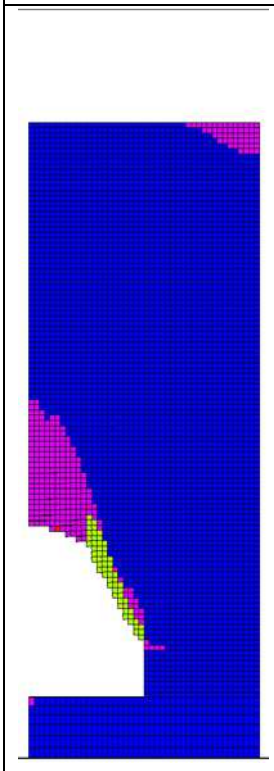	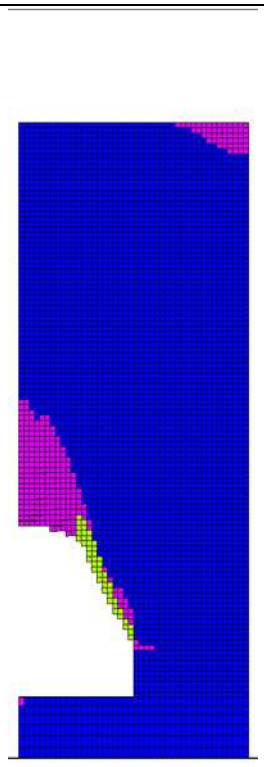	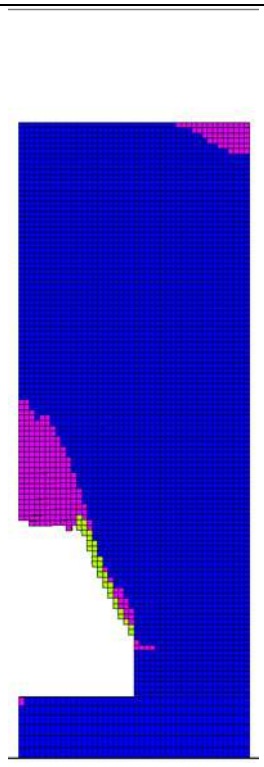
VSI Criterion 3%	VSI Criterion 2%	VSI Criterion 1%

Figure 6.12: Height of void migration for varying values of volumetric strain increment cut off.

From the above it can also be seen that the VSI criterion that most closely results in a collapse cone with a caving angle equal to 90º minus the friction angle of the rock mass is the 5% VSI criterion, however the height of collapse is approximately 0.3 m less than that estimated by the empirical tool or the value that has been assumed in the previous numerical modelling work to be the height of roof collapse based on the height of extent of shearing within the rock mass. It is assumed that this reduced height is because the tool was run after cycling of the model was completed and that if the model were stepped to equilibrium, the failed roof strata that were not removed would continue to deform and would ultimately exceed the yield criterion and be removed from the model. This assumption was tested and the results summarised below.

Once a suitable criterion was identified (in this case a value of volumetric strain increment equal to 5% was selected), a fully coupled model was run whereby the element removal FISH function was linked to the FLAC stepping command using a specialised inbuilt FLAC command known as “Fish Call” which allows custom FISH code to be implemented as part of the standard FLAC stepping routine.

As such for every step / cycle of the model, a full iteration of the element removal function was run. This allowed the model to be stepped to an equilibrium condition whereby no further collapse of the model occurred. The final result of this modelling is summarised in Figure 6.13 below:

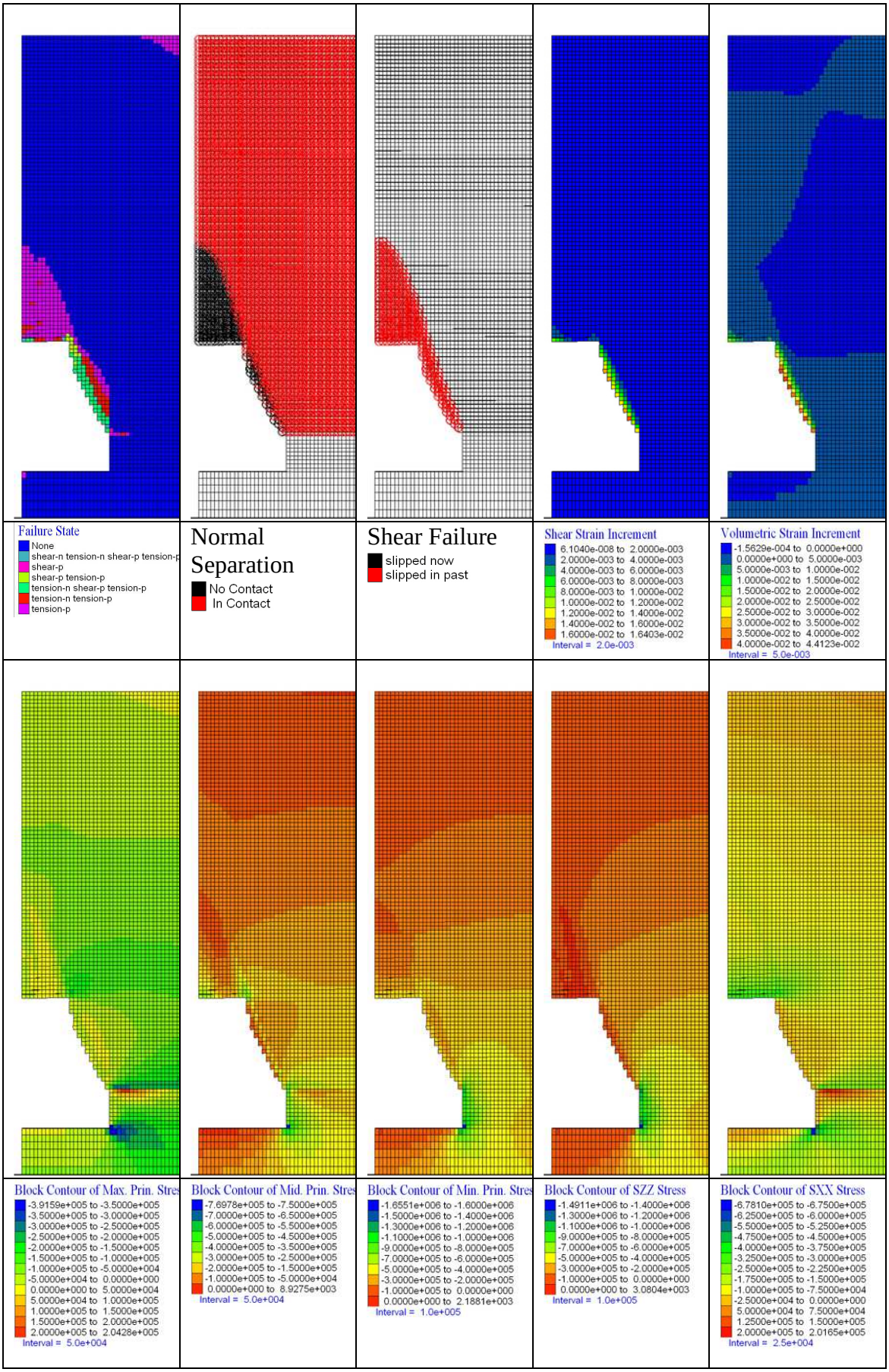

Figure 6.13: Plots related to the failed element removal tool at equilibrium after a fully coupled model run.

In order to validate that the model is behaving as required by the VSI cut off criterion the plot of volumetric strain increment (VSI) in Figure 6.13 should be observed. Here it can be seen that the maximum volumetric strain increment recorded in the model is in the zones immediately adjacent to the collapse boundary / newly formed roof and that these reach a maximum value of around 0.044 (4.4%) which is less than the criterion selected for the cut off. This correlates with the shear strain increment (SSI) plot, whereby the zones which have undergone significant shear strain have also been removed from the model, even though the shear strain is not explicitly accounted for in the tool (rather it is the presence of shear yield that is tested for), the elements that have failed in shear yield have also undergone sufficient volumetric strain to be removed from the model.

It is also clear that only those elements in the roof strata above the excavation and that are within the zone of yielding have been removed from the model. This is indicative that the use of the element removal tool coupled to the FLAC cycling routine is working as expected. This can be seen when the failure geometry is compared side by side with the model allowed to progressive collapse, where it can be seen that in both cases the band of shear has extended to the same height within the rock mass and hence the failed strata have extended to the same height.

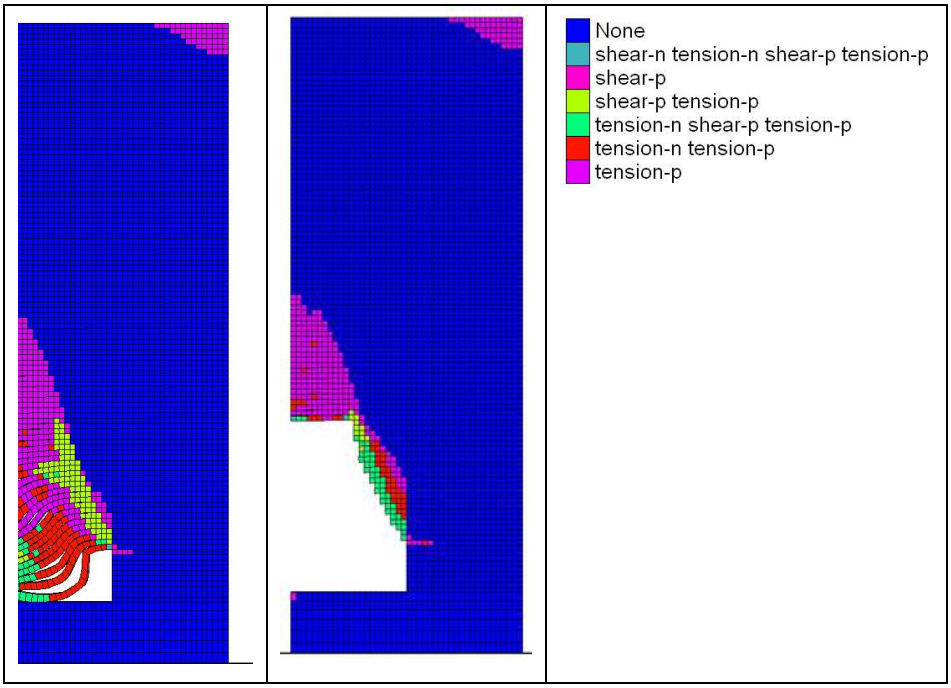

Figure 6.14: Comparison of element removal model with strata sagging model.

The primary differences between the un-coupled and coupled modelling are discussed below along with some more generalised discussion of the results of the coupled modelling.

The first and most obvious difference between the coupled and un-coupled results is the difference in collapse geometry between the two. In the uncoupled model which is not run to an equilibrium state, the collapse boundary follows the left hand boundary of the shear band that runs upwards into the rock mass at an angle equal to 90º minus the friction angle of the rock mass. In the coupled model however the failure boundary is steeper and runs upwards into the rock mass virtually bisecting the zone of shearing. This might suggest that the ultimate height of collapse would be higher, however this does not appear to be the case as the second difference between the coupled and un-coupled model that is of significant interest in this case is the development of a stable span in the roof strata that forms at a level equal to the upper extent of the shear band that develops into the rock mass overlying the excavation. This leads to a very well developed frustum geometry of failure. This geometry has been observed in the field (see Figure 2.17), in laboratory experiments (see Figure 2.15) and in the interpretation of the results of prior modelling undertaken and summarised in this thesis.

When the block state plot of the coupled and un-coupled modelling is compared, it can also be seen that there is a difference in the yield state of the rock mass whereby a region of tensile yielding has formed within the rock mass in the coupled model to the right of the zone of shearing over the excavation. This corresponds to a region of tensile stress with values reaching up to approximately 50 kPa (yellow contour region) which can be seen on the contour plot of maximum principal stress in Figure 6.13. This is assumed to be caused due to the loss of support of the cave roof that occurs when the failed roof strata are removed from the model. In the work undertaken here, the model reached equilibrium suggesting that this was ultimately stable, however it is possible that at lower rock mass strengths or in rock masses where discontinuities with unfavourable orientations relative to the excavation / collapse geometry were present, that this may also result in failure, effectively increasing the angle of caving of the rock mass even further. For example in rock masses with steeply dipping near vertical and persistent joints the angle of caving will be equal to the angle of joint dip. In this case void migration will only be halted by bulking or the presence of competent strata such as a thick sandstone bed within the rock mass.

Another factor of note is that the final geometry of the coupled model at its stable equilibrium state most closely matches the un-coupled models where the volumetric strain increment yield criterion drops to a value below approximately 3% which can be seen when the models geometries are compared as in Figure 6.15.

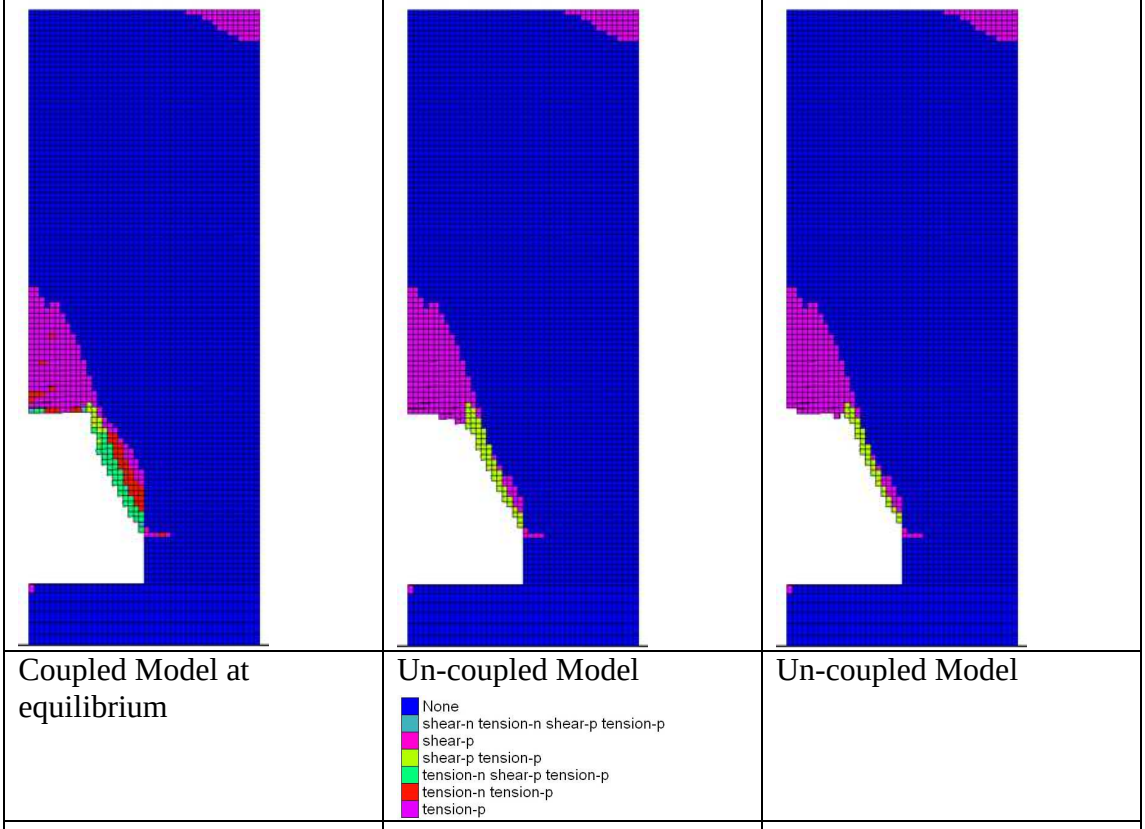

Coupled Model at equilibrium	Un-coupled Model	Un-coupled Model
VSI Criterion 5%	VSI Criterion 2%	VSI Criterion 1%

Figure 6.15: Comparison of coupled and un-coupled modelling at varying VSI criterion values.

This suggests that the un-coupled collapse height block removal tool can be used to approximate the final collapse geometry if a reduced value of the volumetric strain increment is used as the cut off criterion. A number of un-coupled modelling trails were undertaken on a number of higher strength rock masses and the results are summarised in Figure 6.16.

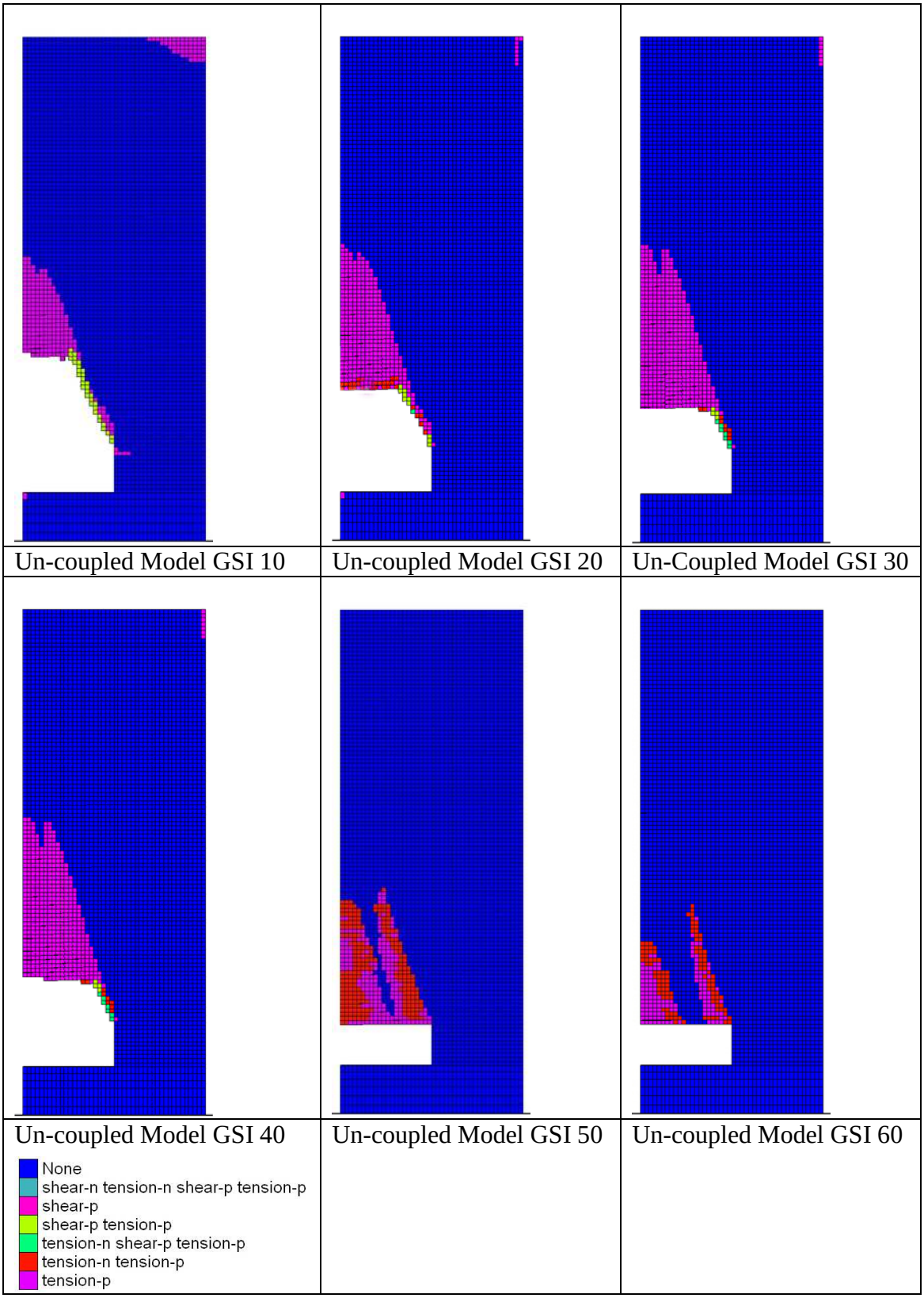

Figure 6.16: Collapse geometry using the un-coupled block removal tool at a VSI criterion of 1%.

Here it can be seen that the resultant failure is shown to occur in strata where shear failure cross cuts the bedding planes which results in collapse but not in those examples where there is no shear failure. This is indicative that the model will be able to capture

the progressive roof collapse behaviour in thicker roof strata that fail by shear / joint parting plane or pure shear failure.

6.6 Conclusions

A pair of empirical tools have been devised to estimate the potential height of collapse of a void when roof collapse occurs. The estimated height is derived based on the angle of caving of the rock mass which based on the work undertaken in section 5.13 is controlled by the rock mass friction angle where the deformation behaviour is not dominated by steeply dipping joints or on the height to which a void may migrate before bulking or choking of the void by rubble may occur. Analysis of varying excavation geometries in the numerical modelling in section 5.7 suggests that in horizontally layered strata, increases in the excavation width lead to increases in the height to which collapse occurs before an arch will form. This behaviour is also reflected in the empirical tool whereby collapse height increases as the width of a span increase due to the simple relationship between caving height and the excavation width as summarised below:

$$\text{Height}_{\text{Collapse}} = \frac{\text{Exc. Width}}{\tan(90 - \textit{C}\text{aving Angle})}$$

It has also been demonstrated that the collapse geometry in a rock mass of uniform strength (*i.e.* caving angle as related to the friction angle) is approximated in three-dimensions as a cone and in layered strata as a series of frustums topped by a cone. It is noted that this assumption is a worst case scenario as the tensile strength of the strata in the rock mass typically result in frustum rather than cone geometry, however this allows the empirical tool to estimate the volume of bulked debris that would have formed as a result of a given collapse geometry which is in turn controlled by the caving angle. This combined methodology can be readily implemented in a spreadsheet allowing an estimation to be made of the potential height of void migration through varying strata.

The above methodology has been combined with a method of estimating the maximum height of void migration that occurs before bulking. This was calibrated using the assumptions made by commonly occurring bulking estimation equations such as that of Tincelin and Wardell and Eynon (Bell, 1975; Bell *et al.*, 1988) whereby the extracted

thickness and the bulking factor or change in density are the only variables and these showed good agreement.

In this chapter, a numerical modelling tool has also been described that is intended to allow the modelling of failure propagation through both thinly and thickly bedded rock masses as it was recognised in the modelling undertaken in the previous section that the discontinuous horizontally layered elements intended to represent bedding planes were effective at capturing self weight sag subsidence which occurs due to tensile delamination along the bedding surfaces but was not able to capture the failure behaviour of thicker strata where a shear fracture would form propagating upwards into the rock mass where the elements where seen to yield in shear, however the continuous nature of the bed meant that the roof beam would not collapse into the void.

As such a tool was developed that relies on an assessment of the failure or yield state of an individual element along with its degree of volumetric strain in order to asses if it should be removed from the model. It has been demonstrated that the model can be coupled to the mechanical stepping to model the collapse behaviour to equilibrium indicating a stable roof state however it is recognised that this is a very inefficient and computationally expensive process. As such a methodology has also been devised and demonstrated that a close approximation of this final state can be derived by decoupling the FISH function from the mechanical time stepping and then running the function after a preset number of time steps before continuing the model run, and repeating the process until an equilibrium state (or potentially a collapse to surface) is reached.

Chapter

7

The Dolphingstone Case Study

7 The Dolphingstone Case Study

7.1 Introduction

During May and June 2001 a pair of crown holes of approximate diameter 1.5 m were found near the East Coast Main Line (ECML) track at a site near Dolphingstone near the track between Prestonpans station and Wallyford Cutting (Dolphingstone is a village located approximately 4 km East of Edinburgh in East Lothian in Scotland, Ordnance Survey Grid Reference NT 381732). The location can be seen in more detail in Figure 7.2 and Figure 7.3. The presence of these crown holes and the possibility of further subsidence at this site prompted Network Rail to divert the ECML over a distance of approximately 1.6 kilometres.

During the desk study carried out by Donaldson Associates Ltd (2002), it was found that mining had taken place in the area from the early 18th century (and anecdotal evidence of mining dates as far back as the 13th century).

The presence of the crown holes and the confirmation of historical mining activity and subsidence at the site, coupled with the risk of further subsidence representing what was considered a significant hazard to the railway, prompted the instigation of a site investigation (S.I.) which commenced in February 2002 (Donaldson Associates Ltd, 2002).

A preliminary SI was undertaken with rotary open and cored holes at 13 locations on both the north and south bound lines during night time possessions. This initial work confirmed the presence of mine voids (with heights of up to 3.2 m) at shallow depths (10.7 m) below the railway with only minimal rock cover (3.3 m) underlying superficial deposits. (Donaldson Associates Ltd, 2002).

The presence of these shallow abandoned workings was considered a significant hazard and prompted Railtrack (now Network Rail) to impose a temporary 32 km/h (20 mph) hour speed limit along the affected portion of the line as well as commissioning an even more extensive ground investigation which was undertaken between March and July 2002. Ultimately 266 bore holes were drilled to investigate the condition of the rock mass below site, 32 of which were fitted with standpipes or piezometers to monitor groundwater levels.

To further complicate matters, during the SI work it was found that new crown holes formed at the surface possibly triggered by vibration caused by the SI operations. Based on the presence of significant mine voids and the occurrence of further crown holes it was established that the most likely cause of the crown hole subsidence was the collapse of abandoned mine workings beneath the area.

The diversion of the ECML required the construction of a continuous raft supported on end bearing piles and although the remedial measures were successful they were highly expensive.

Following these subsidence events, Network Rail commissioned a report with the aim of reviewing current practice associated with the management and treatment of subsurface voids as they influence transport networks (Jones *et al*., 2005). Another aim of the report was to suggest areas where further research was required. One such research topic identified was the use of advanced numerical / computer modelling of the site at Dolphingstone which in turn prompted this research.

Lotian, Scotland. Marker indicates extent of lower image.

Figure 7.1: Satellite maps showing national location of site of interest.

Lothian and the Firth of Forth. Red Marker indicates approximate extent of Figure 7.3.

Figure 7.2: Satellite map showing regional location of site of interest.

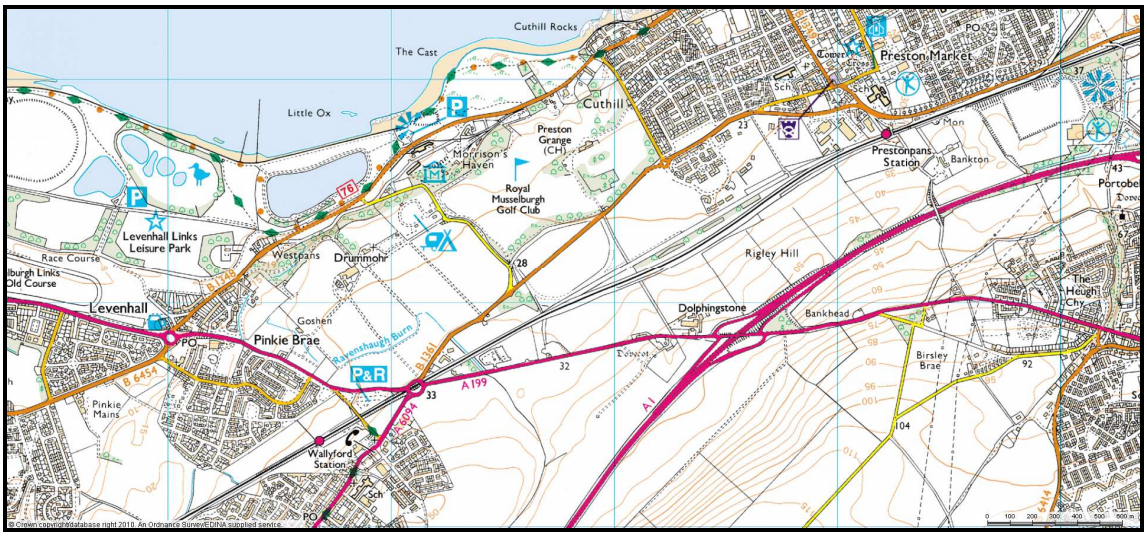

Figure 7.3: Map showing the location of Dolphingstone, the ECML, Prestonpans Station and Wallyford Cutting (Helm, 2010a).

7.2 Desk Study

7.2.1 Superficial Deposits

The report by Donaldson Associates Ltd. (2002) indicates that information from geological maps and other sources indicate that the superficial deposits are composed of high raised beach deposits of the "late glacial era" broadly to the north of the railway line and boulder clay (glacial till) is indicated to the south of the railway line on the site.

Further investigation of the geological map indicates that they are of Devensian age from the Quaternery period. A map showing the drift geology of the Dolphingstone site is included. See Figure 7.4. A list of the annotations for the drift and solid geology maps is included in Table 7.1.

7.2.2 Solid Geology

Information from geological maps studied by Donaldson Associated Ltd (2002) indicate that the solid geology is predominantly of the Limestone Coal Formation of Upper Carboniferous age. The strata involved are described as sandstones, siltstones, mudstones, coals and ironstone.

According to the site investigation report, the strata broadly dip to the North West, however there are no strike or dip markings on the geological map available, so this is impossible to verify. However the map does indicate the hinge of an anticline to the south east of the site which runs broadly normal to the indicated dip direction and so is broadly supportive of this interpretation. In the area of Dolphingstone the site investigation report indicates that the coal seam outcrops trend North East and these can be seen on the plot of solid geology included in Figure 7.5.

The Top Hosie Limestone outcrops to the southeast of the site (the thin, blue band to the south east of the Limestone Coal Formation in Figure 7.5); this limestone delineates the base of the Upper Carboniferous Limestone Coal formation and the top of the Lower Carboniferous Lower Limestone Formation. This latter formation is composed of sandstones, siltstones, mudstones, limestones and a small number of uneconomical coal seams.

Table 7.1: Description of geological map annotations.

Drift Geology		
Annotation	**Material**	**Age**
RMDF	Raised Marine Deposits	Flandrian (12,000 BC to present)
SABD	Shoreface and Beach Deposits	
RMDV	Raised Marine Deposits	Devensian
TILLD	Glacial Till	Devensian
Solid Geology		
Annotation	**Material**	**Period**
ULGS	Upper Limestone Formation	Carboniferous
CSTD	Tholeiitic Dyke	Carboniferous
ILS	Index Limestone	Carboniferous
LSC	Limestone Coal Formation	Carboniferous
TOHO	Top Hosie Limestone	Carboniferous
LLGS	Lower Limestone Formation	Carboniferous
SHLS	Second Hosie Limestone	Carboniferous

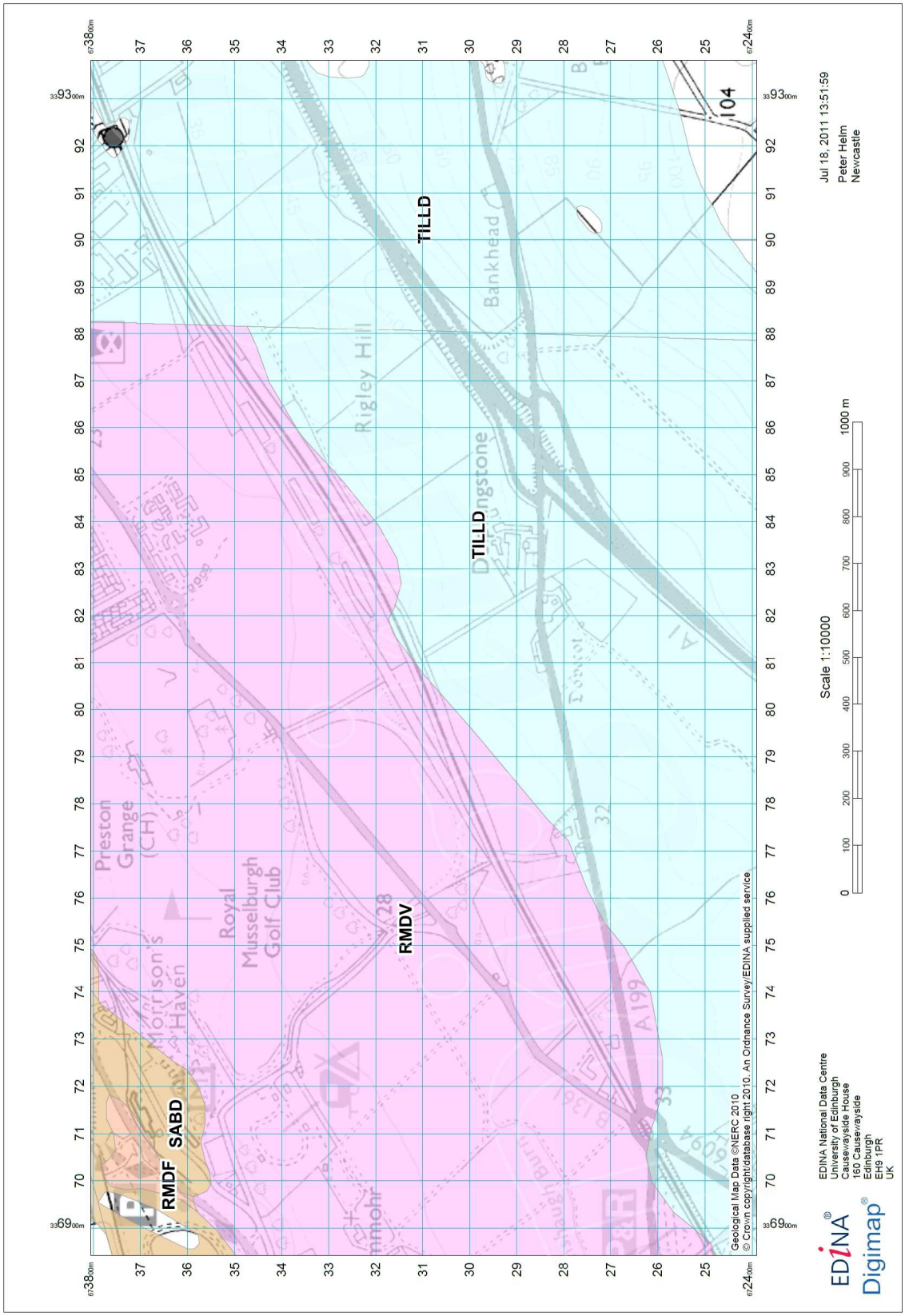

Figure 7.4: Drift geology of the Dolphingstone site. See table for a legend explaining the annotations (Helm, 2011b).

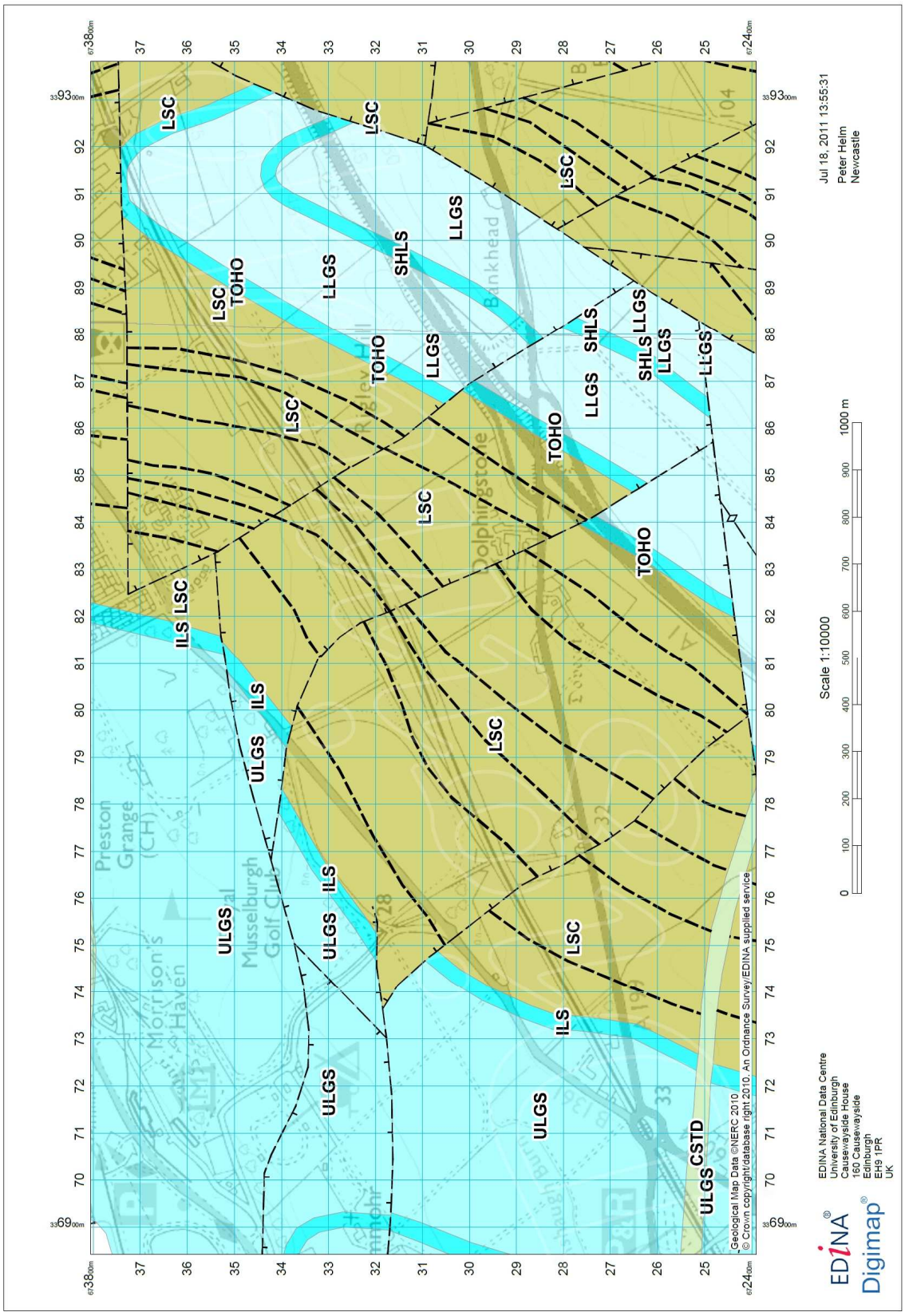

Figure 7.5: Solid geology and structure of the site. See table for a legend explaining the annotations (Helm, 2011c).

7.2.3 Mining History

During the desk study carried out by Donaldson Associates Ltd (2002), it was found that mining had taken place in the area from the early 18th century (and anecdotal evidence of mining dates as far back as the 13th century) through until the closure of the Prestongrange Colliery (see Figure 7.6 and Figure 7.8) during the 1960s. Two former collieries were also present on the site in the late 19th century one of which (Dolphingstone No. 2 colliery) was located directly adjacent to the railway line approximately 200 m east of Prestongrange crossing on the northern side of the ECML. This is visible in a historical Ordnance Survey map from the 1890s (see Figure 7.7) upon which can also be seen a number of old mine shafts and air shafts. The location of the now abandoned colliery is also plotted on the detailed site map (Figure 7.8) and Prestongrange crossing can be seen in the centre of Figure 7.3, trending SSE / NNW immediately north of the village of Dolphingstone. Further to this, crown holes associated with shallow workings had been recorded on mine plans dating from the early part of the 20th century. Mine abandonment plans also confirmed that mining had occurred within two coal seams in the area (the "Clay" and "Five Foot Coals" of Dolphingstone).

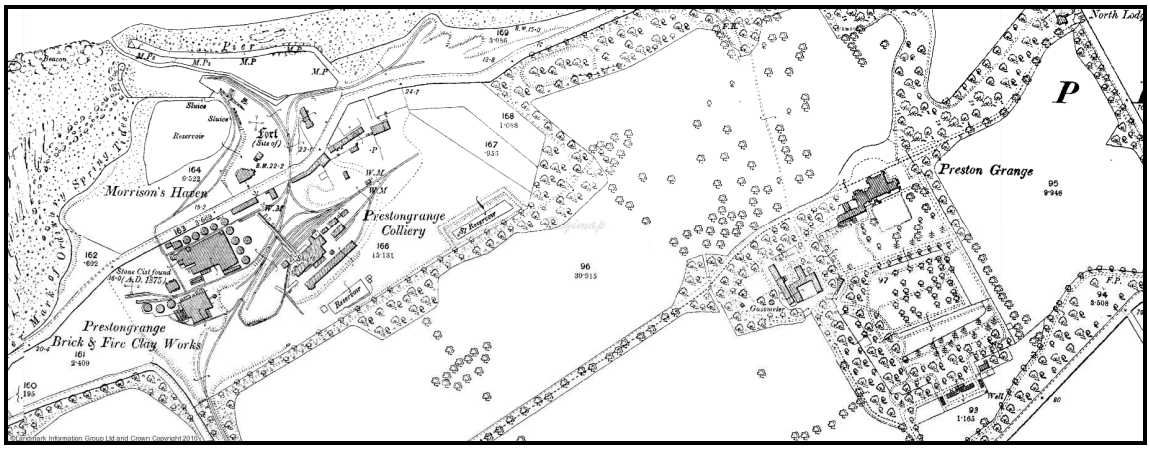

Figure 7.6: Historical (1890) Ordnance Survey map showing the location of Prestongrange Colliery. See Morrison's Haven on Figure 7.3 approximately 1.5 km north west of Dolphingstone for the present day location (Ordnance Survey County Series, 1894a).

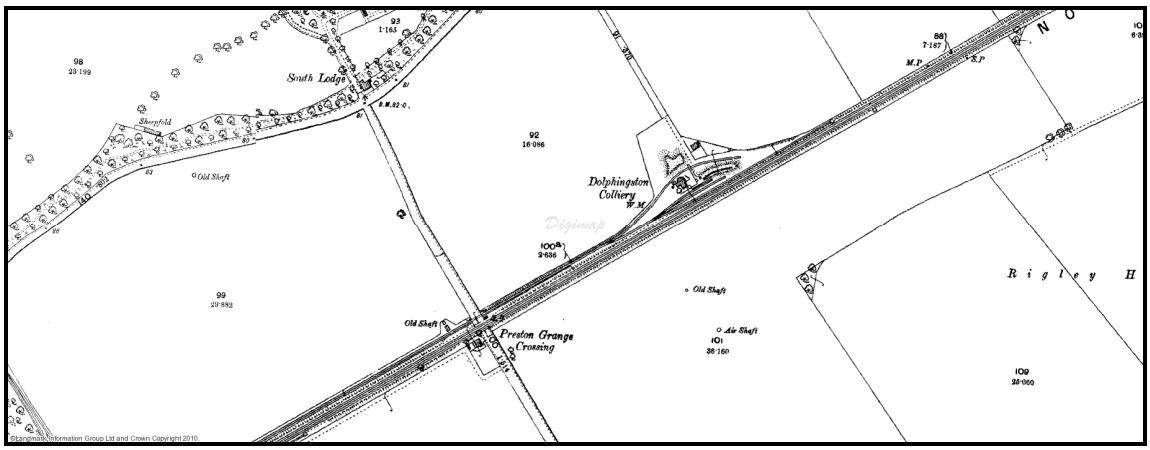

Figure 7.7: Historical (1890) Ordnance Survey map showing the location of Dolphingstone No. 2 colliery in relation to the railway line and Preston Grange crossing. Also note the presence of old mine shafts indicating mining predating the presence of this colliery (Ordnance Survey County Series, 1894b).

7.3 Site Investigation Findings

Trail pits and cable percussion holes were used to investigate the superficial deposits which in general comprise a topsoil layer of between 0.3 to 0.6 m thickness overlying fine to medium grained loose to moderately dense silty sands of approximately 1 to 2 m thickness in turn overlying a stiff to very stiff glacial till of 2 to 3 m thickness (Donaldson Associates Ltd, 2002).

The rotary coring revealed that the sub surface strata predominantly consisted of interbedded sandstones, siltstones and mudstones with frequent coal seams (Donaldson Associates Ltd, 2002). The coal seams ranged in thickness from 0.1 to 2 m and workings were found in the vast majority of coal seams. In all cases, the workings were filled with groundwater (Donaldson Associates Ltd, 2002).

Upon examination of the crown hole location plan and after comparison with the rotary borehole location plan (Donaldson Associates Ltd, 2002) it was noted that a number of crown holes (CrH03, CrH07 CrH10 and CrH12) had formed approximately 50 m to the west of Preston Grange crossing and were also located in close proximity to rotory borehole 1055-S, 1055/T1, 1080-S, 1105-S and 1130-S. A detail plot of Preston Grange crossing in relation to Dolphingstone is shown in Figure 7.8 and a detailed plot of the locations of the crown holes and borehole 1105-S can be seen on Figure 7.9. The full descriptions of the crown holes are outlined in the "Crown Hole Register" which was maintained by Donaldson Associates Ltd. and indicates that of the crown holes listed

above, crown hole CrH10 is especially significant. CrH10 is stated to be typical of the type found at the site and is described as having a surface diameter of 2 m and a depth of 0.3 m. It is stated that when it was located it was over grown with vegetation which is indicative of the fact that it developed before the site investigation was instigated. The site investigation report states that a number of the crown holes formed on site were thought to have collapsed due to the site investigation process and the occurrence dates and comments attached included on the crown hole register support this.

As log data was available for the bore holes described previously; a number of crown holes had developed in close proximity to these holes and as they appeared to capture the general geology and structure of the site (*i.e.* voids at shallow depth with limited rock cover) it was decided to use the sedimentary and soil logs from boreholes 1055/T1, 1055-S, 1080-S, 1105-S and 1130-S to give an overview of the variation in the sub surface in the area near Preston Grange crossing where the crown holes developed. The logs revealed that the depth to rock head was variable with superficial deposit thickness increasing across the site of interest from south west to north east with total thickness of the superficial deposits increasing from approximately 4.5 m in BH-1055/T1 increasing to 5 m in BH-1055-S. BH-1080-S located to the east of BH-1055-S shows a further increase in superficial deposit thickness of 5.5 m. This trend continues across the site whereby at BH-1105-S, the superficial deposits are 6 m thick. The next borehole records available (BH-1130-S and BH-1130-N both record 6 m of superficial deposits. As borehole BH-1105-S was located in very close proximity to the location of crown hole CrH10 (see Figure 7.9), it was decided that this would form the broad basis of the sub surface geology for the numerical modelling work. A sedimentary log derived from the borehole log for 1105-S and which is used to derive the stratigraphy for the numerical model is included in Figure 7.10.

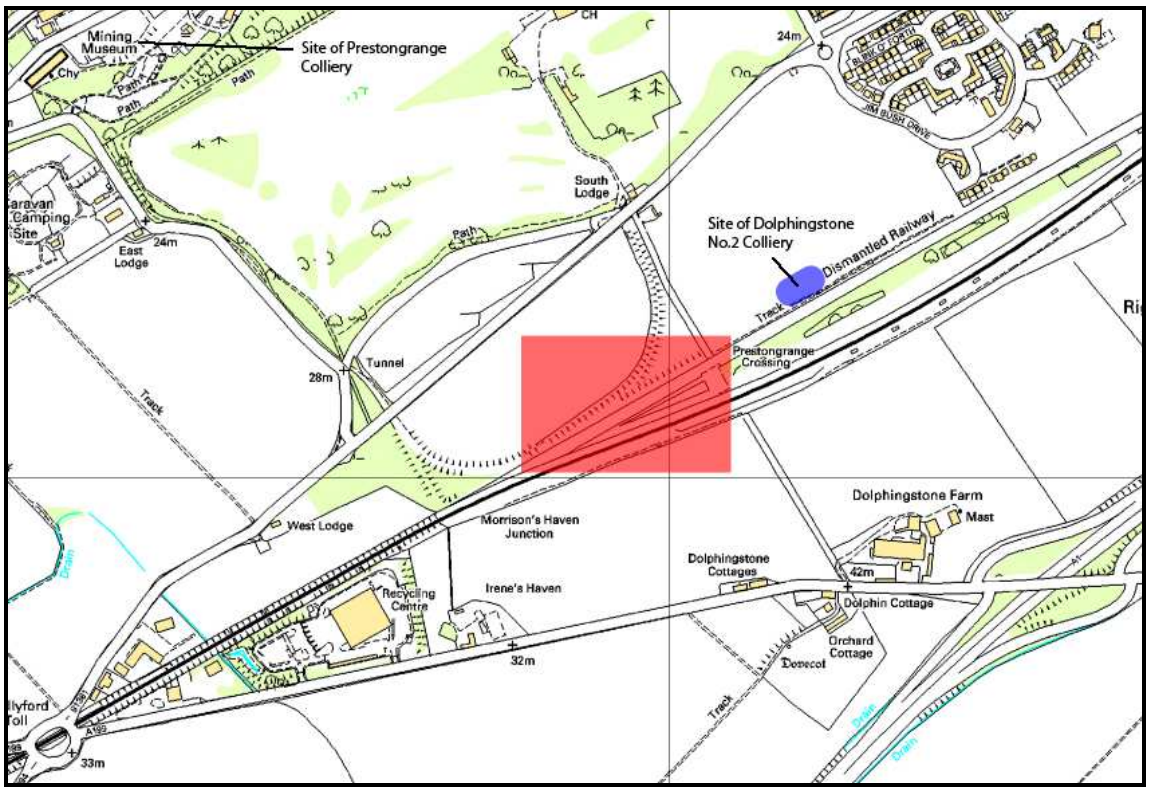

Figure 7.8: Plan showing location of the abandoned Dolphingstone No.2 and Prestongrange Collieries as well as the location of the detail plot of borehole and crown holes (Figure 7.9 - marked in red) relative to Dolphingstone, Prestongrange Crossing and the original and new route of the ECML.

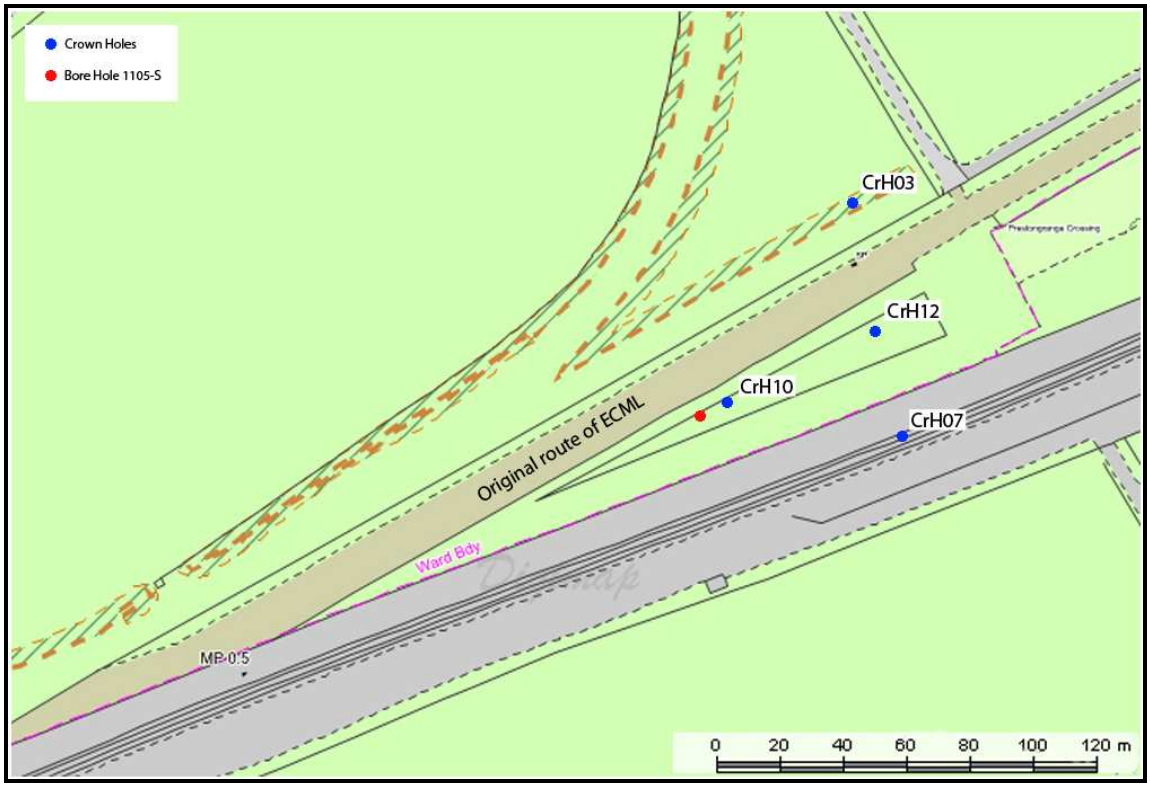

Figure 7.9: Plan showing approximate locations of crown holes and bore hole 1105-S relative to Preston Grange Crossing and the original ECML track.

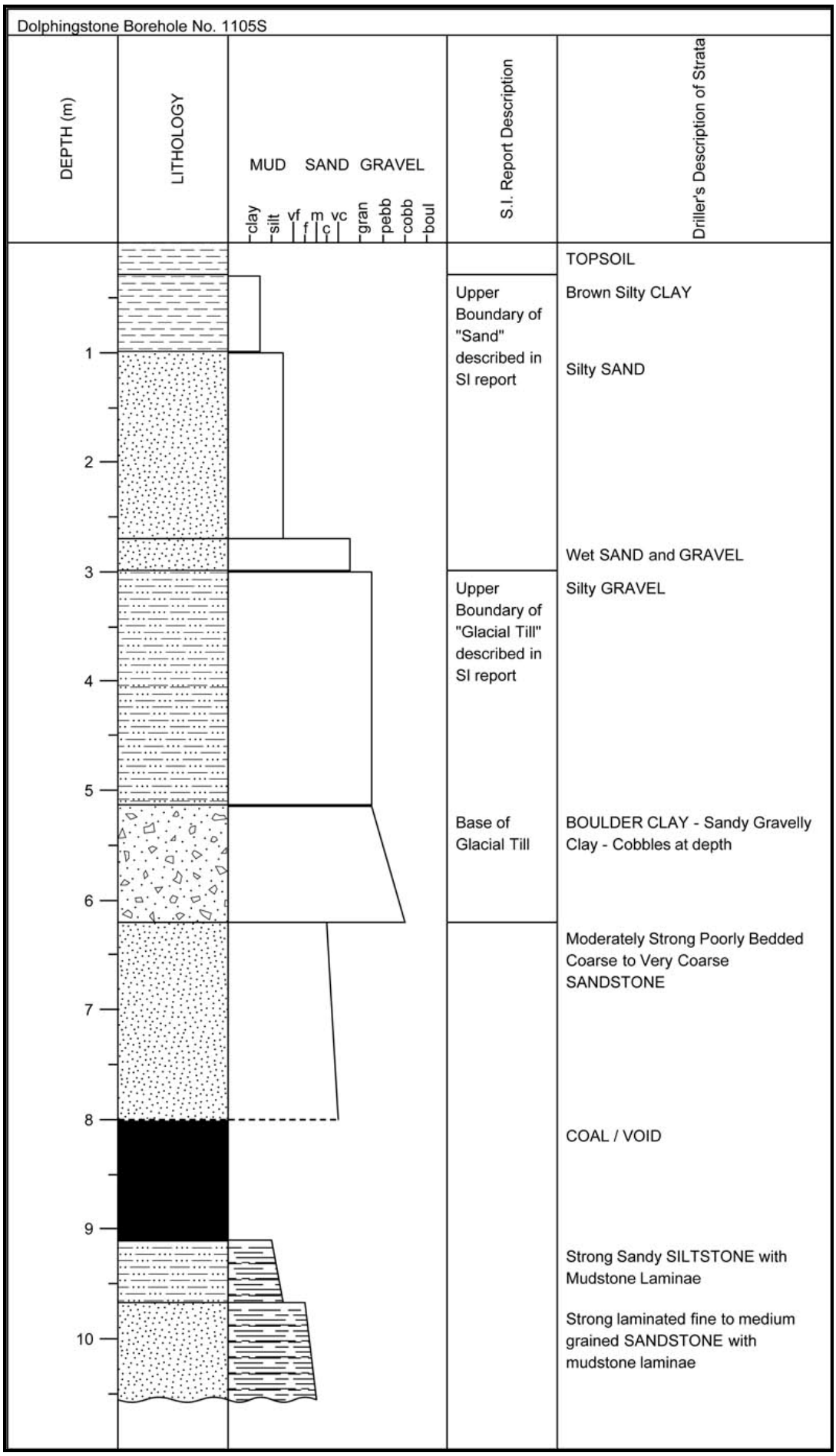

Figure 7.10: Sedimentary log of borehole 1105-S.

A number of features of note are immediately apparent on observation of Figure 7.10. First of which is the presence of a 1.2 m deep void at 8 m depth below surface. The second of which is that the overburden material above the void is predominantly composed of superficial deposits with only 1.8 m of what appears to be competent rock (in this case sandstone).

Unfortunately the driller's description of the sandstone's structure does not follow the British Standard (BS 5930:1999) and so it is unclear whether "poorly bedded" in this context means that there are no notable bedding surface (*i.e.* the bedding is thick or very thick) or whether "poor" may refer to the state of the bedding surfaces in the context of a rock mass description (*i.e.* those used to describe discontinuity alteration / weathering, persistence or orientation *etc*). Reference in the report is made to the presence of joint planes as sub horizontal.

The interpretive report describes that the water table is approximately 3 m below the surface in this area of the site which correlates with the presence of "wet sand and gravel" at approximately this depth.

7.4 *In-situ* and Laboratory Test Results on Soils

The results of *In-situ* and laboratory testing undertaken on the superficial deposits is summarised below and is taken from the site investigation report published by Donaldson Associates Ltd (2002).

7.4.1 Sands

Tests were undertaken on what are described as "Sand" in the site investigation report which according to the descriptions of depth correlates to the brown silty CLAY, silty SAND and wet SAND and GRAVEL on the core logs based on the driller's descriptions.

In-situ testing

Standard penetrations tests undertaken on the sand yielded "N" values from 2 to 16 from 0.5 to 1 m depth and "N" values from 4 to 23 at depths greater than 1m. Cone

penetration tests (CPTs) gave cone resistance values from 1 to 2 MPa from 0.5 to 1 m depth and values of 4 MPa and above, at depths of 1 m and above.

These test results are indicative of a loose to very loose sand below the topsoil down to approximately 1 m depth and then a medium dense to dense sand below 1 m.

Laboratory testing

Particle size analysis indicated that the sand was composed of varying proportions of silt, sand and gravel (from 0% to 13%, 70% to 90% and 1% to 16% respectively) with the silt content increasing with depth ultimately indicating a fine to medium grained sand with silt and gravel. This broadly correlates with the drillers description of the silty SAND and wet SAND and Gravel layers found within borehole 1105-S from 1 to 2 m depth.

Shear box testing undertaken on samples of the silty sand yielded cohesion values (c') from 2 – 11 kPa and friction angle (ϕ') values from 35.5° to 38.5°

7.4.2 Glacial Till

Further tests were undertaken on what is described as "Glacial Till" in the site investigation report which according to the descriptions of depth correlates to the silty GRAVEL and BOULDER CLAY on the core log based on the driller's descriptions.

***In-situ* testing**

Standard penetrations tests undertaken on the till yielded "N" values from 12 to 53 suggesting undrained shear strength from 454-150 kPa. Cone penetration tests (CPTs) gave cone resistance values from 3-10 MPa which indicate firm to very stiff clay.

Laboratory testing:

Direct shear testing of a sample of glacial till yielded a cohesion values (c') of 10 kPa and a friction angle (ϕ') of 29.5°.

7.5 Rock Description and *In-situ* and Laboratory Test Results

7.5.1 Moderately Strong Sandstone

The sandstone is described as slightly weathered containing sub-horizontal clay infilled joints. From the literature (Goodman, 1989; Brady and Brown, 1993 and Zhang, 2005) it is suggested that clay filling material in discontinuities can have friction angles varying from approximately 15° to 30° with residual friction angle values as low as 11°. The driller's description indicates that the sandstone is moderately strong which is assumed to correlate to the BS 5930:1999 description "medium strong" indicating a UCS in the range 25-50 MPa

Laboratory testing

Uniaxial compressive strength (UCS) testing undertaken on a sample of the sandstone from another borehole indicates a UCS value of 11.4 MPa for this material.

7.5.2 Interbedded Sandstones, Siltstones and Mudstones

Below the coal seam / mine void the rock mass is composed of interbedded sandstones siltstones and mudstones.

The sandstone is described in the driller's description as moderately strong to strong containing mudstone lamina. The strength description suggests a UCS value in the range 50 – 100 MPa (BS 5930:1999) however it is likely that the presence of the lamina may reduce this value. The siltstone is also described as strong which also suggests a UCS value in the range 50 – 100 MPa and again the presence of the mudstone lamina may act to reduce these values. The mudstone is described as moderately strong to moderately weak suggesting an unconfined compressive strength of between 5 – 50 MPa. Unfortunately no laboratory test data is reported for these rock types.

7.6 Groundwater Data for Dolphingstone

The Dolphingstone Hydrogeological report (Edmund Nuttall Ltd, 2002) contains data in the form of a graph of borehole water levels for Prestonpans. This data indicates the seasonal variation of the water table in this area (East of the site) is approximately 1.5m.

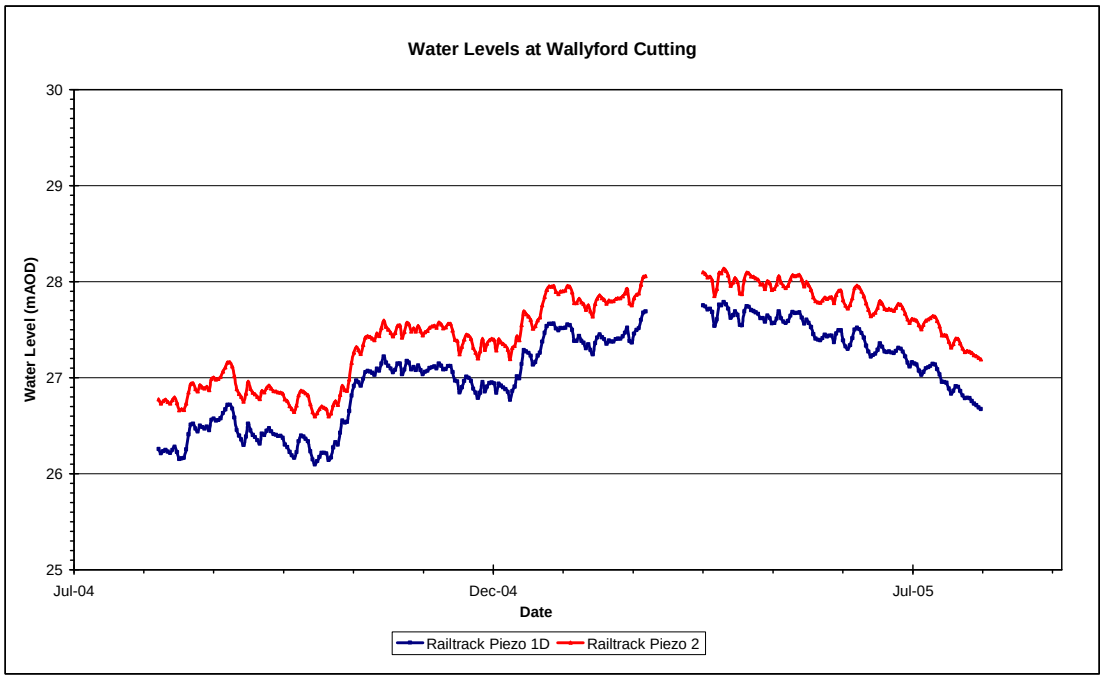

Figure 7.11: Variations in the groundwater table at Wallyford cutting at the west of the Dolphingstone site.

The available data for groundwater levels at the Wallyford site courtesy of K. Whitworth (personal communication, August 2007) is plotted in Figure 7.11 which shows a minimum water table during the summer (August 2004) of around 26 m (Railtrack Piezo 1), increasing through the Autumn and Winter to a maximum of around 27.8 m. This again shows a seasonal variation of a little over 1.8 m. It is possible that the water level increases beyond this value, however unfortunately there is missing data from the 08 March through to the 31 March 2005. It would seem based on the above (Figure 7.11) and the information from the Dolphingstone Hydrogeological report (Edmund Nuttall Ltd, 2002) that the groundwater across the site displays seasonal variations of approximately 1.5 – 1.8 m at a given location. Unfortunately the ordnance datum used to plot the ground water levels above does not match that used on bore hole 1105-S as the data is related to a differing project.

The mine workings at the site and in the surrounding area are all below the level of the groundwater table and are recorded as being flooded in both the site investigation (Donaldson Associates Ltd, 2002) and hydrogeological reports (Edmund Nuttall Ltd, 2002) and originally required drainage to maintain a water table below that of the base of the excavations. The site investigation report indicates that the working were originally drained by "soughs" or "day levels" which are sub-horizontal drainage adits which remove water from a worked seam by the action of gravity. The records studied indicate that these features are up to 250 years old and the present condition is unknown. What can be stated with a degree of certainty however is that the water table has risen to a significant degree since the abandonment of the mine workings.

7.7 Numerical Modelling of the Dolphingstone Collapse

In order to investigate the conditions that may have lead to the initiation of shallow mine subsidence at the Dolphingstone site it was decided to undertake a numerical modelling study.

Due to the large number of unknowns (for example the width of workings) and the potentially extremely variable nature of coal measures strata it was decided that this would be undertaken in the form of a parametric study.

Based on the modelling undertaken previously in chapter 5 it was decided to make use of interface elements to allow the model to behave in a discontinuous manner as this approach has been demonstrated to capture the behaviour seen during the collapse of layered strata such as those that compose coal measures rocks.

7.7.1 Model Geometry and Mesh Discretisation

These models all represent a void of varying height and width at 10 m below surface, with 10 m of underlying rock mass material and square numerical zones. The geometry parameters are outlined in Table 7.2

Table 7.2: Numerical model geometry parameters.

Parameter	Value
Excavation Width	1, 2 and 3 m
Excavation Height	1 m
Pillar Width	1, 2 and 3 m
Zone Size	0.1 m^2
Number of Discrete Strata within overburden rock mass	2, 4, 10, 20
Discontinuity Spacing	1.0, 0.5, 0.2 and 0.1 m

The discontinuity spacing values chosen above broadly correspond to the thin, medium and thick descriptors used in BS5930:1999 for the description of bedding plane thickness (while allowing for the constraints imposed by the discretisation of the model).

The model geometry with geologic profile and with the excavated mine void is illustrated in Figure 7.12. The mesh discretisation and interfaces representing bedding planes are illustrated in Figure 7.13.

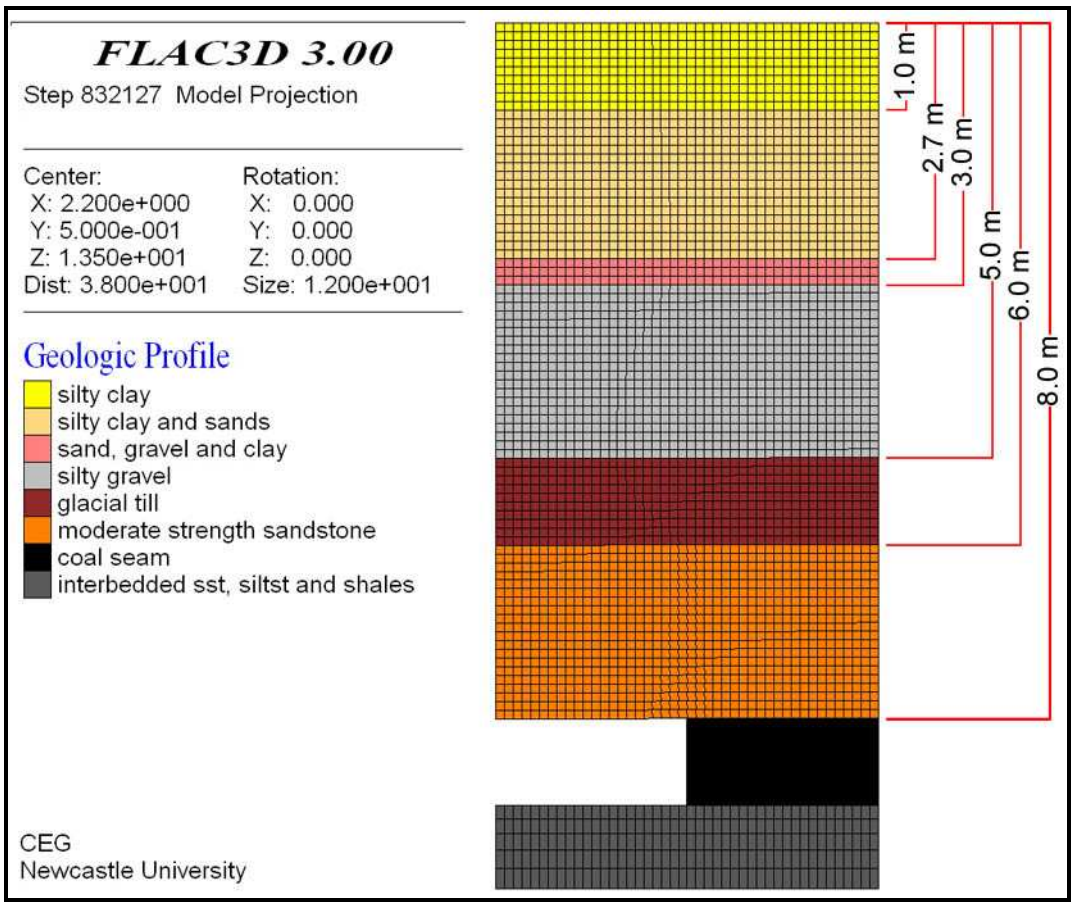

Figure 7.12: Geologic profile of the site of interest at Dolphingstone recreated in FLAC. Example shown is a 3 m wide 1 m high excavation.

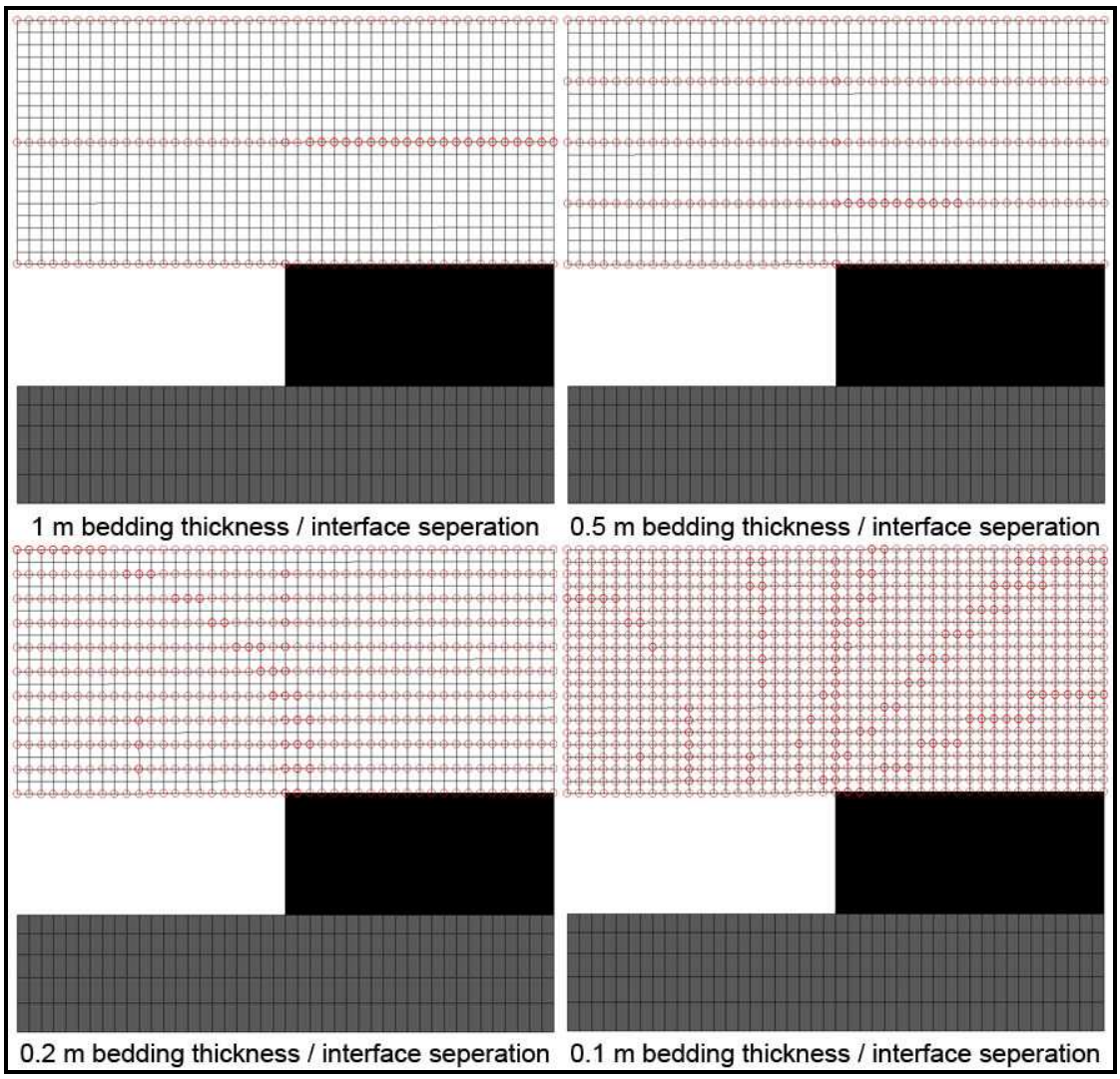

Figure 7.13: Plot showing the interface spacing at differing bedding thicknesses as used in the modelling work for Dolphingstone.

7.7.2 Rock Mass and Soil Properties

This section summarise the numerical model input parameters from site investigation, laboratory data and literature:

Soil Parameters

The soil parameters were derived from information in the site investigation report where possible. Where this was impossible, they are assumed from published literature (Thomlinson, 2001; Craig, 2004; Itasca, 2005).

Table 7.3: Soil Properties as used in the Dolphingstone numerical modelling work.

	Bulk Modulus	Shear Modulus	Cohesion	Friction Angle	Tensile Strength	Density
Silty Clay	3.33	2.0	0.011	38.5	0.0	1540.0
Silty Sand	33.3	20.0	0.002	30.5	0.0	1540.0
Sand, Gravel & Clay	33.3	20.0	0.003	35.5	0.0	1620.0
Silty Gravel	14.0	8.4	0.003	29.5	0.0	1620.0
Glacial Tilll	33.0	20.0	0.011	38.5	0.0	1620.0
	(MPa)	**(MPa)**	**(MPa)**	**(°)**	**(MPa)**	**(kgm^{-3})**

Rock Mass Strength, Stiffness and Density Parameters

The medium strength sandstone overlying the void / coal seam has a uniaxial compressive strength of 11.4 MPa. The drillers log notes that the Moderate Strength Sandstone is poorly bedded and as discussed earlier it is unclear whether this refers to bedding thickness or is a rock mass condition description. As this bed is immediately overlying a mine void and as the only layer of competent rock before the superficial deposits, it is likely to be the key factor in determining stability or otherwise of the excavation and whether void migration occurs. The site investigation report also states that the sandstone in this region of the site commonly contains sub-horizontal joints with clay infills which are likely to act to reduce the shear strength properties of the discontinuities present in the rock mass. Based on the above information a suite of rock mass strength and stiffness properties were created in ROCLAB (Rocscience, 2010) for a range of GSI values.

The confining stress dependent tunnel form of the Hoek-Brown criterion was used to derive the Mohr-Coulomb input parameters for the model due to the shallow depth of the workings involved. The intact uniaxial compressive strength of the sandstone layer as measured in the laboratory was also used as an input to the program. Finally an estimate of the intact elastic modulus of sandstone was used as an input parameter. This value was taken as 13 GPa (Zhang, 2005). The full range of Mohr-Coulomb rock mass strength and stiffness properties as derived by ROCLAB (Rocscience, 2010) and used in this modelling for the Moderate Strength Sandstone can be seen in Table 7.4. In previous work, a GSI of 70 was considered a suitable maximum value at which no significant deformation or failure within the model would occur, however the low uniaxial compressive strength recorded for the sandstone and the relatively low resultant tensile and shear strength parameters derived using the Hoek-Brown criterion suggest

that a rock mass with strength parameters scaled to GSI 70 may not be stable. As such in this work, the full range of GSI values from 10 to 100 are applied to scale the rock mass strength within the model.

7.7.3 Effect of Saturation on the Strength of Rock

In previous modelling undertaken, instability due to variations in the ground water table was related to the decreased effective stress caused by pore water pressures. It is recognised that this is a simplifying assumption that potentially underestimates the effect of water on the rock mass as the literature reports that both the uniaxial compressive strength and tensile strength of rock is affected when it is saturated with water. Zhang (2005) reports that the strength reduction can vary from as little as 3% to as much as a 50% reduction in strength. Vasarhelyi (2003) reports that the typical strength reduction that occurs in sandstones is around 25%. Li and Reddish (2004) report broadly similar results of a 26% reduction in uniaxial compressive stress between dry and saturated samples.

In order to improve the numerical modelling of the effects of changes in the groundwater table / increases in pore water pressure this saturated reduction in rock mass strength must be taken into account. As such in the modelling work undertaken here, both a dry and a saturated series of strength parameters are derived for a given rock mass. In this case it is assumed that the uniaxial compressive strength of the sandstone in the overburden material undergoes a 25% decrease as the water table rises through it. The dry uniaxial compressive strength of the sandstone was recorded as 11.4 MPa; as such the saturated uniaxial compressive strength is estimated from the above as approximately 8.6 MPa.

Table 7.4: Rock mass dry and saturated strength and stiffness parameters.

GSI	Bulk Modulus	Shear Modulus	Cohesion	Friction Angle	Tensile Strength
10	0.55	0.14	0.026	45.0	0.00076
10_{Sat}	0.55	0.14	0.023	73.0	0.000057
20	0.82	0.22	0.039	51.0	0.0016
20_{Sat}	0.82	0.22	0.036	49.0	0.001
30	1.47	0.38	0.054	55.0	0.0035
30_{Sat}	1.47	0.38	0.048	53.0	0.003
40	2.88	0.75	0.071	57.0	0.0073
40_{Sat}	2.88	0.75	0.062	56.0	0.006
50	5.55	1.45	0.098	60.0	0.016
50_{Sat}	5.55	1.45	0.083	58.0	0.012
60	9.39	2.45	0.15	61.0	0.033
60_{Sat}	9.39	2.45	0.12	60.0	0.025
70	13.23	3.45	0.25	62.0	0.07
70_{Sat}	13.23	3.45	0.19	61.0	0.05
80	15.90	4.15	0.45	62.0	0.15
80_{Sat}	15.90	4.15	0.34	61.0	0.11
90	17.31	4.52	0.84	61.0	0.32
90_{Sat}	17.31	4.52	0.64	60.0	0.24
100	17.95	4.68	1.60	60.0	0.68
100_{Sat}	17.95	4.68	1.21	59.0	0.51
	(GPa)	**(GPa)**	**(MPa)**	**(°)**	**(MPa)**

The bedding plane properties were derived using the same methodology as that outlined in section 3.1.5 for the normal and shear stiffness and 4.5.2 for the frictional properties. The full range of bedding plane interface element strength and stiffness parameters is summarised in

Table 7.6. The strain softening properties used in this analysis are summarised in Table 4.1. It should be noted that unlike joints in the Strain Softening Ubiquitous Joint Model as used in previous modelling, the interfaces that allow the mesh to behave in a discontinuous manner do not undergo strain softening behaviour.

Table 7.5: Strain softening parameters showing peak and residual strength values.

GSI	Cohesion	Friction Angle	Tensile Strength	Cohesion at 5% Strain	Friction Angle at 5% Strain	Tensile Strength at 1% Strain
10	0.026	45.0	0.00076	0.019	41.0	0.0
20	0.039	51.0	0.0016	0.019	41.0	0.0
30	0.054	55.0	0.0035	0.019	41.0	0.0
40	0.071	57.0	0.0073	0.019	41.0	0.0
50	0.098	60.0	0.016	0.019	41.0	0.0
60	0.15	61.0	0.033	0.019	41.0	0.0
70	0.25	62.0	0.07	0.019	41.0	0.0
80	0.45	62.0	0.15	0.019	41.0	0.0
90	0.84	61.0	0.32	0.019	41.0	0.0
100	1.60	60.0	0.68	0.019	41.0	0.0
	(MPa)	**(°)**	**(MPa)**	**(MPa)**	**(°)**	**(MPa)**

Table 7.6: Interface / bedding plane properties for 0.1 m and 0.2 m spacing.

Spacing	GSI	Intact Bulk Modulus	Intact Shear Modulus	Interface Normal Stiffness	Interface Shear Stiffness	Interface Cohesion	Interface Friction Angle
0.1 m	10	18.00	4.68	4.1	1.4	0.012	20.0
	20	18.00	4.68	6.2	2.2	0.012	26.0
	30	18.00	4.68	11.5	3.9	0.012	30.0
	40	18.00	4.68	24.7	7.8	0.012	33.0
	50	18.00	4.68	57.8	15.7	0.012	35.0
	60	18.00	4.68	141.8	28.4	0.012	37.0
	70	18.00	4.68	362.7	42.7	0.012	38.0
	80	18.00	4.68	1008.9	53.9	0.012	37.0
	90	18.00	4.68	3613.6	60.4	0.012	37.0
	100	18.00	4.68	64620.0	63.2	0.012	35.0
0.2 m	10	18.00	4.68	2.0	0.7	0.012	20.0
	20	18.00	4.68	3.1	1.1	0.012	26.0
	30	18.00	4.68	5.8	2.0	0.012	30.0
	40	18.00	4.68	12.4	3.9	0.012	33.0
	50	18.00	4.68	28.9	7.9	0.012	35.0
	60	18.00	4.68	70.9	14.2	0.012	37.0
	70	18.00	4.68	181.3	21.4	0.012	38.0
	80	18.00	4.68	504.5	27.0	0.012	37.0
	90	18.00	4.68	1806.8	30.2	0.012	37.0
	100	18.00	4.68	32310.0	31.6	0.012	35.0
		(GPa)	**(GPa)**	**($GPam^{-1}$)**	**($GPam^{-1}$)**	**(MPa)**	**(°)**

Table 7.7: Interface / bedding plane properties for 0.5 m and 1.0 m spacing.

Spacing	GSI	Intact Bulk Modulus	Intact Shear Modulus	Interface Normal Stiffness	Interface Shear Stiffness	Interface Cohesion	Interface Friction Angle
0.5 m	10	18.00	4.68	0.8	0.3	0.012	20.0
	20	18.00	4.68	1.2	0.4	0.012	26.0
	30	18.00	4.68	2.3	0.8	0.012	30.0
	40	18.00	4.68	4.9	1.6	0.012	33.0
	50	18.00	4.68	11.6	3.1	0.012	35.0
	60	18.00	4.68	28.4	5.7	0.012	37.0
	70	18.00	4.68	72.5	8.5	0.012	38.0
	80	18.00	4.68	201.8	10.8	0.012	37.0
	90	18.00	4.68	722.7	12.1	0.012	37.0
	100	18.00	4.68	12924.0	12.6	0.012	35.0
1.0 m	10	18.00	4.68	0.4	0.1	0.012	20.0
	20	18.00	4.68	0.6	0.2	0.012	26.0
	30	18.00	4.68	1.2	0.4	0.012	30.0
	40	18.00	4.68	2.5	0.8	0.012	33.0
	50	18.00	4.68	5.8	1.6	0.012	35.0
	60	18.00	4.68	14.2	2.8	0.012	37.0
	70	18.00	4.68	36.3	4.3	0.012	38.0
	80	18.00	4.68	100.9	5.4	0.012	37.0
	90	18.00	4.68	361.4	6.0	0.012	37.0
	100	18.00	4.68	6462.0	6.3	0.012	35.0
		(GPa)	**(GPa)**	**($GPam^{-1}$)**	**($GPam^{-1}$)**	**(MPa)**	**(°)**

As the initial modelling undertaken in section 3.4.7 indicated that the strength of the coal pillar and the rock mass underlying the excavation were not significant in the stability of the roof (rather they were important in the phenomena of pillar crushing leading to areal or sag subsidence or punching failure of the pillars into the softer underlying rock mass neither of which are thought to have contributed to the collapse at Dolphingstone), the strength of the coal and the underlying rock mass were scaled to an intermediate value whereby the coal was assumed to have a uniaxial compressive strength (UCS) of approximately 15 MPa (Bell, 1975) and the underlying rock UCS was assumed from the drillers descriptions whereby the sandstone is described as moderately strong (UCS of 50 MPa, BS5930:1999), the mudstone is described as moderately weak (UCS of 12.5 MPa, BS5930:1999) and the Siltstone as strong (UCS of 50 MPa, BS5930:1999). As such an average strength value was assumed of 37.5 MPa. The Mohr-Coulomb parameters were then estimated using the Hoek-Brown method as applied by ROCLAB (Rocscience, 2010). See Table 7.8.

Table 7.8: Strength and stiffness properties as used for the coal and underlying rock mass.

Rock Type	Bulk Modulus	Shear Modulus	Cohesion	Friction Angle	Tensile Strength
Coal	1.47	0.38	0.498	49	0.26
Underlying Rock Mass	9.39	2.45	1.21	51	0.651
	(GPa)	**(GPa)**	**(MPa)**	**(°)**	**(MPa)**

7.7.4 Groundwater Table

It should be noted that the water table at Dolphingstone was recorded at approximately 3 m below the surface in borehole 1105-S. The core log for borehole 1105-S indicates it was started and completed on 21 March 2002.

The plot of pore water pressures recorded in Figure 7.11 for Wallyford cutting, would suggest that this period represents the peak level of ground water, however this data was collected from August 2004 – August 2005 and as both the site investigation and hydrogeological reports (Donaldson Associates Ltd, 2002; Edmund Nuttall Ltd, 2002) state that the groundwater recharge at the site is thought to be predominantly reliant on precipitation, it is reasonable to assume that the pore water profile response with time may potentially have been different in the time period when the site investigation was undertaken and when the collapse that triggered the subsidence initially occurred and potentially during its progression; especially given the inherent variability in precipitation.

Therefore a range of pore water pressures will be modelled ranging from a level where the water table lies below the excavation (simulating the time when mine abandonment occurred) to the surface (which would simulate an extreme rise in the groundwater table of 3 m from that recorded in the borehole). These assumptions are considered acceptable in that they increase the potential for instability to occur within in a given model and as such are conservative and will also potentially aid in the understanding of the overall system behaviour.

7.7.5 Modelling Methodology

The parametric study to investigate the instability that occurred at Dolphingstone was run using an automated FISH routine which varied the geometry and strength of the model automatically while stepping to either static equilibrium (a stable solution without collapse) or to an unstable state where a prescribed level of plastic strain within the roof strata was used as a cut off to represent roof instability, in a virtually identical manner to that described in chapter 5. Only changes made to the modelling process are described in more detail below:

Iterations of the Parametric Study

The parametric study is undertaken using an automated model and parameter generation system coded by the user in FISH. This function controls the modelling run and iterates through a series of nested loop commands. The loop command uses an integer counter and the command takes the form: Variable (expression 1; expression 2) where variable is given the value of expression 1 initially, and is incremented by one at the end of each loop execution until it obtains the value of expression 2. In this parametric study the set of loops which control the model run are nested as shown below:

A. Bedding thickness (0.1, 0.2, 0.5, 1.0)

B. Excavation Width (1, 2, 3)

C. Excavation Height (1)

D. Rock mass strength (10, 20, 30, 40, 50, 60, 70, 80, 90, 100)

E. Rising water table (1 m increments)

F. Roof stability criteria

Ultimately this results in this case in 120 model runs (4 x 3 x 10).

Monitoring of the Model Run

A number of parameters are monitored during the model run. These include the vertical displacement in the centre line of the roof strata, the vertical strain of the strata in the roof centre line and the pore water pressure within the immediate roof of the excavation.

The vertical strain within the roof is actually more correctly the vertical axial strain of the zones forming the excavation roof centreline. It is calculated by measuring the

vertical displacement of the gridpoints at the base and the top of the first row of elements within the excavation roof centreline. The difference between these two values is the extension, which is then divided by the original pre-deformation element height. These monitored parameters are all recorded as history files of the specific parameter vs. model timestep.

Strain Measurement and Yield Criteria

The yield criteria used in this modelling are the same as that described previously but with the additional feature of a displacement cut off, whereby the vertical displacement of the roof centreline is monitored and if this value exceeds a prescribed value (0.5 m) the roof is assumed to have failed. This criterion was added as it was found that strata separated by interface elements which failed, would undergo delamination and sag into the void without undergoing significant tensile axial strain and as such the tensile yield criterion was not capturing failure leading to models running for much greater periods than required to investigate roof collapse / collapse initiation.

Saturated Sandstone Rock Mass Strength

To account for the reduction in strength of the rock mass below the water table, the saturated rock mass strength properties are applied to the lower and upper 1 m of the sandstone layer as the pore water pressures reaches said layer.

7.7.6 Results of the Parametric Study on the Stability of the Site of Interest at Dolphingstone

In this section the results of the parametric study into the stability of the site of interest at Dolphingstone are summarised. This summary takes the form of a table in which the conditions leading to failure or resulting in a stable roof for a given working geometry are reported. Significant results or those of further interest are reported in more detail.

Based on experience of the modelling of excavation instability undertaken in the previous chapter and the relatively wide variation in the degree and type of failure that can occur within a numerical representation of a rock mass with variable interface spacing, in order to improve the clarity of the tables, 8 descriptive terms are used to describe the degree of yielding within the rock mass. These terms and their explanations are summarised below:

- Stable – No significant deformations or plastic yielding of the rock mass
- Stable (marginal) – Somewhat subjective – requires a degree of engineering judgement. The block state plot indicates that significant portions of the rock mass have exceeded the constitutive model yield criteria, however the user specified axial strain and or displacement yield criteria have not been reached, However other indicators of instability are visible (*i.e.* increasing magnitudes of deformation for increasing water table levels, increasingly large vertical displacements in the roof centre line on the 10s of mm scale) suggest that the factor of safety of the roof of the excavation is approaching 1.
- Yielding – The model has exceeded the user defined yield criterion for axial strain in the roof centre line. However this does not involve significant deformations of the whole rock mass
- Significant Yielding – As per description for yielding, however the roof strata have also undergone significant deformations (0.2-0.5 m)
- Yielding with Tensile Delamination – As per the description of significant yielding with the addition of visible bed separation that extends < 0.5 m into rock mass
- Significant Strata Delamination – As per the description of yielding with tensile delamination, however the visible bed separation extends > 0.5 m into rock mass
- Very Significant Yielding – As per description for significant yielding, however the region of yielding and deformation extends > 1 m into the rock mass (broadly comparable to the descriptor for Very Significant strata delamination however no visible bedding separation occurs)
- Very Significant Strata Delamination – As per the description of yielding with tensile delamination, however the visible bed separation extends > 1 m into rock mass
- Collapse – Yielding and visible delamination of the whole of the over lying rock mass with significant displacements. May also be significant deformations at surface

To demonstrate the effect of varying rock mass strength on failure and to illustrate the differing descriptors above, a series of failure plots are presented for varying rock mass strengths from GSI 10 to 100 with uniform excavation widths (3 m) and bedding plane separation (0.1 m) with water tables at the level which caused failure to exceed the prescribed yield conditions (if applicable). These can be seen for GSI values of 10 – 40 in Figure 7.14, GSI 50 – 80 in Figure 7.15, and GSI 90 – 100 in Figure 7.16.

The models with rock mass strength for GSI 10 through to 30 are described as being collapsed in Table 7.9. It can be seen that visible deformation has occurred at the surface in the models with GSI values from 10 to 30 and that in all cases, significant levels of shear yielding have occurred across the full height of the rock mass overlying the excavation. The model with a GSI of 40 has been classed as "Very Significant strata delamination" as the bedding panes within the rock strata have undergone visible delamination through a significant thickness of the sand stone bed, however it has not spanned the full thickness and some support is still being provided to the overlying soil mass by the sand stone. However this appears to be a very marginally stable state and even a small change in the groundwater level would most likely trigger collapse.

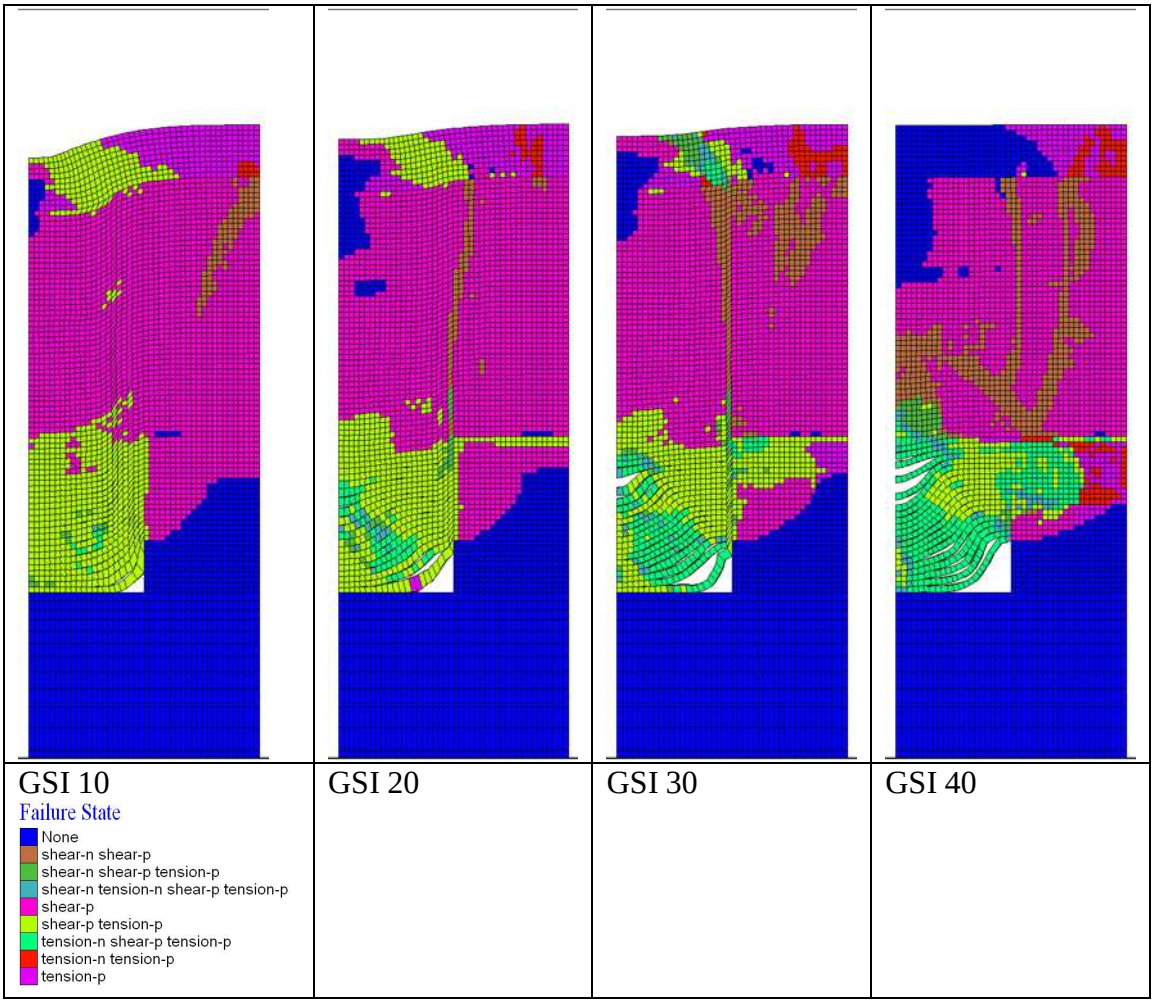

Figure 7.14: Constitutive model yield state plots for a range of models with GSI from 10-40. Excavation width 3 m, interface / bedding plane separation 0.1 m.

The plot of GSI 50 seen in Figure 7.15 is also described as "Very Significant Strata Delamination" as there are displacements greater than 0.5 m and the visible delamination extends more than 1 m into the rock mass over the excavation. From these plots it can be seen that the height of delamination in the rock mass and the level of

vertical deformation / displacement is decreasing as the rock mass strength is increasing. In the plots of rock mass with GSI 60 and 70 it can be seen that although delamination has occurred it has extended into the overlying rock mass by a value between 0.5 and 1 m and therefore is described as “Significant Strata Delamination”. The rock mass with GSI equal to 80 has undergone plastic yielding of the bedding plane in the immediate roof. There is also a small degree of tensile delamination and so is described as “Yielding with Tensile Delamination”. This example can also be used to illustrate “Significant Yielding”, as this descriptor would fit this plot if the tensile delamination of the single bedding plane had not occurred. Finally as the rock mass strength increases further, the deformation / displacements decrease to low values (mm scale) and visible delamination no longer occurs at any level of ground water table. These scenarios are described as stable. These descriptors are used in a series of tables which summarise the results of the modelling undertaken to assess the initial stability of the excavations at Dolphingstone.

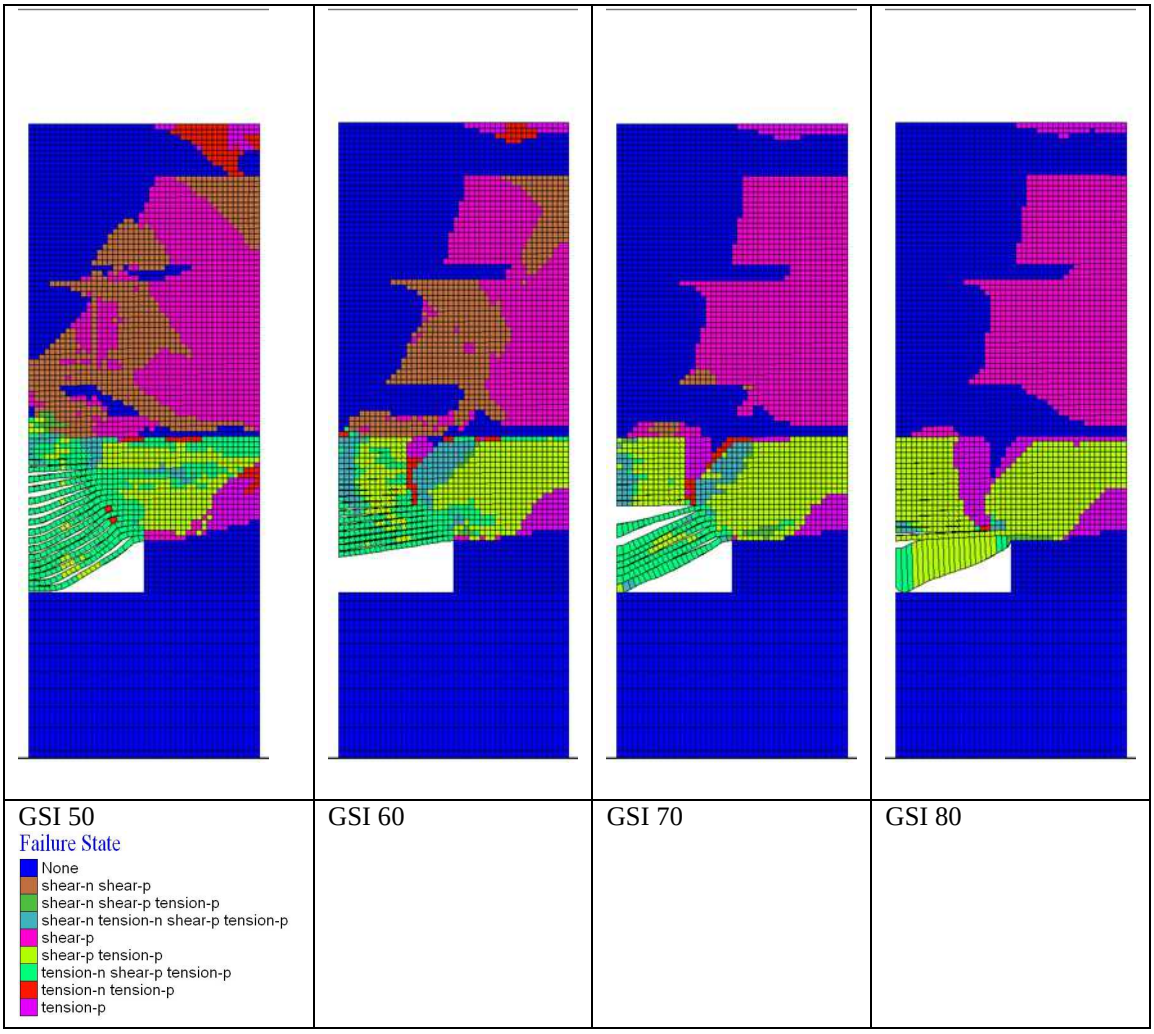

Figure 7.15: Constitutive model yield state plots for a range of models with GSI from 50-80. Excavation width 3 m, interface / bedding plane separation 0.1 m.

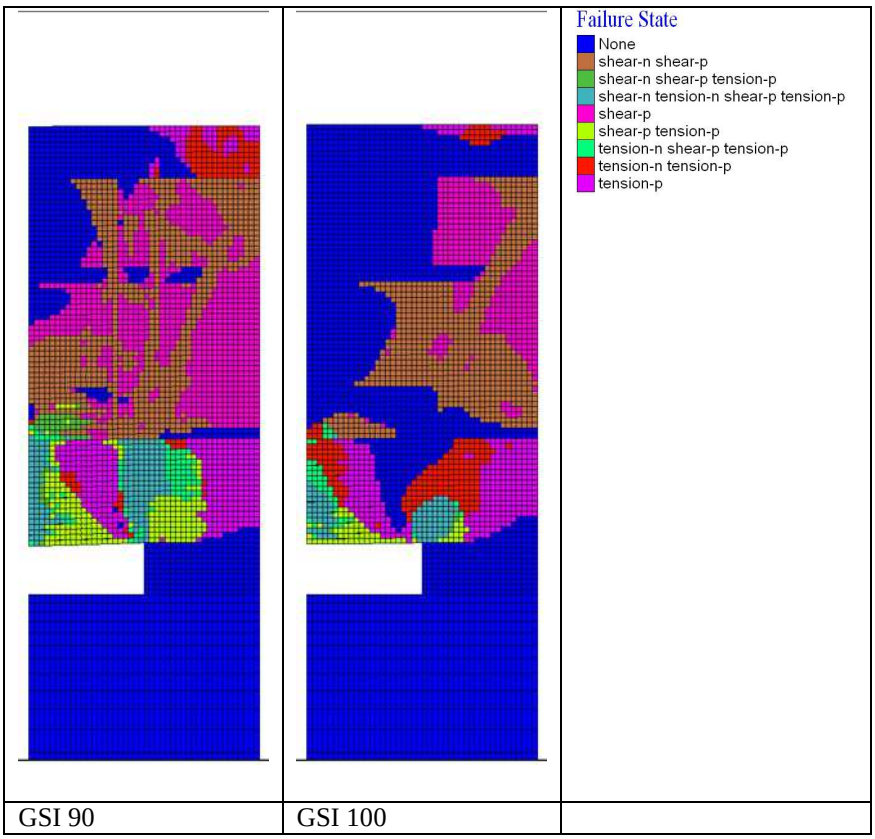

Figure 7.16: Constitutive model yield state plots for a range of models with GSI from 90-100. Excavation width 3 m, interface / bedding plane separation 0.1 m.

A series of tables showing the bedding plane spacing, excavation geometry and height of the ground water table relative to datum (the excavation roof) that causes the modelling to be halted due to the roof deformation exceeding the yield criteria is shown for the full range of results. See Table 7.9 to Table 7.12.

Table 7.9: Summary of stability results for models with 0.1 m bedding plane separation.

Bedding Plane Separation (m)	GSI	Excavation Width (m)	Excavation Height (m)	Hydraulic Head Above Excavation Roof at Instability (m)
0.1	10	1.0	1.0	-1 m - Yielding with Tensile Delamination
0.1	20	1.0	1.0	-1 m - Yielding with Tensile Delamination
0.1	30	1.0	1.0	-1 m - Significant yielding
0.1	40	1.0	1.0	-1 m - Yielding with Tensile Delamination
0.1	50	1.0	1.0	-1 m - Yielding with Tensile Delamination
0.1	60	1.0	1.0	-1 m - Yielding
0.1	70	1.0	1.0	+7m - Yielding
0.1	80	1.0	1.0	Stable
0.1	90	1.0	1.0	Stable
0.1	100	1.0	1.0	Stable
0.1	10	2.0	1.0	-1 m - Collapse
0.1	20	2.0	1.0	-1 m - Collapse
0.1	30	2.0	1.0	-1 m - Significant Strata Delamination
0.1	40	2.0	1.0	-1 m - Significant Strata Delamination
0.1	50	2.0	1.0	-1 m - Yielding with Tensile Delamination
0.1	60	2.0	1.0	+1 m - Yielding
0.1	70	2.0	1.0	+6m - Yielding
0.1	80	2.0	1.0	Stable
0.1	90	2.0	1.0	Stable
0.1	100	2.0	1.0	Stable
0.1	10	3.0	1.0	-1 m - Collapse
0.1	20	3.0	1.0	-1 m - Collapse
0.1	30	3.0	1.0	-1 m - Collapse
0.1	40	3.0	1.0	-1 m - Very Significant Strata Delamination
0.1	50	3.0	1.0	-1 m - Very Significant Strata Delamination
0.1	60	3.0	1.0	-1 m - Significant Strata Delamination
0.1	70	3.0	1.0	+1 m - Significant Strata Delamination
0.1	80	3.0	1.0	+2 m - Yielding with Tensile Delamination
0.1	90	3.0	1.0	Stable (marginal)
0.1	100	3.0	1.0	Stable

Table 7.10: Summary of stability results for models with 0.2 m bedding plane separation.

Bedding Plane Separation (m)	GSI	Excavation Width (m)	Excavation Height (m)	Hydraulic Head Above Excavation Roof at Instability (m)
0.2	10	1.0	1.0	-1 m - Yielding
0.2	20	1.0	1.0	+1 m - Yielding
0.2	30	1.0	1.0	+1 m - Yielding
0.2	40	1.0	1.0	+1 m - Yielding
0.2	50	1.0	1.0	+2 m - Yielding
0.2	60	1.0	1.0	+4m - Yielding
0.2	70	1.0	1.0	+7m - Yielding
0.2	80	1.0	1.0	Stable
0.2	90	1.0	1.0	Stable
0.2	100	1.0	1.0	Stable
0.2	10	2.0	1.0	-1 m - Very Significant Yielding
0.2	20	2.0	1.0	-1 m - Significant Yielding
0.2	30	2.0	1.0	-1 m - Yielding with Tensile Delamination
0.2	40	2.0	1.0	+1 m - Yielding
0.2	50	2.0	1.0	+2 m - Yielding
0.2	60	2.0	1.0	+3 m - Yielding
0.2	70	2.0	1.0	+7m - Yielding
0.2	80	2.0	1.0	Stable
0.2	90	2.0	1.0	Stable
0.2	100	2.0	1.0	Stable
0.2	10	3.0	1.0	-1 m - Collapse - Visible deformation at surface
0.2	20	3.0	1.0	-1 m - Collapse - Visible deformation at surface
0.2	30	3.0	1.0	-1 m - Very Significant Strata Delamination
0.2	40	3.0	1.0	-1 m - Very Significant Strata Delamination
0.2	50	3.0	1.0	-1 m - Yielding with Tensile Delamination
0.2	60	3.0	1.0	2 m - Yielding
0.2	70	3.0	1.0	5 m - Yielding
0.2	80	3.0	1.0	Stable
0.2	90	3.0	1.0	Stable
0.2	100	3.0	1.0	Stable

Table 7.11: Summary of stability results for models with 0.5 m bedding plane separation.

Bedding Plane Separation (m)	GSI	Excavation Width (m)	Excavation Height (m)	Hydraulic Head Above Excavation Roof at Instability (m)
0.5	10	1.0	1.0	-1 m - Yielding
0.5	20	1.0	1.0	+1 m - Yielding
0.5	30	1.0	1.0	+1 m - Yielding
0.5	40	1.0	1.0	+1 m - Yielding
0.5	50	1.0	1.0	+2 m - Yielding
0.5	60	1.0	1.0	+4m - Yielding
0.5	70	1.0	1.0	+7m - Yielding
0.5	80	1.0	1.0	Stable
0.5	90	1.0	1.0	Stable
0.5	100	1.0	1.0	Stable
0.5	10	2.0	1.0	-1 m - Significant Yielding
0.5	20	2.0	1.0	-1 m - Significant Yielding
0.5	30	2.0	1.0	+1 m - Yielding
0.5	40	2.0	1.0	+1 m - Yielding
0.5	50	2.0	1.0	+2 m - Yielding
0.5	60	2.0	1.0	+3 m - Yielding
0.5	70	2.0	1.0	+7m - Yielding
0.5	80	2.0	1.0	Stable
0.5	90	2.0	1.0	Stable
0.5	100	2.0	1.0	Stable
0.5	10	3.0	1.0	-1 m - Collapse - Visible deformation at surface
0.5	20	3.0	1.0	-1 m - Very Significant Yielding
0.5	30	3.0	1.0	-1 m - Significant Yielding
0.5	40	3.0	1.0	+1 m - Yielding
0.5	50	3.0	1.0	+2 m - Yielding
0.5	60	3.0	1.0	+3 m - Yielding
0.5	70	3.0	1.0	+7m - Yielding
0.5	80	3.0	1.0	Stable
0.5	90	3.0	1.0	Stable
0.5	100	3.0	1.0	Stable

Table 7.12: Summary of stability results for models with 1.0 m bedding plane separation.

Bedding Plane Separation (m)	GSI	Excavation Width (m)	Excavation Height (m)	Hydraulic Head Above Excavation Roof at Instability (m)
1.0	10	1.0	1.0	-1 m - Yielding
1.0	20	1.0	1.0	+1 m - Yielding
1.0	30	1.0	1.0	+1 m - Yielding
1.0	40	1.0	1.0	+1 m - Yielding
1.0	50	1.0	1.0	+2 m - Yielding
1.0	60	1.0	1.0	+4m - Yielding
1.0	70	1.0	1.0	+7m - Yielding
1.0	80	1.0	1.0	Stable
1.0	90	1.0	1.0	Stable
1.0	100	1.0	1.0	Stable
1.0	10	2.0	1.0	-1 m - Significant Yielding
1.0	20	2.0	1.0	-1 m - Significant Yielding
1.0	30	2.0	1.0	+1 m - Yielding
1.0	40	2.0	1.0	+1 m - Yielding
1.0	50	2.0	1.0	+2 m - Yielding
1.0	60	2.0	1.0	+4m - Yielding
1.0	70	2.0	1.0	+7m - Yielding
1.0	80	2.0	1.0	Stable
1.0	90	2.0	1.0	Stable
1.0	100	2.0	1.0	Stable
1.0	10	3.0	1.0	-1 m - Collapse - Visible deformation at surface
1.0	20	3.0	1.0	-1 m - Very significant Yielding
1.0	30	3.0	1.0	-1 m - Significant Yielding
1.0	40	3.0	1.0	+1 m - Yielding
1.0	50	3.0	1.0	+2 m - Yielding
1.0	60	3.0	1.0	+3 m - Yielding
1.0	70	3.0	1.0	+7m - Yielding
1.0	80	3.0	1.0	Stable
1.0	90	3.0	1.0	Stable
1.0	100	3.0	1.0	Stable

From observation of the tables, some initial broad trends can be identified:

- Stability increases with increasing rock mass strength and stiffness properties
- Stability decreases with increasing excavation width
- Stability decreases with increasing height of the ground water table above the excavation roof
- Stability decreases with decreased bedding surface separation

This matches the broad conclusions derived from the modelling described in the previous chapter related to the effects of using interface elements to model discontinuous behaviour in the model.

Another factor of note is that a number of the excavations at lower rock mass strengths, lower values of interface separation and with increased excavation widths underwent significant roof failure (*e.g.* collapse or very significant strata delamination) when the water table was below the base of the excavation upon initial excavation. Hence, the excavation had a factor of safety of less than 1 and as such would have required significant support to be in use as a working mine. It is assumed therefore that these scenarios are not a realistic representation of the collapse that occurred at Dolphingstone.

By way of example some sample plots of these types of failure are included below. They also act to further illustrate the descriptions for “collapse” and “very significant strata delamination” as used in Table 7.9 to Table 7.12.

The following is a block state / yield state plot from the 1.0 m interface spacing models with a rock mass GSI of 10 and an excavation width of 3 m which in the table is marked as undergoing collapse with visible deformation at the surface.

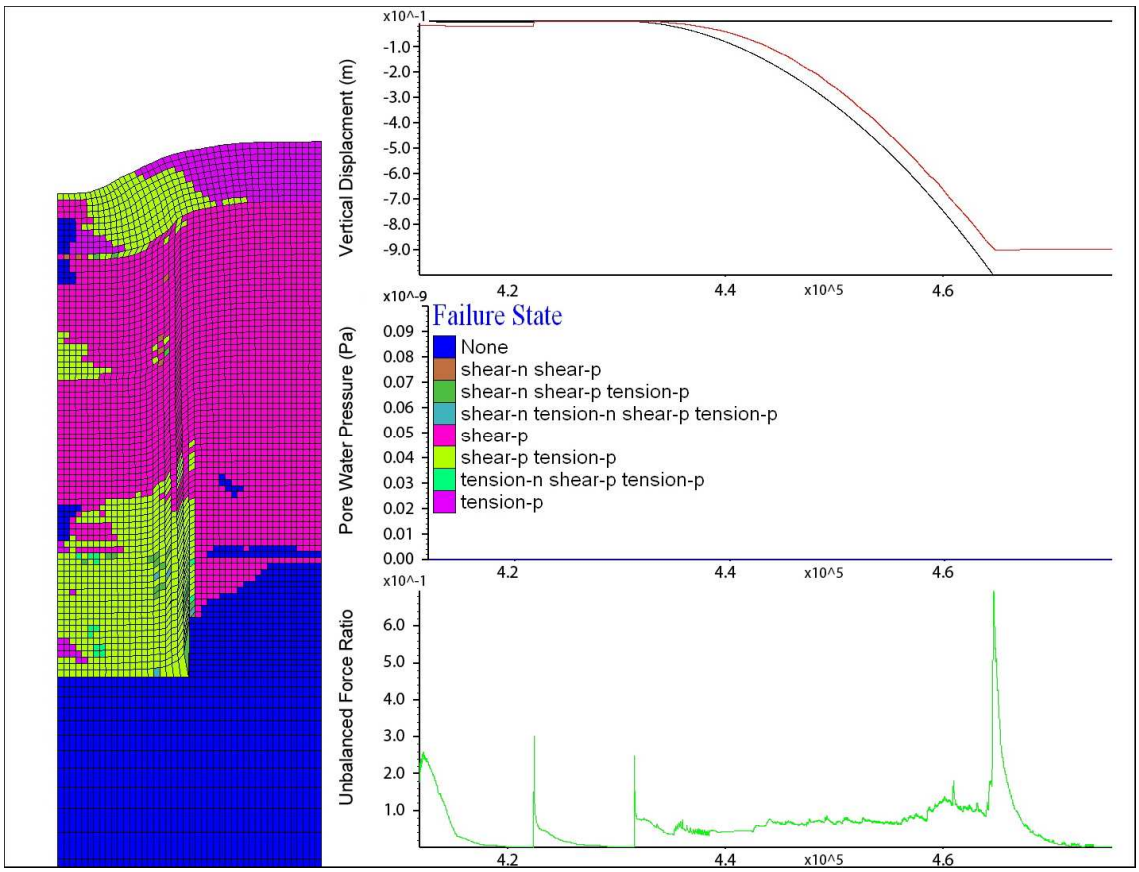

Figure 7.17: Yield sate plot of the over burden for an interface spacing of 1m, rock mass GSI 10 and excavation width, 3m.

In can be seen in Figure 7.17 that the modelled strata over the excavation have undergone significant plastic yielding. This failure and the resultant significant deformations have occurred across the full width of the excavation roof and caused significant visible subsidence of the overburden at the upper boundary of the model. The vertical displacement at the roof centre line is equal to 1 m and the vertical displacement at the surface directly above the roof centreline is equal to approximately 0.9 m. This can be seen on the history plots of vertical displacement in Figure 7.17 whereby the black history line represents displacement of the immediate roof and the red line, displacement at the surface.

An example of what is described as “very significant strata delamination” can be observed in Figure 7.18 below which represents a 3 m wide excavation in a rock mass with GSI 60 and interfaces of 0.1 m separation, where it can be seen the bedding planes have visibly separated to a height of over 1 m in the rock mass over the excavation and the vertical displacement of the roof centre line is equal to 0.3 m.

This is confirmed when the plot of interface normal failure is observed (See Figure 7.19). Whereby it can be seen that interface delamination has occurred for all interfaces in the sand stone bed.

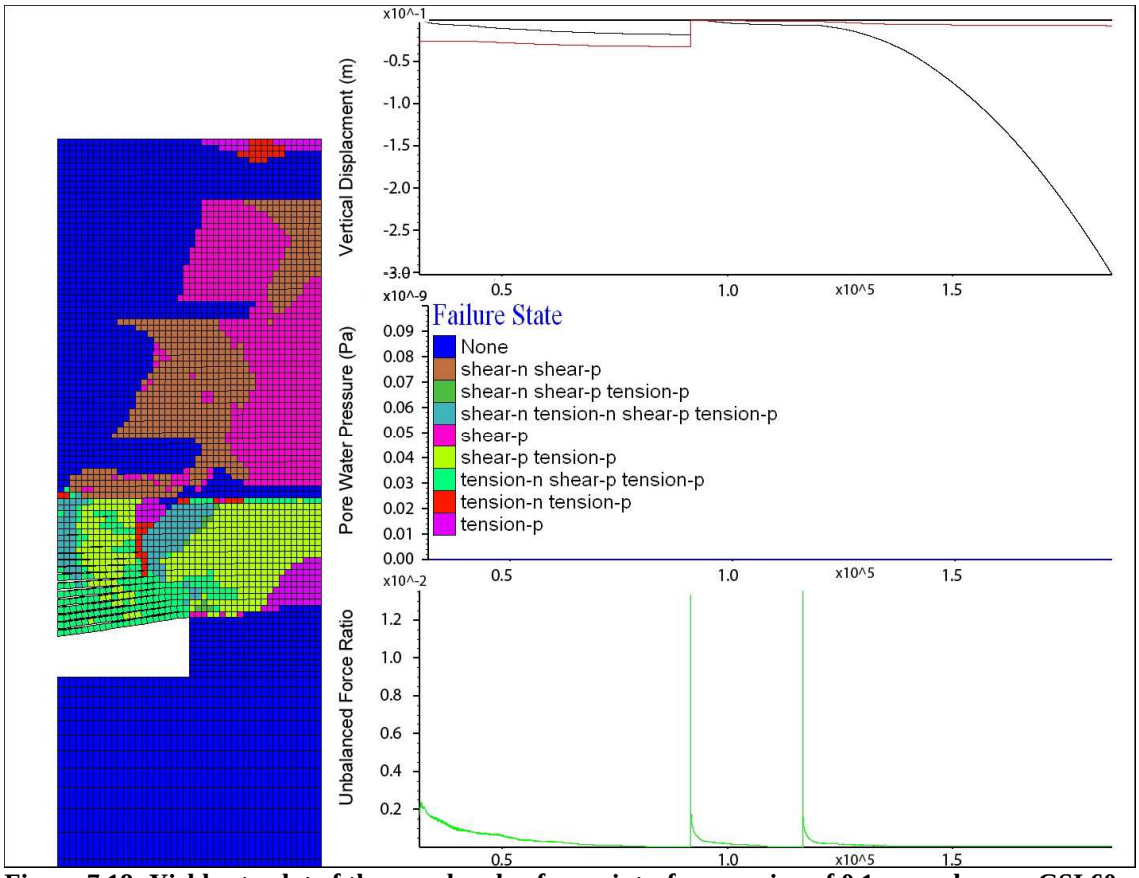

Figure 7.18: Yield sate plot of the over burden for an interface spacing of 0.1 m, rock mass GSI 60 and excavation width, 3m.

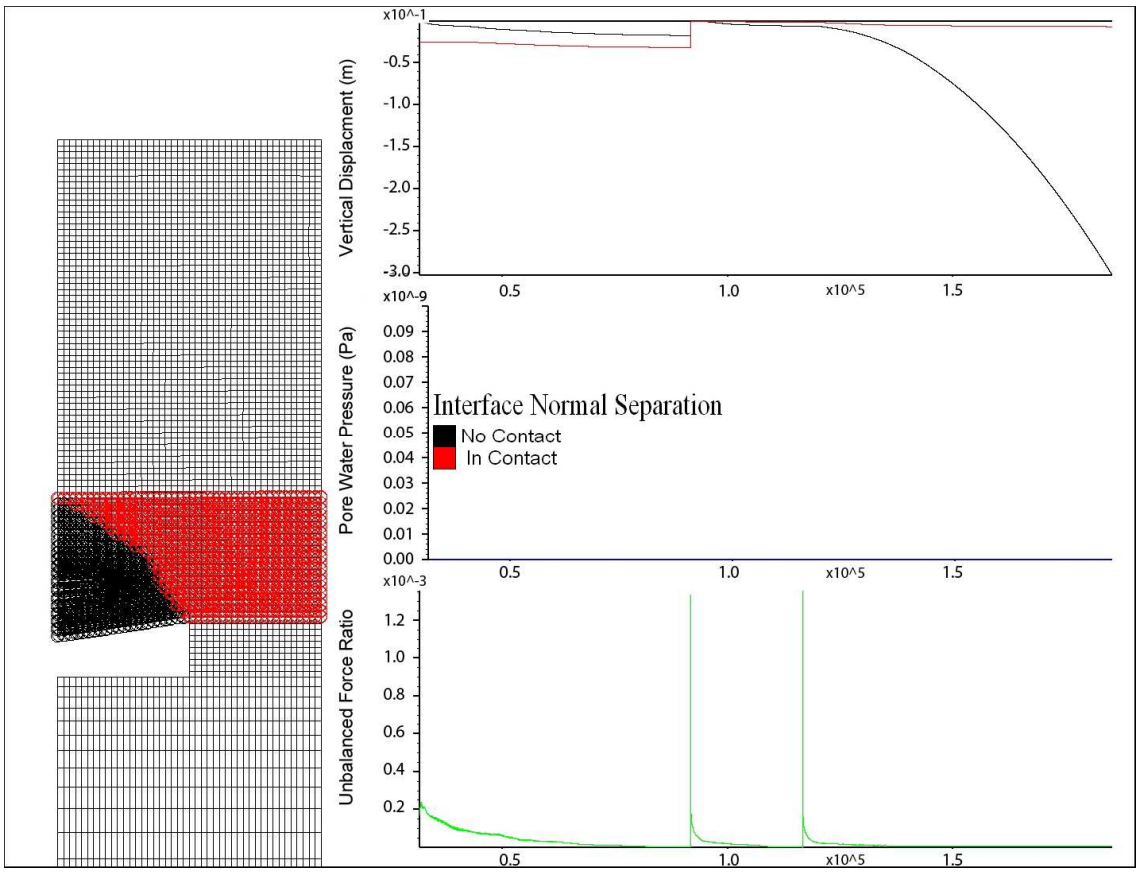

Figure 7.19: Interface normal failure plot for an interface spacing of 0.1 m, rock mass GSI 60 and excavation width, 3m.

Perhaps most significant in light of the occurrence of failure at Dolphingstone are those models where initial instability occurs at a level at or near the current ground water level (3 m below surface). This is equivalent to a pressure head over the excavation or void roof of 6 m (approximately 60 kPa pore water pressure in the immediate excavation roof).

As there have been reported seasonal variations in the ground water level of 1.5 to 1.8 m and it is not clear due to the variable seasonal nature of precipitation as to whether a depth of 3 m represented a maximum, median or minimum value of water table it is assumed that scenarios that showed yielding occurring approximately 2 m shallower (*i.e.* closer to the surface) than this value and at any depth above the excavation roof would span the full potential range of scenarios which may have triggered the Dolphingstone collapse.

In order to narrow this list down even further to identify those models where failure of the roof strata leading to collapse was likely to occur, the plots of block yield state and the interface shear slip were examined. If the yield plot indicated failure of elements

through the entire sandstone bed and also displayed shear failure of the bedding surfaces from the base of the sandstone to the upper boundary then there was assumed to be the potential for roof failure leading to void migration. If this criterion was not met initially, then the plots were compared to those at a later stage of the model run with the water table at the surface, this would identify if there was a potential for failure to occur within the roof strata to the full thickness of the sandstone roof layer leading to void migration due to a rise in the water table from the level where initial yielding occurred.

Scenarios at water tables that were unstable but did not meet this criterion were compared to the model run at maximum water table to observe if a continued increase in water table may have lead to the criterion being exceeded. Examples of a scenario meeting this criterion at the water table where yielding first occurs, another where the criterion is not reached initially, however the increase in water table leads to it being met and a final example where this does not occur in either case are shown below:

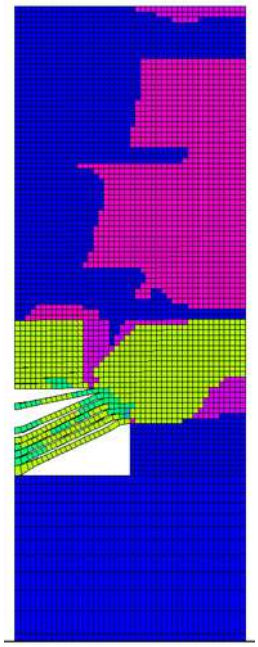	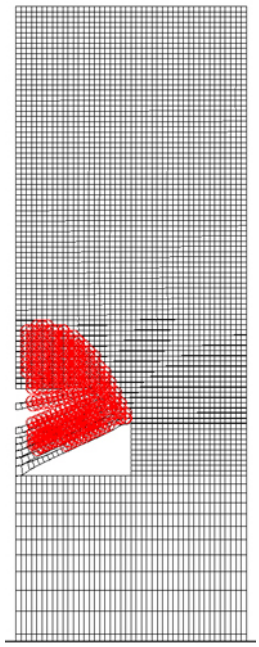	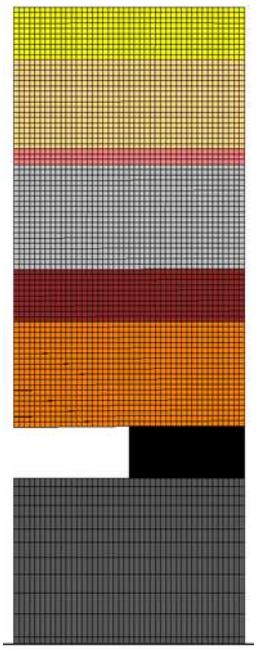
GSI 70, 3 m width, 0.1 m bedding spacing. Water table +1 m. Yielding extends to the full thickness of the sandstone layer.	Shear failure plot of interface indicating shear failure forming an arch. Significantly this intersects the roof, suggesting an unstable span.	Plot of strata. Sandstone is indicated by the orange coloured region.

Figure 7.20: Plot of scenario meeting the full span thickness failure criterion.

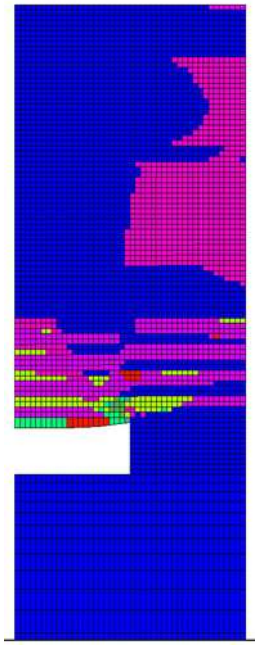	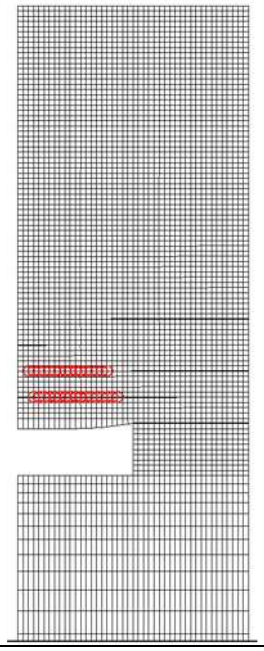	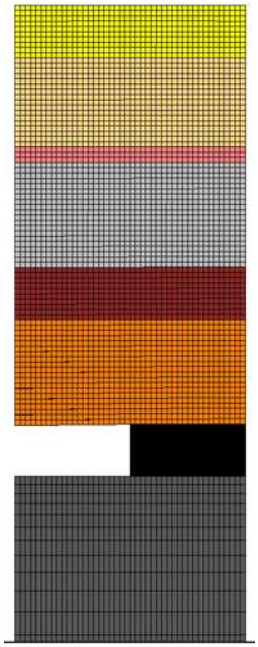
GSI 50, 3 m width, 0.5 m bedding spacing. Water table +2 m. Yielding extends to the full thickness of the sandstone layer.	Shear failure of bedding planes however does not extend from the 3rd to 4th layer. So collapse to the full thickness of the sandstone does not occur	
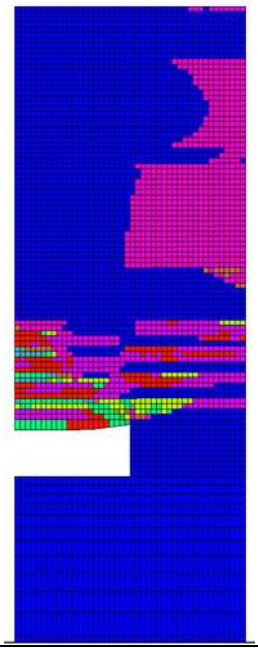	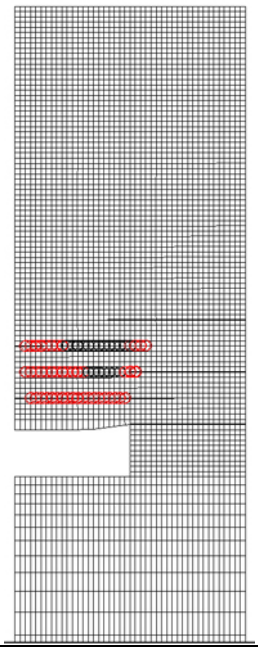	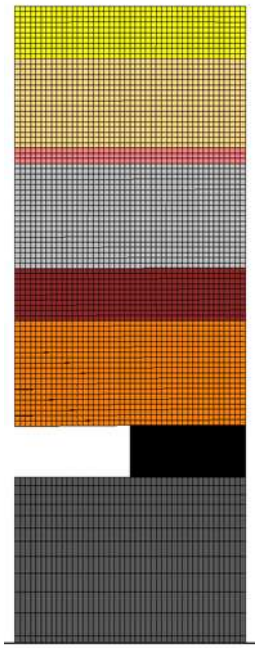
GSI 50, 3 m width, 0.5 m bedding spacing. Water table +8 m. Yielding extends to the full thickness of the sandstone layer.	Shear failure observed in all three bedding planes indicating that collapse to the full thickness of the sandstone possible.	

Figure 7.21: Plot of scenario which initially fails the full span thickness failure criterion until water table increases.

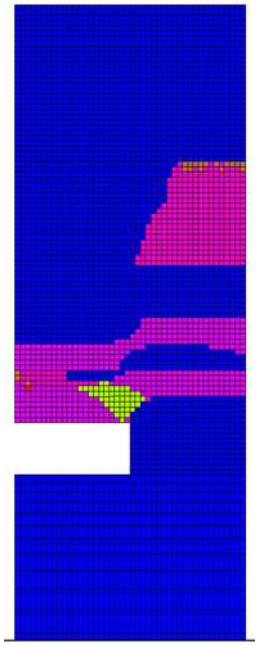	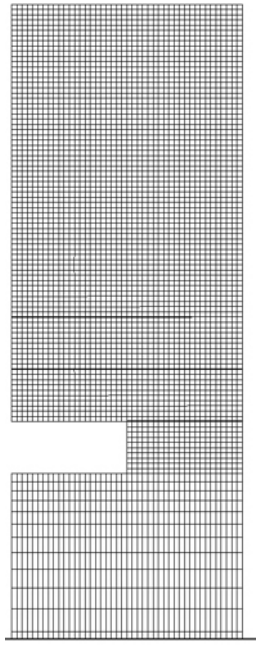	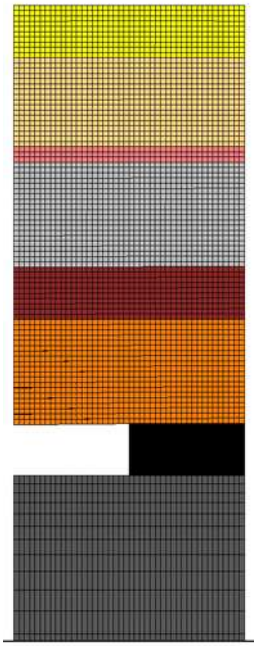
GSI 60, 3 m width, 1.0 m bedding spacing. Water table +2m. Yielding has occurred but does not extend the full thickness of the sand stone bed.	Shear failure plot of interfaces indicating shear failure of the bedding surface has not occurred.	Plot of strata. Sandstone is indicated by the orange coloured region.
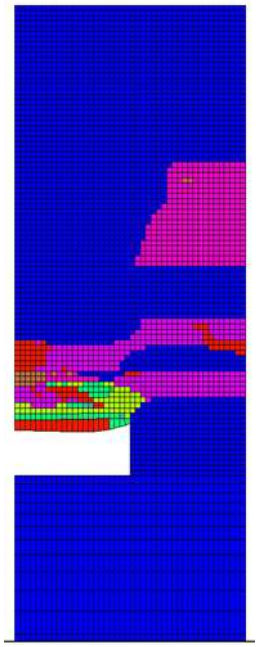	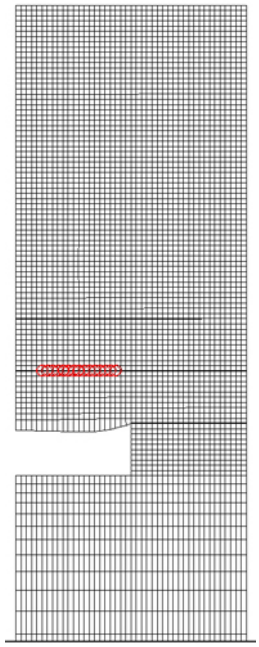	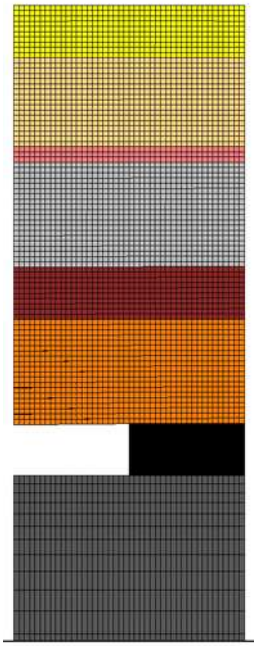
GSI 60, 3 m width, 1.0 m bedding spacing. Water table +8m. Yielding has occurred but still does not extend the full thickness of the sand stone bed.	Shear failure plot of interfaces indicating shear failure of the bedding surface has occurred.	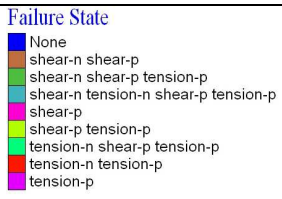

Figure 7.22: Plot of scenario that does not meet the full span thickness failure criterion even after raising the water table to the surface.

The models which fit this new criterion are summarised in Table 7.13 below, where it can be seen that there are thirteen scenarios where void migration may occur, of which nine have geometry with a 3 m wide room / excavation and the remaining four, a 2 m wide excavation geometry. This suggests that the room widths at Dolphingstone were likely to have been a minimum of 2 m as failure spanning the full thickness of the roof strata did not occur at excavation widths below this value. However due to the larger number of failures at the 3 m width mark that could feasibly have caused the roof collapse it is suggested that this is a more realistic minimum room width at the site.

Table 7.13: Scenarios fitting the revised criterion for failure of the full thickness of the sandstone bed.

Bedding plane separation (m)	GSI	Excavation Width (m)	Excavation Height (m)	Hydraulic head above excavation roof at instability (m)
0.1	60	2	1	+1 m Initial Yielding* +7m Exceeds Criterion
0.1	70	2	1	+6m – Yielding
0.1	70	3	1	+1 m – Yielding
0.1	80	3	1	+2 m – Yielding
0.2	40	2	1	+1 m – Yielding* +7m Exceeds Criterion
0.2	60	3	1	2 m – Yielding
0.2	70	3	1	5 m – Yielding
0.5	30	2	1	+1 m – Yielding* +7m Exceeds Criterion
0.5	40	3	1	+1 m – Yielding
0.5	50	3	1	+2 m – Yielding* +3 m Exceeds Criterion
0.5	60	3	1	+3 m – Yielding* +5 m Exceeds Criterion
0.5	70	3	1	+7m – Yielding* +6 m Exceeds Criterion
1.0	40	3	1	+1 m – Yielding* +5 m Exceeds Criterion

***Indicates that the criterion was exceeded on raising the water table to the surface**

The minimum stable strength of the sandstone within the constraints defined (*i.e.* a water table above the level of the workings) was that with a GSI of 80. This occurred in a 3 m width model with 0.1 m bedding spacing. As the bedding spacing thickness increased, the maximum strength at which failure occurred for a given excavation width can be seen to decrease, with the maximum value for a 2 m excavation occurring at a strength equivalent to a GSI value of 70 with 0.1 m wide bedding planes, this reduces to 40 at 0.2 m bedding thickness and 30 at 0.5 m. Failures that may potentially result in

void migration were not recorded for a bedding thickness of 1 m in any of the models tested with a 2 m width between pillars.

The minimum stable strength was broadly independent of the bedding separation or the excavation width and was equal to a value of GSI 80 except for one exception, the 0.1 m bedding, 3 m width model which in this study represented the worst case and was noted as being marginally stable at a rock mass strength equivalent to GSI 90 and totally stable at GSI 100. The strength and stiffness properties represented by these values is summarised in Table 7.14.

Table 7.14: Minimum stable strength at varying geometries and bedding spacing values.

GSI	Bulk Modulus	Shear Modulus	Cohesion	Friction Angle	Tensile Strength
80	15.90	4.15	0.45	62	0.15
80_{Sat}	15.90	4.15	0.34	61	0.11
90	17.31	4.52	0.84	61	0.32
90_{Sat}	17.31	4.52	0.64	60	0.24
100	17.95	4.68	1.60	60	0.68
100_{Sat}	17.95	4.68	1.21	59	0.51
	(GPa)	**(GPa)**	**(MPa)**	**(°)**	**(MPa)**

The results also indicate that the sandstone roof strata most likely did contain bedding surfaces and that these had separations of less than 1 m with the majority of scenarios where yielding occurred had a bedding spacing of 0.5 m although it is recognised that one potential failure scenario (GSI 40, 3 m wide excavation, 1 m bedding thickness) indicates that bedding spacing up to 1 m was a possibility.

It can also be seen that just over ½ of the scenarios show initial roof yielding that does not span the full thickness of the strata until the water table level is raised and a number of those are triggered at a water level table of between 4 and 6 m above the excavation roof which is within plus or minus 1 m of the water table as measured in borehole 1105-S.

This is significant as it is very strongly indicative that the rise in the groundwater table at Dolphingstone after the abandonment of the mine workings was a significant factor in causing the initiation of the collapse. Of further interest are the scenarios where the full

failure of the roof strata did not occur until the water table reached a level in close proximity to that of the present day water table (at 3 m below the ground surface - equal to a pore pressure within the immediate roof of the excavation of approximately 60 kPa). This is potentially significant as these results indicate that the roof strata of the abandoned workings were at a very marginal factor of safety (approaching 1) and that the seasonal fluctuations in the ground water table may have been responsible for triggering the collapse.

As the groundwater table at Dolphingstone is recharged solely by precipitation (Edmund Nuttall Ltd, 2002) this potentially suggests that there may be a meteorological / climate trigger related to unseasonably high rainfall at the site which was responsible for triggering the collapse, however the specific link to a meteorological cause cannot be proven by the modelling work undertaken here (potential methods for undertaking this work are discussed in the section relating to suggestions for further work – see Chapter 7), although this does not lessen the evidence which shows the importance of variations in the water table on stability.

Example plots of the shear failure along the interfaces and the yield state of the rock mass over the excavation roof for the 0.2 m bedding spacing model with a rock mass GSI of 70 and a 3 m wide excavation are presented below.

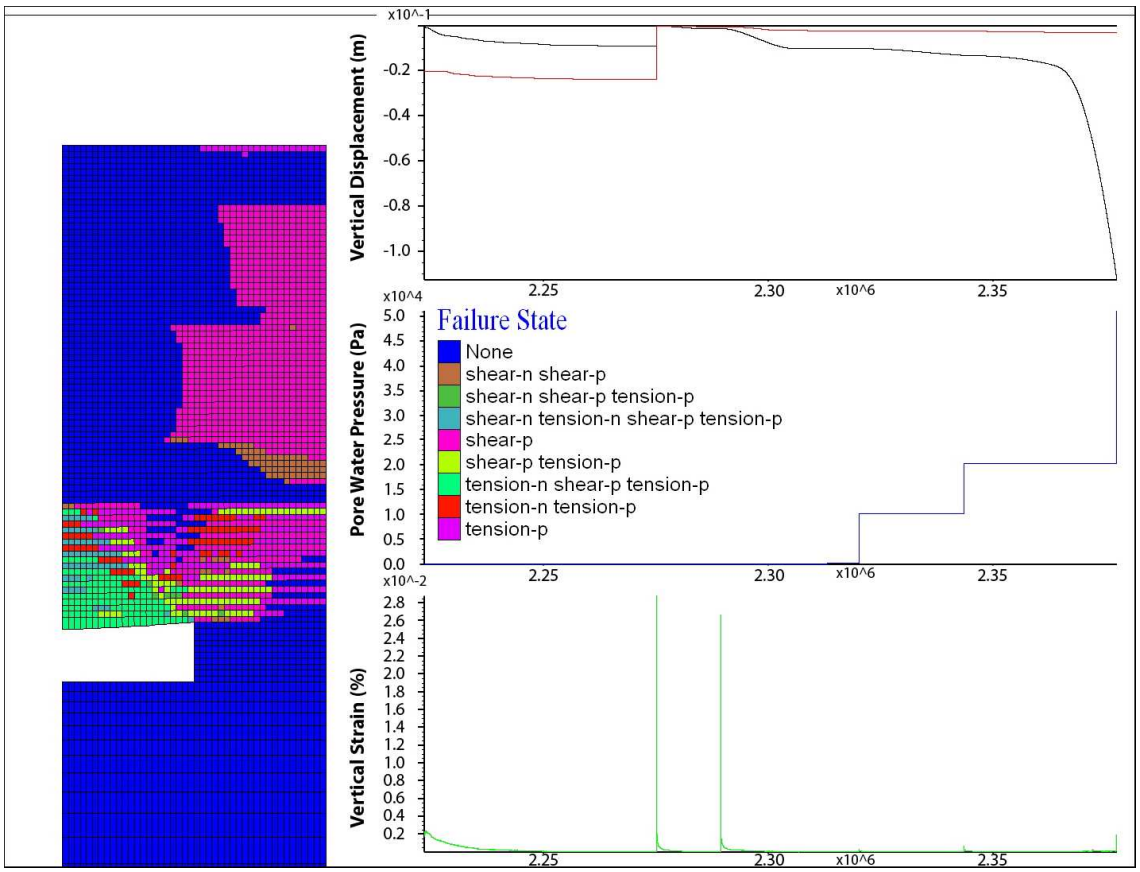

Figure 7.23: Yield plot of the failed rock mass above the excavation.

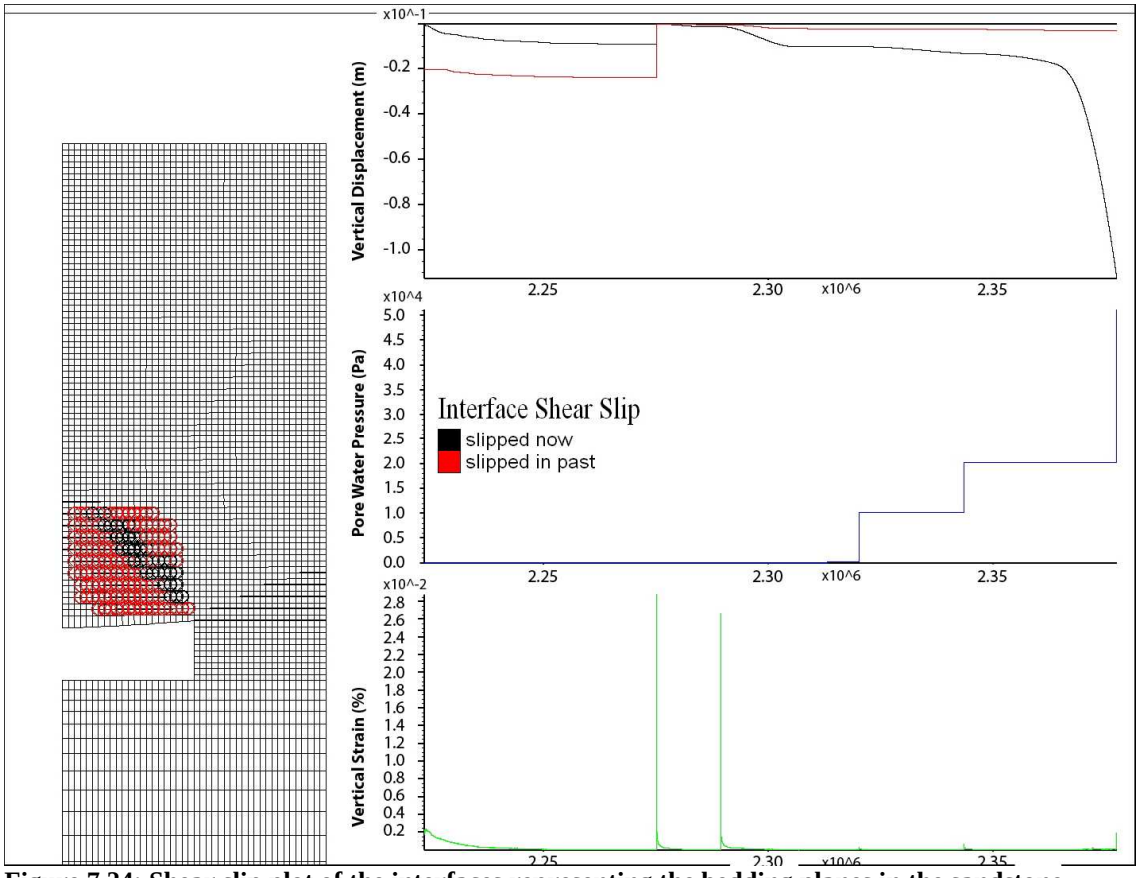

Figure 7.24: Shear slip plot of the interfaces representing the bedding planes in the sandstone overlying the rock mass.

7.8 Conclusions

The modelling work undertaken here suggests that the Dolphingstone collapse was as a result of roof failure in a room width of a minimum of 2 m span (although the majority of scenarios resulting in the potential for roof collapse occurred in rooms with a width of 3 m (equivalent to a maximum span of approximately 4.24 m)

The maximum strength of the sandstone that allowed roof failure to occur within the constraints defined (*i.e.* a water table above the level of the workings) was that with a GSI of 80. This occurred in a 3 m width model with 0.1 m bedding spacing. For all bedding thicknesses and at all other excavation widths, the maximum strength at which roof failure could occur was at a GSI of 70.

The modelling also indicates that the rise in the groundwater table at Dolphingstone after the abandonment of mine workings was a significant factor in causing the initiation of the collapse. Of further interest are the scenarios where the full failure of the roof strata did not occur until the water table reached a level in close proximity to that of the present day water table. This indicates that at these pore water pressures, the excavations stability was very marginal (close to a factor of safety of 1). This in turn suggests that the seasonal fluctuations in the ground water table may have contributed to the instability and so be responsible for triggering the collapse.

Chapter

8

Shallow Abandoned Mine Working Hazard Assessment

8 Shallow Abandoned Mine Working Hazard Assessment

In this section a system used to assess the potential relative hazard posed by abandoned mine workings which was developed by the US Department of Transport's Federal Highway Administration (FHA) to assess the risk posed by mine workings to road infrastructure (Ruegsegger, 1999) is introduced. The main features of the FHA system are summarised and are discussed in terms of the numerical modelling and empirical parametric studies undertaken.

In the FHA system the first phase of the process involves a basic desk study where data is analysed to classify the sites into varying degrees of hazard posed. The sites receiving the highest assessment score are then subject to further investigation to allow a decision to be made as to whether monitoring or remediation of these sites is required.

Currently the recommended strategy in the UK is outlined in the CIRIA report entitled Construction over Abandoned Mine Workings (Healy and Head, 1984) which provides guidance on the desk study and site investigation design required for abandoned mine workings. However, there is very little guidance given as to the analysis or interpretation of those results. The site investigation and remediation decision making portion of scheme outlined by CIRIA are of limited use in terms of assessing the relative hazard posed by various sites. The decision making process is shown more clearly in the FHA system which can be used to rank the relative hazard posed.

N.B. Figure 8.1 represents the management framework outlined by the FHA is an initial framework from which a management strategy for UK railways and rail infrastructure can be derived. This process will include alteration of some of the criteria used in the FHA hazard assessment to take into account the results of numerical modelling work, or to make the criteria more applicable to the UK and UK railway infrastructure and also to include feedback by Network Rail intended to ensure the system can be incorporated into their management process as simply as possible.

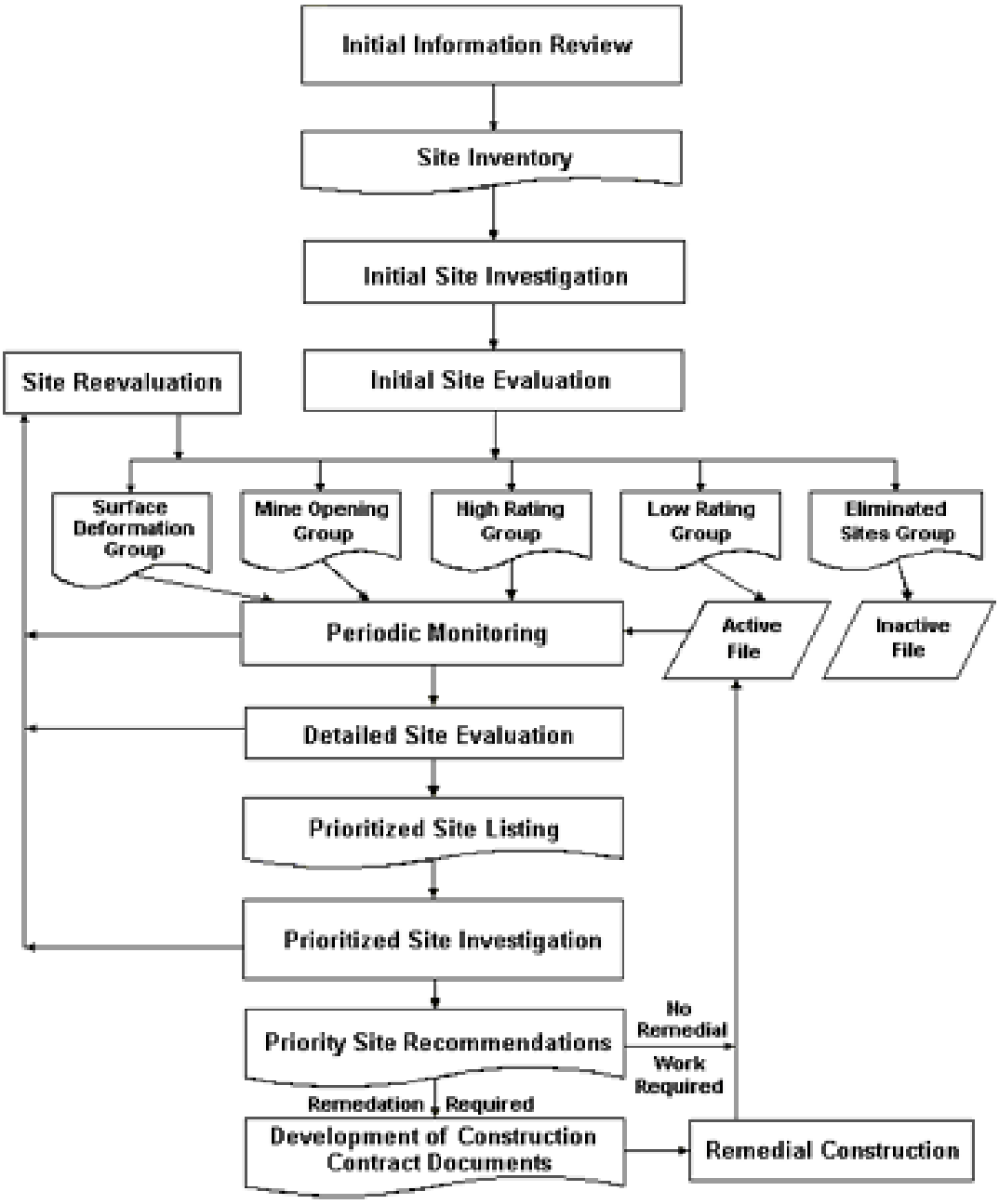

Figure 8.1: Flowchart outlining the FHA hazard assessment scheme (Ruegsegger, 1999).

8.1 The Desk Study Phase

The desk study phase (including a site walkover) is represented by the first three boxes in the flow chart. The recommended sources of data for a desk study in the UK relating to abandoned coal mining are described in the CIRIA report "Construction over abandoned mine workings" (Healy and Head, 1984)

Figure 8.2: Desk Study Phase.

In order to make an initial assessment of the hazard posed by each site, the following initial information should be identified from the sources of data above:

- Where abandoned coal mine plans do exist, a preliminary composite plan view of the workings and the surface topography maps should be compiled
- Any available geological maps and sections should be reviewed to identity presence of and likely depth to coal seams
- Historical maps and aerial photographs should be checked to try and identify historical evidence of previous land use for mining

Once this is completed an initial assessment of the hazard posed by the site can be made.

The above phase is essentially similar in outline to that described as the initial assessment and detailed site reconnaissance phase as described in the CIRIA report (Healy and Head, 1984).

8.2 Initial Site Evaluation

The results of the first three stages are used in the initial site evaluation phase (box 4, Figure 8.2) to rank the hazard posed by various sites using a methodology which shall be described in section 8.2.1 It should be noted that these criteria are to a certain extent qualitative and are intended to give an initial indication of potential hazard posed, purely to allow the prioritisation of site inverstigation (SI).

The Initial Site Evaluation results in the subdivision of sites into five groups of decreasing hazard.

1. Surface Deformation Group:

   Sites with evidence of surface deformation, such as areas of surface settlement, subsidence or irregular drainage conditions which may be mine-related, and may exist or may have historically been observed in areas effecting rail infrastructure.

2. Mine Opening Group:

   Sites with evidence that mine opening(s) exist or have historically been observed or recorded as being in the right-of-way or within view of the right-of-way.

   Note: It is suggested that this be amended to encompass mine openings at any point on site. This would be especially important where abandoned shafts are anticipated as their potential zone of influence if a failure occurs may be large as seen in Figure 8.3.

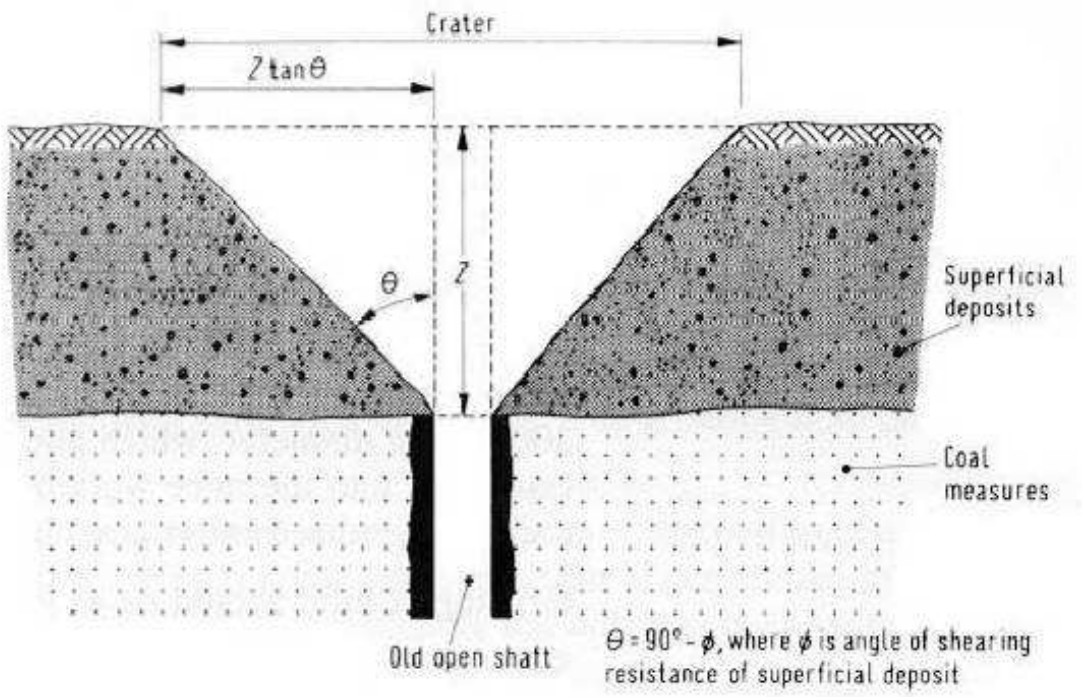

Figure 8.3: Zone of influence if superficial deposits collapse into shaft (Healy and Head, 1984).

3. High Rating Group:

   Of the remaining sites, the top 25% form the High Rating Group. N.B. this is a purely arbitrary cut off point. The FHA manual recommends that this group is made up of the top 10 sites (Ruegsegger, 1999). However as there are an unknown number of sites, it does not seem sensible to quote an absolute number, but rather a percentage.

4. Low Rating Group:

All other sites posing a relatively lower level of hazard as compared to those sites in the high rating group

5. Eliminated Sites:
   Sites eliminated (screened) from further evaluation through the verification that the abandoned underground mine in question in fact does not pose any hazard to rail infrastructure.

Sites rated from 1 to 3 are then studied in greater detail in the next phase of the investigation (entitled Detailed Site Evaluation in the flow chart) process. Initial site evaluation data for sites in group 4 are stored as active files. The highest ranked sites in the 4th group will be promoted into the higher group (group 3) once these sites have been evaluated and a remediation or monitoring strategy implemented.

8.2.1 Evaluation Criteria

Any evidence of subsidence events or of the conditions listed above from the desk study places the site in Category 1 – Highest Potential Hazard. If no evidence of previous subsidence exists the site will be categorised from 2 – 5.

Any evidence that suggests a mine opening (either shaft or adit) exists near the rail track places the site in Category 2 – High Subsidence Hazard. A site with no mine openings will appear in one of the other categories.

A number of other criteria are used to assess in simple terms the potential relative subsidence hazard posed by a site. For each of the following criteria a score between 1 and 10 is allocated for the site. The tallied score at the end of the site evaluation is used to rank the relative hazard posed by each site.

1. Ratio of competent rock to superficial deposits in the overburden material:
This criterion is a simple method of estimating the ratio between strata imposing an overburden load with no structural value (assumed to be any superficial deposit) and those supporting overburden load (assumed to be competent rock).

As such, the authors state that a larger proportion of superficial deposits to competent rock mass will apply a greater dead load on the workings without providing any

significant additional resistance to subsidence which is a credible assertion, however for shallow abandoned mine workings (*i.e.* those below 30 m) the modelling summarised in section 3.2 suggests that this parameter is of limited significance and does not warrant the high rating value applied to it (which is equal to that for the excavation height which has a significant impact on the height of void migration, and is given a higher rating value than that for hydrogeology in terms of flooding of excavations which again has been shown by the modelling work to be an important trigger in excavation instability by altering the effective stress).

Table 8.1: Ratio of competent rock to superficial deposits in the overburden material.

Site Condition:	Rating Value:
Ratio > = 1	10 Points
Ratio < 1	1 Point

2. Traffic Volume:

This criterion is based around the average daily traffic volume of the section of railway potentially affected by subsidence. A greater traffic volume suggests a greater risk to both trains and passengers. This introduces a simple element of risk assessment into the initial hazard ranking.

Table 8.2: Traffic Volume Criterion.

Site Condition:	Rating Value:
>30,000 Vehicles	10 Points
20,000 to 30,000 Vehicles	8 Points
10,000 to 20,000 Vehicles	6 Points
5,000 to 10,000 Vehicles	4 Points
<5,000 Vehicles	2 Points

The above are example values as suggested in the FHA manual (Ruegsegger, 1999) for road vehicle numbers. Values appropriate for the UK rail network should be defined by Network Rail.

3. Hydrogeology:

This criterion takes into account the effect of groundwater on the stability of the workings. The FHA use a simple rule whereby the workings can be assessed as dry, flooded or dewatered and awarded a hazard rank accordingly with dewatering activity assumed to have the greatest affect on stability.

Table 8.3: Hydrogeology Criterion.

Site Condition:	Rating Value:
Dewatered	10 Points
Flooded	8 Points
Not Flooded	1 Points

The numerical modelling undertaken in the earlier sections indicate that this value is of high significance in terms of the stability of subsurface excavations and demonstrates that even small increases in pore water pressure of approximately 10 kPa (circa 1 m increase in the ground water table) can initiate instability of subsurface excavations. Information available in the literature indicates that the uniaxial compressive strength of both intact and broken rocks has been demonstrated to decrease by between 25% and 50% when they are saturated (Vasarhelyi, 2003; Li and Reddish, 2004; Zhang, 2005) which can lead to the potential for even greater instability.

4. Minimum Thickness of Overburden:

This is a simple method of estimating the subsidence potential of a site. It is a measure of the competent rock mass overlying the shallowest coal seam.

Table 8.4: Minimum Thickness of Overburden Criterion.

Site Condition:	Rating Value:
< 5m	10 Points
10m to 20m	8 Points
20 to 30m	5 Points
>30m	1 Points

The literature reviewed in section 2.2.3 as well as the numerical modelling of layered strata using interfaces and the Ubiquitous Joint Model, along with the empirical techniques to estimate collapse height before arching or bulking will occur all suggest that this parameter is extremely significant with regards to halting the movement of a void whereby the greater this value, the lower the chance of a void successfully migrating to surface. This is due to the minimum rock mass height necessary to form a stable stress arch over an excavation if instability leading to collapse does occur (which has been shown to be related to the rock mass friction angle). It also allows the debris pile to increase in volume or "bulk" which will given sufficient over burden thickness result in halting of the void migration.

5. Coal Seam Thickness: This has an influence on the potential maximum height of extraction and hence the severity of any surface subsidence.

Table 8.5: Coal Seam Thickness Criterion.

Site Condition:	Rating Value:
>2m	10 Points
1 m to 2m	5 Points
<1m	1 Points

The numerical modelling suggested that this parameter is relatively insignificant in terms of the stability of excavation roof strata; however it significantly affects the height to which void migration before bulking can occur with even small increases in excavation height affecting the height before bulking can occur, as such the application of the highest potential rating to this category seems appropriate.

6. Ratio of Minimum Thickness of Overburden to Coal Seam Thickness:

It is intended that this criterion will give an indication as to the potential hazard posed by void migration and sink holes.

Table 8.6: Ratio of Minimum Thickness of Overburden to Coal Seam Thickness.

Site Condition:	Rating Value:
Ratio < 5	10 Points
Ratio = 5 to 11	5 Points
Ratio > 11	1 Points

As stated previously the overburden thickness affects the potential height to which void migration can occur before either bulking or arching will halt migration however the addition of the excavation height component indicates that it will have the most significant effect on the bulking.

7. Secondary Mining:

Any evidence of pillar robbing or retreat mining may suggest increased instability of the workings. This may be difficult to assess; however if evidence is available it can be incorporated.

Table 8.7: Secondary Mining.

Site Condition:	Rating Value:
Yes	10 Points
No	1 Points

8.2.2 Site Evaluation Criteria Weighting Factors

To reflect the relative importance of the different criteria, weighting factors are applied. Suggested levels are given in the FHA document manual (Ruegsegger, 1999) and can be seen below:

Criteria	
Evidence of surface deformation	Automatic placement in the Surface Deformation Group for Detailed Site Evaluation.
Presence of mine opening(s)	Automatic placement in the Mine Opening Group for Detailed Site Evaluation.
	Weighting Factor (FHA)
Ratio of competent rock to superficial deposits in the overburden material	9
Average daily volume of traffic	9
Hydrogeologic Setting	8
Minimum Thickness of Overburden	4
Coal Seam Thickness	4
Ratio of Minimum Thickness of Overburden to Coal Seam Thickness	6
Secondary Mining	4

Table 8.8: Weighting factors to reflect the relative importance of the different criteria.

Once these tests have been conducted for each individual site, the inventory can be sorted into 5 different hazard groups. These groups in order of priority are listed in Table 8.9. Once the initial hazard assessment has been performed and the sites have been ranked according to the relative hazard posed, the process enters the next phase. This is an iterative process whereby sites are continually monitored (monitoring ranges from infrequent (bi-annual) walkovers which should be done for all sites, up to constant monitoring using borehole methods such as Time Domain Reflectometry (TDR). The decision to upgrade site monitoring is based on the analysis of SI results. The next phase of the investigation involves a detailed site evaluation to be made. This process is described in the following section.

Table 8.9: Hazard assessment groups.

Priority	Name	Description
1	Surface Deformation Group	Sites with evidence of surface deformation, such as areas of surface settlement, subsidence or irregular drainage conditions which may be mine-related, and may exist or may have historically been observed in the right-of-way or within view of the right-of-way.
2	Mine Opening Group	Sites with evidence that mine opening(s) exist or have historically been observed or recorded as being in the right-of-way or within view of the right-of-way.
3	Higher Rating Group	The top 25% of sites having the highest level of risk to the travelling public and / or damage to the infrastructure resulting from abandoned underground mines.
4	Lower Rating Group	All other sites with a relatively lower hazard rating
5	Eliminated Sites	Sites eliminated from further evaluation through the verification that the abandoned workings do not influence rail infrastructure.

8.2.3 Monitoring Before Priority Site Evaluations

The requirements for monitoring (form and frequency) will depend on the field information and existing information reviewed for the given site at this point in the assessment process. The hazard group into which the site has been placed will determine the forms and corresponding frequencies of site monitoring which will be appropriate (Ruegsegger, 1999). Sites where surface deformation is suspected (Surface deformation group) sites should be assigned the highest level of monitoring. Site specific monitoring, as determined to be appropriate for the observed field conditions, should be undertaken. Detailed Site Evaluations and Priority Site Investigations should be given the highest priority for these sites. The initial monitoring visit should be performed as soon as possible after the initial site visit. Suspected Mine Opening Group Sites should be assigned the second highest level of monitoring. The sites that do not fall into either of the above categories will form a general group which will be subdivided into the high and low rating groups as seen above and will be assigned the third and fourth (lowest) priority levels for monitoring. The suggested frequency for these different types of monitoring are based on the suggested values in the Manual for Abandoned Underground Mine Inventory and Risk Assessment (Ruegsegger, 1999).

Table 8.10: Monitoring of Priority 1 sites before detailed evaluation has occurred (Ruegsegger, 1999).

Forms of Monitoring (Surface Deformation Group Sites – Priority 1)	**Frequency**
I. Visual	
Site walkovers during general track inspections	Daily - weekly
Specific features of interest identified in the initial walkover	Weekly - monthly
Ground photography	Done during walkovers
II. Non - Intrusive	
Ground Survey	Weekly to monthly
Aerial Photography: Conventional (B/W and Colour)	Yearly
Aerial Photography: Infrared (B/W & Colour)	Yearly
Falling Weight Deflectometer[A]	Every 6 months
Ground Penetrating Radar[A]	Every 6 months

[A]Falling weight deflectometers have been used in conjunction with GPR to assess track bed stiffness and the quality of track bed, ballast and immediately underlying formation. These methods combined can give an indication of areas of anomalous behaviour and ballast conditions at shallow depth (Brough *et al.*, 2003, Hugenschmidt, 2000) which may be an indication of a deeper underlying problem such as void migration (Ruegsegger, 1999). These methods are most applicable to surface deformation groups sites as it is assumed that voids may already be near surface as subsidence has occurred in the past.

Table 8.11: Monitoring of Priority 2 sites before detailed evaluation has occurred (Ruegsegger, 1999).

Forms of Monitoring (Mine Opening Group Sites – Priority 2)	**Frequency**
I. Visual	
Site walkovers during general track inspections	Weekly – Every 2 weeks
Specific features of interest identified in the initial walkover	Every 2 weeks - Monthly
Ground photography	Done during walkovers
II. Non - Intrusive	
Ground Survey	Weekly to monthly
Aerial Photography: Conventional (B/W and Colour)	Yearly
Aerial Photography: Infrared (B/W & Colour)	Yearly
Falling Weight Deflectometer	Every 6 months – Site specific[A]
Ground Penetrating Radar	Every 6 months – Site specific[B]

[A]As this method is used on track, it is only applicable if the opening or void is at shallow depth under or very near to the track.

[B]GPR can be run from vehicles travelling on the rail or by hand on the sides of the track, and may be able to detect shallow disturbances which may be an indicator of instability over mine openings. Especially if the magnitude of disturbances vary over time.

Table 8.12: Monitoring of Priority 3 sites before detailed evaluation has occurred (Ruegsegger, 1999).

Forms of Monitoring (High Rating Group – Priority 3)	**Frequency**
I. Visual	
Site walkovers during general track inspections	Every 2 weeks
Specific features of interest identified in the initial walkover	Monthly
Ground photography	Done during walkovers
II. Non - Intrusive	
Ground Survey	Monthly
Aerial Photography: Conventional (B/W and Colour)	Yearly
Aerial Photography: Infrared (B/W & Colour)	Yearly
Falling Weight Deflectometer	Every 12 months – Site specific[A]
Ground Penetrating Radar	Every 12 months – Site specific[A]

[A]If geological cross sections suggest that there may be workings at very shallow depth (<10) these processes may give early warning of any anomalous ground conditions that may relate to void migration.

Table 8.13: Monitoring of Priority 4 sites before detailed evaluation has occurred (Ruegsegger, 1999).

Forms of Monitoring (Low Rating Group – Priority 4)	**Frequency**
I. Visual	
Site walkovers during general track inspections	Monthly
Specific features of interest identified in the initial walkover	Monthly
Ground photography	Done during walkovers
II. Non - Intrusive	
Ground Survey	Every 6 months
Aerial Photography: Conventional (B/W and Colour)	Every 2 years
Aerial Photography: Infrared (B/W & Colour)	Every 2 years
Falling Weight Deflectometer	Every 2-3 years
Ground Penetrating Radar	Every 2-3 years

The results of this monitoring should be fed back into the initial evaluation and if necessary the sites hazard grouping should be altered accordingly.

E.g. a high risk site group walkover shows pooling of surface water, and some localised surface track deflection. Suggests surface deformation is occurring. Site moved into Surface deformation group and new monitoring regime applied accordingly.

This process of repeat monitoring of all sites is necessary because sites that initially appear stable may demonstrate future instability due to their increasing age, or due to variations in other parameters such as ground water.

8.3 Detailed Site Evaluation

The aim of this evaluation is to prioritise the sites within a particular group for site investigation. All sites within group 1 will loop through the full process of evaluation, site investigation and recommendations for monitoring or remediation before starting on the sites in group 2 and finally group 3. This phase of the assessment process is shown in Figure 8.4. The information used to make the detailed site assessment (which augments the initial desk study) includes specialised maps, plans and mining records, and also aerial photographs, old site investigation reports, and original documents (Healy and Head, 1984).

The detailed site evaluation process will reconsider some of the criteria in the first evaluation phase. However it is assumed that a more thorough search for detailed information will be undertaken and a greater range of information will be available as detailed on the previous page. As a result of this evaluation, some sites may be reclassified into lower or higher rated groups.

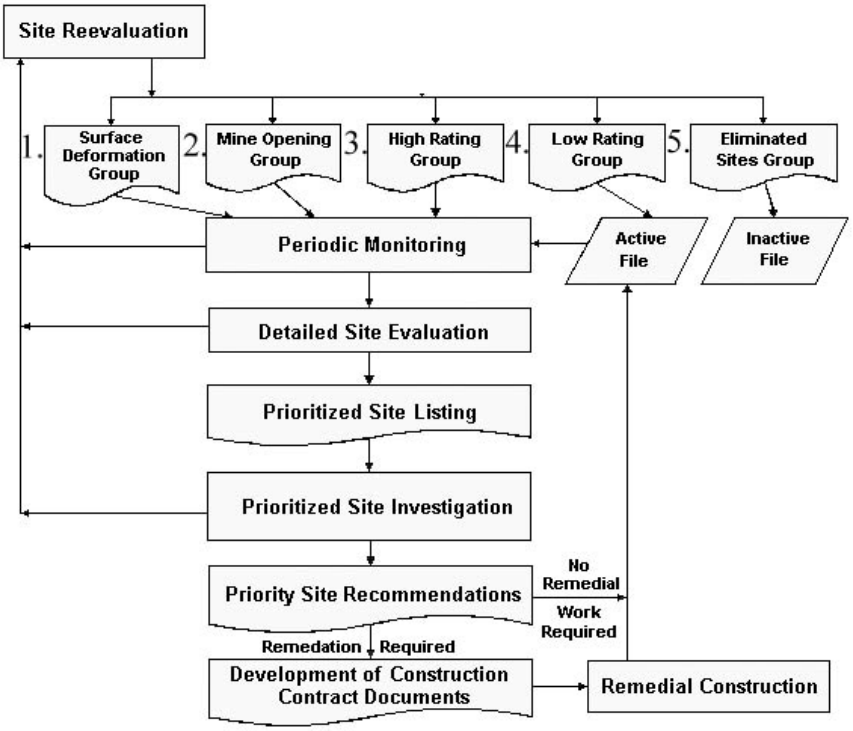

Figure 8.4: Detailed site evaluation phase (after Ruegsegger, 1999).

1. Prior number of subsidence events:

This criterion gives an indication of the susceptibility of a site to subsidence. It is assumed that the larger the number of previous subsidence events, the greater the hazard posed by the site. The rating value used is the number of areas of surface settlement, subsidence, or irregular drainage conditions, which are observed (either in a site walkover, or from desk study documentation) or have historically been observed (from historical maps etc) within the boundaries of the site.

2. Recent Dewatering:

This criterion is an indicator of the potential for instability caused by fluctuations of the water table affecting abandoned workings. Variations in the ground water table can have detrimental effects on the stability of abandoned workings due to the change in stress state leading to weakening of the rock mass as shown by numerical modelling work in sections 3.4.11 and 5.12 and by Li and Reddish (2004) . The site condition is the length of time since each report or incidence of dewatering. The total rating value for a given site will be the sum of all rating values of all dewatering events.

Table 8.14: Recent dewatering criterion.

Site Condition:	Rating Value:
< 1 Year	10 Points
1 to 3 Years	9 Points
4 to 6 Years	4 Points
7 to 9 Years	2 Points
> 9 Years, unknown, or dry mine	1 Points

Example: A site dewatered five years ago and again in the past year. The total site rating value for this criterion would be equal to 4 + 10, or 14.

3. Traffic Volume:

This criterion is identical to that used in the initial site assessment

4. Ratio of Competent Rock to Superficial Deposits:

This criterion is identical to that used in the initial site assessment

Table 8.15: Criterion based on ratio of competent rock to superficial deposits.

Site Condition:	Rating Value:
Ratio >1	10 Points
Ratio <1	1 Point

5. Availability of Reasonable Detour Routes:

This criterion is an indicator of the strategic significance that lost use of the rail infrastructure site would have.

Table 8.16: Criterion based on availability of reasonable detour routes.

Site Condition:	Rating Value:
Main Line – No Diversion	10 Points
Branch Line – No Diversion	5 Points
Goods Line – No Diversion	2 points
Suitable Diversion	1 Point

N.B. This specific example is illustrative. The specific criterion and their relative values must be decided by the asset owner.

6. Presence of Structures:

This criterion is an indicator of the potential consequences of subsidence affecting a structure at the site. Structures may include tunnels, bridges, embankments, culverts and cuttings.

It is assumed that for each of the structures, the result of subsidence will be collapse or partial collapse. This is assumed to be the worst case scenario and to pose the greatest potential hazard to the public.

It is assumed that the overall site value will be the sum of the number of structures.

Table 8.17: Structures criterion.

Site Condition:	Rating Value:
Structures Present	10 Points
No Structures	0 points

E.g. Site with a bridge and a tunnel entrance = 10 + 10 = 20 Points.

7. Minimum Thickness of Overburden:

This criterion is identical to that used in the initial site assessment

8. Mine Opening Location (Excluding Mine Shaft):

This criterion is an indicator of the relative risk to the safety of the travelling public. The site condition is the location of the mine opening relative to the railway line. If multiple openings are located then the rating value should be calculated as the sum of the individual site condition rating values for each of the mine openings on the site. Shafts are excluded from this classification as the area of influence of a shaft collapse may be much larger than for other mine openings. (The F.H.A system included all mine openings in one criterion, however due to the much greater potential area of influence of a shaft collapse it seems sensible to apply a separate criterion).

Table 8.18: Mine opening location criterion.

Site Condition:	Rating Value:
Location not conclusively known	10 Points
< 10 m from track	10 Points
10 - 20 m from track	8 Points
20m - 30m	2 Points
> 30 m from track	1 Point

9. Mine Opening Location (Mine Shaft):

To assess the zone of hazard posed by a mine shaft see the appendices.

Table 8.19: Mine opening location criterion (shafts).

Site Condition:	Rating Value:
Location not conclusively known	10 Points
Site within zone of influence	10 Points
Site outside zone of influence	1 Point

10. Method Used to Seal Mine Openings:

This criterion gives an indication of the potential stability of any materials originally used to seal mine openings.

Table 8.20: Criterion based on method used to seal mine workings.

Site Condition:	Rating Value:
No Information	10 Points
Timber Decking	10 Points
Uncontrolled Random Backfill	6 Points
Concrete Cap	4 Points
Controlled Backfill	2 Points

11. Type of Support:

This criterion is an indicator of the stability of material placed to provide support of the mine opening.

Table 8.21: Support criterion.

Site Condition:	Rating Value:
No Information	10 Points
Timbers	10 Points
Brick	7 Points
Concrete	4 Points

12. Minimum Thickness of Overburden Over Mine Opening:

This criterion is identical to that used in the initial site assessment

13. Type of Mine Opening:

This criterion is an indicator of the relative danger posed to the public by the original type of mine opening. In the case of multiple mine openings, the overall site condition rating value should be calculated as the sum of the individual site condition rating values for each of the mine openings on the site.

Table 8.22: Criterion based on type of mine opening.

Site Condition:	Rating Value:
Shaft (Vertical) Entry	10 Points
Slope Entry	8 Points
Drift (Horizontal) Entry	6 Points

14. Extraction:

This criterion is an indicator of the amount of mine roof support which remains in the mine. Evidence of mineral extraction and pillar scavenging may exist for some sites.

Table 8.23: Extraction criterion.

Site Condition:	Rating Value:
Evidence of Secondary Mining	10 Points
Rate of Mineral Extraction > 50%	7 Points
Unknown	5 Points
Rate of Mineral Extraction < 50%	1 Point

15. Coal Seam Thickness:

This criterion is identical to that used in the initial site assessment

16. Ratio of Minimum Thickness of Overburden to Coal Seam Thickness:

This criterion is identical to that used in the initial site assessment. Upon completion of the detailed evaluation, a prioritised list of sites for site investigation can be prepared based on the relative score for each site in a group.

8.4 Conclusions

The US Department of Transport's Federal Highway Administration's mining hazard assessment tool developed by Ruegsegger (1999) is a comprehensive system that allows the hazard posed to road transport infrastructure sites affected by mining subsidence to be ranked. It incorporates the majority of parameters identified in the literature and the modelling work undertaken in this project as significant (*e.g.* the prior occurrence of subsidence or prior evidence of the undermining of the site, fluctuations in the ground water table, the worked seam thickness and overburden thickness) although some additions or alterations are required to make the tool more appropriate fro use in rail infrastructure. Rather than develop an entirely new system it seems a sensible approach to modify an existing tool to make it more appropriate for use in managing UK rail infrastructure.

8.4.1 Parameters from Desk Study and Site Investigation to Aid Prioritisation of Sites Potentially Affected by Shallow Abandoned Mine Workings

Based on the modelling results and the empirical study of the effects of variations in parameters on the potential height of void migration along with the literature review undertaken, a number of variables appear to be significant in terms of the potential for initial excavation instability and the height to which void migration may occur.

1. The succession of strata, in particular the presence of high strength strata which may act to halt void migration.
2. The depth to workings
3. The thickness or height of the excavated seam
4. Excavation width
    - This parameter appears to be important in both estimating the height of void migration before bulking or arching will occur; however finding a method to assess this value is proving difficult. Down hole cameras are one possibility. (Onions *et al*., 1996).
5. The depth to the groundwater table as it is apparent from the literature that the presence of water acts to reduce the strength of both intact rock (Li and Reddish, 2004; Zhang, 2005; Whittles *et al., 2007*) and broken rock (Li and Reddish, 2004) and so will effect the rock mass strength. Increased pore water pressures will also have an impact on effective stress and so affect the strength properties of the rock mass and have been demonstrated in the modelling work undertaken here to be a cause of instability.

6. The friction angle of the rock mass has been shown in the modelling work undertaken in chapter 5 to be an extremely significant parameter in the control of the geometry of failure above an excavation. In horizontally bedded strata the rock mass friction angle is a composite of that for the intact rock and the friction angle of the bedding surfaces. Discontinuity friction angle properties would be a very useful parameter in a detailed assessment of stability, however it is recognised that there are difficulties in acquiring these values.
7. The uniaxial compressive strength (UCS) of the main strata encountered during drilling.
    - The uniaxial compressive strength of the rock can be found using UCS tests of intact rock core samples with no discontinuities. The length to diameter ratio of 2:1 is a minimum for cylinders. From this test the Young's modulus and Poisson's ratio would also be derived (Geological Society Engineering Group Working Party, 1999)
    - UCS can also be estimated using the point load test on broken rock samples that would not be suitable for the standard laboratory UCS test (Franklin, 1985). Further to this the UCS value can be used to estimate the bulking factor of the rock mass using the relationship outlined by Palchik (2002) which allows an estimate to be made of the maximum collapse height. .
8. Presence of bed separation, jointing / fracturing and joint / fracture orientation in the rock mass
    - These features can be identified and their orientations measured on borehole television images (Onions *et al*., 1996)
    - Bedding spacing has been shown to significantly impact on stability in the work undertaken in this thesis as well as in laboratory (Goodman, 1989) and field observations (Healy and Head, 1984) and is a key parameter in halting void migration.
    - The presence of steeply dipping weakness planes such as joints will significantly affect stability and will potentially invalidate the relation ship between arch height and the friction angle of the rock mass. Especially in cases where the joints are persistent. In these cases it is likely that the void migration will only be stopped wither by bulking (if the collapse debris in this case increase in volume). This can significantly increase the height to which void migration can occur.

Chapter

9

Conclusions and Suggestions for Further Work

9 Conclusions and Suggestions for Further Work

In the following sections the research undertaken in this thesis and the major conclusions of this research are summarised and suggestions made for further work.

9.1 Conclusions

In terms of the numerical modelling work to investigate shallow excavation stability, a number of observations have been made in this work relating to the effects of various parameters on shallow mine excavation stability. This included two main phases of modelling work.

The initial phase intended to identify the broadly significant parameters in stability and which was undertaken using an equivalent continuum approach and the elastic-perfectly plastic Mohr-Coulomb constitutive model and then a second phase in which the parameters identified as of primary significance in the first phase were investigated in more detail.

The second phase involved the modelling of the rock mass overlying the excavation as an anisotropic strain softening material making use of the Strain-Softening Ubiquitous-Joint Mohr-Coulomb constitutive model to investigate the effect of the presence of variably dipping discontinuities in the rock mass on stability as well as the use of the Strain-Softening Mohr-Coulomb model with embedded interfaces which allowed the model to behave as a discrete assemblage of layers as opposed to a continuum and which more accurately captures the behaviour that occurs in stratified materials (such as Coal Measures strata).

The parameters investigated and significant observations and conclusions are summarised below:

The effect of variations in the geometry of the excavation, including the excavation width and height were investigated where it was found that variations in the width of the coal pillar were shown to have virtually no effect on the stability of the roof with yielding occurring to the same extent for a given excavation width and rock mass strength in all cases. Excavation width however was demonstrated to be a very significant parameter in all the numerical modelling work undertaken here with increases in the excavation width leading to significant increases in the height to which failure of roof strata and yielding extended into he rock mass over the excavation roof. This was shown to be significantly effected by the presence of discrete discontinuities in the rock mass as modelled using interface elements whereby tensile yielding extended to significantly greater heights in the modelled rock mass when interface elements were present than when they were not (*i.e.* in the equivalent continuum modelling). The results of the modelling of varying excavation height indicate that this parameter appears to have a limited impact on the stability of excavations with the rock mass strength and the height of the groundwater table being far more significant parameters. It is however observed that the excavation height has an impact on excavation stability that is related to the ratio of width of excavation to excavation height. Whereby excavation stability increases as the excavation width to height ratio approaches one and decreases as this parameter diverges from 1. However from the results it was determined that the decrease in roof stability due to variations in height of an excavation for a given rock mass strength caused significantly less instability than increases in excavation width.

The modelling undertaken to investigate the effect of overburden thickness on excavation stability was surprising as it demonstrated that it has virtually no effect on excavation stability at higher strength levels tested (those equivalent to a GSI value of 60). The influence of the overburden thickness was seen to increases progressively as the strength of the rock mass decreased, but only caused very small changes in deformations recorded in the roof strata (on the order of 10^{-3} m) which were not considered significant in terms of initial stability . It is recognised however that the thickness of the overburden is a significant factor with regards to the potential for collapse progression / void migration.

The effects of material anisotropy and discontinuity of the model were investigated using both an anisotropic constitutive model as well as by the use of interface elements to allow the model grid to be separated into discrete layers representing bedding.
In this work it was demonstrated that a discontinuous model with interface planes or elements used to represent the bedding surfaces was able to display behaviour observed in laboratory experiments (such as those in outlined in Bieniawski, 1984 and Goodman, 1989) whereby the strata would delaminate in the roof centreline and fail in shear at the pillar intersection. In the laboratory experiments this would result in the formation of a discrete fracture leaving a series of abutments that acted to support the overlying layer and so progressively decreased the excavation span. In the continuum modelling the sagging and delamination where observed to occur by normal failure of the interface elements. Shear yielding was also observed to occur at the pillar roof boundary however this did not take the form of a discrete fracture due to the continuum nature of the model. This effect is discussed in more detail below. It was also observed in the modelling undertaken using interface elements that the stress within a bed / stratum that had undergone delamination and was self supporting was shown to form a compression arch whereby the upper portion of the beam was in compression and the lower portion in tension as would be expected to occur in a compression arch showing that the use of discrete modelling more realistically captures the behaviour of roof strata than would be observed in an equivalent continuum model. See Figure 9.1.

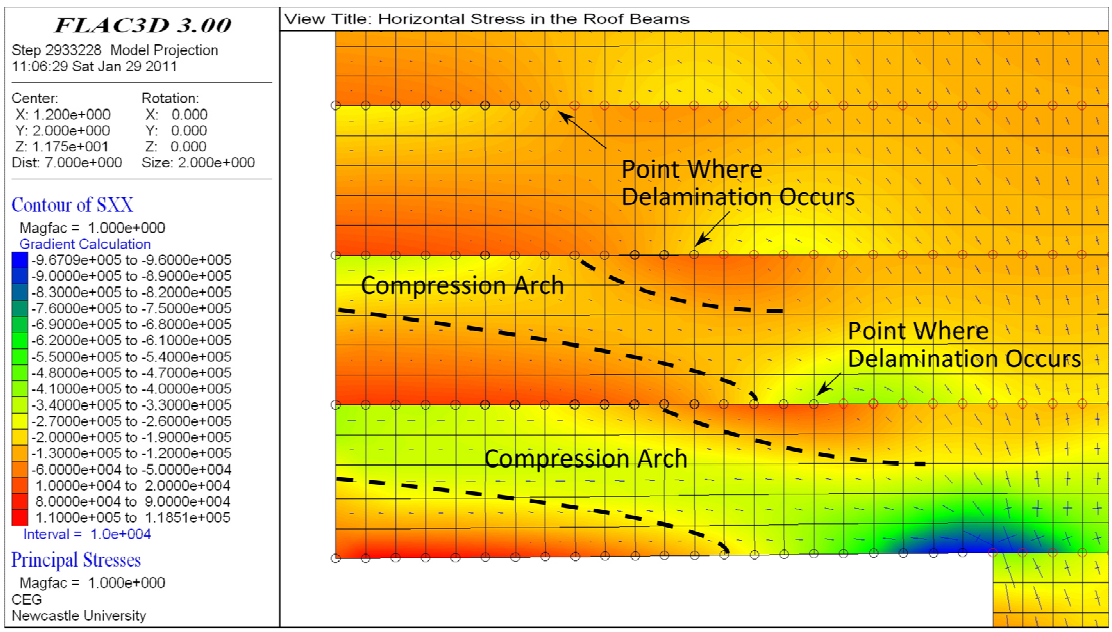

Figure 9.1: Plot showing the formation of compression arches in roof beams. Locations of compressive arch boundaries are approximate.

The modelling also demonstrated that a region of tensile delamination of the strata extended upwards into the rock mass above the excavation even in those strata that did not ultimately fail. This would reduce the shear strength of those bedding planes to zero, which would in turn cause all the strata within this region to behave as compression arches and transmit stress into the rock mass over the pillar.

The effects of variations in the rock mass strength and stiffness properties were investigated in both phases of the modelling as they had been shown to be significant. The effect of variable pillar strength on stability of excavations in an equivalent continuum rock mass was investigated, where it was observed that the strength of the coal pillar can have a significant impact on the type of subsidence that will occur. Where the coal pillar strength is low compared to the strength of the overlying and underlying rock mass, significant shear yielding can occur along with large horizontal displacements within the pillar and pillar margins. This represents pillar crushing. This is unlikely to lead to void migration and instead results in sag subsidence.

The effect of variations in the underlying rock mass strength on stability in an equivalent continuum rock mass were also investigated where the effect of decreasing underlying rock mass strength leads to a uniform increase in both the pillar vertical displacements and the roof centreline displacements. It is not indicative of roof failure or collapse that would lead to void migration. The yielding within the underlying rock mass beneath the pillar suggests this may represent the coal pillar punching into the underlying material. This is most significant when the strength of the coal pillar and overlying rock mass are significantly higher than that of the underlying rock mass. It may also be significant in multi seam workings however these were not investigated here.

The effect of material anisotropy in the form of a “weak plane” within the numerical model intended to represent the presence of (steeply) dipping or vertical discontinuities (*e.g.* joints) was investigated where it was observed that the frictional angle of the intact matrix and the joints along with the angle of dip were the dominant factors in controlling the geometry of failure in dipping strata, except for those that dip at 90° whereby the dip angle is the single dominant factor in controlling failure geometry. In more detail, at shallow dip angles, (*i.e.* those below the friction angle of the joints) the boundary of the zone of yielding is controlled by the joint friction angle and joint dip.

As the dip angle increases past the friction angle of the joint planes, the tensile failure boundary begins to be defined to the up-dip or left hand side by the rock mass matrix friction angle, the upper boundary by the joint dip and the down-dip or right hand side by the joint friction angle of the rock mass and the joint dip. This forms a broadly trapezoidal shape.

It was also demonstrated in the modelling that variations in the bedding plane spacing clearly impacted on the stability of the strata overlying sub surface excavations. It was observed that the larger the bedding thickness the greater the excavation stability for a given stress state. It was also observed that if roof failure did occur it would extend to a lesser height into the rock mass as the bedding thickness was increased. Also the ability of the individual strata to form a stable compression arch was found to significantly increase as the bedding thickness / bedding plane separation increases. The bedding thickness / bedding plane separation also has a significant effect on the height to which "damage" in the form of tensile yielding and bedding plane delamination propagate upwards into the overlying rock mass, whereby the thicker the bedding / strata, the lower the height that damage extends vertically into the rock mass.

In this phase of the study FLAC was observed to be capable of modelling the self weight sagging of thinly bedded low strength strata directly when use was made of horizontally layered interfaces to represent bedding however this failed to totally capture the collapse behaviour in thicker bedded strata (>0.2 m) where shear failure and shear joint / parting plane failure occurred. It was observed that the shear failure occurred in the rock mass extending upwards into the excavation roof over the void as would be expected, crossing thicker roof spans and this resulted in shear failure occurring within the bedding planes (parting plane failure), however the continuum nature of a thick roof beam meant that the shear fractures that would form resulting in the span collapse could not be modelled effectively. As such it was necessary to devise an alternative method for modelling the progressive roof collapse in thickly bedded strata dominated by shear joint / parting plane failure, using a methodology summarised in the section below relating to void migration.

Observations of variations in the frictional strength properties of bedding surfaces as represented by interface elements which allow the model to behave in a discontinuous /

discrete manner indicate that the interface / bedding plane friction angle is a dominant parameter in controlling the geometry of the resultant region of failure within the rock mass over an excavation or void, whereby in horizontally layered strata the angle at which the failure arch forms over the excavation is related to 90° – the effective angle of friction of the rock mass. In this case the effective angle of friction is a combination of the friction angle parameter applied to the strata and the (lower) angle of friction of the interfaces which represented the bedding surfaces. This can be seen in Figure 9.2 where the bedding surface friction angle varies and the individual beds are composed of material with a friction angle fixed at 47° whereby the angle of collapse from the vertical is closely related to the joint friction angle

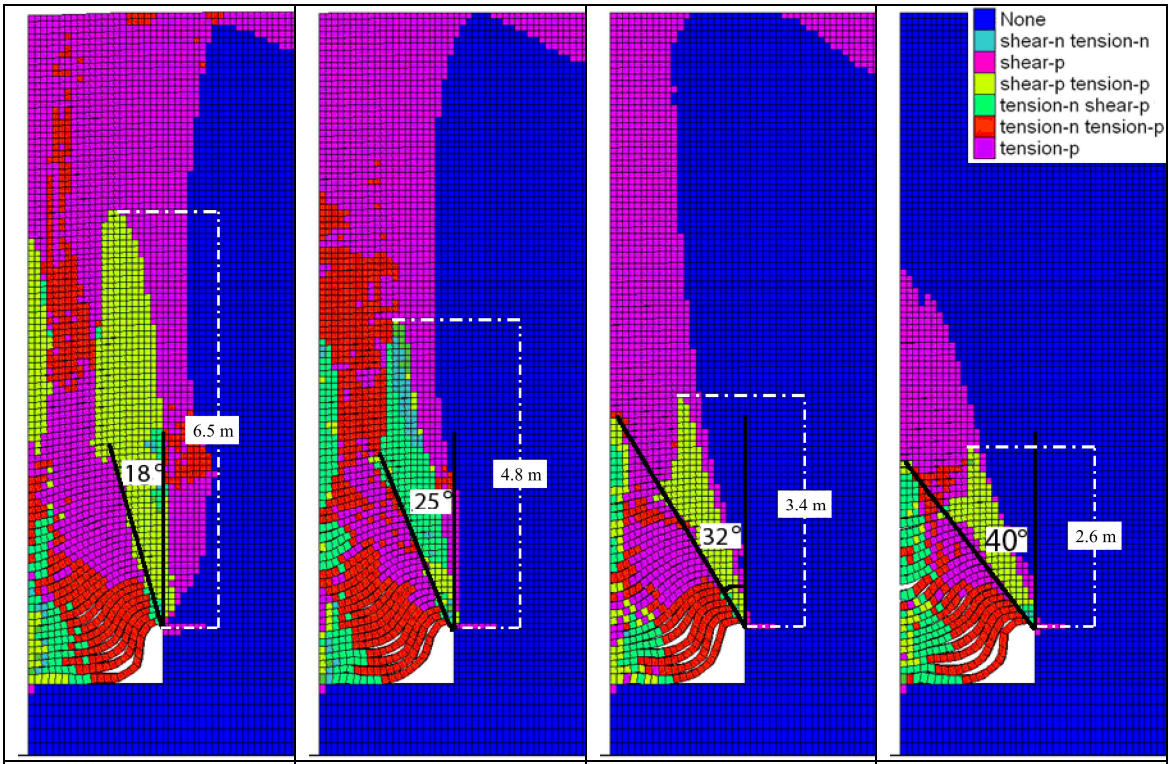

Figure 9.2: Effect on angle of collapse of roof strata of the friction angle of the bedding surfaces.

Observations of the results of the modelling also indicated that the collapse geometry takes the form of a frustum in three-dimensions where the height of collapse was controlled both by the angle of friction of the rock mass and also the tensile and cohesion strength properties. This causes the roof failure progression to halt when the span width became low enough that the tensile stress within it drops below the tensile strength. This led to a phenomenon whereby for a given set of strength and stiffness values for the strata, the height to which roof instability extended into the rock mass

decreased with increases in the friction angle, however the width of the stable span is always the same.

Modelling of the effect of increases in the groundwater table on stability due to effective stress changes was also undertaken. This demonstrated that pore water pressures were a significant factor in the initiation of yielding of the roof strata under all conditions and were shown to cause yielding to occur in initially stable roof strata as the ground water table increased.

A tool that can be used to estimate the height of void migration was also devised based on assumptions about the potential caving angle and bulking factor of the overburden. This empirical tool was validated against the numerical modelling results. The height of collapse of roof strata estimated by the tool was shown to be in close agreement to that derived by the numerical modelling work.

A numerical modelling tool was also developed that relies on an assessment of the failure or yield state of an individual element along with its degree of volumetric strain and or shear strain in order to asses if it should be removed from the model. This was undertaken to allow the progressive failure of thickly bedded roof strata to be modelled which fail due to the propagation of shear fractures within the rock mass and cannot be modelled effectively within a continuum.

Using the modelling capability and knowledge derived during the phased numerical modelling study, a large parametric study was undertaken to investigate the significant factors in the subsidence event that occurred in Dolphingstone in Scotland which lead to the formation of surface crown holes. A total of 120 initial scenarios were investigated and the analysis of the results indicated that there were 13 scenarios that may have caused the collapse of the roof strata of the workings which could cause void migration. Broadly it was observed that the minimum width necessary for a roof collapse to occur was 2 m, however the majority of scenarios resulting in roof instability occurred at a width of 3 m suggesting that this is a more realistic minimum estimate for the room size of the underlying workings. The majority of collapses that may feasibly have caused the void migration occurred at a bedding spacing of 0.2 to 0.5 m.

In a number of these cases where the excavation state was initially stable the increases in pore water pressures related to increases in the height of the water table were shown to either cause failure of the rock mass overlying the excavation or increase it's extent so that it ultimately spanned the full thickness of the sandstone bed. From this it is suggested that the increase in the water table after mine abandonment was a significant cause of the collapse.

A tool developed by the US FHA in order to allow the relative hazard posed by differing mining sites to be derived and hence ranked to allow the prioritisation of further investigation, monitoring or remediation is discussed in relation to the numerical modelling work undertaken to investigate the significant parameters affecting shallow mine working roof stability. The tool is shown to include variables which account for the parameters determined to be significant in the numerical modelling work including the thickness of over burden (in terms of potential height of collapse before void migration may be halted by bulking or arching), the excavated thickness of the mined seam, again related to the height of potential void migration which can be estimated by the bulking factor method.

9.2 Suggestions for Further Work

In this section, the potential for further work is discussed with respect to the work undertaken in this thesis.

The modelling undertaken in this work was two-dimensional due the limitations imposed on the maximum size of model that can be created in FLAC3D version 3.00. This in turn is due to the limitations of 32 bit architecture in terms of memory usage (FLAC3D 3.00 can only make use of 2GB of RAM and 3D models with a reasonable mesh discretisation significantly surpass this limit even for the relatively simple Mohr-Coulomb model. This is even more pronounced when more complex constitutive models or interface elements are used in the modelling. However the newer versions of FLAC3D (from version 3.1 onwards – Itasca, 2011) were programmed to make use of 64 bit architecture and so are not constrained by this limitation and are capable of almost unlimited model size (limited only by the available RAM within the computer). As such use of the updated version of FLAC if available would be recommended for undertaking the modelling at high mesh density of the type undertaken in this thesis in three-dimensions.

It is recognised that the modelling of void migration in FLAC does not capture the true behaviour of this form of subsidence as in the model; the collapse debris is not re-emplaced into the void. This debris would offer support to the excavation walls and would act ultimately to halt void migration which would affect the height to which void migration could occur where as currently this is controlled purely by the formation of a stable arch within the rock mass. As such a numerical modelling tool that fully captures the void migration process would need to either model the re-emplacement of collapse debris and allow bulking to occur or devise a method for calculating the forces applied to the void wall and the varying area across which they act as collapse progresses in order to simulate this process.

A preliminary attempt to model void migration and the bulking of debris was undertaken by the author, by altering the original FISH collapse parameter to apply an elastic constitutive model to the first available null zone at the base of the void, when an element that had failed was nulled from the mesh above. A function was also written that counted the number of elements removed due to collapse and at every nth number emplaced a random block at the base of the void. In this way, bulking of the collapse debris was approximated. However this process was very computationally intensive and the process tended to create debris piles with unrealistic final geometries (*e.g.* sides significantly steeper than the friction angle would allow as the emplacement of bulked debris was random), however this appears to be an avenue worthy of further study as it would potentially fully capture the migration of voids in rock masses and potentially also in soils where the support provided by the bulked debris is very significant in allowing the modelling of a realistic final geometry.

The work undertaken here strongly suggests that pore water pressures are significant in the initiation of excavation instability. However this work is not able to indicate a time frame or rate of collapse. Only that a collapse event may be initiated by a given set of excavation geometry, rock mass strength and stiffness conditions and a given stress state. One potential avenue that may be pursued to introduce the element of time into the modelling of collapse would be the use of a coupled fluid mechanical model where flow occurs per unit time as opposed to unit timestep in the purely mechanical modelling.

It is also recognised that this work does not investigate the effects of dewatering in the triggering of instability. It is theorised that this could be initially approximated quite simply by maintaining pore water pressure within the rock mass while removing the applied stress simulating the loss of water pressure acting normally to the excavation roof and hence a loss of support. It is assumed that the pore water pressures within the rock mass would take much longer to dissipate than the rate of water table reduction in the workings due to the lower permeability of the rock mass and that this loss of support coupled with elevated pore water pressures may trigger instability. The approach suggested here may be undertaken relatively quickly as a proof of concept. However the detailed modelling would have to be undertaken with a coupled fluid mechanical model in FLAC or another piece of geomechanics software and derivation of realistic hydrological parameters may prove difficult requiring a large scale parametric study to be undertaken.

The modelling of the Dolphingstone subsidence event is assumed to be triggered here by the rise in water table and then presumed to have been a progressive collapse of the roof strata, however as per the earlier statement regarding pore water pressures there is no way to asses the timeframe except perhaps by indicating the number of timesteps required to achieve a final state.

There is some anecdotal evidence that crown hole collapses are related to periods of heavy rainfall. As it has been demonstrated here that small changes in the water table / pore water pressure are capable of initiating instability and as the site investigation (Donaldson Associates Ltd, 2002) and hydrological reports (Edmund Nuttall Ltd, 2002) for Dolphingstone states that rainfall is the primary recharge method for the groundwater table at the site and leads to a variation in water table of approximately 1.8 m, there is the potential for significantly wetter periods to increase this level beyond that which would normally occur and which may potentially induce instability. It may also be possible to model the meteorological inputs into a site such as Dolphingstone and their influence on the water table within the site using software such as SHETRAN (Ewen *et al*., 2000) to investigate the potential maximum water table that may occur on site. This modelling could be calibrated against the site pore water profiles in the hydrological report and then used to study the period leading up to the collapse. This data could then be used to re-asses the geotechnical modelling undertaken in light of

any significant fluctuations in the ground water table, especially if coupled fluid-mechanical modelling were to be undertaken.

In order to run the large scale parametric studies of the sort required in this work to investigate the site conditions at Dolphingstone, the use of three-dimensional modelling would also have been far to time consuming, however now that the most significant scenarios related to the potential for collapse to occur have been identified, further investigation of these models in three-dimensions may be possible at a reduced level of mesh discretisation and the resultant loss of accuracy and resolution in order to investigate the effects if any of the third-dimension on stability.

Chapter

10

Reference List

10 Reference List

Alehossein, H. and Korinets, A. (2000). Mesh-Independent Finite Difference Analysis Using Gradient-Dependent Plasticity. *Communications in Numerical Methods in Engineering*. Vol. 16, No. 5. pp. 363-375.

Alejano, L. R., Taboada, J., García-Bastante, F. and Rodriguez, P. (2008). Multi-Approach Back-Analysis of a Roof Bed Collapse in a Mining Room Excavated in Stratified Rock. *International Journal of Rock Mechanics and Mining Sciences*. Vol. 45, No. 6. pp. 899-913.

Attewell, P. B. and Taylor, R. K. (Eds.) (1984). *Ground Movements and Their Effects on Structures*. Blackie & Son Ltd, London.

Badr, S., Ozbay, U., Kieffer, S. and Salamon, M. (2003). Three-Dimensional Strain Softening Modeling of Deep Longwall Coal Mine Layouts. In: *FLAC and Numerical Modeling in Geomechanics* (Eds., Andrieux, P., Brummer, R., Detournay, C. and Hart, R.), Lisse: Swets & Zeitlinger. pp. 233-239.

Barton, N. (2002). Some New Q-Value Correlations to Assist in Site Characterisation and Tunnel Design. *International Journal of Rock Mechanics and Mining Sciences*. Vol. 39, No. 2. pp. 185-216.

Barton, N. (2007). Rock Mass Characterization for Excavations in Mining and Civil Engineering. In: *Proceedings of the International Workshop on Rock Mass Classification in Underground Mining* (Eds., Mark, C., Pakalnis, R. and Tuchman, R. J.), Pittsburgh, PA: U.S. Department of Health and Human Services, Public Health Service, Centers For Disease Control and Prevention, National Institute For Occupational Safety and Health, 2007. pp. 3-14.

Barton, N., Lien, R. and Lunde, J. (1974). Engineering Classification of Rock Masses for the Design of Tunnel Support. *Rock Mechanics and Rock Engineering*. Vol. 6, No. 4. pp. 189–236.

Bell, F. G. (1975). *Site Investigations in Areas of Mining Subsidence*. Butterworth and Co. London.

Bell, F. G. (1992). *Engineering Properties of Soils and Rocks*. Butterworth-Heinemann, London.

Bell, F. G, Cripps, J. C., Culshaw, M. G. and Lovell, M. A. (1988). A Review of Ground Movements Due to Civil and Mining Engineering Operations. In: *Engineering Geology of Underground Movements* (Eds., Bell, F. G, Cripps, J. C., Culshaw, M. G. and Lovell, M. A.), Geological Society Engineering Geology Special Publication No. 5, pp. 3-32.

Bell, F. G. and De Bruyn, I. A. (1999). Subsidence Problems due to Abandoned Pillar Workings in Coal Seams. *Bulletin of Engineering Geology and the Environment*. Vol. 57, No. 3. pp. 225-237.

Bieniawski, Z. T. (1984). *Rock Mechanics Design in Mining and Tunnelling*. Balkema, Rotterdam.

Bieniawski, Z. T. (1989). *Engineering Rock Mass Classifications - A Complete Manual for Engineers and Geologists in Mining, Civil, and Petroleum Engineering*. John Wiley and Sons, Chichester.

Brady, B. H. G. and Brown, E. T. (1993). *Rock Mechanics for Underground Mining*. Second Edition. Chapman and Hall, London.

Brinkgreve, R. B. J., Swolfs, W. M. and Engin. E. (2010). *Plaxis 2D 2010 Scientific Manual*. Plaxis BV, Delft.

British Standards Institution (1999). *BS 5930:1999 Code of Practice for Site Investigations*. Milton Keynes, BSI.

Brough, M., Stirling, A., Ghataora, G. and Madelin, K. (2003). Evaluation of Railway Trackbed and Formation: A Case Study. *NDT & E International*. Vol. 36, No. 3. pp. 145-156.

Cai, M., Kaiser, P. K., Tasaka, Y. and Minami, M. (2007). Determination of Residual Strength Parameters of Jointed Rock Masses Using the GSI System. *International Journal of Rock Mechanics and Mining Sciences*. Vol. 44, No. 2. pp. 247-265.

Carter, J. P., Desai, C. S., Potts, D. M., Schweiger, H. F. and Sloan, S. W. (2000). Computing and Computer Modelling in Geotechnical Engineering. In: *Proceedings of GeoEng2000, Melbourne, Australia*. Vol. 1 - Invited Papers, Technomic Publishing, pp. 1157-1252

Crabb, G. I. (1997). *Ground Classification Systems in Tunnel Construction*. Transport Research Laboratory, TRL Report 280.

Craig, R. F. (2004). *Craig's Soil Mechanics*. Seventh Edition. Taylor and Francis, London.

Das, S. K. (2000). Observations and Classification of Roof Strata Behaviour Over Longwall Coal Mining Panels in India. *International Journal of Rock Mechanics and Mining Sciences*. Vol. 37, No. 4. pp. 585-597.

Deb, D. and Choi, S. O. (2006). Analysis of Sinkhole Occurrences Over Abandoned Mines Using Fuzzy Reasoning: A Case Study. *Geotechnical and Geological Engineering*. Vol. 24, No. 5. pp. 1243-1258.

Deere, D. U. (1964). Technical Description of Rock Cores for Engineering Purposes. *Journal of the International Society of Rock Mechanics - Rock Mechanics and Engineering Geology*. Vol. 1. pp. 16-22.

Deere, D. U and Deere, D. W. (1988). The Rock Quality Designation (RQD) Index in Practice. In: *Rock Classification Systems for Engineering Purpose, ASTM STP 984* (Ed., Kirkaldie, L.), Philadelphia, PA: American Society for Testing and Materials, 1988. pp. 91-101

Diederichs, M. S. (1999). *Instability of Hard Rock Masses: The Role of Tensile Damage and Relaxation*. Phd Thesis. Dept. of Civil Engineering, University of Waterloo.

Diederichs, M. S. and Kaiser, P. K. (1999). Stability of Large Excavations in Laminated Hard Rock Masses: The Voussoir Analogue Revisited. *International Journal of Rock Mechanics and Mining Sciences*. Vol. 36, No. 1. pp. 97-117.

Donaldson Associates Ltd. (2002). *ECML Dolphingstone Remediation Works Geotechnical Interpretive Report*. Edmund Nutall Ltd.

Duff, D. (1993). *Holmes' Principles of Physical Geology*. Fourth Edition. Taylor & Francis, London.

Dyne, L. A. (1998). *The Prediction and Occurrence of Chimney Subsidence in Southwestern Pennsylvania*. MSc Thesis. Dept. of Mining and Minerals Engineering, Virginia Polytechnic Institute and State University.

Eberhardt, E. (2003). *Rock Slope Stability Analysis - Utilisation of Advanced Numerical Techniques,* University of British Columbia, Vancouver, Canada.

Eberhardt, E., Stead, D., Coggan, J. S. and Willenberg, H. (2003). Hybrid Finite-Discrete Element Modelling of Progressive Failure in Massive Rock Slopes. In: *10th Congress of the International Society for Rock Mechanics ISRM 2003 – Technology Roadmap for Rock Mechanics, Johannesburg,* (Eds., Handley, M. and Stacey, D.) pp. 275-279.

Edelbro, C. (2004). *Evaluation of Rock Mass Strength Criteria*. Licentiate Thesis. Luleå University of Technology.

Edmund Nuttall Ltd. (2002). *Hydrological Summary Report – Dolphingstone Remediation Works*. Report No. SC/MG/512/8.

Ellenberger, J.E., Chase, F.E., Mark, C., Heasley, K.A and Marshall, J.M. (2003). Using Site Case Histories of Multiple Seam Coal Mining to Advance Mine Design. *Proceedings, 22nd International Conference on Ground Control in Mining*. West Virginia University, Morgantown, WV, Aug. 3-5, 2003. pp. 59-64.

Esterhuizen, G. S. and Karacan C. O. (2005). Development of Numerical Models to Investigate Permeability Changes and Gas Emission around a Longwall Mining Panel. In: *Proceedings of the 40th* U.S. *Symposium on Rock Mechanics (USRMS).* Anchorage, University of Alaska-Anchorage, 25-29 June 2005.

Ewen, J., Parkin, G. and O'Connell, P.E. (2000). SHETRAN: Distributed River Basin Flow and Transport Modelling System. *Journal of Hydrologic Engineering*. Vol. 5, No. 3. pp. 250-258.

Farmer, I. (1992). Room and pillar mining. In: Hartman, H. L. (Ed.), *SME Mining Engineering Handbook*. Vol. 2, pp 1681-1701.

Fernando, D. A. (1988). Review of Subsidence and Stabilization Techniques. In: *Mine Induced Subsidence: Effects on Engineered Structures: Geotechnical Special Publication No. 19, Proceedings of the symposium sponsored by the Geotechnical Engineering Division of the American Society of Civil Engineers, Nashville, Tennessee,* (Ed., Siriwardane, H. J.) pp. 189-206.

Geological Society Engineering Group Working Party. (1988). Engineering Geophysics: Report by the Geological Society Engineering Group Working Party. *Quarterly Journal of Engineering Geology and Hydrogeology*. Vol. 21, No. N/A. pp. 207-271.

González-Nicieza, C., Menéndez-Díaz, A., Álvarez-Vigil, A. E. and Álvarez-Fernández, M. I. (2008). Analysis of Support by Hydraulic Props in a Longwall Working. *International Journal of Coal Geology*. Vol. 74, No. 1. pp. 67-92.

Goodman, R. E. (1989). *Introduction to Rock Mechanics*. Second Edition. John Wiley and Sons, New York.

Gray, R. E. (1988). Coal Mine Subsidence and Structure. In: *Mine Induced Subsidence: Effects on Engineered Structures: Geotechnical Special Publication No. 19, Proceedings of the symposium sponsored by the Geotechnical Engineering Division of the American Society of Civil Engineers, Nashville, Tennessee,* (Ed., Siriwardane, H. J.) pp. 69-86.

Harrison, J. P. and Hudson, J. A. (Eds.) (2000) *Engineering Rock Mechanics*. *Part 2: Illustrative Workable Examples*. Oxford: Elsevier.

Healy, P. R. and Head, J. M. (1984). *Construction over abandoned mine workings*. Construction Information and Research Association. CIRIA Special Publication No. 32.

Helm, P. (2010). *ECML between Wallford and Prestonpans* [PNG map], Scale 1:10,000 (OS 1:25,000 Raster [geospatial data], updated May 2010; Land-Form PROFILE [geospatial data], updated August 2003), Ordnance Survey, GB. Using: EDINA Digimap Ordnance Survey Service, <http://edina.ac.uk/digimap>, Created: December 2010.

Helm, P (2011a). *Drift Geology of Dolphingstone* [PDF map], Scale 1:10,000, BGS 1:50,000 [geospatial data], updated Jan 2007, Version 1.10, British Geological Survey (BGS), UK. Using: EDINA Geology Digimap Service, http://edina.ac.uk/digimap. Created: July 2011.

Helm, P (2011b). *Solid Geology of Dolphingstone* [PDF map], Scale 1:625,000, BGS 1:50,000 [geospatial data], updated Jan 2007, Version 1.10, British Geological Survey (BGS), UK. Using: EDINA Geology Digimap Service, http://edina.ac.uk/digimap. Created: July 2011.

Hibbeler, R. C. (1999). *Structural Analysis*. Prentice-Hall, London.

Hoek, E. (1999). Putting Numbers to Geology – An Engineer's Viewpoint. *Quarterly Journal of Engineering Geology*. Vol. 32, No. 1. pp. 1-19.

Hoek, E. (2007). *Practical Rock Engineering*, Rocscience Inc.

Hoek, E. and Brown, E. T. (1980). Empirical Strength Criterion for Rock Masses. *Journal of the Geotechnical Engineering Division of the American Society of Civil Engineers*. Vol. 106, No. GT9. pp. 1013-1035.

Hoek, E. and Brown E. T. (1997). Practical Estimates of Rock Mass Strength. *International Journal of Rock Mechanics and Mining Sciences*. Vol. 34, No. 8. pp. 1165-1186.

Hoek, E., Carranza-Torres, C. and Corkum, B. (2002). Hoek-Brown Failure Criterion - 2002 Edition. *Proceedings of the NARMS-TAC Conference*. Toronto, 2002. Vol. 1. pp. 267-273.

Hoek, E., Kaiser, P. K. and Bawden, W. F. (1995). *Support of Underground Excavations in Hard Rock*, Balkema, Rotterdam.

Hoek, E., Marinos, P and Benissi, M. (1998). Applicability of the Geological Strength Index (GSI) Classification for Weak and Sheared Rock Masses - The Case of the Athens Schist Formation. *Bulletin of Engineering Geology and the Environment*. Vol. 57, No. 2. pp.151-160.

Hoek, E., Marinos, P. G. and Marinos, V. P. (2005). Characterisation and Engineering Properties of Tectonically Undisturbed but Lithologically Varied Sedimentary Rock Masses. *International Journal of Rock Mechanics & Mining Sciences*. Vol. 42, No. 2. pp. 277-285.

Hugenschmidt, J. (2000). Railway Track Inspection Using GPR. *Journal of Applied Geophysics*. Vol. 43, No. 2-4. pp. 147-155.

Hung, C. J., Monsees, J., Munfah, N. and Wisniewski, J. (2009). *Technical Manual for Design and Construction of Road Tunnels - Civil Elements*. US Dept. of Transportation, Federal Highway Administration, Report No: FHWA-NHI-09-010.

Hutchinson, D.J. and Diederichs, M.S. (1996). *Cablebolting in Underground Mines*. Bitech Publishers Ltd, Vancouver.

Itasca Consulting Group Inc. (2005). *FLAC3D - Fast Lagrangian Analysis of Continua in 3 Dimensions Version 3.0, User's Guide*. Itasca, Minneapolis.

Itasca Consulting Group Inc (2005a) *UDEC: Universal Distinct Element Code User's Guide, Version 4,* Itasca Consulting Group, Inc., Minneapolis, MN.

Itasca Consulting Group Inc. (2005b). *3DEC Three-Dimensional Distinct Element Code User's Guide, Version 3.00,* Itasca Consulting Group, Inc., Minneapolis, MN.

Itasca Consulting Group. (2011). *New in FLAC3D 3.1* [online] Available at: http://www.itascacg.com/flac3d/newin31.html [Accessed 15 January 2011].

Jing, L. (2003). A Review of Techniques Advances and Outstanding Issues in Numerical Modelling for Rock Mechanics and Rock Engineering. *International Journal of Rock Mechanics and Mining Sciences*. Vol. 40, No. 3. pp. 283-353.

Jing, L. and Hudson, J. A. (2002). Numerical Methods in Rock Mechanics. *International Journal of Rock Mechanics and Mining Sciences*. Vol. 39, No. 4. pp. 409-427.

Jones, C. J. F. P., Lamont-Black, J. and Davies, O. (2005). *Review of Current Practice Associated with the Management and Treatment of Subsurface Voids as they Influence Transport Networks*. University of Newcastle upon Tyne, 2005. (Phase 1 Report).

Lawrence, W. (2009). A Method for the Design of Longwall Gateroad Roof Support, *International Journal of Rock Mechanics and Mining Sciences*. Vol. 46, No. 4. pp. 789-795.

Li, Z. and Reddish, D. J. (2004). The Effect of Groundwater Recharge on Broken Rocks. *International Journal of Rock Mechanics and Mining Sciences*. Vol. 41, No. 3. pp. 280-285.

Marinos, P. and Hoek, E. (2001). Estimating the Geotechnical Properties of Heterogeneous Rock Masses Such as Flysch. *Bulletin of Engineering Geology and the Environment*. Vol. 60, No. 2. pp. 85-92.

Marinos, P. and Hoek, E. (2007). A Brief History of the Development of the Hoek-Brown Failure Criterion. *Soils and Rocks*, No. 2.

Marinos, V., Marinos, P and Hoek, E. (2005). The Geological Strength Index: Applications and Limitations. *Bulletin of Engineering Geology and the Environment*. Vol. 64, No. 1, pp. 55-56.

Mark, C. (1999). Development and Application of the Coal Mine Roof Rating (CMRR) to Extended Cuts. *Journal Mining Engineering*. Vol. 51, No. 4. pp. 52-56.

Mark, C. and Molinda, G. M. (2005). The Coal Mine Roof Rating (CMRR) - A Decade of Experience. *International Journal of Coal Geology*. Vol. 64, No. 1-2. pp. 85-103.

Mark, C. and Molinda, G. M. (2007). Development and Application of the Coal Mine Roof Rating (CMRR). In: *Proceedings of the International Workshop on Rock Mass Classification in Underground Mining*. (Eds., Mark, C., Pakalnis, R. and Tuchman, R. J.), Pittsburgh, PA: U.S. Department of Health and Human Services, Public Health Service, Centers For Disease Control and Prevention, National Institute For Occupational Safety and Health, 2007; pp. 95-109.

Mark, C, Molinda, G. M. and Barton, T. M. (2002). New Developments with the Coal Mine Roof Rating. In: *Proceedings of the 21st International Conference on Ground Control in Mining* (Eds., Peng, S. S., Mark C., Khair. A. W. and Heasley, K. A.), Morgantown, WV: West Virginia University, 2002 Aug; pp. 294-301.

McNally, G. H. (2000). Geology and Mining Practice in Relation to Shallow Subsidence in the Northern Coalfield, New South Wales. *Australian Journal of Earth Sciences*. Vol. 47, No. 1. pp. 21-34.

Molinda, G. M. (2003). *Geologic Hazards and Roof Stability in Coal Mines*. Pittsburgh, PA: U.S. Department of Health and Human Services, Public Health Service, Centers For Disease Control and Prevention, National Institute For Occupational Safety and Health, DHHS (NIOSH) Publication No. 2003-152, Information Circular 9466; pp. 1-33.

Molinda, G. M., Mark, C. and Debasis, D. (2001). Using the Coal Mine Roof Rating (CMRR) to Assess Roof Stability in U.S. Coal Mines. *Journal of Mines, Metal and Fuels (India)*. Vol. 48, No. 12. pp. 314-321.

Okubo, S. and Fukui, K. (1996). Complete Stress-Strain Curves for Various Rock Types in Uniaxial Tension. *International Journal of Rock Mechanics and Mining Sciences Abstracts*. Vol. 33, No. 6. pp. 549-556.

Onions, K. R., Whitworth, K. and Jackson, P. (1996). Application of Geophysical Methods to Site Investigations at Contaminated Old Collieries. *Quarterly Journal of Engineering Geology and Hydrogeology*. Vol. 29, No. N/A. pp. 219-231.

Ordnance Survey County Series. (1894a). 1st Edition [PNG map], Scale 1:2,500, Edinburghshire County, Published 1894, Landmark Information Group, UK. Using: EDINA Historic Digimap Service, <http://edina.ac.uk/digimap>, Downloaded: December 2010.

Ordnance Survey County Series. (1894b). 1st Edition, Revision 1 [PNG map], Scale 1:2,500, Haddingtonshire County, Published 1894, Landmark Information Group, UK. Using: EDINA Historic Digimap Service, <http://edina.ac.uk/digimap>, Downloaded: December 2010.

Parry, R. H. G. (2004). Mohr Circles, Stress Paths and Geotechnics. Second Edition. London, Spon Press.

Price-Jones, A. (2004) *Rock Mechanics and Rock Engineering*. In: Civil Engineer's Reference Book (Ed., Blake, L. S.) Elsevier Butterworth-Heinemann, London.

Roberts, D. P., Roberts, M. K. C., Jager, A. J. and Coetzer, S. (2005). The Determination of the Residual Strength of Hard Rock Crush Pillars with a Width-to-Height Ratio of 2:1. *The Journal of the South African Institute of Mining and Metallurgy*. Vol. 105. pp. 401-408.

Rocscience. (2010). *Rocscience Products – Roclab* [online] Available at: http://download.rocscience.com/products/RocLab.asp [Accessed 18 November 2010].

Ruegsegger, L. R. (2009). *Manual For Abandoned Underground Mine Inventory and Risk Assessment*. United States Department of Transportation, Federal Highway Administration, Infrastructure Division and the Ohio Department of Transportation, 1999. (FHWA IF-99-007).

Singh, G. S. P and Singh U. K. (2009). A Numerical Modelling Approach for Assessment of Progressive Caving of Strata and Performance of Hydraulic Powered Support in Longwall Workings. *Computers and Geotechnics*. Vol. 36, No. 7. pp. 1142-1156.

Singh, K. B. and Dhar, B. B. (1997). Sinkhole Subsidence Due to Mining. *Geotechnical and Geological Engineering*. Vol. 15, No. 4. pp. 327-341.

Stead, D., Eberhardt, E., Coggan, J. and Benko, B. (2001). Advanced Numerical Techniques in Rock Slope Stability Analysis - Applications and Limitations. In: *Proceedings of the International Conference on Landslides – Causes, Impacts and Countermeasures, Davos, Switzerland, 17-21 June 2001*, United Engineering Foundation, pp. 615-624.

Swart, A. H. and Handley M. F. (2005). The Design of Stable Stope Spans for Shallow Mining Operations. *The Journal of the South African Institute of Mining and Metallurgy*. Vol. 105. pp. 275-286.

Thigpen, L. (1984). On the Mechanics of Strata Above Underground Openings. *American Society of Civil Engineers Journal of Geotechnical Engineering*. Vol. 122, No. 12. pp. 14-44.

Tomlinson, M. J. (2001). *Foundation Design and Construction*. Seventh Edition. Pearson Education Ltd, Harlow, Essex.

Twiss, R. J. and Moores, E. M. (1992). *Structural Geology*. W.H. Freeman, New York.

Vasarhelyi, B. (2003). Some Observations Regarding the Strength and Deformability of Sandstones in Dry and Saturated Conditions. *Bulletin of Engineering Geology and the Environment*. Vol. 62, No. 3. pp. 245-249.

Waltham, A. C. (1989). *Ground Subsidence*. Blackie & Son Ltd, London.

Whittles, D. N., Reddish, D. J. and Lowndes, I. S. (2007). The Development of a Coal Measure Classification (CMC) and its Use for Prediction of Geomechanical Parameters. *International Journal of Rock Mechanics and Mining Sciences*. Vol. 44, No. 4. pp. 496-513.

Wiles, T. D. (2006). Reliability of Numerical Modelling Predictions. I*nternational Journal of Rock Mechanics and Mining Sciences*. Vol. 43, No. 3. pp. 454-472.

Xie, H., Chen, Z and Wang, J. (1999). Three-Dimensional Numerical Analysis of Deformation and Failure During Top Coal Caving. *International Journal of Rock Mechanics and Mining Sciences*. Vol. 36, No. 5. pp. 651-658.

Yasitli, N. E. and Unver, B. (2005). 3D Numerical Modelling of Longwall Mining with Top-Coal Caving. *International Journal of Rock Mechanics and Mining Sciences*. Vol. 42, No. 2. pp. 219-235.

Zhang, L. (2005). *Engineering Properties of Rocks*. Elsevier Ltd, London.

Zipf, K. (2005). Failure Mechanics of Multiple Seam Mining Interactions. *In: Proceedings of the 24th International Conference on Ground Control in Mining* (Eds., Peng, S. S., Mark, C., Finfinger, G. L., Tadolini, S. C., Heasley, K. A., Khair, A. W.) West Virginia University, 2 - 4 August 2005, Morgantown. pp. 93-106.

Zipf, K. (2006). Numerical Modelling Procedures for Practical Coal Mine Design. *In: Proceedings of the 41st* U.S. *Symposium On Rock Mechanics - Golden Rocks 2006* (Ed.,Yale, D. P.) 17 - 21 June 2006, Curran Associates, Golden, Colorado.